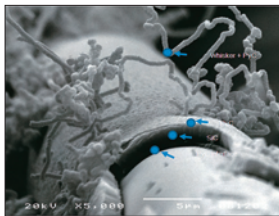
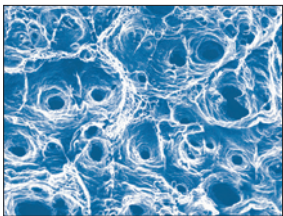


Structural Materials for Innovative Nuclear Systems (SMINS-2)

Workshop Proceedings
Daejon, Republic of Korea
31 August-3 September 2010



**Structural Materials for Innovative Nuclear Systems
(SMINS-2)**

Workshop Proceedings, Daejon, Republic of Korea
31 August-3 September 2010

© OECD 2012
NEA No. 6896

NUCLEAR ENERGY AGENCY
ORGANISATION FOR ECONOMIC CO-OPERATION AND DEVELOPMENT

ORGANISATION FOR ECONOMIC CO-OPERATION AND DEVELOPMENT

The OECD is a unique forum where the governments of 34 democracies work together to address the economic, social and environmental challenges of globalisation. The OECD is also at the forefront of efforts to understand and to help governments respond to new developments and concerns, such as corporate governance, the information economy and the challenges of an ageing population. The Organisation provides a setting where governments can compare policy experiences, seek answers to common problems, identify good practice and work to co-ordinate domestic and international policies.

The OECD member countries are: Australia, Austria, Belgium, Canada, Chile, the Czech Republic, Denmark, Estonia, Finland, France, Germany, Greece, Hungary, Iceland, Ireland, Israel, Italy, Japan, Luxembourg, Mexico, the Netherlands, New Zealand, Norway, Poland, Portugal, the Republic of Korea, the Slovak Republic, Slovenia, Spain, Sweden, Switzerland, Turkey, the United Kingdom and the United States. The European Commission takes part in the work of the OECD.

OECD Publishing disseminates widely the results of the Organisation's statistics gathering and research on economic, social and environmental issues, as well as the conventions, guidelines and standards agreed by its members.

*This work is published on the responsibility of the OECD Secretary-General.
The opinions expressed and arguments employed herein do not necessarily reflect the views of all member countries.*

NUCLEAR ENERGY AGENCY

The OECD Nuclear Energy Agency (NEA) was established on 1 February 1958. Current NEA membership consists of 30 OECD member countries: Australia, Austria, Belgium, Canada, the Czech Republic, Denmark, Finland, France, Germany, Greece, Hungary, Iceland, Ireland, Italy, Japan, Luxembourg, Mexico, the Netherlands, Norway, Poland, Portugal, the Republic of Korea, the Slovak Republic, Slovenia, Spain, Sweden, Switzerland, Turkey, the United Kingdom and the United States. The European Commission also takes part in the work of the Agency.

The mission of the NEA is:

- to assist its member countries in maintaining and further developing, through international co-operation, the scientific, technological and legal bases required for a safe, environmentally friendly and economical use of nuclear energy for peaceful purposes, as well as
- to provide authoritative assessments and to forge common understandings on key issues, as input to government decisions on nuclear energy policy and to broader OECD policy analyses in areas such as energy and sustainable development.

Specific areas of competence of the NEA include the safety and regulation of nuclear activities, radioactive waste management, radiological protection, nuclear science, economic and technical analyses of the nuclear fuel cycle, nuclear law and liability, and public information.

The NEA Data Bank provides nuclear data and computer program services for participating countries. In these and related tasks, the NEA works in close collaboration with the International Atomic Energy Agency in Vienna, with which it has a Co-operation Agreement, as well as with other international organisations in the nuclear field.

This document and any map included herein are without prejudice to the status of or sovereignty over any territory, to the delimitation of international frontiers and boundaries and to the name of any territory, city or area.

Corrigenda to OECD publications may be found online at: www.oecd.org/publishing/corrigenda.

© OECD 2012

You can copy, download or print OECD content for your own use, and you can include excerpts from OECD publications, databases and multimedia products in your own documents, presentations, blogs, websites and teaching materials, provided that suitable acknowledgment of the OECD as source and copyright owner is given. All requests for public or commercial use and translation rights should be submitted to rights@oecd.org. Requests for permission to photocopy portions of this material for public or commercial use shall be addressed directly to the Copyright Clearance Center (CCC) at info@copyright.com or the Centre français d'exploitation du droit de copie (CFC) contact@cfcopies.com.

Cover picture credits: China Institute of Atomic Energy; KAERI.

Foreword

Materials research is a field of growing relevance for innovative nuclear systems, such as Generation IV reactors, critical and subcritical transmutation systems and fusion devices. For these different systems, structural materials are selected or developed taking into account the specificities of their foreseen operational environment. However, material development projects require both cross-cutting research programmes and advanced experimental/simulation facilities in order to characterise and evaluate the performance of the selected materials.

Since 2007, the OECD Nuclear Energy Agency (NEA) has begun organising a series of workshops on Structural Materials for Innovative Nuclear Systems (SMINS). The objective of these workshops is to stimulate an exchange of information on current materials research programmes for different innovative nuclear systems with a view to identifying and developing potential synergies. The first workshop was organised in Karlsruhe, Germany in 2007.

The second workshop was organised on 31 August–3 September 2010 in Daejeon, Republic of Korea. It was hosted by the Korea Atomic Energy Research Institute (KAERI) and co-sponsored by the European Commission (EC) and the International Atomic Energy Agency (IAEA). A total of 78 papers were presented during the oral and poster sessions.

These proceedings include all the papers presented at the second workshop. The opinions expressed are those of the authors only, and do not necessarily reflect the views of the NEA, any national authority or any other international organisation.

Acknowledgements

The OECD Nuclear Energy Agency (NEA) is grateful to the Korea Atomic Energy Research Institute (KAERI) for hosting the second Workshop on Structural Materials for Innovative Nuclear Systems (SMINS). The Agency also extends its gratitude to the European Commission (EC) and the International Atomic Energy Agency (IAEA) for their co-operation.



Table of contents

Executive summary	11
Opening Session	17
Chair: J.H. Hong	
M-S. Yang KAERI welcome address	19
Y-J. Choi NEA welcome address	21
Plenary Session I	23
Chairs: T. Allen, J-Y. Park	
J-H. Chang, D.H. Hahn Summary of international design needs for advanced reactors	25
S. Zinkle Novel pathways for improving nuclear reactor structural materials performance	27
Session I: Metal – VHTR Environmental Effects and High-temperature Properties	29
Chairs: F. Balbaud-C��lerier, S. Kislitsin	
W.R. Corwin VHTR materials issues	31
C-H. Jang, D. Kim, D. Kim, I. Sah, M. Kim, W-S. Ryu, D.J. Yoon Environmental effects of nickel-based superalloys on mechanical properties for VHTR applications	33
K. Maile, E. Roos, A. Klenk, M. Hoffmann Optimisation of Ni-based Alloy 617	39
M.A. Sokolov Fracture toughness of two advanced structural alloys	53
R.K. Nanstad, M.A. Sokolov, R.N. Wright High-temperature fracture toughness of Inconel 617	55
Y-D. Kim, T-S. Jo, J-H. Lim, J-Y. Park Oxidation behaviour of Alloy 617 during ageing at various temperatures	57
Session II: Ceramics-composite	59
Chairs: C. Fazio, W.J. Kim	
J.Y. Park, W.J. Kim Development of SiCf/SiC composite for innovative structural materials	61
T. Shibata, J. Sumita, T. Takagi, T. Makita, K. Sawa, E. Kunimoto Irradiation-induced property change of C/C composite for application of control rod elements of very-high-temperature reactor (VHTR)	69

T. Donomae, K. Maeda Behaviour of irradiated boron carbide	79
S. Kislitsin, K. Kadyrzhanov, V. Uglov, D. Rusalski, G. Abadias, S. Dub Study of heavy ions irradiation on structure of triple titanium nitride basis coating.....	87
Y-K. Yang, T. Gerczak, D. Morgan, I. Szlufarska, S-T. Kim, T. Allen Diffusion of silver in zirconium carbide inside tristructural-isotropic nuclear fuel	89
Session III: Metal – Materials Compatibility – Molten Salt and Sodium	99
Chair: Y. Dai	
V. Ignatiev, A. Surenkov Alloys compatibility with selected molten salt environments for molten salt fast reactor breeders and burners.....	101
B. Long, Y. Xu, J. Zhang, H. Li, D. Zhang Investigation on the compatibility of weldments of main component materials with sodium in the Chinese experimental fast breeder reactor (CEFR).....	121
Plenary Session II	131
Chairs: Ph. Dubuisson, W.W. Kim	
K.O. Pasamehmetoglu, Ph. Dubuisson Innovative fuels state-of-the-art assessment	133
A. Kimura, R. Kasada, N. Iwata, J. Isselin, P. Dou, J.H. Lee, T. Okuda, M. Inoue, S. Ukai, S. Ohnuki, H. Sano, T. Fujisawa, F. Abe Super ODS steels R&D for fuel cladding of advanced nuclear systems	135
Session IV: Metal – Materials Compatibility – LFR Corrosion.....	149
Chairs: M. Toloczko, S. Ukai	
F. Balbaud-Célérier, L. Martinelli, F. Gabriel Corrosion of structural materials in nuclear systems involving liquid metals.....	151
G. Coen Effect of temperature and strain rate on the fracture toughness of T91 steel in lead-bismuth eutectic environment.....	153
A. Pramutadi, A. Mustari, M. Takahashi Effect of welding on corrosion properties of ferritic-martensitic steels in liquid lead-bismuth.....	155
I-S. Hwang, J. Lim, S-G. Lee Development of alumina forming ferritic steels for lead-bismuth eutectic- cooled applications	165
A. Weisenburger, A. Jianu, A. Heinzl, M. DelGiacco, G. Müller, V.D. Markov, A.D. Katanov Corrosion barrier development using electron beams for application in lead alloys with focus on recent creep to rupture tests.....	175
Y. Kurata, H. Sato, H. Yokota, T. Suzuki Development of aluminium powder alloy coating for innovative nuclear systems with lead-bismuth	177

Session V: Fundamental – Radiation Effects	189
Chairs: G.J. Ackland, J. Wallenius	
Ph. Dubuisson, Y. de Carlan, V. Garat, M. Blat ODS ferritic-martensitic alloys for sodium fast reactor fuel pin cladding.....	191
S.A. Maloy, M. Toloczko, J. Cole, T.S. Byun Materials issues in cladding and duct reactor materials.....	193
R. Kasada, J.H. Lee, A. Kimura, T. Okuda, M. Inoue, S. Ukai, S. Ohnuki, T. Fujisawa, F. Abe Radiation response of super ODS steels for fuel cladding of advanced nuclear systems	195
C. Shin, Y. Osetsky, R. Stoller, J. Kwon Formation of dislocation loops at the onset of plasticity during single crystal nanoindentation	201
Session VI: General	203
Chair: S.S. Hwang	
L. Edwards Developing advanced nuclear structural materials for use in high-radiation environments: An Australian perspective.....	205
T. Shikama, T. Muroga Development of materials for nuclear fusion reactors: Summary of the 14 th International Conference on Fusion Reactor Materials	207
J. Wallenius, N. Sandberg, P. Szakalos, A. Nordlund Structural materials research in the Swedish GENIUS Project.....	209
Plenary Session III	211
Chairs: S. Zinkle, C.H. Jang	
G.J. Ackland, T.P.C Klaver, D.J. Hepburn Binding of impurities in austenitic iron: An <i>ab initio</i> study.....	213
F. Tavassoli Fission-fusion cross-cutting issues related to structural materials	223
Session VII: Novel Materials – Nano-structured Materials	225
Chairs: A. Kimura, J.S. Jang	
S. Ukai, R. Miyata, S. Hayashi, K. Tanaka, T. Kaito, S. Ohtsuka Structural control and high-temperature strength of 9 Cr ODS steels.....	227
C. Fazio, J. Knebel Development of cladding materials: Past and present experience.....	237
M.D. Mathew, T. Jayakumar, B. Raj Advances in the development of core and out-of-core structural materials for sodium-cooled fast reactors	251
Session VIII: Fundamental Radiation Effects – Helium Effect	261
Chairs: R. Nanstad, S-H. Chi	
Y. Dai Challenges of structural materials for applications in spallation targets of ADS	263

C. Heintze, E. Altstadt, F. Bergner, M. Hernández Mayoral, M. Xie, U. Birkenheuer Hardening and microstructure of neutron- and ion-irradiated Fe-Cr alloys.....	265
G-H. Kim, K. Shiba, T. Sawai, I. Ioka, K. Kiuchi, J. Nakayama Microstructural evolution and void swelling in extra high purity Ni-based superalloy under multi-ion irradiation	273
S. Obara, T. Wakai, T. Asayama, Y. Yamada, T. Nakazawa, M. Yamazaki, H. Hongo Effects of heat treatments on long-term creep properties of 9Cr-W-Mo-V-Nb steel	281
Poster Session	297
Chairs: T. Allen, J-Y. Park	
Session I: Fundamental – Irradiation	299
Chairs: J-H. Kwon, G-G. Lee, C-S. Shin	
J-H. Kwon, G-G. Lee, C-S. Shin Multi-scale modelling approach to the estimation of radiation hardening of stainless steels in LWR and SFR environments	301
S-H. Kim, W-S. Ryu, Y-W. Kim A study on the change of impact properties by neutron irradiation in modified 9Cr-1Mo steel.....	303
K. Field, A. Certain, Y. Yang, T. Allen Radiation response of ferritic/martensitic cladding steels	305
J-H. Yoon, S-H. Kim, D-S. Kim, B-S. Lee, W-S. Ryu Irradiation-induced shifts in master curve reference temperature of ferritic/martensitic steels and welds.....	307
D-W. Kim, S-H. Kim, W-S. Ryu Mechanical properties of welded and irradiated 9Cr-1Mo-1W steel	309
G.G. Lee, J.H. Kwon Computer simulation on the isochronal annealing of irradiated Fe using the kinetic Monte Carlo method	313
W.G. Kim, S.N. Yin, G.G. Lee, J.Y. Park, Y.W. Kim Creep properties in air and helium environments of Alloy 617 for a VHTR.....	315
Session II: Metal-Compatibility	317
Chairs: D.Y. Ku, M.Y. Ahn, I.K. Yu, S. Cho, H.G. Lee, K.J. Jung	
D.Y. Ku, M.Y. Ahn, I.K. Yu, S. Cho, H.G. Lee, K.J. Jung Thermal fatigue and thermal ageing test of low activation ferrite/martensitic steel for helium-cooled solid breeder TBM.....	319
X. Fu, B. Long, J. Zhang, F. Chu, Y. Xu, A. Gessi Corrosion behaviour of 316LN in static liquid lead-bismuth eutectic.....	321
J. Zhang, X. Fu, B. Long, F. Chu, Y. Xu, A. Gessi Compatibility of CLAM steel 9Cr2WVTa with flowing lead.....	323
D. Kim, I. Sah, C. Jang Ageing effects of nickel-based superalloys on mechanical properties for VHTR applications	325
D. Kim, I. Sah, C. Jang Effects of carburisation and decarburisation on the mechanical properties of nickel-based superalloys for VHTR applications	329

G.G Lee, D.J. Kim, W.G. Kim, J.Y. Park Effect of He environment on the microstructure and creep properties of Inconel Alloy 617 at high temperature.....	331
H-O. Nam, I-S. Hwan, K-H. Lee Hydrogen effect on nickel and nickel oxide phase transition at hydrogenated water environment	333
Session III: Ceramic	343
Chairs: E-S. Kim, S-H. Chi, Y-W. Kim	
E-S. Kim, S-H. Chi, Y-W. Kim Fracture behaviour of nuclear-grade graphite for VHTR.....	345
J-Y. Park, C-H. Jung, W-J. Kim, J. Sumita, T. Shibata, K. Sawa, I. Fujita, T. Takagi, T. Makita Property changes of nuclear grade C _f /C composite by oxidation	347
G-Y. Gil, N. Alfian, D-H. Yoon, W-J. Kim, J-Y. Park Properties of SiC/SiC _f fabricated by slurry infiltration	349
S-H. Lee, H-D. Kim Low-temperature sintering of SiC using ternary aluminium carbides.....	351
Z. He, Z.L. Pan Determination of the theoretical density and Young's modulus of ceramic ZrO ₂ doped with neutron absorbers	353
Session IV: Novel Materials Pathways	365
Chairs: N.Y. Iwata, T. Liu, R. Kasada, A. Kimura, T. Okuda, M. Inoue, S. Ukai, S. Ohnuki, T. Fujisawa, F. Abe	
N.Y. Iwata, T. Liu, R. Kasada, A. Kimura, T. Okuda, M. Inoue, F. Abe, S. Ukai, S. Ohnuki, T. Fujisawa Influence of processing parameters on the microstructure and Charpy impact properties of ODS ferritic steels	367
J-S. Jang, M-H. Kim, C-H. Han, H-J. Ryu, X. Zhang, D. Foley, K.T. Hartwig Preliminary results of grain refinement of ODS alloy by equal channel angular pressing.....	369
S-H. Noh, R. Kasada, A. Kimura Effect of different insert materials on transient liquid phase bonded ODS ferritic steels for advanced nuclear systems.....	371
B-J. Kim, R. Kasada, H. Tanigawa, A. Kimura Fracture toughness and Charpy impact properties of cold-worked F82H steels.....	381
I. Ioka, J. Suzuki, K. Kiuchi, J. Nakayama Study of optimum composition of extra high purity Ni-Cr-W-Si alloy for advanced reprocessing plant.....	391
J-H. Baek, C.H. Han, J.H. Kim, T.K. Kim, W.G. Kim, S.H. Kim, C.B. Lee Effects of lower nitrogen and higher boron in ferritic/martensitic steels for a SFR fuel cladding	401
Y-S. Kim, S-S. Kim, D-W. Kim Hydrogen cracking of structural materials for innovative nuclear systems: Crack growth mechanism in metals	403
J. Wallenius, N. Sandberg, G. Ackland A spin-polarised potential for Fe with charge transfer.....	405

Session V: General	407
Chairs: A. Zeman, N. Dytlewski, V. Inozemtsev, G. Mank, F. Mulhauser, D. Ridikas, A. Stanculescu	
A. Zeman, N. Dytlewski, G. Mank, F. Mulhauser, D. Ridikas, A. Stanculescu, V. Inozemtsev IAEA activities on co-ordinated research of structural materials for advanced reactor systems.....	409
C.S. Kim, V. Barabash, M. Merola, R. Raffray Contribution of ITER to research of internal component materials	417
Annex 1: List of participants	433

Executive summary

The main topics of the workshop covered: fundamental studies, modelling and experiments on innovative structural materials including cladding materials for the range of advanced nuclear systems such as thermal/fast systems, subcritical systems and fusion systems. During the workshop, four topics were discussed:

- fundamental studies;
- metallic materials;
- ceramic materials;
- novel materials pathways.

The fundamental studies focused on multi-scale modelling, links between scales, numerical methods, the limitation of displacement per atom (DPA) assessments, radiation damage, etc. The metallic and ceramic materials include in-and out-core applications taking into account the scope of data availability and gaps (considering also licensing issues); experimental and modelling needs for specific components or degradation modes; links between R&D, standardisation and experimental protocols; and coolant effects and mechanical properties. The novel materials pathways comprise nano-grained materials, grain boundary engineered materials and nano-precipitation-strengthened materials and micro-laminates among other topics. It should be noted that fuel-cladding interaction is not covered in this edition of the workshop.

A total of 83 participants from 18 countries and 3 international organisations attended. The list of participants is provided in Annex 1. The total number of presentations amounted to 78 (34 oral presentations and 44 posters).

The workshop opened with the welcome address by M.S. Yang (KAERI, Republic of Korea) and Y-J. Choi, on behalf of Thierry Dujardin (NEA). The opening session was followed by three plenary and eight technical sessions.

Three plenary sessions covered current R&D issues on structural materials as well as fuel and fusion aspects, such as:

- a summary of international design needs for advanced reactors;
- novel pathways to improve the performance of structural materials for nuclear reactors;
- innovative fuels state-of-the-art assessment;
- super ODS steels R&D for fuel cladding of advanced nuclear systems;
- binding of impurities in austenitic iron;
- fission-fusion cross-cutting issues related to structural materials.

The following topics were covered in the technical sessions:

- Session I: Metal – VHTR Environmental Effects and High-temperature Properties;
- Session II: Ceramics-composite;
- Session III: Metal – Materials Compatibility – Molten Salt and Sodium;

- Session IV: Metal – Materials Compatibility – LFR Corrosion;
- Session V: Fundamental – Radiation Effects;
- Session VI: General;
- Session VII: Novel Materials – Nano-structured Materials;
- Session VIII: Fundamental Radiation Effects – Helium Effect.

The theme of the summary session was “Critical experiments, modelling needs and round robin opportunities”. All sessions were summarised based on the following questions:

- What are the critical issues to be solved?
- What are the associated experiments?
- What specific modelling issues can provide an answer to the above two questions?
- What are the opportunities for round robin experiments?

After the summary session, a special lecture on the *Generation IV Materials Handbook: A Structural Materials Database for International VHTR Development* was presented by B. Corwins (United States).

The main conclusions of the workshop were that:

- the issues surrounding innovative structural materials have been identified;
- technical readiness level (TRL) can be a proper tool to evaluate current R&D levels;
- an international database on structural materials for innovative nuclear systems is needed;
- further collaboration with material scientists in non-nuclear fields is needed;
- the SMINS workshop should be continued, covering both the modelling and experiment communities.

Technical tours were organised to the Hanaro reactor, Material Irradiation Test Facility (at KAERI) and Doosan Heavy Industries (Changwon, Republic of Korea).

Highlights of the plenary sessions

In Plenary Session I, D.H. Hahn (KAERI, Republic of Korea) summarised the international design needs for advanced reactors, presented on behalf of S. Zinkle (ORNL, United States). T. Allen (University of Wisconsin, United States) also presented on novel pathways for improving nuclear material performance for nuclear reactors. Some of the main conclusions were the following:

- materials have to maintain integrity in irradiated environments;
- the optimisation of ODS, corrosion and embrittlement were the main issues of the discussion;
- a round robin on corrosion and embrittlement was suggested;
- modelling simple irradiation effect and material coating effectiveness should be reviewed;
- for ODS, performing key experiments on a common material is necessary;
- the value of a technology readiness level should be estimated;
- the necessity of an international materials database should be studied.

In Plenary Session II, the innovative fuel state-of-the-art assessment was presented by T. Allen on behalf of K.O. Pasamehmetoglu (INL, United States) and super ODS steels R&D for fuel cladding of advanced nuclear systems was presented by A. Kimura (U. Kyoto, Japan). The conclusions were that:

- the critical issues of fuel are the compatibility with cladding, transient tests and cladding ODS under irradiation;
- the transfer of ions into neutrons can be used as associated experiments;
- for fuel tests, transient tests, the use of cladding with different fuels and the use of ODS under irradiation are needed;
- for modelling, calculations on stability of different oxides of ODS material are necessary.

Plenary Session III comprised two presentations: binding of impurities in austenitic iron by G. Ackland (University of Edinburgh, United Kingdom); and fission-fusion cross-cutting issues related to structural materials by F. Tavassoli (CEA, France). The main findings were that:

- modelling of experiments is needed to understand behaviour;
- for fission/fusion cross-cutting issues, characterisation is required to optimise modelling issues;
- creep-fatigue test can be the round robin experiments.

Highlights of the technical sessions

Session I: Metal-VHTR environmental Effects and High-temperature properties

One invited speech, five oral presentations and seven posters were presented in Session I. The main conclusions of session were that:

- the session covered the status of knowledge on Ni-based alloys and others for high temperature in He including issues such as chemistry control;
- a key requirement is the understanding of long-term creep strength;
- modelling and fracture behaviour of IN617 and its oxidation were discussed;
- a key comment in Session I referred to the possibility of round robin experiments on VHTR materials, including corrosion issues, as these are the only available tests in the short-term for HTR.

Session II: Ceramics-composite

Five oral presentations and seven posters were presented in Session II. The main findings were that:

- this session covered mainly SiC/SiC, the production of properties, fabrication processes, upgrading of laboratories to a larger scale and for control rod applications;
- the importance of experiments, irradiated properties, modelling, database and round robin tests have been highlighted including experiments on coatings;
- for B₄C, swelling profile has been reviewed; experiments in the Joyo facility and modelling may offer opportunities for round robin tests;

- the characterisation of ZrC in TRISO fuel and Ag diffusion effect have been reviewed; the experimental devices have been difficult to set; methods of measurement can be selected as a round robin test;
- TiN coating can prevent corrosion by deposited process; a microstructural evolution study is needed;
- production methods and joining could be a round robin test; using modelling can optimise fabrication/architecture and get the most out of irradiation programmes.

Session III: Metal – Materials Compatibility – Molten Salt and Sodium

Two oral presentations and five posters were presented in Session III. The main issues were alloy compatibility with molten salt and weldments for CEFR.

Session IV: Metal – Materials Compatibility – LFR Corrosion

One invited speech, five oral presentations and eight posters were presented in Session IV. The main conclusions were that:

- one of the main issues of the session is to determine the different methods of corrosion prevention such as: use of barriers; experiments to evaluate reliability of coatings and degradation mechanisms;
- coating techniques could be a round robin test;
- corrosion mechanisms on materials could be a good subject for modelling; corrosion fundamentals should be studied in an experimental manner;
- studies on the effect of LBE on welds and thermal ageing are necessary.

Session V: Fundamental – Radiation Effects

One invited speech, three oral presentations and two posters were presented in Session V. The main findings were that:

- more experiments should be conducted in order to look at variants; activation characteristics of Al and limits of embrittlement should be studied;
- the FFTF post-irradiation experiment needs over 440°C to avoid embrittlement and 100°C lower in the EUROFER test;
- the modelling of oxide particle and the effect of Al result in the fact that the interpolation of data across a range can reduce experimental costs.

Session VI: General

Three oral presentations were given in Session VI. The national programmes from newly involved countries were reported. The identified challenges of ODS design were the experiments on corrosion compatibility. The round robins are important to share updated information and to aid new programmes in order to look at key issues.

Session VII: Novel Materials – Nano-structured Materials

One invited speech and two oral presentations were presented in Session VII. The main conclusions were that:

- past and present programmes on nano-structured materials and cladding were summarised;

- from the European fast reactors (EFR) programme, improvement of swelling through modification of elements can be achieved;
- planned new irradiation experiments and modelling programmes have been reviewed.

Session VIII: Fundamental Radiation Effects – Helium Effect

Four oral presentations were presented in Session VIII. The highlights of the session were that:

- austenitic steels and LBE embrittlement effects have been summarised;
- for cladding, new alloys with swelling resistance can bring benefits;
- heat treatments can give better performance for long life;
- standard experiments and comparison with other materials are needed to explain ion damage compared with neutron displacement damage;
- more round robin tests on microstructures are needed and the results should be shared.

Additional comments

- relative effects of ion versus neutron irradiation, such as comparison between evaluation types, should be very well understood;
- benchmark studies and a common set of information are necessary;
- collaboration and comparison with IAEA expert groups could help identify needs for NEA expert groups;
- the European fast reactors (EFR) set new targets for high burn-up; the schedule is set for the next 30 years. However, clear milestones should be set to show the viability and maturity of the reactor type, e.g. GFR, parameters, materials and human resources should be estimated;
- technical readiness level is one of the options which allows for the identification of critical steps to verify feasibility. This can set the roadmap for material development which links to up-scaling and validating requirements for reactor usage; hence, technical readiness level for material R&D should be developed;
- the need for ODS for SFR and LFR should be evaluated;
- it is necessary to keep modelling up to speed with materials development and to collaborate with the fusion or non-nuclear communities;
- it is important to promote young engineers and to develop methods to support new starters in the technology;
- it is necessary to identify the main obstacles for improving ODS and to study the characterisation of ODS for SFR use;
- common objectives are needed for the different round robins which could be defined in conjunction with Generation IV.

Opening Session

Chair: J.H. Hong

KAERI welcome address

M-S. Yang
President
KAERI, Republic of Korea

I would like to welcome all of you to this 2nd International Workshop on Structural Materials for Innovative Nuclear Systems (SMINS-2).

I am glad that KAERI provides the venue for this workshop, which will be a great opportunity to share cutting-edge scientific and technological knowledge among key researchers in nuclear science and technology.

In the Republic of Korea, nuclear energy provides 40% of the country's total generation of electricity. With 20 nuclear power plants currently operating in the Republic of Korea, the importance of materials and safety related research on nuclear components cannot be overemphasised. Moreover, considering the global trend towards safe and environmentally friendly energy sources, the development of material technology surrounding nuclear power plants is of common interest to the global community.

In 2009, South Korea became the world's 6th nation to export nuclear power plants by securing a contract with the United Arab Emirates to build four APR1400 nuclear power plants in their country. A consortium led by state-run Korea Atomic Energy Research Institute (KAERI) and Daewoo Engineering and Construction also won a bid to build a nuclear research reactor for Jordan in December 2009. These successes have been made possible through our long-term commitment to research and development activities in materials science.

Last year was truly significant for KAERI as it marked the 50th anniversary of its foundation. Over the past 50 years since its inception, the institute has made great contributions to the progress of nuclear science and technology through the combination of the institute's well-established systems and high quality research workforce.

For example, localisation of CANDU fuel was completed in 1985, the research reactor HANARO has been operated since 1995. The Korea Standard Nuclear Power Plant (KSNP) was developed in 1996.

To enhance the thermal hydraulic safety of nuclear power plants with thorough simulations, KAERI designed the advanced thermal hydraulic test loop for accident simulation ATLAS in 2002.

In 2010, the research reactor HANARO unit was upgraded and transformed to produce "cold neutrons" and incorporate a fuel test loop (FTL) system.

The main research areas of the Nuclear Materials Research Division, which has had a key role in the organisation of this workshop, are the development of corrosion control and protection technology, characterisation of pressure vessel materials, radiation damage research, non-destructive characterisation, control of steam generator degradation, water chemistry control, high temperature material technology, etc. These technologies will be utilised for sodium fast reactors, high-temperature gas-cooled reactors and Generation IV nuclear reactor research work.

This SMINS-2 (2nd International Workshop on Structural Materials for Innovative Nuclear Systems) is a valuable opportunity to further strengthen the role of KAERI in promoting knowledge sharing and co-operation at international levels. Since the initiation of the workshop by the German research institute “Forschungszentrum”, the workshop has come through several expert meetings, subsequent approvals and its first official meeting at OECD, where KAERI was chosen as the venue of the second workshop, held this week from 31st August to 3rd September 2010. Hosted by the NEA of the OECD, this second workshop provides a place of in-depth discussions on structural materials for future nuclear reactor systems. With the participation of approximately 100 domestic and overseas experts from 18 countries, this workshop at KAERI will deal with current technological trends, new findings in research and future directions of nuclear materials research.

The scope of these workshops will cover fundamental studies, modelling and experiments on innovative structural materials for nuclear systems with four areas such as “fundamental studies”, “metallic materials”, “ceramic materials” and “novel materials pathways”. They will encompass the whole range of advanced nuclear systems including thermal/fast systems, subcritical systems, as well as fusion systems.

I wish all the participants a fruitful experience this week. Once again, I welcome all of you to KAERI and wish you an enjoyable stay in Korea.

NEA welcome address

Yong-Joon Choi

OECD Nuclear Energy Agency (NEA)

It is a great pleasure for me to welcome you to the second international workshop on Structural Materials for Innovative Nuclear Systems on behalf of Thierry Dujardin, Deputy-Director of the OECD Nuclear Energy Agency (OECD/NEA).

First of all, I would like to express my sincere appreciation to our hosts, the Korea Atomic Energy Research Institute and the honourable workshop chair Dr. Myung-Seung Yang, the President of KAERI, as well as to all KAERI staff and the members of both the scientific and the organising committees, who have worked hard in preparing and supporting this workshop.

I would also like to thank the European Commission and the International Atomic Energy Agency for their co-operation in the organisation of this workshop.

Structural materials research is a field of growing relevance in the nuclear sector, especially for the different innovative reactor systems, such as critical or subcritical advanced nuclear systems including Generation IV and fusion energy systems. As you well know, the goals defined for innovative nuclear systems call for demanding material-related operating conditions, such as very high temperatures, high fuel burn-ups, long service life and compatibility with different coolants. All these conditions imply new challenges with respect to current nuclear industry experience with structural materials.

In this context, the Nuclear Science Committee (NSC) of the OECD/NEA organised a first workshop on Structural Materials for Innovative Nuclear Systems in June 2007. The objectives of this workshop were to exchange information on structural materials research issues and ongoing programmes for different types of reactor concepts, as well as to foster the development of synergies. The workshop was held in Karlsruhe, Germany, hosted by the *Forschungszentrum Karlsruhe*, which is now the Karlsruhe Institute of Technology.

About 60 papers were presented. There were about 60 presentations by the participants from the various NEA member states and from the Russian Federation. As a follow-up to this workshop, the NEA established two activities in the field of material science, one more theoretical devoted to multi-scale modelling of fuels and structural materials for nuclear systems and one more application-oriented on innovative structural materials.

The NEA Working Party on Multi-scale Modelling of Fuels and Structural Materials for Nuclear Systems, which is chaired by M. Stan (United States), deals with the scientific and engineering aspects of fuels and structural materials, aiming at establishing multi-scale models and simulations as validated predictive tools for the design, fuel fabrication and performance of nuclear systems. The working party organises five expert groups on: multi-scale modelling methods, multi-scale modelling of fuels, structural materials modelling, validation and benchmarks of methods and primary radiation damage.

The NEA Expert Group on Innovative Structural Materials, which is chaired by T. Allen (United States), is conducting joint and comparative studies to support the development, selection and characterisation of innovative structural materials that can be

implemented in advanced nuclear fuel cycles, under extreme conditions such as high temperature, high dose rate and corrosive chemical environment and long service lifetime. A status report on structural materials for innovative nuclear systems is now being finalised and will be published by the end of 2012.

The NEA Nuclear Science Committee attaches great importance to the development of new structural materials for nuclear applications and has therefore decided to organise this second SMINS workshop. This year, about 80 papers will be presented either by oral or poster sessions covering scientific issues of fundamental studies, metals, ceramics and novel materials pathways. The plenary lectures on the key issues such as summary of international design needs for advanced reactors, candidate cladding and duct materials, novel material pathways, perspectives on modelling materials far from equilibrium and perspectives on fuel development for advanced reactors will be presented during the three days of the workshop. At the end of the workshop, there will be a summary session, which will cover critical experiments, modelling needs and round robin opportunities.

I hope that this workshop will be very fruitful and useful for scientists to get an overall picture of ongoing and planned research activities in this specific area and also to get the opportunity to establish further international collaborations.

Plenary Session I

Chairs: T. Allen, J-Y. Park

Summary of international design needs for advanced reactors*

Jonghwa Chang, Dohee Hahn
Korea Atomic Energy Research Institute

Abstract

Global warming and rising energy demand are key issues in worldwide economic development. The role of nuclear energy to overcome the problems accompanying massive use of fossil resources is ever increasing. Though the current fleet of LWR is commercially successful, there are many more possibilities for nuclear energy. Current LWR can utilise only small amounts of uranium resources, leaving problems of extremely long-term waste management. Their application is limited to electricity generation.

The Generation IV International Forum was established in 2002 to develop reactor systems which have better safety, economics and sustainability and proliferation resistance. Six reactor concepts, GFR, LFR, MSR, SCWR, SFR and VHTR, are selected as Generation IV reactors. The Republic of Korea has opted for SFR and VHTR system development. A fusion reactor is another possibility to solve the problems. The Republic of Korea joined the ITER project and operated the domestic KSTAR facility. The current R&D status of fusion is far from energy production. However, when we acquire a technology to control the stability burn plasma, we need an energy conversion system, which is not much different from Generation IV reactors in technological aspect.

Global R&D collaborations on Generation IV reactors and ITER save effort by avoiding duplication and by co-ordinating required work among the participants. Thus, demonstration and commercial deployment can be achieved. The material issue for realising the Generation IV reactor system is taking quite a long time and great effort. VHTR has decreased its outlet temperature several times from 1 000°C to current 800°C mainly due to the gap between the timeline when VHTR could be demonstrated and the date when a material design code is available. Recently, there have been discussions on developing SMR which is supposed to have a very long service interval with a high safety standard. The material for SMR will suffer very high radiation fluence, with which we have little experience.

To help future nuclear systems develop more efficiently, a common database, such as a Generation IV material database or the IAEA irradiated graphite database is necessary. The database will help to advance material property modelling capability, establish the mechanical design code, derive required experiments, as well as to set up the goal of innovative reactor in a more realistic manner. To promote the common database, the author proposes to first establish and publish an internationally agreed upon data exchange format for bibliographical and numerical data.

* The full paper being unavailable at the time of publication, only the abstract is included.

Novel pathways for improving nuclear reactor structural materials performance*

S. Zinkle

Oak Ridge National Laboratory, United States

Abstract

Future innovative nuclear energy systems will be increasingly dependent on advanced structural materials to deliver the requisite improved plant performance. The increased operating temperatures for these innovative nuclear energy systems will require structural materials with improved high-temperature strength for prolonged operating periods and engineered corrosion resistance for the candidate coolants and other materials in the system, while maintaining acceptably high toughness, good fabricability and moderate cost for the finished parts. The high radiation fluxes in innovative nuclear energy systems will require the structural materials to have superior radiation resistance compared to currently available materials. This presentation will review some of the current and emerging strategies being employed to develop structural materials with simultaneous high radiation resistance, high strength, good toughness, corrosion resistance and moderate fabrication cost. Materials systems to be covered include steels, refractory alloys, bulk amorphous metals and ceramic composites. Engineering approaches to design improved performance include the introduction of nanostructures in the form of high densities of second phases (precipitates or inert particles) or nanolayered interfaces, the development of tailored composite materials systems, the creation of high strength, radiation-stable amorphous alloys and the design of optimised engineered grain boundaries. In the future, the utilisation of advanced manufacturing processes to produce near-net shape parts with precise microstructural control will be of increasing importance to control fabrication costs.

* The full paper being unavailable at the time of publication, only the abstract is included.

Session I

Metal – VHTR Environmental Effects and High-temperature Properties

Chairs: F. Balbaud-Célrier, S. Kislitsin

VHTR materials issues*

William R. Corwin

Oak Ridge National Laboratory, United States

Abstract

Very-high-temperature reactor (VHTR) systems provide numerous challenges for the structural materials used in many of their high-temperature components. The key design parameters that will affect the choice of VHTR structural materials and therefore, their needed R&D, include the reactor coolant inlet and outlet temperatures and pressure, as well as the choice of the secondary-side coolant and its associated temperatures and pressures. Expected service conditions include a near-term core coolant outlet temperature between 750°C and 850°C, for which existing materials may be used, and a longer-term goal of 1 000°C that will require the development of new materials. The inlet core temperature for such systems could range from about 300°C to 600°C and the primary coolant system pressures from 5 to 9 MPa. Reactors currently being developed, such as the Next Generation Nuclear Plant (NGNP) or the high-temperature gas-cooled reactor-pebble-bed module (HTR-PM), focus on the lower range of core outlet temperatures and will largely utilise existing structural materials, but will serve a vehicle for developing and evaluating the enhanced materials, codes and design methods, and condition monitoring techniques needed for their anticipated 60-year lifetimes and design envelopes, as well as some of the materials needed for higher temperature systems, such as the Nuclear Hydrogen Development & Demonstration Project (NHDD). Materials development and qualification, design codes and standards, as well as construction methodologies for VHTRs require new investigations for the design and construction of the key components. The developments of new material grades, as well as the extended qualification of existing materials, are key issues for meeting the higher temperature and longer lifetime requirements of VHTR normal and off-normal operating conditions, including:

- graphite for the reactor core and internals;
- high-temperature metallic materials for internals, piping, valves, high-temperature heat exchangers, steam generators and turbomachinery;
- ceramics and composites (e.g. C/C, SiC/SiC, etc.) for control rod cladding and other specific reactor internals, as well as for advanced intermediate heat exchangers for very high temperature conditions.

To provide for a co-ordinated international structural materials research programme to support the development of VHTR systems, several countries with ongoing R&D activities have joined together in a formalised project arrangement (PA) within the framework of the Generation IV International Forum. The PA addresses the three major categories of materials-graphite, high temperature alloys, and ceramics and composites. The VHTR materials PA includes major shared contributions of both newly generated and protected historical information from its partners that currently include Canada, EURATOM, France, Japan, the Republic of Korea, the Republic of South Africa, Switzerland and the United States.

* The full paper being unavailable at the time of publication, only the abstract is included.

Environmental effects of nickel-based superalloys on mechanical properties for VHTR applications

Changheui Jang^{1,2}, Daejong Kim¹, Donghoon Kim¹, Minu Kim¹,
Injin Sah¹, Woo-Seog Ryu³, Duk Joo Yoon⁴

¹Korea Advanced Institute of Science and Technology, Republic of Korea

²Khalifa University of Science, Technology and Research, United Arab Emirates

³Korea Atomic Energy Research Institute, Republic of Korea

⁴Korea Electric Power Research Institute, KEPCO, Republic of Korea

Introduction

Currently, nickel-based superalloys are being considered for use in the IHX due to a combination of good oxidation resistance, high-temperature strength and creep resistance. However, once they are subjected to high-temperature helium environments, they can be carburised or oxidised/decarburised depending on the gas compositions and temperature, which will degrade mechanical properties significantly [1-3]. In this study, the environmental effects of Alloy 617 and Haynes 230 on low temperature embrittlement and creep properties were evaluated for VHTR applications.

Experimental

Commercial wrought nickel-base superalloys Alloy 617 and Haynes 230 were used in this study. Oxidation and ageing heat treatment were carried out for 500 h at 900°C and 1 000°C. The impure helium chemistries to simulate the VHTR environments are listed in Table 1. After ageing heat treatment, tensile tests were carried out at room temperature. Creep tests were carried out in air and high purity helium environments to evaluate the effect of oxygen concentration on creep rupture life.

Table 1: Composition of impurities in He gas (in µbar)

	He	H ₂	H ₂ O	CO	CO ₂	CH ₄
He-K1 at 900°C	Bal.	40	0.7	50	10	20
He-K1 at 1 000°C	Bal.	50	0.7	50	10	15
He-K2 at 900°C	Bal.	-	0.7	50	10	-
He-K2 at 1 000°C	Bal.	-	0.7	50	10	-

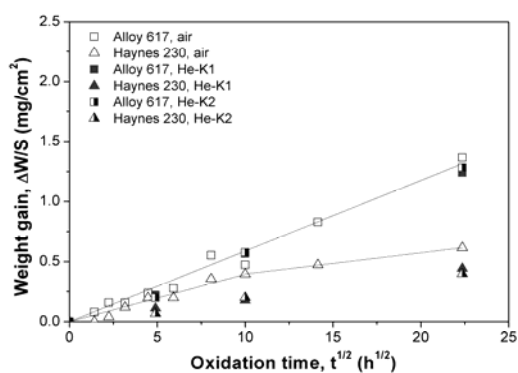
Results and discussion

Oxidation behaviours of nickel-base superalloys

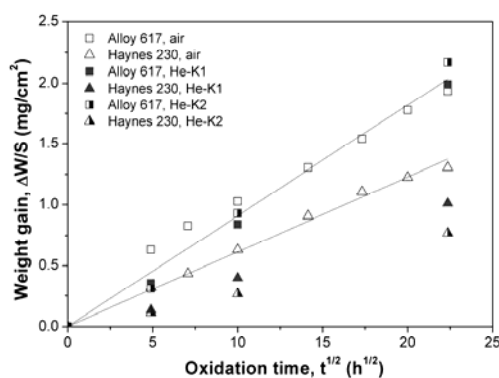
Figure 1 shows the weight gain vs. time ($t^{1/2}$) plots of Alloy 617 and Haynes 230 after isothermal oxidation at 900°C and 1 000°C up to 500 hours in air and impure helium environments, He-K1 and He-K2. It is clear from the Figure that the weight gain of Alloy 617 was considerably greater than that of Haynes 230 in all environments.

Oxides like NiO and NiCr₂O₄, which were stable in air, did not form in the impure helium environments because of very low oxygen activities. Instead, a Cr₂O₃ layer, TiO₂ ridges on the grain boundaries, and isolated MnCr₂O₄ grains on top of the Cr₂O₃ layer were formed for Alloy 617, while a Cr₂O₃ inner layer and a MnCr₂O₄ outer layer were formed for Haynes 230. As shown in Figure 2, the formation of a MnCr₂O₄ outer layer with the Mn depletion below was an important factor in increasing oxidation resistance of Haynes 230, which resulted in slower oxidation kinetics.

Figure 1: Weight change vs. time plots of Alloy 617 and Haynes 230 in air and impure helium environments: (a) at 900°C, (b) at 1 000°C

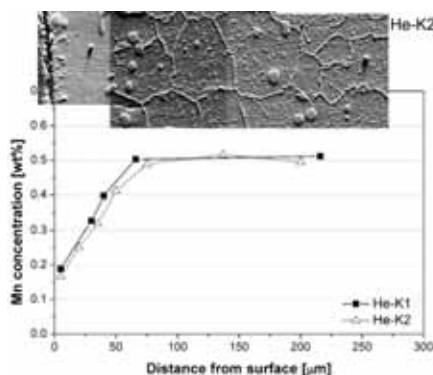


(a)



(b)

Figure 2: EPMA analysis results showing depletion of Mn for Haynes 230 after 500 hours exposure to He-K1, He-K2 at 1 000°C



Tensile properties after ageing heat treatment

One of the important changes was decarburisation depth depending on gaseous impurities. In spite of the negligible difference between oxidation kinetics in He-K1 and He-K2, decarburisation was much more extensive below the oxide layer of alloys in a He-K1 environment that contained CH_4 and H_2 than in He-K2, as shown in Figure 3. As shown in Figure 4, the reduction in elongation was more significant in He-K2 because decarburisation reduced the amount of inter-granular fracture, a major cause of ductility loss.

Figure 3: Decarburization depth of Alloy 617 and Haynes 230 after ageing in He-K1 and He-K2 at 900°C and 1 000°C

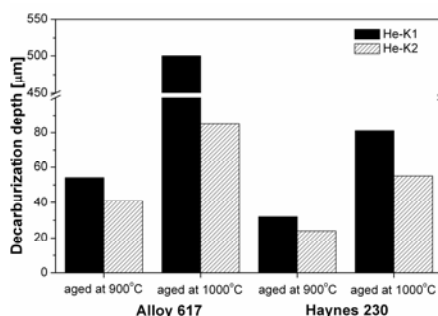
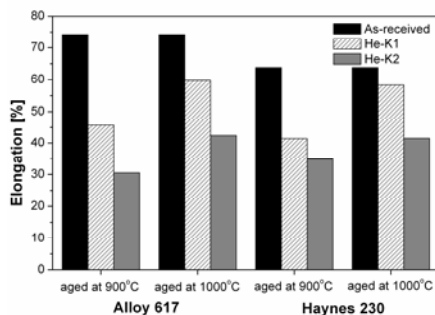


Figure 4: Change in elongation after ageing at 900°C and 1 000°C under He-K1 and He-K2 conditions for 500 hours



Oxidation and creep behaviours

Figure 5 shows the creep rupture properties of Alloy 617 tested in the temperature range of 800°C to 1 000°C in air and in a flowing helium environment that contained about 2 ppm O₂ and H₂O. Creep rupture life was shorter in a flowing helium environment than in air, which suggests that the oxidation behaviour may affect the creep resistance of the alloys. When Alloy 617 was oxidised/decarburised for 72 hours at 900°C in various environments, oxidation and decarburisation behaviours changed depending on oxygen concentration, as shown in Figure 6. Creep rupture life can be reduced when a carbide free zone is more extensive in the helium environment.

Inter-granular oxide Al₂O₃ formed on grain boundaries could attribute to the fracture of the Cr₂O₃ layer after detachment of the interface between inter-granular oxides and metal [Figure 7(a)]. It also could provide preferential sites for crack initiation. Creep cavities were predominantly formed where grain boundary carbides were grown parallel to tensile load through redistribution [Figure 7(b)].

Figure 5: Creep rupture life of Alloy 617 tested in air and flowing helium environment

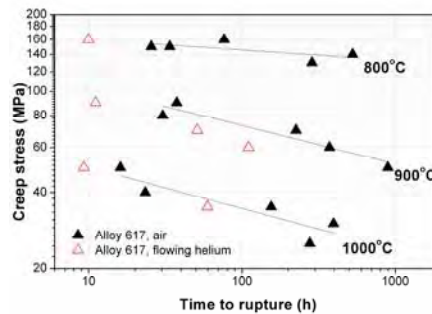


Figure 6: Weight change and decarburisation depth of Alloy 617 depending on oxygen concentration after oxidation at 900°C

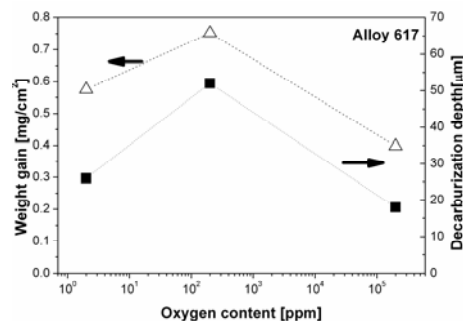
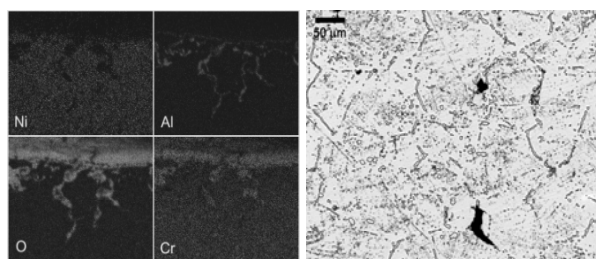


Figure 7: Surface cracks and creep cavities of Alloy 617 formed during creep deformation at 900°C in helium



(a)

(b)

Conclusions

The formation of MnCr_2O_4 outer layer increased oxidation resistance of Haynes 230. A small amount of CH_4 and H_2 hardly influenced the oxidation kinetics of the alloys. However, these impurities led to the extensive decarburisation, which resulted in less ductility loss at room temperature. Meanwhile, extensive decarburisation led to a reduction in the creep life of Alloy 617. Creep rupture life was shorter in helium with low oxygen content. Inter-granular oxidation and the redistribution of carbide contributed to the formation of surface cracks and creep cavities.

References

- [1] B. Huchtemann (1989), *Materials Science and Engineering*, A121, 623.
- [2] F. Abe, Y. Sakai, T. Tanabe, H. Araki, T. Suzuki, H. Yoshida, R. Watanabe (1985), *Transactions ISIJ* 25, 1087.
- [3] R. Wright, J. Simpson, A. Wertsching, W. D. Swank (2008), *Proceedings of the 4th International Topical Meeting on High Temperature Reactor Technology*, United States.

Optimisation of Ni-based Alloy 617

K. Maile, E. Roos, A. Klenk, M. Hoffmann

Materialprüfungsanstalt Universität Stuttgart, Stuttgart, Germany

Abstract

The Ni-based Alloy 617 is a candidate material for use in fossil-fired power plants as well as in nuclear high-temperature reactor (HTR). Based on experience with this material in the former German HTR projects, the material has been qualified for use in high efficient fossil-fired power plants within the temperature range up to 725°C. This paper describes the ongoing investigations on the qualification of Ni-based Alloy 617 within the framework of the German national funded R&D initiative COORETEC. A comparison with the steels normally used in power plants with this new class of materials shows that there are distinctive differences regarding physical and mechanical properties. Specific damage mechanisms have to be investigated in order to have a safe design and operation of components. New design methods are required to make full use of the strength potential but also taking into account their specific stress-strain and relaxation behaviour. The verification of material laws is demonstrated by simulation of component-like specimens.

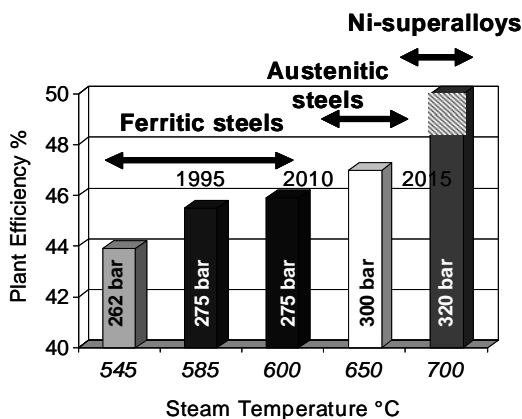
Results of basic qualification programmes with standard specimens including welded joints show the applicability of candidate materials. In parallel, component tests with waterwall panels and thick-walled pipes have been carried out. These tests reveal the need for the identification of specific failure mechanisms especially with the Ni-alloys. This paper will present and discuss typical damage mechanisms assessed so far.

Introduction

In the future coal will also provide a significant contribution to energy production. In steam power plants a more resource – saving application is possible using new technologies which include a significant rise in the degree of efficiency and thereby a considerable reduction of pollution. This technology is suitable to substitute old power plants and thereby contribute to compliance with climate protection agreements. The implementation of new technologies in low-emission high performance power plants is based primarily on a clear increase in the steam parameters pressure and temperature. Materials used up to now are not applicable for highest demand; the shift to nickel-based alloys at a progressive rate has to be intensified, as shown in Figure 1. One of the candidate materials is well known not only for its application in gas turbines and heat exchangers but also for developments in former high-temperature reactor projects. The material is therefore also an option for use in components for future high-temperature reactors. In the case of its application in fossil power plants the rise in temperature places considerable demands on the evidence of long-term stability/resistance concerning corrosion (oxidation), the strength and the deformation ability of the structural materials to be used. Furthermore, the manufacturing technologies e.g. production of components with large wall thickness are challenging. Therefore, the steps in production e.g. welding in piping or turbine production have to be investigated and processing procedures have to be established, especially for welded joints of nickel-based materials as well as dissimilar metal welds between nickel-based alloys and ferritic/martensitic steels. In the new high efficient 700°C power plant membrane walls will be exposed to temperatures up to 620°C, headers, turbine casings and rotors up to 735°C. One well-known candidate material among the nickel-based alloys is Alloy 617. Experience was gained with this material during developments in the frame of the German high-temperature gas-cooled reactor. This could be used as a basis for the further qualification of the material in the temperature range 600 to 750°C.

Research and development for material qualification and results from basic investigations

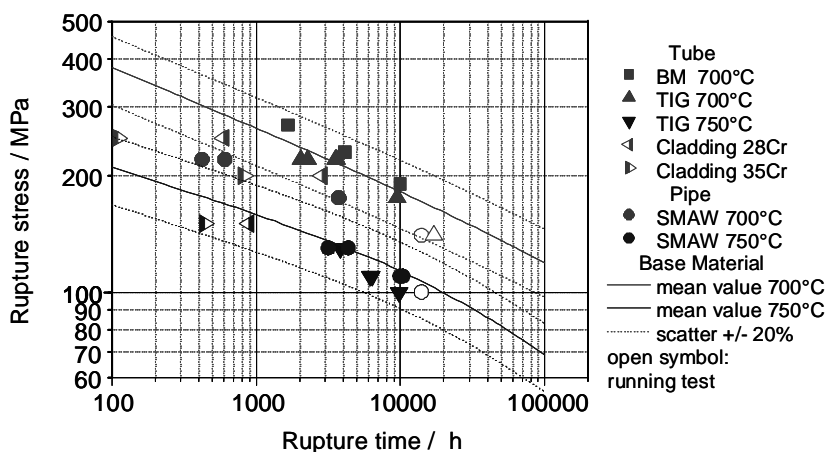
Figure 1: Main developments in the near future



Using the experience from research programmes on design criteria and material qualification for high-temperature reactors [1] several research projects were initiated to investigate behaviour and properties of nickel-based alloys. As a first step the MARCKO-DE2 programme fulfilled the aim of providing a suitable material for temperatures up to 750°C [2] [3]. The compilation of data from creep tests is shown in Figure 2. The

evaluation and further data assessments based on the results of previous projects resulted in the development of a modification of Alloy 617 with controlled chemistry, as shown in Table 1. For this material a creep strength of 119 MPa at 700°C and more than 100 MPa at 750°C could be demonstrated, which was one of the aims of the project. As a first step towards the demonstration of component behaviour creep tests with cross weld specimens of different welds (SMAW, GTAW) were performed. Specific welding problems arise especially with thicker components. These issues are addressed more closely in the follow-up projects. Various investigations on corrosion protection systems were carried out. As a result, a weld-on of Ni-based alloys with high chromium contents was selected. Creep tests with clad tubes are ongoing. Besides creep tests on base material and welds, a field test was performed in a plant.

Figure 2: Creep rupture tests Alloy 617 – base material mean values and welded joints



In the various investigation programmes, e.g. the MARCKO700 Programme [4] and running projects within the COORETEC-Initiative [5], long-term investigations on creep properties of base materials and welded joints are one of the focal points. For Alloy 617 mod. a reasonably good long-term data base for base material and welded joints of tubes and pipes obtained by crossweld tests already exists [2] [3] [4]. The results obtained with crossweld specimens from SMAW- and TIG-girth welds of tubes and pipes for temperatures of 700°C and 750°C are within the base material scatter band. Creep tests longer than 10 000 h show a tendency towards the base material mean values (see Figure 2).

Table 1: Chemical composition of Alloy 617mod

Material		C %	Al %	Co %	Cr %	Mo %	Nb %	Ti %	B %	Fe %	Ni %	
A617	Min.	0.050	0.80	11.0	21.0	8.0		0.30	0.002			Alloy 617 mod.
	Max.	0.080	1.30	13.0	23.0	10.0		0.50	0.005	1.50	Bal.	
	Min.	0.05	0.60	10.0	20.0	8.0		0.20		-		VdTUV 485
	Max.	0.10	1.5	13.0	23.0	10.0		0.50		2.0	Bal.	

Experimental examinations (creep tests, component tests) lay the basis for the long-term behaviour of the tested materials under operating conditions and hence for their

accreditation as construction materials in pressure vessel construction. Hereby, the focus is placed on scientific aspects like deformation and failure behaviour, damage mechanisms and micro-structural modifications and damage development. The results of the project will allow the planning of periodic testing which corresponds to the actual material capabilities. Moreover, possibilities arise to use modern design methods e.g. finite element analyses which are going to be introduced into technical practice – design by analysis. It has to be assumed that the design by formula will not be able to fully exploit the material potential, leading to sub-optimal degrees of efficiency for constructions with high wall thickness. The optimised design of components is based on the availability and reliability of material data and the knowledge about deformation and damage behaviour. Material testing must consider specific service conditions like physical and chemical properties, mechanical properties (strength, crack initiation and growth), creep properties and influence of manufacturing and ageing on these properties. The aim of metallographic investigations is the identification of microstructural changes under service conditions and the characterisation of damage development.

Microstructural characterisation and damage mechanisms of Alloy 617

Alloy 617 is a solid-solution strengthened and carbide-hardened material. This nickel-based alloy from the type NiCr22Co12Mo is characterised by high resistance and creep properties and good resistance against carbonisation as well as oxidation resistance at temperatures up to 1 100°C [6]. Alloy 617 mainly consists of nickel, chromium, molybdenum and cobalt. Solid-solution hardened superalloys are subjected to a solution annealing treatment. An optimal carbide distribution can already be achieved at cooling down.

According to [7], the typical temperature area of solution annealing for the Alloy 617 is 1 140°C to 1 200°C with different holding times for various semi-finished components. The structure of Alloy 617 consists of an austenitic matrix with unevenly spread carbides. Often the material shows many twins and tends to build banded structures. The grain size in this material is inhomogeneous. Titan carbon nitrides M(C, N)-Ti (C, N) are counted among the primary precipitations which are distributed irregularly in the structure. Furthermore, among them there are primary and secondary carbides rich in chromium which precipitate at the grain boundaries as well as inside the grains (see Figure 3).

Normally the $M_{23}C_6$ precipitations become visibly bigger at the grain boundaries than inside the grain as the growth kinetics of inter- and intra-crystalline precipitations are different [2] [8]. Molybdenum and M_6C carbides rich in chromium can be found equally at the grain boundaries and within the grain [8] [9]. In the initial condition, the γ' -phase had been rarely detected [8] [10]. The γ' -phase will be identified only after thermal mechanic stress in the inner grain. The part of this phase stays below 8 vol.% [11]. The number and the size of the $M_{23}C_6$ precipitations do not vary considerably according to creep stress. However, due to the size of the γ' -particles, no effect on the grain strength is to be expected, which is influenced mainly by the solid-solution hardening. Thus, the results of the tests available do not indicate if and how the grain resistance, having a significant influence on the possibilities of the relaxation crack formation, has an effect. Further precipitations which may build due to the thermo-mechanic stress are carbon nitrides Cr, Mo (C, N), nitrides TiN as well as δ -Phase [8] [9] [12]. For the most part, precipitation hardening occurs by the formation of carbides (Cr, Mo) $_{23}C_6$.

Microstructural changes during the creep process give information about the situation regarding precipitation and the evolution of dislocation structure. These data can be correlated to actual material properties and therefore give information which can be used for the determination of long-term behaviour and damage evolution in new materials. This microstructural evolution of materials is investigated using SEM and TEM analyses. The change of microstructure of the nickel-based alloy 617 is shown in Figure 3

as an example. For three states of a thick walled pipe precipitation characteristics and dislocation density has been determined. The first two states represent the initial state and a creep state after around 10 000 hours for a stress of 110 MPa and a temperature of 750°C. The third state results from a creep test of 26 700 hours at 700°C for a stress level of 140 MPa. The initial state is presenting an average grain size of 51 μm . Precipitates of M_{23}C_6 were detected (see Figure 3) inside the grain but also at the grain boundary. They differ only in their average size (50 nm inside the grain and 250 nm at the boundary). In the received state, no γ' phase (Ni_3Al or Ni_3Ti) could be detected. For the creep damaged specimen, there is a rise in the number of dislocations and subgrains. The average grain size is, for instance, growing from 50 μm (as received state) through 75 μm (after 10 000 hours) to end at a 90 μm level (after 26 700 hours). The dislocation density also rises from $4.0 \cdot 10^9 \text{ cm}^{-2}$ in the initial state to $6.1 \cdot 10^9 \text{ cm}^{-2}$ after 10 000 hours to finally end at $8.2 \cdot 10^9 \text{ cm}^{-2}$ after 26 700 hours of creep test. By systematically analysing the microstructure, some other parameters like precipitation size and number can be extracted. Inside the grain, the M_{23}C_6 grow and the amount of particles increases to a high level after 26 700 hours. At the grain boundary, the number of M_{23}C_6 precipitates after the creep process decreases. At the grain boundary M_6C precipitates have been identified before and after the creep period of 26 700 hours. TEM analyses as described above can be used for qualitative analyses of the material behaviour. A future challenge will be to correlate these findings with quantitative measures with regard to material behaviour and damage development. Such investigations deliver information on the physical mechanisms of creep deformation and damage. Multi-scale modelling approaches and thermodynamical calculations will be used in the near future to determine the macroscopic behaviour on the basis of microstructural findings.

The formation of creep cavities can also be observed for Alloy 617 after long-term creep. In the further damage process inter-granular micro cracks are formed crossing several grain boundaries. Both the grain boundaries on which the cavities are positioned and the micro cracks are orientated towards the maximum principal stress. The temperature and time dependent precipitation behaviour in the microstructure influences the appearance of cracks under creep loading. Lower temperature favours the formation of cracks at the grain boundaries and its coalescence into inter-granular micro cracks. In the case of high mechanical stress the grain boundaries directly crack. Figure 4 shows crack formation in the weld region after high creep stress and short running time. Formation of creep cavities cannot be observed, the grain boundaries cracked in a relatively coarse grain region. Figure 5 shows the macrograph of a long-term strained, broken creep crossweld sample. The crack appeared in the weld metal. The formation of creep cavities could be observed in the base material near the fusion line. The cavities at grain boundaries are perpendicular to the direction of loading.

Figure 3: TEM-analysis of the evolution of precipitations and dislocations during creep in Alloy 617

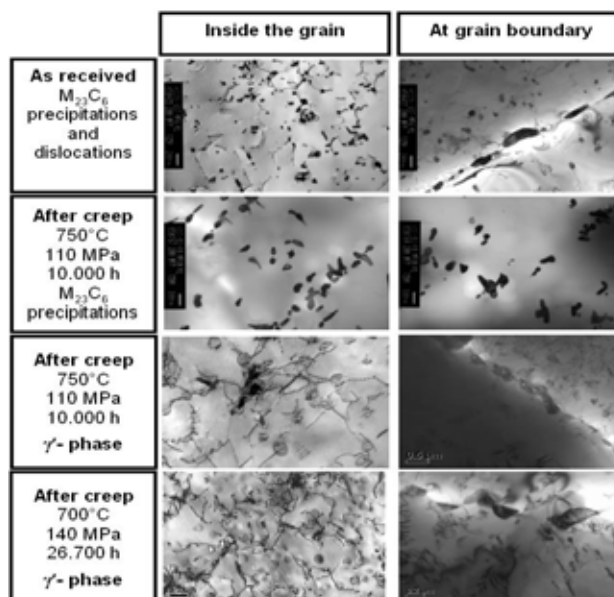


Figure 4: Crack formation after short creep strain

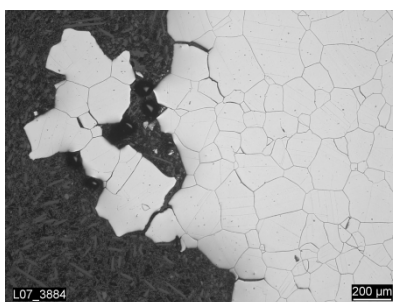
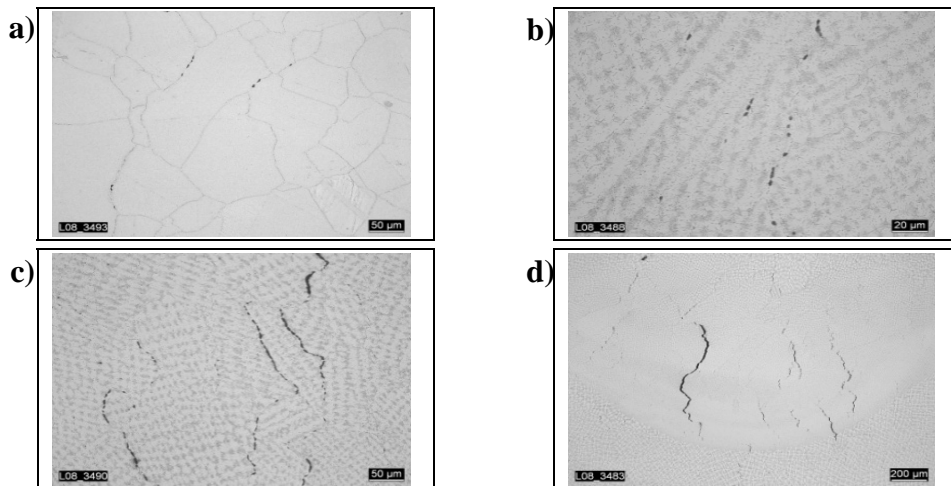


Figure 5: Macrograph of welded joint specimen of Alloy 617, 700°C/26 744 h



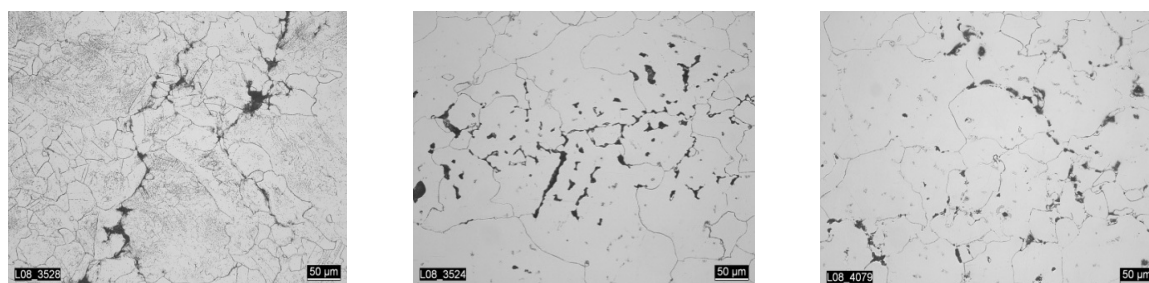
The same mechanism as in base metal can also be observed in Alloy 617 weld metal: interdendritic cavity formation, formation of cavity chains and microcracks, as shown in Figure 6. A strong orientation towards the main direction of stress can be noticed. In this context, it has to be pointed out that a thorough preparation with appropriate etchant is required for the identification of the stadium of the beginning creep damage with creep cavities and short microcracks [13].

Figure 6: Cavity formation in the base material (a) and weld metal (b), (c), (d)



In general, welding may cause problems like hot cracking and different types of relaxation cracking in Ni-based alloys. Therefore, welding processes, especially for thick-walled weldings, have to be defined precisely and must be followed very accurately during the welding process. In order to investigate this behaviour, tensile specimens of Alloy 617 were exposed to a weld simulation at a peak temperature of 1 330°C and a respective cooling down rate in order to create a structure close to the fusion line. After this a hot tensile test with low strain rate 10⁻⁵/s at 700°C was carried out. When reaching a plastic elongation > 5%, the test was stopped. A specimen was subjected to an annealing heat treatment which was proposed and investigated for example in [14] [15] at 980°C/30 min and at 980°C/3 h prior to the tensile test. Longitudinal micrographs were made of all specimens. The occurring crack appearances were illustrated during the tensile test (see Figure 7). In all tests the crack formation orientates to the grain boundaries. The condition of the specimens without stabilising annealing tends to show longer coherent inter-crystalline crack formations. Tests are still underway concerning the changes of the condition of precipitation in the grain and at the grain boundary by annealing.

Figure 7: Crack appearance after tensile-test at 750°C in welding simulated structure, without annealing (left), with annealing at 980°C/0.5h (centre) and at 980°C/3 h (right)



Material data and concepts for design and lifetime evaluation

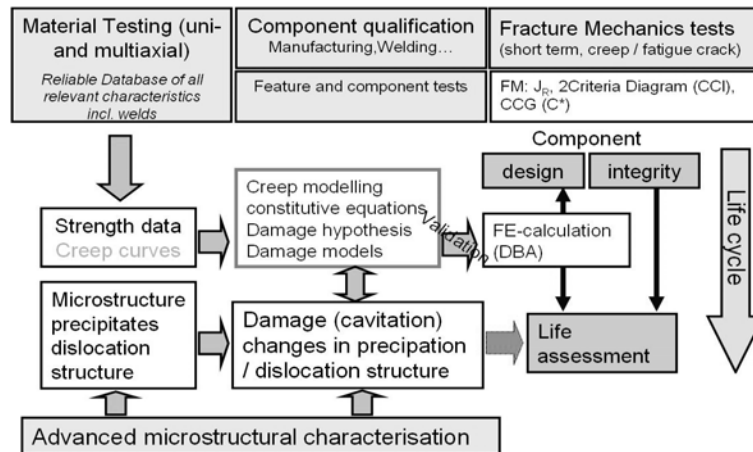
Up to now, components have been designed according to codes and standards, mainly by design by formula (DBF). In order to reduce the cost related to the new nickel-based alloys and an economic and efficient use of other materials, a tailor-made design of components is required. Extended steam conditions would also yield high wall thickness and thick-walled components and piping if they are designed according to currently existing codes and standards. However, in some cases these requirements are contrary to the possibilities of manufacturing. Furthermore, high thermal stresses during start-up and shut-down would have to be taken into account in such components due to high wall thickness. Actual codes and standards do not take into account the inelastic material response (for example the relaxation of secondary stresses). One way to improve the design of new high-temperature components is the use of modern constitutive equations. Indeed, the European Pressure Equipment Directive (PED) or the ASME code allows, for example, the use of design by analysis (DBA). Consequently, finite element method (FEM) can be used to predict the creep and relaxation behaviour of boiler components for 700°C fossil power plants. Since these models are mostly phenomenological, a detailed experimental database is necessary to fit simulation parameters [16].

In the design of high-temperature components for the development of 700°C plants, many aspects still require research efforts (see Figure 8)[17]. In order to use design by analysis, appropriate constitutive equations need firstly to be derived from a large and reliable experimental database to describe the thermo-mechanical behaviour of the investigated materials. Since these equations have to describe the behaviour in multiaxial conditions, experiments under multiaxial conditions such as hollow cylinders are required to quantify the influence of multiaxiality on each material response. In the last few years, a lot of effort has also been put to combine physical aspects of damage with phenomenological constitutive equations. The analysis of the evolution of the microstructure during creep, fatigue or creep-fatigue tests with help of transmission electron or scanning electron microscopy gives hints (e.g. dislocation density, creep pores) for the implementation of mechanistic based damage evolution laws into materials equations.

Another important aspect in the design of 700°C fossil power plants is the consideration of manufacturing; especially properties of weldments have to be considered. Information is needed on material behaviour in the component state including changes due to the manufacturing process. In the case of weldments, two main aspects have to be considered. Firstly, residual stresses coming from the welding process could influence the behaviour. Secondly, heat affected zones need to be taken into account because of their different mechanical behaviour in comparison to the base

material. In order to properly take into account all these aspects, a verification of design and qualification procedures by component tests is necessary.

Figure 8: Representation of a design and assessment concept for new fossil power plants



Last but not least is the aspect of integrity assessment. Creep crack initiation (CCI) and creep crack growth (CCG) assessments need to be quantified both in base materials and welded structures to guarantee the component's reliability. Fracture mechanics tests are then required for the determination of fracture parameters such as the J-Integral (strain energy release rate) and the creep crack parameter C^* . In the following sections, the concept is illustrated through examples covering some of the aspects shown in Figure 8 for the critical components of boilers for the 700°C technology, which are the membrane and furnace walls, the final superheater and reheater stages, boiler tubes (hot sections), in- and outlet headers (hot sections) as well as the thick-walled components, mainly the high-pressure outlet headers and the piping to the turbine. Besides the material qualification for large forgings the dissimilar rotor weld is the most important issue to be considered for the turbine.

Constitutive equations are an essential part of any structural calculations. Depending on the load type and complexity, they differ in their complexity. While in monotonic and low cycle fatigue, some standards based on rate independent models widely used in the industry, modelling the creep behaviour of materials need the introduction of rate dependent laws. Unified viscoplastic equations combine, if complex enough, the global behaviour of a material under a wide range of load type. Nevertheless, such unified models require a huge and precise database to describe qualitatively enough the complete behaviour of a material. Most of the time, this amount of information is not available and the complexity for the model calibration is so high that most authors limit their investigation to a defined purpose. In order to assess the lifetime of components submitted to creep, an incremental constitutive equation covering all creep stages is required. The basic creep equation (see Equation 1) was formulated in the 1950s by Graham and Walles [18].

$$\dot{\varepsilon}_{cr} = A_1 \sigma^{m_1} \varepsilon_{cr}^{m_1} + A_2 \sigma^{m_2} \varepsilon_{cr}^{m_2} + A_3 \sigma^{m_3} \varepsilon_{cr}^{m_3} \quad (1)$$

This creep law was modified and has been successfully used in many R&D projects. In the original formulation, the third creep stage is modelled by introducing a third term. Through the deletion of this third component and the introduction of an effective stress

concept with damage evolution \dot{D} , a good description of the global creep behaviour is ensured. It is advantageous to introduce a parameter able to reproduce the multiaxial stress state. A power law of the quotient of multiaxiality q is then introduced as reported in the modified Graham-Walles creep law in Equation 2.

$$\dot{\varepsilon} = 10^{A1} \cdot \left(\frac{\sigma_{\text{Mises}}}{(1-D)} \right)^{n1} \cdot \varepsilon_{\text{eq}}^{m1} + 10^{A2} \cdot \left(\frac{\sigma_{\text{Mises}}}{(1-D)} \right)^{n2} \cdot \varepsilon_{\text{eq}}^{m2} \quad (2)$$

The damage evolution is defined in Equation 3, where:

$$\dot{D} = 10^{AD1} \cdot \left(\left(\frac{\sqrt{3}}{q} \right)^\alpha \cdot \sigma_{\text{vm}} \right)^{nD1} \cdot \tilde{\varepsilon}^{mD1} + 10^{AD2} \cdot \left(\left(\frac{\sqrt{3}}{q} \right)^\alpha \cdot \sigma_{\text{vm}} \right)^{nD2} \cdot \tilde{\varepsilon}^{mD2} \quad (3)$$

$$\tilde{\varepsilon} = \sqrt{\langle \varepsilon_1 \rangle^2 + \langle \varepsilon_2 \rangle^2 + \langle \varepsilon_3 \rangle^2}; q = \sqrt{\frac{3}{2}} \cdot \frac{\tau_{\text{okt}}}{\sigma_{\text{okt}}} = \frac{1}{\sqrt{3}} \cdot \frac{\sigma_{\text{vm}}}{\sigma_{\text{hyd}}}; \sigma_{\text{hyd}} = \frac{1}{3} \cdot (\sigma_1 + \sigma_2 + \sigma_3)$$

This material model has been used for assessments of Alloy 617 components. The specific material parameters have been determined from creep tests for a variety of melts. Furthermore, to guarantee the transferability of results gained by uniaxial creep tests to real components, the multiaxial state of stress was taken into account. Components in service are indeed exposed to multiaxial loadings. Under such loadings, these components show shorter times to failure for comparable equivalent stresses (Von Mises criterion), as shown in Figure 9 (left). An adequate test to investigate the material behaviour under multiaxial conditions is a creep test using hollow cylinders under internal pressure and axial force. During creep tests involving Alloy 617 cylinders, axial and hoop strains were measured by capacitive high-temperature strain gauges. By using finite element simulations based on the modified constitutive equation presented in the former paragraph, a comparison with experimental results could be done. Simulation results for an internal pressure of 490 bars and temperature of 700°C are presented in Figure 9 (right). The symbols show the experimental hoop strains. The lower graph presents the results of the simulation without considering the quotient of multiaxiality q . Finally, the representation of the simulation with consideration of the quotient of multiaxiality q is in good agreement with the experiment. As expected, the first calculation is well defining the primary and secondary creep stages. In order to describe the global behaviour, i.e. all three creep domains, the introduction of the quotient of multiaxiality was finally required. The calculation result shows the good fit in the tertiary domain by imposing α to 0.3. In the design of high efficiency power plants working up to 700°C, nickel-based alloys are required to ensure a certain creep resistance. Because such alloys are very costly, these materials cannot be used for the all components of the plant. Indeed, ferritic/martensitic (Fe/Ma) steels are still used in components where the temperature is limited to 600°C. These elements need then to be welded to nickel-based alloys. That is why dissimilar welds must also be investigated (see Figure 10 for the welding of Fe/Ma steel – Alloy 617).

In that case, the difference in the expansion coefficient influences the creep behaviour of the welding. In the same way as presented for similar welds, creep calculations have been performed to determine the location of maximal stresses. Metallographic investigations confirm that the specimen failure zone is located in the intercritical zone (HAZ 3 in Figure 10).

Figure 9: Effect of a multiaxial state of stress on the creep behaviour (left), measured hoop strains of an Alloy 617 hollow cylinder compared with simulated results (right)

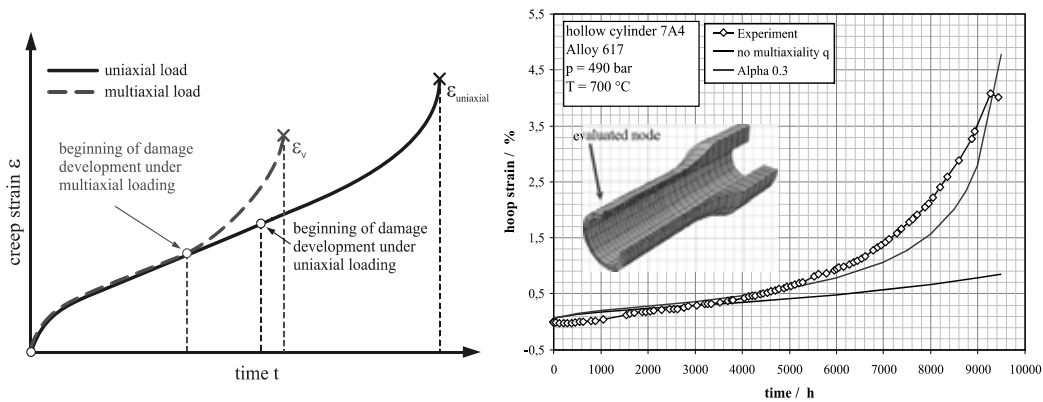
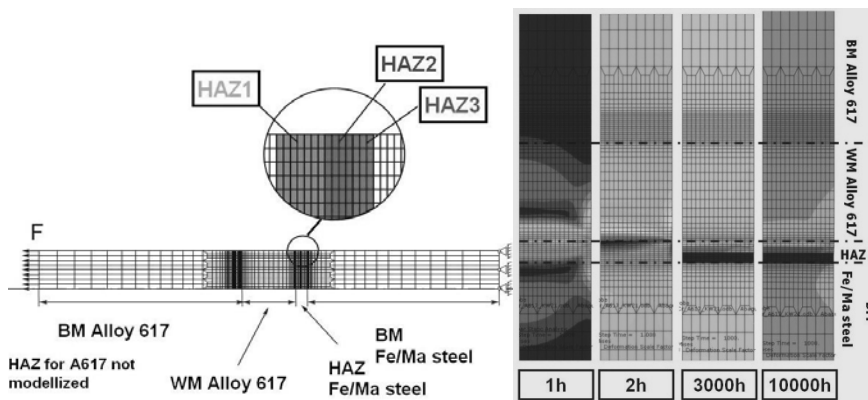


Figure 10: Geometrical model of a weld Fe/Ma steel – Alloy 617 with modelling of the heat-affected zones in the ferritic-martensitic steel and equivalent stress repartition in a cross-weld specimen of a weld Fe/Ma steel – Alloy 617 with HAZ



Summary and conclusions

Based on experience with the developments for high-temperature reactors, results from field tests and a couple of research projects and the development of power plants with 700°C technology are well underway. Design and material needs are described and the requirements for all materials used are outlined. Extensive qualification programmes are underway and with the first results producibility and weldability of the components made of Ni-based alloys could be demonstrated. Thanks to good mechanical properties and oxidation resistance, Alloy 617 has great potential to be applied at operating temperatures over 700°C as components like pipes, membrane walls etc. Investigations and improvements in creep behaviour, manufacturability and component design for this Ni-based alloy will be presented. Special emphasis must be placed on the special characteristic of the material by designing and applying welding procedures. For a reliable description of the long-term behaviour tests, it is necessary to take into account these special characteristics. Knowledge about material behaviour and properties in the manufactured state, i.e. in thick-walled components and in welded joints is necessary. New approaches in design for this material demand knowledge of the inelastic behaviour.

Modern numerical tools are used for more extensive assessments of the material behaviour in life time assessments. Multiaxial behaviour is also taken into account by these methods. In order to get good results with these inelastic approaches, good data bases of uniaxial and multiaxial creep tests as well as creep experiments on welds are required. In order to open a new scope of modelling, TEM and SEM analyses were used to evaluate the evolution of damage by microstructural changes. Damage mechanisms have been analysed. These investigations open the way for future multi-scale simulations taking as input, for example, parameters like dislocation density or precipitates size and number.

Acknowledgements

Some of the results reported in this paper were obtained in projects supported by the AVIF (*Forschungsvereinigung der Arbeitsgemeinschaft der Eisen und Metall verarbeitenden Industrie e.V.*) under contract number A130 and A215 and by the Federal Ministry for Economy and Technology (BMWi) under contracts No 0326894 and 0327754B. This support is acknowledged. Thanks are due to the steering committee members of these projects.

References

- [1] Auslegungskriterien für hochtemperaturbelastete metallische und keramische Komponenten zukünftiger HTR-Anlagen- Teil B (1988), Metallische Komponenten, Research project KFA Jülich, Final Report.
- [2] New pipe materials for steam generators with high efficiency (>50%), (2004), MARCKO-DE2, Final Report, AVIF-A130, BMWi 326894, MPA Stuttgart.
- [3] R. U. Husemann, A. Helmrich, J. Heinemann, A. Klenk and K. Maile (2004), Applicability of Ni-based welding consumables for boiler tubes and piping in the temperature range up to 720°C, 4th Int. Conf. On Advances in Materials Technology for Fossil Power Plants.
- [4] Husemann R.-U, K. Schmidt, A. Klenk, K. Maile and E. Roos (2009), MARCKO 700 Untersuchung von Werkstoffen für das 700°C-Kraftwerk, 32. VV Langzeitverhalten warmfester Stähle, Düsseldorf.
- [5] K. Maile, E. Roos, A. Klenk: Qualifizierung von Hochleistungswerkstoffen für das 700°C-Kraftwerk im Rahmen der Coorettec-Initiative (2007), 30. VV Langzeitverhalten warmfester Stähle, Düsseldorf.
- [6] ThyssenKrupp VDM- Werkstoffdatenblatt (2005), Nr. 4119, Nicrofer 5520Co – Alloy 617
- [7] VdTÜV-Blatt 485: Hochwarmfeste Nickelbasislegierung NiCr23Co12Mo, Werkstoff-No.2.4663 (2001).
- [8] Kirchhöfer, H.: Untersuchungen zum isothermen Ausscheidungsverhalten von Nickelbasislegierungen mit Hilfe der Elektrochemischen Phasenisolierung, Dissertation, RWTH Aachen (1983).
- [9] K. Rao, H. Schiffers, H. Schuster, and H. Nickel (1988), Influence of Time and Temperature De-pendent on Strain Controlled Low Cycle Fatigue Behavior of Alloy 617, Metallurgical Transaction A, 19 A, 359.
- [10] W. L. Mankins, J. C. Hosier and T. H Bassford (1974), Microstructure and Phase of INCONEL Alloy 617 Stability, Metallurgical Transactions, 5, 2579.
- [11] Q. Wu, V. K. Vasudevan, J. P. Shingledecker and R.W. Swindeman (2005), Microstructural Characterization of Advanced Boiler Materials for Ultra Supercritical Coal Power Plants, *Proceedings to the Fourth International Conference on Advances in Materials Technology for Fossil Power Plants.*

- [12] M. Cabbibo et al. (2008), Creep applications of INCOLOY alloy 617, *Journ. Of Mat. Sc.*, 43, 2912.
- [13] K. Maile, R. Scheck, G. Lüdenbach, P. Körner (2008), Ambulante Bauteil-Metallographie an der Nickelbasislegierung Alloy 617. 42. Materialographie-Tagung, Jena.
- [14] H. van Wortel (2007), Control of Relaxation Cracking in austenitic High Temperature Components, *Proc. Corrosion*, NACE International, Nashville.
- [15] R.U Husemann, M. Bader, J. Klöwer (2010), Metallurgical Aspects during Manufacturing of Alloy 617B, 8th Int. NIMS-MPA-IfW-Workshop on Advances In High Temperature Materials for High Efficiency Power Plants, Tsukuba.
- [16] M. Speicher, A. Klenk, K. Maile, E. Roos (2009), Investigations on advanced materials for 700°C steam power plant components, 3rd Symp.on Heat Resistant Steels and Alloys for High Efficiency USC Power Plants Tsukuba, Japan.
- [17] K. Schmidt, C. Feuillette, K. Maile, A. Klenk, E. Roos (2010), New Concepts for Integrity and Lifetime Assessment of Boiler and Turbine Components for Advanced Ultra-Supercritical Fossil Plants, 4, 5th Int. Conf. on Advances in materials for EPRI.
- [18] Graham, A. and K. F. A. Wallis (1955), Relationships between Long-and Short-Time Creep and Tensile Properties of a Commercial Alloy, *Journal of The Iron and Steel Institute*, Vol. 179, pp. 104-121.

Fracture toughness of two advanced structural alloys*

M.A. Sokolov

Oak Ridge National Laboratory, United States

Abstract

Fracture toughness and tensile properties of two advanced structural alloys were characterised in a wide temperature range from room temperature to 650°C. These two alloys are the candidates of high-temperature structural materials in the next generation nuclear systems. The HT-UPS (high-temperature ultrafine precipitate strengthened) austenitic stainless steel with Fe-14Cr-16Ni (wt%) base composition exhibits superior creep strength compared to the advance austenitic stainless. A columnar shape cast ingot of 4 in. (102 mm) diameter and 5 in. (127 mm) length was hot-forged and hot-rolled at 1 200°C, which resulted in a plate sample with the size of 0.8 x 0.5 x 16 in (20x12.7x407 mm). The plate showed uniform solutionised microstructure with an average grain size of around 100 µm, together with a lot of TiN dispersions with less than 5 µm size which was introduced during the solidification process. As a result, tensile tests did not reveal any significant differences for specimens in the rolling and transverse directions. Another candidate alloy in this study was the ferritic-martensitic steel NF616 (9Cr-1.8WNbV). Both alloys exhibited considerable fracture toughness to 650°C. Additionally, thermo-mechanical treatment is being developed on the as-received NF616. Preliminary results of Vickers microhardness and tensile tests showed enhancement in microhardness, strength and ductility compared to the as-received NF616. Microstructural characterisation is being performed to explain the properties enhancement induced by the thermo-mechanical treatment.

* The full paper being unavailable at the time of publication, only the abstract is included.

High-temperature fracture toughness of Inconel 617*

R.K. Nanstad¹, M.A. Sokolov¹, R.N. Wright²

¹Oak Ridge National Laboratory, United States, ²Idaho National Laboratory, United States

Abstract

The expected service life of the Next Generation Nuclear Plant (NGNP) is 60 years. Based on technical maturity, availability in required product forms, experience base, and high-temperature mechanical properties, preconceptual design studies have specified Alloy 617 as the material of choice for heat exchangers. Structural analyses of the intermediate heat exchanger will require knowledge of the properties of Alloy 617 as a consequence of thermal ageing effects due to long time exposure at high temperatures. One of the properties of interest is fracture toughness and although there are no fracture toughness data for thermally aged Alloy 617, there are Charpy impact data that show a significant loss of toughness in Alloy 617 after long-term exposure at high temperatures. The programme plan incorporates thermal ageing of both base metals and welds at 750 and 1 000°C and for times from 200 to 120 000 hours, followed by fracture toughness testing to evaluate the effects of ageing on the J-integral resistance (J-R) behaviour. In this paper, fracture toughness test results of unaged base metal and welds with 0.5 T and/or 0.8 T compact specimens [0.5 TC (T) and 0.8 TC (T)] at various temperatures from room temperature to 950°C are described. Charpy impact tests have also been performed to enable direct comparisons with data in the literature and to provide data for potential correlations between Charpy impact toughness and fracture toughness for the thermally aged materials. Additionally, microstructural and fractographic evaluations have been performed with the unaged specimens and will be performed for specimens tested in the aged conditions as well.

* The full paper being unavailable at the time of publication, only the abstract is included.

Oxidation behaviour of Alloy 617 during ageing at various temperatures*

Young Do Kim¹, Tae Sun Jo¹, Jeong Hun Lim¹, Ji Yeon Park²

¹Division of Materials Science and Engineering, Hanyang University, Republic of Korea

²Nuclear Materials Research and Engineering, Korea Atomic Energy Research Institute, Republic of Korea

Abstract

As a wrought Ni-based superalloy, Alloy 617 (Ni-22.6Cr-9.53Mo-13.1Co-1.07Al-0.4Ti-0.09C, wt.%) is a solid-solution strengthened alloy which shows excellent strength, creep-rupture strength, stability and oxidation resistance at high temperatures. This alloy is a candidate tube material of intermediate heat exchanger (IHX) and hot gas duct (HGD) in VHTRs for H₂ production, under severe operating conditions of pressures over 8 MPa and temperatures over 950°C in He gas with some impurities (H₂, H₂O, CO, CO₂, and CH₄ etc.). This work studied the oxidation behaviour of Alloy 617 by exposure at 900°C, 950°C, 1 000°C and 1 050°C in air and He atmosphere and discussed the behaviour of high-temperature degradation in detail with microstructural changes during the surface oxidation. The specimens for oxidation test were machined to an appropriate size (12 x 5 x 9 mm³). The samples for microstructural observation were prepared by chemical etching with HCl (100 ml), C₂H₅OH (100 ml) and CuCl₂ (5 g). The oxidation behaviour of each sample was observed by scanning electron microscopy (SEM). The chemical composition of the oxide layer was analysed by an electron probe micro-analyser (EPMA). The degree of oxidation during ageing at high temperature was evaluated by the Cr-depleted zone and the carbide free zone. The Cr-depleted zone was estimated by concentration profiles of Cr element from surface to matrix. The carbide free zone was estimated by the dissolution region of carbides on grain boundary. The oxide layer can be distinguished as two regions for both environments; the external oxide scale on the surface and internal oxide on the grain boundaries. The external oxide layer was confirmed to be Cr₂O₃ and the internal oxide was confirmed to be Al₂O₃ along the grain boundary. The Cr-depleted zone was formed below the external oxide layer due to the formation of Cr₂O₃. During the ageing, carbides on grain boundary were dissolved in the matrix. A carbide free zone was observed in the Cr-depleted zone. Vickers hardness in the region of the Cr-depleted zone and the carbide free zone was lower than that of the matrix due to depletion of the alloying element. The depth of the carbide free zone increased with exposure time. Also, the depth of the carbide free zone at relatively low temperatures was formed similar to both environments. However, as the ageing temperature increased, the depth of the carbide free zone in air environment was higher than that in He environment.

* The full paper being unavailable at the time of publication, only the abstract is included.

Session II

Ceramics-composite

Chairs: C. Fazio, W.J. Kim

Development of SiC_f/SiC composite for innovative structural materials

Ji Yeon Park, Weon Ju Kim

Korea Atomic Energy Research Institute, Daejeon, Republic of Korea

Abstract

To improve the matrix filling behaviours and the strength of SiC_f/SiC composite, the whisker growing assisted CVI (WA-CVI) and a hybrid of slurry infiltration and hot-pressing (HP) process were developed by KAERI. To get a similar density of 2.65~2.8 g/cm³, the processing time of the WA-CVI process was 13 ± 3 h and that of the conventional CVI process was 24 ± 8 h. The flexural and tensile strength of WA-CVI composite were 600~701 MPa and 286 MPa and those of CVI composite were 498~521 MPa and 232 MPa, respectively. These suggested the intentionally grown whiskers acted as the new deposition sites for matrix filling and additional reinforcement of the matrix. The porosity of a hybrid of slurry impregnation and hot pressed SiC_f/SiC composite was less than 1%, while a degradation of the interphase was observed.

Introduction

Some components of next generation nuclear energy systems – VHTR, GFR and the fusion reactor – are subject to high temperature, rather high irradiation fluence and slightly oxidising environments under normal operating conditions. These extreme conditions lead to the choice of ceramic matrix composites (CMC, like C_f/C, C_f/SiC or SiC_f/SiC) as potential materials for these components. Among them, the SiC_f/SiC composite has potential advantages for structural applications due to their unique properties such as good irradiation resistance and thermo-mechanical properties, less severe waste generation due to neutron activation and improved plant conversion efficiencies by higher operating temperatures [1] [2]. Therefore, SiC_f/SiC composite is being considered as control rod components and core internals for VHTR, fuel clad for GFR and blanket structures for fusion reactor [2] [3]. Generally, CMC are flexible materials that can be tailored for each application to meet design requirements. There are many fabrication parameters to be adjusted depending on requirements and the geometry of the parts [4].

Several processing methods for SiC_f/SiC composites have been suggested: chemical vapour infiltration (CVI) [5], polymer impregnation and pyrolysis (PIP) [6], reaction sintering (RS) [7], slurry impregnation and hot pressing (nano-infiltrated transient eutectoid process: NITE) [8], etc. The CVI process is an effective method which can produce a high-quality SiC matrix [5]. The conventional CVI process, however, takes a long processing time to make a sound composite with a high density. In fact, the composites by the conventional CVI process have large pores in the inter-bundle/inter-laminar regions, which cause a degradation of the mechanical and thermal performances of SiC_f/SiC composites. We developed the “whisker growing process”, in which SiC deposits with high aspect ratios such as whiskers and nanowires are introduced into the fiber preform before the matrix infiltration step, results in composites with a lower porosity and an uniform distribution of the pores when compared with the conventional CVI [9-11]. The slurry impregnation and hot pressing process is an effective method to make a dense SiC_f/SiC composite [5] [12]. Instead of vacuum impregnation, we applied the electrophoretic deposition (EPD) method with an ultrasonification for slurry impregnation [13].

In this paper, the current status of development of SiC_f/SiC composites for innovative structural applications in KAERI will be reviewed focusing on different fabrication technologies and evaluations of their mechanical properties.

Experimental

Composites were prepared by different fabrication processes such as the conventional chemical vapour infiltration (CVI), the whisker growing assisted CVI (WA-CVI) and a hybrid of slurry infiltration and hot-pressing (HP) process.

In the conventional CVI and WA-CVI process, disk-shaped fabrics with a diameter of 50 mm were punched out from a plain weave Tyranno-SA™ SiC fabric (Ube Industries, Japan). The preforms were prepared by pyrolytic carbon (PyC) coating on SiC fibers. The PyC interlayer with a thickness of 150-200 nm was coated on the fibers and/or whiskers surface by a decomposition of methane (CH₄) for 180 min at 1 100°C. Methyltrichlorosilane (MTS, CH₃SiCl₃, 99%, Aldrich Chemical Co. Ltd.) was used as a source precursor for the matrix filling. Purified H₂ was used as both a carrier and a diluent gas. The matrix infiltration process was performed at 1 000°C for various times with the input gas ratio ($\alpha = F_{\text{(diluent+carrier gas)}}/F_{\text{MTS}}$) of 10 and the system pressure of 6.3–13.3 kPa. In the WA-CVI process, the SiC whiskers were grown into the fiber preform before matrix filling. The growth of the SiC whiskers was carried out at 1 100–1 150°C under a total pressure of 0.74 kPa. The input gas ratio of H₂ to MTS was 60 and the total flow rate was 800 sccm. For reinforcement of the matrix, the PyC coating on SiC whiskers was also tried.

In a hybrid of slurry infiltration and hot-pressing (HP) process, nano-sized β -SiC ($D_m=52$ nm, 97.5% pure, 620KE, Nano-Amor Inc., United States) and 12 wt% of an $Al_2O_3:Y_2O_3:MgO$ mixture at a weight ratio of 6.4:2.6:1.0 were used as the matrix phase and sintering additive, respectively. Two-dimensionally woven Tyranno™-SA fabrics were used as reinforcements after being coated with different thicknesses of PyC and/or SiC layers through the same deposition conditions in the CVI process. After dissolving the PVB resin in a solvent, slurries were synthesised by adding the SiC powder containing the sintering additive and 20 wt% of a polyester/polyamine co-polymeric dispersant (Hypermer KD1, ICI, UK) to the binder solution. The slurries were ball-milled for 36 h using 6 mm SiC balls. Two types of impregnation methods were applied for slurry impregnation into the preform; vacuum impregnation and electrophoretic deposition (EPD). The EPD was performed using a disc-shaped SiC fabric sample by dipping into the slurry under an applied voltage of 135 V for ten minutes. A dual electrode system was used for efficient infiltration from both sides. The anode and cathode were varied according to the sign of the zeta potential of the slurry used because SiC particles move to the electrode with an opposite charge. After drying the infiltrated fabrics at 70°C for 3 h, 15 layers of the infiltrated fabrics were stacked with a fabric layer orientation of 0°/90° and laminated uniaxially under a pressure of 10 MPa at 80°C. Hot pressing was carried out at 1750°C in an Ar atmosphere under the pressure of 15~20 MPa.

The microstructural examination was carried out using a scanning electron microscopy (SEM, JS-5200, Jeol, Japan) at 20 KeV and a transmission electron microscopy (JEM-2000FX, JEOL, Japan) operated at 200 KeV. The FIB milling system was used for preparing the TEM samples. The mechanical properties such as flexural and tensile strength were measured and the fracture behaviours were also analysed.

Results and discussion

Figure 1 shows the microstructure of SiC_f/SiC composite in the intermediate stage of the CVI prepared by the conventional CVI and the WA-CVI, respectively. As shown in Figure 1 (b), the SiC whiskers (arrow marks) were grown in the void between fibers by the WA-CVI. The SiC whiskers were also observed in the void between SiC bundles. These SiC whiskers within the fiber preform increased the surface area for the SiC deposition and reduced the void size between fibers or bundles. Therefore, the efficiency of the matrix filling was increased and resulted in a higher density with a shorter CVI time. The remaining pore size of the composites was also decreased.

Figure 1: Microstructure of SiC_f/SiC composite prepared by the conventional CVI (a) and the WA-CVI (b)

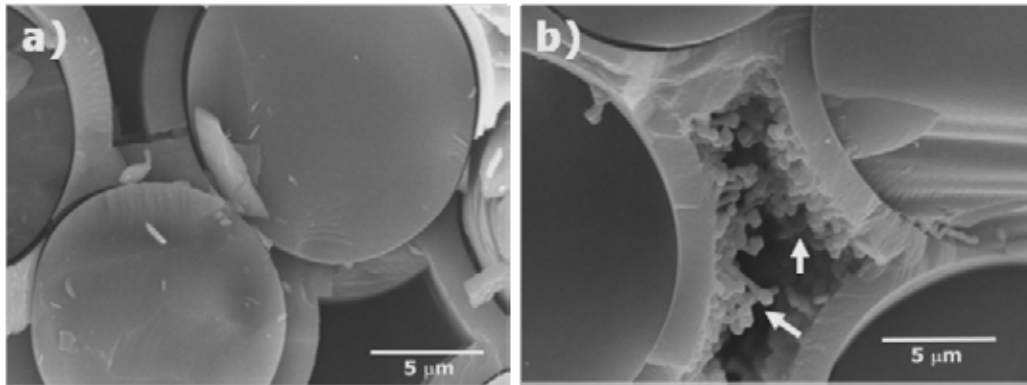


Figure 2 shows the microstructures of the matrix phase of SiC_f/SiC composite by different fabrication processes. While fine columnar SiC grains with radial growth direction (Figure 2 a) were observed in conventional CVI composite, fine columnar and equiaxed (showing black dots and arrow marks) grains were observed in the WA-CVI composite, as shown in Figure 2 b. The fine equiaxed grains were the whiskers which were intentionally grown before the matrix filling process. The incorporation of the SiC whiskers into the SiC matrix would increase the fracture toughness and flexural strength of the SiC_f/SiC composites. On the other hand, the matrix phase of slurry impregnated and hot pressed SiC_f/SiC composite showed the same microstructure with sintered SiC (Figure 2 c).

Figure 2: Microstructures of the matrix in SiC_f/SiC composite prepared by different process: (a) conventional CVI, (b) WA-CVI and (c) hybrid of slurry impregnation and hot press

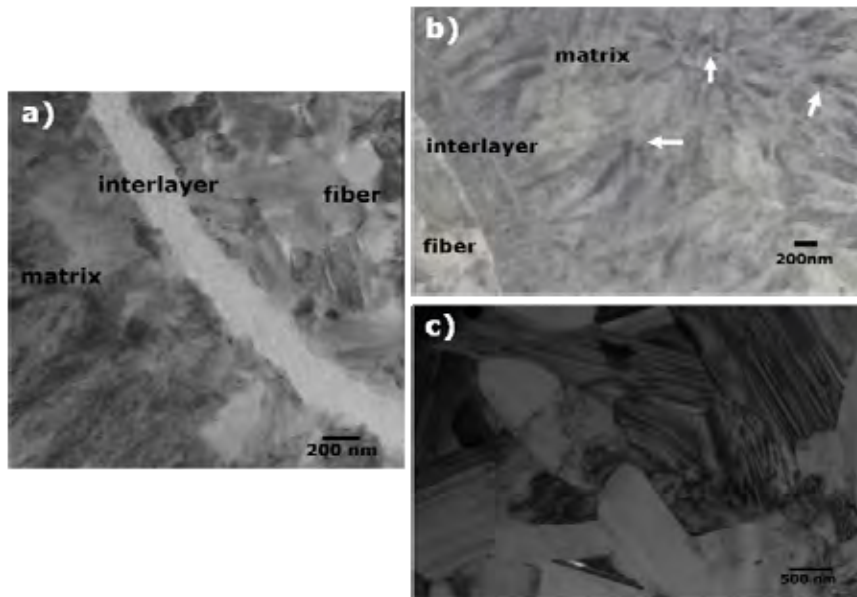
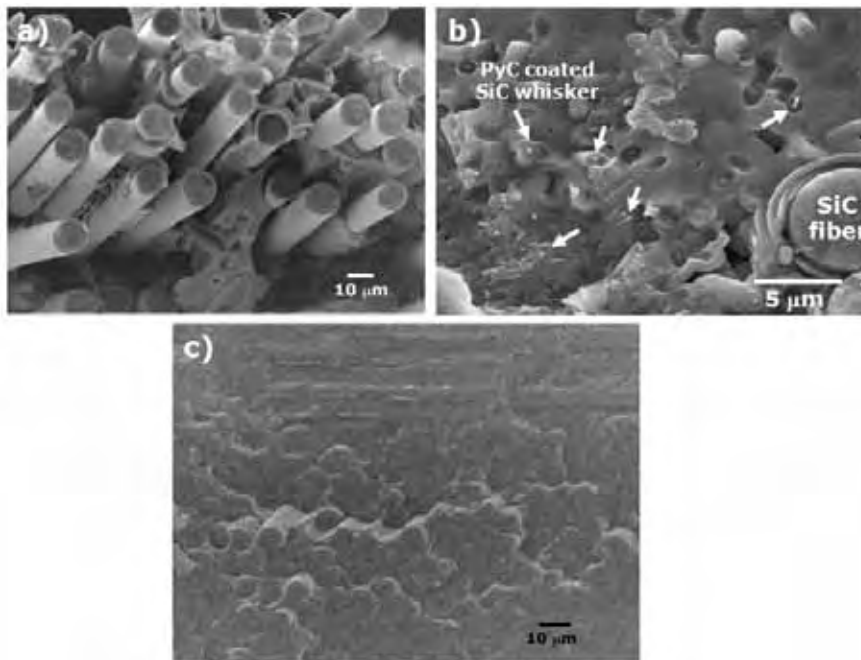


Figure 3: Fracture surface of SiC_f/SiC composite by different fabrication processes: (a) WA-CVI, (b) WA-CVI with PyC coated SiC whisker and (c) hybrid of slurry impregnation and hot press



The fracture surface of SiC_f/SiC composites by different fabrication processes was also observed. Figure 3 (a) is the microstructure of the fracture surface of WA-CVI composite which shows the pull-out behaviour of the SiC fibers. Figure 3 (b) shows the fracture surface of SiC_f/SiC composite prepared by the WA-CVI with PyC coating process. White particles (arrow marks) were the pulled-out PyC coated whiskers and voids with circular or rectangular shape seem to be traces of the completely pulled-out PyC coated whiskers. The PyC coated whiskers can improve the fracture toughness of SiC_f/SiC composite, which resulted in the additional crack deflection around PyC layers coated on the whiskers and pull-out of the PyC coated whiskers. Figure 3 (c) shows the fracture surface of slurry impregnated and hot pressed SiC_f/SiC composite. The fracture of hot pressed SiC_f/SiC composite proceeded with brittle mode, which seemed to have resulted from a degradation of the PyC interphase during hot pressing.

In Table 1, some properties of SiC_f/SiC composite prepared by different fabrication processes are summarised. Compared with the processing time for the CVI process, the WA-CVI processing time was the shortest to get a similar density and the flexural strength and the tensile strength is the strongest. This suggests the intentionally grown whiskers acted as the new deposition sites for matrix filling and additional reinforcement of the matrix. The density of hot pressed composites was near theoretical density but their flexural strength was relatively low. In order to improve the strength of hot pressed composite, a further study on the fine control of the interphase will be carried out.

Table 1: Properties of SiC_f/SiC composite prepared by different processes

Process	Density (g/cm ³ , Max.)	Flexural strength (MPa, Max.)	Tensile strength (MPa)	PLS (σ_0 , MPa)	Processing time (h)
Conventional CVI	2.65-2.7	498-521	232	143	24 ± 8
WA-CVI	2.65-2.8	600-701	286	232	13 ± 3
WA-CVI with PyC	2.64-2.73	562	261	211	15 ± 5
Hybrid of slurry impregnation and hot press	3.1-3.13	340-530	-	-	-

Summary

SiC_f/SiC composites were fabricated by four different processes – the conventional chemical vapour infiltration (CVI), whisker growing assisted CVI (WA-CVI), WA-CVI with PyC coating, as well as a hybrid of slurry impregnation and hot press. The matrix densification behaviour was effectively improved by whisker growth before matrix filling in the CVI process. To get a similar density of 2.65~2.8 g/cm³, the processing time of the WA-CVI process was 13 ± 3 h and that of the CVI process was 24 ± 8 h. The flexural and tensile strength of WA-CVI composite was higher than that of the CVI composite. A hybrid of slurry impregnation and hot press was an effective method to make a high dense composite with a porosity less than 1%. However, a degradation of the interphase during hot pressing took place and fractured with a brittle mode.

Acknowledgements

This work was supported by the National Research Foundation of the Republic of Korea (NRF) grant funded by the Korean government (MEST). The authors would like to express their gratitude to Professor Dang Hyok Yoon, Dr. Seok Min Kang and Mr. Myeong Hoon Jung for their technical support.

References

- [1] T. Nozawa, T. Hinoki, A. Hasegawa, A. Kohyama, Y. Katoh, L.L. Snead, C.H. Henager Jr., J.B.J. Hegeman (2009), *J. Nucl. Mater.* 386–388; 622.
- [2] W.R. Corwin (2009), *Proceedings of GIF Symposium*, pp 131, Paris, France, 9-10 September 2009.
- [3] L. Brunel, N. Chauvin, T. Mizuno, M.A. Pouchon and J. Somers (2009), *Proceedings of GIF Symposium*, pp 135, Paris, France, 9-10 September, 2009.
- [4] A. Kelly, C. Zweben (2000), *Comprehensive composite materials*, Elsevier.
- [5] T.M. Besmann, B.W. Sheldon, R.A. Lowden, D.P. Stinton (1991), *Science Vol.* 253. 1104.
- [6] M. Kotani, Y. Katoh, A. Kohyama (2002), *Ceram. Trans.*, Vol. 144, 97.
- [7] S.P. Lee, Y. Katoh, J.S. Park, S. Dong, A. Kohyama, S. Suyama and H.K. Yoon (2001), *J. Nucl. Mater.* 289. 30.
- [8] Y. Katoh, S.M. Dong and A. Kohyama (2002), *Fusion Eng. Design*, 61-62. 723.
- [9] B.J. Oh, Y.J. Lee, D.J. Choi, G.W. Hong, J.Y. Park and W.-J. Kim (2001), *J. Am. Ceram. Soc.* Vol. 84. 245.

- [10] S.M. Kang, J.Y. Park, W.-J. Kim, S.G. Yoon and W.-S. Ryu (2004), *J. Nucl. Mater.* Vol. 329–333. 530.
- [11] W.-J. Kim, S. M. Kang, C. H. Jung, J.Y. Park, W.-S. Ryu, *J. Crystal Growth* (2007), 300. 503.
- [12] K.-Y. Lim., D.-H. Jang, Y.-W. Kim, J. Y. Park, and D.-S. Park (2008), *Metals and Mater. Int.*, 14[5]. 589.
- [13] J.H. Lee, G.Y. Gil and D.H. Yoon (2009), *J. Kor. Ceram. Soc.*, 46[5]. 447.

Irradiation-induced property change of C/C composite for application of control rod elements of very-high-temperature reactor (VHTR)

Taiju Shibata¹, Junya Sumita¹, Kazuhiro Sawa¹,
Takashi Takagi², Taiyo Makita³, Eiji Kunimoto⁴

¹Japan Atomic Energy Agency, Japan; ²IBIDEN Co. Ltd., Japan

³Tokai Carbon Co. Ltd., Japan; ⁴Toyo Tanso Co. Ltd., Japan

Abstract

The high-temperature gas-cooled reactor (HTGR) is an attractive nuclear reactor to obtain high-temperature helium gas about 950°C at reactor outlet. The very-high-temperature reactor (VHTR) is one of the Generation IV reactor systems being focused and developed internationally. Since the core components in the VHTR will be used at severe temperature conditions, it is important to develop heat-resistant ceramic composite materials. Carbon fiber reinforced carbon matrix composite (C/C composite) is a major candidate material and its application for control rod elements is one of the important subjects for the VHTR development.

JAEA (Japan Atomic Energy Agency) is carrying out an application study on two-dimensional (2D-) C/C composite to the control rod. Since the 2D-C/C has great anisotropy in thermal and mechanical properties in parallel and perpendicular lamina directions, it is important to consider the anisotropy for control rod design.

In this study, a PAN-based and plain-woven 2D-C/C composite, CX-270G grade (Toyo Tanso Co.), was used to evaluate the change of material properties for each direction by neutron irradiation. It is graphitised at 2 800°C in its manufacturing process. The samples were irradiated at O3M-47AS capsule by JMTR of JAEA at 600°C up to the neutron fluence of 8.2×10^{24} n/m² (E>1.0MeV) corresponding to 1.2 dpa (displacements per atom). The irradiation-induced dimensional change, thermal conductivity, coefficient of thermal expansion and Young's modulus were evaluated through post-irradiation examination. The test results were evaluated in comparison with the irradiation database of JAEA's graphite material. It was shown that the graphite material database can be used to support the evaluation of the irradiation test results of the graphitised C/C composite.

Introduction

The high-temperature gas-cooled reactor (HTGR), graphite-moderated and helium gas-cooled, is an attractive nuclear reactor to obtain high-temperature helium gas of about 950°C at reactor outlet. It is possible to utilise the high-temperature helium gas not only for power generation but also for process heat source in a hydrogen production system [1] [2]. Its inherent and passive safety feature is also attractive. The HTGR shows slow temperature change behaviour under accident conditions due to graphite components with large heat capacity in the core. Japan Atomic Energy Agency (JAEA) developed the high-temperature engineering test reactor (HTTR), which is a test reactor and the first HTGR in Japan [3]. It was demonstrated that the HTTR can produce high-temperature helium gas about 950 °C to the reactor outlet at high temperature operation mode. A long-term high-temperature operation test, 50 days continuous operation with the outlet temperature of 950°C, was successfully carried out in 2010. Valuable data about fuel performance, reactor physics, impurities in primary helium gas, etc. were obtained throughout the test.

The very-high-temperature reactor (VHTR) is a promising candidate for the Generation IV nuclear energy systems. An international collaboration has been carried out through the Generation IV International Forum (GIF) [4]. As for commercial HTGR/VHTR projects for individual countries, the United States focuses on the next generation nuclear plant (NGNP) and China has started the construction of high-temperature reactor – pebble bed module (HTR-PM). The design of pebble bed modular reactors (PBMR) in South Africa has been discussed. The Nuclear Hydrogen Development and Demonstration (NHDD) has been studied in the Republic of Korea. JAEA has also carried out R&D on the design of an original VHTR based on the technologies established through the HTTR construction and operation. JAEA's design is for a prismatic block type reactor, gas turbine high-temperature reactor 300-cogeneration (GTHTR-300C) [5] [6]. It can generate electricity and produce hydrogen by a thermochemical hydrogen production cycle, the IS (iodine-sulphur) process.

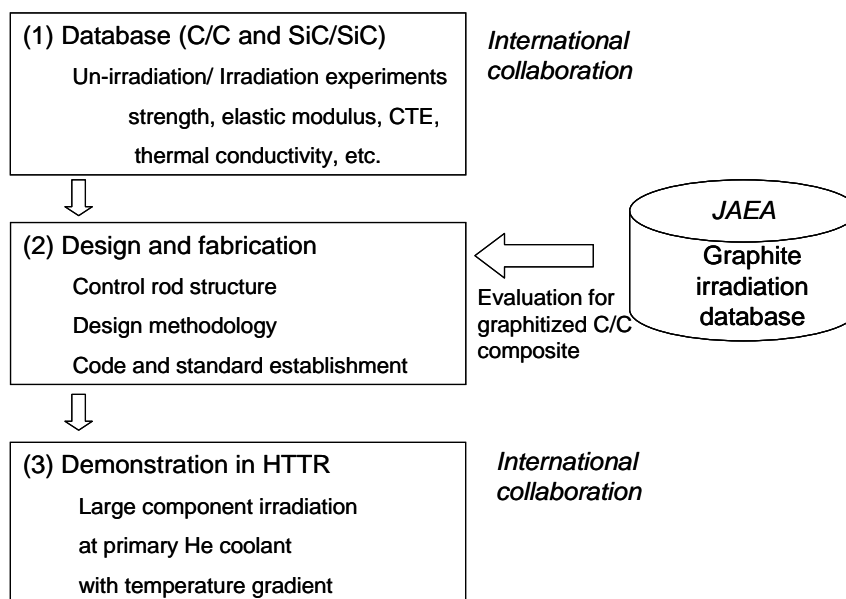
The application of ceramics composite materials to the control rod is one of the important subjects for the VHTR development. For the HTTR, ferritic superalloy Alloy 800H is used for the metal parts of the control rod [7]. Its maximum allowable temperature to be used repeatedly after scrams is 900 °C. On the other hand, for the VHTR, it is important to develop heat-resistant ceramic composite material substitute for metallic materials, since the core components in the VHTR will be used at more severe conditions than in the HTTR. The heat-resistant ceramic composite, carbon fiber reinforced carbon matrix composite (C/C composite) and SiC fiber reinforced SiC matrix composite (SiC/SiC composite) are major candidate materials substitute for the metallic materials of the control rod to use higher temperature.

JAEA focuses especially on a two-dimensional C/C composite (2D-C/C composite) which has the layer structure of laminas composed of fibers and matrix [8]. Since the 2D-C/C composite has great anisotropy in thermal and mechanical properties in parallel and vertical to lamina directions, it is important to consider the anisotropy for the components design. Neutron irradiation effects on the properties are also anisotropic and important. On the other hand, JAEA has an irradiation database on graphite materials. It is expected to use this database to support the evaluation on the irradiation effects on C/C composite material. This paper includes the R&D plan of the composite control rod development. The test results and the irradiation effects on the C/C composite have been also discussed.

R&Ds for control rod element with C/C composite

JAEA studies on the application of composite materials for the control rod of VHTR [8]. The scheme of the control rod element development consists of the following phases: (1) database establishment, (2) design and fabrication, and (3) demonstration test by HTTR. The scheme of the R&Ds is shown in Figure 1.

Figure 1: Scheme of R&Ds for C/C composite control rod



For the database establishment in phase (1), material properties data at un-irradiated and irradiated conditions are necessary. They are strength, elastic modulus, coefficient of thermal expansion (CTE), thermal conductivity, etc. JAEA is carrying out studies to obtain these data for several kinds of candidate composite materials. An international collaboration study with the Korea Atomic Energy Research Institute (KAERI) has been carried out for the un-irradiated material properties evaluation for three C/C composite materials. Characterisations of Japanese C/C composites were conducted for fracture toughness and oxidation effect on material properties [9].

For the design and fabrication in phase (2), it is necessary to determine the control rod structure. Since the 2D-C/C composite has great anisotropy in thermal and mechanical properties in parallel and vertical to lamina directions, it is important to consider the anisotropy for component design. The connecting method for the component parts is one of the key technologies for the fabrication of the control rod. Appropriate design methodology, e.g. fracture theory, for the fiber reinforced ceramics has not been fully developed yet. It is also an important issue for the C/C and also SiC/SiC composite application.

The demonstration test by HTTR in phase (3) is the final stage for the composite control rod development. It is possible to carry out irradiation tests by material test reactors with small size specimens to establish a material database. On the other hand, it is difficult to find the irradiation field which can irradiate real scale control rod structure except the HTTR [10]. This demonstration test is expected to be carried out through international collaboration.

Experimental

Irradiation test

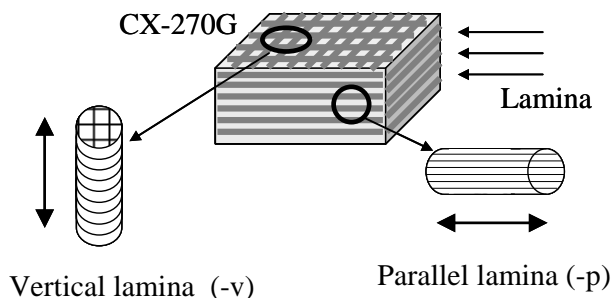
A PAN-based and plain-woven 2D- C/C composite, CX-270G grade (Toyo Tanso Co.), is one of the candidate materials for the control rod application [11]. It is graphitised at 2 800°C in its manufacturing process. Table 1 shows its typical material properties in comparison with fine-grained isotropic IG-110 graphite (Toyo Tanso Co.) used in the core components of the HTTR. Two types of the samples were prepared. One to measure the irradiation-induced dimensional change, coefficient of thermal expansion and Young's modulus ($\phi 5 \times 20$ mm) and the other to measure thermal conductivity ($\phi 10 \times 2$ mm). The samples were prepared from the block of CX-270G, as shown in Figure 2, to measure the anisotropy of the material properties and the irradiation effects. The prepared samples were irradiated at O3M-47AS capsule in the Japan Material Testing Reactor (JMTR) of JAEA to the fast neutron fluence of 8.2×10^{24} n/m² ($E > 1.0$ MeV) at 600°C. This irradiation damage for the graphite material corresponds to 1.2 dpa (displacements per atom) and the neutron energy range can be converted through atomic displacement damage evaluation as 1.3×10^{25} n/m² ($E > 0.18$ MeV). IG-110 was also irradiated as a reference material.

Table 1: Typical material properties of CX-270G and IG-110

Grade	Bulk density (Mg/m ³)	Bending strength (MPa)	Tensile strength (MPa)	Compressive strength (MPa)	Elastic modulus (GPa)	Coefficient of thermal expansion (10 ⁻⁶ /°C)	Thermal conductivity (W/m/°C)
CX-270G-p	1.63		167	69	81	0.2	129
CX-270G-v	1.63	133		89		10.8	26
IG-110	1.77	39	25	78	10	4.6	116

Figure 2: Specimens for vertical and parallel lamina directions

-p: parallel lamina direction, -v: vertical lamina direction



Post-irradiation examination

Irradiation-induced dimensional change, thermal conductivity, coefficient of thermal expansion and Young's modulus were measured [12] [13]. Test methods of the irradiation effects are summarised in Table 2. Thermal conductivity is calculated by density, specific

heat and the measured thermal diffusivity. Young's modulus is calculated by density and the measured sound velocity.

Table 2: Test methods of irradiation effects on CX-270G

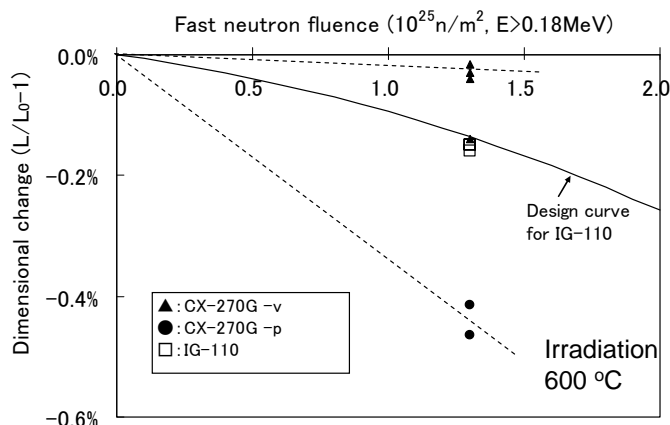
Property	Specimen size	Number of specimen	Measurement method
Dimensional change	φ5x20 mm	4	Digital micro meter
Thermal conductivity	φ10x2 mm	3	Laser flash method from room temperature to 1 400 °C, for every 100 °C
Coefficient of thermal expansion	φ5x20 mm	3 (measurements: 2 times for each)	Thermo-mechanical analysis (TMA) method from 50 to 1 000 °C, 10 °C /min standard material: Al ₂ O ₃
Young's modulus	φ5x20 mm	4	Longitudinal wave probe: φ6 mm, 1MHz

Results

Irradiation-induced dimensional change

Irradiation-induced dimensional change L/L_0-1 is shown in Figure 3, where L_0 and L are respectively the length of specimen before and after the irradiation. The obtained data are plotted in comparison with the design curve of the IG-110 graphite for the HTTR [14]. It is obvious that the shrinkage for the parallel lamina direction (-p) is much larger than that for the vertical lamina (-v) direction. The neutron irradiation causes shrinkage of fibers along their length and swelling in their diameter [15]. Although the change in -p direction shows shrinkage, the change in -v direction does not show swelling. It is probable that the swelling of the fiber would be accommodated pores and matrix among lamina. It is possible to evaluate the dimensional change of IG-110 graphite by a linear line approximately in this irradiation condition. It was shown in the previous study that the dimensional change curves in this neutron range for the both -p and -v directions can be described linearly [8]. It has been suggested that the knowledge of the irradiation damage on graphite can be used to support the evaluation of the irradiation damage on the graphitised C/C composite.

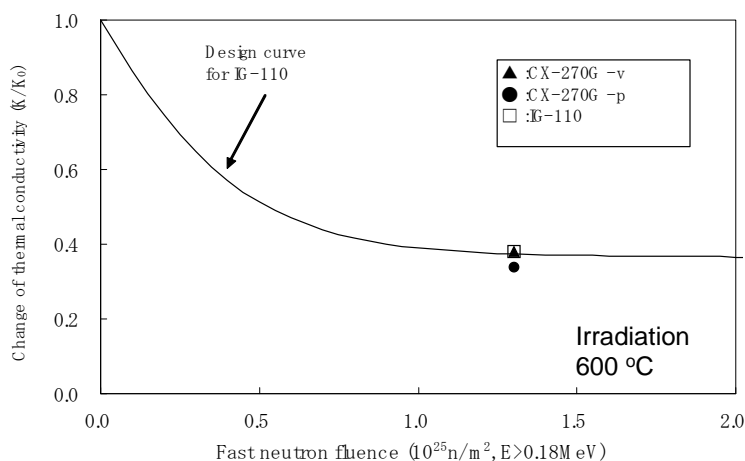
Figure 3: Irradiation-induced dimensional change of CX-270G in comparison with IG-110 design curve



Thermal conductivity

Thermal conductivity was calculated by the measured thermal diffusivity. The change of thermal conductivity K/K_0 by irradiation was evaluated, where both K_0 and K are conductivity before and after irradiation. Figure 4 shows the change of thermal conductivity of CX-270G in comparison with the IG-110 design curve for the measurement temperature of 600°C. The average values of five times measurement for each sample are plotted in the figure. It is obvious that the change of thermal conductivity of CX-270G for both directions is in good agreement with that of IG-110, although the geometric structures of the three samples are quite different. It was also shown in the previous study that the measurement temperature dependency of conductivity is almost the same for the both directions of CX-270G and IG-110 [8] [12]. It was reported that the heat transport in graphite takes place by lattice wave conduction (phonon conduction). The thermal conductivity of graphite reduces when irradiated, because phonons are scattered by irradiation defects in the graphite crystal structure. From this point of view, a graphite irradiation database would be effective in evaluating the graphitised C/C composite thermal properties.

Figure 4: Change of thermal conductivity of CX-270G in comparison with IG-110 design curve for the measurement temperature of 600°C

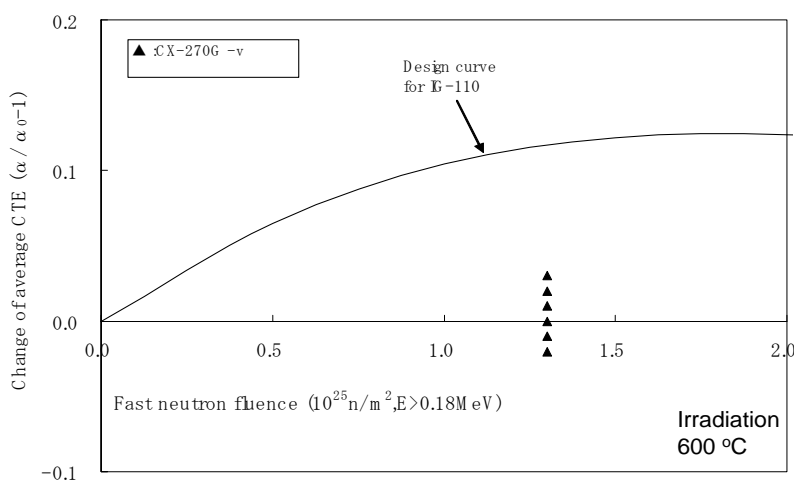


Coefficient of thermal expansion

The change of average coefficient of thermal expansion (CTE), $\alpha/\alpha_0 - 1$, in the temperature range from 50 to 1 000°C was measured, where both α_0 and α are the CTE before and after the irradiation.

Although it is possible to directly compare the change ratio in -v direction with that for IG-110, it is difficult to do so in -p direction. The ratio in -p direction shows a large negative value and the data contain some scattering. Figure 5 shows the change of CTE just for CX-270G in -v direction in comparison with the IG-110 design curve. The obtained data of -v direction is smaller than the design curve of IG-110. Since the pores and matrix among the lamina can accommodate the thermal expansion in the -v direction, it must result in the small change shown in the Figure. It seems to be difficult to use the graphite database directly to evaluate the CTE of CX-270G. On the other hand, although the obtained data of the change of CTE in -p direction show negative values, the absolute value of the change in -p direction is about 10^2 times smaller than that in -v direction. The change in the -p direction would be negligible in the component design of the control rod.

Figure 5: Change of CTE of CX-270G (-v) in comparison with IG-110 design curve

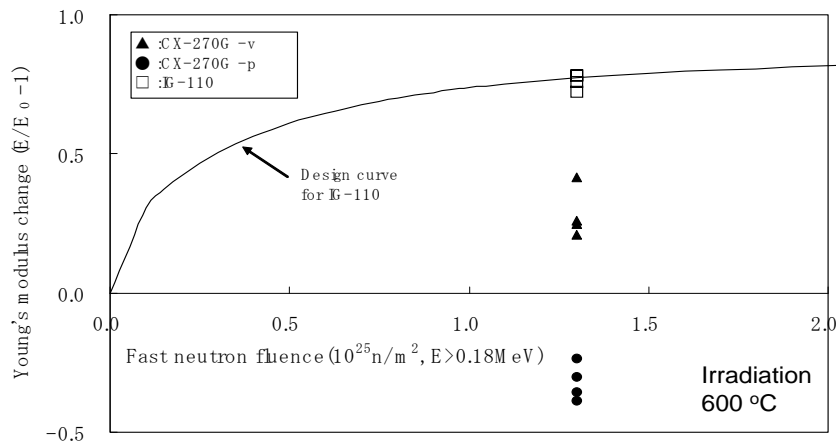


Young's modulus

Young's modulus was calculated by the measured longitudinal wave velocity and density. It was simply evaluated through multiplying the density and square of velocity. The change of Young's modulus $E/E_0 - 1$ was evaluated, where both E_0 and E are the modulus before and after irradiation. Figure 6 shows the change of Young's modulus of CX-270G in comparison with the IG-110 design curve. For the graphite material, it is known that the rapid increase in Young's modulus at the initial irradiation stage is caused by the pinning effect on dislocations in crystals (pinning factor). The gradual increase in the next irradiation stage is caused by irradiation-induced dimensional shrinkage (structure factor). In this Figure, the increase of the modulus by the irradiation in -v direction is about half of that of the IG-110. As shown in Figure 3, the irradiation-induced shrinkage in -v direction is much smaller than that for IG-110. It would be one of the major reasons for the smaller increase in -v direction than that of IG-110. It is

suggested that the knowledge of the graphite irradiation damage would be used to support the evaluation on CX-270G. On the other hand, the change of Young's modulus in -p direction shows a negative value. It is due to the large decrease in wave velocity in -p direction.

Figure 6: Change of Young's modulus of CX-270G in comparison with IG-110 design curve



Conclusions

As the material for the control rod element of the VHTR, C/C composite is a promising candidate substitute for the metallic material. Irradiation effects on the graphitised 2D-C/C composite, CX-270G, were investigated in comparison with IG-110 graphite. An irradiation test was carried out by JMTR at 600°C to the fluence of $8.2 \times 10^{24} \text{ n/m}^2$ ($E > 1.0 \text{ MeV}$) corresponding to 1.2 dpa. The results obtained by the post-irradiation examination were summarised as follows:

- The dimensional change of the CX-270G shows a similar linear decreasing trend to IG-110 graphite.
- The change of thermal conductivity of CX-270G is in good agreement with that of graphite and is due to the graphitised treatment of CX-270G.
- The change of CTE in -v direction is smaller than that of graphite. The change in -p direction would be negligible, since its absolute value is much smaller than that in -v direction.
- The change of Young's modulus of CX-270G in -v direction is about half of that of graphite. The structure factor on the irradiation-induced change of Young's modulus would be one of the major reasons.

Although the 2D-C/C composite has anisotropy in material properties, it is effective in evaluating the irradiation effects on graphitised C/C composite taking the knowledge of graphite irradiation database into consideration. The evaluation on thermal conductivity by using the graphite database is especially effective. On the other hand, the evaluation on CTE directly from the graphite database seems to be difficult, because it is strongly affected by geometric structure, JAEA carries out R&D for composite control rod based on the experience of HTTR construction and operation. International collaboration is effective in establishing composite material databases and demonstrating composite control rod in the future.

Acknowledgements

The authors express their sincere appreciation to the members of hot laboratory of JMTR for their technical support of the post-irradiation examination.

References

- [1] K. Matsui, S. Shiozawa, M. Ogawa and X. L. Yan (2008), Present Status of HTGR Development in Japan, *Proc. 16th Pacific Basin Nuclear Conference (16PBNC)*, Aomori, Japan, 13-18 October 2008, PaperID P16P1355.
- [2] S. Shiozawa, et al. (2007), Status of the Japanese Nuclear Hydrogen Program, ANS 2007 Annual Meeting, "Embedded Topical on Safety and Technology of Nuclear Hydrogen Production, Control and Management", (ST-NH2), 24-28 June 2007, Boston, MA, United States.
- [3] S. Saito, et al. (1994), Design of High Temperature Engineering Test Reactor (HTTR), JAERI 1332.
- [4] T. J. O'Connor (2010), Gas Reactors - A Review of the Past, an Overview of the Present and a View of the Future, *Proc. of GIF Symposium*, pp.77-92, 9-10 September 2010, Paris, France.
- [5] K. Kunitomi, S. Katanishi, S. Takada, et al. (2004), Reactor core design of Gas Turbine High Temperature Reactor 300, *Nucl. Eng. Design*, 230, 349-366.
- [6] K. Kunitomi, X. Yan, T. Nishihara, et al. (2007), JAEA's VHTR for hydrogen and electricity cogeneration: GTHTR300C, *Nucl. Eng. and Technol.*, 39[1], 9-20.
- [7] Y. Tachibana, S. Shiozawa, J. Fukakura, F. Matsumoto and T. Araki (1997), Integrity assessment of the high temperature engineering test reactor (HTTR) control rod at very high temperatures, *Nucl. Eng. and Design* 172, 93-102.
- [8] T. Shibata, J. Sumita, T. Makita, T. Takagi, E. Kunimoto, K. Sawa (2009), Research and developments on C/C composite for Very High Temperature Reactor (VHTR) application, *Ceramic Engineering and Science Proceedings (CESP)*, Vol.30, Issue 10, pp. 19-32.
- [9] T. Shibata, J. Sumita, T. Makita, T. Takagi, E. Kunimoto, K. Sawa, W. J. Kim, C. H. Jung and J. Y. Park (2010), Characterization of 2D-C/C composite for application of Very High Temperature Reactor, *Transactions of Japan Society of Mechanical Engineers A*, Vol. 76, No. 764, pp. 383-385. [In Japanese].
- [10] T. Shibata, T. Kikuchi, S. Miyamoto and K. Ogura (2003), Assessment of irradiation temperature stability of the first irradiation test rig in the HTTR, *Nucl. Eng. and Design*, 223, 133-143.
- [11] T. Sogabe, M. Ishihara, et al. (2002), Development of the Carbon Fiber Reinforced Carbon-carbon Composite for High Temperature Gas-cooled Reactors, JAERI-Research 2002-026. [In Japanese].
- [12] T. Shibata, J. Sumita, E. Kunimoto and K. Sawa (2008), Characterization of 2D-C/C composite for application to in-core structure of Very High Temperature Reactor (VHTR), *Proc. Carbon 2008*, P0370, 13-18 July 2008, Nagano, Japan.
- [13] T. Takagi, T. Makita, E. Kunimoto, T. Shibata and K. Sawa (2009), Measurement on Irradiation-induced Property Change of Carbon Composite Material for Very High Temperature Reactor - Irradiation-induced Dimensional Change, Coefficient of Thermal Expansion and Elastic Modulus, *JAEA-Technology 2008-094*. [In Japanese].

- [14] HTTR Design Laboratory, *et al.* (1989), “Graphite Structural Design Code for the High Temperature Engineering Test Reactor”, JAERI-M 89-006, Japan Atomic Energy Research Institute (1989). [In Japanese].
- [15] Burchell T. D, CONF-940412-3.

Behaviour of irradiated boron carbide

Takako Donomae, Koji Maeda
Japan Atomic Energy Agency, Japan

Abstract

Boron carbide (B_4C) is used extensively as a material for control rods in fast reactors because of its superior properties, such as a large neutron absorption cross-section, high melting temperature, light weight and chemical stability at up to approximately 2 400°C. So far, B_4C pellet swelling was measured only at low irradiation temperatures up to a burn-up of 80×10^{26} cap/m³. In this investigation, swelling data were measured under this burn-up condition using irradiated B_4C pellets in the experimental fast reactor Joyo. This investigation has revealed that B_4C pellet swelling behaviour is the same up to a high burn-up of 100×10^{26} cap/m³ regardless of the difference in irradiation temperatures. It is necessary to perform irradiation tests under higher burn-up conditions and clarify the boundary of saturation of B_4C pellet swelling.

Introduction

Boron carbide (B_4C) is used extensively as a material for control rods in fast reactors because of its superior properties, such as large neutron absorption cross-section, high melting temperature, light weight and chemical stability at up to approximately 2 400°C. In the experimental fast reactor Joyo, B_4C pellets are covered by a cladding tube of stainless steel as a pin, and 7 pins are installed in each control rod. There is a difference in the irradiation temperature of approximately 300°C between the center and the outer circumference of the B_4C . Pellet temperature at the center is higher than at the outer circumference, with the difference in thermal expansion inducing thermal stress. Neutron-irradiated B_4C pellets usually show extensive grain cracking due to thermal stresses and structure damage [1] [2] [3]. In larger diameter pellets, these thermal expansion gradients are large and it has been observed that pellet cracking occurred at an early operational stage [4].

Since cracked B_4C pellet fragments relocate and swell, absorber-cladding mechanical interaction (ACMI) occurs [5] [6]. ACMI may cause cracking of the cladding tubes [7].

The helium produced by $^{10}B(n, \alpha)^7Li$ reaction is released from the pellets, and causes an increase in the gas pressure inside the absorber pins. This problem was addressed by the employment of a bent-type pin in Joyo.

The swelling behaviour of B_4C pellets was investigated by both volume measurement and microstructural observation. The change in volume was determined by measuring the change in the diameter or length of B_4C pellets. When B_4C pellets are irradiated at high burn-ups, significant cracking and pellet fracturing occur. Consequently, it is very difficult to obtain an accurate swelling value from the measurement of dimensional changes alone. Therefore, it is necessary to perform density measurements on the high burn-up pellets using mercury picnometry [5]. Results showed that the swelling of the B_4C pellets tends to increase linearly, overall. Specifically, B_4C pellets tend to increase linearly at low burn-up up to 80×10^{26} cap/m³. When burn-up exceeds 100×10^{26} cap/m³, the gradient of the swelling curve tends to decrease gradually. It is suggested that the increase in released helium quantities may contribute to the decrease in the gradient of the swelling curve. Above 100×10^{26} cap/m³, swelling values tend to saturate and the pellets break into small fragments.

For a microstructural investigation, lattice parameters of B_4C were measured using X-ray powder diffraction [2]. Microstructures were observed using optical micrography, scanning electron micrography and transmission electron microscopy [2] [3] [5].

The crystal structure of B_4C is rhombohedral; however, it is usually categorised into the hexagonal system. Lattice parameter changes were measured by annealing the B_4C pellets that were irradiated at elevated temperatures up to a burn-up of 4.1×10^{26} cap/m³. During annealing at progressively higher temperatures, the lattice parameter a was decreased below the original value at first and then recovered. The lattice parameter c showed a sharp increase up to 900°C and then suddenly decreased to the original value of the unirradiated specimen. Therefore, the changes in unit cell volume decrease slightly around 500°C and reached a maximum value at approximately 750°C [2].

These results and the appearance of irradiated B_4C pellets show that the pellets are not easily broken at around the irradiated temperature of 700°C-800°C [1]. At high temperatures, above 500°C, it is known that lenticular bubbles with helium gas gather along the c -plane [1] [3]. The generation of helium bubbles depends on the number of ^{10}B and burn-up [8].

Thus far, the swelling of B_4C pellets has been measured only at low irradiation temperatures up to 80×10^{26} cap/m³.

Experimental procedure

In the present investigation, B₄C pellets were irradiated in the experimental fast reactor Joyo MK-III core to a ¹⁰B burn-up of up to 100×10²⁶cap/m³, and a maximum temperature of approximately 780°C, as shown in Figure 1 [9]. The configuration of absorber pins in the control rod, together with the B₄C pellets in the absorber pin, is illustrated in Figure 2. The B₄C pellets were fabricated by hot-pressing using isotopic enriched B₄C with 90 at% of ¹⁰B. B₄C pellet density was 90% TD. The specifications of B₄C content are shown in Table 1. The diametrical dimensions of the B₄C pellet, shroud tube, and cladding tube are φ16.3 mm, φ_{od}16.8 mm-0.1 mm thickness and φ_{od}18.9 mm-0.5 mm thickness, respectively. This high burn-up-low-temperature condition was achieved by using sodium for bonding material.

Burn-up was calculated using the HESTIA code [9]. The maximum temperature at the pellet center was calculated using the universal computer code HEATING-5 (heat engineering and transfer in nine-geometries, Vol. 5). [5] [6].

Absorber pins were removed from the irradiated control rods after withdrawal from the Joyo core. Burn-up values were approximately 20, 40, 50, 80 and 100×10²⁶cap/m³. The pieces of B₄C pellets were observed visually and the density of the pellets was measured. The B₄C pellets were cut by diamond blade to a height of 2 mm and their appearance is shown in Figure 3. Fragment size decreased with increasing burn-up.

First the specimen was weighed to 0.1 mg. Next, the pycnometer was filled with Hg and weighed. After that, the specimen was placed into the Hg-filled pycnometer and weighed. Finally, these values were inserted into the following equation:

$$T.D. = (Ws \times \rho_{hg}) / (W1 + Ws - W2) \quad (1)$$

where T.D. is theoretical density, Ws is weight of specimen, ρ_{hg} is density of Hg, W1 is the weight of the pycnometer filled with Hg, W2 is weight of specimen in the pycnometer filled with Hg. Each specimen was measured three times. After that, the swelling value was calculated from density.

Determined density values were converted into swelling values. These values were calculated from the following equation:

$$S = \Delta V / V = \rho_0 / \rho - 1 \quad (2)$$

where S is swelling value, ΔV is the change in volume, V is unirradiated volume of specimen, ρ₀ is un-irradiated B₄C density and ρ is irradiated B₄C density. This equation is useful as an empirical definition of the swelling behaviour of various materials on a comparative basis.

These results are shown in Figure 4.

Results and discussion

Figure 4 shows the burn-up dependence of B₄C pellet swelling. Open triangle symbols and cross symbols were measured prior to this investigation. The temperature data were divided into low and high temperatures at 1 000°C. Open triangle data were measured largely by dimensional change and parts of the cross symbol data were measured by density.

Swelling data were not recorded around temperatures of 100×10²⁶ cap/m³. Apart from 100×10²⁶ cap/m³, the gradient of increasing swelling is changed. In terms of irradiation temperature, low-temperature swelling data are classified into the low burn-up condition and high-temperature swelling data are classified into the high burn-up condition. B₄C pellets that were irradiated at low temperatures up to 80×10²⁶ cap/m³, the swelling of B₄C

pellets increased linearly; however, above $100 \times 10^{26} \text{cap/m}^3$, the gradient of the swelling curve tended to decrease gradually.

The closed triangle symbols overplotted show that B_4C pellet swelling behaviour is the same between the low-temperature-low burn-up condition and the low-temperature-high burn-up condition, up to $100 \times 10^{26} \text{cap/m}^3$.

All closed triangle symbol data were taken from the same control rod and cut from absorber pins along the axial direction. These data were measured by density and they showed nearly the same tendency as that of the diameter measurement described above. Therefore, the method of determining swelling from diameter change is considered reasonable.

In this investigation, B_4C pellet swelling data of low temperature-high burn-up were measured. These results suggest the behaviour of B_4C pellet swelling at higher and lower temperatures.

As is generally known, B_4C pellet helium retention is greater at low temperatures and smaller at high temperatures. Therefore, B_4C pellet swelling increases as a result of helium retention. Figure 5 shows the relation between burn-up and helium retention [5]. As can be seen from this Figure, helium retention in B_4C pellets decreases with increasing burn-up and the rate of retention decreases at lower temperatures. Kaito *et al.* reported that the appearance of B_4C pellets that were irradiated at around 800°C and a burn-up of about $40 \times 10^{26} \text{cap/m}^3$ and irradiated around 1100°C and a burn-up of about $100 \times 10^{26} \text{cap/m}^3$ [6]. Later pellets were broken into small pieces. According to the results in Figure 3, B_4C pellet appearance shows the tendency of smaller pellet fragment size observed in this study. Therefore, it has been suggested that helium release from B_4C pellets would start and then swelling would be decreased. It is necessary to perform irradiation tests under higher burn-up conditions and clarify the boundary of saturation of B_4C pellets swelling.

Table 1: Specifications of B_4C content

	Specification	B_4C specimen
^{10}B enrichment (wt%)	90.0 ± 1.0	90.1
Total B (wt%)	77.0 ± 1.0	76.8
Total B+ Total C	≥ 99.0	99.2

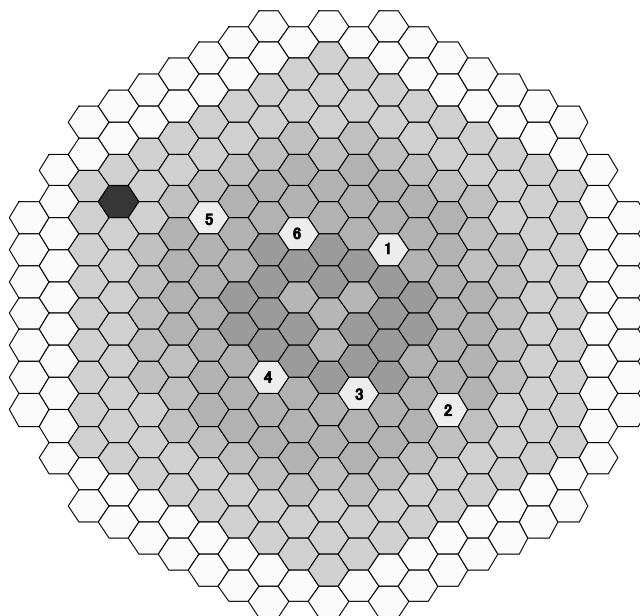
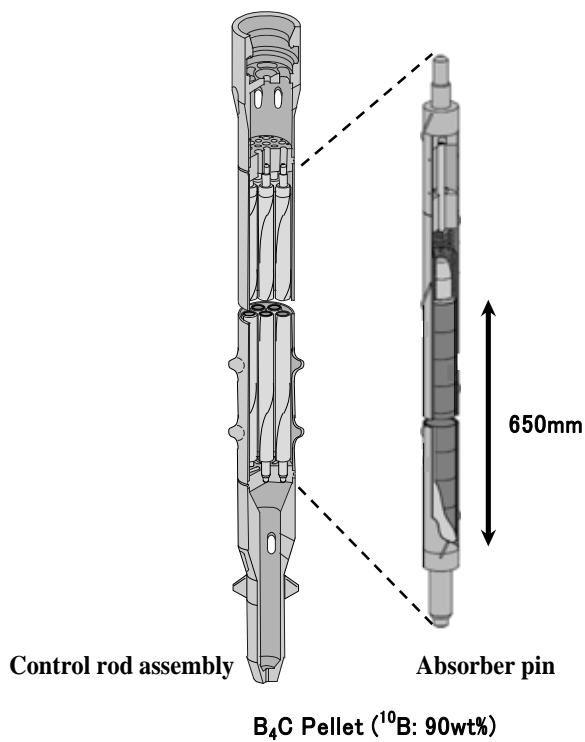
Figure 1: Position of control rods in the Joyo MK-III core [1]**Figure 2: Joyo MK-III control rod [1]**

Figure 3: Appearance of B₄C specimens

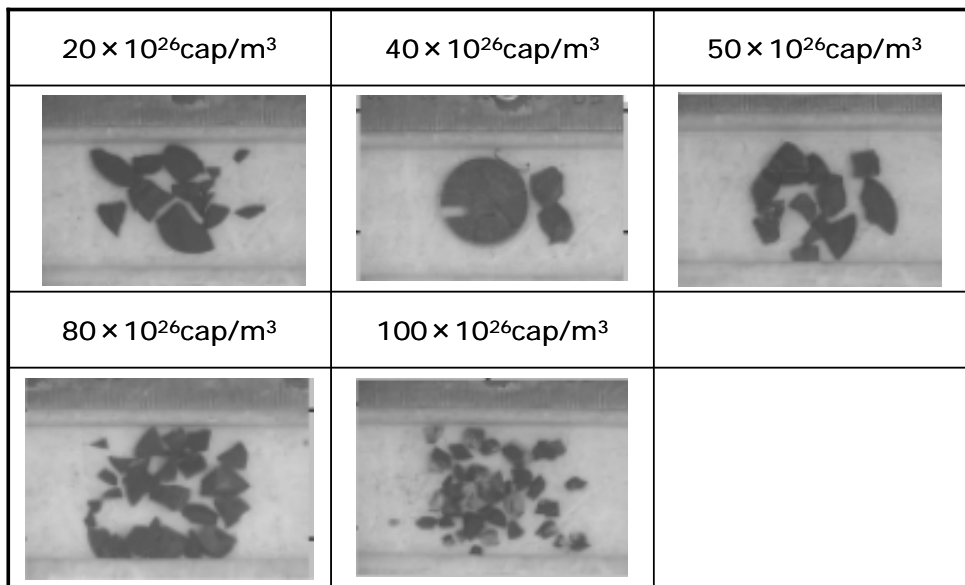


Figure 4: Volume swelling of B₄C

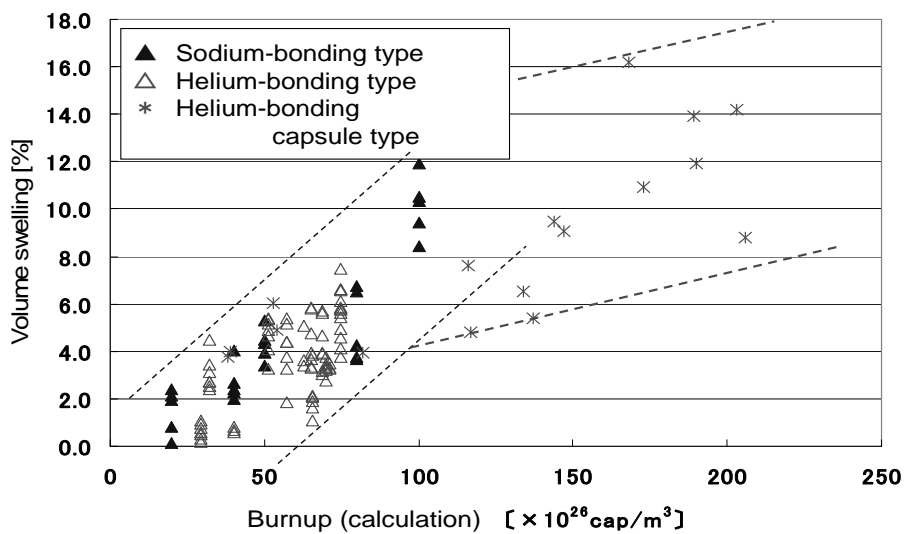
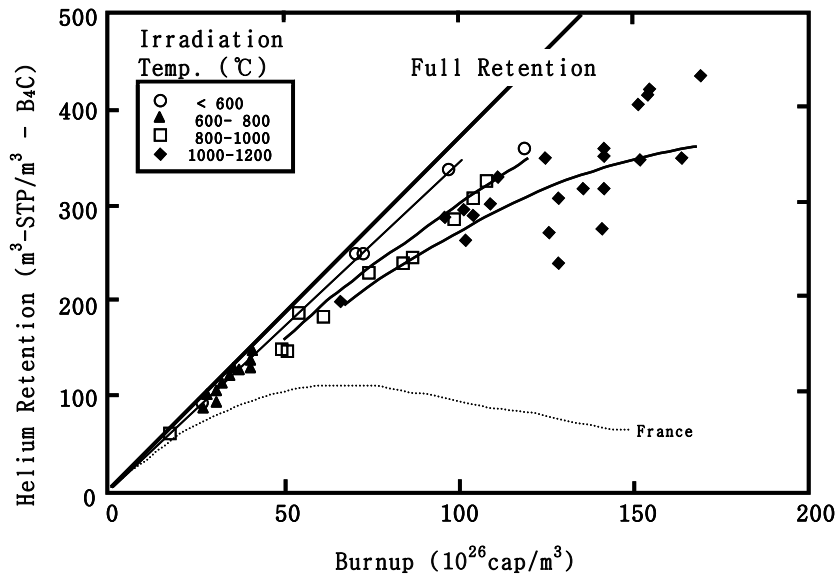


Figure 5: Burn-up dependence of helium retention [5]



Conclusion

In this investigation, swelling data were measured under the given irradiation conditions using irradiated B_4C pellets in the experimental fast reactor Joyo. This investigation has revealed that B_4C pellet swelling behaviour is the same up to a high burn-up of $100 \times 10^{26} \text{ cap}/\text{m}^3$ regardless of the difference in irradiation temperatures. It is necessary to perform irradiation tests under higher burn-up conditions and clarify the boundary of saturation of B_4C pellets swelling.

References

- [1] M Itoh (2004), Neutron Absorber and Control Rod Materials, Bulletin of the Ceramic Society of Japan, 39(10), 822-825 [in Japanese].
- [2] H Suzuki, T Maruyama and T Wakasa (1979), Post irradiation annealing of boron carbide pellet irradiated in fast breeder reactor, *J. Nucl. Sci. Technol.*, 16, 588-595.
- [3] T. Stoto, N. Housseau, L. Zuppiroli and B. Kryger (1990), Swelling and microcracking of boron carbide subjected to fast neutron irradiations, *J. Appl. Phys.*, 68(7), 3198-3206.
- [4] G. W. Hollenberg and J. A. Bsmajian (1982), Crack propagation in irradiated B_4C induced by swelling and thermal gradients, *J. Amer. Cer. Soc.*, 65(4), 179-181.
- [5] T. Maruyama, S. Onose, T. Kaito and H. Horiuchi (1997), Effect of fast neutron irradiation in the properties of boron carbide pellet, *J. Nucl. Sci. & Tech.*, 34(10), 1006-1014.
- [6] T. Kaito, T. Maruyama, S. Onose and H. Horiuchi (1995), Irradiation behavior of boron carbide neutron absorber, IAEA-TECDOC—884, 161-171.
- [7] T. Maruyama (2008), Development of control rods for fast breeder reactor, *Taikabutsu*, 60(10), 516-526 [in Japanese].

- [8] T. Donomae, Y. Tachi, M. Sekine, Y. Morohashi, N. Akasaka and S. Onose (2007), Neutron irradiation effects on $^{11}\text{B}_4\text{C}$ and recovery by annealing, *J. Cer. Soc. of Japan*, 115(9), 551-555.
- [9] T. Aoyama, T. Sekine, S. Maeda, A. Yoshida, Y. Maeda, S. Suzuki and T. Takeda (2007), Core performance tests for the JOYO MK-III upgrade, *Nuclear Engineering and Design*, 237, 353-368.

Study of heavy ions irradiation on structure of triple titanium nitride basis coating*

Sergey Kislitsin¹, Kairat Kadyrzhanov¹, Vladimir Uglov²,
Dmitriy Rusalski², Gregory Abadias³, Sergey Dub⁴

¹Institute of Nuclear Physics of National Nuclear Center of Kazakhstan, Almaty, Kazakhstan, ²Belarusian State University, Minsk, Belarus,

³Laboratoire PHYMAT, Université de Poitiers, Cedex, France,

⁴Institute of Superhard Materials, Kiev, Ukraine

Abstract

Titanium nitride and triple titanium nitride is a technologically important refractory material combining the physical properties of ceramics and metals. In addition to its wide use as protective hard coating for different applications or metallisation layer in microelectronics, triple titanium nitride coating can be considered as a shell material for nuclear fuel in future high-temperature nuclear reactors. This work studied the influence of low and high energy heavy ions irradiation on the surface structure and physical-mechanical properties of CrTiN and ZrTiN coating on silicon and steel. Irradiation by He and Xe ions can be regarded as interaction of fission products of nuclear fuel with shell material surrounded nuclear fuel. Chromium-titanium-nitrogen and zirconium-titanium-nitrogen coating were deposited on the surface of silicon or carbon steel substrates by magnetron sputtering or vacuum arc coating deposition. The series of Cr₅₀Ti₅₀N coatings on silicon and carbon steel with a thickness of 50.200 nm were formed by vacuum arc technique. Ti_(x)Zr_(1-x)N (x=0, 0.25, 0.50, 0.75, 1) thin films (~300 nm thickness) were deposited on (100) Si substrate using unbalanced reactive magnetron co-sputtering. Irradiation of specimens with CrTiN and ZrTiN coating on silicon was performed in the low energy canal of the heavy ion cyclotron DC-60 of the Astana branch of INP NNC RK. Specimens with CrTiN coating on silicon underwent irradiation of He (Z=+2) ions, i.e. ion energy consists E = 40 keV, irradiation fluence – F = 1×10¹⁸ ions/cm². Ti_(x)Zr_(1-x)N (x=0, 0.25, 0.50, 0.75, 1) was irradiated in the low energy canal of the heavy ion cyclotron DC-60 with Xe (Z=+18) ions, E= 360 keV and F = 8×10¹⁴ ions/cm². Irradiation with Ar ions was performed at the high energy canal of cyclotron DC-60 by Ar ions (E=1 MeV/nucleon) F=1.6 × 10¹⁷ ions/cm². Structure and properties of the irradiated coating were studied by SEM, XRD, AFM, RBS and nanohardness measurements methods. It was established that He ions irradiation up to fluence F = 1×10¹⁸ ions/cm² leads to the appearance of blisters on the surface, Ar ions – formation of bubbles on the surface. Irradiation of ZrTiN coating by Xe ions up to fluence 1×10¹⁸ ions/cm² does not significantly influence the structure of the coating surface. Nanohardness of Ti_(x)Zr_(1-x)N with x=0.25, 0.50, 0.75 increases after xenon ions irradiation.

* The full paper being unavailable at the time of publication, only the abstract is included.

Diffusion of silver in zirconium carbide inside tristructural-isotropic nuclear fuel

**Youngki Yang, Tyler Gerczak, Dane Morgan, Izabela Szlufarska,
Sungtae Kim, Todd Allen**
University of Wisconsin-Madison, United States

Abstract

The fuel of choice for the very-high-temperature reactor (VHTR) is TRistructural-ISotropic (TRISO) particle fuel. Traditionally, TRISO fuel construction has consisted of a UO_x or UCO kernel, surrounded by successive layers of a porous carbon buffer, dense inner pyrocarbon, SiC and a dense outer pyrocarbon. During operation, however, the SiC layer has been known to release Ag and is subjected to Pd attack. ZrC has been regarded as a promising alternative to the SiC fission product barrier. ZrC exhibits high-temperature stability and possesses superior Pd resistance, while the retention properties are unknown for the ZrC/Ag system. In this work a liquid encapsulation method has been developed to construct a constant source diffusion couple between ZrC_{0.84} and Zr-6.9% Ag solid solution. The resultant impurity diffusion coefficient of Ag in ZrC_{0.84} at 1 500°C was experimentally determined to be about $5.0 \times 10^{-17} \text{ m}^2/\text{sec}$.

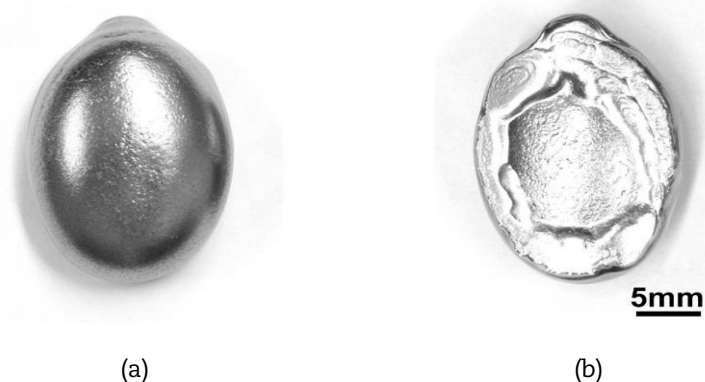
Introduction

The very-high-temperature reactor (VHTR) is a Generation IV reactor concept that can operate at high outlet temperature (up to about 1 000°C). The fuel of choice for the VHTR is TRistructural-ISotropic (TRISO) particle fuel. Traditionally, TRISO fuel construction has consisted of a UO_x or UCO kernel, surrounded by successive layers of a porous carbon buffer, dense inner pyrocarbon, SiC and a dense outer pyrocarbon. The SiC and graphite layers enable the reactor to operate more safely and at higher temperatures due to their thermal stability. Consequently, high temperatures allow for high efficiencies and new opportunities for process heat applications such as H_2 production. During operation, however, the SiC layer has been known to release Ag and is subjected to Pd attack and rupture at high temperatures [1] [2]. ZrC has been considered as a promising alternative to the SiC fission product barrier [3]. This material exhibits high-temperature stability and possesses superior Pd resistance, while the retention properties are unknown for the ZrC/Ag system. In particular, there are no (or very few) reliable measurements of Ag diffusion coefficients in ZrC, a paucity stemming not from lack of interest but from the difficulty of obtaining reliable data at high temperatures such as 1 500°C. The major complications arise from the lower melting point of Ag, poor wettability of Ag on ZrC and oxidation of ZrC at those high test temperatures judging from our previous experience in this research. To overcome these difficulties, a new liquid encapsulation method has been developed and tested.

Table 1: Composition of pure zirconium in ppm (wt% base)

Al	Si	Fe	Zn	N	C	Cr	Hf	H	O	Zr
28	14	910	30	44	62	90	63	7	750	Bal.

**Figure 1: Zr-Ag solid solution alloy ingots prepared by arc-melting:
(a) top view, (b) bottom view of Zr-6.9% Ag ingot**



Experimental

A Zr-Ag solid solution was alloyed from pure Hafnium-free Zr (99.9 wt%) and silver (99.9 wt%) using an arc melter. The composition of zirconium used for alloying is shown in Table 1. Arc melting was conducted under an argon back-filled atmosphere. The alloy was melted four times with the ingot flipped over between successive operations for better homogenisation. The resultant alloy weighed about 10 grams. The composition was Zr-6.9% Ag according to a post-fabrication wavelength dispersive X-ray spectroscopy (WDS) measurement. All compositions quoted in this paper are given in atomic percent unless otherwise specified. An example of the arc-melted alloy is shown in Figure 1. The alloy appeared to be microscopically inhomogeneous while macroscopically homogeneous according to microstructure analysis. Selecting any 200 μm by 200 μm square area of Zr-6.9% Ag randomly, for instance, appears to represent average composition and so the Zr-6.9% Ag alloy can be described as macroscopically homogeneous.

Figure 2: Experimental set-up for encapsulation of ZrC with Zr-Ag alloy: (a) before encapsulation, (b) after encapsulation

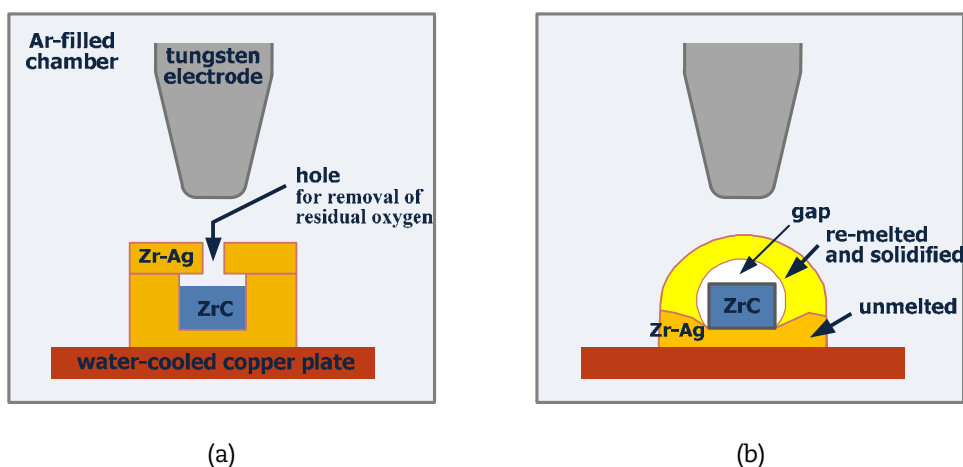
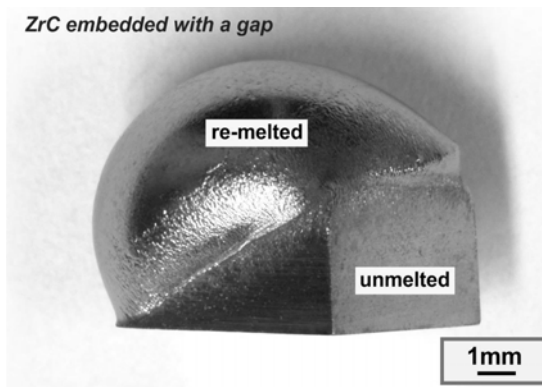


Figure 3: External appearance of ZrC encapsulated with Zr-6.9% Ag alloy

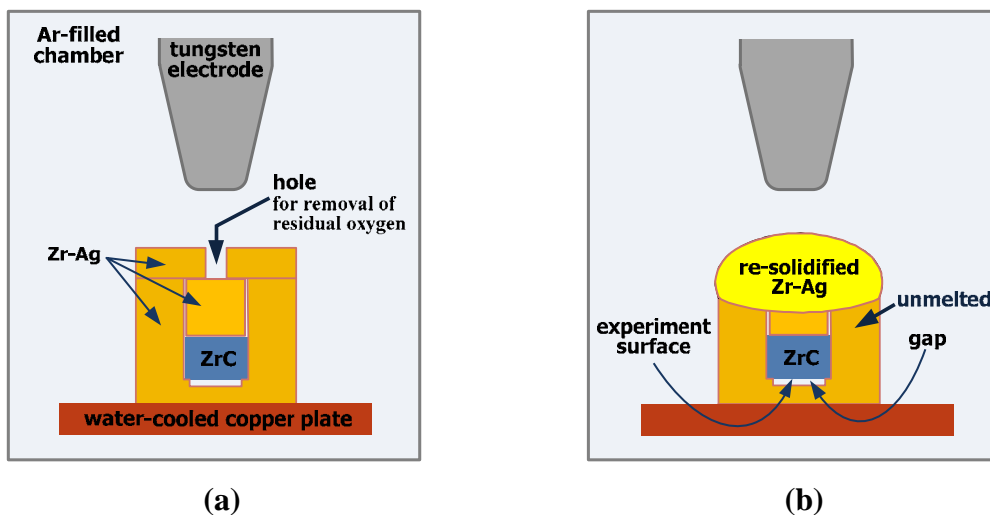


A float-zone refined $ZrC_{0.84}$ disk custom-manufactured by applied physics technologies, Inc. was used. It was 2 mm tall and 3 mm in diameter. Arc melting was conducted under an argon back-filled atmosphere. The Zr-6.9% Ag alloy was used to encapsulate the $ZrC_{0.84}$, with a gap between the ZrC disk and the Zr-Ag alloy. The sample was loaded into the arc melter as shown in the schematic illustration of Figure 2(a) and the chamber was evacuated, purged with Argon and evacuated again. This procedure was repeated five times to remove most of the oxygen. The chamber was then filled to 0.5 atm with Ar. Pure Ti (99.7 wt%) was arc-melted first to act as an oxygen getter, to minimise any trace amounts of oxygen remaining after purging. However, pure Zr instead of Ti will be used in the future experiments to prevent possible contamination since Zr is indigenous and thermodynamically more reactive with oxygen than Ti [4]. The encapsulation was performed in the arc melter with one melt cycle of 1 or 2 seconds to completely encapsulate but prevent dissolution as schematically illustrated in Figure 2(b). Figure 3 shows such a sample right after liquid encapsulation before annealing and cross-sectioning.

A sample prepared using the method outlined above was then located inside a graphite rod to prevent oxidation during further exposure at high temperatures. It was placed in an alumina tube furnace, heated up at 200°C/hr to $1\,500^{\circ}\text{C}$, annealed for 50 hours, and finally cooled at 200°C/hr under an Ar atmosphere. This diffusion annealed sample was then cross-sectioned and analysed with WDS. The standards used for this analysis technique were 99.9 wt% pure Ag and Zr, respectively.

Results and discussion

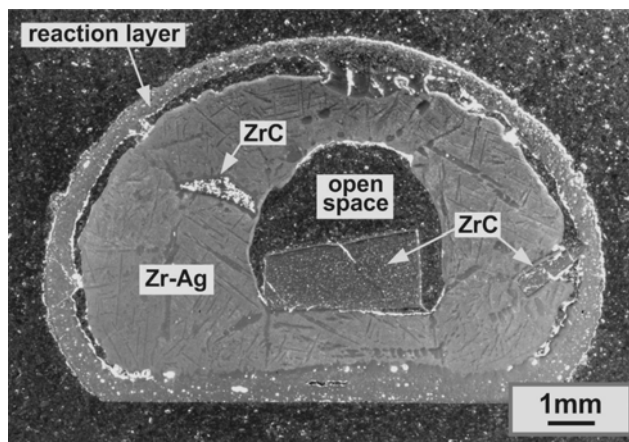
Figure 4: Schematic illustration of an improved experimental setup for encapsulation: (a) before encapsulation, (b) after encapsulation



The experimental results show this newly-developed encapsulation method is a promising start as will be discussed later. Further improvements upon this method are feasible and can be implemented as well. One of these improvements is using an analytical method with higher detection sensitivity, such as secondary ion mass spectroscopy (SIMS), because of the free surface available. It has been known that the diffusion coefficients measured are in the range, 10^{-16} - 10^{-23} m^2/sec , the SIMS technique is suitable while the electron probe micro analysis (EPMA) techniques such as WDS are most effective in determining diffusion coefficients above 10^{-15} m^2/sec [5]. Another planned area of improvement is better control over the volume of open space within the encapsulation and the concentration of the sample by using a larger volume of sample,

making it less sensitive to potential concentration changes due to oxidation, evaporation or phase reaction. This improved control, as demonstrated in Figure 4, will help to quickly reach and maintain a constant equilibrium vapour pressure of Ag in the open space. Encapsulation with a gap or open space can provide a space for Ag gas to form and diffuse into ZrC. The gaps shown in Figure 2(b) can allow Ag to achieve an equilibrium vapour pressure assuming that the solid solution dominates the overall vapour pressure. Since ZrC is very stable at high temperatures, this assumption holds. Rapid heating and cooling will also help better define diffusion annealing conditions more accurately and clearly.

Figure 5: Optical macrograph showing a cross-section of a sample annealed at 1 500°C for 50 hours in an argon atmosphere



Note: The reaction layer of the Zr-6.9% Ag alloy.

Figure 6: SEM image of an area in Figure 5

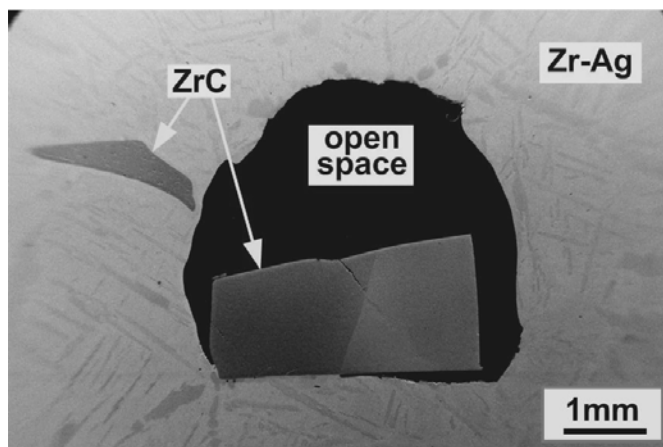


Figure 5 shows a cross-sectional photo of the diffusion annealed sample. This photo also shows that a part of the ZrC was broken off and two small pieces were embedded in the melt although ZrC is thermally stable and resistant to thermal shock. This seems likely to have occurred due to the large grain size of the sample. It was confirmed that the ZrC disk consists of only two single grains as shown in Figure 6 using electron

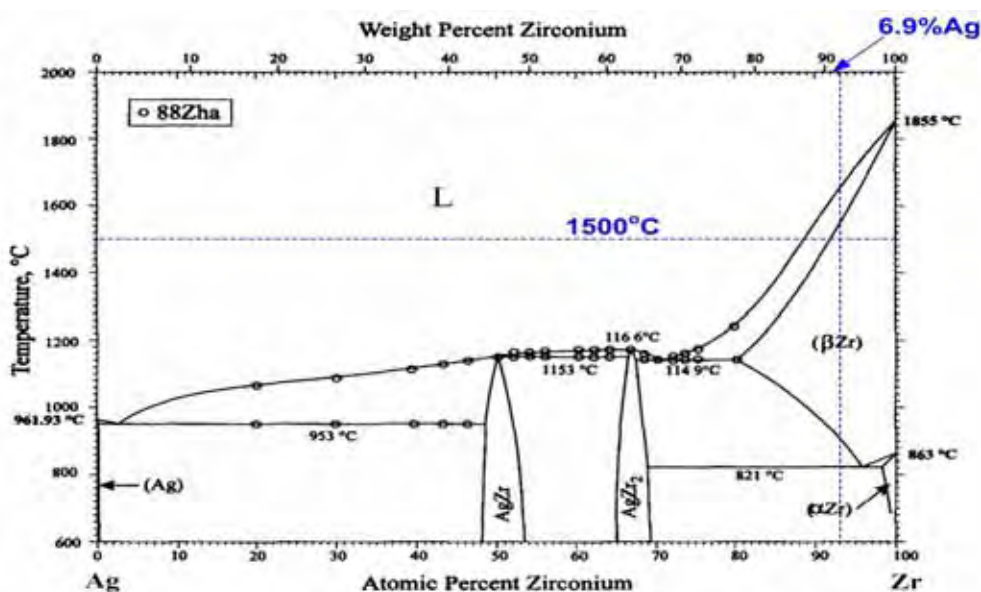
backscatter diffraction pattern (EBSP) analysis. It should be noted that this bi-crystallinity of the given ZrC disk is especially important since it can eliminate complexities of the measurement data analysis arising from both diffusional anisotropy and high-diffusivity paths. There is no diffusional directionality relative to the crystal axes at a fixed temperature, pressure, and composition since ZrC has cubic symmetry in the crystal structure [6]. No fast diffusion paths of interfaces and grain boundaries exist since the analyzed area is virtually a cubic (cF8) single crystal [7].

Equation 1 is the starting point of our analysis. For the diffusion couple between gas and solid, an analytical solution for the Fickian diffusion equation has been well established, where the boundary conditions for this equation are that the concentration of a diffusing element, C at a position $x > 0$, i.e. anywhere below the surface at time $t = 0$ is 0 and that the surface concentration remains constant, C_s . The analytical solution for Fick's second diffusion equation with these boundary conditions is:

$$C(x, t) = C_s \left[1 - \operatorname{erf} \left(\frac{x}{2\sqrt{Dt}} \right) \right] \quad (1)$$

where erf is the mathematical error function [7]. Once an experimental concentration profile has been determined, it can be compared with the analytical curve to determine the diffusion coefficient.

Figure 7: Binary Zr-Ag phase diagram showing that the solidus of 6.9% Ag is above 1 500°C [8]



Note that dotted lines and "1500 °C, 6.9% Ag" words were added by the authors.

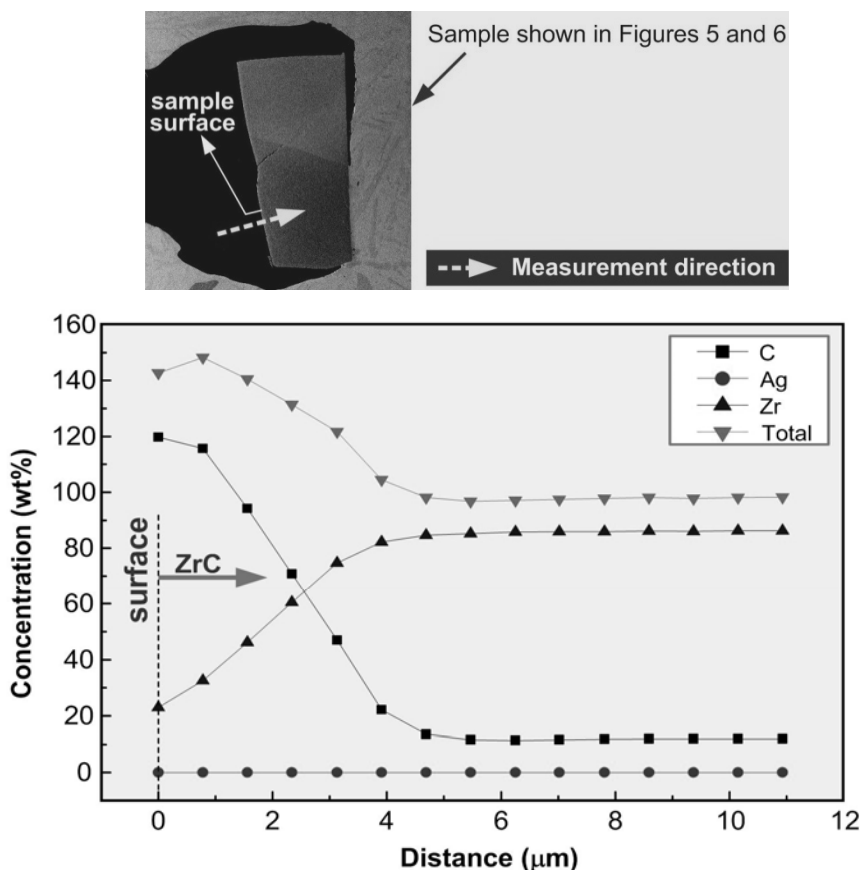
To obtain an experimental concentration profile for Ag, the diffusion annealed sample was mounted and cross-sectioned. The concentration was measured from the surface to the bulk of the ZrC using WDS. One of the measurement results showed that the bulk composition of the sample was about Zr-6.9% Ag as already mentioned earlier.

Figure 7 shows the binary Zr-Ag phase diagram. The solidus of Zr-6.9% Ag alloy is sufficiently higher than 1 500°C to avoid liquation during diffusion annealing. The cross-section of the sample annealed at 1 500°C for 50 hours showed a reaction layer where carbon from the graphite containment reacted with the Zr in solid solution as shown in Figure 5. This seems to act as a protective layer of solid solution preventing further loss of

Zr. The area of Zr-6.9% Ag solid solution looks to be inhomogeneous, which is most likely caused by the phase transformation from 1 500°C to room temperature. According to the binary Zr-Ag phase diagram, the solid solution of Zr-6.9% Ag will undergo phase transformations while cooling, since the cooling rate is quite slow (200°C/hr). During annealing, we expect the concentration to remain constant as a single phase. One way to improve on this is to increase the volume of Zr-Ag alloy to make sure the alloy is less affected by potential compositional changes.

Assuming a binary Zr-6.9% Ag alloy and looking at the phase diagram in Figure 7, at 1 500°C no melting should occur with the 6.9% Ag alloy used for this experiment. This means a gas-solid interface should be present inside the gap in the diffusion couple. Even at 2 366°C, the vapour pressure of pure Zr is only 1 Pa [9]. Therefore, the Zr diffusion from the gaseous Zr is not likely to change the concentration of ZrC, making it possible to define the impurity diffusion coefficient of Ag in ZrC.

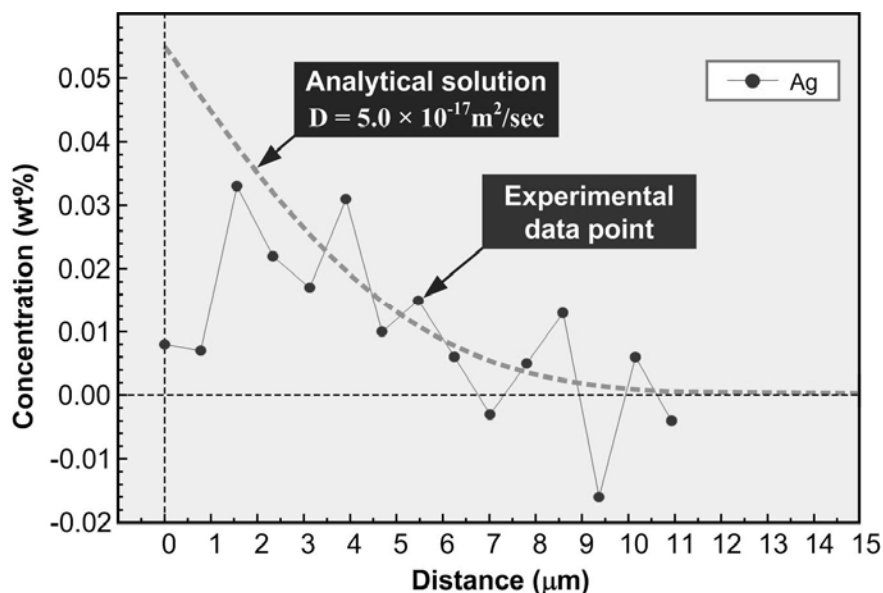
Figure 8: Measured area and concentration profiles of diffusion at 1 500°C, 50 hours



Before presenting a measured diffusion coefficient, it is worth noting that the measured concentration is pushing the limits of the resolution of the EPMA technique. One of the assumptions when performing EPMA is that the analysed volume is homogenous. However, in practice the secondary fluorescence of the beam across the boundary between the carbons containing mounting material and the ZrC, detects carbon from the mounting material, which skews the concentration of carbon [10]. This is why the carbon content alone is over 100 wt% in Figure 8. The total is the sum of the absolute concentration of each element; ideally it should be 100 wt%. Zr concentration also decreases as the depth of ZrC decreases since the interaction volume of incident

electrons begins to include the outside of the sample as well as the bulk sample itself. Due to limitations of EPMA, measured data may not be very accurate for curve fitting with an analytical solution. This is especially the case when the concentration of the diffusing element is very low and a very shallow area is measured. Although an optimal EPMA standard sample for accurate quantitative analysis is not available, the concentration profile demonstrates a measurable variation, at least, in the relative concentrations of silver.

Figure 9: Concentration profile of Ag in ZrC diffusion heat-treated at 1 500°C, 50 hours



Figures 8 and 9 are concentration profiles from measurements using WDS. Although the Ag concentration is very low, Ag was detected only near the original diffusion surface and not elsewhere in the ZrC. Figure 9 presents the same Ag data as in Figure 8, but the scale is shifted to clearly show the concentration of Ag. The dashed curve represents the fitting of a concentration profile from the solved diffusion equation. Using Equation 1 and curve fitting with experimental data points, the diffusion coefficient of Ag in $\text{ZrC}_{0.84}$ was determined as $5.0 \times 10^{-17} \text{ m}^2/\text{sec}$.

Experiments with better sample design, rapid heating and cooling procedures and a more suitable measurement technique, specifically SIMS, are also in progress to obtain more accurate diffusion data for Ag in ZrC.

Conclusions

A new liquid encapsulation method has been developed to construct a constant source diffusion couple between ZrC and Zr-6.9% Ag solid solution using an arc melter. Implementing this method, the diffusion coefficient of Ag in $\text{ZrC}_{0.84}$ at 1 500°C was experimentally determined to be about $5.0 \times 10^{-17} \text{ m}^2/\text{sec}$. This is the first known value of this diffusion coefficient.

Acknowledgements

The support of the Department of Energy, Office of Nuclear Energy Deep Burn projects is gratefully acknowledged for providing funding support. The authors would like to thank Dr. J. Fournelle for expert guidance with EPMA measurements and analysis.

References

- [1] D. A. Petti, J. Buongiorno, J. T. Maki, R. R. Hobbins, G. K. Miller (2003), "Key differences in the fabrication, irradiation and high temperature accident testing of US and German TRISO-coated particle fuel, and their implications on fuel performance", *Nuclear Engineering and Design*, 222, pp. 281-297.
- [2] R. N. Morris, D. A. Petti, D. A. Powers, and B. E. Boyack (2004), "TRISO-Coated Particle Fuel Phenomenon Identification and Ranking Tables (PIRTs) for Fission Product Transport Due to Manufacturing, Operations, and Accidents", NUREG/CR-6844, Vol. 1, US-NRC.
- [3] K. Sawa and S. Ueta (2004), "Research and Development on HTGR fuel in the HTTR project", *Nuclear Engineering and Design* 233, pp. 163-172.
- [4] G. Wang and J. J. Lannutti (1995), "Chemical Thermodynamics as a Predictive Tool in the Reactive Metal Brazing of Ceramics", *Metallurgical and Materials Transaction A*, Vol. 26, No. 6, pp. 1499-1505.
- [5] H. Mehrer (2009), *Diffusion in Solids*, Springer.
- [6] M. E. Glicksman (2000), *Diffusion in Solids*, John Wiley & Sons.
- [7] A.N. Christensen (1990), "A Neutron Diffraction Investigation on Single Crystals of Titanium Oxide, Zirconium Carbide and Hafnium Nitride", *Acta Chem. Scand*, Vol. 44, pp. 851-852.
- [8] H. Okamoto (1997), *Journal of Phase Equilibria*, Vol. 18, No. 3, p. 312.
- [9] <http://en.wikipedia.org/wiki/Zirconium>
- [10] S. J. B. Reed (1993), *Electron Microprobe Analysis*, Cambridge University Press.

Session III

Metal – Materials Compatibility – Molten Salt and Sodium

Chair: Y. Dai

Alloys compatibility with selected molten salt environments for molten salt fast reactor breeders and burners

Victor Ignatiev, Alexandr Surenkov

RRC-Kurchatov Institute, Moscow, Russian Federation

Abstract

The molten salt reactor (MSR) has a long-term vision for highly sustainable reactors that requires significant development in a number of technical areas. Within GIF Generation IV an overall plan for the MSR is underway with its design features, processing systems and operating parameters to be developed within the next decade. This paper summarises the results of recent work done and the present state of knowledge about container materials for molten salt breeder and burner concepts. Key physical and chemical factors that influence material compatibility are analysed for screening candidate salts, as applied to different applications. Methods for purification of molten salt compositions and for improvement of Ni-based container alloys compatibility by maintaining the salt at low redox potential are discussed. The effect of fuel (uranium / plutonium fluorides) and fission product (tellurium) additions to different solvent systems on materials compatibility is considered. Results from our studies with corrosion facilities with thermal gradient at temperatures up to 750°C are presented.

Introduction

Recent years have demonstrated a growing interest in the circulating-fuel nuclear systems based on molten salt fluorides. These systems present a promising flexible option in response to the goals and criteria assigned to future nuclear systems: fuel cycle sustainability, safety, environmental impact, proliferation resistance, diversity of applications and economics.

Nuclear power systems employing molten salt fluorides have been investigated by ORNL, (United States) in the 1960s and 1970s. The favourable experience gained from the 8 MWt MSRE test reactor [1] operated from 1965 to 1969 led to the design of a 1 000 MWe molten salt breeder reactor (MSBR) with a thermal spectrum graphite moderated core, and thorium-uranium fuel cycle [2]. At the Kurchatov Institute (KI, Russian Federation), the molten salt programme was started in the second half of the 1970s [3]. The experimental and theoretical studies were mainly directed at the improvement of the MSBR type concepts.

The past decade's R&D on MSR has focused mainly on fast spectrum concepts (MSFR), which have been recognised as long-term alternatives to solid fuelled fast neutron reactors with attractive features (very negative feedback coefficients, smaller fissile inventory, easy in-service inspection and simplified fuel cycle). MSFR designs are already available for long-lived actinides burning and Th-U breeding [4-7]. For example, within the ISTC#1606 project (from 2001 to 2007) special focus was placed on the experimental and theoretical evaluation of the single stream Molten Salt Actinide Recycler and Transmuter (MOSART) system with homogeneous core fuelled only by transuranium elements (TRU) trifluorides from UOX and MOX PWR spent fuel [4]. Recent molten salt Th-U breeder developments in CNRS, France [5] [6] address advanced large power units without graphite in the Li, Th, U/F core. Unification of the MOSART system with Th containing molten salt blanket, which is now under study within the ISTC#3749 project [7], can provide (1) core operation with minor actinide bearing fuels basing on additional ^{233}U support or (2) effective production of ^{233}U required for starting uranium loading of MSFR.

An extremely large body of literature exists on the corrosion of metal alloys by molten fluorides. Much of this work was done at ORNL and involved either thermal convection or forced convection flow loops. In order to select the alloy best suited to this application, an extensive programme of corrosion tests was carried out on the available commercial nickel-base alloys and austenitic stainless steels [8-13].

These tests were performed in a temperature gradient system with various fluoride media and different temperatures (maximum temperature and temperature gradient). Chromium, which is added to most alloys for high-temperature oxidation resistance, is quite soluble in molten fluoride salts. Metallurgical examination of the surveillance specimens showed corrosion to be associated with outward diffusion of Cr through the alloy. It was concluded that the chromium content should be maintained as low as reasonably possible to keep appropriate air oxidation properties. Corrosion rate is marked by initial rapid attack associated with dissolution of Cr and is largely driven by impurities in the salt. This is followed by a period of slower, linear corrosion rate behaviour, which is controlled by a mass transfer mechanism dictated by thermal gradients and flow conditions. Minor impurities in the salt can enhance corrosion by several orders of magnitude and must be kept to a minimum. Dissolution can be mitigated by a chemical control of the redox in salts, for example by small additions of elements such as Be or Zr. Corrosion increased dramatically as the temperature was increased and was coupled to plate-out in the relatively cooler regions of the system, particularly in situations where high flow was involved.

Hastelloy N alloy was the only structural material used in the Li, Be, Zr, U/F MSRE test and contributed significantly to the success of the experiment [1]. Chemical compositions of Hastelloy N and its later modifications developed for MSBR are given in Table 1. Less

severe corrosion attack ($<10 \mu\text{m}/\text{yr}$) was seen for the Hastelloy N in contact with the MSRE fuel salt at temperatures up to 704°C for three years (26 000 hours). The most striking observation is the almost complete absence of corrosion for Hastelloy N during the 3-year exposure to MSRE coolant Li, Be/F salt.

Table 1: Chemical composition of nickel-based alloys (% mass)

Element	Hastelloy-N (INOR-8)	Hastelloy-N Ti-mod.	Hastelloy-N Nb-mod.	MONICR	HN80M-VI	HN80MTY (EK-50)	HN80MTV
Ni	base	base	base	base	base	base	base
Cr	7.52	6-8	6-8	6.85	7.61	6.81	6.94
Mo	16.28	11-13	11-13	15.8	12.2	13.2	9.35
Ti	0.26	2	—	0.026	0.001	0.93	1.68
Fe	3.97	0.1	0.1	2.27	0.28	0.15	< 0.33
Mn	0.52	0.15-0.25	0.15-0.25	0.037	0.22	0.013	< 0.1
Nb	—	0—2	1—2	< 0.01	1.48	0.01	—
Si	0.5	0.1	0.1	0.13	0.040	0.040	< 0.05
Al	0.26	—	—	0.02	0.038	1.12	—
W	0.06	—	—	0.16	0.21	0.072	5.5
Cu	0.02	—	—	0.016	0.12	0.020	< 0.01
Co	0.07	—	—	0.03	0.003	0.003	—
Ce	—	—	—	< 0.003	0.003	0.003	—
Zr	—	—	—	0.075	—	—	—
B	< 0.01	0.001	0.001	< 0.003	0.008	0.003	< 0.0005
S	0.004	0.01	0.01	0.003	0.002	0.001	< 0.001
P	0.007	0.01	0.01	0.003	0.002	0.002	< 0.001
C	0.05	0.05	0.05	0.014	0.02	0.025	0.003

- The elements were neither added to the melt nor determined.

Two main problems of Hastelloy N requiring further study were observed during the construction and operation of the MSRE. The first was that the Hastelloy N used for the MSRE was subject to a kind of “radiation hardening”, due to accumulation of helium at grain boundaries [1]. Later, it was found that modified alloys with fine carbide precipitates within the grains would hold the helium and avoid this migration to the grain boundaries. Nevertheless, it is still desirable to design MSR in which the exposure of the reactor vessel wall to fast neutron radiation is limited. The second problem was the discovery of tiny cracks on the inside surface of the Hastelloy N piping for the fuel circuit. It was found that these cracks were caused by the fission product tellurium [12]. Later work showed that tellurium attack could be controlled by keeping the fuel on the reducing side. This is done by adjustment of the chemistry so that about 2% of the uranium is in the form of UF_3 , as opposed to UF_4 . This can be controlled rather easily now

that good analytical methods have been developed. If the UF_3 to UF_4 ratio becomes too low, it can be raised by the addition of some beryllium metal, which, as it dissolves, will take some of the fluoride ions from the uranium.

Research towards finding a material for constructing a MSR that has adequate resistance to irradiation embrittlement and inter-granular cracking by tellurium has progressed [11-12]. The latest ORNL findings suggest very strongly that a MSR could be constructed of 1- to 2%-Nb-modified Hastelloy N and operated very satisfactorily at 650°C.

Methods and facilities

At KI, a material testing for MSRs was started in 1976 [3]. It was substantiated by data accumulated in the ORNL MSR programme on Ni-Mo alloys for UF_4 -containing salts. Our MSR programme included: (1) development of structural material for the MSR primary circuit on the base of Hastelloy-N, which is compatible with its environments, has acceptable mechanical properties, both non-irradiated and irradiated after exposure to maximum temperatures up to 750°C; (2) tests of corrosion resistance of domestic alloys and steels under various operation conditions and the selection of most promising among them.

In KI corrosion studies the Ni-Mo alloy HN80MT was chosen as a base. Its composition (in wt.%) is Ni-6.9%Cr-0.02%C-1.6%Ti-12.2%Mo. The development and optimisation of the HN80MT alloy was mainly envisaged to be performed in two directions: (1) improvement of alloy resistance to selective chromium corrosion and (2) increase in alloy resistance to tellurium inter-granular corrosion and cracking (IGC). The alloy resistance to IGC was estimated from parameter "K", which is the value equal to the product of cracks number on 1 cm length of longitudinal section of specimen subjected to tensile strain, multiplied by an average cracks depth in micrometers.

The corrosion resistance of materials was studied by two methods. The first is the method of ampoule static isothermal test of reference specimens in various molten-salt mixtures. The second method involves tests of materials in forced and natural convection loops with thermal gradient. Not only high purity, but also high oxidation conditions were present in the loops. The latter circumstance made it possible to estimate the limiting corrosion characteristics of the materials. The summary of Ni-based loop corrosion tests for fluoride fuel salts is presented in Table 2.

Special attention was paid to the purification of molten salt from impurities. In general, before filling the loop for main corrosion test, there are two options: (1) to refill the loop with fresh pure salt and (2) to remove oxygen, nickel and iron impurities from the flash salt. The second way led us to the necessity of salt charge purification from oxidants in order to reduce its redox potential down to values acceptable for corrosion studies.

On the basis of the available data and thermodynamic assessment of molten salt state, the following order of the technological operations for salt purification was accepted [4] [13]: (1) hydrofluorination of salt by a mixture of hydrogen fluoride and helium in order to remove solid and dissolved oxides; (2) electrolysis of the salt aimed at removing the main amount of dissolved nickel and (3) treatment of salt by metallic beryllium in order to remove the rest of nickel and iron ions.

Table 2: Summary of Ni-based loop corrosion tests for molten fluoride salts [19] [20]

Loop	Salt, in mole %	Specimens material	T _{max} , °C	ΔT, °C	Exposure time, hr	Corrosion rate, μm/yr
F1	71.7LiF-16BeF ₂ -12ThF ₄ - 0.3UF ₄ +Te	HN80MT	750	70	1 000	3
F2		HN80MTY	750	70	1 000	6
NC-1	LiF-NaF-BeF ₂ +PuF ₃	HN80M-VI	700	100	1 600	5
		HN80MTY				5
		MONICR				19
NC-2	LiF-BeF ₂ -ThF ₄ +UF ₄	HN80M-VI HN80MTY HN80MTV	720	100	Under exposure	-
Te-1	LiF-NaF-BeF ₂ +Cr ₃ Te ₄	HN80M-VI	700	10	400	3
		HN80MTY				3
		MONICR				15
Te-2	LiF-ThF ₄ +UF ₄ +Cr ₃ Te ₄	HN80M-VI HN80MTY HN80MTV Ni-25W-6Cr	720	10	250	-

Note that recent facilities of NC-1, 2 and Te-1, 2 types (see Table 2) include the systems for redox potential measurement during corrosion studies. Details of these loops designs have been described previously [4] [13]. The first type of facility, the thermal convection corrosion loop, makes it possible to carry out experiments with molten salt heat up to about 80-100°C and its flow rate up to 5 cm/s. The second type of facility was developed for the tests of Ni-based alloy resistance in the presence of chromium telluride in stressed and unloaded conditions at temperatures up to 700-750 °C. Auxiliary systems have been developed and installed to both facilities to carry out the melt decontamination from impurities and to provide melt sampling in the course of the corrosion tests, to make addition of UF₄ or PuF₃ and fission product simulators, gaseous and solid oxidants (HF, FeF₂), reducing agents (H₂, Be) and fluoride agents, affecting the melt's redox potential (HF-H₂).

To measure the redox potential of the BeF₂ and PuF₃ containing salts diaphragm-free three-electrode meter with a nonstationary (dynamic), a beryllium reference electrode was developed [14]. The results of corrosion experiments in the corrosion loops NC-1 and Te-1 demonstrated reliability of the developed design for measuring the redox potential in 15LiF-58NaF-27BeF₂ salt mixture containing plutonium and tellurium. It was shown that the three-electrode meter with a dynamic reference electrode is highly sensitive to changes in the redox potential of the melt and measures these changes to within ±5 mV.

Recent studies [15] with molten LiF-ThF₄ mixture containing up to 2.5 mol.% of UF₄ have revealed that well reproducible and analysable cathodic and cyclic voltammograms can be measured only in partially reduced melts with UF₃ additions, which are free from electropositive impurity ions. Linearity of the dependences i_p^c vs. [UF₄] and i_p^c vs. $v^{1/2}$, as well as the independence of the E_p^c of v in the experiment is qualitatively consistent with the voltammetric criteria of reversibility of the investigated electrode process. Platinum, tungsten or molybdenum can be used as the material of the reference and working electrodes. If the electrodes are made of different materials, the thermal emf affects the results of potentiometric and voltammetric measurements.

Breeders

About 70 differently alloyed specimens of the HN80MT were studied in ampoule tests with the molten Li, Be, Th, U/F mixture. The alloying elements included: W, Nb, Re, V, Al, Mn and Cu. It was found that mechanical properties and corrosion rate depend slightly on the type of alloying, remaining practically in all cases at an acceptable level.

The combined results of the investigation of mechanical, corrosion and radiation properties of various alloys of HN80MT permitted the KI to suggest the Ti- and Al-modified alloy as an optimum container material for the MSR design [3] [16]. This alloy, named HN80MTY (or EK-50), has the composition given in Table 1.

In the thermal convection loop F1 operated with the molten Li,Be,Th,U/F salt system, the HN80MTY alloy specimens showed a maximum uniform corrosion rate of 6 $\mu\text{m}/\text{year}$ (see Table 2). As for the HN80MT alloy, it was twice lower [3] [16]. The corrosion was accompanied by selective leaching of chromium into the molten salt, which is evidenced by the 10-fold increase in its concentration for 500 hours of exposure. Similar oxidising conditions, characterised by the same content of Fe and Ni impurities in the salt, existed in testing a standard Hastelloy N alloy on the NCL-21A loop operated with a molten Li, Be, Th, U/F salt system at ORNL [17]. For the NCL-21A loop, uniform corrosion rate of Hastelloy N specimens was about 5 $\mu\text{m}/\text{year}$. However, in the NCL-21A loop, the maximum temperature was somewhat lower (704°C) than in the KI experiments (750°C) and in addition, fission products, including Te, were not added to the circuit.

Comparison with corrosion data obtained at ORNL [10] indicates the HN80MT and HN80MTY resistance is higher than that of the standard Hastelloy N. This conclusion is confirmed by the microphotographs of HN80MT and HN80MTY alloy specimens after corrosion tests (see Figures 1 and 2). Physical metallurgy studies were done on longitudinal metallographic sections of specimens subjected to tensile tests (see Table 3).

Under static conditions at $T=600^\circ\text{C}$, there is only a slight tendency of HN80MT to IGC(IGC), and corrosion defects are observed along grain boundaries at a depth of 20 to 30 μm . As temperature increases to 750°C, the defect depth increases to 60 μm . Transition to loop tests at $T=750^\circ\text{C}$ show even more expressed IGC (see Figure 1c). Massive defects in the material along the grain boundaries at full depth and further cracking over boundaries of the following grains are found. The defect area reaches 130 μm . The estimated value for the parameter "K" in these conditions (ampoule isothermal tests at $T=750^\circ\text{C}$) amounts to 1 300 $\text{pc}\cdot\mu\text{m}/\text{cm}$. For the HN80MT alloy, this value is more than five times lower than that of a standard Hastelloy N alloy subjected to similar testing conditions [12].

Therefore, the maximum operating temperature for HN80MT alloy in a reactor should be reduced at least down to 700°C and rigorous control of oxidation-reduction potential of the fuel salt is necessary. A completely different picture was observed in testing HN80MTY alloy specimens. No IGC traces were found, either in static tests under stress conditions (at 650 to 800°C up to 245 MPa) or in thermal convection loops up to $T=750^\circ\text{C}$ [3] [16]. The thermal convection tests show that corrosion proceeds uniformly along the entire grain volume, giving rise to a small porous layer near the material surface in contact with the fuel salt at the depth of 15 to 30 μm (see Figure 2).

Table 3: Mechanical characteristics of nickel-molybdenum alloys before and after 1 200 hours corrosion test in thermal convection loop NC-1

Alloy	Specimens conditions	Temperature, °C	$\sigma_{0.2}$, MPa	σ_B , MPa	δ , %
HN80M-VI	Before test (hot deformed)		1 110	1 210	10
	After test	605...645 °C	870	1 025	21
		650...700 °C	725	970	35
	Before tests (quenched in water after thermo-mechanical treatment and 2 h annealing at 1 100°C)		470	800	47
	After test	605...645 °C	400	780	50
		650...700 °C	370	800	50
HN80MTY	Before test (quenched in water after 1 h annealing at 1 100°C)		450	800	46
	After test	605...645 °C	400	820	47
		650...700 °C	410	815	53
MONICR	Before test (conditions of delivery)		510	760	52
	After test	605...645 °C	515	763	50
		650...700 °C	514	759	53
	Before test (quenched in water after thermo-mechanical treatment and 2 h annealing at 1 100 °C)		540	890	35
	After tests	605...645 °C	545	898	33
		650...700 °C	602	895	36

A material study of Ni-Mo alloys specimens after 250 h exposure in test loop Te-2 (see Table 2) under different mechanical loadings, including 0; 25 and 50 MPa at 720°C in molten 78LiF-20ThF₄-2UF₄ (mole%) mixture containing chromium telluride addition is executed within ISTC#3749. Note that before the corrosion test preliminary purified fuel salt was additionally treated by metallic beryllium during 9 h. Figure 3 shows microphotographs of HN80M -VI with 1.5% Nb; HN80MTY with 0.9% Ti, 1.1% Al and HN80MTV with 1.7% Ti, 5.5% W alloys surface layer after testing under stress in the tellurium containing melt. As can be seen from Figure 3, no inter-granular corrosion for alloys under study was observed in this test.

Thus, choosing effective alloying additions and proper control of oxidation-reduction potential of the fuel salt can solve the problem of IGC for nickel alloys in fuel salts containing fission products. The corrosion and other characteristics of developed HN80MTY alloy make it possible to consider it as a promising structural material for Th-U MSR with a maximum working temperature of 750 to 800°C.

Burners

In the ISTC#1606 corrosion study, special focus was placed on the compatibility of Ni-based alloys with a molten Li,Na,Be/F salt mixture fuelled by PuF_3 [4]. Different HN80MT type alloys, including particularly: HN80M-VI with 1.5% Nb, HN80MTY with 1% Al and MONICR with about 2% Fe were chosen for the study in the corrosion facilities (see Table 1).

The results of a 1 200-hr loop corrosion test [4] [13] with on-line redox potential measurement demonstrated that high-temperature operations with molten 15LiF-58NaF-27BeF₂ (mole%) salt are feasible using carefully purified molten salts and loop internals. In the established interval of salt redox potential 1.25-1.33 V relative to a Be reference electrode, corrosion is characterised by uniform loss of weight with low rate from sample surfaces. Under such exposure, the salt contained less than (in mass%): Ni-0.004; Fe-0.002; Cr-0.002. Specimens of HN80M-VI and HN80MTY alloys from the hot leg of the loop exposed at temperatures from 620°C to 695°C showed a uniform corrosion rate from 2 $\mu\text{m}/\text{yr}$ to 5 $\mu\text{m}/\text{yr}$. For the MONICR alloy, this value was up to 20 $\mu\text{m}/\text{yr}$ (see Table 2). As shown in Figure 4, the metallurgical examination of the specimens after 1 200 h exposure in the corrosion loop with 15LiF-58NaF-27BeF₂ melt showed corrosion associated with outward diffusion of Cr through the alloy surface layer. The data from the chemical analysis of the specimen's surface layer showed a decrease in chromium content by 10 to 20 μm . The mechanical characteristics of nickel-molybdenum alloys before and after 1 200 h corrosion test in thermal convection loop NC-1 are given in Table 3.

No significant change in the corrosion behaviour of material samples was found in the melt due to the presence of 0.5 mole% PuF_3 addition in 15LiF-58NaF-27BeF₂ (mole%) salt. Specimens of HN80M-VI exposed during 400 h at 650°C in the loop showed a uniform corrosion rate of about 6 $\mu\text{m}/\text{yr}$ (see Table 2). Under such exposure, the salt contained (in mass%): Ni - 0.008; Fe -0.002; Cr- 0.002. No traces of IGC were found for all specimens after tests at NC 1 loop, even in the melt with PuF_3 addition.

Tellurium IGC testing of the Ni-Mo alloys [4] [13] without and under mechanical load for the 15LiF-58NaF-27BeF₂ (mole%) melt in ampoule and dynamic conditions at Te-1 facility (see Table 2) was done at 700°C with exposure times of about 100 and 250 hours. Figures 5-8 and Table 4, respectively, present microphotographs of the specimens surface layer and characteristics of IGC for different Ni-Mo alloys under study after exposure in this melt with the addition of chromium telluride (Cr_3Te_4) at different redox potentials (established, particularly, by the addition of NiF_2 oxidant or metallic Be reducer) without and under mechanical stress.

Table 4: Characteristics of inter-granular corrosion for different Ni-Mo alloys after 240 hours exposure in 58NaF-15LiF-27BeF₂ melt containing chromium telluride without and with 80 MPa stress at 700°C in test loop Te-1

Alloy specimens	Stress, MPa	Number of cracks per 1 cm length	Average depth of cracks, μm	Maximum depth of cracks, μm	K, $\text{pc}\cdot\mu\text{m}/\text{cm}$
HN80M-VI	no	16	43	75	690
	yes	24	65	125	1 560
HN80MTY	no	14	27	37	380
	yes	21	42	75	880
MONICR	no	115	31	44	3 590
MONICR ¹	yes			220	>1 0000
Ni-7Cr-12Mo-0.5Ti-1Nb	yes	23	164	220	3 770
Ni-7Cr-12Mo-0.5Ti-1Nb-1Re	yes	14	80	175	1 120
Ni-7Cr-12Mo-0.5Ti-1Nb-0.01Y	yes	15	79	156	1 190

Note: MONICR specimen has shown brittle fracture at minimum stress and with very low relative elongation at rupture, that many of surface cracks were not opened.

For each of the tested alloys the intensity of tellurium IGC was essentially lower: (1) in unstressed state than in stress condition and (2) in reducing than in oxidising melt conditions. It was particularly apparent for alloys with low IGC resistance. So, for the MONICR alloy in unstressed state (see Figure 5.a) the grain boundary disruption was observed over the whole template surface to the depth up to 44 μm ($K = 3\,590\text{ pc}\cdot\mu\text{m}/\text{cm}$). As shown in Figures 5.b, for MONICR specimens under stress the depth of cracks reached 220 μm ($K > 10\,000\text{ pc}\cdot\mu\text{m}/\text{cm}$) and the intensity of cracking was maximum as compared to other alloys tested under similar conditions. Mechanical testing of the MONICR specimens after exposure in the melt led to their brittle failure at minimum stress and with very low relative elongation at rupture. As can be seen from Figure 8, for MONICR alloy the tellurium IGC without stress at a low redox potential (1.2 V) was essentially lower compared to the experiment with melt under strongly oxidising conditions (about 1.6 V).

For the HN80M-VI alloy the resistance to IGC was much higher than that for MONICR alloy (see Figures 5 c, d). For a HN80M-VI specimen tested without stress rather low IGC ($K = 690\text{ pc}\cdot\mu\text{m}/\text{cm}$) was observed. Under stress the intensity of the HN80M-VI alloy cracking increased more than twice and the cracks' depth reached 125 μm . Niobium contents in the alloy of 1.5% looks optimal as our tests showed worse resistance to IGC compared to HN80M-VI alloy, as Nb decreased to 1.0% (see Figures 5 e, f).

Of all tested alloys the HN80MTY 1.1% Al has the best resistance against IGC (see Figures 5 e, f). The intensity of its IGC under stress is $K = 880\text{ pc}\cdot\mu\text{m}/\text{cm}$ (twice as low as that of the HN80M-VI alloy). Assuming that for these alloys, the process of tellurium diffusion along the grain boundaries follows general regularities, the temperature conditions for the HN80MTY alloy can be somewhat higher than those for the HN80M-VI.

Results of Nb, Ti, Re, Y, W, Al and Mn addition to the HN80M alloy on IGC after 240 h exposure in 15LiF-58NaF-27BeF₂ melt containing chromium telluride at 700°C with 1.2 V redox potential under 80 MPa stress are presented in Figure 6. According to ORNL data [12], even small Ti additions to an alloy doped only with Nb had a negative effect on the alloy resistance

to IGC. Figure 6 shows a microphotograph of alloy HN80MT 0.5% Ti and 1.0% Nb surface layer after testing. It is seen that the tellurium IGC was rather intense ($K = 3\,590\text{ pc}\cdot\mu\text{m}/\text{cm}$) and much higher than for the HN80M-VI alloy doped with Nb alone, which is in compliance with the ORNL data.

The data show that Re, Y and W additions (see Figures 6. b, c, and d) only slightly increase the alloys' resistance to tellurium IGC. The alloy doped with Nb alone exceeds them significantly concerning IGC resistance. The addition of Al and Mn can give an essential advantage in alloy resistance to tellurium IGC (see Figures 6e, f and Figures 8c, d, g, h). Thus, niobium is not the only one and optimal alloying element to enhance the Ni-based alloy's resistance to tellurium IGC.

As can be seen from Figure 7, a significant increase in IGC resistance was found for alloys with a decrease in Ti down to 0.8-1.0% and Al contents of 1.0-2.0%. Further decrease in Ti content down to 0.5% with a parallel increase in Al up to 3.0% leads to worse results related to tellurium IGC in the alloy.

Conclusion

Reliable materials for MSR with fuel salt temperatures up to 700-750°C are at present available. Our findings in developments of Ni-Mo alloys for MSRs shift the emphasis from alloys modified with titanium and rare earths to those modified with niobium and aluminum.

The problem of uniform Cr corrosion for Ni-Mo alloys was solved both by a decrease in Cr contents with compensation of heat resistance loss by an additional alloying and owing to the alloying alone by elements decreasing Cr thermodynamic activity in the alloy. The problem of tellurium IGC can be minimised or completely eliminated by alloying such elements as Nb, Al or Mn. Since all corrosion reactions are of an oxidation reduction character, monitored control of salt redox potential is a powerful means to suppress corrosion of the container material.

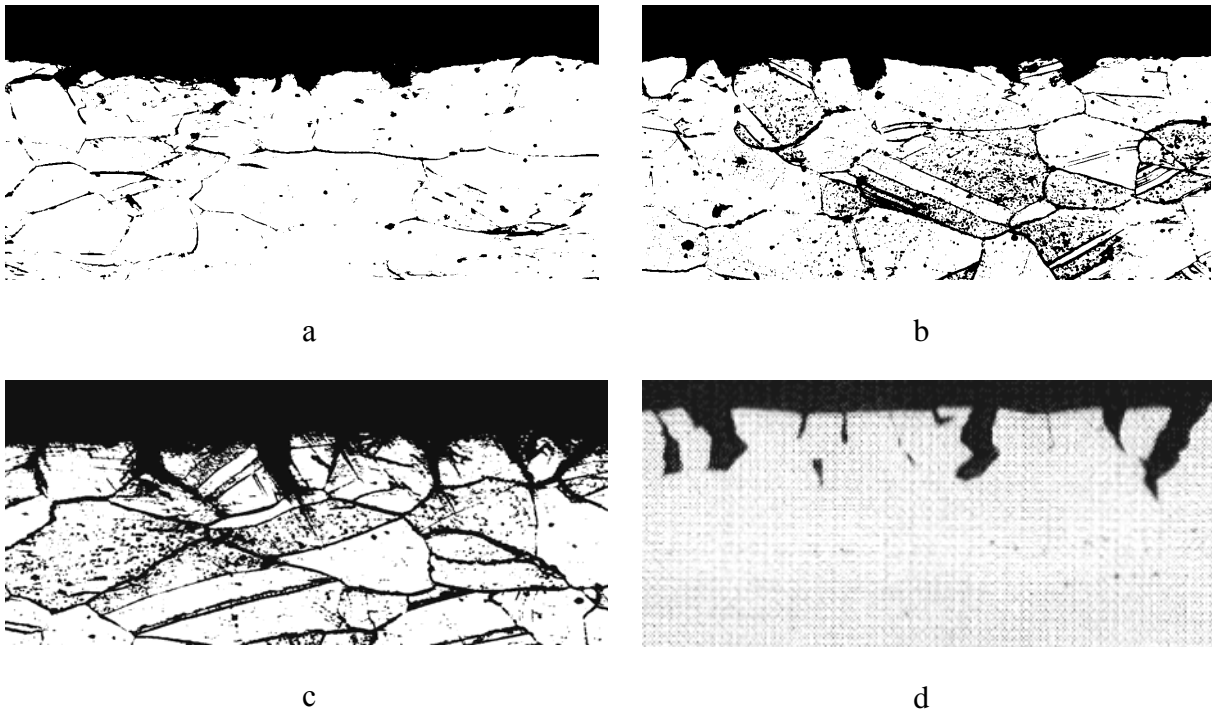
The results of combined investigation of mechanical, corrosion and radiation properties of various alloys of HN80MT type permitted to suggest the Ti-and Al-modified alloy as an optimum container material for the MSR burner and breeder designs with fuel salt temperatures up to 750°C. HN80MTY alloy 1% of Al is the most resistant to tellurium IGC of Ni-Mo alloys under study.

Further steps for this type of metallic materials development must involve: (1) irradiation, corrosion, tellurium exposure, mechanical property and fabrication tests to finalise the composition for scale up; (2) procurement of large commercial heats of the reference alloy; (3) mechanical property and corrosion tests of at least 10 000 h exposure; and (4) development of design methods and rules needed to design a MSR (breeder or burner) to be built of the modified alloy.

Acknowledgements

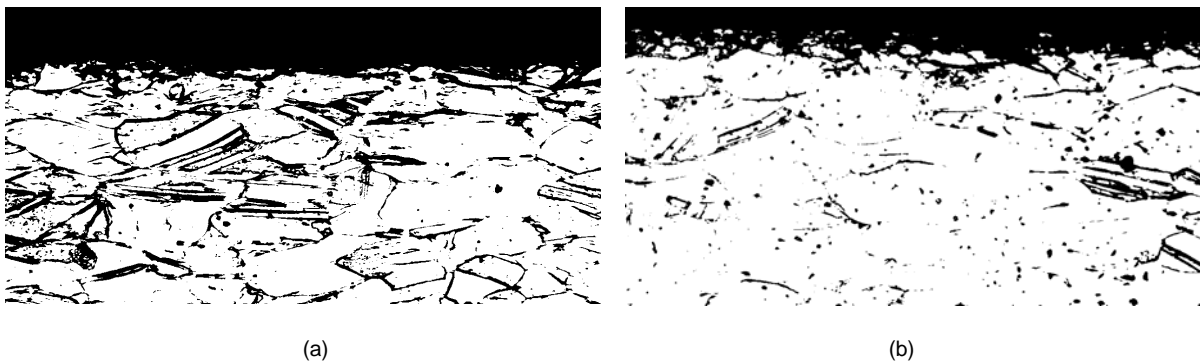
This work was supported in 2010 by the Russian Foundation for Basic Research grant No. 10-08-00097-a. This research utilised ISTC#1606 and ISTC #3749-supported facilities at the Kurchatov Institute (Moscow), VNIITF (Snezinsk) and IHTE (Ekaterinburg). The authors also would like to thank personally Ivan Gnidoi and Vadim Uglov (Kurchatov Institute), Valery Afonichkin and Alexander Bove (IHTE) as well as Vladimir Subbotin (VNIITF) for participation in the development of corrosion facilities and materials tests.

Figure 1: Microphotographs of the Ni-Mo alloy specimens (enlargement $\times 100$) after 500 hours exposure in melt $71.7\text{LiF}-16\text{BeF}_2-12\text{ThF}_4-0.3\text{UF}_4$ containing tellurium



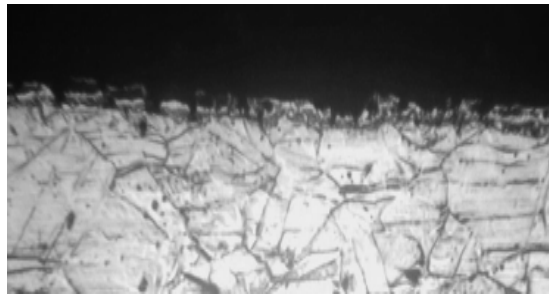
a - HN80MT, isothermal test, Texposure = 6000C; b - HN80MT, isothermal test, Texposure = 7500C, c - HN80MT, nonisothermal loop test, Texposure =750 0C; d - standard Hastelloy-N, isothermal test Texposure =700 0C [20]

Figure 2: Microphotographs of HN80MTY alloy specimens (enlargement $\times 100$) after 500 hours exposure to the tellurium containing melt $71.7\text{LiF}-16\text{BeF}_2-12\text{ThF}_4-0.3\text{UF}_4$

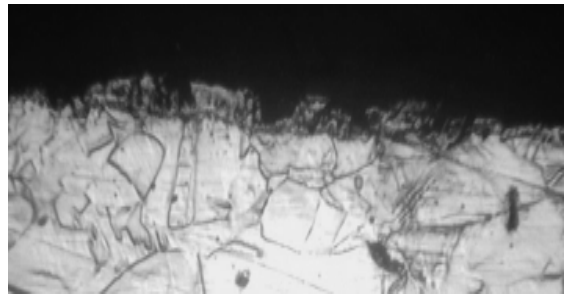


a- isothermal test, T = 750 °C; b- nonisothermal loop test, T = 750 °C.

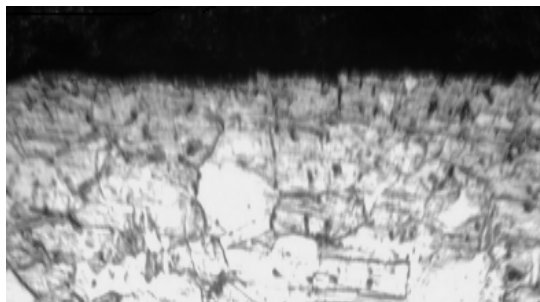
Figure 3: Microphotographs of the Ni-based alloy specimens (enlargement $\times 250$) after 250 hours exposure at 720°C in molten $78\text{LiF}-20\text{ThF}_4-2\text{UF}_4$ (mole %) mixture containing chromium telluride addition under different mechanical loadings (0, 25, 50 MPa)



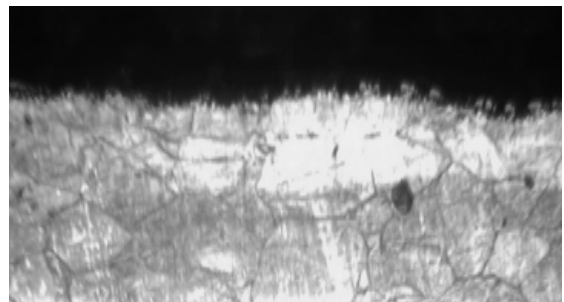
a)



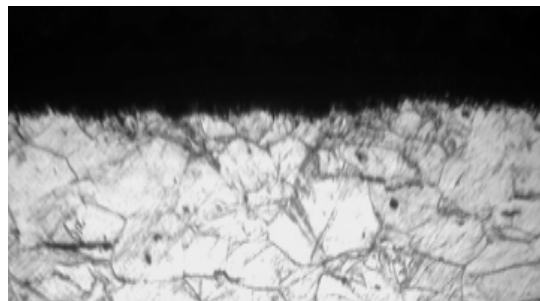
b)



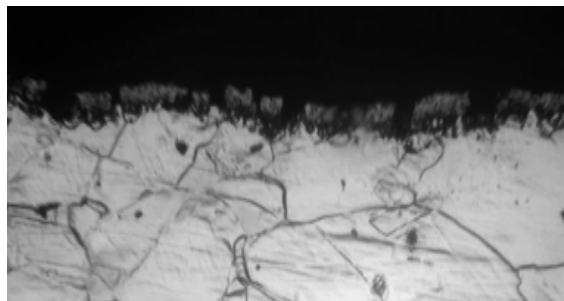
c)



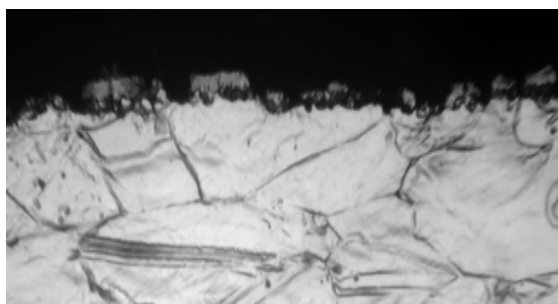
d)



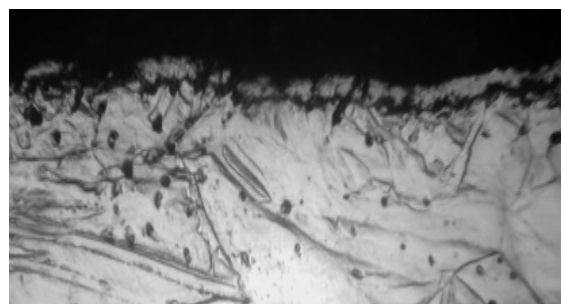
e)



f)



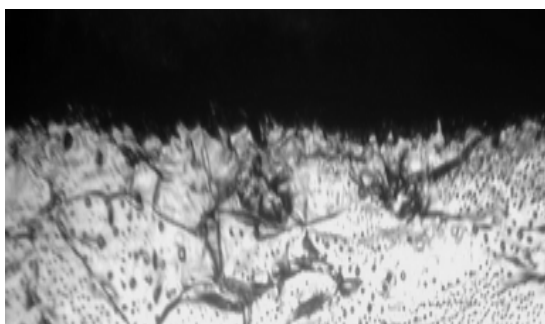
g)



h)



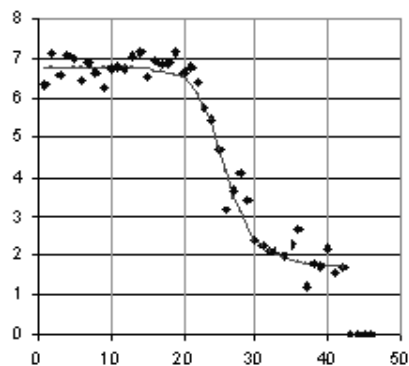
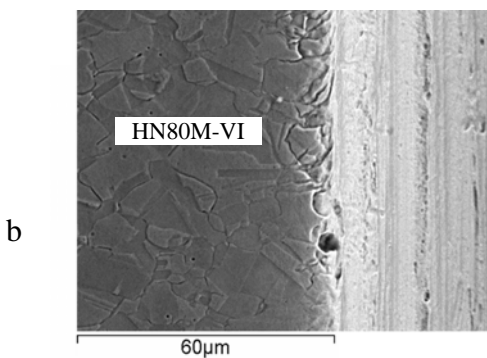
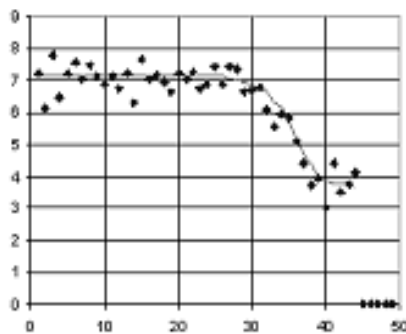
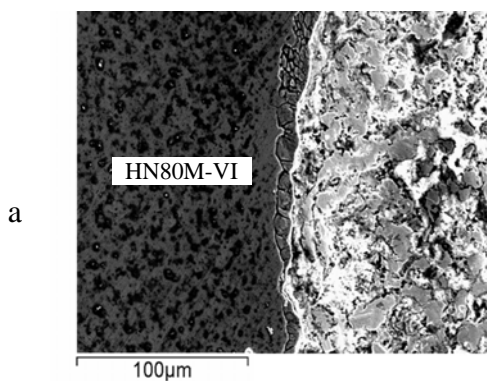
i)

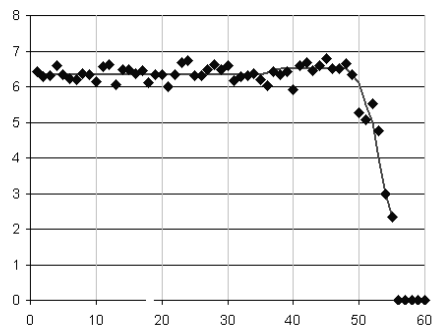
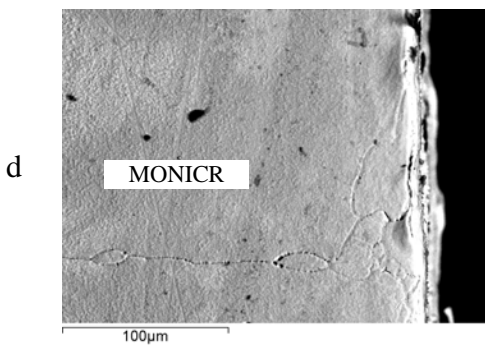
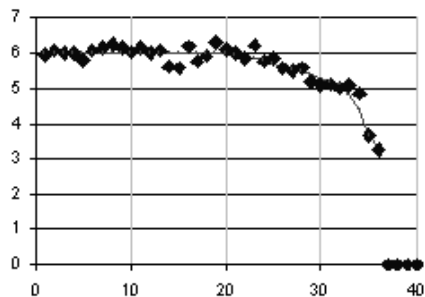
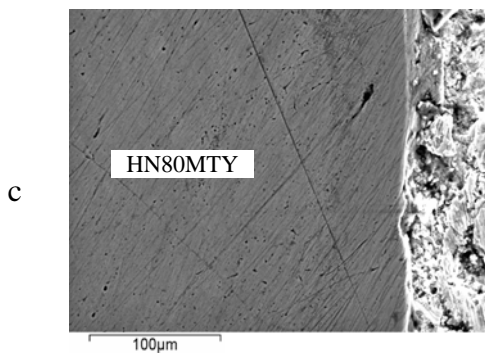


j)

a,b,c) HN80M-VI 1.5% Nb; d,e,f) HN80MTY 1.1% Al; g,h,i) HN80MTV 1.7% Ti, 5.5% W; j) HN80MTVB 1.5% Ti, 5.4% W, 1.0% Nb

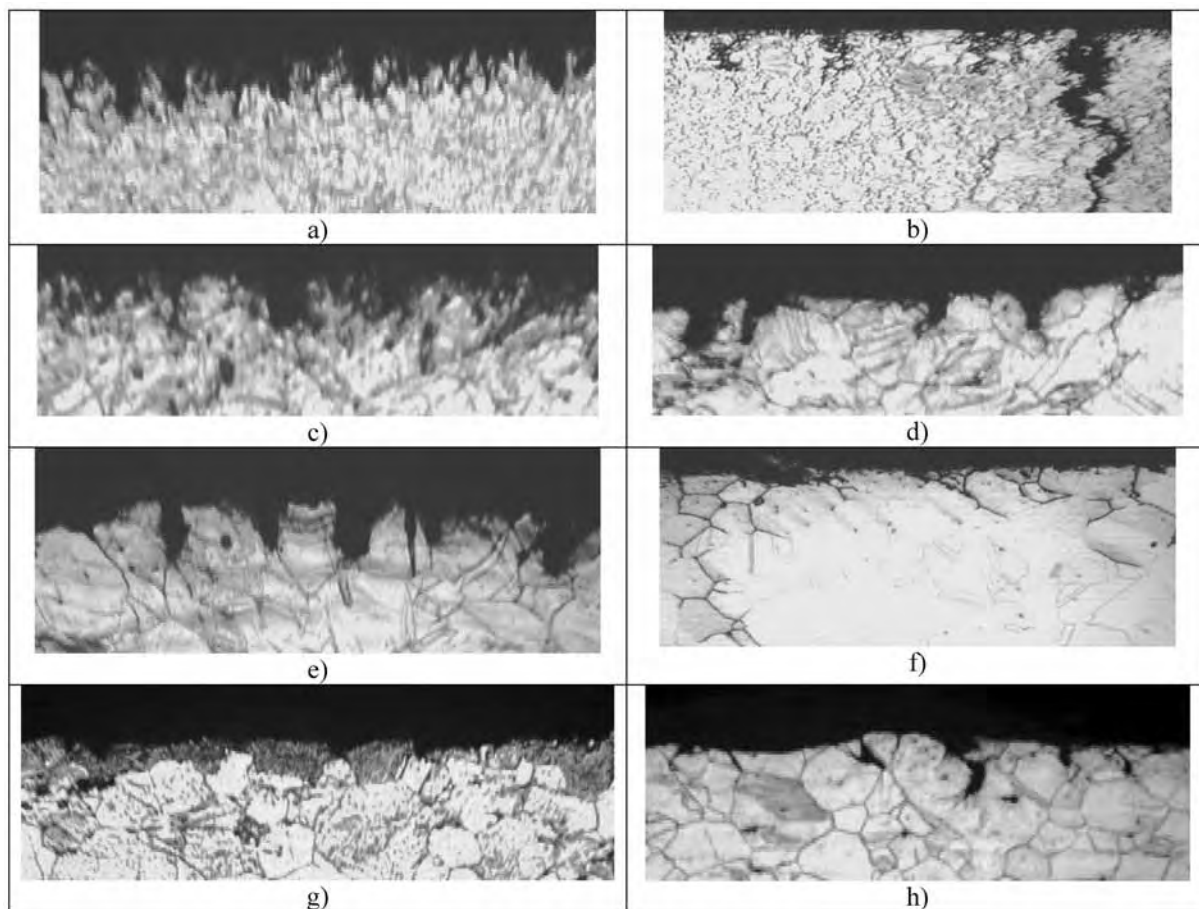
Figure 4: Chromium distribution (mass.%) vs. depth of the specimens surface layer (μm) after 1 200 hours exposure in corrosion loop with melt $15\text{LiF}-58\text{NaF}-27\text{BeF}_2$ at 1.25-1.33 V redox potential





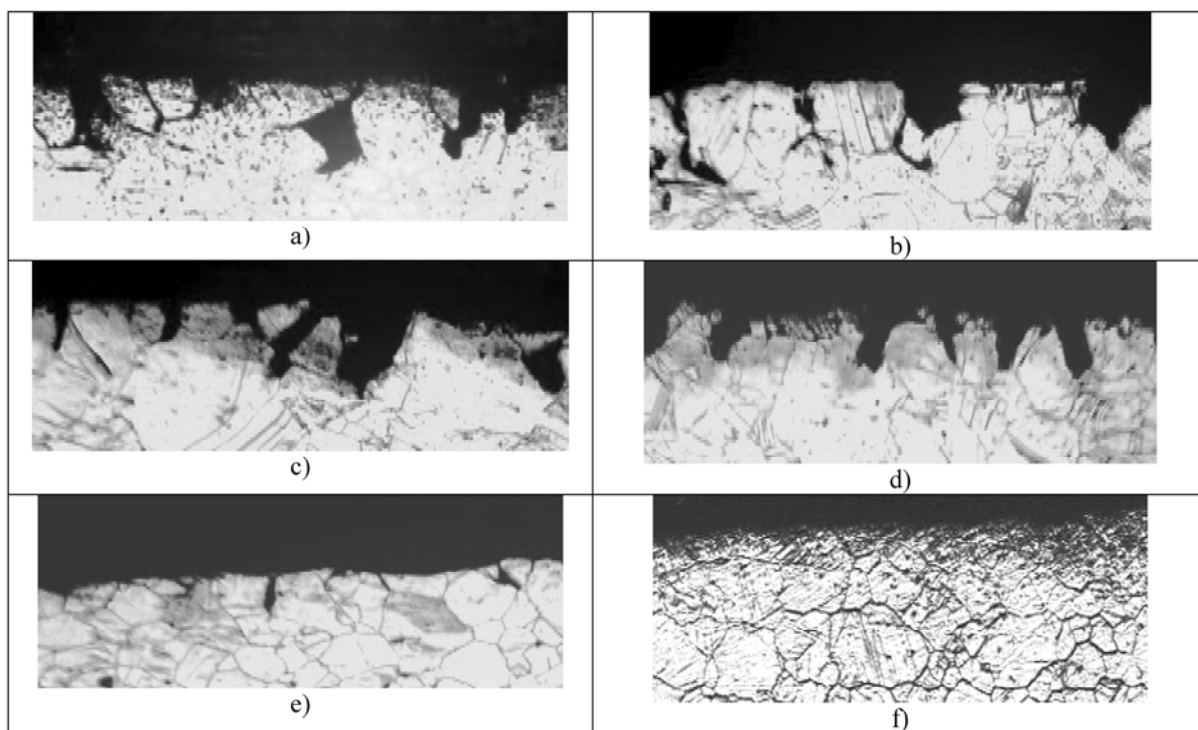
a - quenched HN80M-VI, T = 690°C; b - hot deformed HN80M-VI, T = 670°C; c - quenched HN80MTY, T = 620°C; d - MONICR, T = 690°C

Figure 5: Microphotographs of the Ni-based alloy specimens (enlargement $\times 160$) after 240 hours exposure in melt $15\text{LiF}-58\text{NaF}-27\text{BeF}_2$ with addition of chromium telluride (Cr_3Te_4) at 700°C and 1.2 V redox potential without and under 80 MPa stress



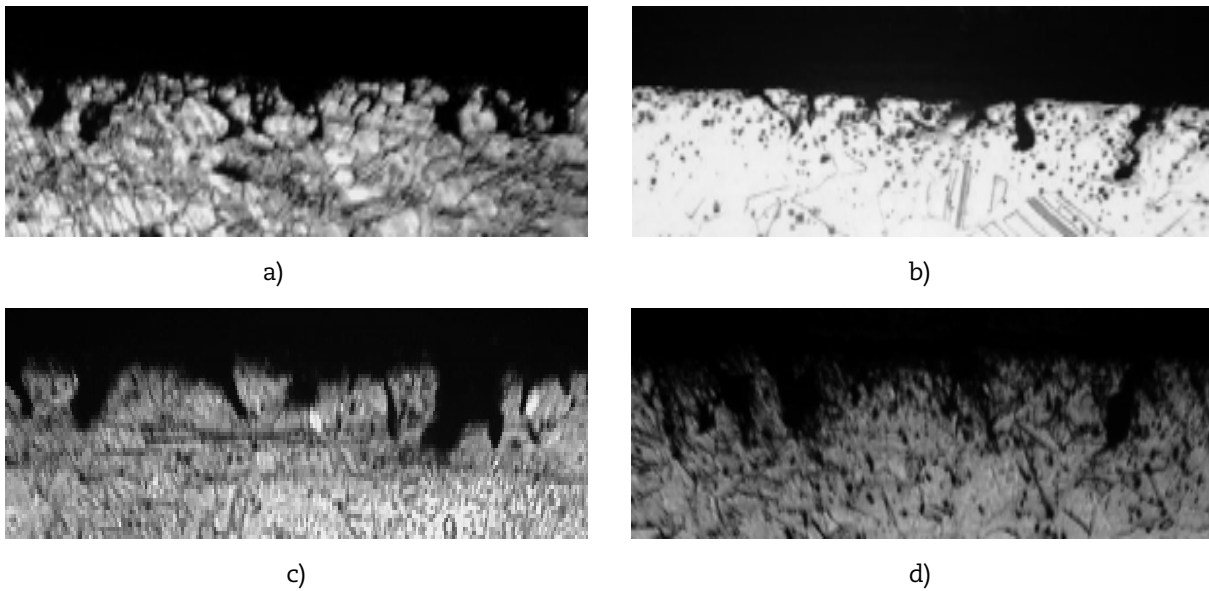
a,b) MONICR; c,d) HN80M -VI; e,f) HN80M 1,0 % Nb; g,h) HN80MTY 0.9% Ti and 1.1% Al

Figure 6: Effect of Nb, Ti, Re, Y, W, Al and Mn addition to the HN80M alloy specimens (enlargement $\times 160$) on IGC after 240 hours exposure in melt $15\text{LiF}-58\text{NaF}-27\text{BeF}_2$ containing chromium telluride at 700°C with 1.2 V redox potential under 80 MPa stress



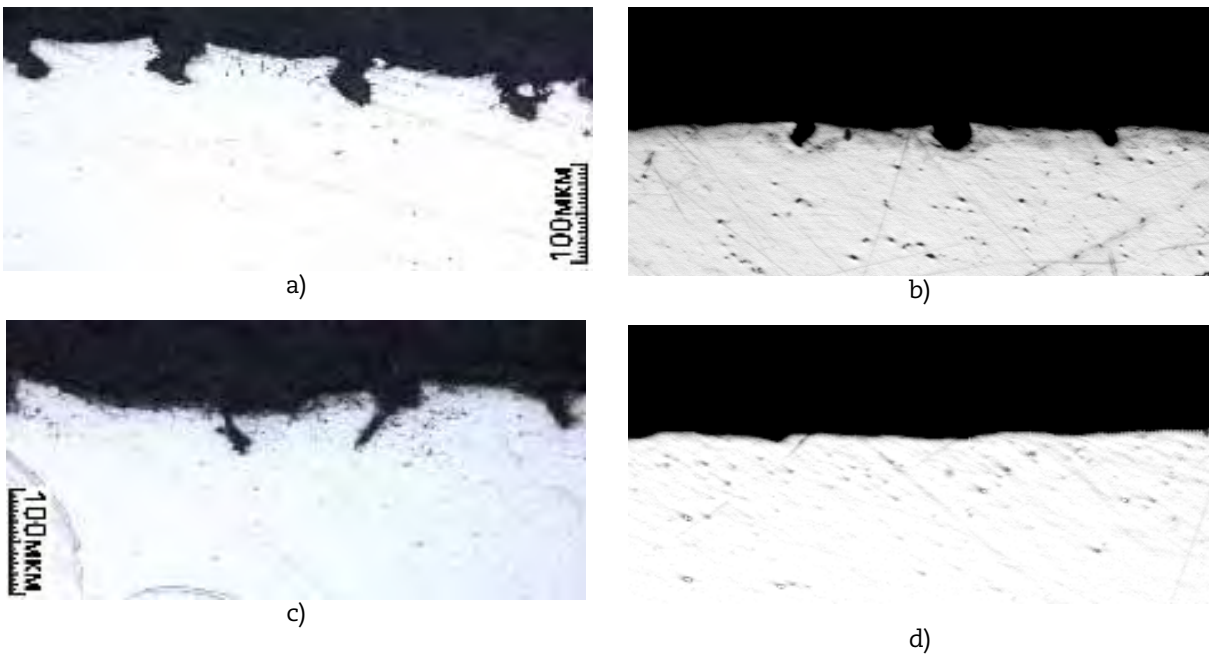
a) HN80M 0.5% Ti and 1.0% Nb; b) HN80M 0.5% Ti, 1.0% Nb and 1.0% Re; c) HN80M 0.5% Ti, 1.0% Nb and 0.01% Y; d) HN80M 9.4%Mo, 1.7%Ti, 5.5% W; e) HN80MTY 0.9 % Ti and 1.1% Al; f) HN80M 0.5% Ti, 1.0% Nb and 0.25% Mn

Figure 7: Microphotographs of the HN80M alloy specimens with different Ti and Al addition (enlargement $\times 160$) after 240 hours exposure in melt $15\text{LiF}-58\text{NaF}-27\text{BeF}_2$ with chromium telluride at 700°C and 1.2 V redox potential under 80 MPa stress



a) 1.7% Ti, 0.5% Al; b) 5.0% Cr, 1.0% Ti, 1.5% Al and without stress; c) 5.0% Cr, 0.5% Ti, 2.0% Al; d) 5.0% Cr, 0.5% Ti, 3.0% Al

Figure 8: Microphotographs of various Ni-based alloys specimens





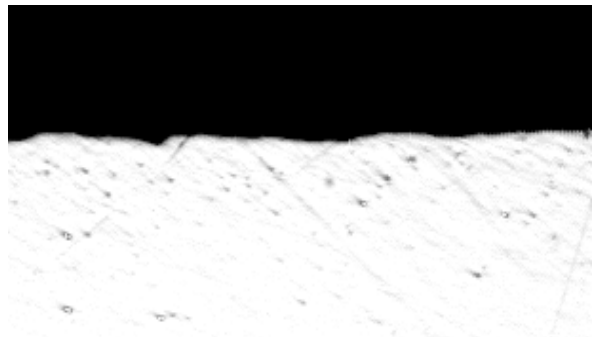
e)



f)



g)



h)

Note: Enlargement $\times 100$ without mechanical load after 114 hours exposure at 700°C in melt $15\text{LiF}-58\text{NaF}-27\text{BeF}_2$ containing chromium telluride with additions of NiF_2 (a,c,e,g – redox potential 1.6V) and metallic Be (b,d,f,h - redox potential 1.2V) respectively: a,b) MONICR 7% Cr; c,d) HN80M -VI 1.5% Nb and 0.2% Mn; e,f) HN80M 0.5% Ti, 1.0% Nb and 0.25% Mn; g,h) HN80MTY 0.9% Ti, 1.1% Al and 0.13% Mn.

References

- [1] PN. Haubenreich, JR. Engel (1970), Experience with the molten-salt reactor experiment; *Nuclear Applications and Technology* 8 (2), 107-140.
- [2] ES. Bettis et al. (1970), The design and performance feature of a single fluid molten salt reactor; *Nuclear Applications and Technology* 8 (2), 190.
- [3] VM. Novikov, VV. Ignatiev, VI. Fedulov, VN. Cherednikov (1990), Molten Salt Reactors; Perspectives and Problems. Moscow, USSR: Energoatomizdat.
- [4] ISTC # 1606 project final report (2007), International scientific and technical centre, Moscow, July 2007.
- [5] C. Renault et al. (2009), European molten salt reactor; *Proceedings of the Seventh European Commission Conference on Euroatom Research and Training in Reactor System*, Prague, Czech Republic, 22 - 24 June 2009.
- [6] S. Delpech et al. (2009), Material issues and the effect of chemistry control; *Proceedings of Global 2009*, Paris, France, 9-10 September 2009.
- [7] V. Ignatiev, O. Feynberg (2009), Molten Salt Actinide Recycler & Transmuter System; Fuel Cycle and Safety Related Issues, *Proceedings of ICENES 2009*, Ericeira, Portugal, 29 June -2 July 2009.
- [8] ORNL (1971), Preparation and handling of salt mixtures for the molten salt reactor experiment, Shaffer JH. ORNL-4616, Oak Ridge, TN, United States.
- [9] WD. Manly et al. (1960), Metallurgical problems in molten fluoride systems, *Progress in Nuclear Energy* 2 (4): 164-179.
- [10] ORNL (1962), Corrosion behavior of reactor materials in fluoride salt mixtures, DeVan JH and Evans III RB. ORNL/TM-328, Oak Ridge, TN, United States.
- [11] ORNL, Mc Coy HE et al. (1978), Status of materials development for molten salt reactors, ORNL-TM-5920. Oak Ridge, TN, United States.
- [12] ORNL (1977), Status of tellurium-Hastelloy N studies in molten fluoride salts, Keiser JR. ORNL-TM-6002, Oak Ridge, TN, United States.
- [13] VV. Ignatiev et al. (2008), Compatibility of selected Ni-base alloys in molten Li, Na, Be/F salts with PuF₃ and tellurium additions, *Nuclear Technology* 164 (1), 130-142.
- [14] VK. Afonichkin et al. (2009), Dynamic Reference Electrode for Investigation of Fluoride Melts Containing Beryllium Difluoride, *J. of Fluorine Chemistry* 130 (1), 83-88.
- [15] VK. Afonichkin et al. (2010), Salts purification and redox potential measurement for the molten LiF-ThF₄-UF₄ mixture, *Proceedings of the First ACSEPT International Workshop*, Lisbon, Portugal, 31 March - 2 April 2010.
- [16] Institute of Atomic Energy, VV. Ignatiev et al. (1993), The state of the problem on materials as applied to molten-salt reactor, problems and ways of solution, Preprint IAE-5678/11. Moscow, USSR.
- [17] ORNL (1977), Compatibility studies of potential molten-salt breeder reactor materials in molten fluoride salts, Keiser JR. ORNL-TM-5783. Oak Ridge, TN, United States.

Investigation on the compatibility of weldments of main component materials with sodium in the Chinese experimental fast breeder reactor (CEFR)

I. The weldments of upper diaphragm with liquid sodium

B. Long, Y. Xu, J. Zhang, H. Li and D. Zhang
China Institute of Atomic Energy, Beijing, China

Abstract

This study presents one of a series of verification tests on the compatibility of sodium with welds on structural core material of the Chinese experimental fast breeder reactor (CEFR). The corrosion tests in static liquid sodium (at 425°C for 3 000 hours) on chromium nitride coated weldments of 304 stainless steel, which is used as upper diaphragm material in CEFR, were performed with subsequent post-corrosion characterisation PCC [optical microscopy (OM) and scanning electron microscopy (SEM)]. In addition, in order to investigate the changes in mechanical properties due to sodium exposure mechanical tests (tensile test and micro-hardness) were performed on the pre- and post-exposed welds. This investigation shows that the Cr-N coating film has maintained its integrity after the corrosion test and no inter-granular attack has been observed on the interface of steel with sodium for either base or weldment parts. The average corrosion rate has been found to be as low as $3.42 \times 10^{-4} \text{ g/m}^2 \cdot \text{h}$ (equivalent to $0.39 \mu\text{m/a}$). The tensile test results show that there is no change of mechanical properties due to liquid sodium exposure.

Introduction

Due to the fast industrial development of the Chinese economy an enormous increase in energy consumption is expected. While fulfilling this demand it has been realised that greenhouse gas emissions cannot be increased by the same rate, leaving nuclear power as the only virtual emission free energy source. While most of the electrical power is produced by light-water reactors, sodium-cooled fast breeder reactors are the key to the advanced closed fuel cycle allowing for a reduction in spent fuel. The Chinese experimental fast breeder reactor (CEFR) has by now been completed and went critical in July 2010.

Because the CEFR is sodium-cooled, it needs to be ensured that the structural components and their welds are inert against liquid metal embrittlement and corrosion. Therefore, a series of verification tests on the materials compatibility with sodium for CEFR have been conducted at the China Institute of Atomic Energy (CIAE).

This paper presents the results of the corrosion tests and mechanical property investigations on the upper diaphragm welds used in the CEFR exposed to liquid sodium at elevated temperature. The diaphragm, which supports the fuel assembly in the reactor core, is fabricated out of 304 austenitic stainless steel while the weld filler is 308L.

In order to prevent fretting and surface welding of fuel assembly with the diaphragm, a chromium nitride coating was applied on the materials surface of the upper diaphragm using a chromisation method. The objective of the present study is to provide experimental information on the corrosion behaviour and the coating of the upper diaphragm material 304 stainless steel and its welds after exposure to elevated temperature in liquid sodium.

Experimental

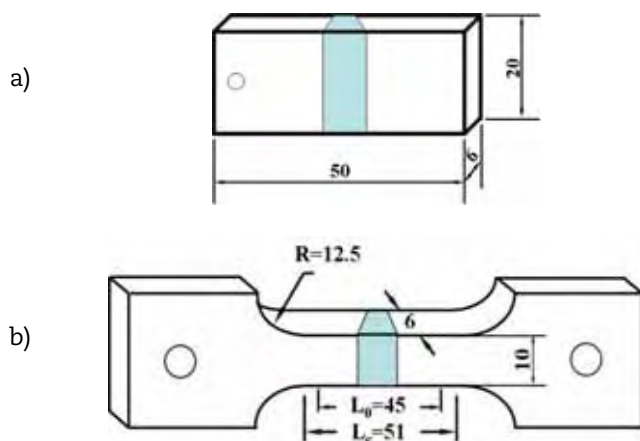
Materials and specimens

The 304 SS testing was carried out by China Nantong special-type steel factory, one of the main suppliers of CEFR. The weld filler ER308L was purchased from AVESTA, Sweden. The nominal chemical compositions of the base metal and filler wire are presented in Table 1. The specimens were cut from the welding plate, which uses the same welding procedure and coating surface treatment process as the upper diaphragm of CEFR. The procedure for welding and surface treatment was the following: single V-groove welds were performed using TIG (tungsten inert gas) welding; then the samples were heated to 1 050°C for 1 h (solution treatment). After welding and heat treatment, the samples were chromised and azotised and a chromium nitride layer was formed on the surface of the steel. The chromisation procedure was chromised by pack method in the powder mixture consisting of ferro-70% chromium at 1 100°C for 17 h, then azotised in high pure N₂ at 1 100°C for 4.5 h.

Table 1: Nominal chemical composition of 304 SS weldment for CEFR upper diaphragm (wt%, bal. Fe)

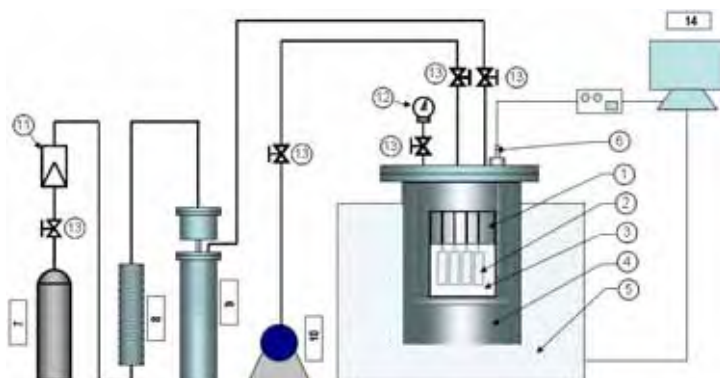
	C	Mn	P	S	Si	Ni	Cr	B	Mo	N	Cu	Co
base	0.034	1.09	0.03	0.016	0.38	9.5	18.3	0.0007	-	0.052	-	0.03
filler	0.016	1.84	0.022	0.012	0.40	9.86	19.89	-	0.32	-	0.15	0.071

The as-received weldment was machined into two types of specimens: a flat corrosion specimen with 50 mm x 20 mm x 6 mm and a flat tensile specimen with 10 x 6 mm² and a gauge length of 45 mm (see Figure 1). Regardless of the type, all specimens were machined along the direction of perpendicular to the weld joint part and the specimens for tensile test were non-standard specimens to avoid damage on the surface coating layer.

Figure 1: Schematic sketch of the corrosion test coupons (a) and tensile test specimens (b)


Test process

After degreasing in acetone and dried, the dimensions of specimens were measured using a micrometer with an accuracy of 0.01 mm, the weight measurement was performed with an analytical balance with an accuracy of 0.1 mg. After dimensional and weight measurements the specimens were exposed to sodium in the static-sodium corrosion test (SCT) facility at CIAE. The SCT consists of a test section, cover gas purification system, temperature control and monitor system (see Figure 2). The crucible containing the sodium is made out of 0Cr18Ni9 steel which is also used in CEFR. The sodium was analysed using chemical processes before the corrosion test in order to quantify the O and C, content. It was found that the content of oxygen and carbon were about 18 ppm and less than 10 ppm, respectively. The corrosion test temperature was 425°C for 3 000 h. The ratio of specimen surface to sodium volume in crucible is around $1/20 \text{ cm}^{-1}$.

Figure 2: Schematic diagram of the static-sodium corrosion test (SCT)


(1) crucible, (2) specimens, (3) liquid sodium, (4) test section, (5) furnace, (6) thermal couple, (7) argon tank, (8) molecular sieve, (9) Na-K eutectic purification tank, (10) vacuum pump, (11) flow-meter, (12) gauge, (13) vacuum valve, (14) temperature monitor and control unit.

After the corrosion test had been completed, the specimens were cleaned in ethanol in order to remove the remaining solid sodium on the specimen surface. Tensile tests were performed at constant strain velocity with an initial strain rate of $3 \times 10^{-3} \text{ s}^{-1}$ using an electro-mechanical test machine. Control specimens (no exposure to sodium) were tested in the same manner. An analytical balance with an accuracy of 0.1 mg was used to make weight measurements performed for corrosion test specimens using the same tool as measured before the test to evaluate the corrosion rate of the weldment of 304 SS.

After the corrosion tests, all specimens were analysed using OM, SEM, energy dispersive X-ray spectroscopy (EDS), X-ray diffraction (XRD) analysis and Vickers micro-hardness tests.

Results and discussion

Weight loss measurements

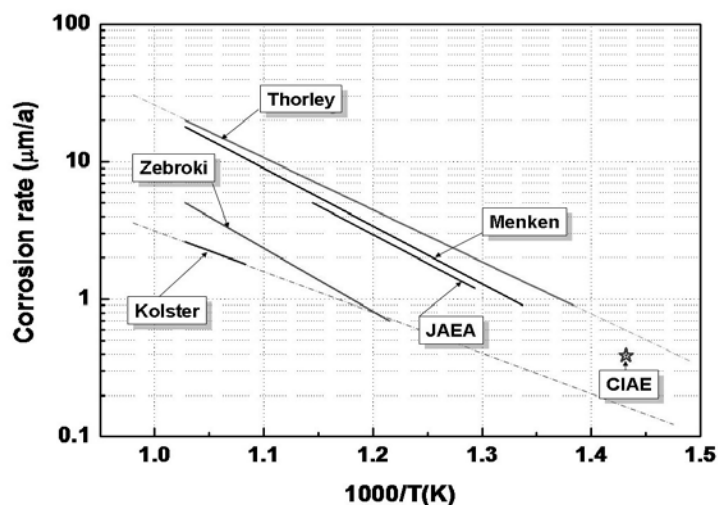
The pre- and post-exposure weight measurement of specimens shows the corrosion rate of 304 SS weldment with Cr-N coating is less than $0.0009 \text{ g/m}^2\cdot\text{h}$ which indicates that the material has high corrosion resistance to liquid sodium according to the National Standard of Corrosion Resistant for Metallic Material [1].

Table 2: Corrosion rate of upper diagrid materials after exposed in sodium at 425°C for 3 000 hours

Materials	Average corrosion rate	
	$\text{g/m}^2\cdot\text{h}$	$\mu\text{m/a}$
Upper diagrid	3.42×10^{-4}	0.39

In a liquid metal system, corrosion is a function of the rate of dissolution or the rate of deposition, while temperature is one of the main parameters in a static system affecting the corrosion rate [2]. Figure 3 shows temperature dependence on the corrosion rate of austenitic stainless steel. The corrosion rate of 304 SS with chromium nitride coating ($\text{CR}_{304\text{SS}} = 0.39 \mu\text{m/a}$ at 425°C with 18 ppm oxygen content) obtained by the present work is within the data band obtained by the others [2-6]. The test results reveal that the 304 SS welds have sufficient corrosion resistance in high-temperature sodium under the current testing conditions.

Figure 3: Comparison of corrosion rates as a function of test temperature for austenitic stainless steel

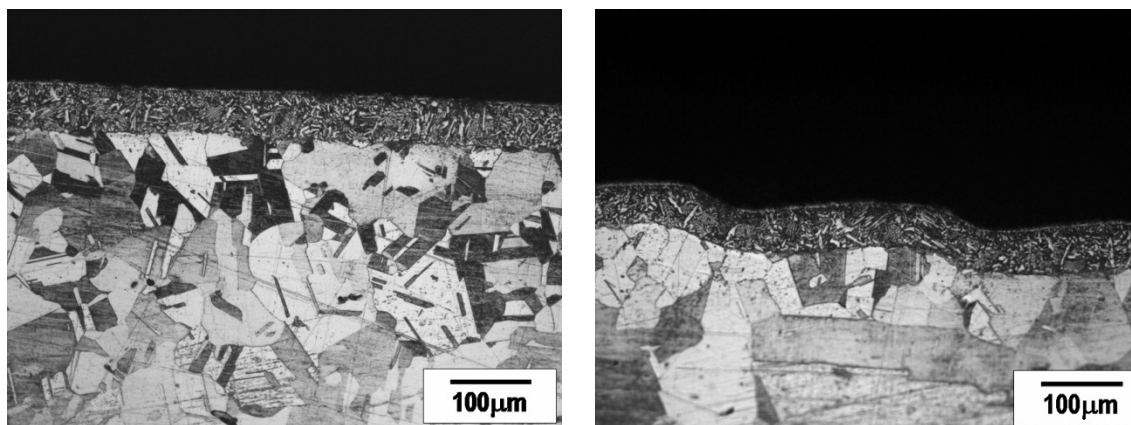


Note: The present test data are within the values reported in the following literature: Thorley [3], Menken [4], Zebroki [5], Kolster [6] and JAEA [2].

Surface morphology and structure

The coating morphology was investigated on cross-section samples. Figure 4 shows the surface morphologies on the matrix and weld zone of the specimens after exposure to liquid sodium. It can be seen that the Cr-N coating formed on the surface of the steel is about 60 µm thick and well-bonded to the substrate (304 SS). The coating thickness is uniform along the surface of the specimens. A comparison between the exposed and unexposed samples reveals that no significant material loss or microstructural changes can be observed. SEM/EDS line analysis for the specimens (Figure 5) illustrates that there is no significant difference between the control and the not exposed sample. However, in both cases the coating seems to slightly alter the local composition. It appears that the iron decreases in the 304 steel towards the coating while the chromium increases, with nickel content remaining uniform throughout the matrix and coating layer. It should be noted that the chromium content decreased slightly on the surface of the coating layer, which indicates that a small amount of chromium has been dissolved into liquid sodium. This result is consistent with weight loss measurement.

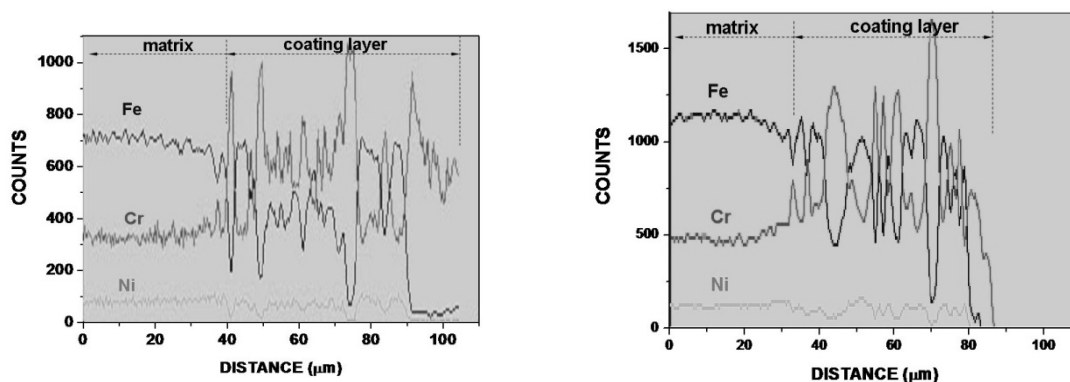
Figure 4: Surface morphology of upper diagrid specimens exposure to liquid sodium at 425°C for 3 000 hours



(left: base metal; right: weld zone)

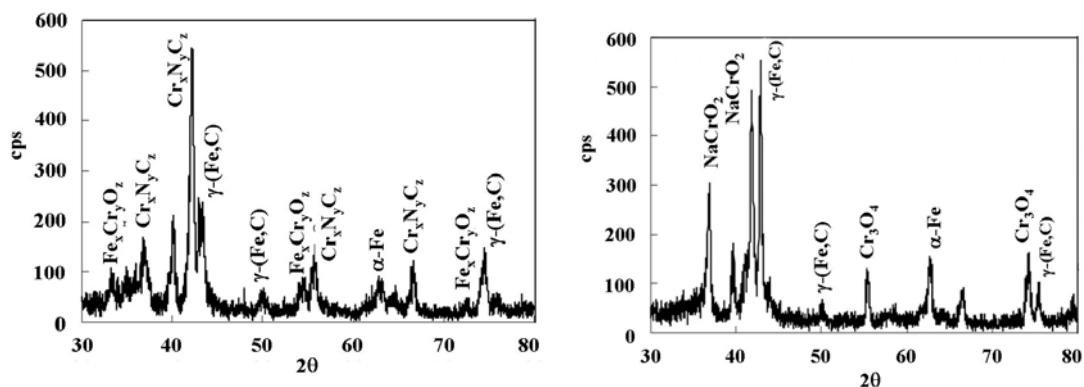
Figure 5: EDS line analysis on the upper diagrid specimens before and after exposure to liquid sodium

(left: as-received; right: tested in sodium at 425°C for 3 000 hours)



The structure of the coating layer was determined by X-ray diffraction. The XRD results on specimens before and after exposure to liquid sodium are shown in Figure 6. The surface layer for as-received specimen was identified to be predominantly $\text{Cr}_x\text{N}_y\text{C}_z$ phase due to the chromising and azotising treatment on the surface of the upper diagrid, while the peak of $\gamma\text{-(Fe,C)}$ was also detected (see Figure 6). After testing in liquid sodium, a small amount of NaCrO_3 and Cr_2O_3 compounds were formed on this coating layer (see Figure 6). NaCrO_3 is a soluble corrosion product and it could be dissolved into liquid sodium with the extending of test time [7], finally, the protection Cr_2O_3 film remained on the surface of the coating, which could prevent further attack by liquid sodium.

Figure 6: X-ray diffraction patterns of upper diagrid before and after exposure to liquid sodium at 425°C for 3 000 hours



(left: as-received; right: after exposed to sodium)

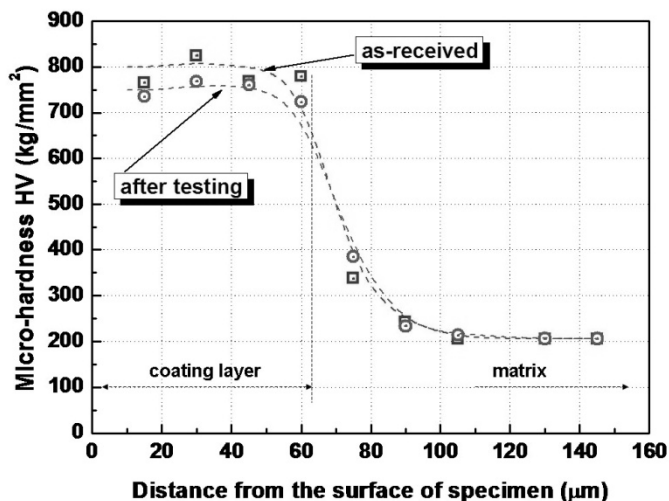
Micro-hardness test

The micro-hardness measurement was performed according to the ASTM standard (ASTM E92-82 standard test method for Vickers hardness of metallic materials). Vickers hardness tests were performed both on the coating layer of Cr-N on the surface and the weld joint part with a test weight of 0.05 kg, the error of this measurement is ± 20 HV0.05.

Micro-hardness tests on the coating layer

Figure 7 shows the micro-hardness test results on the coating layer before and after exposure to liquid sodium at 425°C. The result shows that the Vickers hardness of the Cr-N coating can reach 700-800 HV0.05, while the base steel is about 200 HV0.05. As can be seen from Figure 7, the curves dropped sharply at around 60 μm distance from the outer surface of the coating layer which indicates that the thickness of the Cr-N coating layer is about 60 μm . Comparing the curves obtained before and after corrosion tests in liquid sodium, it has been assumed that the hardness is reduced slightly after test, but the variation is well within the error. The reduction on the hardness is due to the nitride dissolved into sodium during the corrosion test. The SEM surface observation reveals that no crack appears for specimens both before and after exposure in liquid sodium. The results show that the liquid sodium has virtually no effect on the hardness of the Cr-N coating or the substrate steel and this type of coating can prevent effectively the wear and tear from the fuel sub-assembly.

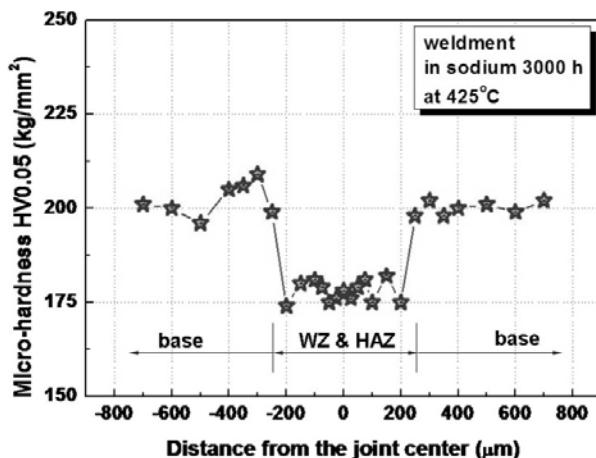
Figure 7: Micro-hardness profile of Cr-N coating on the surface of upper diagrid



Micro-hardness test on the weld part

Figure 8 shows the micro-hardness data measured perpendicular to the weld center along the line from base metal, HAZ and weld zone. The hardness value of 304 base metal is around 200 HV0.05. No hardening in weld metal and adjacent HAZ is clearly observed. The value of microhardness is around 175 HV0.05. The softening on the weld zone and HAZ occurs due to the solution heat treatment after welding and chromised at high temperatures (1 100°C). In these processes the carbon dissolved into austenitic combined with lower carbon content in the weld zone using low carbon 308L filler wire. The result shows that no significant hardness variation has been found after exposure to high-temperature sodium.

Figure 8: Micro-hardness profile of the 304 SS weldment for CEFR diagrid after exposure to sodium at 425°C for 3 000 hours



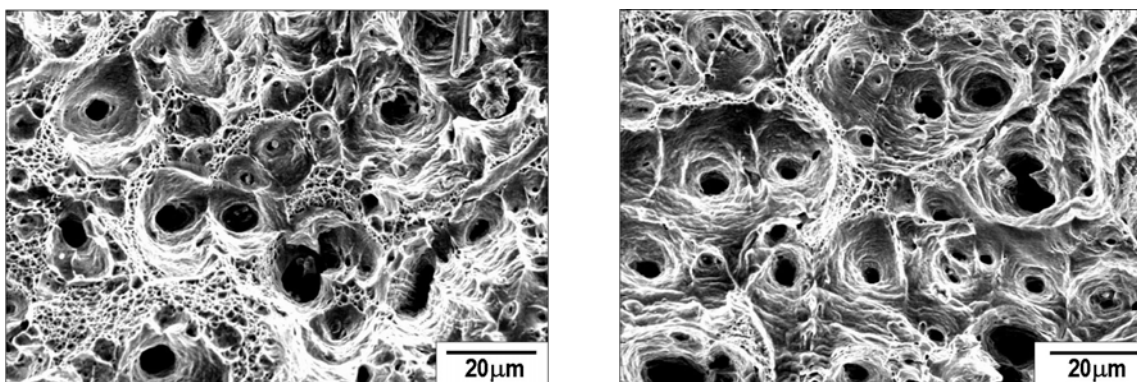
Mechanical properties

The main results of the tensile test of 304 SS weldment with Cr-N coating are listed in Table 3, where the average values of yield strength (YS), ultimate tensile strength (UTS) and total elongation percentage (TE) are given. It can be seen that the exposure of steel to liquid sodium does not dramatically affect its mechanical properties. The yield stress gets a slight decreasing, it has been observed that the reduction on the coating layer ($CR=0.39 \mu\text{m/a}$) may be the reason for the decrease. Its ductility does not show any degradation by liquid sodium attack. The comparison of the tensile test results of 304 steel with and without Cr-N coating shows that the coating layer has no effect on its mechanical properties. Figure 9 gives SEM micrographs of the fracture surfaces of upper diagrid specimens after tensile test. It shows that the fracture behaviour is the same before and after exposure to liquid sodium, the fracture surfaces exhibit typical ductile fracture characterised by the presence of dimples.

Table 3: The tensile test results of 304 SS weldment with Cr-N coating after exposure to liquid sodium at 425°C for 3 000 hours

	YS(Rp0.2) (MPa)	UTS(σ_b) (MPa)	TE (%)
As-received	185±10	535±15	60±5
After exposure to Na	165±20	530±15	65±2

Figure 9: SEM micrograph of fracture surface of 304 SS with Cr-N coating



(left: as-received; right: after exposure to sodium at 425°C for 3 000 hours)

Conclusion

Under present test conditions, the average corrosion rate of the weldment of 304 SS with Cr-N coating on the surface is $3.42 \times 10^{-4} \text{g/m}^2 \cdot \text{h}$ (equivalent to $0.39 \mu\text{m/a}$), which reveals that it has sufficient corrosion resistance to high-temperature sodium, no intergranular attack has been observed on the interface of steel with sodium either for base or weldment parts.

The tensile test results show that there is no degradation of mechanical properties after exposure to liquid sodium, with the fracture surface after tensile test exhibiting dimple-ductile fracture.

The Cr-N coating film has maintained its integrity after the corrosion test. The hard coating ($\text{HV}0.05=700\text{-}800 \text{ kg/cm}^2$) could prevent effectively the wear and tear from the fuel sub-assembly.

Acknowledgements

The authors would like to acknowledge the technical help of S.Y. Chen, X.C. Yu and Y.T. Jia on this work. Especially, the authors would like to thank Professor Dr. Peter Hosemann from University of California Berkeley for his excellent editorial suggestions.

References

- [1] G. Yimig (1992), *Handbook on Corrosion of Steels*, China Metallurgy Industry Press.
- [2] T. Furukawa, S. Kato and E. Yoshida (2009), *J. Nucl. Mater.*, 392. 249-254.
- [3] A.W. Thorley, C. Tyzack (1973), *Corrosion and mass transport of nickel alloys in sodium system*, *Liquid Alkali Metals*, BNES, London.
- [4] G. Menken (1980), *Second International Conference on Liquid Metal Technology in Energy Production*, XIII-2-3, Richland.
- [5] E.L. Zebroski (1973), *Liquid Alkali Metals*, BNES, London.
- [6] R.H. Kolster (1976), *Proceedings of International Liquid Metal Technology in Energy Production*, *Champion*, p.368. PA, United States.
- [7] H. Borgstedt, K. Mathews (1987), *Applied Chemistry of the Alkali metals [M]*, p. 201-204, New York and London, Plenum Press.

Plenary Session II

Chairs: Ph. Dubuisson, W.W. Kim

Innovative fuels state-of-the-art assessment*

Kemal O. Pasamehmetoglu, Ph. Dubuisson
Idaho National Laboratory, United States

Abstract

Under the guidance of the Nuclear Science Committee (NSC) and the mandate of the Working Party on Scientific Issues of the Fuel Cycle (WPFC), an Expert Group on Innovative Fuels (EGIF) has been formed with the objective to conduct joint and comparative studies in order to support the development of innovative fuels (including innovative clad materials) that can be implemented in advanced nuclear fuel cycles.

A state-of-the-art report on innovative fuel concepts is being prepared for publication. The scope of the report covers the technical issues associated with the development of innovative fuels and clad materials targeted for use in advanced fuel cycles.

The fuel types of interest for EGIF are those that contain minor actinides (MA) as opposed to standard fuels (i.e. uranium or uranium-plutonium fuels that are currently being used in the fuel cycle). Thorium-fuels (e.g. Th-MA oxides) also fall within the scope of the expert group.

The following technical issues associated with innovative fuel development are covered in the report:

- *innovative fuel fabrication techniques;*
- *irradiation performance of innovative fuels (including advanced clad materials);*
- *characterisation and post-irradiation examination methods.*

The report also covers the following fuel types:

Metallic fuels: The compilation of the international metallic fuel development activities is being led by Dr. Takanari Ogata (CRIEPI, Japan).

Oxide fuels: The compilation of the international oxide fuel development activities is being led by Dr. Natalie Chauvin (CEA, France).

Nitride fuels: The compilation of the international nitride fuel development activities is being led by Dr. Kazuo Minato (JAEA, Japan).

Dispersion fuels: CERCERs and CERMETs. The compilation of the international dispersion fuel development activities is being led by Dr. Joseph Summers (ITU, EU).

Special mechanical fuel forms: such as sphere-pac, vibro-pac, and coated particle fuels, etc. The compilation of the international development activities is being led by Dr. Manuel Pouchon (PSI, Switzerland).

The paper provides a summary of the state-of-the-art on innovative fuels. The paper also includes a discussion of the technical maturity assessment methodology in the form of a definition of technology readiness levels (TRLs) as applied to nuclear fuel technology.

* The full paper being unavailable at the time of publication, only the abstract is included.

Super ODS steels R&D for fuel cladding of advanced nuclear systems

Akihiko Kimura¹, Ryuta Kasada¹, Noriyuki Iwata¹, Jerome Isselin¹, Peng Dou¹, Jae-hoon Lee¹, Takanari Okuda², Masaki Inoue³, Shigeharu Ukai⁴, Somei Ohnuki⁴, Hiroyuki Sano⁵, Toshiharu Fujisawa⁵, Fujio Abe⁶

¹Institute of Advanced Energy, Kyoto University, Kyoto, ²KOBELCO Research Institute, Kobe, ³Japan Atomic Energy Agency, Oarai, Ibaraki, ⁴Hokkaido University, Sapporo, ⁵Nagoya University, Nagoya, ⁶National Institute of Materials Science, Tsukuba

Abstract

The development of high-performance fuel cladding is essential for the realisation of Generation IV systems. The 9Cr-ODS martensitic steel was developed as the cladding material for sodium-cooled first breeder reactors in Japan and the steel showed a good performance in sodium, while the corrosion resistance is poor in supercritical water (SCW) and lead-bismuth eutectics (LBE).

High-Cr ODS steels added to Al showed a drastic improvement in corrosion resistance in SCW and LBE. High-temperature strength, however, was reduced by Al addition because of the characteristic changes in the dispersion morphology of oxide particles. Recently, “super ODS steels” have been developed by means of the third element alloying method, i.e. a small addition of Zr, which results in the improvement of high-temperature strength while maintaining high resistance to corrosion in SCW and LBE.

The high performance of the super ODS steels stems from the fine nano-scaled (Y, Zr)-oxide particle dispersion. Dispersion morphology of the oxide particles, such as size, number density, chemical compositions, coherency between matrix and particles, are characterised by FE-TEM/EDS observations, high-temperature XRD measurements and analyses by FE-EPMA and FE-AES. The chemical compositions of the main particles, which were (Y, Zr) oxide particles rather than (Y, Al) oxide particles, were influenced by the addition of a small amount of Zr. The size and the number density of Zr-added steel were reduced and increased, respectively. The coherency of the (Zr, Y) oxide particles depended on the size of the particle. Characteristic features of the oxide particles for strengthening mechanism will be summarised for the super ODS steels.

This presentation shows recent experimental results of mechanical properties at elevated temperatures, corrosion behaviour in SCW and LBE and phase stability under ion irradiation of super ODS steel to demonstrate that “super ODS steel” is a promising fuel cladding material for next generation nuclear systems.

Introduction

A scenario of high burn-up operation over 150 GWd/t of next generation nuclear systems, such as supercritical pressurised water-cooled reactor (SCWR), lead-bismuth-cooled reactors (LFR), high-temperature helium-cooled reactor (GFR), as well as sodium-cooled reactor (SFR), imposes a number of requirements for cladding materials, which include 1) resistance to neutron irradiation embrittlement, 2) dimensional stability under irradiations, 3) corrosion resistance, 4) low susceptibility to stress corrosion cracking (SCC) and 5) hydrogen and/or helium embrittlement, 6) high-temperature strength, 7) long creep life, etc.

The requirement of materials performance strongly depends on the operation temperature. Below 673 K, the irradiation embrittlement coupled with corrosion-induced hydrogen embrittlement is most critical for the cladding, because in many metallic materials irradiation induces embrittlement accompanied by hardening at these temperatures and with a decrease in irradiation temperature, the embrittlement becomes more significant [1]. When the cladding is highly susceptible to hydrogen and/or helium embrittlement, synergistic degradation by irradiation embrittlement and H/He embrittlement becomes crucial for determining the lifetime of the cladding. SCC often determines the lifetime of the claddings. High-temperature properties, such as tensile strength, creep, void swelling and corrosion are critical for application to highly efficient next generation nuclear systems. When the irradiation temperature is higher than 673 K, irradiation induces non-hardening embrittlement, which is due to irradiation-induced phase changes, such as precipitation [1], phase transformation and helium bubble formation of the grain boundaries. The phase changes often increase susceptibility to irradiation embrittlement, H/He embrittlement, swelling and even corrosion. Thus, phase stability is more critical for high-temperature usage.

Oxide dispersion strengthening (ODS) ferritic/ martensitic steels, which contain chromium at least 12%, have been developed to be applied as fuel cladding material of SFR [2] [3]. Recent irradiation experiments clearly showed that the ODS ferritic/martensitic steels were rather highly resistant to neutron irradiation embrittlement at temperatures between 573 and 773 K up to 15 dpa [4] [5]. They showed a very limited loss of elongation by irradiation, i.e. the ODS steels showed irradiation hardening accompanied by almost no loss of ductility. A remarkable improvement was attained in high-temperature strength of ferritic steels by dispersing nano-scale oxide particles. However, it is well known that the corrosion resistance of 9Cr-ferritic/martensitic steel is not good enough in SCPW and LBE at high temperatures. Thus, for 9-12% Cr-ODS ferritic steels, the most critical issue for their application to SCWR and LFR is to improve their corrosion resistance. A programme to develop corrosion-resistant ODS steels started at Kyoto University [5] [6].

In our previous research [5-10], it was reported that the addition of chromium (>13 wt.%) and aluminum (4.5 wt.%) to the ODS steels are very effective in suppressing corrosion in a SCPW (783 K, 25 MPa) environment. Recent corrosion experiments in lead-bismuth have clearly shown that Al added ODS steels are much more resistant than ODS steels without the addition of Al. The addition of Al also improves the Charpy impact property of high Cr ODS steels. In general, however, an increase in the Cr concentration of the steels often results in an increase in susceptibility to thermal ageing embrittlement. Furthermore, the addition of Al significantly reduced strength at high temperatures as well as at ambient temperature.

According to the preliminary irradiation experiments, the ODS steels did not show irradiation-induced dislocation recovery at temperatures above 673 K, which indicates that the dispersed oxide particles played a role in stabilising microstructure.

In this report, it is demonstrated that high-Cr ODS steels are very promising as fuel cladding materials for high burn-up operation of SCWR and LFR, based on recent work on mechanical properties, corrosion resistance and radiation tolerance at elevated temperatures, as well as some other properties obtained so far.

Materials

The elemental high purity powders of the targeted compositions for ODS steels were mechanically alloyed using a high-energy attritor with pre-alloyed Y_2O_3 powder. The mechanically alloyed (MA) powders were canned, degassed and extruded at 1 423 K to make cylindrical rods. In order to avoid oxygen contamination by air exposure, the MA powder was transferred from the attritor into extrusion capsules in a series of glove boxes throughout the processes. During these processes, oxygen contamination was reduced to less than 10 wt.ppm, which is good enough to control excess oxygen concentration. After the hot-extrusion, re-crystallisation heat treatment was performed at 1 423 K for 1 hr. Table 1 shows the chemical compositions of ODS steels used in this work. The compositions range from 11.6 to 17.3 wt.% for Cr and 0 to 4wt.% for Al to optimise the adequate compositions of high-Cr ODS steel with added Al. Minor elements, such as Ce, Hf and Zr were added to investigate the effects on oxide particles morphologies. Carbon was not intentionally added, but contaminated during MA treatment from steel balls, which contained a high concentration of carbon.

Table 1: Chemical compositions of ODS steels used in this work

	C	Si	Mn	P	S	Ni	Cr	W	Al	Ti	Y	O	N	Ar	Ce	Hf	Zr	Y2O3	Ex.O
SOC1	0.02	0.02	0.03	<0.005	0.002	-	16.11	-	3.44	0.09	0.27	0.14	0.002	0.005	-	-	-	0.34	0.07
SOC2	0.04	0.01	0.02	<0.005	0.002	-	13.65	-	3.35	0.07	0.28	0.14	0.016	0.006	-	-	-	0.36	0.06
SOC3	0.05	0.02	0.04	<0.005	0.003	-	17.33	-	3.5	0.09	0.27	0.14	0.006	0.006	-	-	-	0.34	0.07
SOC4	0.02	0.01	0.03	<0.005	0.002	-	15.77	-	1.85	0.09	0.27	0.14	0.003	0.007	-	-	-	0.34	0.07
SOC5	0.04	0.01	0.01	<0.005	0.002	-	15.95	-	-	0.09	0.27	0.15	0.007	0.007	-	-	-	0.34	0.08
SOC6	0.03	0.01	0.03	<0.005	0.002	-	16.08	1.61	3.36	0.09	0.27	0.13	0.002	0.005	-	-	-	0.34	0.06
SOC7	0.04	<0.01	<0.01	<0.005	0.002	-	15.68	-	1.7	0.09	0.28	0.15	0.003	0.005	0.37	-	-	0.36	0.07
SOC8	0.15	<0.01	<0.01	<0.005	0.001	0.93	11.61	-	1.34	-	0.28	0.15	0.003	0.005	-	-	-	0.36	0.07
SOC9	0.03	0.02	0.05	<0.005	0.002	-	15.42	1.85	3.8	0.1	0.28	0.16	0.004	0.0068	-	-	-	0.36	0.084
SOC10	0.017	0.02	0.04	<0.005	0.002	-	15.42	1.92	3.46	0.11	0.52	0.25	0.005	0.0068	-	-	-	0.66	0.11
SOC11	0.018	0.02	0.02	<0.005	0.002	-	15.39	0.28	3.78	0.1	0.56	0.25	0.006	0.007	-	-	-	0.7	0.1
SOC12	0.022	0.02	0.04	<0.005	0.002	-	15.29	1.91	3.88	0.09	0.98	0.18	0.007	0.0059	-	-	-	1.24	-0.08
SOC13	0.035	0.02	0.04	<0.005	0.002	-	15.12	1.89	3.78	0.1	0.34	0.16	0.011	0.0063	-	1.28	-	0.43	0.07
SOC14	0.052	0.03	0.05	<0.005	0.002	-	14.85	1.84	3.73	0.09	0.27	0.17	0.009	0.0061	-	-	0.63	0.34	0.1
SOC15	0.024	0.01	0.01	<0.005	0.002	-	15.12	1.92	3.93	0.1	0.28	0.25	0.006	0.0066	1.32	-	-	0.36	0.17
SOC16	0.043	0.02	0.02	<0.005	0.002	-	14.54	1.93	3.01	0.13	0.28	0.16	0.007	0.0064	-	0.62	-	0.36	0.08
SOCH1	0.054	0.02	0.03	<0.005	0.002	-	12.19	1.89	2	0.19	0.28	0.21	0.01	0.0065	-	-	-	0.36	0.13
SOCH2	0.033	0.02	0.05	<0.005	0.002	-	14.91	1.84	2.29	0.15	0.27	0.2	0.009	0.0063	-	-	-	0.34	0.13
SOCP1	0.029	0.02	0.02	<0.005	0.001	-	14.52	1.9	3.2	-	0.26	0.11	0.004	0.006	-	-	0.48	0.33	0.04
SOCP2	0.035	0.02	0.02	<0.005	0.001	-	14.73	1.9	3.2	-	0.25	0.1	0.004	0.006	-	0.47	-	0.32	0.03
SOCP3	0.046	0.03	0.03	<0.005	0.001	-	13.32	1.9	3.2	0.16	0.26	0.11	0.004	0.007	-	-	-	0.33	0.04
SOCP4	0.027	0.03	0.02	<0.005	0.002	-	15.33	1.9	3.8	0.12	0.26	0.14	0.009	0.006	-	-	0.32	0.33	0.07
SOCP5	0.031	0.03	0.02	<0.005	0.002	-	15.15	1.9	3.9	0.11	0.26	0.14	0.005	0.005	-	-	0.58	0.33	0.07
SOCP6	0.028	0.03	0.01	<0.005	0.002	-	15.41	1.8	3.87	0.12	0.26	0.14	0.007	0.005	-	0.59	-	0.33	0.07

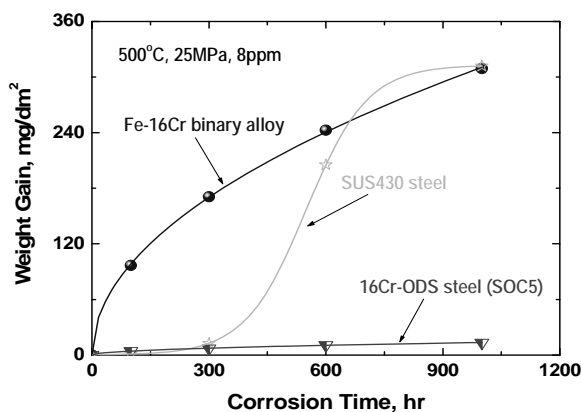
Corrosion resistance

Supercritical pressurised water

Weight gain

Figure 1 shows the weight gain of a Fe-16Cr binary alloy (not ODS alloy), SUS430 steel (16Cr) and 16Cr-ODS steel (SOC-5) exposed at 773 K up to 1 000 hr. None of the materials contains Al. The weight gain of binary ferritic alloy and that of SUS430 steel are similar for 1 000 hr, suggesting that corrosion resistance seems to be controlled by Cr concentration. However, the corrosion rate of 16Cr-ODS steel was much smaller than that of those two materials which contain the same amount of Cr. This suggests that there are more important factors than Cr content. It has been proposed that fine oxide dispersion and fine grains influence corrosion resistance.

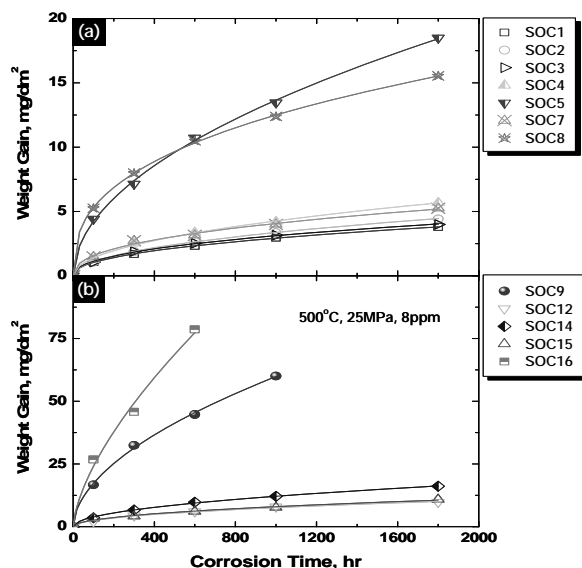
Figure 1: Weight gain as a function of corrosion time of a ferritic alloy, SUS430 and an ODS ferritic steel (SOC5) after exposure to SCPW at 773 K with 8 ppm dissolved oxygen under a pressure of 25 MPa



Note: All the materials contain no Al.

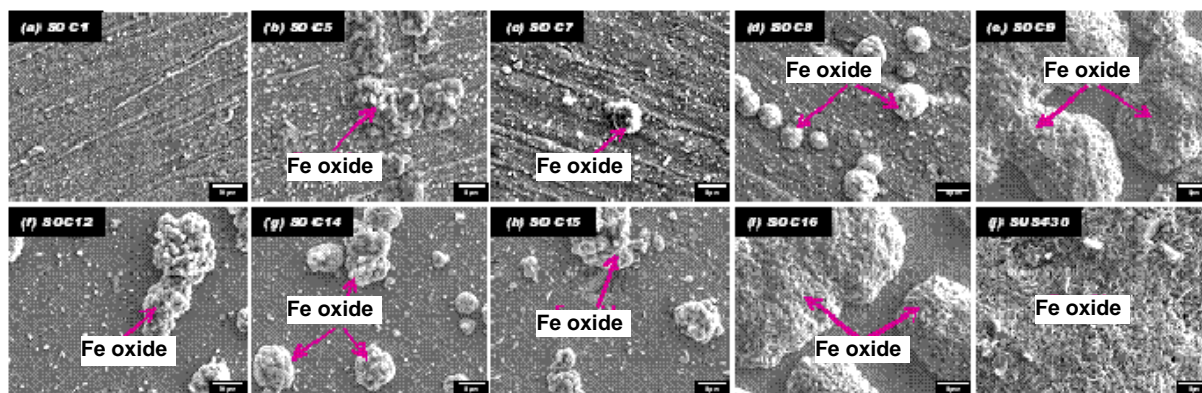
The weight gains of ODS steels with various compositions are shown in Figure 2. The corrosion resistance of Al added to ODS ferritic steels with different Cr content between 13.5 and 17.5 wt.% is almost identical, while the corrosion rate of SOC-5, which does not contain Al, is much larger than that of the ODS steels with Al (Figure 2a). It has also been found that the corrosion resistance of ODS ferritic/martensitic steel (SOC-8), whose Cr content is 11.6 wt.%, is lower than that of ODS ferritic steels, although SOC-8 contains 1.3 wt.% Al. In comparison to the standard ODS ferritic steel (SOC-9) which contains W, the ODS steels with Zr addition and high content of Y_2O_3 have shown better corrosion resistance (Figure 2b). However, the addition of Hf has not been effective in increasing corrosion resistance.

Figure 2: Weight gain as a function of corrosion time of ODS ferritic steels after exposure to SCPW at 773 K with 8 ppm of dissolved oxygen under a pressure of 25 MPa



Surface morphology

Surface morphologies of ODS ferritic steels and SUS430 steel exposed at 773 K up to 1 800 h are shown in Figure 3. In comparison to the other ODS steels, only fine oxides are observed on the surface of Al-added SOC-1 (Figure 3a). On the other hand, many corrosion products are observed on the surface of SOC5 without Al (Figure 3b). It is also found that the addition of Ce does not affect the formation of surface oxide (Figure 3c), but in the case of ferritic/martensitic steel (SOC-8) with 11 wt.% Cr, the corrosion products increase (Figure 3d). Note that W-added SOC-9 has large corrosion products, even though the material is only exposed for 300 h (Figure 3e). The addition of Zr and Ce and increasing Y₂O₃ content decreased the corrosion products of W-added ODS ferritic steels (Figures 3f, g and h). However, the corrosion products of SOC-16 with W and Hf are almost identical to those of SOC-9 (Figure 3i). The FE-EPMA analysis has revealed that the corrosion products are mainly Fe oxide. These results indicate that Al addition reduces the formation of Fe oxide. Also, adding Zr and Ce and increasing Y₂O₃ content in W-added ODS steels appear to reduce the formation of the surface oxide. However, the addition of W or Hf increases the growth of the oxides. As for the SUS430 steel, the whole specimen surface was covered by corrosion products (Figure 3j).

Figure 3: Surface morphologies of specimens after corrosion test

(a) SOC-1, (b) SOC-5, (c) SOC-7, (d) SOC-8, (f) SOC-12, (g) SOC-14 and (h) SOC-15 were exposed at 773K for 1 800 hours, while (e) SOC-9 and (i) SOC-16 were exposed at 773K for 300 hours. Note that SUS430 was exposed at 773K for 1 000 hours.

Recent corrosion tests up to 5 000 h in SCPW (773 K, 25 MPa, 8 ppm DO) have clearly showed that super ODS steel candidates showed better corrosion resistance than nickel-based super alloys, such as Inconel-625 and Incoloy-800, Hastelloy C-276, and SUS310 alloys.

It can be concluded that corrosion resistance of 16 wt.% Cr-ODS steel is much higher than that of SUS430 steel whose Cr content is 16 wt.% but is not dispersed with oxide particles, suggesting that the fine oxide dispersion and fine grains play a role in increasing the corrosion resistance of ferritic steels. The improvement of the corrosion resistance in Al added ODS steels is due to alumina formation on the surface of the ODS steels. The addition of 4 wt.% Al has been effective in increasing the corrosion resistance of the 16 wt.% Cr-ODS steel. Since previous results showed no remarkable improvement by Al addition for 19 wt.% Cr-ODS steel, the beneficial effects of Al addition on corrosion resistance in SCPW depends on Cr concentration. It has been proposed that the adequate contents of Cr and Al of candidate super ODS steel for application to SCPWR range 14 to 16 wt.% for Cr and 3.5 to 4.5 wt.% for Al.

Lead-bismuth eutectics

Experimental method

Lead and bismuth were carefully weighed for a composition of LBE and charged into a mullite crucible. The crucible was heated at 973 K in an electric resistance furnace under Ar-5% H₂ atmosphere for 1.8 ks. A part of prepared LBE was shaved by a knife and was dissolved into 3N- HNO₃. Lead, bismuth, iron, chromium and aluminum contents were measured by ICP-AES. Oxygen content in LBE was also measured by the helium gas fusion-infrared absorptiometry method. Iron, chromium and aluminum contents in initial LBE were less than 10 mass ppm, respectively. Oxygen content was less than 1 mass ppm. The conditions of the partial pressure of oxygen were selected from the above potential diagrams as follows: lower condition at which (Fe, Cr, Al)₃O₄ coexisted with iron alloy and higher condition at which stable (Fe,Cr,Al)₃O₄ certainly formed.

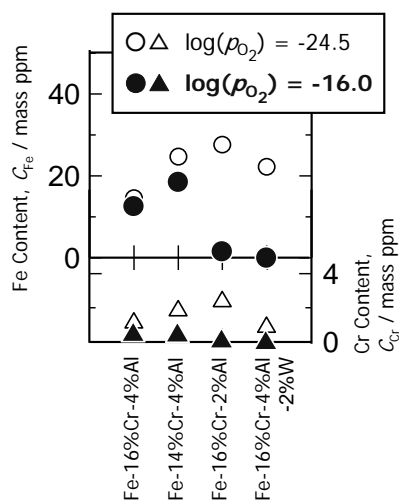
Prepared LBE and Fe-Cr-Al alloy or the developed super ODS steel candidates were charged in an alumina crucible, which was covered with an iron lid to prevent LBE from evaporating during the heating. The crucible was set at the top of a furnace heated at a desired temperature. H₂-H₂O gas mixture, which was controlled at a desired mixing ratio, began to flow close on the crucible through an alumina tube at a flow rate of 4.98×10^{-6} Nm³·s⁻¹ (200 ml·min⁻¹). It was maintained for a while to replace the gas in the furnace for the experimental atmosphere. Then the container was moved down to the hot zone in the furnace with the gas flow and was kept there for a desired time period. The container was pulled out of the furnace and quenched rapidly by a jet of helium gas.

After the experiments, the sample was subjected to the optical microscope, SEM and EPMA for interfacial observations. A part of LBE was subjected to the ICP-AES and iron, chromium and aluminium contents in LBE were analysed. Lead and bismuth contents were also analysed and it was confirmed that the composition of LBE had not changed.

At lower oxygen partial pressures than the pressure that was sufficient for the formation of the stable oxide layer, a rough oxide layer mixed with iron alloy was formed at the interface between LBE and the steel in all samples. This is because $(\text{Fe, Cr, Al})_3\text{O}_4$ coexisted with the iron alloy under this condition. The oxide layer was clearly observed to increase the aluminium content in steel and it tended to become thinner. When the aluminium content was lower, the oxide layer became thick or more rough.

Figure 4 shows the iron and chromium content in LBE after the experiments. Open symbols represent the condition of the lower oxygen partial pressure, while closed symbols represent the condition of the higher one. As expected from such interfacial behaviour, iron and chromium in the steel dissolved into LBE through the oxide layer. However, the aluminum content in LBE had not changed from the initial one and it is thought that the aluminum in steel or crucible hardly dissolved into LBE.

Figure 4: Iron and chromium content in LBE at 973 K for 144 ks



The results of the interfacial observation of two kinds of the developed super ODS steel candidates, Fe-16% Cr-4% Al and Fe-16% Cr-4% Al-2% W, under higher partial pressure of oxygen, $\log(p_{\text{O}_2}) = -16$, at 973 K for 144 ks (40 h) indicates that at the oxygen partial pressure to form stable oxide layer, a dense and very thin oxide layer was formed especially on the higher aluminium content steel. The thin oxide layer seemed to be alumina and it prevented the alloy dissolution into LBE. The results show that aluminium and chromium content in steel is very important in preventing corrosion by LBE.

In summary, dissolution experiments of synthetic Fe-Cr-Al alloys and developed super ODS steel candidates into LBE under several partial pressures of oxygen were conducted in this study. In addition, partial potential diagrams of the Fe-Cr-4% Al-O system at 973 K and 873 K were established as basic data. At lower oxygen partial pressures than the pressure that is sufficient for the formation of the stable oxide layer, a rough oxide layer was formed at the interface in all samples and the alloy elements dissolved into LBE through it. On the other hand, at the oxygen partial pressure to form stable oxide layer, a dense and very thin oxide layer was formed especially on the higher aluminum content steel, preventing the alloy dissolution into LBE. As can be seen from

the results, aluminum and chromium contents in steel were very important in preventing the corrosion by LBE.

Strengthening

Reduction of strength by Al addition

Although Al addition is very effective in improving the corrosion resistance of ODS ferritic steels, the most serious problem of Al addition is the reduction of strength. Tensile test results showed that Al addition to 19Cr-4Al-ODS steel significantly reduced the tensile strength, although the tensile strength of 19Cr-4Al-ODS steel is still much higher than ordinary ferritic/martensitic steel. A dispersion of yttria (Y_2O_3) particles increased the strength of ferritic steels. The hardening mechanism in the ODS steels is interpreted in terms of dispersion barrier model against moving dislocations, in which the number density and the size of the particles are controlling factors of the strengthening.

In order to investigate the mechanism of this softening by Al addition, TEM observations were performed and revealed that the structure and dispersion morphology of the oxide particles were different between the steels with and without Al addition. In the Al added steel, the average diameter of the oxide particles is 7 nm but less than 3 nm in the steel without Al addition. The number density of the oxide particles was reduced by almost one order of magnitude by Al addition. The structure of the oxide particle is also changed by Al addition. The fine oxide particles in the steel without Al addition are mainly yttrium-titanium pylochore, while those in the steel with Al addition are mostly larger YAT and YAH.

Since oxide particles control the strength of the ODS steel, the addition of Al, which changes the characteristics of oxide particles dispersion morphologies, remarkably influences the strength of ODS steels. As for the Al added ODS steel, the most critical issue is the improvement of high-temperature strength by alternation of oxide particle morphology.

Strengthening by oxide particles modification

YAT and YAH are not adequate for highest strengthening of ODS ferritic steel, while yttrium-titanium pylochore is effective in strengthening it. Although the oxides of Al and Y are known to be stable, the possible selection of other sort of oxides is conceived on the basis of thermodynamics.

There are many stable oxide former elements, such as Y, Al, Ti, V, Ta, Nb, Hf, Zr, etc. Table 2 shows the oxide formation energy of each alloy element at 1 500 K. Among them yttria is known as a component of ODS alloys. The oxide formation energy ranges widely from -520 for Nb to -995 kJ/mol O_2 for Y at 1 500 K. Since the formation energy of yttria and alumina is -995 and -800 kJ/mol O_2 , respectively, Zr and Hf may influence the oxide formation and their characteristics.

Table 2: Oxide formation energy of alloy elements (1 500 K)

Family	3A	4A	5A	3B	4B
Elements	Sc	Ti	V	Al	Si
Atomic #	21	22	23	13	14
Oxide	Sc ₂ O ₃	TiO ₂	V ₂ O ₅	Al ₂ O ₃	SiO ₂
Formation energy	-990	-770	-570	-800	-
Elements	Y	Zr	Nb		
Atomic #	39	40	41		
Oxide	Y ₂ O ₃	ZrO ₂	Nb ₂ O		
Formation energy	-995	-800	-500		
Elements	La	Hf	Ta		
Atomic #	57	72	73		
Oxide	La ₂ O ₃	HfO ₂	Ta ₂ O ₅		
Formation energy	-	-900	-570		

Table 3: Creep test results at 973 K of each candidate ODS steel

Materials	Creep strength (973K, 10 k hr)
16 Cr-ODS	100 MPa
16Cr-4Al-ODS	60 MPa
16Cr-4Al-ODS-Zr	120 MPa
16Cr-4Al-ODS-Hf	110 MPa

The effects of a small addition of Zr and Hf were investigated for 16Cr-4Al ODS steel. Figure 5 shows the tensile strength at 973 K of each candidate ODS steel. SOC-1 is a standard candidate ODS steel whose chemical compositions are 16Cr-4Al-2W-0.15Ti-0.35Y₂O₃. SOC-5 is 16 Cr-ODS steel without Al addition, showing much higher strength than SOC-1. SOC-14 and SOC-16 contain a small amount of Zr and Hf. The addition of a small amount of Zr and Hf is very effective in increasing strength at 973 K.

TEM observation has revealed that the addition of Zr or Hf reduces and increases the size and the number density of oxide particles, which causes matrix hardening by barrier dispersion mechanism. The strength factor in the Orowan model is a measure of the strength of barrier to dislocation motion and the factor depends on the structure of oxide particles, namely, the strain field of the particle/matrix boundary. Furthermore, the number density of grain boundary precipitates, such as carbides and oxides were increased remarkably by the addition of Zr and Hf. Grain boundary precipitates are known to be as obstacles for grain boundary sliding, which is a typical deformation mode at elevated temperatures. This effect

also resulted in a significant increase in long-term creep properties of the ODS alloy, as summarised in Table 3.

Thus, the positive effects of the addition of Zr and Hf are superior to the negative effects of Al addition on high-temperature strength. Zr addition is more recommended than Hf addition in terms of neutron absorption or neutron efficiency.

Figure 5: Ultimate tensile strength at 973 K of each candidate ODS steel (bar), the tensile specimen axis is parallel to extrusion direction and right axis is a measure of an isotropy in tensile strength

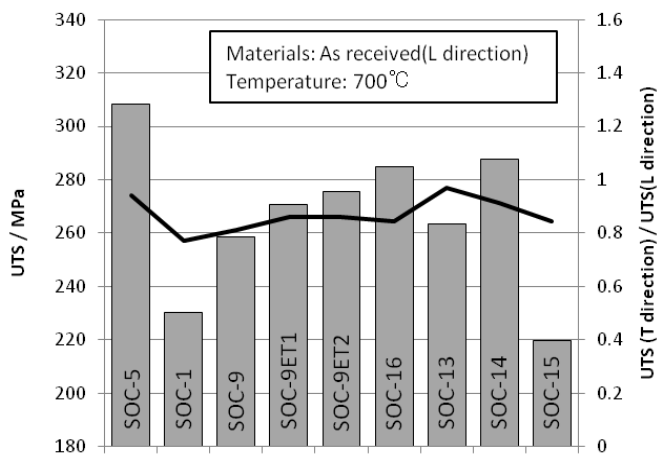
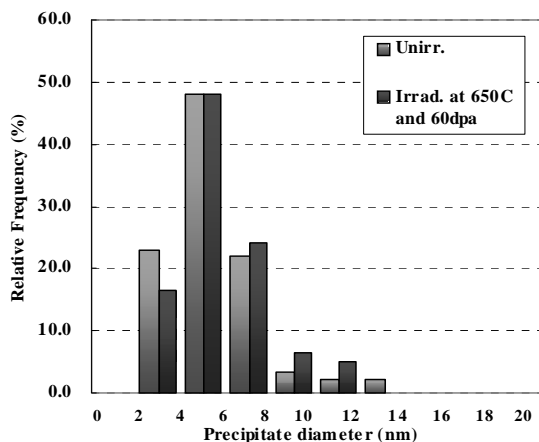


Figure 6: Size distribution of oxide particles before and after ion irradiation at 923 K up to 60 dpa



Radiation tolerance

Phase stability under irradiation

The phase stability of the oxide particles under irradiation is essential for the application of ODS steels to nuclear power plants. Ion irradiation experiments were performed at temperatures 573, 773 and 923 K up to 60 dpa for super ODS steel candidates. The specimens were irradiated with 5.1MeV Fe³⁺ by ion accelerator.

As shown in Figure 6, microstructure observations revealed that ion irradiation at 923 K up to nominal displacement of atom of 60 dpa, which corresponds to 150 dpa at the peak position in the damage depth profile, did not cause the shape change of oxide particles, indicating that the oxide particles in 16Cr-4.5Al-ODS are stable under ion irradiation.

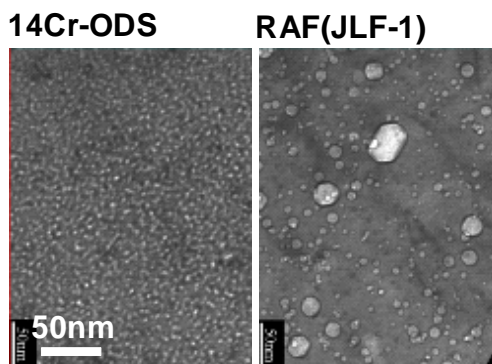
As for damage structure, a number of small dislocation loops were observed after irradiation at 573 K, although no significant change was observed for the other structures such as voids and precipitates. Furthermore, at 773 K, no significant effects such as formation of dislocation loops, voids and precipitation of secondary phases were observed. Fine precipitates in grains did not grow significantly during ion irradiation. At 973 K, however, the irradiation caused a change in the precipitation behaviour, showing that carbides precipitated both in grains and along grain boundaries. The TEM-EDX analysis of matrix, grain boundaries and precipitates in grains were performed. The normalised atomic ratio of chromium on grain boundaries was higher than the others, the carbides were considered to be chromium-rich phase. In contrast, the normalised atomic ratio of aluminum was almost uniform in the matrix and along grain boundaries. It is expected that the segregation of aluminum at grain boundaries would not occur under irradiation at 973 K.

Irradiation hardening was measured for the specimens irradiated at 573 and 773 K up to 10 dpa. The normalised irradiation hardening of $H_v^{\text{irr}}/H_v^{\text{unirr}}$ was measured using nano-indenter. H_v^{irr} and H_v^{unirr} was the hardness of 19Cr-4.5Al ODS steel before and after ion irradiation, respectively. Irradiation hardening increased as irradiation dose increased at 573 K. On the other hand, no hardening was observed at 773 K for 19 Cr ODS steel. It has previously been reported that high-Cr ODS steels often suffer irradiation embrittlement caused by phase decomposition of Fe/Cr. In previous works, Cr-rich phases were observed in the 12 Cr ferritic (not ODS) steel after the neutron irradiation at 653 K to 15 dpa in JOYO (about one year) being accompanied by large irradiation hardening. In this work, the ion irradiation hardening at 573 K is considered to be due to irradiation-induced dislocation loops but not Cr-rich phases, since no such phase was observed after irradiation.

In our neutron irradiation experiments, irradiation-induced hardening with almost no loss of elongation has been observed in high-Cr ODS ferritic steels irradiated in HFIR at 573 K to 3 dpa and in JMTR at 673 K to 0.1 dpa and in JOYO at 873 K to 4 dpa, which is interpreted in terms of suppression of localised deformation caused by nano-sized oxide particles dispersed at a high number density.

Low susceptibility to helium embrittlement

Transmutation helium causes helium embrittlement by forming helium bubbles along grain boundaries. TEM observation of the microstructure of a ODS steel and martensitic steel (JLF-1) irradiated with 5.1 MeV Fe ions (60 dpa) and 1 MeV He ions (900 at.ppm) simultaneously at 773 K indicated that large voids were formed in JLF-1 steel but no such large void was observed in ODS steels, as shown in Figure 7. This is because the oxide particles trap helium and prevent it from gathering to form large bubbles.

Figure 7: He bubbles in ODS steel and JLF-1 steel (60 dpa, 900 at.ppmHe, 773 K)

Helium implantation by cyclotron with 40 MeV He ions caused a large shift of the ductile brittle transition curve of a martensitic steel, which was accompanied by fracture mode change from cleavage fracture to grain boundary fracture in the implanted area with 1 000 at.ppm He at 823 K. In contrast, the 19Cr-ODS steel showed little shift of ductile brittle transition curve and no change in fracture mode under the same implantation conditions.

SCC susceptibility

SCC in SCPW

Susceptibility to SCC was evaluated by means of slow strain rate tests (SSRT) in the loop system of SCPW at 673 and 773 K at a pressure of 25 MPa. Dissolved oxygen (DO) was 8 ppm. Strain rates were 6.7×10^{-4} and $5 \times 10^{-7} \text{ sec}^{-1}$. For comparison, similar tests were carried out for the SUS316L. In both the 19Cr-ODS and 19Cr-4.5Al-ODS steels, ductility was independent of the strain rate, indicating that the ODS steels show very low SCC susceptibility, while SUS316L showed a reduction of tensile elongation and SCC fracture only at a strain rate of $5 \times 10^{-7} \text{ sec}^{-1}$. It should be noted that the tensile stress of ODS steels significantly depended on strain rate, a trait was also observed in ordinary ferritic steels.

Summary

Super ODS steels research and development have been carried out to fabricate fuel cladding of highly efficient next generation nuclear systems. The alloy design study suggests that 14-16 Cr plus 4 Al is necessary to keep corrosion resistance in SCPW and to suppress a severe ageing embrittlement. In particular, the addition of Al is very effective in increasing corrosion resistance of 16Cr-ODS steels in SCPW and in LBE. However, the addition of Al remarkably decreases tensile strength because of the change in oxide particles dispersion morphology. An effort was made to reduce and increase the size and the number density of the nano-scaled oxide particles, respectively, which was realised by the addition of Zr and Hf. The positive effects of Zr and Hf addition are superior to the negative effects of Al addition on high-temperature strength. Zr addition is preferred over Hf addition in terms of neutron absorption and neutron efficiency. 16Cr-4Al ODS steels were highly resistant to ion irradiation up to 150 dpa. Helium bubble growth and segregation at grain boundaries were suppressed by oxide particles dispersion. It is considered that the nano-sized oxide dispersion resulted in the increase in phase stability, which is essential for good material performance under irradiation.

“Super ODS steel”, which has a high strength at elevated temperatures and high-resistance to corrosion and irradiation embrittlement, has been developed. It is demonstrated that “Super ODS steel” has a high potential as fuel cladding material for SCWR and LFR as

well as SFR. Long-term experiments, such as neutron irradiation experiments, creep tests and long-period corrosion and ageing tests, are necessary to assess performance of high-Cr ODS steels as fuel cladding for advanced nuclear systems with high efficiency and high burn-up. After the evaluation of baseline properties of “super ODS steel”, R&D is ready to proceed to the engineering evaluation stage which includes joining technology development and massive production method towards practical application to nuclear systems.

Acknowledgements

The present study includes the result of “R&D of corrosion resistant super ODS steel for highly efficient nuclear systems” entrusted to Kyoto University by the Ministry of Education, Culture, Sports, Science and Technology of Japan (MEXT).

References

- [1] A. Kimura, T. Morimura, M. Narui and H. Matsui (1996), “Irradiation Hardening of Reduced Activation Martensitic Steels”, *J. Nucl. Mater.*, 233-237, 701-706.
- [2] S. Ukai, T. Nishida, H. Okada, T. Okuda, M. Fujiwara and K. Asabe (1997), “Development of Oxide Dispersion Strengthened Ferritic Steels for FBR Core Application (1) Improvement of Mechanical Properties by Recrystallization Processing”, *J. Nucl. Sci. Technol.*, 34[3], 256.
- [3] S. Ukai, T. Nishida, T. Okuda and T. Yoshitake (1998), “Development of Oxide Dispersion Strengthened Ferritic Steels for FBR Core Application (II) Morphology Improvement by Martensite Transformation”, *J. Nucl. Sci. Technol.*, 35[4], 294.
- [4] T. Yoshitake, T. Ohmori and S. Miyakawa (2002), “Burst properties of irradiated oxide dispersion strengthened ferritic steel claddings”, *J. Nucl. Mater.*, 307-311, 788.
- [5] A. Kimura, S. Ukai and M. Fujiwara (2004), “R&D of Oxide Dispersion Strengthening Steels for High Burn-up Fuel Claddings”, *Proc. Int. Cong. Advances in Nuclear Power Plants*, (ICAPP-2004) ISBN: 0-89448-680-2, CD-ROM file, paper 2070-2076.
- [6] A. Kimura, S. Ukai and M. Fujiwara (2003), “Development of Fuel Clad Materials for High Burn-up Operation of LWR”, *Proc. Int. Conf. Of Global Environment and Advanced Nuclear Power Plants*, (GENES4/ANP 2003), ISBN 4-901332-01-5, CD-ROM file, paper 1198.
- [7] H. S. Cho, A. Kimura, S. Ukai and M. Fujiwara (2004), “Corrosion properties of oxide dispersion strengthened steels in super-critical water environment”, *J. Nucl. Mater.* 329-333, 387-391.
- [8] H. S. Cho, A. Kimura, S. Ukai and M. Fujiwara (2005), “Development of Fuel Clad Materials for High Burn-up Operation of LWR”, *Journal of ASTM International*, 2[7], 194-205.
- [9] J.S. Lee, A. Kimura, S. Ukai and M. Fujiwara (2004), “Effects of Hydrogen on the Mechanical Properties of Oxide Dispersion Strengthening Steels”, *J. Nucl. Mater.* 329-333, 1122-1126.
- [10] J.S. Lee, A. Kimura, S. Ukai, M. Fujiwara and I.S. Kim (2004), “Hydrogen Embrittlement of Oxide Dispersion Strengthening Steels under in-situ Cathodic Charging”, (ICAPP-2004) ISBN: 0-89448-680-2, CD-ROM file, paper 1616.

Session IV

Metal – Materials Compatibility – LFR Corrosion

Chairs: M. Toloczko, S. Ukai

Corrosion of structural materials in nuclear systems involving liquid metals*

F. Balbaud-Célérier¹, L. Martinelli¹, F. Gabriel²

¹CEA, DEN, DPC, SCCME, Laboratoire d'Étude de la Corrosion Non Aqueuse, Gif-sur-Yvette, France, ²CEA, DEN, DM2S, SERMA, Laboratoire de Protection, d'Études et de Conception, Gif-sur-Yvette, France

Abstract

Due to their satisfying properties of heat transfer such as high thermal conductivity, high heat capacities and low vapour pressures, liquid metals are considered for several nuclear systems: Pb-Li is considered as liquid breeder in blanket concepts of future fusion reactors, Pb-Bi as spallation target of accelerator-driven systems for the transmutation of nuclear wastes, Pb, Pb-Bi, Na, Ga as coolant of Generation IV fast reactors. However, structural materials as well as cladding materials are subject to degradation in these liquid metal environments. Liquid metal corrosion can take various forms: dissolution, formation of intermetallic compounds at the interface, penetration of liquid metal along grain boundaries. The corrosion kinetics depends on experimental factors such as: temperature, thermal gradients, solid and liquid compositions, velocity of the liquid metal. In this paper, corrosion processes in these various environments will be presented together with the structural materials considered as well as the protection means foreseen: F/M steels, ODS steels, austenitic steels, coatings, etc. The main parameters affecting corrosion in these environments will be focused on, and comparison of the behaviour of structural materials in these various liquid metals will be performed using predictive models.

* The full paper being unavailable at the time of publication, only the abstract is included.

Effect of temperature and strain rate on the fracture toughness of T91 steel in lead-bismuth eutectic environment*

Gunter Coen
SCK•CEN, Belgium

Abstract

One of the problems of using heavy liquid metals like lead-bismuth eutectic (LBE) as coolant and/or spallation source in future accelerator-driven systems, like the MYRRHA system which is under development at SCK•CEN, is the compatibility of the coolant with the structural materials. One of the possible issues is liquid metal embrittlement (LME), which is a reduction of the ductility and fracture toughness of a metal when subjected to stress and when in direct contact with a liquid metal.

One of the structural materials chosen for parts of the system working at higher temperatures under high neutron doses is T91 ferritic-martensitic steel. Slow strain rate tests (SSRT) of T91 in LBE environment show a reduction of the ductility. However, although SSRT tests show the occurrence of LME, fracture toughness data are needed to quantify its effect.

Fracture toughness tests of T91 steel were performed using sub-sized disc shaped compact tension specimens. The fracture toughness data published show a reduction of up to 30% at 200°C and at a displacement rate of 0.25 mm min⁻¹ [1]. However, as shown by performing SSRT tests, there is an effect of temperature and strain rate on the occurrence of LME. Therefore, the fracture toughness of T91 steel was determined as a function of temperature and strain rate in both air and LBE environment.

Reference

- [1] G. Coen, J. Van den Bosch, A. Almazouzi, J. Degrieck (2009), "Investigation of the effect of lead-bismuth eutectic on the fracture properties of T91 and 316L", DOI: 10.1016/j.jnucmat.

* The full paper being unavailable at the time of publication, only the abstract is included.

Effect of welding on corrosion properties of ferritic-martensitic steels in liquid lead-bismuth

Asril Pramutadi, Andi Mustari¹ and Minoru Takahashi²

¹ Department of Nuclear Engineering

² Research Laboratory for Nuclear Reactors,
Tokyo Institute of Technology, Japan

Abstract

Evaluating the compatibility of LBE with the welded parts of steels is one of the key issues for the development of lead alloy-cooled fast reactors (LFR) and accelerator-driven systems (ADSs). A corrosion test in lead-bismuth eutectic (LBE) was conducted for welded ferritic-martensitic steels. The ferritic-martensitic steels tested in this study were HCM12 and HCM12A. Specimens were prepared by TIG and laser welding with particular parameters. The specimens were categorised with specific combinations. The corrosion test was conducted in liquid LBE at 550°C for 1 000 hours. Oxygen concentration was controlled to be $\sim 5 \times 10^{-3}$ wt% by using Ar-H₂-H₂O mixture gas. The results show that Cr-oxide layers were formed on base metal and the welded parts. The oxide layers were thicker on the welded parts than on the base metal. It was found that the oxidation corrosion of ferritic-martensitic steels in liquid LBE was enhanced at the welded parts. The Vickers hardness showed higher value of hardness on fusion zone (FZ) than base metal (BM).

Introduction

LBE is the candidate material to be used as a spallation target and coolant for accelerator-driven systems (ADSs). In addition to this, LBE also has been proposed as coolant for Generation IV lead alloy-cooled fast reactor (LFR). However, for years, the corrosion has been one of the main concerns for research due to utilisation of LBE in contact with structural materials. Several materials have been tested under LBE environment in order to see the corrosion behaviour.

Welding is the most common method used for joining structural materials. However, a welded part could be a critical point which can generate accidents. For this reason, welded part should have good compatibility with the liquid LBE environment. Several studies were conducted regarding the compatibility of steel welds with LBE [1] [2]. However, there have been very few studies of steel weld under liquid LBE.

This study investigated the corrosion behaviour of welded ferritic-martensitic steels under liquid LBE at 550°C with low oxygen concentration. The effects of welding power and welding speed on the corrosion behaviour were compared. In addition, mechanical properties were also investigated.

Experimental

Ferritic-martensitic steels, HCM12 and HCM12A were used as base metals (BMs). Their chemical compositions can be seen in Table 1. The fusion zones (FZs) in the base metals were made by applying TIG and laser welding with particular parameters. The geometry and surfaces of the specimen are shown in Figures 1 and 2, respectively. The specimens with particular conditions were categorised by specific combinations, as shown in Table 2.

Table 1: Chemical composition of steels (wt%)

	Fe	Cr	Mo	W	Si	others
HCM12	Bal.	12.1	1.1	1	0.3	-
HCM12A	Bal.	12	0.3	1.9	0.3	0.9Cu

Figure 1: Shape and sizes of specimen

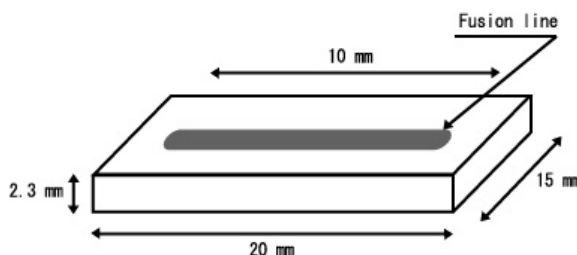
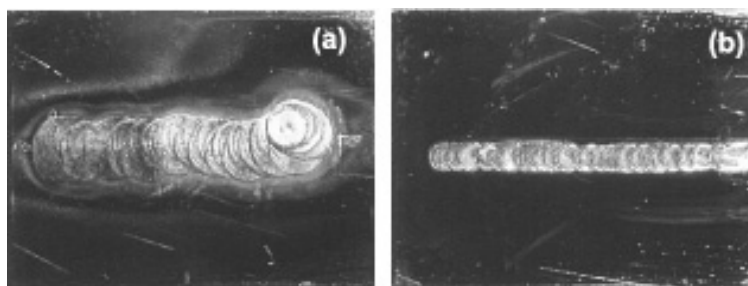


Figure 2: Typical specimen surfaces: (a) TIG welding FZ (b) laser welding FZ

The apparatus used in this experiment was a static corrosion test apparatus, as shown in Figure 3. The specimens had been immersed in hot liquid LBE for several days. In order to maintain the oxygen concentration, Ar-H₂-H₂O mixture gas was supplied. Oxygen concentration and temperature were measured by using an oxygen sensor and a thermocouple, respectively. Oxygen concentration was controlled to 5×10^{-9} wt%, which is under that of Fe₃O₄ formation (Figure 4). Table 3 shows the details of all the experimental procedures.

After the corrosion test, the specimens were rinsed with hot glycerine (at 130°C) and hot water (at 80°C). Copper coating was used to protect the oxide layer formed on the surface during machining. The specimens were then cut at the middle and mounted in resin. In order to have grain boundary image, the specimens were etched using dilute aqua regia (15 ml HCl, 5 ml HNO₃, 100 ml H₂O, at room temperature). Macrostructural and microstructural analyses were conducted using an optical microscope and SEM/EDX, respectively. For each specimen, five or more micrographs were used. Vickers hardness test was used to obtain hardness data.

Table 2: Specimens combination

Combinations	Steels	Welding specifications and condition
I	HCM12	Type: Inverter ELECON 300p (<i>TIG</i>) Power: <i>480 W</i> welding speed: approx. <i>137 mm/min</i>
II	HCM12A	
III	HCM12	Type: YLM-500P (<i>Laser</i>) Power: <i>287 W</i> welding speed: approx. <i>780 mm/min</i>
IV	HCM12A	

Figure 3: Schematic of apparatus

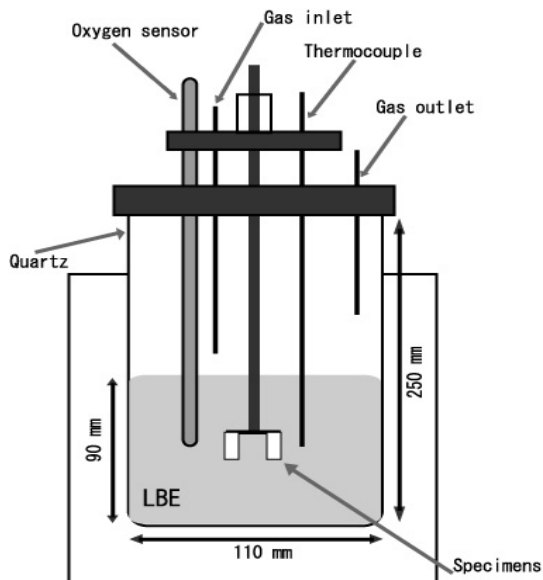


Figure 4: Diagram of oxygen potential

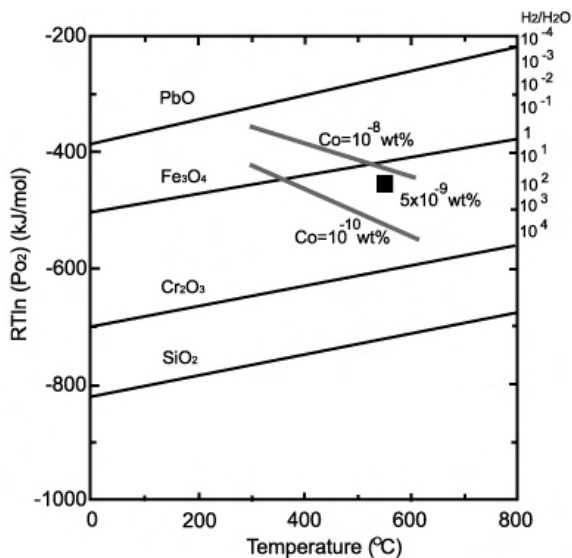


Table 3: Corrosion test condition

Temperature of LBE (°C)	550
Exposure time (h)	1 000
Amount of LBE in pot (kg)	7
Oxygen sensor type	YSZ-tube type (Y--8mol%)
Injection gas	Ar+4%H ₂ and Ar
Oxygen concentration (wt%)	5x10 ⁻⁹

Result

Figure 5 shows SEM images of BM and FZ of the specimens after the corrosion test. The BMs show ferritic-martensitic type of grain structure. On the other hand, FZs show coarse grain structure as a result of the welding process.

Figure 6a indicates a SEM image of HCM12 base metal (BM) after the corrosion test. Cr-rich spinel oxide was formed on the surface (Figure 6c), but it was observed that LBE penetrated into the oxide layer (Figure 6a). The thickness profiles of the formation of the oxide layer and the penetration of LBE are shown in Figure 9. It is found that the thickness of the oxide layer on the HCM12 BM was about 3-7 μm , while penetration was 3.0-7.7 μm . Figure 6b shows the cross-section of HCM12A BM. LBE penetration was dominant on the surface of the BM. Very few oxide layers formed on the surface. Cr-rich spinel oxide thickness was 6.3-6.3 μm . However, penetration of LBE of 9-15 μm was more severe than that of HCM12 material (Figure 9).

Figure 7 shows SEM and EDX observation of cross-section of FZ of combination I and II specimens. Figure 7a shows the formation of an oxide layer on the surface of combination I FZ. It was confirmed by EDX line analysis that the oxide layer was Cr-rich spinel oxide (Figure 7c). Figure 7b shows the SEM result of combination II FZ. Similarly to FZ of combination I, it was found that an oxide layer formed on the surface of the FZ. EDX analysis shows Cr-rich spinel oxide formation on the surface of combination II FZ (Figure 7d). Formation of Cr-rich spinel oxide was thicker on FZ of combination I (7.2-9.6 μm) than combination II (3-7 μm) (Figure 9).

Figure 5: SEM images: (a) HCM12 BM (b) combination I FZ (c) combination III FZ (d) HCM12A BM (e) combination II FZ (f) combination IV FZ

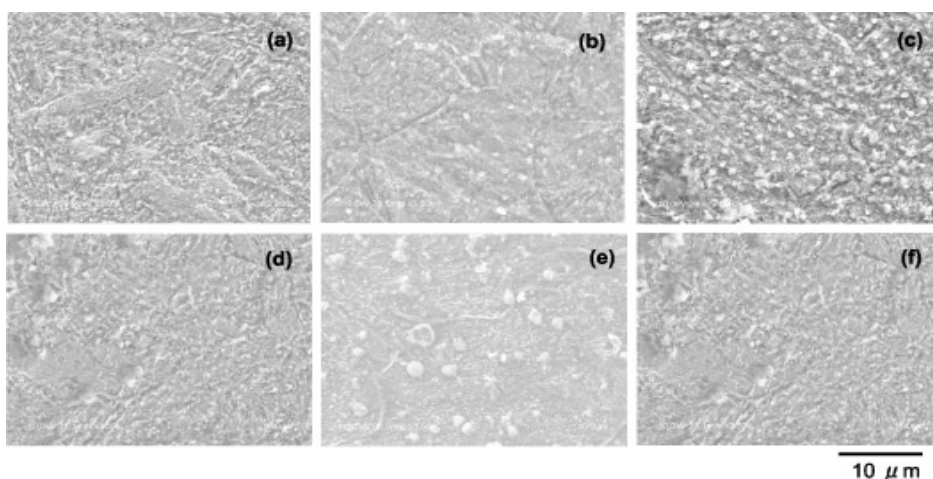


Figure 8 shows SEM and EDX results of combination III and IV FZs. The surface of the combination III FZ after the corrosion test showed oxide layer formation illustrated in Figure 8a. However, it consists of two layers, X and Y. The X layer was Cr-rich spinel oxide (Figure 8c), with a thickness of about 7-11.3 μm , as shown in Figure 9. The Y layer showed the oxygen diffusion layer, where only peak of oxygen indicating a diffusion zone was observed (Figure 8c). Figure 8b shows the penetration of LBE in the combination IV specimen. EDX analysis shows the formation of Cr-rich spinel oxide on the surface. However, the Cr-rich spinel oxide could not prevent the penetration of LBE. The thickness of the oxide layer, i. e. Cr-rich spinel oxide, was only about 1.6-3 μm (Figure 9).

Figure 10 shows the Vicker's hardness number for all specimens after the corrosion test under liquid LBE. The BM of HCM12 and HCM12A showed the hardness of 299-319 HV and 263-284 HV, respectively. FZs of all combination specimens show higher hardness than BMs. The HV values of combination I varied between 349 and 369, which was higher than combination II (from 317 to 351 HV₁₀). The V (HV) value of combination III was about 369-393, while combination IV was 322-360 HV.

Figure 6: SEM/EDX micrographs observation of base metal of HCM12 and HCM12A: (a) SEM result of HCM12 BM (b) SEM result of HCM12A BM (c) EDX line analysis result of HCM12 BM (d) EDX line analysis result of HCM12A BM

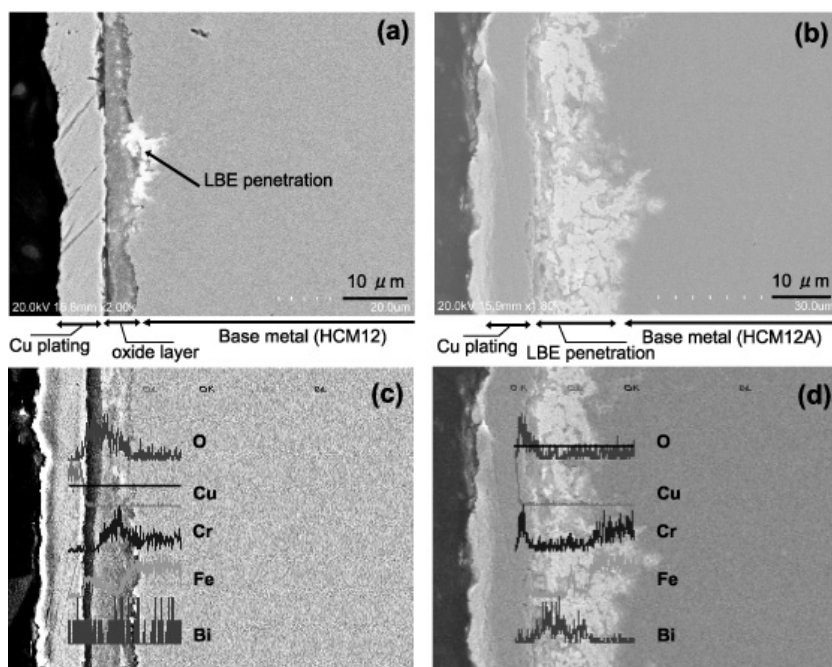


Figure 7: SEM/EDX micrographs observation of FZ of combination I and II specimens: (a) SEM result of combination I (b) SEM result of combination II (c) EDX line analysis result of combination I (d) EDX line analysis result of combination II

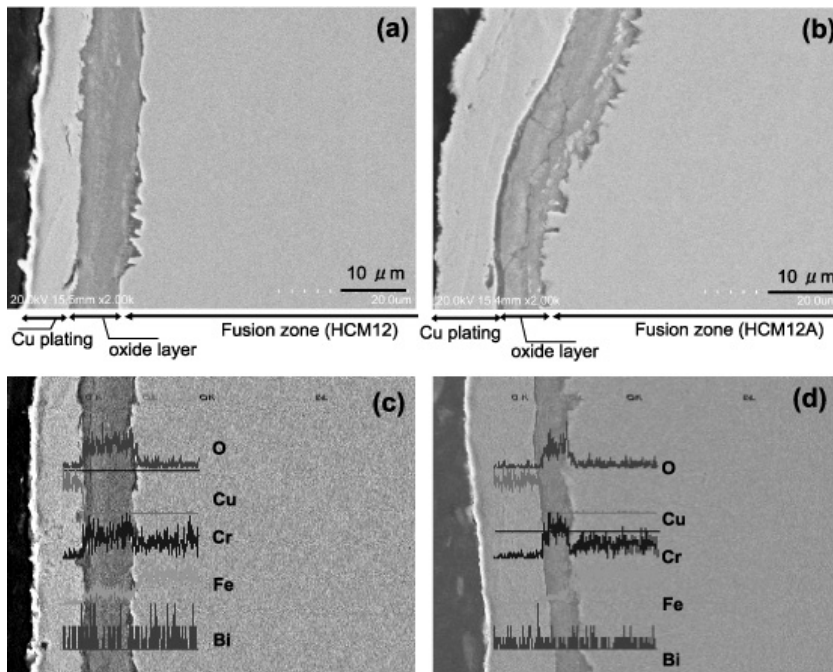


Figure 8: SEM/EDX micrographs observation of FZ of combination III and IV specimens: (a) SEM result of combination III (b) SEM result of combination IV (c) EDX line analysis result of combination III (d) EDX line analysis result of combination IV

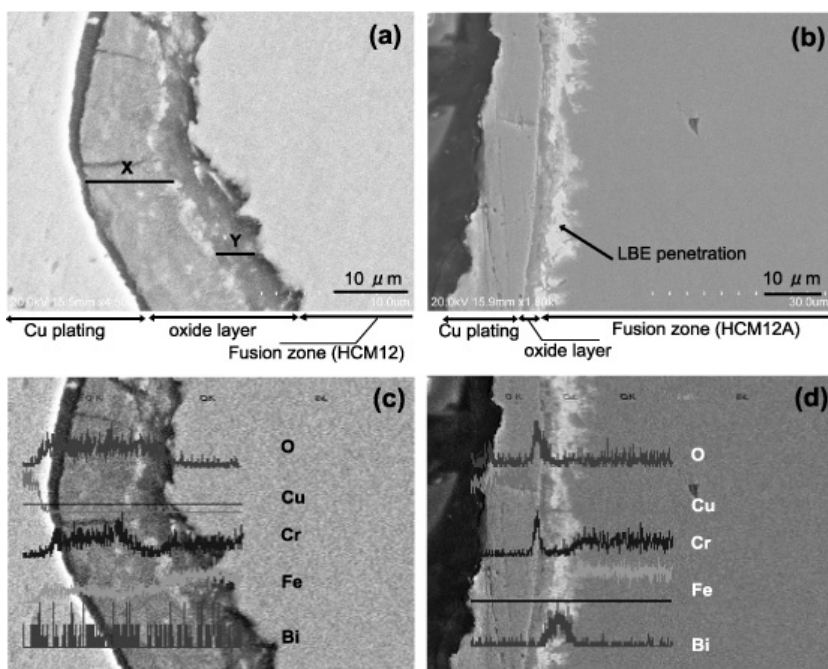


Figure 9: Oxide layer formation and LBE penetration profile of specimens

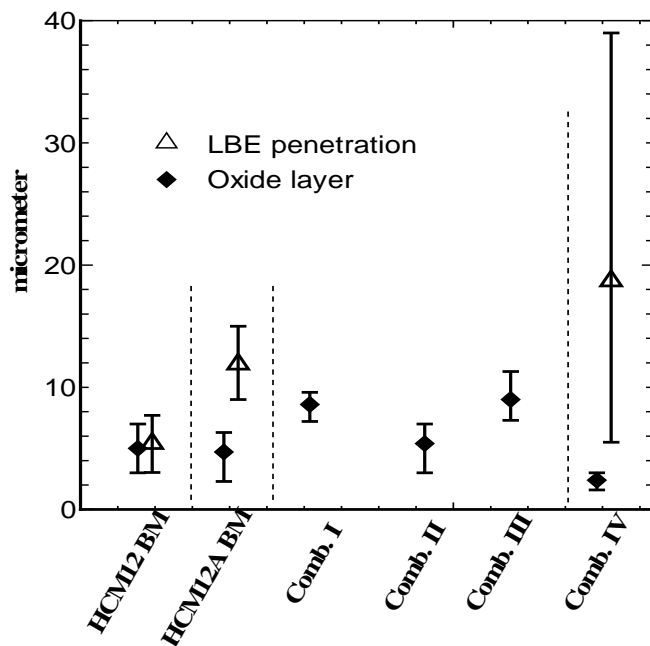
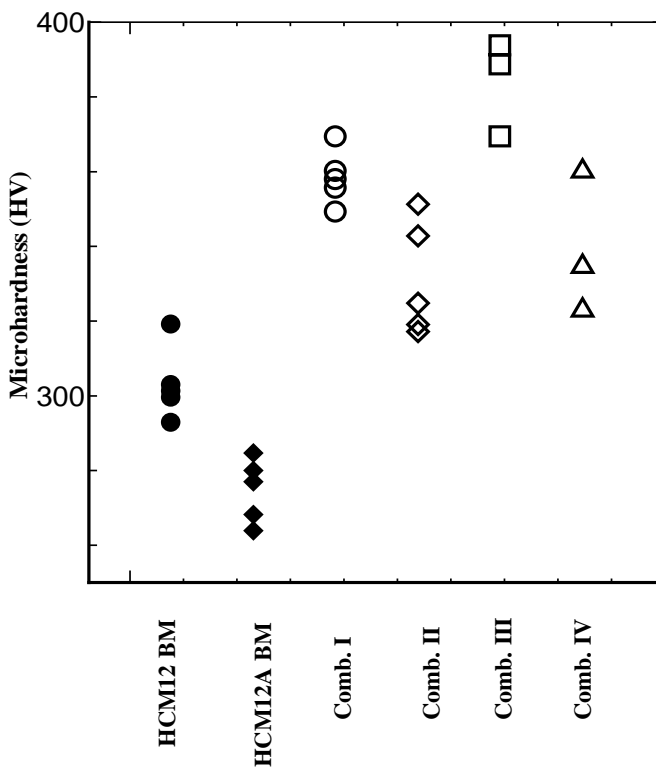


Figure 10: Vicker's hardness profile of specimens



Discussion

In all the cases of HCM12 and HCM12A, oxide of Cr-rich spinel oxide was observed on the specimen surfaces of both BM and FZ after the exposure of specimens to LBE at 550°C in the static corrosion apparatus (Figures 6, 7, 8). This result was in agreement with the result of the experiment for the ferritic-martensitic steels conducted under the same conditions [3]. No formation of magnetite was observed in this study, which may be caused by the low oxygen concentration of the experiment. The condition of oxygen potential at 550°C with the oxygen concentration of 5×10^{-9} wt% is in the area of Cr_2O_3 formation while below Fe_3O_4 formation.

Since the oxide layer seems to be porous and easy to detach, LBE can easily penetrate into the oxide layer and bulk. Kurata *et al.* reported that ferritic-martensitic steels exhibited formation of oxide layer but failed to prevent LBE penetration at 550°C with the oxygen concentration of 5×10^{-9} wt% [3]. LBE penetrated more deeply in BM of HCM12A than in HCM12, as indicated from the thickness of LBE penetration.

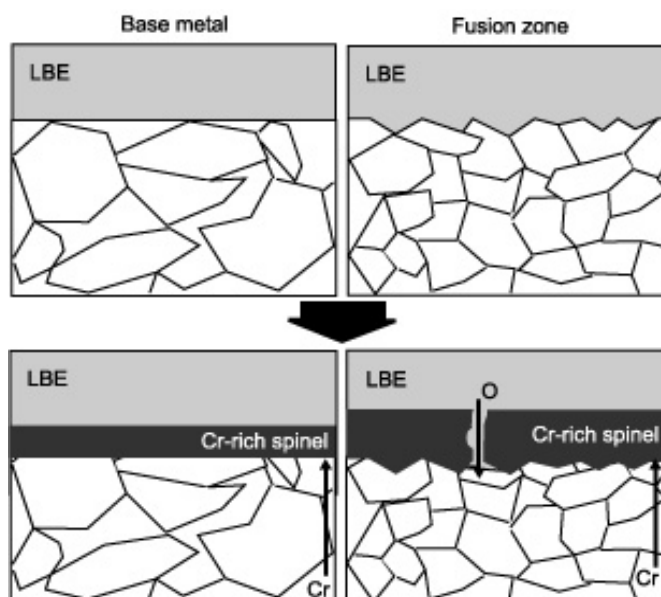
It seems that the FZs were more corrosive, exhibiting more significant oxide formation and LBE penetration than BM, as shown in Figure 9. Even though combination IV FZ has a lower value of oxide layer formation than HCM12A BM, the LBE penetration was higher. More corrosive phenomena of FZ than BM might be caused by the specific feature of surface roughness and grain structure of FZ. After the welding process the surface of the specimens became rough (see Figure 2). Surface roughness may influence the formation of an oxide layer. Kondo reported that rough surface might form an unstable oxide layer due to crack formation [4]. The crack lets oxygen easily diffuse to the bulk and form a diffusion layer.

Another reason for the more corrosive phenomenon of FZ is its specific feature of grain structure. The FZs show coarse grain structure, as shown in Figure 5. The coarse grain structure may influence oxide layer thickness [5]. In this experiment, the grain structure changed by welding exhibited rapid diffusion of oxygen.

The mechanism of oxide layer formation due to surface roughness and grain boundary changing is shown schematically in Figure 11. The illustration shows the diffusion of various species on BM and FZ. Under liquid LBE, an oxide layer is formed on the surface of the material. However, due to coarse grain structure, oxygen diffuses rapidly in the fusion zone and Cr enriches the oxide layer. This condition leads to thicker oxide layer formation. In addition, due to rough surface conditions on the FZ, a crack is formed in the oxide layer. The oxygen then passes through the crack to continue to contact with bulk, then it thickens the oxide layer.

FZ of combinations I and II used TIG welding which has high power and low welding speed in comparison to laser welding (low power and high welding speed) in FZ of combinations III and IV showed a similar trend of oxide layer formation while combination IV FZ showed a little lower oxide formation compared to combination II FZ. However, high power with low welding speed may change the grain structure more than low power with high welding speed, which may lead to more corrosive conditions.

The hardness values of all FZs are higher than BM. This is because of the welding treatment which decreases the ductility of the material while increasing hardness. H. Zhang *et al.* reported that the welded part of the T91 had higher hardness value in comparison with BM [6]. In order to have a similar hardness value between the welded part and BM, post-welding heat treatment (PWHT) is necessary.

Figure 11: Schematic illustration of corrosion mechanisms

Conclusion

From the investigation of the static corrosion experiment at 550°C for 1 000 h with low oxygen concentration, 5×10^{-9} wt%, the following conclusions can be drawn:

- (1) All the investigated specimens showed formation of Cr-rich spinel oxide. The formation of oxide layer on FZ was slightly higher than on BM, although in some specimens penetration of LBE occurred.
- (2) FZ, which was welded by TIG welding with high power and low welding speed, showed almost the same oxide formation as FZ with low power and high welding speed of laser welding.
- (3) The hardness values of FZ of combination specimens were higher than BMs after corrosion test. However, the hardness values among FZs were almost similar.

Acknowledgements

The authors would like to express their gratitude to Dr. Yuji Kurata for his valuable assistance.

References

- [1] J. Van den Bosch, A. Almazouzi (2009), *Journal of Nuclear Materials* 385, 504–509.
- [2] J. Van den Bosch et al. (2010), *Journal of Nuclear Materials* 396, 57–64.
- [3] Y. Kurata et al. (2008), *Journal of Nuclear Materials* 373, 164–178.
- [4] Kondo, Masatoshi (2006), Ph.D. Thesis, Tokyo Institute of Technology, Japan.
- [5] A. Weisenburger et al. (2006), *Journal of Nuclear Materials* 358, 69–76.
- [6] H. Zhang et al. (2008), *Journal of Nuclear Materials* 377, 122–131.

Development of alumina forming ferritic steels for lead-bismuth eutectic-cooled applications

Il Soon Hwang, Jun Lim, Seung Gi Lee

Nuclear Transmutation Energy Research Center of Korea (NUTRECK),
Seoul National University, Republic of Korea

Abstract

Like liquid lead-bismuth eutectic (LBE) cooled fast reactors, PEACER (proliferation-resistant, environment-friendly, accident-tolerant, continual, and economical reactor) was first developed in 1996 for the transmutation of long-living radioactive isotopes from spent nuclear fuels. The LBE coolant has excellent safety and neutronic characteristics whereas the lifetime of the primary structural components is still in question due to corrosion issues. By reducing hot-leg temperature to 400°C, the primary coolant boundary components of PEACER-300 are designed for a 60-year life based on AISI 316L. With a maximum outer temperature of 450°C fuel claddings are designed to assure adequate strength, ductility and corrosion-resistance over about a three-year life using ferritic-martensitic steels. While materials durability is shown to be adequate for PEACER-300, advanced corrosion resistant alloys have been developed in order to allow higher hot-leg temperatures and longer fuel lives in PASCAR, a new long-burning small modular reactor. New Si- and Al-containing ferritic steels are shown to have excellent corrosion-resistance for up to 600°C. However, their radiation-resistance is modest and a hybrid approach has been made. All materials requirement can be satisfied by developing a hybrid tube with the new alloy forming an outer layer of radiation-resistant ferritic martensitic steels. Manufacturing processes for hybrid tubes are being developed for both fuel cladding and steam generator tubes for PASCAR.

Introduction

As a highly promising option for fast reactors, heavy liquid metal coolant (HLMC) including lead and lead-bismuth eutectic (LBE,) has been extensively investigated since the release of the Russian submarine experience incident in the mid-1990s. To improve the safety and economy of fast reactor systems, HLMC offers three important advantages over liquid sodium. First, HLMC's do not react exothermically with water or air. Second, high boiling points (~1 700°C) of HLMC's provide significantly greater safety margins against hypothetical core damage accidents and higher potentials to operate at higher temperatures. Finally, the coolant to fuel volume ratio can be significantly increased to reduce the risk of local flow blockages and mechanical interactions.

However, HLMC's also have several disadvantages, including relatively low heat transfer capability, significant corrosivity to fuels and structural materials, heavy weight and the generation of alpha-emitting Po-210. Lower heat transfer capability was addressed by reduced power densities with open core lattice. The structural burden of coolant weight in the case of medium-large units including PEACER-300 has been overcome by installing base isolations against earthquakes.

Po-210 is expected to reach a steady state concentration of about 10^{-8} wt.% in LBE coolant. With the help of liquid lead-polonide formation at the design temperature range, no significant vapourisation is expected. It should be noted that no submarine crew members received overdoses of Po-210. Hence remote maintenance practices typically used in fast reactors may be adequate to control the issue. With consideration to these advantages and ways to overcome disadvantages, the HLMC technology has been chosen for recent official launches for fast reactor development including Belgian MYRRHA and Russian commercial small modular reactor SVBR-100 [1-3].

The Nuclear Transmutation Energy Research Center (NUTRECK) of Seoul National University (SNU) continues to develop the PEACER design. Recently an LBE cooled small modular reactor PASCAR-35 (proliferation-resistant, accident-tolerant, self-supported, capsular and assured reactor) has been designed with a rating of 35 MWe (100 MWt) operating solely by natural circulation without primary coolant pump [4-7]. The pump-less design has been derived from multiple natural circulation experiments conducted using HELIOS (heavy eutectic liquid metal loop for integral test of operability and safety of PEACER). PASCAR design targets for 20 years of fuel life with a high proliferation resistance. The class of small modular reactors can also have improved economy from longer refueling period and higher reliability [8-9].

In this paper, we confirm, based on new data, that available nuclear-grade materials can be used to ensure a 60-year design life of PEACER design. It is also shown that improved corrosion-resistant materials are needed to be developed for HLMC-cooled small modular reactors for a core-life of 20 years and beyond.

Characteristics of PEACER and PASCAR

PEACER is a dedicated nuclear transmutation system with integral arrangement of a loop-type lead-bismuth cooled reactor and an advanced pyrochemical spent nuclear fuel processing facility [4]. In order to assure high proliferation resistance a PEACER park is proposed to be constructed, operated and managed under an international control. Metallic U-TRU-Zr fuel with HT-9 cladding developed by the integral fast reactor (IFR) technology was adjusted to be compatible with lead-bismuth coolant. In addition, the Russian corrosion database available in the 1990s was analysed for stainless steels to find a high sensitivity of corrosion rate to temperature and dissolved oxygen concentration in lead-bismuth coolant. On this ground the hot-leg temperature of PEACER was limited to 400°C while placing special emphasis on high proliferation resistance, a high transmutation rate, high safety and economy. Thermal trap regions contain long-living

fission products including Tc-99 and I-129 in calcium hydride matrix in order to transmute the isotopes important to the radiological dose in the final waste repository [5] [7].

As a proliferation-resistant capsular small modular reactor (SMR), PASCAR-35 has been developed to operate for a period of 20 years without refueling [8]. Principal applications of PASCAR can be made to at least two areas: 1) a proliferation-resistant SMR for remote deployment in single unit or in cluster for electricity and heat supply and 2) a small-scale technology development for nuclear transmutation of spent nuclear fuels. For the former use, it is expected that a long-core life is desired to make a hermetically sealed reactor for adequate proliferation resistance. The main design characteristics of PEACER and PASCAR are summarised in Table 1.

Table 1: Main design characteristics of PEACER-300 and PASCAR-35

Parameter	PEACER-300	PASCAR-35
Power (MWe/MWt)	300/850	35/100
Fuel compositions (wt%)	U/TRU/Zr (58/32/10)	U/TRU/Zr (Inner : 75.5/14.5/10.0 Outer : 69.9/20.1/10.0)
Fuel assembly type	Square open lattice	Square open lattice
Coolant	Lead-bismuth eutectic	Lead-bismuth eutectic
Plant design life (year)	60	60
Fuel lifetime (year)	3	20
Cladding outer diameter (mm)	8.32	25
Cladding wall thickness (mm)	1.0	0.85
Fuel pitch to diameter ratio	1.44	1.40
Active core height (cm)	50	150
Coolant temperature(°C)	300(inlet) / 400(outlet)	300(inlet) /400(outlet)
Average linear power (kW/m)	24	34.5
Average burn-up (GWD/kg)	77	70
Maximum dpa damage of fuel cladding (dpa)	100	160

Development of material for PEACER and PASCAR

Based on literature data on mechanical properties, irradiation performance, fabricability and availability, two ferritic/martensitic steels (HT9, T91) and a nuclear grade austenitic steel (AISI 316L) have been evaluated for PEACER design. The typical chemical compositions of these steels are given in Table 2.

Table 2: Nominal composition of T91, HT9 and AISI 316L (wt %)

Steel	Fe	Cr	Ni	Mo	W	Mn	V	Nb	Si	C	N
T91	Bal.	9.0	0.10	1.0	-	0.40	0.20	0.08	0.40	0.10	0.05
HT9	Bal.	12.0	0.50	1.0	0.50	0.60	0.25	-	0.40	0.20	-
AISI 316L	Bal.	17.2	10.9	2.1	-	1.6	-	-	0.30	0.02	-

For fuel cladding materials of PEACER and PASCAR, ferritic/martensitic steels (FMS) are preferred in fast neutron environments due to higher irradiation resistance compared with austenitic stainless steels [10-11]. The maximum swelling temperature of FMS is observed at around 400–420°C, where less than 2% swelling was observed for HT9 and modified 9Cr-1Mo (T91) irradiated to 200 dpa in the Fast Flux Test Facility (FFTF) [12]. In addition, a fuel rod performance analysis shows adequate creep resistance for burn-up duties described in Table 1.

The corrosion of materials in LBE has been a controversial issue with lead fast reactor development. Corrosion of structural materials in contact with liquid lead alloys occurs primarily as a classical dissolution process driven by the solubility of a species in the liquid. The solubility of most elements of structural materials in the lead alloy increases with temperature. In order to retard the corrosion process a novel technique of oxygen addition to coolant was developed and successfully applied to develop passivating oxide layers in lead-bismuth coolant. The oxygen injection to the desired concentration, however, does not oxidise the chemically inert coolant constituents including lead and bismuth.

The corrosion behaviours of structural materials such as HT9, T91 and AISI 316L in LBE have been extensively studied under the oxygenated lead-bismuth to predict the materials performance [13]. While the corrosion rate is drastically reduced by dissolved oxygen, the temperature dependence of corrosion rate remains pronounced due to the fact that the diffusion of chemical species across the passivating oxide layer on the materials surface is accelerated exponentially with temperature. The latest fleet of lead-bismuth cooled submarines of the former Soviet Union had operated with a hot-leg temperature of 540°C. Recent studies led by OECD/NEA have demonstrated that both FMS and AISI 316L maintain protective oxide layer at temperatures below 500°C with an adequate oxygen concentration in LBE [13].

The adequacy of reduced hot-leg temperatures for PEACER and PASCAR is re-examined using the database. Correlations for the oxide layer thickness on FMS and AISI 316L in LBE have been derived using experimental data from the literature [13-19].

$$X(t) = [K(T) \cdot t]^{1/2}$$

where $X(t)$ is the thickness in cm and t is time in seconds.

The parabolic rate constant $K(T)$ for FMS and AISI 316L, respectively, has been derived as follows:

$$K(T) = 1.156 \times 10^{-3} \exp\left(-\frac{117675}{RT}\right) \quad \text{for HT9 and T91}$$

$$K(T) = 3.027 \times 10^{-3} \exp\left(-\frac{161626}{RT}\right) \quad \text{for AISI 316L}$$

Where, R is the universal gas constant (8.3144 J/mol-K) and T is temperature in K.

Figure 1 shows the predicted oxide layer thickness together with the experimental data, as a function of temperature for FMS and AISI 316L. The oxide thicknesses of fuel cladding and reactor vessel of PEACER and PASCAR at the end of designed life have been estimated based on the above correlations, as summarised in Table 3.

In the case of PEACER, the oxide thicknesses of both fuel cladding and the reactor vessel are predicted to be acceptably small for their three-year and 60-year lifetime, respectively. In the case of PASCAR, the fuel cladding made of FMS steels can develop an oxide greater than 100 μm during a 20-year life. It has been observed in the laboratory tests that such a thick oxide can develop a high surface stress and hence release oxide scales to coolant, leading to accelerated corrosion behaviour.

Figure 1: Comparison between the experimental data (symbol) in LBE and the predictions (lines) (a) FMS, (b) AISI 316L

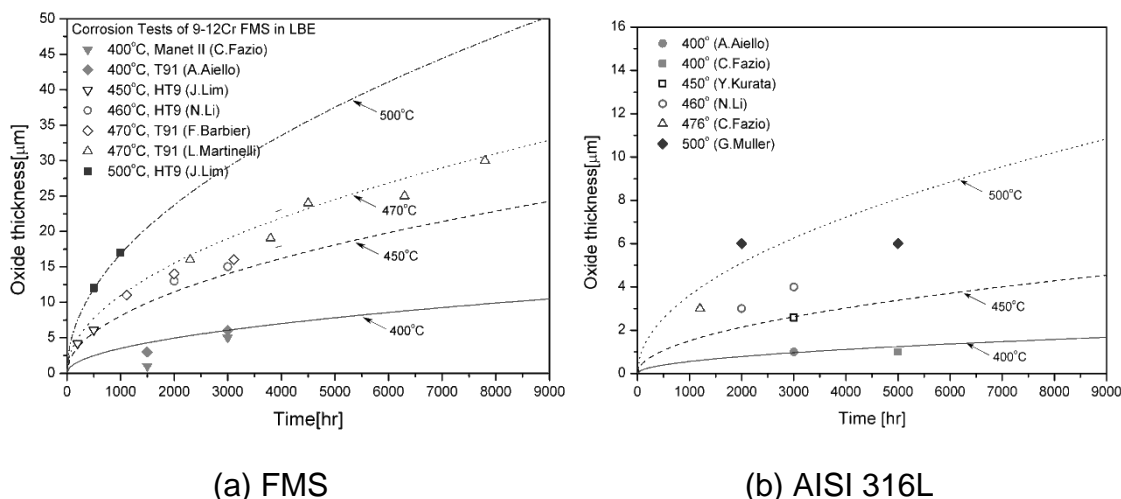


Table 3: Estimated oxide thickness of components of PEACER and PASCAR at the end of design life

Component (material)	PEACER		PASCAR	
	Design life [yr]/maximum temperature [°C]	Oxide thickness [μm]	Design life [yr]/maximum temperature [°C]	Oxide thickness [μm]
Fuel cladding (HT9 or T91)	3 / 450	41	20 / 450	107
Reactor vessel (AISI 316L)	60 / 400	13	60 / 400	13

Considering that a long-burning reactor will be required to have a very high reliability, it is essential that for critical components including fuel rods, the oxide thickness should not develop oxide layers with excessive thickness. Therefore, advanced corrosion-resistant materials are being developed for fuel cladding of PASCAR, as described below.

Corrosion of fuel materials by HLMC is one of the critical issues of PEACER and PASCAR design development in which metallic fuels are employed to allow for higher compatibility with pyrochemical processes. Following the successful experience at EBR-II, liquid sodium is employed as bonding metal for fuel-cladding gap. The cladding inner surface is designed to be lined with vanadium layer to prevent fuel-cladding chemical interaction.

Adequate margin has been given in fuel design to minimise the occurrence of cladding defects. Based on a conservative fuel cladding thickness and the vanadium liner as well as low burn-up, the frequency of cladding perforation during normal operation will be suppressed to an adequately low level. The total amount of sodium will be too small to disturb oxygen concentration in the primary coolant in the event of cladding failures.

Development of hybrid cladding materials

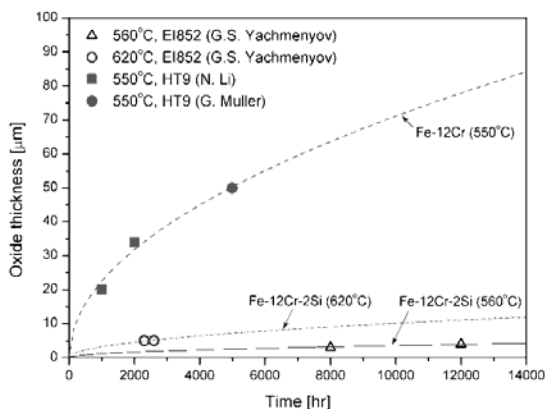
It has been shown that commercially nuclear-grade alloys can provide a 60-year design life for structural components and a three-year fuel life of PEACER with a reduced hot-leg temperature. There is a demand to increase the corrosion resistance of structural materials in HLMC for applications to higher temperature and/or for longer service time, as discussed earlier in relation with PASCAR design.

From the Russian development it is well established that the passivity of oxide layers on structural steels can be enhanced by Si-alloying. Several Si-containing ferritic/martensitic steels have been developed by Russians for applications to LBE-cooled fast reactors. The chemical composition of the two types of Russian FMS designated EP823 and EI852 for LFR are given in Table 4. Figure 2 shows that the corrosion resistance of EI852 is far superior to that of HT9. The oxide thickness of EI852 at 450°C and 560°C, respectively, is predicted to be about 2 µm and 15 µm after 20 years. Therefore Si-containing alloys can solve the corrosion of PASCAR fuels cladding.

Table 4: Typical chemical composition of EP823 and EI853 (wt%)

Steel	Fe	Cr	Ni	Mo	W	Mn	V	Nb	Si	C	N
EP823	Bal.	11.40	0.70	0.67	0.65	0.60	0.40	0.20	1.0	0.18	0.040
EI 852	Bal.	12.85	0.22	1.66	-	0.52	0.40	-	1.9	0.13	0.034

Figure 2: Comparison of oxide growth rate in LBE between HT9 (Fe-12Cr) and EI852 (Fe-12Cr-2Si) [17] [21]



Recently it has been discovered by G. Müller that Al-addition can be even more effective in corrosion control than Si-addition because the Al_2O_3 layer provides a better protection against the corrosion in HLMC. G. Müller applied FeCrAl coating followed by pulsed electron beam mixing treatment named GESA to gain an outstanding corrosion resistance [22]. However, the coating process requires extraordinary attention to homogenise its chemistry and special mechanical protection against abrasion damage.

For this reason, J. Lim has developed new Al_2O_3 forming FeCrAl ferritic steels with a balance of corrosion resistance and mechanical properties [24]. The parabolic rate constants K (T) for the new FeCrAl alloys in LBE have been derived based on the experimental results, as follows:

$$-K(T) = 8.38 \times 10^{-9} \exp\left(-\frac{13247}{RT}\right)$$

where, R is the universal gas constant (8.3144 J/mol-K), T is temperature in K.

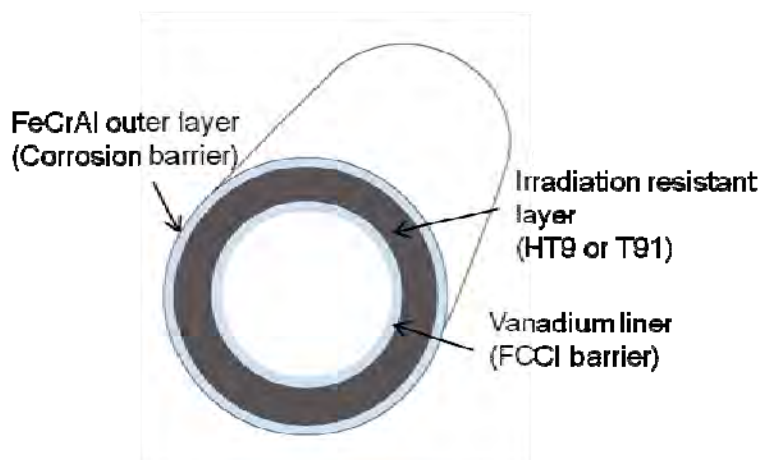
The oxide thickness of the Al_2O_3 forming FeCrAl ferritic steels at 450°C and 600°C for 20 years are predicted to be only about 0.5 μm and 2.5 μm , respectively. The oxide layer thickness less than 1 μm can retain shiny surfaces of pristine materials. Therefore Al-containing alloys are chosen for further qualifications for advanced fast reactors cooled by HLMC, including PASCAR.

However, both Si-containing FMS steels and Al-containing ferritic steels display significant radiation embrittlement as a result of the radiation-induced segregation of Si or Al to grain boundaries and Cr-rich α' phase formation at the temperature range of 300~500°C [25]. Therefore, high Si- or Al-containing steels are unreliable to be used for structural applications including fuel cladding as load-bearing metals. One solution to achieve corrosion resistance while keeping good mechanical properties of FMS is the hybrid tube approach. The novel approach by weld overlay of Si-containing alloys on radiation-resistant FMS has been developed by R. Ballinger. The cladding production process makes use of standard commercial practice. The extrusion billet of FMS is weld overlaid on either the OD or the ID, depending on the desired product form. After weld overlay the extrusion billets are pre-machined to achieve the desired ration of cladding to functional layer thickness in the final form. After pre-machining, the extrusion billets are reduced by a combination of hot extrusion/cold pilgering to final pipe-product dimensions [26].

Figure 3 shows the schematics of the proposed hybrid tube for fuel cladding of PASCAR. It will be manufactured according to the same process as described above. The proposed hybrid cladding tube is expected to meet the requirements for corrosion resistance and resistance against irradiation embrittlement of PASCAR design.

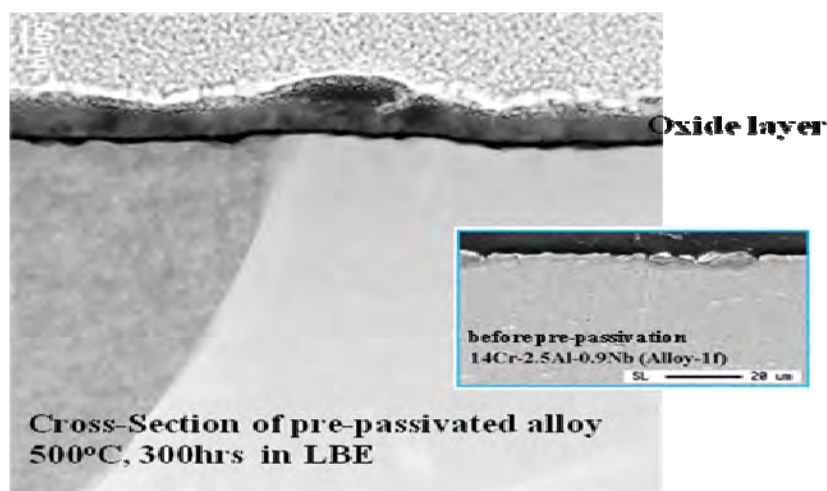
Pre-passivation approach

Based on the corrosion experiments and theoretical calculations it has been confirmed that higher Cr and Al contents are necessary to form an external Al_2O_3 layer at lower temperature regions. The pre-oxidation methods of FeCrAl alloys in higher temperature regions could be one solution to minimise the formation of iron oxide and increase corrosion resistance at lower temperature regions.

Figure 3: Schematic of hybrid tube for fuel cladding of PASCAR

To evaluate the pre-oxidation approach, a corrosion experiment was conducted for pre-passivated Fe-14Cr-2.5Al-0.9Nb in LBE at 500°C for 300 h. The alloy was pre-oxidised at 600°C for 24 h under air condition before exposure to LBE. Alloy-1f did not form a continuous external Al_2O_3 layer in LBE at 500°C before pre-oxidation. As shown in Figure 4, the pre-passivated Fe-14Cr-2.5Al-0.9Nb alloy showed good corrosion resistance by stable growth of continuous Al_2O_3 layer in LBE at 500°C. The thickness of the oxide layer was thinner than 100 nm after exposure to LBE at 500°C for 300 h. This result indicates that pre-oxidation at higher temperatures could suppress the formation of Fe-oxide at lower temperatures and could increase corrosion resistance by forming a continuous Al_2O_3 layer.

By using the pre-passivation approach, it could be possible to minimise Fe-oxide formation and increase corrosion resistance at a lower temperature range with minimal Cr and Al content necessary to form external Al_2O_3 at higher temperatures.

Figure 4: Pre-passivation effect of FeCrAl alloy

Conclusions

Heavy liquid metal coolant including lead and lead-bismuth has the advantages of chemical inertness, high boiling point and excellent neutron transparency. Solutions to overcome several disadvantages, including lower heat transfer capability, heavy weight and the generation of Po-210 have been developed to enable the construction plans for MYRRHA and small modular reactor SVBR-100 by 2020.

Materials corrosion issues are addressed with reference to the design of PEACER-300 and PASCAR-35. At the reduced temperature range of 300°C~400°C, primary boundary components of PEACER and PASCAR are shown to meet a 60-year life goal. Based on a new corrosion database, fuel claddings made of ferritic martensitic steels are shown to meet a three-year life goal. In order to avoid metallic fuel corrosion, however, a very high cladding reliability is pursued by employing adequate design margins.

A long-burning small modular reactor, PASCAR has been designed to operate for a period of 20 years without refueling at a maximum temperature of 450°C. To ensure the long-term operation without excessive corrosion, a new Al-containing alloy has been developed. To retain good mechanical properties of ferritic martensitic steels, a hybrid tube has been developed. The weld overlay technique developed by MIT will be applied to produce cladding materials with the outer layer of Al-containing alloy. The pre-passivation approach can also provide the structural material with additional corrosion resistance.

Acknowledgements

This work is an outcome of the fostering project of the Ministry of Knowledge Economy and Brain Korea 21 Programme of the Ministry of Education, Science and Technology.

References

- [1] B.F. Gromov et al. (1997), *Nuclear Engineering and Design*, 173, 207-217.
- [2] T.R. Allen et al. (2007), *Science and Technology of Nuclear Installations*, 1-11.
- [3] Ning Li (2007), *Progress in Nuclear Energy*, 1-12.
- [4] I. S. Hwang et al. (2002), *Progress in Nuclear Energy*, 37, 217-222.
- [5] J-Y. Lim et al. (2007), *Progress in Nuclear Energy*, 49, 230.
- [6] W.C. Nam et al. (2007), *Nuclear Engineering and Design*, 237, 316-324.
- [7] S. I. Kim et al. (2007), *Progress in Nuclear Energy*, 49, 14-19.
- [8] I. S. Hwang et al. (2008), *Proceeding of International Conference on Advances in Nuclear Power Plants*, ICAPP, pp. 601-610.
- [9] I. S. Hwang et al. (2008), *10th Information Exchange Meeting on Actinide and Fission Product Partitioning and Transmutation*, Mito, Japan, 2008.
- [10] F. A. Garner et al. (2000), *Journal of Nuclear Materials*, 276, 123.
- [11] IAEA (1999), *Status of liquid metal cooled fast reactor technology*, IAEA-TECDOC-1083.
- [12] R.L. Klueh et al. (2007), *Journal of Nuclear Materials*, 371, 37.
- [13] OECD-NEA (2007), *Handbook of lead-bismuth eutectic alloy and lead properties, material compatibility, thermal hydraulics and technologies*.
- [14] C. Fazio et al. (2001), *Journal of Nuclear Materials*, 296, 243.

- [15] A. Aiello et al. (2004), *Journal of Nuclear Materials*, 335, 169.
- [16] J. Lim et al. (2008), *10th Information Exchange Meeting on Actinide and Fission Product Partitioning and Transmutation*, Mito, Japan, 2008.
- [17] J. Zhang et al. (2005), *Journal of Nuclear Materials*, 336, 1.
- [18] F. Barbier et al. (2001), *Journal of Nuclear Materials*, 296, 231.
- [19] L. Martinelli et al. (2008), *Corrosion Science*, 50, 2537.
- [20] Y. Kurata et al. (2008), *Journal of Nuclear Materials*, 373, 164.
- [21] G.S. Yachmenyov et al. (1999), *Proceedings of Heavy Liquid Metal Coolants in Nuclear Technology*, Vol-1, Obninsk, Russia.
- [22] G. Müller et al. (2000), *Journal of Nuclear Materials*, 278, 85.
- [23] A. Weisenburger et al. (2008), *Journal of Nuclear Materials*, 376, 274.
- [24] J. Lim (2010), Ph.D thesis, Seoul National University.
- [25] A.M. Dvoriashin et al. (2007), *Journal of Nuclear Materials*, 367, 92.
- [26] R.G. Ballinger (2009), Project report (DOE award number: DE-FC07-06ID14742), MIT.

Corrosion barrier development using electron beams for application in lead alloys with focus on recent creep to rupture tests*

A. Weisenburger¹, A. Jianu¹, A. Heinzl¹, M. DelGiaccio¹, G. Müller¹,
V.D. Markov², A.D. Kastanov²

¹Institute for Pulsed Power and Microwave Technique, KIT, Germany

²Prometey Central Scientific-Research Institute – CRISM PROMETHEY, Russian Federation

Abstract

Compatibility problems of structural materials (steels) with the coolant are one of the key issues for the development of lead alloy fast reactors. Dissolution of metallic components into the lead alloy and extensive oxide scale growth are challenges that have to be met for both systems. Oxide scales formed on steels act as diffusion barriers for cations and anions and provide the best protection against dissolution attack. At temperatures above 500°C austenitic steels suffer from severe dissolution attack, while martensitic steels form thick oxide scales, which hinder heat transfer from the fuel pins and which may break off and eventually lead to a blocking of the coolant channel. Therefore, above 500°C steels have to be protected by stable, thin oxide scales. Alloying with strong oxide formers like aluminium (Al) into the steel surface combines protection against dissolution with slow growing oxide scales. Alumina scales that grow only very slowly due to low diffusion coefficients for cations and anions are formed on steel surface with an Al content above 4 wt%. However, this value depends on temperature, oxygen content and chromium concentration. FeCrAlY coatings followed by GESA treatment is the method used to obtain thin alumina scales. A number of corrosion experiments showed the good protective behaviour of Al-scales in LBE with 10⁻⁶ wt% oxygen up to 650°C and for exposure times up to 10 000 hours. Mechanical properties of steels were not influenced by the surface modification treatment as was proved during LCF and pressurised tubes experiments. This contribution will be focused on creep to rupture tests of T91 and surface modified T91 in LBE and air at different temperatures. At high stress levels a significant influence of the LBE namely at 550°C on the T91 in original state was already reported. At lower stress levels the negative influence diminishes and below a threshold stress level similar results like in air are expected. The level of this threshold stress was determined in additional tests. Surface modified specimens (GESA) tested at high stress levels instead had creep to rupture times similar to T91 (original state) tested in air. The thin oxide layers formed on the surface modified steel samples are less susceptible to crack formation and therefore suspend LBE enhanced creep.

* The full paper being unavailable at the time of publication, only the abstract is included.

Development of aluminium powder alloy coating for innovative nuclear systems with lead-bismuth

Yuji Kurata¹, Hidetomo Sato², Hitoshi Yokota², Tetsuya Suzuki²

¹Japan Atomic Energy Agency, Japan

²Ibaraki University, Japan

Abstract

Liquid lead-bismuth is a promising candidate material for high power spallation targets and core coolants of accelerator-driven systems (ADSs) for the transmutation of long-lived radioactive wastes and of coolants of fast critical reactors (FRs). However, one difficulty inherent in applying lead-bismuth to nuclear systems is its high corrosiveness to structural materials. Corrosion attacks become severe for most structural steels above 500°C in lead-bismuth. It is necessary to improve corrosion resistance at 550°C in case, taking fluctuation of oxygen concentration in liquid lead-bismuth into consideration. It is well known that aluminium can produce a protective oxide film under various environments. It is necessary to control aluminium concentration within a certain range for use in lead-bismuth because high concentrations of aluminium cause dissolution into liquid lead-bismuth. In this study, we investigated aluminium powder alloy coating for nuclear systems with lead-bismuth. Aluminum, iron and titanium powders were used to produce surface coating on type 316 SS plate. Surface coating of aluminum alloy was accomplished by means of laser heating a thin film made from aluminum, iron and titanium powders on 316 SS plate. Aluminium concentration in the coating was adjusted by means of changing the composition ratio of aluminium and iron powders. The 316 SS plates with coatings of different aluminium concentrations were prepared and tested in liquid lead-bismuth at 550°C. Static corrosion tests were conducted for 1 000 hours and 3 000 hours in lead-bismuth with controlled oxygen concentration of 10^{-6} to 10^{-4} wt%. Oxygen concentration in liquid lead-bismuth was measured during corrosion tests using an oxygen sensor with a solid electrolyte of yttria-stabilised zirconia and a Pt/gas reference electrode. The 316 SS suffered severe grain boundary corrosion and ferritisation followed by lead-bismuth penetration without the coating. In contrast, the coating layer produced by an aluminium powder alloy technique protected the corrosion attack peculiar to austenitic stainless steels. A thin oxide film with high aluminium concentration prevented corrosion by lead-bismuth. Cracks were formed during the coating process in coatings with 12 wt% to 19 wt% of aluminium. Improvement of the coating condition mitigated crack formation and resulted in a good coating layer. Efforts to improve the coating process and corrosion tests in lead-bismuth are in progress. Progress in development of aluminium powder alloy coating on 316 SS is presented.

Introduction

Liquid lead-bismuth eutectic (LBE) is a promising candidate material of high power spallation targets and core coolants of accelerator-driven systems (ADSs) for transmutation of long-lived radioactive wastes and of coolants of fast critical reactors (FRs). One difficulty involved in applying liquid LBE to nuclear systems is its high corrosiveness to structural materials. Studies on LBE corrosion have been conducted in the Russian Federation since the early stages of nuclear reactor development [1] [2]. The recent results of extensive LBE research, which has received significant attention and been performed worldwide, are compiled in OECD/NEA handbook [3].

Corrosion attacks in LBE are generally severe for most steels above 500°C. It is necessary to improve the corrosion resistance of steels above 550°C in LBE [4]. For this purpose, the addition of elements such as Si and Al, which are expected to form protective oxide films in LBE, seems effective. EP823, a ferritic/martensitic steel containing Si, has been developed in the Russian Federation [2]. Recently, developments of ODS steels containing Al have been also conducted [5-7]. In Si-containing steels and Al-containing steels, it is anticipated that these elements affect mechanical and irradiation properties of the steels except for corrosion properties. The Si-containing steel, EP823, showed severe embrittlement at irradiation temperatures below 460°C [8]. Furthermore, it is necessary to balance corrosion resistance and creep strength for Al-containing ODS steels [6] [7]. In contrast, coating and surface treatment are promising as the method by which only high corrosion resistance is added to steels with good mechanical and irradiation properties. Several Al-alloy coating methods have been proposed for the development of corrosion-resistant steels in LBE [9-13]. The Al-alloy coating by GESA (Gepulste Elektronenstrahlanlage) treatment [10] [11] is known worldwide as a method to produce a thin and compact coating layer.

It is a problem that Al dissolves into LBE in alloys with high Al concentration [9] [13]. It is necessary to control Al concentration in the coating layer precisely because Al concentration above a certain level is needed for the appearance of corrosion resistance [10] [11]. Adequate Al concentration range in the coating layer was reported to be 8-15 wt% [10] or 4-15 wt% [11]. However, the lower and upper limits of Al concentration in the coating layer should be further investigated from several technical viewpoints. Recently, authors have developed an Al-powder-alloy coating method in order to apply the coating method using Al and Ti powders [14] to nuclear systems. It is predicted that the method will enable us to control Al concentration and to produce good coating layers by using eutectic reaction in tertiary Al-Ti-Fe system. In this study, the current status of development of the Al-powder-alloy coating method is described on the basis of results of corrosion tests for Al-powder-alloy coated 316 SS in LBE.

Experimental

Al-powder-alloy coating

Figure 1 shows a schematic illustration of Al-powder-alloy coating. Thin sheets were produced from Al, Ti and Fe powders. A laser beam was scanned on the sheet stuck to the substrate in this method. An Al-alloy layer was coated on the substrate using this treatment. It was found from previous experiments that good coating layers were produced by setting the atomic ratio of Al to Ti at 4 to 1. The Al concentration in a sheet was adjusted by changing the Fe ratio in the sheet. Type 316 SS was used as a substrate because its data of mechanical and irradiation properties are abundant and suitable for nuclear reactors. The main parameters of coating conditions are the chemical composition of sheet materials and the scanning rates of a laser beam. Table 1 summarises the chemical composition of sheet materials used in this study. A YAG laser beam of Nd was scanned on the specimen under Ar

gas environment. Pulse energy of the laser beam and voltage were adjusted to be 0.60-0.86J and 195-205V, respectively.

Figure 1: Schematic illustration of Al-powder-alloy coating

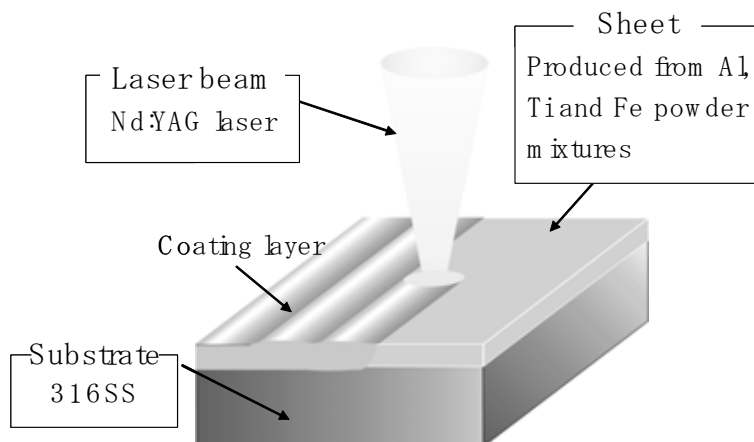


Table 1: Chemical composition of sheet materials for Al-alloy coating (wt %)

Sheet	Al	Ti	Fe
I	8.5	3.8	87.8
II	24.8	11.0	64.2
III	31.6	14.0	54.4
IV	39.2	17.4	43.4
V	43.4	19.2	37.4
VI	47.8	21.2	30.9
VII	57.8	25.6	16.6

Corrosion tests in liquid LBE

Corrosion tests were performed using Al-alloy coated 316 SS specimens in oxygen-controlled LBE. Figure 2 shows a schematic of static corrosion apparatus in liquid LBE. Oxygen concentration was measured using an oxygen sensor installed in the corrosion apparatus. Yttria-stabilised zirconia (YSZ) as a solid electrolyte and a Pt/air reference electrode were employed in the oxygen sensor. Oxygen concentration was controlled using Ar-H₂, Ar-H₂-H₂O and Ar-air-H₂O gas flow over LBE during the corrosion tests. The corrosion tests were conducted at 550°C for 1 000 h and 3 000 h. Figure 3 depicts the variation of outputs of the oxygen sensor and oxygen concentration in LBE during the corrosion test for 1 000 h. It was found that oxygen concentration was controlled in the range of 10⁻⁶ wt% ~ 10⁻⁴wt% for 1 000 h. Similar oxygen control was made in the corrosion test for 3 000 h where Ar-air-H₂O gas was also used at the early stage. Corrosion specimens were rectangular plates with a size of 15 mm x 30 mm x 2 mm. About 7 kg of fresh LBE was used in each corrosion test.

After the corrosion tests, the test specimens were cleaned in silicone oil at about 180°C and their surfaces were plated with copper to protect corrosion films during polishing. Observation and analyses were made using an optical microscope and a field emission scanning electron microscope (FE/SEM) with energy dispersion X-ray equipment (EDX).

Figure 2: Schematic of static corrosion apparatus in liquid LBE

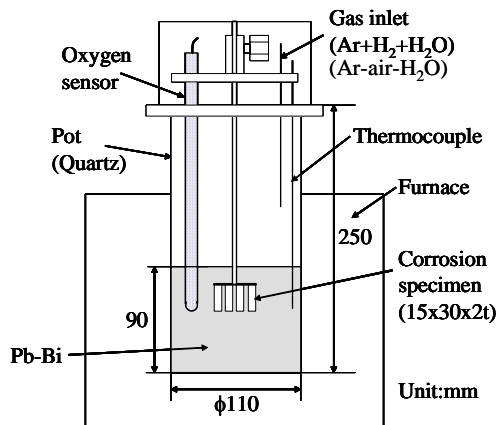
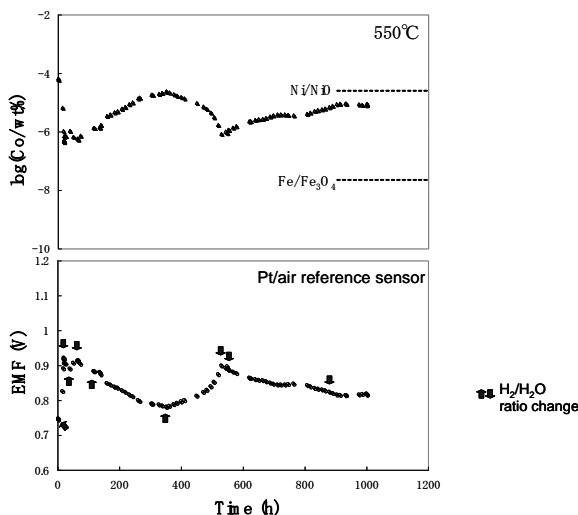


Figure 3: Oxygen concentration in liquid LBE during exposure test at 550°C for 1 000 hours



Results and discussion

Relationship between crack formation and Al concentration in coating layers

Cracks were sometimes found in the coating layers when Al-powder-alloy coating was made using sheets with high Al concentration. Figure 4 shows the relationship between Al concentration in the coating layer and in the sheet. The Al concentration in the coating layer was calculated from the results of point analyses on the coating layer by EDX. The datum points of the average Al concentration (open symbols) in the coating layer are plotted in Figure 4 and Al concentration in the crack area (solid symbols) is also plotted in the case where cracks are formed. This figure has shown that Al concentration in the coating layer decreases with the decreasing scanning rates of a laser beam.

Al concentration in the area near cracks is above 12 wt%. Although it was previously reported that cracks were also formed in Al-alloy layers coated by other coating methods [10] [13], no quantitative relationship between crack formation and Al concentration has been shown. It is indicated that cracks are found above 12 wt% of Al concentration in the coating layer when Al-alloy coating is made on 316 SS using laser beam heating. Figure 5 shows the relationship between the numbers of cracks and the average Al concentration in the coating layer. Cracks are found when the average Al concentration in the coating layer is above about 8 wt%. This indicates that cracks are generated in the coating layer with the average Al concentration above 8 wt% due to the scattering of the Al concentration in the coating layer.

Figure 4: Relationship between Al concentration in coating layer and that in sheet material

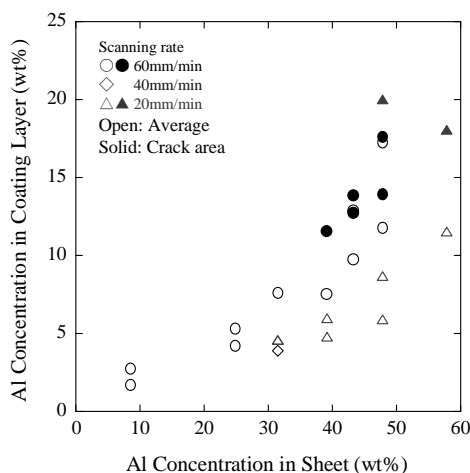
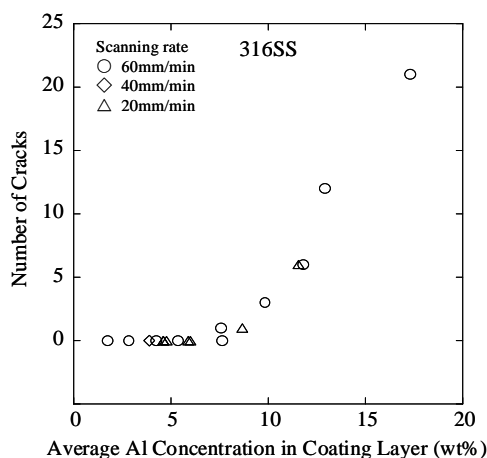


Figure 5: Relationship between number of cracks and average Al concentration in coating layer



Corrosion test for 1 000 hours

Figure 6 depicts some optical micrographs of cross-sections of specimens after corrosion test in liquid LBE at 550°C for 1 000 h. As shown in Figure 6(a), the formation of surface oxides and grain boundary corrosion are found on 316 SS substrate without Al-

alloy coating. The Al-alloy coating specimens were produced using sheet materials (I), (II) and (VI) in Table 1. The scanning rate of a laser beam was 60 mm/min. The average Al concentration of the coating layer shown in Figures 6(b), (c) and (d) is 2.8, 4.2 and 17.3 wt%, respectively. Although cracks are found in the coating layer, as can be seen from Figure 6(d), it appears that Pb and Bi do not penetrate into the cracks. As shown in Figures 6(b), (c) and (d), Al-alloy coating layers where the average Al concentrations are 2.8 to 17.3 wt% protect surface oxidation, with grain boundary corrosion being observed on 316 SS in the corrosion test at 550°C for 1 000 h. Figure 7 demonstrates the concentration profile of Al, Ti, Cr and Ni of Al-alloy coated 316 SS using sheet material (II) after corrosion test in liquid LBE at 550°C for 1 000 h. Al concentration is 5 to 6 wt% in the coating layer and fluctuation of the Al concentration is small, ranging about 70 μm of depth of the coating layer. The concentration of Ti, Cr and Ni in the coating layer is 2 to 4 wt%, about 12 wt% and about 8 wt%, respectively. Elements of Cr and Ni, which diffused from 316 SS substrate during the coating process, are found in the coating layer. Titanium dissolved in the coating layer does not have a bad influence on the corrosion resistance improved by Al. Based on the results of the corrosion test in liquid LBE at 550°C for 1 000 h, Al-powder-alloy coating is promising as a corrosion-resistant coating method in liquid LBE.

Figure 6: Optical micrographs of cross-sections of specimens after corrosion test in liquid LBE at 550°C for 1 000 hours (a) 316 SS substrate, (b) coated 316 SS using sheet material (I), (c) coated 316 SS using sheet material (II) and (d) coated 316 SS using sheet material (VI)

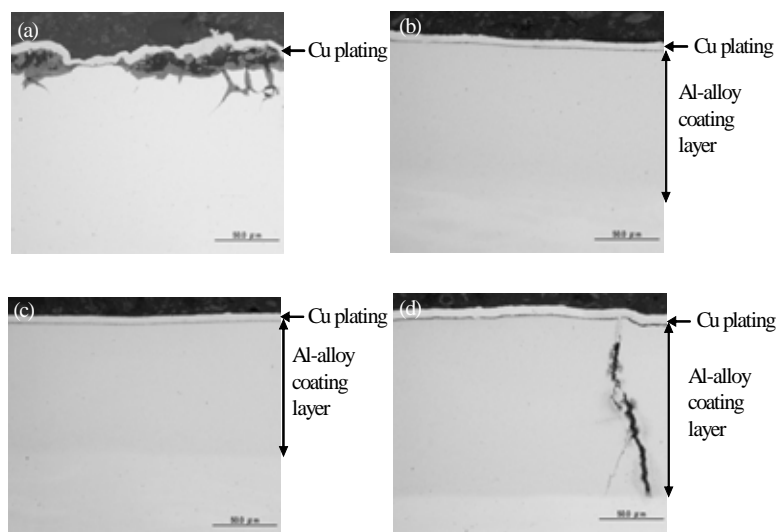
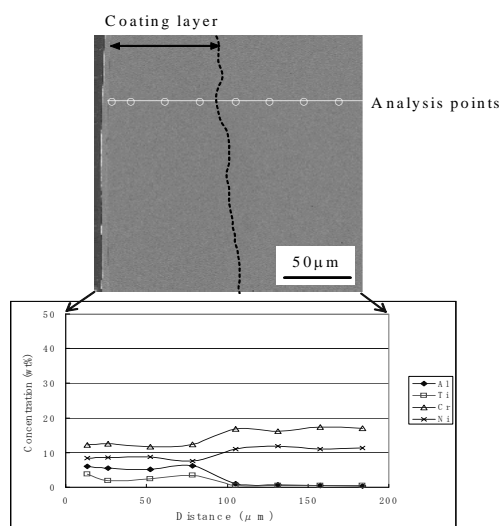


Figure 7: Concentration profile of Al, Ti, Cr and Ni of Al-alloy coated 316 SS after corrosion test in liquid LBE at 550°C for 1 000 hours, sheet material (II) was used for coating



Corrosion test for 3 000 hours

The Al-alloy coating specimens produced using sheet materials (I), (II), (III) and (VI) at the scanning rate of 60 mm/min were employed in the corrosion test for 3 000 h. In addition, the Al-alloy coating specimens produced from sheet material (III) at the scanning rates of 40 mm/min and 20 mm/min were also employed to investigate the effect of the scanning rate. Figure 8 depicts element mapping of the cross-section of 316 SS substrate without Al-alloy coating after corrosion test in liquid LBE at 550°C for 3 000 hours. Ferritisation due to selective dissolution of Ni is observed near the surface of 316 SS. Furthermore, areas where ferritisation has occurred peel off and intrusion of Pb and Bi is observed in a wide range. Grain boundary corrosion by liquid LBE is also recognised. Corrosion attacks become severe for 316 SS, increasing in corrosion time from 1 000 h to 3 000 h at 550°C. This type of severe corrosion attack characterised by Ni dissolution, penetration of Pb and Bi and partial loss of grains is often observed in austenitic stainless steels such as 316 SS and it makes it difficult for austenitic stainless steels to be used in nuclear systems using LBE [4].

Although Al-alloy coating layers produced at the scanning rate of 60 mm/min prevented corrosion attacks by LBE in several places, LBE penetration was observed in some places. Figure 9 shows SEM images of cross-sections of Al-alloy coating specimens after corrosion test in liquid LBE at 550°C for 3 000 h. Specimens shown in Figures 9 (a), (b), (c) and (d) are 316 SS coated using sheet materials (I), (II), (III) and (VI) at the scanning rate of 60 mm/min, respectively. The average Al concentration of the coating layer shown in Figures 9(a), (b), (c) and (d) is 1.7, 5.3, 7.6 and 11.8 wt%, respectively. A crack is found in the coating layer, as shown in Figure 9(d). In addition, as typically indicated in Figures 9 (a), (b) and (d), penetration (white part) of Pb and Bi is found near the surface of the coating layers. Figure 10 depicts a SEM image and results of point analyses for a part of the view shown in Figure 9(a). White parts exhibit penetration of Pb and Bi. Al concentration is low in the area shown in Figure 10. Furthermore, Ni does not diffuse from 316 SS substrate in analysis points, 1, 3 and 4. Since Pb and Bi penetrate around grains in the coating layer, it is estimated that the melting and diffusion of elements by laser heating were insufficient. Figure 11 depicts element mapping for the cross-section of a part of the view shown in Figure 9(d). The Al concentration is low near areas where Pb and Bi penetrate. Diffusion of Ni and Cr from 316 SS substrate is also little. In contrast, Ti is enriched in this area. It is considered that there were un-melted Ti or aggregate Ti grains on account of

insufficient heating by fast laser beam scanning. It is estimated that the melting and diffusion of elements by laser heating were also insufficient for sheet materials with high Al and Ti contents.

Since laser beam heating was not sufficient at the scanning rate of 60 mm/min, the effect of decreasing the scanning rates of a laser beam was investigated. Figure 12 shows SEM images of cross-sections of 316 SS coated using sheet material (III) at the scanning rates of (a) 40 mm/min and (b) 20 mm/min. As a result of broad observation for cross-sections of specimens after the corrosion test at 550°C for 3 000 h, surface defects where Pb and Bi penetrate are not found, as indicated in Figure 12. The average Al concentration of the coating layer shown in Figures 12(a) and (b) is 3.9 and 4.6 wt%, respectively. While decreasing scanning rates of a laser beam from 60 mm/min to 40 or 20 mm/min, it causes lower Al concentration in the coating layer and results in more homogenous coating layers without surface defects. Figure 13 shows a line analysis of the cross-section of 316 SS coated using sheet material (III) at the scanning rate of 20 mm/min after corrosion test at 550°C for 3 000 h. The thin corrosion film whose thickness is 100 to 200 nm is formed on the Al-alloy coating layer during the corrosion test at 550°C for 3 000 h. Since peaks of Al and O are high at the thin corrosion film, it is estimated that a very thin alumina film is formed. Because penetration of Pb and Bi, and formation of a multilayer oxide film composed of Fe and Cr are not observed, the thin oxide film prevents diffusion of Pb, Bi, Fe and O. The Al-alloy coating layer with 4 to 5 wt% Al produced by GESA treatment exhibited good corrosion resistance by formation of a thin alumina film in the corrosion test at 600°C for 2 000 h using LBE loop [11]. Furthermore, it was reported that a multilayer oxide film was formed without a protective alumina film in some places where Al concentration in the coating layer was below 4 wt% [11]. It is recommended that the adequate values of Al concentration in the coating layer range from 4 to 12 wt% at the laser beam scanning rate of 20 mm/min in Al-powder-alloy coating on 316 SS, taking account of the present results and the above-mentioned result [11].

Figure 8: EDX analysis of the cross-section of 316 SS substrate after corrosion test in liquid LBE at 550°C for 3 000 hours

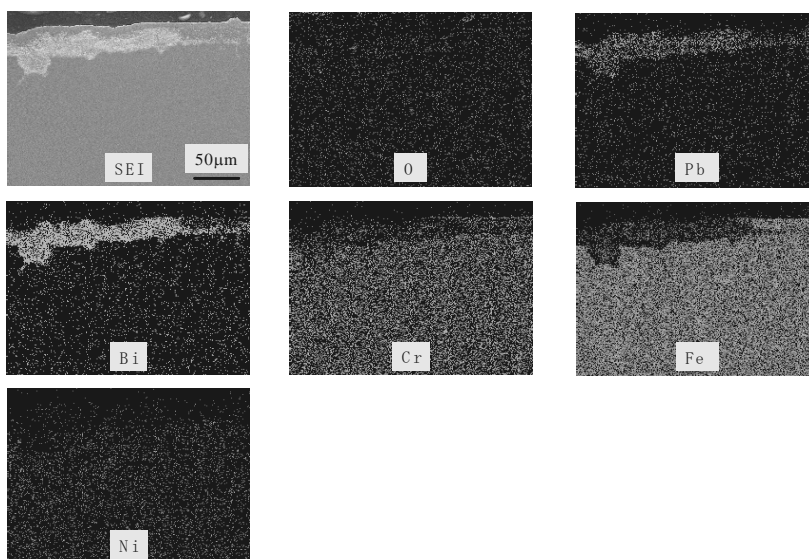


Figure 9: SEM images of cross-sections of specimens after corrosion test in liquid LBE at 550°C for 3 000 hours (a) coated 316 SS using sheet material (I), (b) coated 316 SS using sheet material (II), (c) coated 316 SS using sheet material (III) and (d) coated 316 SS using sheet material (VI)

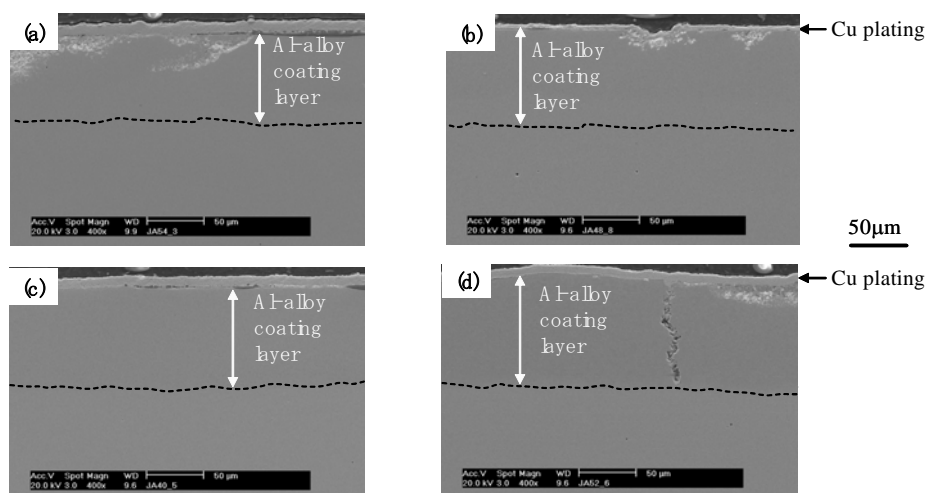
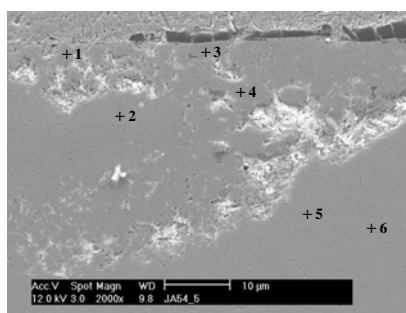


Figure 10: SEM image of cross-section of 316 SS coated using sheet material (I) after corrosion test in liquid LBE at 550°C for 3 000 hours, point analyses were conducted by use of EDX



(wt %)

No.	Al	Pb	Bi	Ti	Cr	Fe	Ni
1	0.86	7.72	1.81	1.89	9.25	78.47	0
2	1.69	2.66	1.02	1.08	8.1	81.33	4.13
3	1.27	3.22	0.87	0.99	8.18	85.47	0
4	1.54	6.14	0	0.69	6.46	85.17	0
5	1.51	4.87	0.54	1.97	13.82	73.41	3.88
6	1.44	4.56	1.1	1.92	13.14	72.86	4.98

Figure 11: EDX analysis of cross-section of 316 SS coated using sheet material (VI) after corrosion test in liquid LBE at 550°C for 3 000 hours

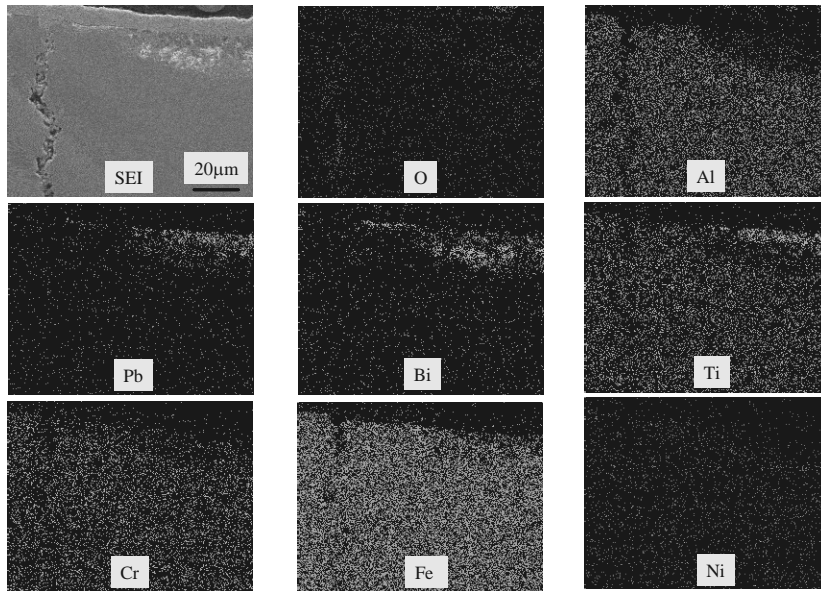


Figure 12: SEM images of cross-section of 316 SS coated using sheet material (III) after corrosion test at 550°C for 3 000 hours, laser beam speed: (a) 40 mm/min and (b) 20 mm/min

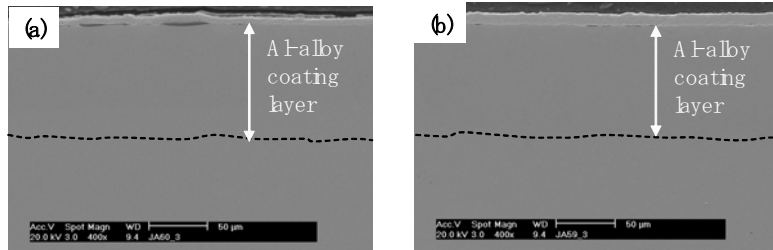
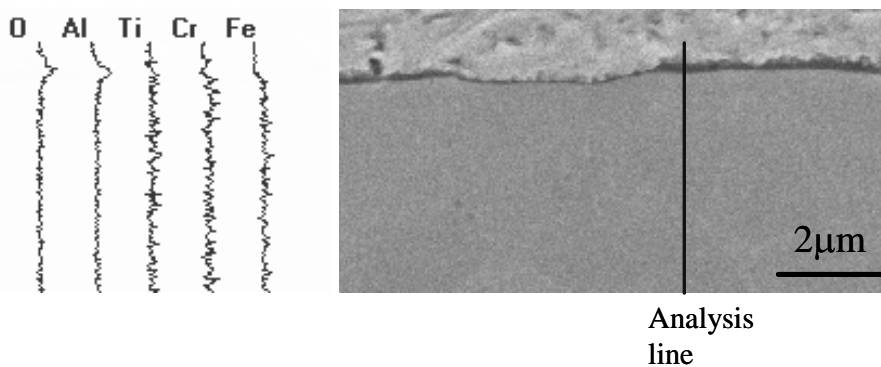


Figure 13: Line analysis of cross-section of 316 SS coated using sheet material (III) after corrosion test in liquid LBE at 550°C for 3 000 hours, laser beam speed: 20 mm/min



Conclusions

A new Al-powder-alloy coating method using Al, Ti and Fe powders has been developed and the Al-alloy coating has been made on 316 SS plates. The 316 SS plates with coating layers of different Al concentrations were prepared and tested at 550°C for 1 000 h and 3 000 h in liquid LBE with controlled oxygen concentration of 10^{-6} to 10^{-4} wt%. The main results obtained in this study are summarised as follows:

When Al-alloy coating is made on 316 SS using laser beam heating, cracks are found above 12 wt% of Al concentration in the coating layer. It is possible to produce Al-alloy coating layers without cracking if the average Al concentration in the coating layer is below 8 wt% at the low scanning rate of a laser beam.

Although significant corrosion attacks such as surface oxidation and grain boundary corrosion occur on 316 SS without Al-alloy coating in the corrosion test at 550°C for 1 000 h, the Al-alloy coating prevents the corrosion attacks and is promising as a corrosion-resistant coating method in liquid LBE.

Nickel dissolution, penetration of Pb and Bi and partial loss of grains occur on 316 SS substrate in corrosion at 550°C for 3 000 h in addition to surface oxidation and grain boundary corrosion. Although Al-alloy coating layers produced at the scanning rate of a laser beam of 60 mm/min prevent corrosion attacks by LBE in several places, LBE penetration is observed in some places where surface defects are formed on account of insufficient laser heating. In contrast, Al-alloy coating layers produced at lower scanning rates are homogenous, surface-defect free and corrosion-resistant.

It is effective to adjust Al concentration in the coating layer to a range between 4 and 12 wt% at low scanning rates of a laser beam in order to produce corrosion-resistant layers without cracks and surface defects.

Acknowledgements

This work was supported in part by JSPS KAKENHI, Grant-in-Aid for Scientific Research (C), 21560876.

References

- [1] I. V. Gorynin, G. P. Karzov, V. G. Markov, V. S. Lavrukihin and V. A. Yakovlev (1999), *Proc. of Heavy Liquid Metal Coolants in Nucl. Technol. HLMC'98*, October 5-9, 1998, Obninsk, Russia, p. 120.
- [2] G.S. Yachmenyov, A.Ye. Rusanov, B. F. Gromov, Yu. S. Belomytsev, N. S. Skvortsov, A. P. Demishonkov (1999), *Proceedings of Heavy Liquid Metal Coolants in Nuclear Technology, HLMC'98*, October 5-9, 1998, Obninsk, Russia, p. 133.
- [3] Handbook on Lead-bismuth Eutectic Alloy and Lead Properties, Materials Compatibility, Thermal-hydraulics and Technologies (2007).
<http://www.nea.fr/html/science/reports/2007/nea6195-handbook.html>
- [4] Y. Kurata, S. Saito (2009), *Mater. Trans*, 50, 2410.
- [5] S. Takaya, T. Furukawa, K. Aoto, G. Mueller, A. Weisenburger, A. Heinzl, M. Inoue, T. Okuda, F. Abe, S. Ohnuki, T. Fukjiwara, A. Kimura (2009), *J. Nucl. Mater*, 386–388, 507.
- [6] R. Kasada, N. Toda, K. Yutani, H.S. Cho, H. Kishimoto, A. Kimura (2007), *J. Nucl. Mater*, 367–370, 222.
- [7] S. Takaya, T. Furukawa, M. Inoue, T. Fujiwara, T. Okuda, F. Abe, S. Ohnuki, A. Kimura (2010), *J. Nucl. Mater*, 398, 132.

- [8] S.I. Porollo, A.M. Dvoriashin, Yu.V. Konobeev, F.A. Garner (2004), *J. Nucl. Mater*, 329-333, 314.
- [9] G. Mueller, A. Heinzl, J. Konys, G. Schumacher, A. Weisenburger, F. Zimmermann, V. Engeliko, A. Rusanov, V. Markov (2002), *J. Nucl. Mater*, 301, 40.
- [10] G. Mueller, G. Schumacher, A. Weisenburger, A. Heinzl, F. Zimmermann, T. Furukawa, K. Aoto (2003), JNC report, JNC TY9400 2003-026, Study on Pb-Bi Corrosion of Structural and Fuel Cladding Materials for Nuclear Applications Part III.
- [11] A. Weisenburger, A. Heinzl, G. Mueller, H. Muscher, A. Rousanov (2008), *J. Nucl. Mater*, 376, 274.
- [12] Ph. Deloffre, F. Balbaud-Celerier, A. Terlain (2004), *J. Nucl. Mater.*, 335, 180.
- [13] Y. Kurata, M. Futakawa (2004), *J. Nucl. Mater.*, 325, 217.
- [14] T. Suzuki, S. Terada, Y. Tomota (2005), *Tetsu-to-Hagane*, 91, 206 [in Japanese].

Session V

Fundamental – Radiation Effects

Chairs: G.J. Ackland, J. Wallenius

ODS ferritic-martensitic alloys for sodium fast reactor fuel pin cladding*

Ph. Dubuisson¹, Y. de Garlan¹, V. Garat², M. Blat³

¹CEA – Nuclear Materials Department, France

²AREVA NP, France

³EDF, France

Abstract

The sodium fast reactor (SFR) is considered in France the most mature technology of the different Generation IV systems. In the short term, the designing work is focused on the identification of the potential tracks to improve competitiveness, safety, efficiency and to reduce cost. To improve safety, efforts have been mainly focused on core designs with limited burn-up reactivity and reduced coolant void reactivity. The option large fuel pin diameter ($\phi \approx 10$ mm) and low spacer diameter ($\phi \approx 1$ mm) was regarded as the conceptual design basis for SFR cores, in order to both decrease the sodium fraction and increase the fuel fraction inside the core, with regards to standard SFR cores.

This design leads to proposing for fuel pin cladding, materials which present very low deformation under flux, especially very good resistance to swelling. These materials also have to be stable at elevated temperatures, up to 700°C. Oxide dispersion-strengthened ferritic-martensitic steels (ODS) have appropriate mechanical properties at high temperatures such as high creep rupture strength thanks to reinforcement by homogeneous dispersion of nano-oxides and a good resistance to very high doses thanks to the ferritic-martensitic matrix. But other key technologies must be mastered for the definitive choice of the ODS cladding materials and among the more important ones, the potential embrittlement induced by irradiation (Cr content), compatibility with environments (oxide fuel for one side and Na for the other side). This kind of materials elaborated by mechanical alloying requires a very rigorous control of the manufacture parameters.

The objective of this paper is to describe the present status of the French Research and Development Programme launched by CEA, AREVA NP and EDF to establish the viability of these ODS materials.

* The full paper being unavailable at the time of publication, only the abstract is included.

Materials issues in cladding and duct reactor materials*

S.A. Maloy¹, M. Toloczko², J. Cole³, T.S. Byun⁴

¹Los Alamos National Laboratory, Los Alamos, NM, United States

²Pacific Northwest National Laboratory, Richland, WA, United States

³Idaho National Laboratory, Idaho Falls, ID, United States

⁴Oak Ridge National Laboratory, Oak Ridge, TN, United States

Abstract

The Fuel Cycle Research and Development Programme is investigating methods of burning minor actinides in a transmutation fuel. To achieve this goal, the fast reactor core materials (cladding and duct) must be able to withstand very high doses (>300 dpa design goal) while in contact with the coolant and the fuel. Thus, these materials must withstand radiation effects that promote low-temperature embrittlement, high-temperature helium embrittlement, swelling, accelerated creep, corrosion with the coolant and chemical interaction with the fuel (FCCI). Research is underway which includes determining radiation effects in ferritic/martensitic steels at doses up to 200 dpa, minimising FCCI and developing advanced alloys with improved irradiation resistance.

To develop and qualify materials to a total fluence greater than 200 dpa requires the development of advanced alloys and irradiations in fast reactors to test these alloys. Test specimens of ferritic/martensitic alloys (T91/HT-9) previously irradiated in the FFTF reactor up to 210 dpa at a temperature range of 350-700°C are being tested. This includes analysis of a duct made of HT-9 after irradiation to a total dose of 155 dpa at temperatures from 370 to 510°C. Compact tension, charpy and tensile specimens have been machined from this duct with mechanical testing as well as SANS and Mossbauer spectroscopies currently being performed.

* The full paper being unavailable at the time of publication, only the abstract is included.

Radiation response of super ODS steels for fuel cladding of advanced nuclear systems

**R. Kasada¹, J.H. Lee¹, A. Kimura¹, T. Okuda², M. Inoue³,
S. Ukai⁴, S. Ohnuki⁴, T. Fujisawa⁵, F. Abe⁶**

¹Institute of Advanced Energy, Kyoto University, Kyoto, ²KOBELCO Research Institute, Kobe, ³Japan Atomic Energy Agency, Oarai, Ibaraki, ⁴Hokkaido University, Sapporo, ⁵Nagoya University, Nagoya, ⁶National Institute of Materials Science, Tsukuba

Abstract

Oxide dispersion-strengthened (ODS) ferritic steels are expected to be used for advanced nuclear systems, such as fusion reactors and the Generation IV nuclear fission systems. The present paper deals with the latest results of the effect of neutron irradiation on the mechanical properties of newly-developed "SUPER-ODS" steels irradiated in JOYO and BR-2. Tensile properties after the irradiations clearly showed irradiation temperature dependence. Though the BR-2 irradiation at a temperature of 290~300°C resulted in irradiation hardening, the JOYO irradiations at 531°C and 756°C showed no change in the tensile properties and Charpy impact properties.

Introduction

Oxide dispersion-strengthened (ODS) ferritic steels are expected to be used for the first-wall component in fusion reactors as well as for fuel pin cladding in Generation IV nuclear fission systems [1]. Recently, we have developed “SUPER-ODS steels” as a high performance fuel cladding material for the realisation of Generation IV systems [2]. The SUPER-ODS steels containing Al showed good corrosion resistance in supercritical water (SCW) and lead-bismuth eutectics (LBE) [3] [4]. Here, the neutron irradiation response of SUPER-ODS steels is one of the most important issues to be unveiled for the material realisation. The present paper shows the tensile properties and Charpy impact properties of the SUPER-ODS steels after neutron irradiation experiments using JOYO and BR-2.

Experimental procedure

The chemical compositions of the SUPER-ODS used in the present study are listed in Table 1. These steels were developed for checking the role of alloying elements on the material properties. The source elemental powder of the ODS steels was mechanically alloyed with Y_2O_3 powder in Ar atmosphere. The mechanically alloyed powders were consolidated as cylindrical rods by hot-extrusion processing at about 1 423 K. After that, homogenisation heat treatment was performed at 1 423 K for 1 hour followed by air cooling.

Table 1: The chemical compositions (wt.%) of SUPER-ODS steels used for the present study

	C	Si	Mn	P	S	Cr	Al	Ti	N	Ar	Y_2O_3	Others	Fe
SOC-1	0.02	0.02	0.03	<0.005	0.002	16.11	3.44	0.09	0.002	0.005	0.34	-	Bal.
SOC-2	0.04	0.01	0.02	<0.005	0.002	13.65	3.35	0.07	0.016	0.006	0.36	-	Bal.
SOC-3	0.05	0.02	0.04	<0.005	0.003	17.33	3.5	0.09	0.006	0.006	0.34	-	Bal.
SOC-4	0.02	0.01	0.03	<0.005	0.002	15.77	1.85	0.09	0.003	0.007	0.34	-	Bal.
SOC-5	0.04	0.01	0.01	<0.005	0.002	15.95	-	0.09	0.007	0.007	0.34	-	Bal.
SOC-6	0.03	0.01	0.03	<0.005	0.002	16.08	3.36	0.09	0.002	0.005	0.34	1.61 (W)	Bal.
SOC-7	0.04	<0.01	<0.01	<0.005	0.002	15.68	1.7	0.09	0.003	0.005	0.36	0.37 (Ce)	Bal.
SOC-8	0.15	<0.01	<0.01	<0.005	0.001	11.61	1.34	-	0.003	0.005	0.36	0.93 (Ni)	Bal.

Tensile tests were carried out for the SS-J type miniaturised tensile specimens, the gauge dimensions of which were 5 mm × 1.2 mm × 0.50 mm, at a strain rate of $6.7 \times 10^{-4} \text{ s}^{-1}$ at the ambient temperature of ~293 K.

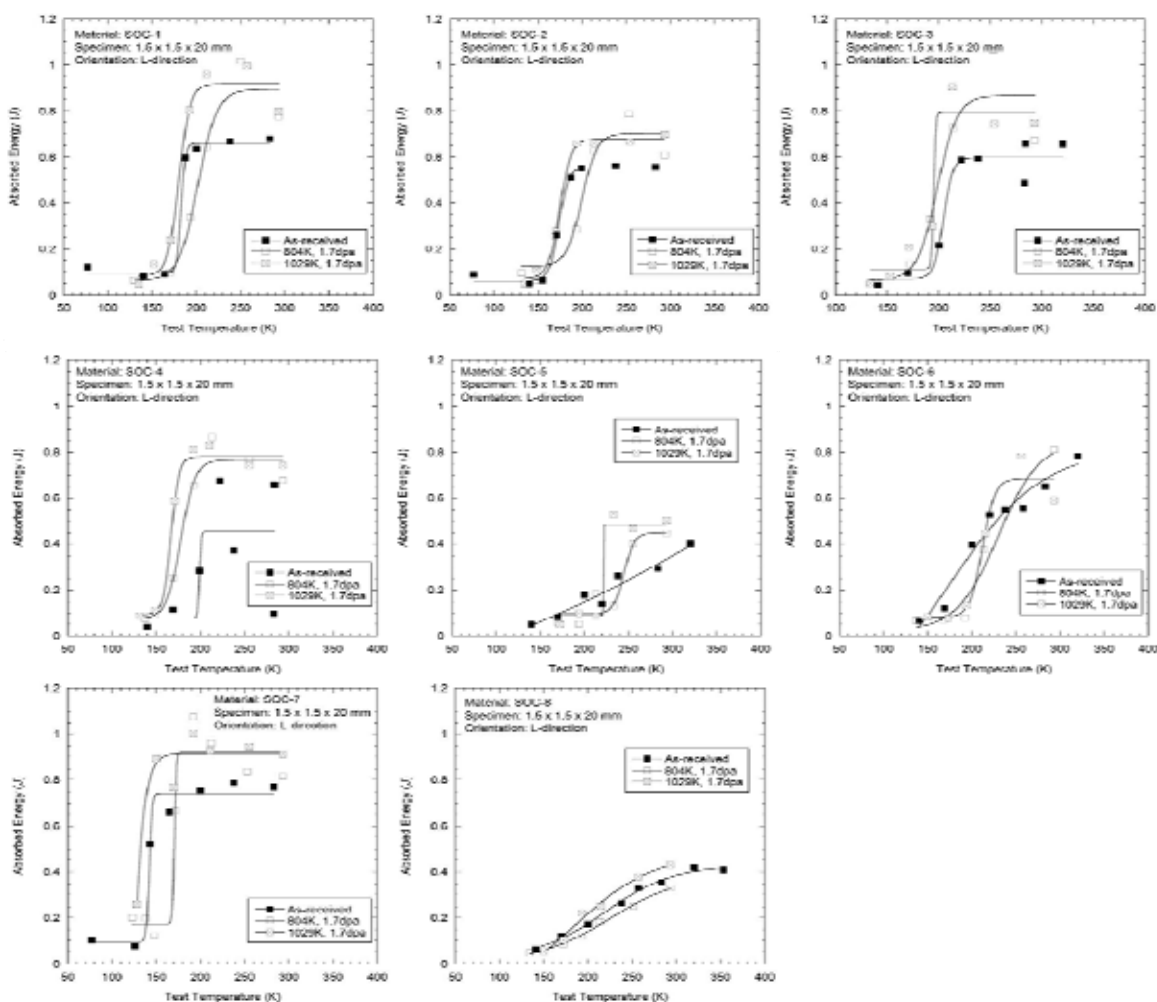
Charpy impact tests were performed for the 1.5 mm × 1.5 mm × 20.0 mm V-notched specimens. These specimens were cut from the hot-extruded bar as the longitudinal direction of specimens has to be parallel to the extruded direction.

JOYO irradiation was carried out in the two capsules of SMIR-27(2) irradiation campaign. The irradiation temperatures at the specimens were evaluated as 804 and 1029 K. The fast neutron doses (≥ 0.1 MeV) were monitored as $3.3\text{--}3.4 \times 10^{25}$ n/m² (1.7 dpa). BR-2 irradiation was also performed in the capsule of 06M-4BR at a temperature of 563–573 K. The fast neutron doses (≥ 1 MeV) were monitored as 4.0×10^{24} n/m².

Results and discussion

Figure 1 shows the absorbed energies in Charpy impact measured in SUPER-ODS steels in as-received and irradiated conditions in JOYO. Note that the irradiation damage resulted in an improvement, rather than degradation, of the impact properties. Superior impact properties of ODS ferritic steels after JOYO irradiation at temperatures between 646 and 845 K were also reported by Kuwabara *et al.* [7].

Figure 1: Temperature dependence of absorbed energy obtained from Charpy impact tests on SUPER-ODS steels before and after JOYO irradiations



The dependence of the increases in the ultimate tensile strength and the total elongation on irradiation temperature is shown in Figure 2 for the SUPER-ODS steels irradiated in BR2 and JOYO. Irradiation hardening is observed only for the BR-2 irradiation

at 563~573 K. Our previous studies investigated the dependence of tensile properties and microstructural evolution in the proto-type SUPER-ODS steels (named K-series) on irradiation temperatures at 563, 673 and 873 K in JMTR [8]. The paper revealed that irradiation hardening of the ODS steels irradiated at 563 K could be explained by the formation of dislocation loops. Ion-irradiation experiments on the ODS ferritic steels at 573 K p to 10 dpa also support the irradiation hardening mechanism [9].

In the present JOYO irradiation, differences of the ultimate tensile strength between as-received and irradiated specimens could no longer be observed except for SOC-5. Change in the tensile properties after the irradiation at 873 K in JMTR was also negligible [8]. These results indicate that the irradiation at temperatures above about 800 K would not cause a significant irradiation hardening in the ODS ferritic steels. A possible reason to explain the reduction of ultimate tensile strength in SOC-5 is recovery of dislocation during irradiation at high temperatures because the no-Al-added SOC-5 contains smaller grain and smaller nano-oxide particles than the other Al-added SUPER-ODS steels [10].

Irradiation hardening in the high Cr ODS ferritic steels is likely to be more significant when the irradiation temperature is around 748 K because of a combination of thermal ageing and irradiation damage. In fact, after irradiation at 673 K in JMTR, the measured hardening increases with Cr concentration because of Cr-rich phase formation through the phase separation phenomenon [8]. The dependence of the increases in the ultimate tensile strength on Cr contents is shown in Figure 3 for the SUPER-ODS steels irradiated in BR2 and JOYO. The present results show no Cr dependence of irradiation hardening of SOC steels after the irradiations in both BR-2 and JOYO. Higher dose neutron irradiation experiments at around 748 K are necessary to make clear the irradiation hardening behaviour of ODS ferritic steels.

Figure 2: Irradiation temperature dependency of the change in a) ultimate tensile strength and b) total elongation for SUPER-ODS steels

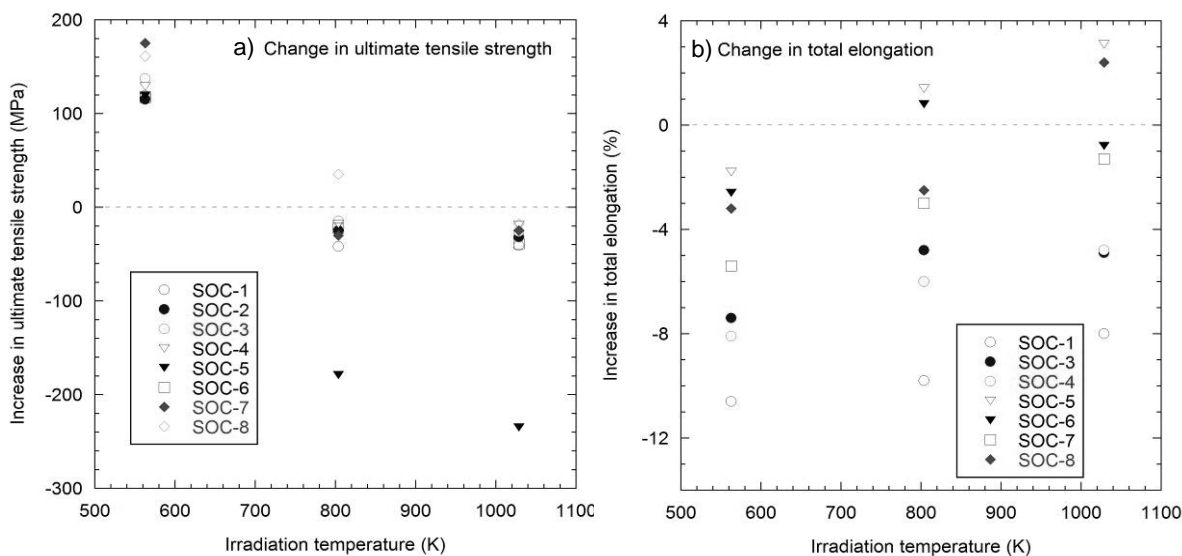
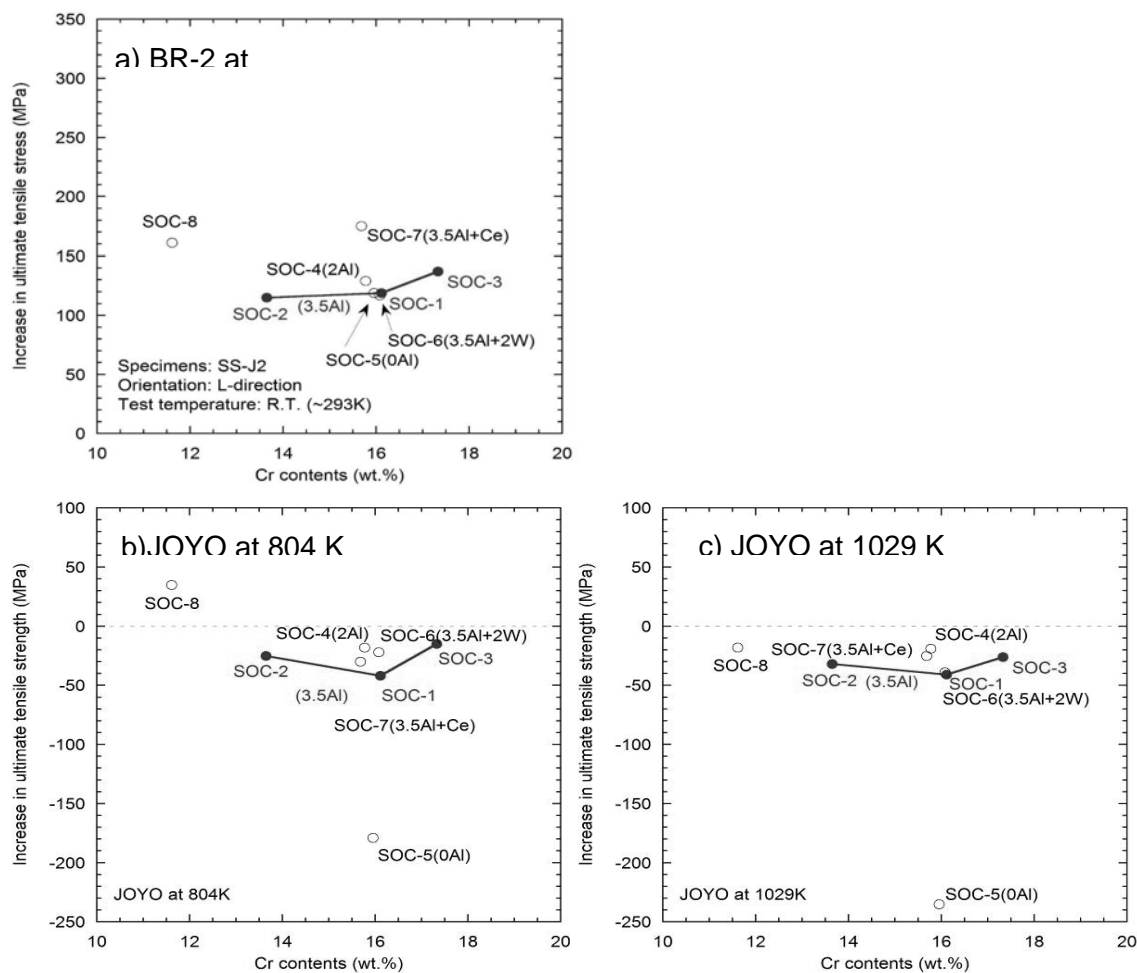


Figure 3: Cr contents dependency of the increase in ultimate tensile strength after irradiations in a) BR-2, b) JOYO at 804 K and c) JOYO at 1 029 K



Conclusion

The effects of neutron irradiation on the tensile properties and Charpy impact properties of SUPER-ODS steels were investigated.

- (1) JOYO irradiations at 804 and 1 029 K resulted in an improvement of Charpy impact properties of SUPER-ODS steels rather than degradation.
- (2) Irradiation hardening was observed after irradiations at 563–573 K in BR-2 while no significant hardening was observed after irradiations at 804 and 1 029 K in JOYO.
- (3) Irradiation hardening after the BR-2 irradiation at 563–573 K was independent of the Cr contents.

Acknowledgements

The present study includes the result of “R&D of corrosion-resistant super ODS steel for highly efficient nuclear systems” entrusted to Kyoto University by the Ministry of Education, Culture, Sports, Science and Technology of Japan (MEXT).

References

- [1] A. Kimura, H.S. Cho, N. Toda, R. Kasada, K. Yutani, H. Kishimoto, N. Iwata, S. Ukai, M. Fujiwara (2007), “High burn-up fuel cladding materials R&D for advanced nuclear systems nano-sized oxide dispersion strengthening steels”, *Journal of Nuclear Science and Technology*, 44, 323-328.
- [2] A. Kimura, R. Kasada, A. Kohyama, H. Tanigawa, T. Hirose, K. Shiba, S. Jitsukawa, S. Ohtsuka, S. Ukai, M.A. Sokolov, R.L. Klueh, T. Yamamoto, G.R. Odette (2007), “Recent progress in US-Japan collaborative research on ferritic steels R&D”, *Journal of Nuclear Materials*, 367-370, 60-67.
- [3] A. Kimura, R. Kasada, N. Iwata, J. Isselin, P. Dou, J.H. Lee, T. Okuda, M. Inoue, S. Ukai, S. Ohnuki, T. Fujisawa, F. Abe, “Super ODS steels R&D for fuel cladding of advanced nuclear systems”, in the present proceedings.
- [4] J. Isselin, R. Kasada, A. Kimura, “Corrosion behaviour of 16%Cr-4%Al and 16%Cr ODS ferritic steels under different metallurgical conditions in a supercritical water environment”, *Corrosion Science*, in press.
- [5] S. Takaya, T. Furukawa, K. Aoto, G. Müller, A. Weisenburger, A. Heinzl, M. Inoue, T. Okuda, F. Abe, S. Ohnuki, T. Fujisawa and A. Kimura (2009), “Corrosion behavior of Al-alloying high Cr-ODS steels in lead-bismuth eutectic”, *Journal of Nuclear Materials*, 386-388, 507-510.
- [6] J. Isselin, R. Kasada, A. Kimura, “Corrosion behaviour of 16%Cr-4%Al and 16%Cr ODS ferritic steels under different metallurgical conditions in a supercritical water environment”, *Corrosion Science*, in press.
- [7] T. Kuwabara, H. Kurishita, S. Ukai, M. Narui, S. Mizuta, M. Yamazaki, H. Kayano (1998), “Superior Charpy impact properties of ODS ferritic steel irradiated in JOYO”, *Journal of Nuclear Materials*, 258-263, 1236-1241.
- [8] H.S. Cho, R. Kasada, A. Kimura (2007), “Effects of neutron irradiation on the tensile properties of high-Cr oxide dispersion strengthened ferritic steels”, *Journal of Nuclear Materials* 347-370, 239-243.
- [9] K. Yutani, R. Kasada, H. Kishimoto, A. Kimura (2007), “Irradiation hardening and microstructure evolution of ion-irradiated ODS ferritic steels”, *Journal of ASTM International* 4.
- [10] R. Kasada, N. Toda, K. Yutani, H.S. Cho, H. Kishimoto, A. Kimura (2007), *Journal of Nuclear Materials* 347-370, 222-228.

Formation of dislocation loops at the onset of plasticity during single crystal nanoindentation*

Chansun Shin^{1,2}, Junhyun Kwon¹, Yuri Osetsky², Roger Stoller²

¹Nuclear Materials Research Division, Korea Atomic Energy Research Institute, Daejeon, Republic of Korea, ²Materials Science and Technology Division, Oak Ridge National Laboratory, United States

Abstract

Initiations of deformation and plastic flow at small scales have been drawing much attention in the last decades in both experiments and simulations. Needs for a better understanding of deformation mechanisms at a nanometer scale are surging up along with the development of nanometer scale materials and components. Nanoindentation has been a widely used technique in this study owing to its experimental simplicity: pressing a hard tip into a sample material and measuring the applied force and tip displacement.

A sharp elastic-plastic transition is often observed during indentations on single crystals. This sudden transition appears as a displacement burst (pop-in) on a load-displacement (P-h) curve. Recent studies have suggested that the onset of plasticity during nanoindentation is associated with homogeneous dislocation nucleation for small indenter size and/or low initial dislocation density. The activation of a dislocation source within a critical volume of material is believed to be involved in large indenter size and/or high initial dislocation density.

Our intention is to explore the interactions of irradiated defects with dislocations activated and propagated under the indenter. Experimentally measured P-h curves of an ion-irradiated single crystal have been compared with those of a pristine single crystal. We have also investigated dislocation nucleation and defect formation at the onset of plasticity during nanoindentation of FCC and BCC single crystals using atomistic simulations. The results of atomistic simulations have shown that the type of homogeneously nucleated dislocations depends on the crystallographic orientation and the crystal structure of indented single crystals. The formation and destruction of defect structures will be discussed based on the theory of dislocation reactions.

* The full paper being unavailable at the time of publication, only the abstract is included.

Session VI

General

Chair: S.S. Hwang

Developing advanced nuclear structural materials for use in high-radiation environments: An Australian perspective*

Lyndon Edwards

Head, Institute of Materials Engineering
Australian Nuclear Science and Technology Organisation (ANSTO)

Abstract

The world is undergoing a nuclear power renaissance using current technology. Next generation nuclear power systems are designed to address global energy needs later this century. If the materials community are to be successful, they will need to identify, design and produce materials that can withstand the extreme conditions of radiation, temperature, chemical environment and stress inherent in these advanced nuclear systems. Meeting these requirements is both challenging and exciting. We then must understand and develop predictive models of the failure mechanisms so that we can develop design codes and defect-assessment criteria that ensure structural integrity [1].

The Institute of Materials Engineering at the Australian Nuclear Science and Technology Organisation is a major centre of materials engineering expertise in Australia with a multidisciplinary team of scientists and engineers. The institute plays a significant role in maintaining Australia's international profile in the field of nuclear science and technology. The institute's core mission is to: develop, manufacture, characterise, model and ultimately, utilise materials in support of the advanced nuclear fuel cycle and next generation nuclear power generation systems.

The Structural Integrity Programme within the institute undertakes research underpinning the assessment of structural integrity of advanced nuclear power system components. It has two major themes:

- 1. Advanced nuclear structural materials: the development and assessment of structural materials and design methodologies for advanced nuclear power generation systems including the use of advanced structural materials for use in high stress, high-temperature and high-radiation environments.*
- 2. Nuclear structural integrity modelling: the use of advanced structural materials modelling to predict both weld residual stress and high-temperature structural integrity.*

Following the commissioning of OPAL, the Australian research reactor, the institute is investing in new ion and neutron irradiation and post-irradiation examination facilities to aid the development of advanced structural and waste form materials for use in high-radiation environments. This presentation will present ANSTO's strategy in this field and will illustrate our current progress using examples of our current work on advanced, very high strength zirconium alloys, novel ODS materials and recent progress on both ion and neutron radiation damage in ternary carbide (MAX) alloys which have the potential for use in both fission and fusion systems.

* The full paper being unavailable at the time of publication, only the abstract is included.

Reference

- [1] G. Robin, R. Konings, L. Edwards (2008), "Greater Tolerance for Nuclear Materials", *Nature Materials*, 7, pp. 683-685.

Development of materials for nuclear fusion reactors: Summary of the 14th International Conference on Fusion Reactor Materials*

Tatsuo Shikama¹, Takeo Muroga²

¹Institute for Materials Research, Tohoku University, Sendai, Japan

²National Institute for Fusion Science, Toki, Japan

Abstract

The implementation of the ITER project opened a new era for the development of materials for nuclear fusion applications. There, the development of appropriate materials in a due time schedule is a key issue. In the meantime, more clear perspectives are demanded beyond the ITER, to make nuclear fusion energy a realistic energy supply option, where more innovative materials must be taken into consideration. The set-up of an international collaboration between the EU and Japan, namely the BA (broader approach) project aims to develop technologies needed for the economically feasible nuclear fusion energy systems. The current status was reported and extensively discussed at the 14th International Conference on Fusion Reactor Materials (ICFRM-14) held at Sapporo, Japan, on 7-11 September 2009. The present paper will review and summarise the presentations and discussions there.

As a structural material, the general consensus will be on the so-called reduced activation ferritic/martensitic steels (RAFM) and their innovative version will be oxide dispersion-strengthened (ODS) one. For ITER application, it is essential to establish a large-scale production of the RAFM with a high-quality control, with co-operation between academic and industrial societies. For the ODS-RAFM, appropriate control of nano structures, especially dispersion properties of oxide particles will be important. There, several innovative experimental techniques are applied, such as small angle neutron scattering (SANS) and three-dimensional atom probe tomography (3D-APT). For more innovative structural materials, vanadium-based alloys and SiC_f/SiC (silicon carbide fibre reinforced silicon carbide matrix) composites have several attractive features, especially for more energy efficient and longer-life systems. There, properties other than conventional interests are important research topics to be studied, such as properties related to functional ceramic coatings. Functional properties such as thermal and electrical conductivity will also be important research topics there. Finally, the advance of multi-scale modelling should be emphasised and the understandings of radiation effects on property changes are steadily going ahead with detailed and more reliable experimental results obtained in various irradiation tools such as fission reactors, multi-beam ion accelerators, etc.

* The full paper being unavailable at the time of publication, only the abstract is included.

Structural materials research in the Swedish GENIUS Project*

Janne Wallenius, Nils Sandberg, Peter Szakalos, Anders Nordlund
KTH, Sweden

Abstract

Within the Swedish research programme on Generation IV reactors at the universities of Sweden (GENIUS), investigations on radiation damage in Fe-Cr alloys, ODS steels and corrosion of steels in lead alloys are performed. In the present contribution, the scope of these activities is reviewed and preliminary results are presented.

* The full paper being unavailable at the time of publication, only the abstract is included.

Plenary Session III

Chairs: S. Zinkle, C.H. Jang

Binding of impurities in austenitic iron: An *ab initio* study

G.J. Ackland, T.P.C. Klaver and D.J. Hepburn

School of Physics, University of Edinburgh, Scotland

Abstract

We present the results of the first principles calculations of austenitic iron using the VASP code. We determine an appropriate reference state for collinear magnetism to be the anti-ferromagnetic double-layer (AFM-d), which is both stable and lower in energy than other possible models for the low-temperature limit of paramagnetic fcc iron. We then consider the energetics of dissolving typical alloying impurities (Ni, Cr) in the materials and their interaction with point defects typical of the irradiated environment. We show that using standard methods has a very strong dependence of calculated defect formation energies on the reference state chosen. Furthermore, there is a correlation between local free volume magnetism and energetics. The effect of substitutional Ni and Cr on defect properties is weak, so it is unlikely that small amounts of Ni and Cr will have a significant effect on the radiation damage in austenitic iron.

Introduction

Austenitic (face-centred cubic) steels are key materials in many nuclear applications. Their main advantages over their ferritic (body-centred cubic) counterparts are in performance and stability at high temperatures, which makes them especially applicable in Generation IV reactors, where thermodynamic efficiency is increased through high operating temperatures.

First-principles calculations have proved to be a very reliable method of obtaining information about radiation-induced defects in transition metals. In early works on non-magnetic elements such as Mo and V it was shown that the pseudopotential plane wave method reproduced formation energies and barriers to within 0.1eV [1]. It was also shown that the strain fields associated with interstitials were much smaller than had been predicted by interatomic potentials, such that reliable values could be calculated with supercells as small as 100 atoms.

Application to steels is a more complicated task on account of their multi-component nature and the crucial role of carbon in mechanical properties; however, work on ferritic Fe and FeCr bcc alloys has shown a number of unexpected outcomes. In particular, the binding energy of a Cr atom in Fe is positive, in apparent conflict with the phase diagram which shows a miscibility gap. This conundrum was resolved when it was shown that two Cr atoms in bcc iron strongly repel one another due to anti-ferromagnetic frustration [2] [3], such that a dilute solution of Cr in Fe has positive binding, but a concentrated alloy phase-segregates, because Cr-Cr interactions are unavoidable. This theme of frustration carried over into studies of defects in alloys, however, the non-linear variation of cohesive energy with concentration meant that determining unambiguous energies for quantities such as the binding of an interstitial to a Cr proved impossible in concentrated alloys [4], since the calculated energy had a complex dependence not only on the defect, but also on concentration and the precise location of the atoms.

Modelling the high-temperature stability of austenitic steel is particularly challenging, because its pure form, gamma-iron is metastable under the zero-temperature conditions typically used in quantum mechanical calculation. The body centred cubic ferromagnetic structure has significantly lower energy than any magnetic arrangement for face-centred cubic (Figure 1). Furthermore, austenite exists naturally only in the paramagnetic state, and paramagnetism is an intrinsically high-temperature phenomenon involving dynamically disordered spins which break local symmetry but produce the fcc structure on average. First principles calculations use density functional theory to calculate electronic ground states (Born-Oppenheimer dynamics), and so do not include thermal excitations of the magnetic state. Finally, although there remain some debates about whether the paramagnetism is itinerant or involves localised moments on the ions, throughout this paper we will interpret our results through the localised-moment picture.

There are difficulties from a purely numerical point of view, too. The Kohn-Sham functional applied in non-magnetic density functional theory has a single minimum with respect to the wavefunctions. By contrast, collinear-magnetic density functional theory, as used for iron, may have up to 2^N minima for an N-atom supercell, corresponding to possible permutations of the spin. In practice, most of these will be unstable but one can never be sure that the lowest energy structure has been reached: indeed, since the lowest energy is ferritic, to study austenite one must avoid that structure. The concept of metastability is also slippery, since the numerical tricks used to find the minimum electronic energy do not correspond to physical pathways which the material can follow: the very definition of metastability depends on the computational algorithm.

Calculations

The energy of a defect in any material is defined as:

$$E_{def} = E(N, \{M_i\}) - NE_{Fe} - M_i E_{i,ref}$$

where the first term is the energy of a supercell containing N host atoms and M_i defects of type i . This typically involves a large calculation. The second term is the energy of “austenitic” iron and the third term the reference structure for the defect. For formation energies, this would be zero for topological defects and the cohesive energy for Ni and Cr impurities. For migration barrier energies and binding energies, the formation energy is the reference state (substitutional impurity for Ni, Cr, monovacancy or [001] interstitial).

For topological defects (vacancies, interstitials) there is no contribution from the final term. The first challenge of this work is to determine a sensible reference state for austenitic iron. This is critical, since if the supercell undergoes a transition from one spin state to another, the calculated defect energy will become extensive (i.e. it will scale with the size of the system).

The specific difficulty in austenite is that calculation of defect energies by static relaxation is implicitly a zero-temperature process and the fcc structure is unstable in iron at zero kelvin. Furthermore, the ground state of fcc iron is believed to be a spin-spiral structure describable only by non-collinear magnetism and highly sensitive to stresses and strains. The material of interest is a paramagnetic fcc crystal where the spins are disordered and bear little resemblance to any ordered state. Thus, there is no unambiguously correct way to deal with the magnetism.

In addition to this, there is a general problem of whether to relax the supercell shape. Again, there are several considerations. If one is considering a periodic array of defects, one should relax the cell shape. If one is considering a random distribution of defects, one should relax the volume. For an isolated defect the lattice parameter is dictated by the material and so constant volume is indicated: this is normally the case for radiation-induced defects, although an Eshelby-type elastic correction for finite size [5] of $P^2V/2B$ can be applied. Even relaxation at constant volume leaves open the question of which volume to use: the minimum energy according to the calculation? The extrapolated 0K volume of austenite [6] ($a=3.56\text{\AA}$)? The volume of the reference state? There is no unambiguously correct answer.

There are numerous possible approaches, but the minimal requirements for a reasonable reference state are as follows:

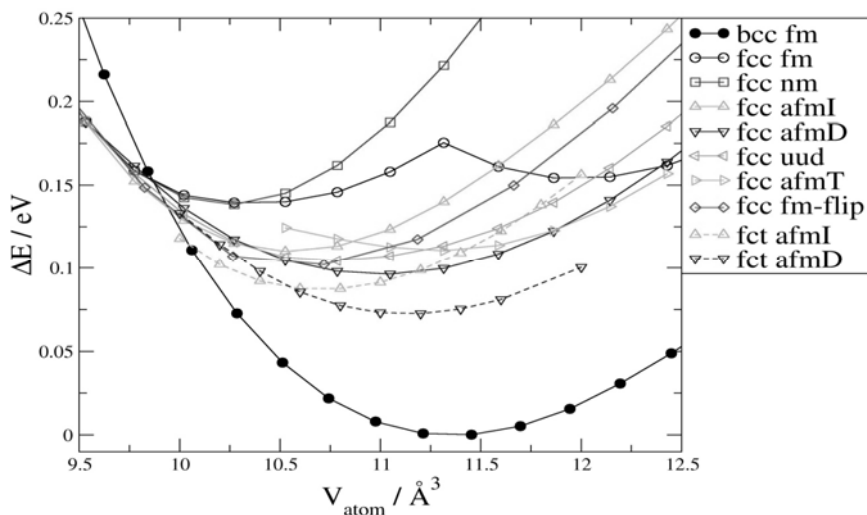
- local minimum of energy, stable against introduction of defects;
- crystal structure close enough to fcc to be regarded as austenitic;
- low energy;
- lattice parameter close to extrapolated values from austenite;
- local moment comparable with paramagnetic iron;
- stable against single-spin flips;
- elastically stable.

Energy and elasticity calculations for candidate reference structures

Calculations were carried out using the plane wave pseudopotential code VASP using a PAW pseudopotential to represent the ions with a plane wave cut-off of 400 eV and a k-point sampling of 16^3 for the conventional 4-atom cell and similar sampling densities for other cells. Various metastable magnetic configurations were set up by a judicious

choice of initial magnetic configuration and their energies were determined for a range of densities. Full relaxation of the atomic positions was allowed in each case, while the unit cell was either allowed to relax tetragonally, or constrained to remain cubic.

Figure 1: Energies of possible reference states for austenite (γ -iron)



In addition to those discussed in the text, uud is alternating (001) layers of two spin-up, one spin down, afmT is three up, three down while fm-flip is a conventional fcc cell with one spin reversed.

The energies of the possible phases are given in Figure 1. We see that the high-spin FM phase used by Jiang and Carter [7] in previous work has the highest energy and is therefore rather unstable. The AFM-D has the lowest energy, this double-layered (001) structure being more stable than either single layer (AFMI) or triple layer (AFMT).

We also considered the effects of flipping a single spin in a 256-atom unit cell and relaxing the structure.¹ Both AFM-1 and AFM-D are stable with one spin flipped, the increase in energy being about 0.05 eV.² In the high-spin FM state the flipped spin is reduced in magnitude close to zero. In low-spin FM a single spin flip triggers a transformation of the entire spin state to a lower energy configuration.

We also calculated the elastic moduli using the method of Karki *et al.* [8] (Table 1). These moduli are only well-defined about the zero stress state, which, in the case of AFM-I and AFM-D, is the tetragonally distorted state.

1. It is important to be clear precisely what this means. We use the Born-Oppenheimer approximation, that the electronic structure energy is fully minimised. In a magnetic system there are multiple minima and we are testing the stability of a “nearby” minimum to each possible reference state. The minimum energy with respect to plane wave coefficients is found using the residual minimisation method with preconditioning and direct inversion in the iterative subspace. This mathematical algorithm does not correspond to any physical trajectory which the electron could follow (c.f. time dependent DFT). Consequently “local minimum” means a minimum from which this algorithm cannot escape in this basis set. It does not guarantee that the spin-state will be a local minimum in reality.

2. In an Ising model, this would correspond to $J=0.04$ eV and a Neel temperature of about 5K.

Table 1: Elastic constants, relative energies and spins (with tetragonal-distorted values in brackets) for candidate reference structures

	FM (low-S)	FM (high-S)	AFM1	AFMd
C11	243	331	324	212
C33	243	331	242	214
C12	35	318	234	207
C13	35	318	100	94
C44	201		173	74
C66	201		252	200
Energy (meV)	62	77	13	0
Spin	0.59	2.57	1.22 (1.48)	1.80 (1.99)

All the structures are mechanically stable at their equilibrium volume. The tetragonal distortion increases the atomic spacing perpendicular to the spin layers and allows an increase in the spin.

Comparison of possible magnetic reference states

Ferromagnetic

In an early work concerning carbon in fcc iron Jiang and Carter [8] took the high-spin ferromagnetic state as a reference. One difficulty with this is that there is also a low-spin state with lower energy and a discontinuous transition between them (Figure 1) and this transition may occur locally without breaking global symmetry. We found this transition (or a transition to a disordered state) could be triggered by topological defects, or even by the energy minimisation algorithm and concluded that carbon is a special case, perhaps because it is non-magnetic itself and stabilises the fcc structure. In defect and impurity calculations we found cases where the impurity induced a transition to the ferrite or to one of the AFM structures.

Non-magnetic

There is little merit to considering the non-magnetic phase as a model for paramagnetism. The compensation of spins throughout means that there is no magnetic moment on a given atom. As a consequence of this, there is less Pauli repulsion between onsite electrons, and the atoms are “too small”. The lattice parameter lies some 10-20% below the spin states.

AFM-1

The AFM-I structure breaks cubic symmetry. This means that the fcc structure is unstable with respect to a tetragonal distortion (it is not even an extremum of the energy). It is possible to relax to the tetragonal minimum, which is elastically stable. The density is significantly higher than the paramagnetic phase. Furthermore, several possible defects which we examined induced a change of spin-state from cubic AFM-1. We note that although the energy of AFM-1 is higher than for AFM-D pure iron, in some concentrated alloys the situation is reversed. For $\text{Fe}_{70}\text{Cr}_{20}\text{Ni}_{10}$ composition it proved impossible to stabilise the AFM-D ordering at all. This raises yet another tricky issue: should one compare supercells with the same magnetic structure (as is natural for atomic structure) or should the magnetic structure be relaxed to the ground state (as is natural for the electronic structure)?

AFM-D

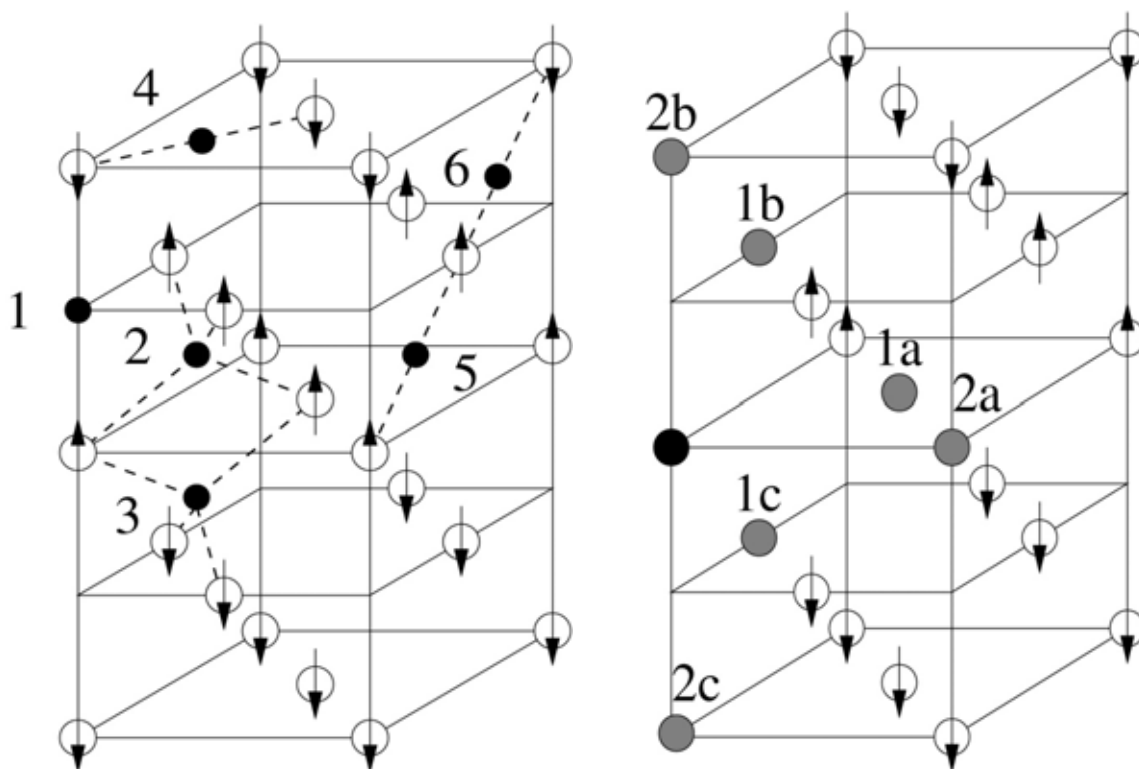
The AFM-D structure also breaks cubic symmetry, such that one has to choose between “cubic” and tetragonal supercells. It has the advantage of being the lowest energy collinear structure we have found and a lattice parameter and spin much closer to the paramagnetic state. Its equilibrium volume is closer to the 0 K extrapolated austenite. However, it has a very low C' shear modulus, which becomes negative at increased volume. For calculations at negative pressure (e.g. the density of gamma-iron under temperature conditions where it is actually stable) the ground state of AFM-D has a further, orthorhombic distortion.

Randomised spins

It would be possible to randomise the spins on each site, or to consider a set of “special quasi-random structures” to represent all possible paramagnetic arrangements in the same way as one deals with random alloys. However, preliminary calculations showed that defect calculations were extremely sensitive to spin-flips: details of the minimisation process could change the magnetic state leading to differences in energy of tenths of eV for apparently identical configurations. Similarly, the energy of the reference state is not well-defined: an average over SQS structure is required and since each SQS structure breaks symmetry in a different way, some decisions must be reached regarding the relaxation of cell and atoms, bearing in mind the possibility of collapse to ferritic states. Thus, this approach was found to be impractical.

Defect calculations

We have extended our calculations of austenitic iron to encompass point defects, self-interstitials, substitutional Cr and Ni, these being commonly-used components of steels. Given the instability of the FM states against single spin flips and the high energy/low volume of AFM-1, we concentrate on the two AFM-D states with supercells based on the minimum energy cubic or tetragonal cell as the best reference state for impurities in gamma-iron. In each case the reference state is the isolated substitutional atom of Cr or Ni in Fe. Because of the symmetry-breaking effect of the AFM ordering, there are more distinct defects and migration barriers than in a homogeneous system. We have calculated many of them: some are unstable to reconstructions and only the lowest ones are considered.

Figure 2: Numbering scheme for defect positions considered in this work


Left, interstitial sites; right, neighbour positions from defect (unmarked black circle). Arrows show relative spin direction for collinear AFM reference state.

Point defects

The various defects considered here are shown in Figure 2 and the defect energies are given in Table 2. The most striking feature is the difference between the different reference states. Even the vacancy formation energy differs by 0.15 eV. The migration barrier is the lowest for those configurations which do not require a spin flip, but varies by up to 0.8 eV. Vacancies on adjacent sites are bound, but again the strength of binding depends on the spin state. Turning to the interstitial, the [001] dumbbell is the most stable structure, with various possible migration paths lower than those available to the vacancy. Again, there is a strong dependence on the reference state, with cubic giving lower formation energies: a consistent difference of some 0.3 eV, significant, albeit much lower than the strain energy. The interstitial atom breaks the fcc symmetry and allows the unstable fcc-AFMd to relax towards the stable fct-AFMd. This is evidence in favour of using the lowest energy state (AFMd).

The position relative to like and unlike spin layers also has an effect. The magnetisation around the defects is more understandable: the magnetisation increases with the free volume around the atom. Thus, atoms around the vacancy and in the tensile region beside the interstitial have enhanced magnetisation. Meanwhile those in the compressive region have reduced magnetisation. The AFMd structure is stable around these defects, consistent with its status as the lowest energy AFM state. Of course, the interstitial atoms themselves acquire a magnetisation, and in the case of the [001] dumbbell the magnetic defect extends to the first neighbour shell, flipping four spins so as to have four (enhanced) parallel spins in the tensile plane, with adjacent compressive layers being antiparallel.

Effect of Cr and Ni impurities

We define the solution energy for adding a Cr or Ni atom to Fe relative to the pure fcc Ni or Cr. This eliminates systematic energies arising from the poor description of the free atom by non-magnetic DFT, which is the default reference state in VASP. We also calculated interactions between these substitutional impurities and with point defects. Results are shown in Table 3. The main feature of this table is the small value of all the energies, rather close to the difference between the two reference states. It appears that Ni and Cr are almost invisible to one another and to defects in iron. The only process in which they behave significantly differently from the host is in the exchange with a vacancy, where the Cr has a lower barrier than for pure Fe, while the Ni has a higher one. Even this result is tempered by the very high energy to exchange Fe between layers of opposite spin, although this is probably anomalous, since in collinear magnetism the symmetry requires that the migrating atom has zero spin, a high energy state for iron.

Table 2: Energies of point defects calculated with AFM-D and cubic or tetragonal supercells, fixed volume with all atomic positions and magnetic moments relaxed

Defect	AFMd (c)	AFMd (t)
E _{f,V}	1.672	1.819
E _{m,V} (1a)	1.046	0.743
E _{m,V} (1b)	0.712	1.098
E _{m,V} (1c)	1.268	1.581
E _{b,VV} (1a)	0.205	0.037
E _{b,VV} (1b)	0.056	0.127
E _{b,VV} (1c)	0.075	0.175
E _{b,VV} (2a)	0.022	-0.064
E _{b,VV} (2b)	-0.079	-0.018
octa (1)	rlx (8)	Rlx(8)
tetra uu (2)	3.581	3.864
tetra ud (3)	3.332	3.663
[110] crowdion (4)	rlx (3)	rlx(3)
[011] crowdion (5)	3.771	4.255
[01-1] crowdion (6)	3.874	4.168
[100] dumbbell (7)	2.978	3.316
[001] dumbbell (8)	2.790	3.195
[110] dumbbell (9)	4.289	4.311
[011] dumbbell (10)	rlx (8)	Rlx(8)
[111] dumbbell (11)	rlx (3)	Rlx(3)

Note: E_f, E_m and E_b refer to formation, migration and binding energies respectively. V refers to vacancies. Numbers in brackets in the first column refer to defect positions given in Figure 2. rlx () indicates that the defect relaxes to the position shown in the bracket. The Eshelby corrections are negligible for all cases apart from the interstitials, where they are of order 0.05 eV, meaning the choice of constant volume vs constant pressure relaxation introduces an uncertainty of around 2%.

Table 3: Binding energies of Ni and Cr to vacancies and interstitial clusters, interstitial configurations other than [001]-type are higher in energy

	AFMd (c)	AFMd (t)
Solution energy Ni	-0.033	0.084
Solution energy Cr	0.106	0.268
V-Ni (1a)	0.043	0.564
(1b)	0.013	0.027
(1c)	-0.036	0.016
(2a)	0.026	-0.002
(2b)	-0.048	-0.011
(2c)	-0.051	-0.005
V-Cr (1a)	-0.087	0.0038
(1b)	-0.066	-0.075
(1c)	-0.088	-0.091
(2a)	-0.025	-0.016
(2b)	-0.039	-0.066
(2c)	-0.036	-0.004
Ni-Ni Ni-Cr Cr-Cr binding		
1a	0.024, -0.016, -0.044	0.055, 0.025, -0.027
1b	-0.004, -0.018, -0.005	0.024, -0.012, -0.012
1c	-0.043, -0.021, -0.093	-0.014, 0.027, -0.098
2a	0.359, -0.021 0.043	0.017, -0.016, 0.023
2b	-0.045, -0.021 -0.001	-0.014, -0.015, -0.011
Vac migration (Ni, Fe, Cr)		
1a	1.304, 1.046, 0.846	0.891, 0.743, 0.560
1b	0.883, 0.711, 0.572	1.172, 1.048, 0.742
1c	0.932, 1.268, 0.657	1.179, 1.581, 0.844
Interstitials		
100 Ni, Fe, Cr	3.416, 2.977, 3.049	3.717, 3.315, 3.385
001 uu Ni, Fe, Cr	3.069, 2.790, 2.933	3.229, 3.195, 3.197
001 ud Ni, Fe, Cr	3.097, 2.790 2.850	3.469, 3.195, 3.270

Conclusions

We have calculated defect energies for a number of configurations using two possible representations for AFM austenite. The choice of relaxation strategy is clearly important: our results suggest that the lowest energy structure AFMd (t) is the best reference structure to use for point defects in pure gamma-iron. Failure to pick a minimum energy supercell can lead to spurious “energy gains” when the unstable structure relaxes around a defect: this is illustrated best by the comparison of interstitials in AFMd (c) with AFMd (t).

The large differences between states which would be identical in fcc need to be interpreted: could such configurations exist locally in high-temperature austenite, such that the formation and migration energies should be taken as the minimum of those we have found? Or should we consider these as extreme cases in a continuum of complicated local spin states, and take a mean? Whether we are really modelling austenite remains open to question.

However, some conclusions are quite robust. The solution energy of Cr and Ni in iron is small and their binding to vacancies and interstitials are weak. As a consequence, the evolution of the primary damage in the dilute alloy is relatively insensitive to these elements.

References

- [1] S.Han, L.A. Zepeda-Ruiz, G.J.Ackland, R.Car, D.J.Srolovitz (2002), *Phys Rev B* 66 220101.
- [2] P. Olsson, I. A. Abrikosov, L. Vitos, J. Wallenius (2003), *J.Nucl. Mater.* 321, 84.
- [3] T. P. C. Klaver, R. Drautz, M. W. Finnis (2006), *Phys.Rev.B* 74, 094435.
- [4] T. P. C. Klaver, P. Olsson, M. W. Finnis (2007), *Phys. Rev. B* 76, 214110.
- [5] G.J. Ackland, R. Thetford (1987), *Phil. Mag.A*, 56, 15.
- [6] M. Acet, H. Zahres, E.F. Wassermann, and W. Pepperhoff (1994), *Phys. Rev. B* 49, 6012.
- [7] DE Jiang and EA Carter (2003), *Phys.Rev. B* 67, 214103.
- [8] BB. Karki, SJ Clark, MC Warren, HC Hseuh, GJ Ackland, J Crain (1997), *J.Phys.CM* 9 375.
- [9] A.Zunger, S.-H. Wei, L. G. Ferreira, J.E. Bernard (1990), *Phys. Rev. Lett.* 65, 353.

Fission-fusion cross-cutting issues related to structural materials*

Farhad Tavassoli

Département de Matériaux pour le Nucléaire, Direction d'Énergie Nucléaire
Commissariat à l'Énergie Nucléaire, France

Abstract

After a brief recall of the past interactions between fission and fusion materials development work, six types of structural materials are retained for cross-cutting detailed examinations and future perspectives. For each type of material, important issues regarding their application in fission Generation IV, fusion DEMO and fusion power reactors are discussed.

It is noted that the austenitic stainless steels will continue to be favoured for main vessel and other critical structural components in any system. Likewise, conventional Mod 9Cr-1Mo steel and its equivalent low-activation derivatives, such as Eurofer and F82H steels, should continue to be the preferred choice for internal structures exposed to high-irradiation doses and steam generators of sodium-cooled fast reactors (SFR). In the immediate future, ODS grades of these steels and in the not so distant future, ODS ferritic steels, could be considered in support of or in replacement to increasing their service temperature window. Development of higher temperature materials, such as SiC_f/SiC composites and refractory alloys (tungsten and vanadium alloys) will need more time and in the long term could allow more efficient high-temperature fission and fusion designs.

* The full paper being unavailable at the time of publication, only the abstract is included.

Session VII

Novel Materials – Nano-structured Materials

Chairs: A. Kimura, J.S. Jang

Structural control and high-temperature strength of 9 Cr ODS steels

**Shigeharu Ukai¹, Ryota Miyata¹, Shigenari Hayashi¹
Kenya Tanaka², Takeji Kaito², Satoshi Ohtsuka²**

¹Hokkaido University, Japan

²Japan Atomic Energy Agency, Japan

Abstract

The 9Cr oxide dispersion-strengthened (ODS) steels are promising fuel cladding materials for advanced sodium-cooled fast reactors. It is known that the 9Cr-ODS steel is composed of both residual ferrite and tempered martensite. The formation process of the characteristic residual ferrite and the resultant high-temperature strength of 9Cr-ODS ferritic steels were investigated.

The formation of residual ferrite is dominated by a competition between the driving force for the α to γ reverse transformation and the pinning force of α - γ interface by oxide particles. The γ -phase formation is enhanced by dissolution of carbides into the matrix at A_{C1} , but this force is reduced on approaching the equilibrium carbon content at temperatures above A_{C3} . This situation induces a partial retention of the ferrite, which is designated as a residual ferrite and identified as metastable phase. The residual ferrite contains finer nano-sized oxide particles, which are responsible for hardening in the residual ferrite. The tensile strength of 9Cr-ODS steels is linearly improved with increasing the fraction of the residual ferrite up to 30% volume.

Introduction

Oxide dispersion-strengthened (ODS) ferritic steels are known to be promising candidates for use as advanced fission and fusion materials that require excellent radiation resistance and high-temperature capabilities [1–3]. We focus here on the development of 9Cr-ODS steels [4–9], their microstructures can be easily controlled by a reversible martensite phase transformation with a remarkably high driving force of a few hundred megajoules per cubic meter as compared to the driving force of irreversible recrystallisation of a few megajoules per cubic meter for 12Cr-ODS ferritic steels [10]. 9Cr-ODS steel claddings are currently being manufactured for use in fast reactor fuel elements in the Japan Atomic Energy Agency by inducing reversible α/γ phase transformation.

From a series of extensive experiments, it has been recognised that 9Cr-ODS steel claddings manufactured in an engineering process exhibit a dual phase structure comprising tempered martensite and ferrite. The high-temperature strength of the manufactured 9Cr-ODS steel claddings is significantly improved by the presence of the ferrite phase [11–15]. The formation of the ferrite phase in 9Cr-ODS steels is extremely unusual, because under normalising and air-cooling conditions only the full martensite phase can be present in 9 Cr steels without yttria. We designated this characteristic ferrite phase as a residual ferrite. Cayron *et al.* also reported the same ferritic grains in 9Cr-ODS Eurofer steels [16].

In this study, an origin and a formation process of the residual ferrite in 9Cr-ODS steels were elucidated on the basis of thermodynamic analyses. The high-temperature tensile strength of 9Cr-ODS steels associated with the residual ferrite was also investigated.

Experimental procedure

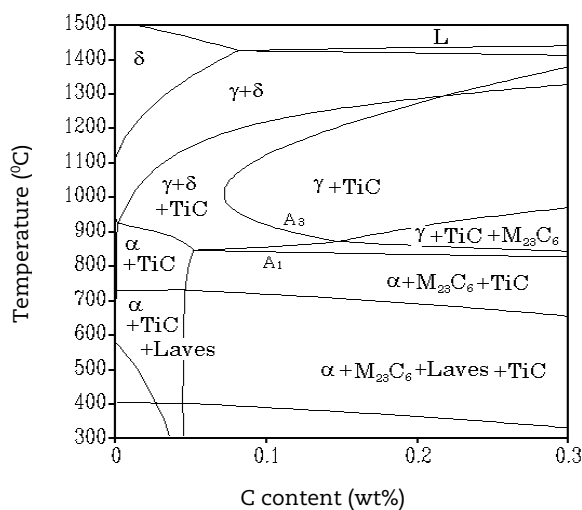
Pure elemental powders of iron (99.5 mass%, 45–100 μm), carbon (99.7 mass%, 5 μm), chromium (99.9 mass%, under 250 μm), tungsten (99.9 mass%, 4.5–7.5 μm), and titanium (99.7 mass%, under 150 μm) were mechanically alloyed (MAed) together with Y_2O_3 powder (99.9 mass%, 20 nm) in an argon gas atmosphere using a planetary-type ball mill (Fritsch P-6). The MAing duration was selected to be 48 h, based on the previous results that the hardness of MAed powders is sufficiently saturated at 48 h. The rotation speed is 400 rpm and powder to ball ratio is 1:10. The standard composition of 9 Cr-ODS steels is 9Cr-0.13C-2W-0.2Ti-0.35 Y_2O_3 (mass%), and carbon content was increased up to 0.34 mass% to change a volume fraction of the residual ferrite phase. The excess oxygen content of mechanically alloyed powders was measured to be 0.09 mass%, where excess oxygen enables the Y-Ti oxide particles to form.

The MAed powders were consolidated by spark plasma sintering at 1 100°C and for 1 h, then consolidated ones were hot-rolled at 1 000°C. After normalising at 1 050°C for 1 h followed by tempering at 800°C for 1 h, tensile tests were conducted at 700°C. Dilatometric measurements were performed using a Rigaku TMA-8140C during heating at a rate of 0.083°C/s. The computation of the thermodynamic analyses of the Fe–9Cr–0.13C–2W–0.2Ti system was performed using the Thermo-Calc code and the TCFE6 database and the Gibbs energy difference between α and γ phases was considered for predicting the driving force for the reverse transformation of the α -phase to the γ -phase.

Residual ferrite formation

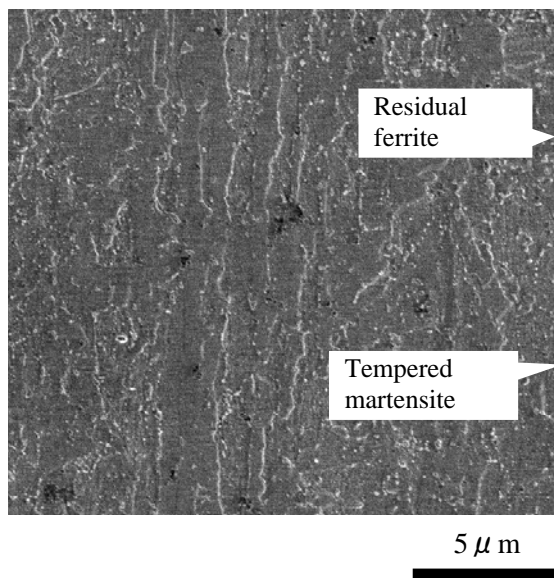
A phase diagram computed by using the Pandat code and PanFe database with respect to carbon content in the Fe-9Cr-0.2Ti-2W system is shown in Figure 1. This diagram does not include oxide particles and displays the equilibrium state. Corresponding to a carbon content of 0.13 mass%, 9Cr-0.13C-0.2Ti-2W is composed of α -ferrite and carbides, including $M_{23}C_6$ and TiC and Laves-phase at room temperature, where the main precipitate is $M_{23}C_6$. When the temperature rises to the A_{c1} point, the α to γ reverse transformation begins to proceed in association with the dissolution of $M_{23}C_6$ carbide in the γ -phase. Only the γ -phase is stable and it includes small amounts of TiC carbide at the normalising temperature of 1 050°C above A_{c3} point. Thus, the structure of the single tempered martensite is expected at normalising and tempered (N-T) heat treatment.

Figure 1: Computed phase diagram with respect to carbon content for Fe-9Cr-xC-0.2Ti-2W system without Y_2O_3



However, the specimen of the standard 9Cr-ODS steel with 0.13 mass% carbon after N-T treatment exhibits a dual phase comprising a tempered martensite and residual ferrite appeared as a flat contrast, as shown in Figure 2. In the SEM micrographs, there are small dots of carbides in the tempered martensite.

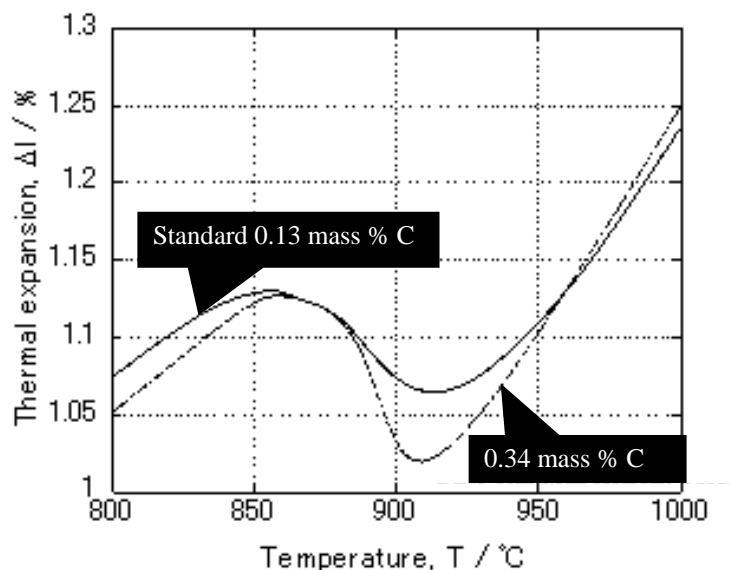
The results of dilatometric measurement for both specimens of standard and 0.34 mass% carbon are shown in Figure 3. The decrease in linear thermal expansion takes place between the A_{c1} point of 860°C and the A_{c3} point of 910°C due to the α to γ reverse transformation and the linear thermal expansion increases at temperatures above the A_{c3} point. It is found that standard 9Cr-ODS steel exhibits a smaller reduction during the α - γ reverse transformation and a lower slope of linear thermal expansion against rising temperature, compared to 0.34 mass% carbon 9Cr-ODS steel. These results indicate that the entire α -phase was not transformed to γ -phase in standard 9Cr-ODS steel. This untransformed ferrite phase is the residual ferrite.

Figure 2: SEM micrograph of standard 9Cr-ODS steel containing 0.13 mass% carbon

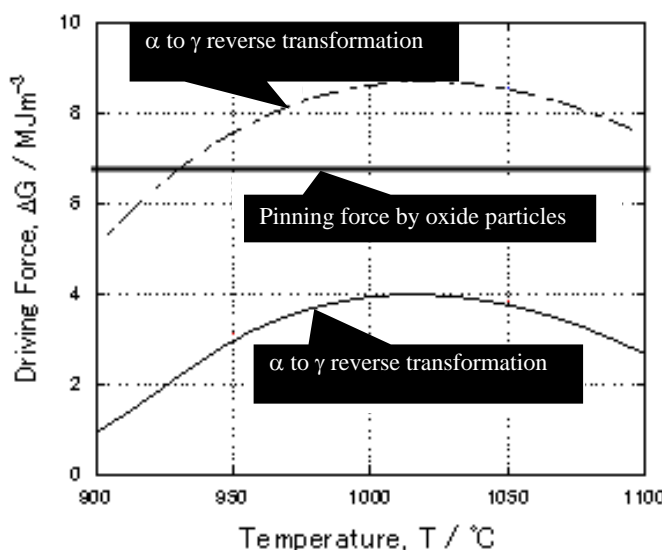
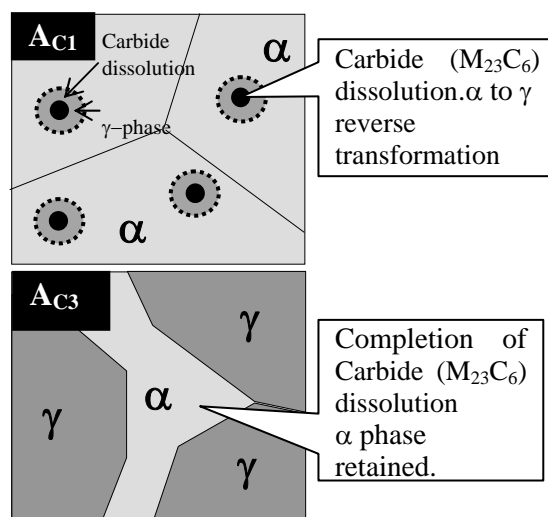
In order to evaluate whether the α to γ reverse transformation proceeds or not at the A_{C1} point for the standard 9 Cr-ODS steel, we calculated a chemical driving force (ΔG) for the α to γ reverse transformation and pinning force (F) for the α - γ interfaces by oxide particles. The ΔG corresponds to a Gibbs energy difference in γ - α phase, where Gibbs energy of γ and α phase can be derived by using the Thermo-Calc code and the TCFE6 database. The pinning force F for the motion of the α - γ interface can be expressed by the equation below [17];

$$F = \frac{3 \sigma \cdot f_p^{2/3}}{8 r}$$

where σ is the α - γ interfacial energy and its value was selected as 0.56 J/m [18]. The r is the radius of the oxide particle and its volume fraction is expressed as f_p . The ΔG and F are competitive; $\Delta G > F$ indicates that the α - γ reverse transformation takes place and $\Delta G < F$ indicates that the α - γ interface can be pinned by oxide particles and the α -phase is retained.

Figure 3: Dilatometric measurement of 9Cr-ODS steels: A_{C1} point: 860°C, A_{C3} point: 910°C

At the A_{C1} point, $M_{23}C_6$ carbide dissolves into the matrix and the carbon concentration at the carbide-matrix interface becomes relatively high. For example, a carbon content of 0.2 mass% leads to ΔG calculated by Thermo-Calc higher than the pinning force F by an oxide particle at 1 050°C, as shown in Figure 4. This result suggests that the α to γ reverse transformation proceeds from the carbide-matrix interface, where $M_{23}C_6$ carbide dissolves into the matrix.

Figure 4: Results of Thermo-Calc calculation for driving force of α to γ reverse transformation and pinning force by oxide particles**Figure 5: Schematic illustration of the residual ferrite formation in standard 9Cr-ODS steel**

When temperature rises beyond the A_{C3} point, $M_{23}C_6$ carbide completely dissolves into the matrix and the average carbon concentration approaches the initial content of 0.13 mass%, where the pinning force F is higher than the driving force ΔG , as shown in Figure 4. This result of calculation implies that α -ferrite can be partially retained at the final stage. These calculations can reasonably explain the formation of dual phase in the standard 9Cr-ODS steel comprising a tempered martensite and residual ferrite shown in Figure 2. Figure 5 schematically illustrates the formation process of the residual ferrite through carbide dissolution at A_{C1} point and saturation of carbon content at A_{C3} point.

Relation between fraction of residual ferrite and carbon content

In order to analyse the volume fraction of the residual ferrite in 9Cr-ODS steels, hardness measurements using both nanoindenter and Vickers were conducted for the specimens with various carbon contents. Figure 6 shows the load vs. indent depth curves of nanoindentation for both tempered martensite and residual ferrite in the standard 9Cr-ODS steel containing 0.13 mass% carbon after N-T condition. In the nanoindentation measurement, a size of Berkovich type of indent was selected to be $1 \mu\text{m}$ by 300 mg loading, which makes it possible to separately measure the nano-hardness in each phase. As can be seen from Figure 6, nano-indentation hardness was estimated to be $H_m 830 \text{ mgf}/\mu\text{m}^2$ for the residual ferrite and $600 \text{ mgf}/\mu\text{m}^2$ for the tempered martensite. Based on our previous study [19], nanoindentation hardness can be converted to Vickers hardness by using the equation below:

$$H_v = \frac{1}{1.4} H_m .$$

$H_v 590$ and $H_v 430$ were derived for the residual ferrite and the tempered martensite, respectively. This hardness belongs to individual ones for both phases.

On the other hand, the size of Vickers type of indent is as large as $40 \mu\text{m}$. As shown in Figure 2, $40 \mu\text{m}$ areas cover both residual ferrite and tempered martensite. Thereby, Vickers hardness comes from both.

Figure 6: Nanoindentation hardness measurement of 9Cr-ODS steels

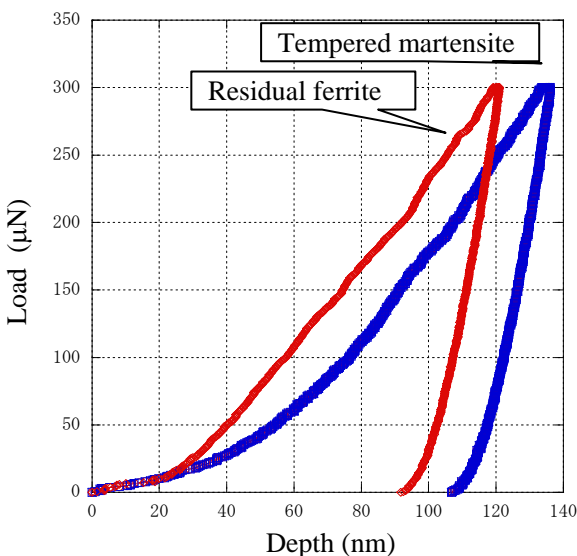


Figure 7: Vickers hardness measurement of the 9Cr-ODS steels containing various carbon contents

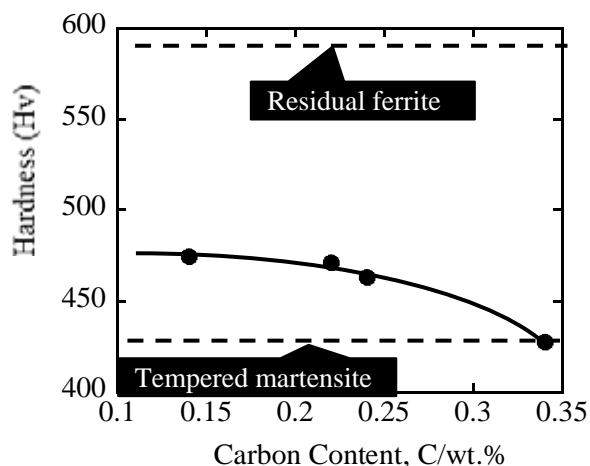
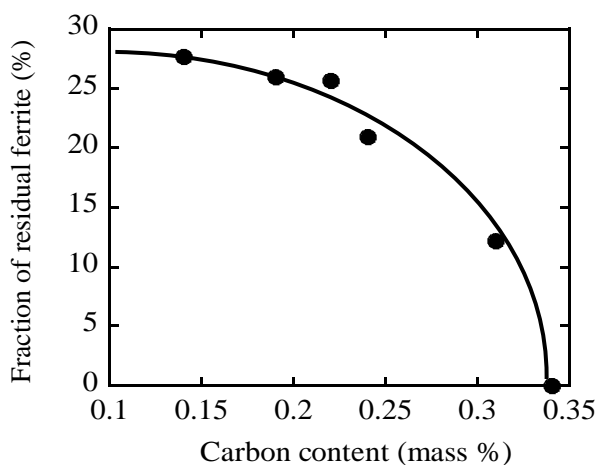


Figure 7 shows the Vickers hardness measured for the 9Cr-ODS steels containing various carbon content from 0.13 to 0.34 mass%. Vickers hardness decreases with increasing carbon content. These results imply that a volume fraction of the residual ferrite decreases with increasing carbon content. The equation below correlates the overall Vickers hardness (Hv) with the volume fraction of the residual ferrite (f_α);

$$Hv = Hv_\alpha \cdot f_\alpha + Hv_{\alpha'} \cdot (1 - f_\alpha)$$

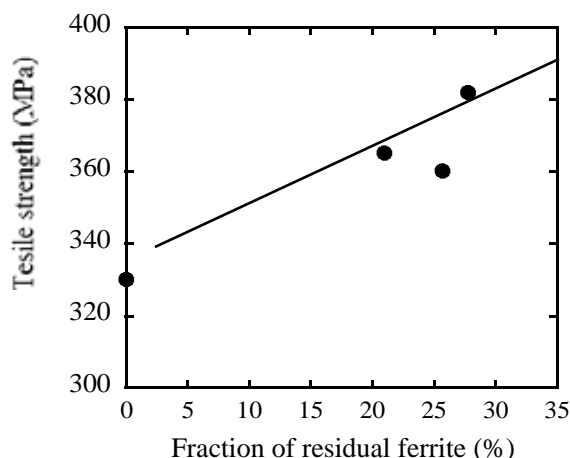
where Hv_α (590) and $Hv_{\alpha'}$ (430) are Vickers hardness for the residual ferrite and the tempered martensite, respectively. According to the Vickers hardness measured in Figure 7, the volume fraction of the residual ferrite (f_α) was estimated; the results are shown as a function of carbon content in Figure 8. The volume fraction of 28 % for the residual ferrite was attained in the standard 9Cr-ODS steel with 0.13 mass% carbons and it decreases to zero at 0.34 mass% carbons, which corresponds to the full martensite. The overall trend that the volume fraction decreases with increasing carbon content is qualitatively consistent with the fact that the driving force for α to γ reverse transformation increases with increasing carbon content.

Figure 8: Measured fraction of residual ferrite as a function of carbon content in 9Cr-ODS steels



Tensile strength improvement by embedding residual ferrite

The tensile tests were conducted for 9Cr-ODS steels with various carbon contents from 0.13 mass% to 0.34 mass%, after N-T condition. Test conditions are a strain rate of $1 \times 10^{-3} \text{ s}^{-1}$ and a temperature of 700°C under flowing argon gas. Figure 9 shows the results of the tensile tests with respect to the fraction of the residual ferrite. It is obvious that the tensile strength is almost linearly improved with increasing the fraction of the residual ferrite. This is attributed to the fact that a crack propagation proceeds inside the soft tempered martensite and stops at hard residual ferrite. It can be said that the 9Cr-ODS steels are reinforced composite materials consisting of hard and soft materials. We are planning to investigate tensile strength behaviour at the fraction of residual ferrite exceeding over 30% in order to find an optimum fraction of residual ferrite.

Figure 9: Relation between tensile strength and fraction of residual ferrite

Concerning the hard residual ferrite with higher hardness of Hv_{α} 590, compared with tempered martensite of Hv_{α} 430, this is due to a dense distribution of finer oxide particles within the residual ferrite rather than in the tempered martensite. This issue has previously been discussed in detail [20]. A different distribution of oxide particles could be associated with α - γ reverse transformation. A change of matrix phase from α (bcc crystal structure) to γ (fcc) by reverse transformation could disturb the interface coherency. The coherent to incoherent transition at the oxide particle interfaces within the martensite phase could induce coarsening of oxide particles, following from the analogy of carbide coarsening by recrystallization of the surrounding matrix reported by Yazawa *et al.* [21]. In contrast, oxide particles keep the coherency inside the residual ferrite. This is attributed to the fact that a fine distribution of the oxide particles in the residual ferrite.

Conclusion

9Cr-ODS steels have been developed by the Japan Atomic Energy Agency as promising fuel cladding materials for advanced sodium-cooled fast reactors. Their structure is composed of residual ferrite and tempered martensite. It has been found that the residual ferrite is formed by pinning of α - γ interface through oxide particles. Thereby, the residual ferrite is metastable phase and its volume fraction decreases with increasing carbon content to 0.34 mass%. This means that the structure approaches an equilibrium condition by increasing driving force for α - γ reverse transformation beyond α - γ pinning force. In contrast, tensile strength can be improved by increasing the fraction of residual ferrite up to 28 volume%.

References

- [1] G.R. Odette, M.J. Alinger and B.D. Wirth (2008), *Annu. Rev. Mater. Res.* 38, 471–503.
- [2] S. Ukai and M. Fujiwara (2002), *J. Nucl. Mater.* 307–311, 749–757.
- [3] T.R. Allen (2002), Workshop on Higher Temperature Materials for Advanced Nuclear Energy Systems, DOE Office of Nuclear Energy, Science and Technology, La Jolla, CA, March 18 2002.
- [4] S. Ukai, T. Nishida, T. Okuda and T. Yoshitake (1998), *J. Nucl. Sci. Technol.* 35, 4, 294–300.
- [5] S. Ukai, T. Nishida, T. Okuda and T. Yoshitake (1998), *J. Nucl. Mater.* 258–263, 1745–1749.
- [6] S. Ukai, S. Mizuta, M. Fujiwara, T. Okuda and T. Kobayashi (2002), *J. Nucl. Sci. Technol.* 39, 7, 778–788.
- [7] S. Ukai, S. Mizuta, M. Fujiwara, T. Okuda and T. Kobayashi (2002), *J. Nucl. Mater.* 307–311, 758–762.
- [8] S. Ukai, T. Kaito, S. Otsuka, T. Narita, M. Fujiwara, T. Kobayashi (2003), *ISIJ International* 43, 12, 2038–2045.
- [9] S. Ukai, T. Narita, A. Alamo and P. Pamentier (2004), *J. Nucl. Mater.* 329–333, 356–361.
- [10] T. Nishizawa (2005), *Micro-Soshiki no Netsurikigaku*, Japan Institute of Metal, p. 218, [in Japanese].
- [11] S. Ukai, S. Ohtsuka, T. Kaito, H. Sakasegawa, N. Chikata and S. Hayashi (2009), *Materials Science and Engineering A*, 510-511, 6, 115-120.
- [12] S. Ohtsuka, S. Ukai, M. Fujiwara, H. Sakasegawa, T. Kaito and T. Narita (2007), *J. Nucl. Mater.* 367–370, 160–165.
- [13] S. Ohtsuka, S. Ukai, M. Fujiwara, T. Kaito and T. Narita (2005), *J. Phys. Chem. Solids.* 66, 571–575.
- [14] S. Ohtsuka, S. Ukai, M. Fujiwara, T. Kaito and T. Narita (2004), *J. Nucl. Mater.* 329–333, 372–376.
- [15] S. Ohtsuka, S. Ukai and M. Fujiwara (2006), *J. Nucl. Mater.* 351, 241–246.
- [16] C. Cayron, E. Rath, I. Chu and S. Kaunois (2004), *J. Nucl. Mater.* 335, 83–102.
- [17] T. Nishizawa, I. Ohnuma, K. Ishida (1997), *Materials Transaction*, Vol.38, No.11, 920-956.
- [18] J. W. Marton and R. D. Doherty (1976), *Stability of Microstructure in Metallic Systems*, Cambridge University Press, 173.
- [19] N. Chikata, S. Hayashi, S. Ukai, S. Ohnuki, S. Ohtsuka and T. Kaito (2009), *Heat Treatment and Surface Engineering*, p.557-560.
- [20] M. Yamamoto, S. Ukai, S. Hayashi, T. Kaito and S. Ohtsuka, *J. Nucl. Mater.*, forthcoming publication.
- [21] Y. Yazawa, T. Furuhashi, T. Maki (2004), *Acta Metall.* 52, 3727-3736.

Development of cladding materials: Past and present experience

Concetta Fazio¹, Joachim U. Knebel¹

¹Karlsruhe Institute of Technology, Nuclear Safety Research Programme, Germany

Abstract

In the context of partitioning and transmutation (P/T) of nuclear waste, with the objective to reduce the burden on a geological repository, fast neutron spectrum has been considered the most suitable for the transmutation of transuranics (TRU). The technologies under consideration are accelerator-driven subcritical (ADS) systems and critical fast reactors (FR). Moreover, advanced fuel cycles including P/T have been included in the studies of Generation IV type FR. Here the objectives are the optimisation of resource utilisation and waste management through e.g. the transmutation of the minor actinides (Np, Am and Cm).

The current design of fast neutron systems (SFR, LFR/ADS, GFR) foresees demanding conditions such as high burn-up, high core temperature and temperature gradients and possibly corrosive environment like in the case of heavy-liquid-metal-cooled systems. Moreover, materials of core components like the fuel clad are subject during in-service operation to mechanical stresses [hoop stress due to fission gas, fuel-clad, mechanical interaction both radial and axial, thermal stresses, pressure and dynamical stresses (as e.g. friction) due to the coolant circulation in the channels, etc.], neutron irradiation (which can induce mechanical and geometrical properties change) and corrosion/erosion. For these conditions and given the stringent requirements (e.g. tightness, dimensional stability) on the fuel cladding, the selection of the proper material becomes a challenge.

The objective of this contribution to the SMINS-2 workshop is to analyse fuel clad requirements and related materials development and characterisation as performed in the past (e.g. within the German SFR project) and to possibly extend that experience to novel appropriate materials under consideration for future systems. In particular, the development and characterisation of the austenitic stainless steel X10CrNiMoTiB 15 15 (Din 1.4970) will be discussed as well as the present status of ODS steels.

Introduction

Fast reactor systems have been developed since studies performed by E. Fermi with the idea to close the nuclear fuel cycle. The first fast reactors (e.g. EBR-I) were put in operation in 1950-1951 with the objective of demonstrating their feasibility and were used to generate electricity. During the period 1960-1970, the increase in energy demand and the development of water-cooled reactors raised the question of resources availability. The opportunities to use fast reactors as breeder to vastly improve resource utilisation motivated the launching of important fast reactor programmes e.g. in France, Germany, the United Kingdom, the United States, Japan, the Russian Federation, etc. However, during the 1980s a decline of nuclear development and the perception of plentiful resource availability triggered a strong slow down of fast reactor programmes. In fact, in countries like the United States (and others) the strategy was based on the once through fuel cycle and the development of a geological repository. At the same time, in countries like France or Japan closed fuel cycles were still pursued and conceived also as a means of solving waste issues. Since the late 1990s there has been a generalised rebirth of closed cycle research and development to improve waste management and critical and subcritical fast neutron systems have been put back on stage. At present there is a renewal of fast reactor programmes in order to address long-term energy security, to expand the role of nuclear reactors due to the increasing energy demand and to address nuclear waste issues.

The fast neutron Generation IV systems, i.e. sodium, lead-and gas-cooled fast reactors are regarded as reference for resource optimisation and waste management [1]. Moreover, these systems as well as the accelerator-driven systems (ADS) are considered for TRU management. The advantages and disadvantages of the coolants envisaged for these systems are shown in Figure 1.

Figure 1: Advantages and disadvantages of the different coolants for fast neutron systems

<p>Sodium = first choice</p> <ul style="list-style-type: none"> ✓ High thermal conductivity ✓ Liquid from 98°C to 883°C (at 1 bar) ✓ Low viscosity ✓ Compatible with steels ✓ Industrial fluid ✓ Low cost <p>But reactive with air and water, and opaque</p>	<p>Lead is a variant also for ADS</p> <ul style="list-style-type: none"> ✓ No reactivity with air and water ✓ Liquid from 327°C to 1745°C (at 1 bar) ✓ Low cost ✓ Good thermal conductivity <p>But corrosive, toxic, very dense, opaque (and solid...)</p>	<p>Helium is an alternative</p> <ul style="list-style-type: none"> ✓ No temperature constraints ✓ No phase change ✓ Inert ✓ Transparent <p>But low density, high pressure</p>
---	---	--

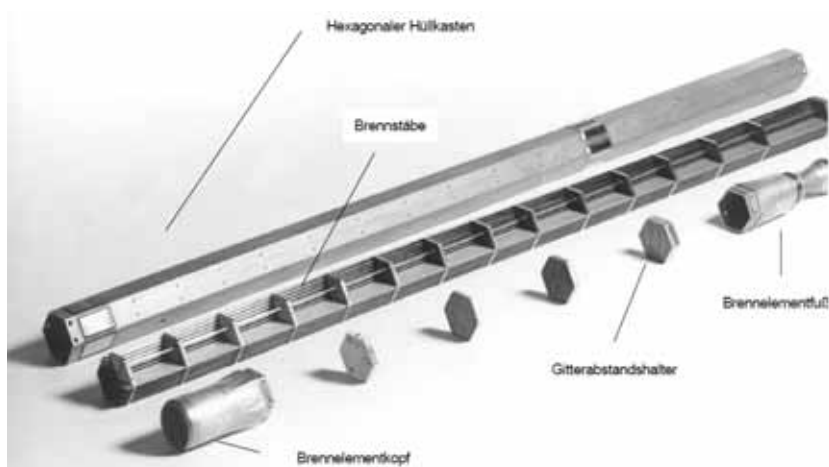
Development of structural materials for core components of fast neutron systems

The most hostile environment in a fast neutron reactor is clearly found inside the core, where high neutron flux, high burn-up, high temperature and flowing cooling medium (liquid metals, gas) impose severe requirements on the materials selected for the core components.

The core fuel assemblies are typically formed by fuel pins inside a wrapper tube. The fuel pins are separated by spacers, which can be wire or grids. In Figure 2, a fuel sub-assembly developed in the frame of the German FR programme is shown [2], where grid spacers have been used.

The fuel pins consist of a cylindrical cladding tube closed at both ends by plugs. Inside the cladding the fuel pellets are accommodated and a plenum for the release of fission gas is expected. Normally at the interface between the pellets and the cladding, a gap is designed to allow for fuel swelling and mitigate fuel/clad mechanical interaction.

Figure 2: A fuel sub-assembly is shown with grid spacer [2]



Hexagonaler Hüllkasten = hexagonal wrapper tube; Brennstäbe = fuel pin;
Gitterabstandhalter = grid spacer; Brennelement kopf / fuß = top and bottom plug of the sub-assembly.

Fuel pin requirement and design issues

The clad of a fuel pin has the function to contain the fuel and to act as safety barrier. The basic requirements of the fuel pin are: resistance to high power and high fuel burn-up, which means high-irradiation dose. In addition, it is essential that the fuel pin maintains its dimensional stability within a narrow tolerance (to allow the flowing of the coolant in the sub-assembly channels in order to remove the heat produced from the nuclear reactions) and remains tight (to contain the fission products) over its operational lifetime.

Moreover, in the selection of materials for the clad one should also consider that it should have low neutron cross-section, therefore high Z materials as W, Mo, Ta etc. must be excluded or at least reduced to a minimum.

Key dimensional requirements and stresses to which the clad will be subjected are summarised hereafter:

Geometrical items:

- clad diameter: is related to the power density and is usually in the range of 6-9 mm;
- clad wall thickness: should be as low as possible (reduce neutron absorption and leaking through high volume and control thermal stresses);
- clad length: not too high due to issues related to sub-assembly movement, height of reactor building and increase of pressure drop. However, the height should accommodate the stresses originated by e.g. the fission gas.

Stresses:

Internal overpressure (at fabrication the pin is filled with He and during heating up degassing of H₂O) can occur. This overpressure increases with burn-up due to fission gas release (mostly Krypton, Xenon and some volatile, e.g. Cs).

- radial stresses due to fuel swelling;
- axial stresses due to fuel expansion in axial direction;
- thermal stresses:
 - thermal gradients along the fuel pin;
 - thermal gradients which take place during reactor startup and power increase;
- external pressure of the coolant;
- dynamical stresses due to the coolant flow and the forces that can originate in the spacer configuration;
- fuel/clad chemical interaction and *clad/coolant* interaction.

Past experience for SNR300

Research and development activities have been conducted for about 30 years on the sodium-cooled fast reactor (SNR 300) [2] [3]. In this frame, fuel elements were developed which reached burn-ups of about 200 GWd/t. An essential prerequisite for that was the selection of suitable structural materials for fuel elements and wrappers. The behaviour of these materials under the extreme conditions of high accumulated dose rates, which resulted in some completely new irradiation phenomena, i.e. swelling, irradiation induced creep and embrittlement, turned out to be life-time-limiting factors. In the following paragraphs these factors will be discussed in more detail. Of course, other factors, e.g. tensile properties, thermal creep resistance, fracture toughness, coolant and fuel compatibilities are also essential for clad qualification. However, these factors are not discussed in this work.

Alloy selection for SNR300

The alloy selection for the SNR300 clad material has been based on the following considerations:

- Ni alloys did show:
 - He embrittlement;
 - low corrosion resistance in Na;
 - higher neutron absorption.

- V alloys did show:
 - missing technological basis (low level of knowledge);
 - first results made evident the low corrosion resistance in Na.
- Ferritic, martensitic steels did show:
 - low creep-to-rupture strength.
- Austenitic stainless steels (the stabilised variants have been considered due to reduced intergranular corrosion e.g. at weld) did show:
 - high thermal creep resistance;
 - high structural stability;
 - low He embrittlement.

The heat-resistant austenitic stainless steel of type X10CrNiMoTiB 15 15 (W.-Nr. 1.4970) was therefore selected for further development, qualification and validation. In Table 1 the composition of this steel together with the modified variant (Din 1.4970 mod.) are reported. Elements that have been investigated to optimise creep resistance and under irradiation behaviour are Ti/C, Si, Mo, B and P. In numerous irradiation experiments neutron dose rates up to 3×10^{23} n/cm² could be reached.

Table 1: Chemical composition of the austenitic steels 1.4970 and 1.4970 mod [2]

Element (wt.-%)	C	Si	Mn	P	S	Al
Spec. 1.4970	0.08-0.12	0.25-0.40	1.60-2.00	≤ 0.030	≤ 0.015	-----
1.4970 mod.	0.08-0.10	0.70-0.90	1.00-2.00	0.03-0.05	≤ 0.015	≤ 0.015
Element (wt.-%)	Cr	Cu	Mo	Ni	Ti	V
Spec. 1.4970	15.0-16.0	-----	1.05-1.25	14.5-15.5	0.35-0.55	-----
1.4970 mod	14.0-16.0	≤ 0.03	1.3-1.7	14.0-16.0	0.3-0.5	≤ 0.03
Element (wt.-%)	B	Zr	W	Nb/Ta	Co	Ca
Spec. 1.4970	0.003-0.006	-----	-----	-----	-----	-----
1.4970 mod	0.004-0.008	≤ 0.03	≤ 0.03	≤ 0.03	≤ 0.03	≤ 0.03

Irradiation effect

Microstructure

In general, it has been observed that radiation-produced changes of the microstructures of the austenitic steels of the 300 series can be related to the changes of mechanical properties and dimensional stability such as hardening, swelling and embrittlement [4]. The most pronounced changes in the microstructural behaviour of austenitic stainless steels occur as a function of irradiation temperature. In this context, at very high temperatures, microstructural evolution during reactor irradiation becomes almost indistinguishable from that occurring during thermal ageing.

In general, the type of defects that can be observed on austenitic stainless steel of type 15Cr-15Ni Ti stabilised upon irradiation can be classified as follows:

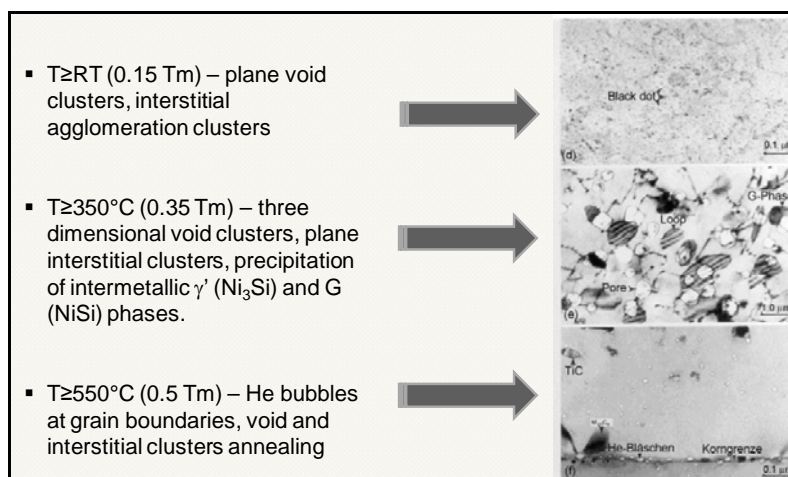
- Dislocations:
 - Without irradiation dislocation network concentration depends on thermo-mechanical treatment. After solution annealing the concentration is lower (~ 4 order of magnitude) with respect to the concentration after cold working.
 - Neutron irradiation produces Frank (faulted) loops, which are usually interstitials (extrinsic): At low irradiation doses Frank loops can be tiny and appear as black dot damage. Frank loops can also grow into dislocation network, depending on the irradiation dose.
- Radiation-induced cavities (clusters of vacancies and gas atoms) can be generally classified as voids or bubbles. Depending on cavity size, cavities can be either stable (slow growth) or unstable with an accelerated growth and become voids.
- Precipitation of phases: Phases as MC (M=Ti, Mo), $M_{23}C_6$ (M= Fe, Cr) and M_2B (M=Fe, Cr) can be observed upon thermal ageing. The neutron-irradiated steel shows mainly the formation of irradiation-induced precipitation of γ' -phase (Ni_3Si) and G-phase ($NiSi$), while MC as the TiC can return in solution.

The formation and growth of these defects during irradiation depend on the temperature. The trend can be described as reported in Table 2.

Figure 3 shows micrographs of the cross-section of irradiated samples at relevant temperatures where the observed defects have been highlighted.

Table 2: Trend of defect formation/microstructural changes of 1.4970 as a function of irradiation temperature [2]

Microstructure changes of the steel 1.4970 due to irradiation	
$\geq RT$ (0.15 T_m)	Observation of "black-dot"-defects Plane defect-cluster on the {111}-plane with $\bar{b} = a/3 < 111 >$ Vacancy clusters Interstitial-cluster build through agglomeration No visible cavity formation (voids or bubbles) No visible radiation produced precipitation
$\geq 350^\circ C$ (0.35 T_s)	Three dimensional vacancy-cluster, boundary planes: {111}- and {100}
	Bi dimensional interstitial clusters, nucleation on the {111}-plane with $b = a/3 < 111 >$
	Observation of irradiation induced precipitation: intermetallic γ' -phase - coherent and G-phase - non coherent; with nucleation on voids
$\geq 550^\circ C$ (0.5 T_s)	Observation of He bubbles at grain boundaries, at coherent precipitation of TiC boundaries with the matrix and at dislocation

Figure 3: Microstructural changes of steel 1.4970 irradiated at different temperatures [2]

Irradiation void swelling of austenitic steels

The mechanism of void swelling can be explained by taking into account defects generated during fast neutron irradiation. The large flux of high energy neutrons in a fast reactor core results in a very high rate of point defect production ($\sim 10^{-6} \text{dpa} \times \text{sec}^{-1}$) being interstitials and vacancies. These vacancies and interstitials produced during neutron irradiation can recombine or can be absorbed at sinks such as dislocations, grain boundaries or existing voids, and are therefore lost. Those defects that survive can aggregate to form embryonic interstitial dislocation loops and voids.

The recombination process and the various types of sinks compete for point defects. If all sinks accept vacancies and interstitials equally well, each void, e.g. will receive both an interstitial and a vacancy and will not grow. There must be at least one sink that exhibits a preferential for interstitials, thereby altering the relative steady-state concentration of vacancies and interstitials; in this case each of the other sinks that normally exhibit no bias will trap more vacancies.

The dislocations act as biased sinks for the preferential absorption of interstitials as a consequence of a more strong interaction with the strain fields associated with these point defects compared with vacancies. The resultant excess vacancy flux into neutral sinks such as the void embryos then leads to their growth, whilst the enhanced input of interstitials into the interstitial loops causes their expansion, coalescence and final incorporation into the dislocation network.

The dislocations that are originally present in the material appear to be less important as preferential sinks for interstitials than the dislocations that are formed during irradiation.

The voids are stabilised by residual surface active gases present in the metal and/or helium generated during neutron irradiation by fast (n, α) transmutation in, for example, isotopes of Fe, Cr and Ni.

The dependence of swelling on temperature can be predicted. At low temperatures the vacancies and interstitials cannot move quickly to sinks and the steady-state concentrations build up. In these conditions recombination predominates and there is little void growth.

In the intermediate temperature range ($0.3 - 0.5 T_m$) recombination is no longer the main mechanism of point defect interaction. The interstitials can move quickly to sinks

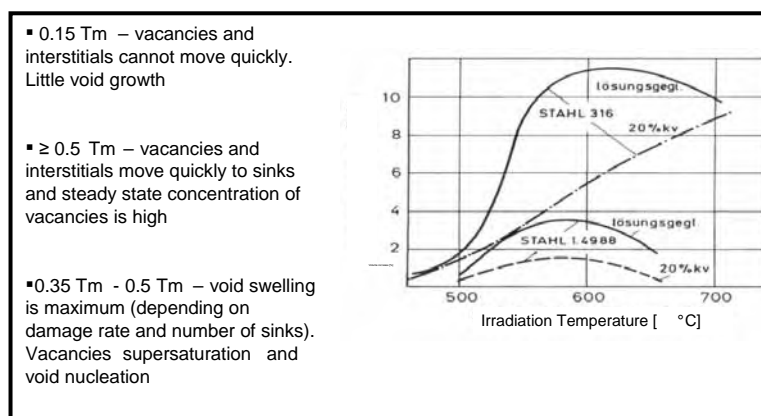
and the void swelling can be driven by vacancy supersaturation (in this temperature range the thermal equilibrium of vacancies is not that high). Void swelling should be the highest at this intermediate temperature range (depending obviously also on damage rate and number of sinks).

At high temperatures the vacancies and the interstitials move quickly to sinks and the steady state concentration of vacancies remains low. In addition, the thermal equilibrium of vacancies increases with temperature so that the vacancy supersaturation that provides the driving force for void nucleation is much reduced at high temperatures.

Moreover, void formations have also been observed under damage rate, temperature and sink density conditions at which vacancy supersaturation does not occur. In these conditions void nucleation and stabilisation occurs at gas atoms. In particular, He produced from transmutation can be effective in aiding void nucleation.

Figure 4 summarises the void swelling as a function of temperature.

Figure 4: Void swelling as a function of temperature; peak swelling occurs between 500°C and 600°C [2]



Irradiation-induced creep of austenitic steels

Irradiation creep is caused when external non-hydrostatic stresses are applied during irradiation.

The first experiments made evident an enhanced creep of austenitic steels under constant load in a fast neutron irradiation field and showed that in the load range below 150 MPa the irradiation creep has a linear relation with external applied stress and is only weakly dependent on the temperature and increases with neutron fluence. The creep mechanism that best explains this behaviour is stress-induced preferential absorption (SIPA). One feature of SIPA is that the absorption of defects at existing dislocations depends upon their orientation with respect to external stress and therefore causes a macroscopic creep strain. The origin of the SIPA mechanism is the elastic interaction of a point defect with the dislocation. The magnitude of this interaction is quadratic in the total strain field. If external stress is applied in addition to the strain field of the dislocation, this superimposed strain field leads to interaction energies which depend on the type and orientation of the dislocation. In this respect, a group of SIPA mechanisms can be observed, where interstitials are preferentially absorbed by dislocations which have a certain orientation with respect to the imposed external stress. In this way, a preferential gliding of the dislocation can occur, which induces the creep of the material.

The SIPA creep can be expressed in first approximation as $\epsilon_{cr} \sim \text{SIPA} \cdot \phi t \cdot \sigma$, where SIPA is a term expressed in $\text{MPa}^{-1} \cdot \text{dpa}^{-1}$; ϕt = dose (dpa); σ = applied external stress. A more

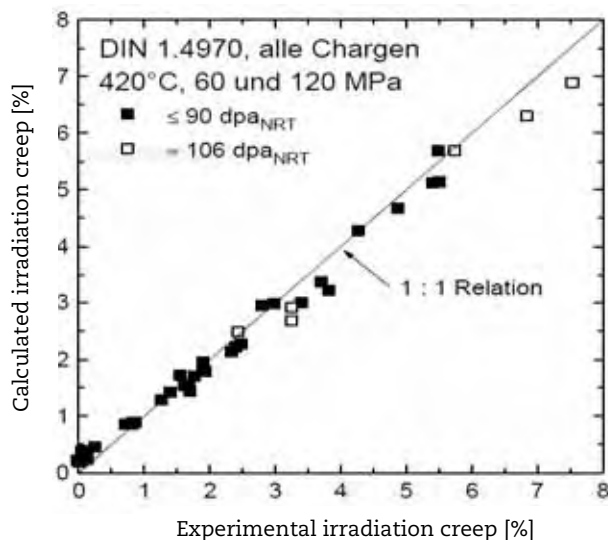
complex description of the SIPA term, where concentrations of dislocations and loops as well as bias factors are considered, can be found in reference [5].

By comparing measured irradiation creep deformations and expected values according to the SIPA model it turned out that the SIPA mechanism accounts for a substantial fraction of irradiation creep deformation at moderate neutron fluence and for $T > 450^\circ\text{C}$. However, the model underestimates experimental data at high doses [6]. Under this condition a further mechanism contributes essentially to the irradiation creep. To explain this mechanism a correlation between swelling and irradiation creep has been introduced. The mechanism which includes dislocation glide (climb enabled glide) as a further strain contribution is considered in these cases (i.e. creep rate increases at the onset of swelling). These models of irradiation creep by climb-enabled glide of dislocation require that the net flux of interstitial into dislocations corresponds to the net vacancy flux into other sinks, e.g. voids. Through the net flux of interstitials to dislocations, these can be solved by glide-obstacles more easily. This mechanism is called I-creep. Gittus [7] has defined a further creep strain term as, $I \cdot \varepsilon_{Sw} \cdot \sigma$ where I is expressed in (MPa^{-1}) ε_{Sw} is the total strain due to swelling. In summary, real irradiation creep can be expressed with the two terms SIPA (independent from swelling) and I-creep (swelling dependent):

$$\varepsilon_{cr}(\sigma, \phi t) = \text{SIPA} \cdot \phi t \cdot \sigma + I \cdot \varepsilon_{Sw}^{tot}(\sigma, \phi t) \cdot \sigma^n$$

In Figure 5, the experimental results of apparent irradiation creep are compared with the calculated one. The irradiation experiments have been conducted on the austenitic steel 1.4970 at different temperatures and with a maximum dose up to 106 dpa. More details on the irradiation experiments can be found in reference [8].

Figure 5: Comparison between the experimental and the calculated irradiation creep



Note: The SIPA and I factors of the equation above have been experimentally evaluated [8]. DIN 1.4970, all doses 420°C, 60 and 120 MPa are indicated inside the figure.

Finally, it should be pointed out that in the higher temperature range a transition from irradiation creep to thermal creep should occur until thermal creep is predominant. Under these conditions, an accelerated thermal creep under irradiation has been observed as well.

Improvement strategies for the austenitic steel 1.4970

To improve the performance of the austenitic steel 1.4970, two approaches have been followed, namely the optimisation of the thermo-mechanical treatment and the optimisation of the chemical composition. The main issue that was addressed was the mitigation of void swelling. In order to mitigate swelling, the metallurgical variables which can be addressed are:

- **Dislocation density:** In the absence of preferential sinks for interstitials there should be no void growth; therefore, a material with no dislocation should not swell. At the other extreme, a very high dislocation density will provide so many sinks for vacancies that the vacancy super-saturation will remain too low for void nucleation and growth. A high dislocation density can be obtained through cold working. Indeed, it has been shown that cold working extends the incubation period as a function of dose prior to the onset of linear swelling. However, as soon as linear swelling starts at higher dose, the swelling rate as a function of dose is no longer controlled by the initial dislocation density.
- **Grain size:** A very fine grain size should provide resistance to swelling because the grain boundaries will act as a sink for point defects. If the grain diameters are sufficiently small, the vacancy concentration in the grain interiors will remain too low for void nucleation.
- **Composition:** The void swelling should be inhibited by the addition of minor elements that bind either vacancies or interstitials sufficiently strongly to reduce effective mobility. The reduced mobility would prevent the defects from reaching sinks, thereby promoting recombination. Moreover, the role of insoluble gas in void nucleation suggests that swelling may be reduced by preventing introduction or production of gas atoms. However, the production of He due to transmutation reactions cannot be avoided.

As far as the effect of composition is concerned, the effect of several minor elements such as Si, Ti, Mo, C, P, B on the austenitic steel 1.4970 has been investigated. Hereafter, as examples, the effects of Si and Ti are discussed.

It has been shown that an increase in Si content increases the incubation dose to swelling but has no influence on the swelling rate. These phenomena could be explained by the fact that the increase in Si content induces an increase of vacancy mobility and therefore reduces void nucleation rate. This yields the increase incubation dose and irradiation creep is also delayed by this element. But this mechanism only works if Si is dissolved in the steel matrix. Swelling starts when the amount of dissolved Si is reduced under a certain amount. During irradiation Si precipitates as coherent γ' (Ni_3Si), which can be apparently re-dissolved, allowing the presence of Si in the matrix. However, with the increase in irradiation dose the non-coherent G-phase (NiSi , $\text{Ni}_{16}\text{Si}_7\text{Ti}_6$) precipitates and Si depletion from the matrix occurs [8].

The effect of Ti has been explained by considering a synergistic effect of Ti and C. For Ti content in the order of 0.3 wt.% (for a given C content of 0.1%) finely dispersed TiC precipitates are dynamically re-dissolved during irradiation with the effect of freeing C atoms which can trap vacancies, but the diffusion of C to the grain boundaries is prevented. This mechanism is responsible for reducing the swelling rate with dose. However, the mechanism has no effect on the incubation dose for swelling. If all C atoms are free or are completely bound to Ti (over-stabilisation), this mechanism is not observed. Therefore, the best swell resistance can be observed only if a slight under-stabilisation is achieved, i.e. slight under-stoichiometric relation between Ti and C.

The combination of high Si content with slight under-stabilising Ti content has the double effect of increasing the incubation time and reducing the swelling rate [2] [8].

Present experience for high burn-up and transmutation systems

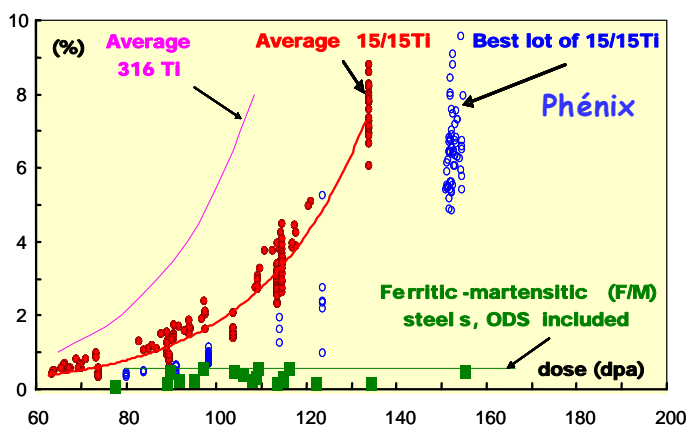
The R&D activities on the 1.4970 steel have been extended from the SNR300 project to the EFR project. The alloy AIM 1 selected for EFR cladding has a composition similar to the 1.4970 mod. [2]. For Generation IV high burn-up reactors and the transmutation systems as reference cladding materials 9Cr F/M steels, ODS and austenitic steels are under consideration.

In view of the large amount of data available, austenitic steels are good candidates to be used as clad material for the first core of prototypes and experimental systems (see e.g. in Europe the ASTRID [9] and MYRRHA [10] designs). However, the lifetime of AIM 1, as explained before, is limited by the swelling and irradiation creep. For the Pb (and Pb alloys)-cooled systems, austenitic steel has a further limiting feature related to its corrosion resistance in this coolant environment [11].

However, it is evident that there could be further “room” for improvement of the austenitic steel to achieve the goals of the high-burn-up and deep waste transmutation reactors as envisaged at present. These improvements can be obtained with a further optimisation of the steel composition to promote a higher delay of the incubation dose to swelling and have a higher reduction of the swelling rate with dose. As for improvement of corrosion resistance, this could be achieved by the development of corrosion protection barriers.

An alternative to this approach is to work on materials which have already a high incubation time for swelling and a low swelling rate. These materials are e.g. the oxide dispersion-strengthened high Cr steels (ODS). Indeed, Figure 6 shows the swelling behaviour of these steels compared to the best lot of austenitic steel.

Figure 6: Swelling of austenitic steels compared to F/M and ODS steels [12]



In the next paragraph, the advantages and challenges for the development of ODS steels will be discussed. The objective is to identify key issues that are needed to elevate this material to nuclear grade material for fast reactor applications.

Advantages and challenges of ODS

Some key advantages of ODS steels are listed hereafter:

- High fuel burn-up can be potentially reached since this steel shows quite good dimensional stability at high fast neutron doses.

- The good dimensional stability opens the way to tighter bundles in SFRs and to a decrease of the sodium flowing in the S/A (favourable feature in order to reduce the sodium-void reactivity coefficient).
- Potentialities to increase operational temperature above 700°C can be envisaged since the creep-to-rupture resistance of this steel can be improved through the dispersion of fine oxide particles.
- The corrosion resistance in HLM should be quite good, since there is no Ni in the steel alloyed. Notably, Ni has high solubility in liquid Pb. However, corrosion resistance can be ensured on these materials by alloying elements as Al or by developing ad hoc corrosion resistant barriers.
- Finally, good acceptable compatibility with fuel and corrosion resistance against fission gas product could be expected.

In order to develop, qualify and verify nuclear grade ODS steels some tough challenges should be tackled. These challenges are related for instance to:

- optimisation of composition, fabrication, manufacturing and welding;
- characterisation and qualification/validation programme in terms of irradiation, fuel and coolant compatibility, fretting;
- standardisation of the materials.

It seems evident that an analysis is required to assess what are the needed efforts and time-line until ODS steels are at a maturity level for fast reactor applications. It is therefore necessary to evaluate the experience available today on this type of material, the experimental and theoretical tools available for materials qualification and to define the qualification and validation programme needed. In the next paragraph an attempt at a qualification/validation programme will be considered. The focus has been placed on the irradiation effects, since irradiation experiments are normally those requiring the most important effort and significant time length.

Future characterisation and validation programme

Given the identified challenges on ODS steels and considering the features of the qualification and validation programme for cladding materials that were set up in the past, it is justified to make an analysis of what are the necessary steps, time-frame and effort in order to produce nuclear grade ODS for high burn-up and transmutation fast neutron reactors.

In this context, assuming that an optimisation (in terms of basic composition, fabrication route and manufacturing items) would be available, the most challenging aspect for the successive qualification programme is the set-up of the irradiation experiments to address:

- screening of materials in different temperature field and neutron fluencies and defining different combination fuel/clad compositions;
- special problems as e.g. experiments with artificially defected pins for safety;
- evaluating pin bundles with original dimensions having different compositions in terms of clad and fuel;
- evaluating one/more fuel assemblies with same specification to confirm statistics of experimental results;
- simulating operational and mild overpower transients as e.g. at reactor start-up or at load-follow-operation and off-normal operational conditions;
- simulating accident conditions e.g. in case of core disruption;

- loading part of a core with selected sub-assembly to show validity of the concept;
- complete loading of a core to confirm validity of the concept.

It is remarkable that some phenomena, e.g. swelling have been observed and investigated only after experimental irradiation tests.

The understandings of these phenomena have been based on metallurgical and microscopic investigations and various mechanisms (sometimes also contradictory among them). Semi-empirical physical models have also been proposed.

It would be of interest to assess the state-of-the-art of novel physical models and computational tools in order to predict materials behaviour under extreme conditions and to support the materials development programme. The materials development programme would here include optimisation of fabrication procedures, chemical composition and thermo-mechanical treatments.

Conclusion

If ODS steels are considered a promising option for clad materials for future high burn-up and transmutation fast reactors, an important R&D programme will be needed. This programme should address all issues related to optimisation (fabrication, manufacturing, composition, etc.) of ODS. Moreover, an important qualification and validation programme including irradiation experiments would also be needed. In addition, the R&D programme should make use of physical and mathematical models available in order to evaluate experimental facilities (i.e. irradiation facilities) available and to define time-frame and efforts needed.

However, when planning such programmes, it would be important to revisit the numerous engineering-relevant reactor irradiation experiments that have been conducted on e.g. various austenitic steels and under different irradiation conditions. It would be interesting to know how this past experience can be used to optimise the future programme. In particular, questions like:

- Is such an extensive characterisation and validation programme, as described in the previous section, fully needed today?
- Are there irradiation facilities available to conduct an extensive irradiation programme (both in steady state and under transient conditions)?
- Are general results that can be used from past experience sufficient?
- Can modelling help in optimising / reducing the number of experiments?

The answer to these questions, together with a careful planning of the R&D programme (where joint and/or shared programmes among different laboratories can create synergistic effects thus helping in optimising time frames and efforts) might help in obtaining suitable materials within the development schedule envisaged for future fast reactor systems.

Acknowledgements

The authors would like to thank H.J. Bergmann, W. Dietz, K. Ehrlich, G. Mühling and M. Schirra, for their preparation of a dedicated report on the Din 1.4970 development.

References

- [1] Generation IV International Forum Annual Report (2007), <http://www.gen-4.org> and the Sustainable Nuclear Energy Technology Platform (SNETP) www.snetp.eu.

- [2] H. J. Bergmann, W. Dietz, K. Ehrlich, G. Mühling and M. Schirra (2003), FZKA Report 6864, June 2003.
- [3] W. Marth, M. Koehler (1993), *Energy* Vol. 23 No. 78, 593.
- [4] P. J. Maziasz (1993), *J. Nucl. Mater.* 205, 118.
- [5] P. T. Heald *et al.* (1975), *Philos. Mag*, 29, 1075.
- [6] K. Ehrlich (1981), *J. Nucl. Mater.* 100, 149.
- [7] W. G. Gittus (1972), *Phil. Mag.* 25, 345.
- [8] R. Hübner (2000), FZKA Report 6372.
- [9] D. Verwaerde, J.-P. Serpantié, J. Rouault (2009), *Proceedings of FR conference 2009*, Kyoto, Japan, December 7, 2009.
- [10] <http://myrrha.sckcen.be/>
- [11] G. Benamati, C. Fazio, H. Piankova and A. Rusanov (2002), *J. Nucl. Mater.* 301 (1) 23-27.
- [12] J.-L. Seran *et al.* (2006), IAEA Technical Committee Meeting on Fast Reactors.

Advances in the development of core and out-of-core structural materials for sodium-cooled fast reactors

M.D. Mathew, T. Jayakumar and Baldev Raj
Indira Gandhi Centre for Atomic Research, India

Abstract

Materials play a crucial role in achieving commercial success with sodium-cooled fast reactor (SFR) technology. Fast reactor components operate at high temperatures under complex loading conditions. The clad and wrapper materials of the fuel sub-assembly are also subjected to intense neutron irradiation in service. These materials should therefore be resistant to irradiation-induced void swelling, irradiation creep, irradiation embrittlement and sodium corrosion. Clad materials should also possess adequate thermal creep strength. For economic viability, the target burn-up required for SFRs is about 200 000 MWd/t. Since the fuel cycle cost is strongly linked with burn-up of the fuel, the focus of core structural materials development is to increase the residence time of fuel elements. This has led to the development of advanced austenitic stainless steels and oxide dispersion-strengthened ferritic steels for fuel clad tubes.

Materials for out-of-core high-temperature structural components should have good creep, low cycle fatigue and creep-fatigue interaction properties, weldability, compatibility with liquid sodium coolant and above all, the design data should be available in international codes. Type 316 stainless steel (SS) and its variants have been used in the early SFRs. A low carbon grade of 316 SS alloyed with nitrogen [called 316L (N) SS] is used for structural components of current SFRs. The recent trend is to increase the design life of SFRs from 40 to 60 years and more, hence it is required to develop structural materials that have higher creep and high-temperature fatigue properties. A significant amount of research is currently focused on developing a high nitrogen grade of 316LN SS.

This paper discusses the progressive evolution of clad and out-of-core structural materials and future trends in alloy development towards mature and economical SFR technology. Research work at IGCAR for the development of these advanced materials is highlighted.

Introduction

Commercial success with sodium-cooled fast reactor technology depends largely upon the performance of core structural materials. The clad and wrapper materials of the fuel sub-assembly should be resistant to irradiation-induced void swelling, irradiation creep, irradiation embrittlement and sodium corrosion; clad material should also possess adequate thermal creep strength. Core structural materials for SFRs have evolved continuously over the years, resulting in a substantial improvement in fuel element performance. The first generation materials belonged to 316 SS grade, but reached unacceptable swelling at burn-ups higher than 50 000 MWd/t. Many improvements were therefore made by changes in the chemical composition of major and minor elements and this has led to the development of advanced austenitic SSs such as alloy 14Cr-15Ni-Ti and 14Cr-15Ni-Ti-Si-P. However, these materials are also unacceptable beyond a burn-up of 150 000 MWd/t. 9-12% Cr ferritic-martensitic steels are regarded as the long-term solution for SFR core structural materials. Though these alloys have excellent swelling resistance to doses even up to 200 000 MWd/t, their creep resistance decreases drastically above 823 K. Thermal creep strength of F-M steels can be improved by dispersion strengthening using nanosized yttria particles.

Criteria which are considered in the selection of materials for out-of-core structural components of SFRs are (i) high-temperature mechanical properties, (ii) compatibility with sodium coolant, (iii) availability of design data, (iv) ease of fabrication, (v) international experience and (vi) cost. Austenitic stainless steel type 316 SS has been the preferred choice for structural components of SFRs. As a SFR structural material, 316 SS has evolved continuously. A low carbon grade of 316 SS-alloyed with nitrogen [called 316L (N) SS] is the preferred material for structural components of current SFRs. In order to increase the design life of SFRs from 40 to 60 years and more, it is necessary to develop structural materials that have superior creep and high-temperature fatigue properties. A significant amount of research is being carried out on developing 316LN SS with high nitrogen content.

Core structural materials

Austenitic SS

For the fast breeder test reactor (FBTR) at Kalpakkam, which has been in operation since 1985, twenty percent cold worked type 316 SS has been used as the clad and wrapper material. Since the reactor has been operating at a lower temperature (<350°C), it has been possible to achieve a record burn-up of 165 000 MWd/t using 316 SS. For the initial cores of the 500 MWe prototype fast breeder reactor (PFBR) nearing completion of construction, the material chosen for clad and wrapper tubes is a 20% cold worked 14Cr-15Ni-Ti stabilised austenitic SS, known as alloy D9. The target burn-up of fuel is 100 000 MWd/t. Thermal creep properties of alloy D9 clad tubes have been studied at various temperatures. Creep deformation of alloy D9 occurred at a much lower rate as compared to 316 SS clad tubes [1]. The minimum creep rates of alloy D9 clad tubes were nearly two orders of magnitude lower than those of 316 SS clad tubes [Figure 1(a)]. The creep rupture lives of alloy D9 were also markedly longer than those of 316 SS [Figure 1(b)]. The improved creep resistance of alloy D9 clad tubes will be beneficial in increasing the fuel burn-up in PFBR.

For future cores of PFBR, it is envisaged that a material of lower swelling will be used so that fuel burn-up of about 150 000 MWd/t can be realised. To this end, a modified composition of 14Cr-15Ni-Ti stabilised stainless steel designated as IFAC-1 is being developed by modifying the amounts of the minor elements titanium, silicon and phosphorous, which have a strong influence on the void swelling of austenitic stainless steel. The influence of these elements on thermal creep properties has been systematically studied by varying titanium in the range of 0.16 to 0.30 wt.%, silicon in the range of 0.75 to 0.95 wt.% and phosphorous in the range of 0.025 to 0.04 wt.%. In cold worked alloy D9, fine TiC precipitates form preferentially on the intra-granular

dislocations which retard recovery and recrystallisation of the cold worked structure, thereby imparting elevated temperature strength to alloy D9. The study showed [2] that maximum creep rupture strength can be realised by limiting Ti content in the range of about 0.25 to 0.29 wt.%, as shown in Figure 2(a). Figure 2(b) shows the influence of titanium on the ion irradiation- induced void swelling of alloy D9I. Increasing the phosphorous content was found to reduce peak swelling (%) and peak swelling temperature in IFAC-1.

Figure 1: Comparison of alloy D9 and 316 SS clad tubes with respect to (a) rupture life and (b) minimum creep rate

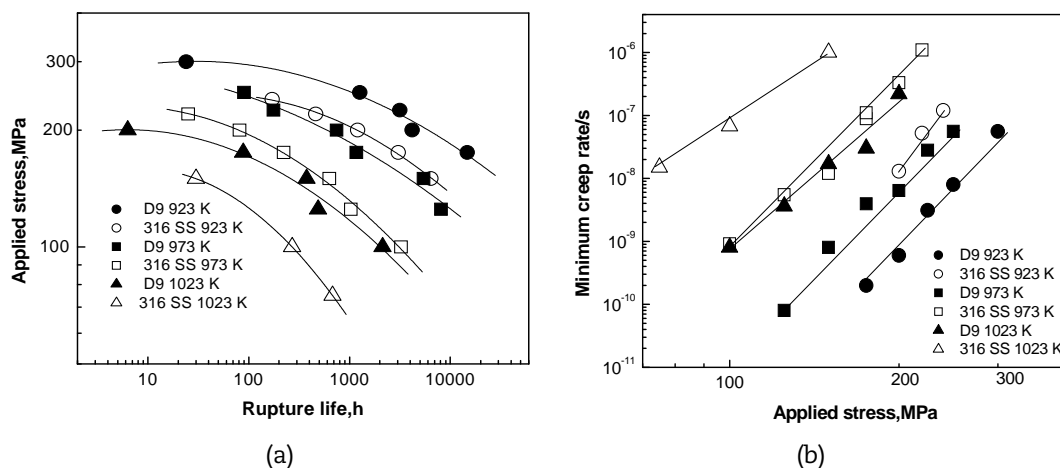
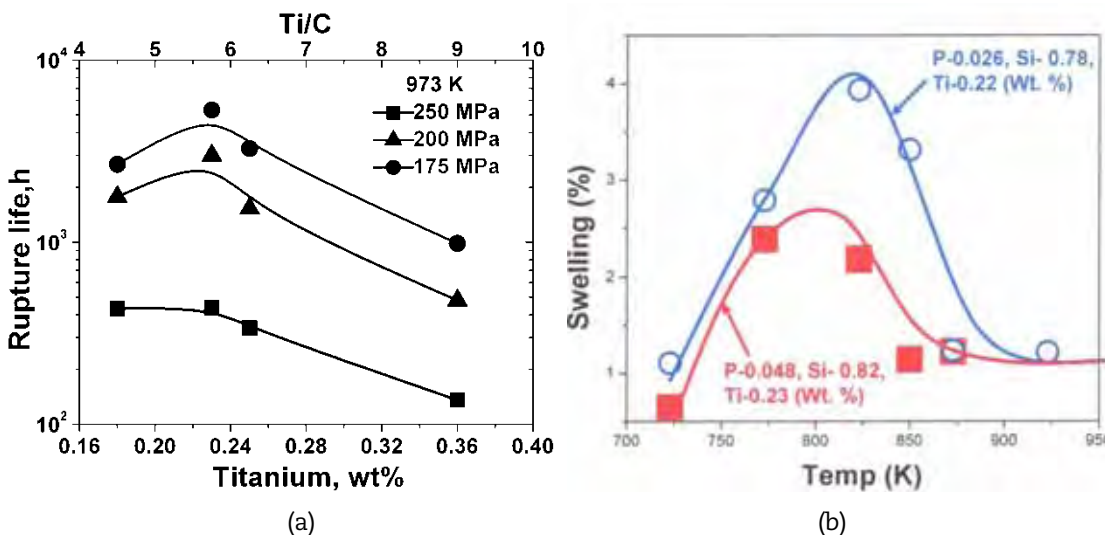


Figure 2: (a) influence of titanium on creep rupture life of IFAC-1 at 973 K and (b) influence of phosphorous on void swelling behaviour of IFAC-1



Oxided dispersion-strengthened ferritic-martensitic steels

9-12% Cr ferritic-martensitic (F-M) steels are considered to be the long-term solution for SFR core structural materials as these alloys have excellent swelling resistance to doses up to 200 000 MWd/t. They are therefore very attractive as wrapper materials since

creep strength is not a primary requirement due to the lower operating temperatures and negligible stresses experienced by the wrapper tubes. The creep resistance of F-M steels decreases drastically above 823 K and these steels are hence not suitable as a cladding material. The thermal creep resistance of F-M steels can be improved by dispersion strengthening using fine yttria particles. Manufacture of oxide dispersion-strengthened ferritic steel tubes is a challenging task. 9 Cr-ODS steel of composition (wt%) Fe-9Cr-0.1C-2W-0.2Ti-0.35Y₂O₃ is being developed as a future clad material for the Indian fast reactor programme. A complex powder metallurgy route consisting of 11 pilger passes with 3 intermediate annealing and a final normalising and tempering heat-treatment was adopted to produce clad tubes of 6.6 mm outer diameter and 0.45 mm wall thickness. The finished tube has a tempered martensitic microstructure with Y-Ti-O nano-complex dispersoids with an average size of less than 10 nm. The clad-tubes are characterised for their microstructure, mechanical properties and irradiation stability of the dispersoids. The tensile and creep strength of the ODS tubes have been substantially increased compared to the properties of Mod. 9Cr-1Mo steel, but are still below typical internationally reported data [3] [4].

Out-of-core structural materials

316 SS and 316(N) SS

For the structural components of FBTR, a modified grade type 316 SS has been used as the principal structural material. The specification for nuclear grade SS differs from the conventional grade of type 316 SS with respect to the following: (i) chemical composition of each of the elements is controlled within close limits to avoid scatter in mechanical properties, (ii) on the carbon content, a lower limit is also specified for better mechanical properties, (iii) a higher degree of cleanliness is specified through lower limits on elements such as S, P and Si and the inclusion content, (iv) lower limits on Ti, Nb, Cu and B from weldability considerations, (v) cobalt content is limited to lower levels from considerations of induced radioactivity and (vi) a finer grain size for ease of ultrasonic inspection of the plates. Despite stringent specifications, the alloy displayed pronounced heat-to-heat variations in the creep rupture properties [5] at 823, 873 and 923K with rupture life as long as 1 40 000 h [6]. The difference in the creep properties resulted from variations in the amounts of minor alloying elements (carbon 0.048-0.057 wt%, nitrogen 0.031-0.045 wt%, boron 0.005-0.015 wt%) and grain size (0.035-0.070 mm); highest creep rupture strength was associated with the heat with the lowest grain size and highest amounts of interstitial elements N, C and B although within the specified ranges. Nuclear grade 316 SS displayed strong microstructural stability over long periods of creep exposure as depicted by the linear variation of the stress dependence of creep rupture life plots shown in Figure 3 for rupture data up to 140 000 hours. This is attributed to the fine scale precipitation of chromium-rich M₂₃C₆ type of carbides on grain boundaries [Figure 4(a)] as well as on dislocations in the intra-granular regions [7] [Figure 4(b)]. The fine precipitates on dislocations prevent the recovery of dislocation substructure, leading to avoidance of a sigmoidal relationship between stress and rupture life. Fine carbides on grain boundaries reduce grain boundary sliding and hence the formation of inter-granular creep cracks and cavities. Understanding the microstructural changes, dislocation evolution and damage mechanisms during long-term creep deformation of 316 SS made possible the selection of a nitrogen-alloyed low carbon (0.02-0.03 wt.%) version of this steel called 316L (N) SS for the high-temperature structural components of the 500 MWe PFBR. In 316(L) N SS, nitrogen is specified in the range of 0.06 to 0.08 wt.%, in order to compensate for the loss in strength due to the reduced carbon content. Although 304L(N) SS and 316L(N) SS are specified by ASME with nitrogen in the range of 0.10 to 0.16 wt.%, for PFBR, nitrogen content is limited to 0.08 wt.% in view of the improved weldability, availability of data in the RCC-MR design codes and for minimising scatter in mechanical properties, which helps in realising better detailed design analyses. Figure 5(a) shows the variation of steady state creep rate of type 316LN SS with applied stress. The creep rates of 316 SS are also superimposed in

Figure 5(a) for comparison. An order of magnitude decrease in steady state creep rate has been observed in type 316LN SS due to addition of about 0.07 wt% nitrogen. A significant increase in creep rupture life has also been obtained [8] [Figure 5(b)].

Figure 3: Influence of test temperature on long-term creep rupture strength of 316 SS

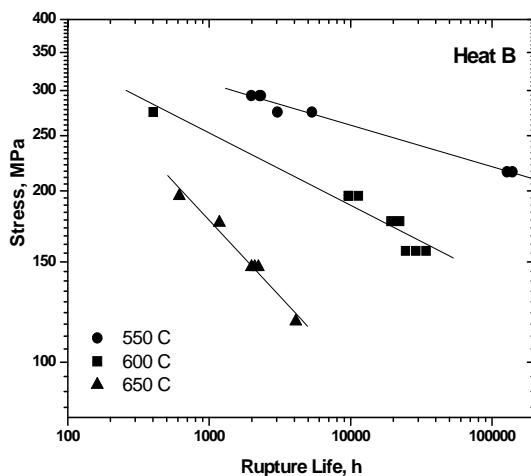
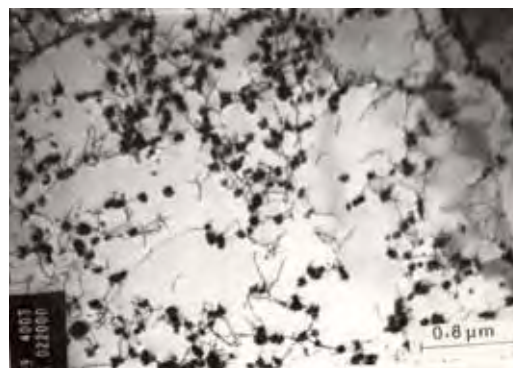


Figure 4: Precipitation of chromium-rich $M_{23}C_6$ type of carbides on (a) grain boundaries (after 22 100 hours of creep at 873 K) and (b) on dislocations in the intra-granular regions (after 8 300 hours at 823 K)

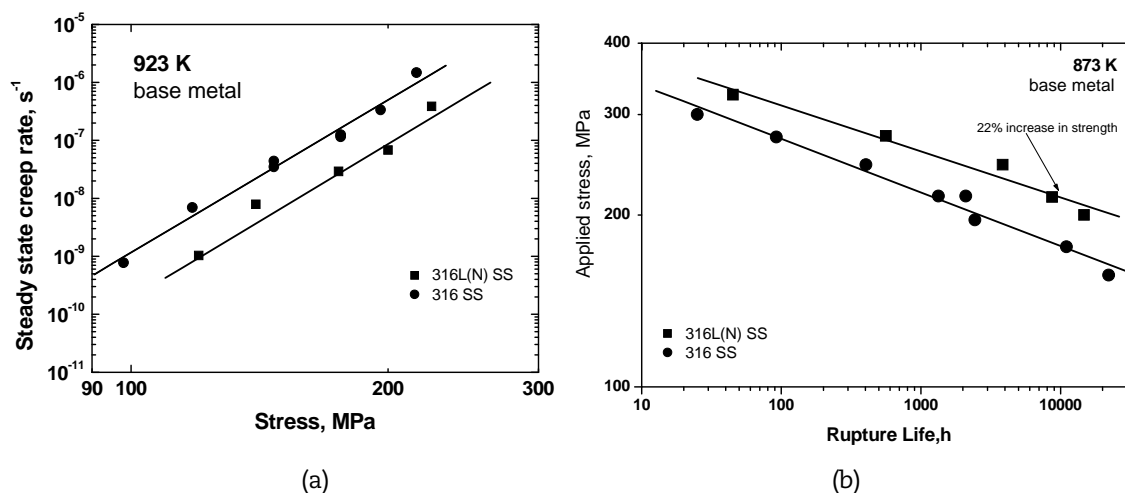


(a)



(b)

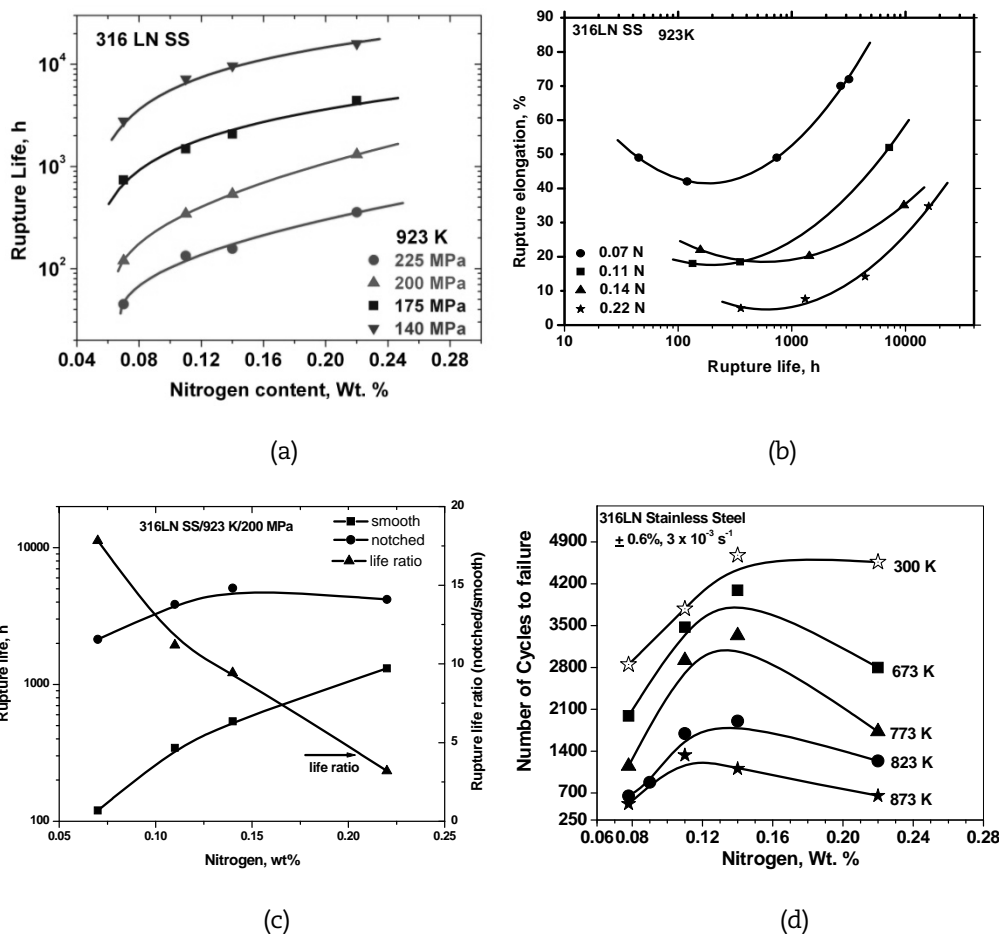
Figure 5: Influence of nitrogen on creep properties of 316L (N) SS
(a) steady state creep rate and (b) rupture life



High nitrogen grades of type 316LN SS

Currently SFRs are designed for 40 years of life. In India, efforts are underway to design six commercial fast reactors (CFRs) with a design life of 60 years in order to reduce the cost of electricity produced. Studies are therefore being carried out to develop a high nitrogen alloyed 316LN SS with superior tensile, creep and low cycle fatigue properties as compared to 316L (N) SS containing 0.06-0.08 wt.% nitrogen. The influence of nitrogen on the creep behaviour of 316LN SS has been studied at nitrogen levels of 0.07, 0.11, 0.14 and 0.22 wt.% by keeping the rest of the composition identical [9] [10]. The carbon content in all these heats was 0.03 wt.%. Creep rupture strength increased substantially with increasing nitrogen content [Figure 6(a)]. Rupture life increased almost 10 times by increasing nitrogen content from 0.07 wt.% to 0.22 wt.%. The increase in creep strength with nitrogen is associated with a decrease in steady state creep rate and an increase in the time spent in primary, secondary and tertiary stages. The beneficial effects of nitrogen arise due to the higher solubility of nitrogen in the matrix as compared to carbon, reduction in stacking fault energy of the matrix and introduction of strong elastic distortions in the crystal lattice, giving rise to strong solid solution hardening. Nitrogen also influences the diffusivity of chromium in austenitic stainless steels, leading to retardation in the coarsening of $M_{23}C_6$ thereby improving the grain boundary strength. Rupture ductility decreased with an increase in nitrogen content and increased with an increase in rupture life; a minimum in ductility was observed, which is a typical trend shown by austenitic SSs [Figure 6(b)]. It was found that the notch sensitivity of the material decreased with an increase in nitrogen content; typically the notched-specimen rupture life increased by a factor of 18 in the steel containing 0.07 wt.% ,which decreased to a factor of just 3 in the steel containing 0.22 wt.% nitrogen, as shown in Figure 6(c). Low cycle fatigue studies in the range 300-873 K showed that the beneficial effect of nitrogen on fatigue life generally increased as nitrogen content increased; fatigue life reached a maximum value [11] between 0.11-0.14 wt% nitrogen at temperatures above 673 K [Figure 6(d)]. Manifestations of DSA have been observed at all the nitrogen contents in the temperature range 673-873 K. It is suggested that the optimum level of nitrogen in 316LN SS lies in the range of 0.12-0.14 wt.% in terms of creep rupture strength, ductility, notch sensitivity and fatigue strength.

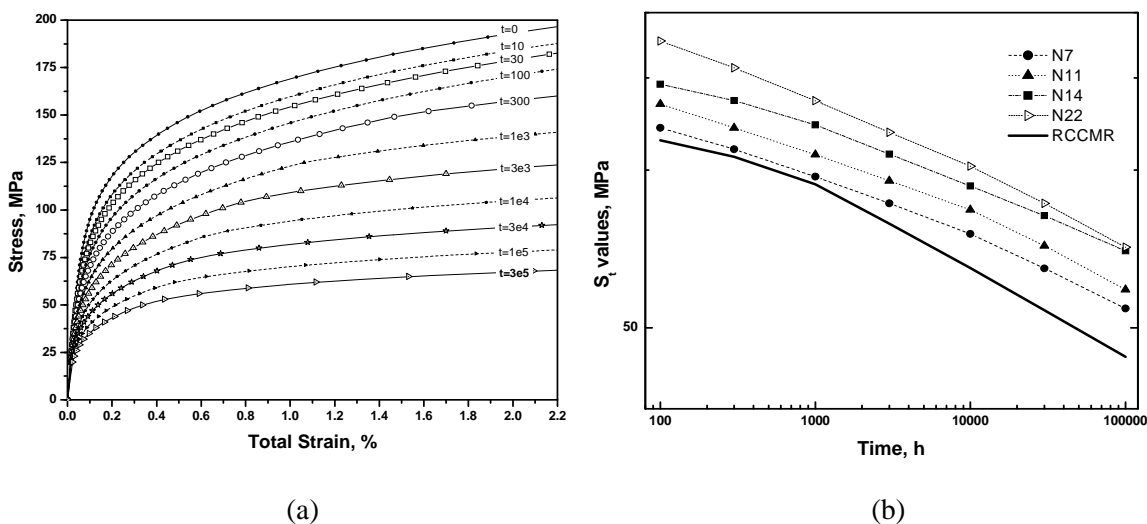
Figure 6: Effect of nitrogen in 316LN SS on (a) creep rupture life, (b) rupture ductility, (c) notch sensitivity and (d) fatigue life



High-temperature design curves for high nitrogen grades of 316LN SS

The large amount of creep data generated on the high nitrogen grades of 316LN SS has been analysed to generate the time dependent design curves. RCC-MR code defines time dependent allowable stress (S_t) as the least value among (i) 2/3 of the minimum stress inducing fracture, (ii) 80% of the minimum stress leading to the onset of tertiary creep and (iii) 100% of the minimum stress inducing 1% total strain (elastic strain+ plastic strain + creep strain), which is determined from the isochronous stress-strain curves. These curves were generated using Young's modulus, average tensile hardening rule and creep strain laws. The detailed analyses for the determination of isochronous and S_t curves are described elsewhere [12]. The isochronous stress-strain curves for the steel containing 0.14 wt.% nitrogen are shown in Figure 7(a) for various time durations up to 300 000 hours. Comparison of the isochronous stress-strain curves showed that the material containing 0.14 wt.% nitrogen has a creep strength higher than the steels with 0.07 and 0.11 wt.% nitrogen. Figure 7(b) shows the influence of nitrogen content on the time dependent allowable stress values. RCC-MR S_t curve for 316L(N) SS containing 0.07 wt.% nitrogen is superimposed in Figure 7(b). It is seen that the S_t values increase as the nitrogen content increases and the values are higher than the corresponding RCC-MR values.

Figure 7: (a) isochronous stress strain curves of 316LN SS containing 0.14 wt.% nitrogen and (b) influence of nitrogen content on the S_t curves of 316LN SS



Summary

Materials for core and structural components of SFRs are evolving gradually and continuously. For the clad materials, the need for resistance to swelling up to a burn-up of 200 000 MWd/t and more, coupled with good thermal creep strength is driving the research for advanced materials. For the structural materials, high-temperature creep, low cycle fatigue and creep-fatigue properties are the major requirements. Clad and wrapper materials which allow very high burn-up and structural materials which can be used for the design of components for 60 years and more, are required in order to make SFRs economically competitive with other sources of electrical energy.

References

- [1] S. Latha, M.D. Mathew, P.Parameswaran K. Bhanu Sankara Rao and S.L. Mannan (2008), Thermal creep properties of alloy D9 stainless steel and 316 stainless steel fuel clad tubes, *International Journal of Pressure Vessels and Piping*, 85. 866.
- [2] S. Latha, M.D.Mathew, P.Parameswaran, M.Nandagopal, K. Bhanu Sankara Rao and S.L.Mannan (2008), Effect of titanium on the creep deformation behaviour of alloy D9I stainless steel, *Proceedings of the 5th international conference on Creep, Fatigue and Creep-Fatigue Interaction (CF-5)*, Kalpakam, 24-26 September 2008.
- [3] National Institute for Materials Science (2007), NIMS Creep Data Sheet, No. D-1, Japan.
- [4] S. Ukai, S.Mizuta, M.Fujiwara, T.Okuda and T.Kobayashi (2002), Development of 9Cr-ODS Martensitic steel claddings for fuel pins by means of ferrite to austenite phase transformation, *J. Nuclear Science and Technology*, 39.778.
- [5] M.D. Mathew, S.Latha, G.Sasikala, S.L.Mannan and P.Rodriguez (1988), Creep properties of three heats of type 316 SS for elevated temperature nuclear applications, *Nuclear Technology* 81.114.
- [6] M.D. Mathew, S.Latha, G.Sasikala, S.L.Mannan and P.Rodriguez (1989), Long term creep behaviour of a modified grade AISI 316 stainless steel in the temperature range 823-923K, *Transactions of the Indian Institute of Metals*, 42(1989), s175.

- [7] M.D. Mathew, M.Sundararaman and S.L.Mannan (1997), Dislocation substructure and precipitation in type 316 stainless steel deformed in creep materials, *Transactions of the Japan Institute for Metals* 38. 37.
- [8] M.D. Mathew, V.S.Srinivasan, U. Kamachi Mudali, B. Raj (2004), Mechanical Behaviour of Nitrogen-bearing Steels, *Monograph on High Nitrogen Austenitic Steels and Stainless Steels*, (Eds.), Narosa Publications, New Delhi, pp.182-204.
- [9] G.V. Prasad Reddy, R. Sandhya, M. Valsan and K. Bhanu Sankara Rao (2008), High temperature low cycle fatigue properties of 316(N) SS weld metals and 316L(N)/316(N) SS weld joints, *Intl. Journal Fatigue*, 30. 538.
- [10] V. Ganesan, M. D. Mathew, K. Bhanu Sankara Rao and B. Raj (2008), Influence of nitrogen on the mechanical behaviour of type 316L SS, *6th European stainless steel conference - science and market*, 10-13 June 2008, Helsinki, Pentti Karjalainen and Staffan Hertzman (Eds.) pp 445-451.
- [11] G.V. Prasad Reddy, R. Sandhya, K. Bhanu Sankara Rao, S. Sankaran (2010), Influence of Nitrogen alloying on Dynamic Strain Ageing regimes in Low Cycle Fatigue of AISI 316LN Stainless Steel, *Procedia Engineering*, 2. 2181.
- [12] J. Ganesh Kumar, M. Chowdary, V. Ganesan, M.D. Mathew, R.K. Paretkar and K. Bhanu (2010), High Temperature Design Curves for High Nitrogen Grades of 316LN Stainless Steel, Sankara Rao, *Nucl. Eng. Design*, 240.1363.

Session VIII

Fundamental Radiation Effects – Helium Effect

Chairs: R. Nanstad, S-H. Chi

Challenges of structural materials for applications in spallation targets of ADS*

Yong Dai

Spallation Neutron Source Division, Paul Scherrer Institute, Switzerland

Abstract

Spallation targets in future accelerator-driven systems (ADS) will use liquid lead-bismuth eutectic (LBE) as the target material. In such spallation targets, structural components in or near the spallation reaction zone will work in an extreme environment with severe irradiation damage induced by high energy protons and spallation neutrons, corrosion and embrittlement induced by flowing LBE and possible high thermal mechanical stresses. As compared to neutron irradiations, irradiation in a spallation target produces not only displacement damage, but also helium and hydrogen at high rates, which can result in more serious embrittlement in structural materials. The corrosion and embrittlement effects of LBE on the structural materials may also result in a strong degradation in the performance of the components. Therefore, it is of critical importance to understand the behaviours of structural materials under such irradiation conditions. To support the R&D of high-power spallation targets, a worldwide effort has been focused on studying the radiation damage effects of high energy protons and spallation neutrons on different structural materials by conducting irradiation experiments in the targets of the Swiss spallation neutron source (SINQ) at the Paul Scherrer Institute (PSI). In the last few years, a large number of specimens irradiated in the SINQ targets have been examined at PSI and at several institutes in Europe, Japan and the United States as well. Significant progress has been achieved in the basic understanding of the radiation effects and a large amount of data has been obtained from the post-irradiation examinations, particularly on ferritic/martensitic (FM) steels and austenitic steel SS 316L. Meanwhile, LBE embrittlement effects on FM steels in irradiated and un-irradiated conditions have been intensively studied at PSI. Not only some important data but also deeper understandings of such phenomena have been obtained. In this presentation, an overview will be given on these results and challenges of materials to be applied in spallation targets of ADS.

* The full paper being unavailable at the time of publication, only the abstract is included.

Hardening and microstructure of neutron- and ion-irradiated Fe-Cr alloys

**Cornelia Heintze¹, Eberhard Altstadt¹, Frank Bergner¹,
Miao Xie¹, Uwe Birkenheuer¹, Mercedes Hernández Mayoral²**

¹ Forschungszentrum Dresden-Rossendorf, Germany, ² CIEMAT Madrid, Spain

Abstract

Understanding the irradiation behaviour of binary Fe-Cr alloys is basic for the optimisation of ferritic/martensitic chromium steels for future applications under conditions of high neutron exposures. In this work, self-ion irradiation with the ion beam scanned over the sample was used in order to simulate neutron damage in Fe-12.5at% Cr. The material irradiated at 300°C up to a damage level of 1 dpa was exposed to isochronal annealing treatments in the range from 300 to 550°C and the indentation hardness was measured as a function of annealing temperature. We have found the presence of two recovery steps. The first one takes place at 300°C, i.e. at irradiation temperature and gives rise to a 45% recovery of the irradiation-induced hardness increase. The second step occurs in the range from 400 to 550°C and gives rise to full recovery. The findings are discussed in terms of the dissolution of hardening features, such as dislocation loops and α' -phase particles. In addition, rate theoretical considerations were used to investigate possible flux effects caused by the pulsed irradiation experienced by the material due to the scanning ion beam. It was found that no significant additional flux effects arise from the pulsing.

Introduction

Ferritic/martensitic Cr-steels are candidate structural materials for application in Generation IV and fusion reactors. Their qualifications for these purposes require experimental characterisation of materials exposed to prototypical environments as well as improved physical understanding [1], which can be achieved by multi-scale modelling in combination with modelling-oriented experiments [2]. The microstructure and mechanical properties of Fe-Cr alloys in the un-irradiated condition and their behaviour under irradiation have been extensively studied in the last decades and a strong influence of Cr on the properties and the irradiation behaviour of Fe-Cr alloys has been observed [3]. In one case [4], the response of the Vickers hardness of neutron-irradiated Fe-15% Cr and Fe-30% Cr to post-irradiation isochronal annealing treatments was used in order to draw additional conclusions about the nature of damage. The irradiation temperature was 127°C. A recovery of the observed irradiation hardening in the range from 400 to 600°C was found.

Due to the well-known advantages, self-ion irradiation has been extensively applied to simulate the damage induced by fast neutrons. Special methods are required to characterise the ion-induced damage, e.g. nanoindentation [5-9], because of the limited penetration depth of the ions. An important issue of the simulation of neutron irradiation by means of ion irradiation is the transferability of the results obtained [10]. Transferability problems may arise both from the parameters of the irradiation itself (e.g. flux) and from the different characterisation techniques (e.g. nanoindentation vs. Vickers hardness).

The present investigation is devoted to the nanoindentation of self-ion irradiated and post-irradiation annealed Fe-12.5% Cr. Post-irradiation annealing treatments of the as-irradiated condition (300°C, 1 dpa) were performed with annealing temperatures ranging from 300°C up to 550°C. The dependence of the indentation hardness on the annealing temperature is discussed.

The Fe-ion beam has been scanned over the sample area of interest during the self-ion irradiation. For a given position at the surface of the specimen, this gives rise to a pulsed mode of irradiation in contrast to an essentially continuous mode for neutron irradiation. As a secondary, but no less important aim of the paper, we have checked by means of simple rate theory arguments, if an additional transferability problem arises because of the pulsed irradiation.

Experimental

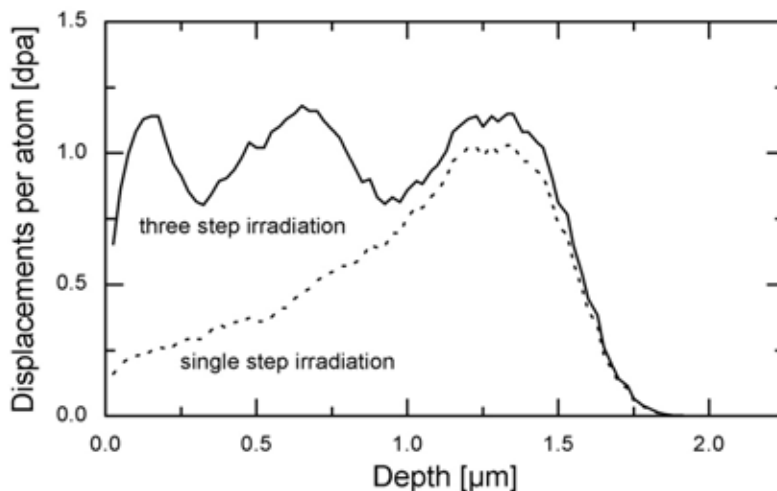
An Fe-Cr model alloy containing 12.5 at% Cr of commercial purity was investigated. The material was provided by SCK-CEN, Mol (Belgium), in the un-irradiated condition. Details about the composition, heat treatment and the characterisation of the un-irradiated material are given in [11].

The specimens were prepared by mechanical grinding and polishing. Ion irradiations were performed with the 3MV-Tandetron accelerator at the Ion Beam Center of FZD, Dresden (Germany). A roughly rectangular damage profile was obtained by applying a three-step irradiation with Fe-ions of different energies as described in [7]. The resulting damage profile calculated by means of the SRIM code version 2006.02 assuming an average displacement energy of 40 eV [12] is shown in Figure 1. To achieve a uniform lateral damage distribution over the specimen area of interest, the ion-beam was scanned over the surface. This procedure results in a locally pulsed mode of irradiation. The irradiations were performed at 300°C up to a fluence of 1 dpa. Depth-sensing nanoindentation was carried out in the load range from 2 mN to 500 mN using a UNAT device (asmec) equipped with a Berkovich indenter. The hardness values for each load

were derived from at least 10 single load-depth curves using the Oliver-Pharr method [13]. Corrections for system stiffness and indenter area function were performed.

The ion-irradiated material was annealed in a vacuum furnace in the temperature range from 300°C to 550°C in steps of 50 K. The annealing time was 1 h for all annealing temperatures. The load dependence of the indentation hardness was measured for the un-irradiated and the as-irradiated material as well as following each annealing step.

Figure 1: Damage profile produced by a three-step irradiation with Fe-ions (solid line) and by a single-step irradiation (dotted line)



Results

Nanoindentation

The load dependence of the indentation hardness for the un-irradiated and the as-irradiated material (300°C, 1 dpa) is shown in Figure 2. The load dependence of the un-irradiated condition shows the well-known indentation size effect, i.e. the indentation hardness increases with decreasing load. For the irradiated material a composite hardness is measured, which results from the hardness of the layer damaged by ion irradiation and the undamaged substrate. The influence of the substrate increases with increasing load, giving rise to a convergence of the load dependencies measured for the un-irradiated and as-irradiated material at high loads. In the present case, significant irradiation-induced hardening of the damaged layer can be observed. Additionally, the load dependence of the indentation hardness is shown for the material ion irradiated and annealed at 300°C for 1 h (Figure 2). It can be observed that there is a partial recovery of the irradiation-induced hardening after annealing.

The residual hardness difference after annealing with the un-irradiated material taken as reference is plotted in Figure 3 as a function of the annealing temperature. Two recovery steps were observed. The first recovery of the irradiation-induced hardening took place at 300°C, i.e. at the annealing temperature equal to the irradiation temperature. We have observed a recovery of about 45 % of the irradiation-induced hardness increase. A second recovery took place at temperatures larger than 400°C, giving rise to full recovery at 550°C.

Figure 2: Load dependence of the indentation hardness for un-irradiated and ion-irradiated (300°C/1 dpa) Fe-12.5at%Cr and of the irradiated material after annealing at 300°C for 1 hour

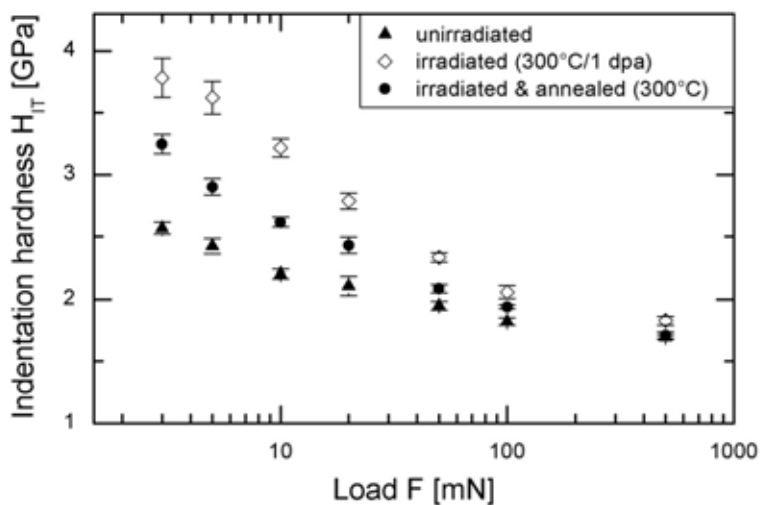
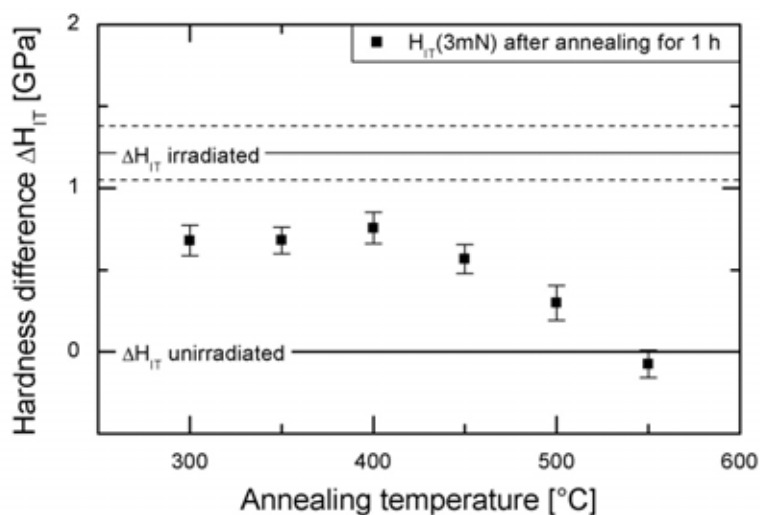


Figure 3: Residual hardness difference after annealing (reference: un-irradiated material) at an indentation load of 3 mN as a function of annealing temperature



Effect of pulsed irradiation

In the past, the irradiation-induced microstructure evolution of iron based materials was mainly discussed under the assumption of a continuous irradiation as is usually the case for neutron irradiation. The question arises whether or not the pulsed irradiation experienced by the material in an ion beam experiment causes additional problems of transferability beyond known flux effects. The actual irradiation can be described in terms of a peak flux during a short pulse of length τ and no flux for the rest of the period T . Here, we introduce the relative pulse width, $\xi = \tau/T$. It is well-known that at low flux the steady-state concentration of vacancies is proportional to the flux while at high flux it only increases like $\phi^{1/2}$. These vacancy concentrations directly enter the mobility of the solute atoms, leading to a flux independent behaviour of the microstructure evolution for a given fluence at low irradiation flux and a flux dependent behaviour ($\phi^{-1/2}$) at high flux. With a value of 0.23×10^{-3} dpa/s for the mean point defect creation rate, $\langle G \rangle$, the above experiments are operating deeply in the flux-dependent regime and the question is what impact the pulsing might have on this non-linear irradiation regime.

For continuous point defect creation rates, G , the solutions $C_x(t)$, $x = i$ (interstitials) or v (vacancies) of the rate equations

$$\frac{d}{dt} C_x = G - k_{vi} C_v C_i - k_x C_x \quad x = v, i \quad (1)$$

for the point defect concentrations reach steady-flux values C_x^{sf} after sufficient time which can directly be related to the applied creation rates [14-16].

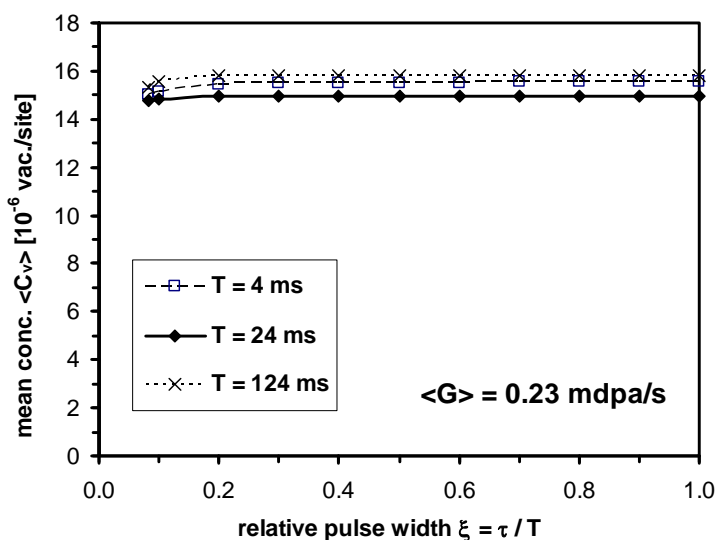
$$C_x^{sf} = \frac{G}{k_x} f\left(\frac{G}{G_{tr}}\right) \quad \text{with} \quad G_{tr} = \frac{k_i k_v}{k_{vi}} \quad \text{and} \quad f(s) = \frac{\sqrt{1+s}-1}{s/2} \quad (2)$$

Here k_x are the decay rates of the point defects at any external sinks (e.g. dislocations or grain boundaries) and k_{vi} is the recombination rate constant. In the case of a periodically pulsed irradiation, the point defect system evolves into a periodic response with steady amplitudes and characteristic mean concentrations, $\langle C_x \rangle = \lim_{t \rightarrow \infty} \frac{1}{T} \int_t^{t+T} C_x(t') dt'$. When solved, the differential Equations (1) for periodic point defect creation rates, $G(T, \xi)$, of various shapes (including the continuous cases for $\xi = 1$) revealed that the basic relation for the flux dependence of the microstructure evolution, Equation (2), can be equally well applied to pulsed beams, i.e.

$$\langle C_x \rangle = \frac{\langle G \rangle}{k_x} f\left(\frac{\langle G \rangle}{G_{tr}}\right) \quad (3)$$

with the same transition creation rate G_{tr} and the same efficiency function $f(s)$ as in Equation (2). The mean concentrations calculated for a given mean flux (or creation rate) are plotted in Figure 4 as a function of ξ for selected values of T . We have found that these concentrations are essentially the same for any value of T and ξ . The experimental situation encountered in the above experiments corresponds to $T = 24$ ms and $\xi = 1/12$.

Figure 4: Mean vacancy concentration $\langle C_v \rangle$ as a function of the period, T and the relative width, $\xi = \tau / T$, for a given mean creation rate $\langle G \rangle$ of 0.23×10^{-3} dpa/s



Discussion

The observed hardening is attributed to the formation of irradiation-induced defects, which were identified as dislocation loops and α' -phase particles in previous works [8] [9] [17]. The formation of dislocation loops with a number density of $1.3 \times 10^{21} \text{ m}^{-3}$ ($\pm 30\%$) and an average diameter of 3.9 nm was found by means of transmission electron microscopy (TEM) in the same ion irradiated material (300°C, 1 dpa) [9]. The formation of α' -phase particles was detected by means of small-angle neutron scattering (SANS) for the same alloy in the neutron irradiated conditions (300°C, 0.6 and 1.5 dpa) with a volume fraction of 4.3 vol% and an average radius of 1 nm reported [17].

The annealing experiment revealed two recovery steps. The first recovery of the irradiation-induced hardening took place at a temperature equal to the irradiation temperature (300°C). This strongly indicates the occurrence of unstable matrix damage (UMD) as introduced by Odette *et al.* [18] in the as-irradiated condition. These authors proposed UMD to include vacancy clusters or possibly mobile interstitial clusters of very small size (< 0.5 nm), which is below the detection limits of both SANS and TEM. It is interesting to note that Suganuma *et al.* [4] did not observe this kind of annealing step. This may be attributed to the much lower flux of about 7×10^9 dpa/s and dpa-level of 0.012 dpa applied in their investigation, but other factors such as lower irradiation temperature and higher Cr level should also be kept in mind.

The second recovery occurred at temperatures higher than about 400°C with full recovery at 550°C. Suganuma *et al.* [4] reported a recovery step in about the same temperature range with complete recovery reached at 600°C for their material. As the irradiation-induced hardening is attributed to the formation of dislocation loops and α' -phase particles (see above) and their interaction with gliding dislocations during plastic deformation, the observed recovery must be connected to the dissolution of those defects or to a change of their character in the direction towards weaker obstacles.

The dissolution of the α' -phase particles would be expected after crossing the boundary of the α - α' two phase region according to the phase diagram. However, the exact position of that boundary in the phase diagram is still under discussion [19] [20]. Shrinkage and dissolution of loops was reported by [21] and [22] for irradiated Fe-Cr alloys

at temperatures of 400 to 500°C and >477°C, respectively. Moreover, [23] has observed that loops of two types of Burgers vectors, $\langle 100 \rangle$ and $\frac{1}{2}\langle 111 \rangle$ co-exist with $\langle 100 \rangle$ -type loops prevailing at higher temperatures and $\frac{1}{2}\langle 111 \rangle$ -type loops prevailing at lower temperatures. The transition temperature between both ranges of dominance was reported to depend on the Cr level [24]. It seems that both α' -phase particles and loops contribute to the observed annealing behaviour in overlapping temperature ranges. Clearly, more work has to be done in order to uncover the detailed mechanisms that control the annealing behaviour.

Conclusions

In this work, self-ion irradiation with the ion beam scanned over the sample was used in order to simulate neutron damage in Fe-12.5at% Cr. We found by means of rate theory arguments that the resulting pulsed irradiation experienced by the material does not cause additional flux effects beyond those known for continuous irradiation. The as-irradiated material was exposed to isochronal annealing treatments and the indentation hardness was measured as a function of annealing temperature. Two recovery steps were observed, one at irradiation temperature and the another one in the range from 400 to 550°C. These recovery steps were compared with reported results and discussed in terms of hardening features. The first step is attributed to the dissolution of so-called unstable matrix damage, whereas the second step, which gives rise to full recovery, can be rationalised by the dissolution of α' -phase particles and dislocation loops.

Acknowledgements

The participation of Vincent Meyer in the experimental work is gratefully acknowledged. The authors would also like to thank Lorenzo Malerba for providing the un-irradiated material.

References

- [1] I. Cook (2006), *Nat. Mater.* 5, 77.
- [2] C. Fazio, A. Alamo, A. Almazouzi, S. De Grandis, D. Gomez-Briceno, J. Henry, L. Malerba, M. Rieth (2009), *J. Nucl. Mater.* 392, 316.
- [3] L. Malerba, A. Caro, J. Wallenius (2008), *J. Nucl. Mater.* 382, 112.
- [4] K. Suganuma, H. Kayano (1983), *J. Nucl. Mater.* 118, 234.
- [5] H. -H. Jin, C. Shin, W.W. Kim (2008), *Solid State Phenom.* 135, 119.
- [6] F. Halliday, A. Almazouzi (2009), *J. Nucl. Mater.* 377, 147.
- [7] C. Heintze, C. Recknagel, F. Bergner, M. Hernández-Mayoral, A. Kolitsch (2009), *Nucl. Instr. Meth. Phys. Res. B* 267, 1505.
- [8] C. Heintze (2010), *Int. J. Nucl. Power – atw* 55 (7), 479.
- [9] C. Heintze, F. Bergner, M. Hernández-Mayoral, Ion-irradiation induced damage in FeCr alloys characterized by nanoindentation, *J. Nucl. Mater.*, submitted.
- [10] G.S.Was (2007), “Fundamentals of radiation materials science – metals and alloys”, Springer, Berlin.
- [11] M. Matijasevic, A. Almazouzi (2008), *J. Nucl. Mater.* 377, 147.
- [12] ASTM Standard E693-01 (2007), Standard practice for characterizing neutron exposures in iron and low alloy steels in terms of displacement per atom (dpa), E 706(ID)

- [13] W.C. Oliver, G.M. Pharr (2004), *J. Mater. Res.* 19, 3.
- [14] L.K. Mansur (1978), *Nucl. Technol.* 80, 5.
- [15] G. R. Odette, T. Yamamoto, D. Klingensmith (2005), *Phil. Mag.* 85, 779.
- [16] F. Bergner, A. Ulbricht, H. Hein, M. Kammel (2008), *J. Phys. Condens. Matter* 20, 104262.
- [17] F. Bergner, A. Ulbricht, C. Heintze (2009), *Scr. Mater.* 61, 1060.
- [18] G.R. Odette, G.E. Lucas (1998), *Rad. Eff. Def. Sol.* 144, 189.
- [19] G. Bonny, D. Terentyev, L. Malerba (2008), *Scr. Mater.* 59, 1193.
- [20] W. Xiong, M. Selleby, Q. Chen, J. Odqvist, Y. Du (2010), *Crit. Rev. Solid State Mater. Sci.* 35, 125.
- [21] R. Sugano, K. Morishita, A. Kimura, H. Iwakiri, N. Yoshida (2004), *J. Nucl. Mater.* 329-333, 942.
- [22] K. Arakawa, M. Hatanaka, H. Mori, K. Ono (2004), *J. Nucl. Mater.* 329-333, 1194.
- [23] Z. Yao, M.L. Jenkins, M. Hernández-Mayoral, M.A. Kirk, *Phil. Mag.*, doi: 10.1080/14786430903430981.
- [24] M. Hernández-Mayoral, Z. Yao, M.L. Jenkins, M.A. Kirk, M.A. (2009), "In-situ TEM observation of microstructure evolution in pure Fe and FeCr under ion irradiation", presented at IAEA Technical Meeting on Physics of materials under neutron and charged particle irradiation, 16 – 19 November 2009, Vienna, Austria.

Microstructural evolution and void swelling in extra high purity Ni-based superalloy under multi-ion irradiation

Gwang-Ho Kim¹, Kiyoyuki Shiba¹, Tomotsugu Sawai¹, Ikuo Ioka¹,
Kiyoshi Kiuchi¹, Jumpei Nakayama²

¹ Japan Atomic Energy Agency, Tokai-mura, Ibaraki-ken, Japan

² Kobe Steel, Ltd., Iwayanaka, Kobe, Hyogo, Japan

Abstract

An ultra high purity Ni-base alloy (EHP(γ): Fe-43Ni-20Cr-1.5Al-1.5Ti-0.3Si) in the ordered γ' phase precipitation-hardened condition was irradiated at temperatures from 673-823 K under single (Fe^{3+} or Ni^{3+}) and triple ($\text{Ni}^{3+} + \text{He}^+ + \text{H}^+$) ion-beams conditions, which were intended to simulate a damage environment of the MA doped MOX fuel claddings for sodium-cooled fast breeder reactors. Single ion-beam irradiations were conducted to 10 dpa and 90 dpa near 673 K and triple ion-beam irradiation was conducted to 90 dpa, 90 appmHe and 1 350 appmH at 825 K. Nanoindentation hardness, dislocation density, cavity density, cavity size and void swelling were determined. In irradiated specimens by single ion-beam at near 673 K, the dominating radiation defect features of EHP (γ) alloy are Frank faulted loops, unfaulted loops and line dislocations. In irradiated EHP(γ) alloy by triple ion-beam at 823 K, swelling occurred about 0.2% due to the formation of bimodal cavities, which consist of voids and bubbles.

Introduction

Cladding materials of nuclear reactors are required to have long excellent performance under irradiation environment. Precipitation-strengthened Ni-based superalloys are known to have excellent high-temperature strength and creep resistance. These alloys also have excellent swelling and creep resistance during irradiation [1] [2] and are, therefore, being considered for fuel cladding in advanced reactors. However, earlier studies on the Ni-based alloys, which are mostly Nimonic PE-16, showed that the Ni-based alloys exhibit ductility loss due to irradiation [2] [3]. The reason for the ductility loss was believed to be attributed to matrix hardening by irradiation-induced point defect clusters at temperatures below 773 K [2] and helium embrittlement at temperatures above 773 K [4].

In the Fast Reactor Cycle Technology Development Project (FaCT Project) by Japan Atomic Energy Agency (JAEA) [5], the cladding materials for MOX fuel used in such high dose irradiations will experience at least 250 dpa of exposure and have a temperature distribution from 673 to 973 K in the steady operation. The candidates of the cladding materials for MOX fuel in the FaCT Project are ODS alloys. ODS alloys show a very good behaviour with respect to swelling at high doses and have a good creep resistance at high temperatures.

In this study, we are seeking an alternative material with better performance and we are developing high purity Ni-based alloys with modified irradiation resistance. In this high purity Ni-based alloy, impurities, such as C, O, N, P, S were reduced to less than 100 ppm in total to improve workability and to prevent irradiation embrittlement and inter-granular corrosion. At low operating temperatures, around 673 K, the cladding materials are strongly affected by matrix hardening due to irradiation-induced point defect clusters [2] [3]. At intermediate operating temperatures, around 823 K, the cladding materials are required to possess above of all, resistance to swelling. In particular, degradation of swelling resistance in a purified austenitic alloy has been reported [6]. In high purity alloys the cavity nucleation is very difficult due to the high surface energy of cavities [7]. However, the growth rate of cavity is very fast because impurities are very low, which interrupt a cavity growth acting as vacancy sinks. Neutrons in the FaCT core condition produce about 1 or 2 appmHe/dpa in high Ni-based alloys. It is less than that in fusion reactors or even in light-water reactors considering the two-step reaction of Ni-58 in stainless steels [8] [9]. Helium production rate is relatively low in the target environment, but, helium may affect the microstructural evolution. Therefore, triple ion-beam irradiation is essential for the adequate evaluation of EHP alloys under radiation environment. This work is focused on the microstructural evolutions and void swelling in EHP Ni-based alloys by the irradiation experiments using single and triple ion-beams.

Experimental procedures

The material used in this study was the ordered γ' -phase-strengthened high purity Ni-based alloy, so called EHP (extra high purity) (γ') alloy. The EHP(γ') alloy was manufactured by the multiple refined melting process, which consisted of cold crucible induction melting (CCIM) and electron beam cold hearth refining (EB-CHR). In CCIM, cold crucible made of water cooling copper was used to prevent contamination from a crucible. The CCIM ingot was refined by EB-CHR to remove volatile impurities at high vacuum. The total impurities, such as C, P, S, B, Mn, in EHP (γ') alloy account for less than 100 ppm. The EB ingot was solution-treated at 1313 K for 4 h. Then 60% cold-work followed by ageing at 923 K for 24 h was carried out to obtain uniform precipitation in the matrix followed by further re-crystallisation carried out at 1 023 K for 24 h. The chemical compositions and the thermo-mechanical treatments of the alloys are given in Table 1. The materials were cut to small coupon type specimens ($6 \times 3 \times 0.4$ mm³). One of the 6×0.4 mm² sides was irradiated after a polishing with SiC paper #4 000 and 0.05 μ m alumina powder.

Table 1: Chemical compositions (wt%) and thermo-mechanical treatment of EHP(γ') alloy

Chemical composition												
Fe	Ni	Cr	Al	Ti	Si	C	Mn	P	S	O	N	B
bal	43	20	1.5	1.5	0.3	0.0013	<0.002	0.0007	0.0005	0.002	0.0009	<0.0001
Thermo-mechanical treatment												
1 313K/4h/AC (ST) + 60% CW + 923K/24h/AC (A) + 1 023K/24h/AC (R)												

Ion irradiation was performed under single (Fe^{3+} or Ni^{3+}) and triple ($\text{Ni}^{3+} + \text{He}^+ + \text{H}^+$) ion beams in the Takasaki Ion Accelerators for Advanced Radiation Application (TIARA) Facility at the Japan Atomic Energy Agency at temperatures 673 K to a dose of 10 dpa and 90 dpa and at 823 K to 90 dpa. Ions of 10.5 MeV Fe^{3+} and 12 MeV Ni^{3+} were injected to produce radiation damage and ions of 1.05 MeV He^{2+} and 380 keV H^+ were implanted through Al degrader foils to simulate a FaCT core irradiation environment. The injection rates for He and H are 1 appm/dpa and 15 appm/dpa, respectively. The irradiations of He and H were controlled using Al foil energy degraders to implant over the depth range from about 0.9 to 1.5 μm . The nominal displacement damage and ion-implantation depth were calculated using TRIM code [10].

Nanoindentation hardness was examined in a direction normal to the irradiated surface on all specimens using an ENT-1100a instrumented nanoindentation device (Elionix, Japan). In this study, specimens were indented up to ~400 nm from the surface (indentation load 18~22 mN) to compare with nanoindentation hardness before and after irradiation. Triangular pyramidal diamond indenter tips with a semiapex angle of 68° were employed. The nanoindentation results were analysed in the manner outlined by Oliver and Pharr [11]. Also, micro-Vickers hardness was measured in un-irradiated EHP (γ') alloy with several different hardness values to determine a conversion factor between the two hardnesses.

Thin foils for transmission electron microscopy (TEM) were fabricated using a FB-2000A (Hitachi, Japan) focused ion beam (FIB) instrument with micro-sampling system. TEM observation was carried out for the evaluation of cavity and dislocation structures with a JEM-2100F (JEOL, Japan) operated at 200 kV.

Results and discussions

TEM observation in EHP (γ') alloy irradiated by single ion-beam near 673 K

Figure 1 shows the damage profiles calculated by TRIM code and the cross-sectional TEM bright field images for single ion-irradiated EHP (γ') alloys to 10 and 90 dpa near 673 K. Defect clusters distribute from 0 to 2.2 μm in depth and this distribution is in good agreement with the TRIM calculation.

Figure 1: (a) TRIM calculations and (b) cross-sectional view in the single (10.5 MeV Fe³⁺) ion-irradiated alloys of EHP(γ') to 10 dpa at 698 K, (c) the cross-sectional view and (d) TRIM calculations in the single (12 MeV Ni³⁺) ion-irradiated alloys of EHP(γ') to 90 dpa at 673 K

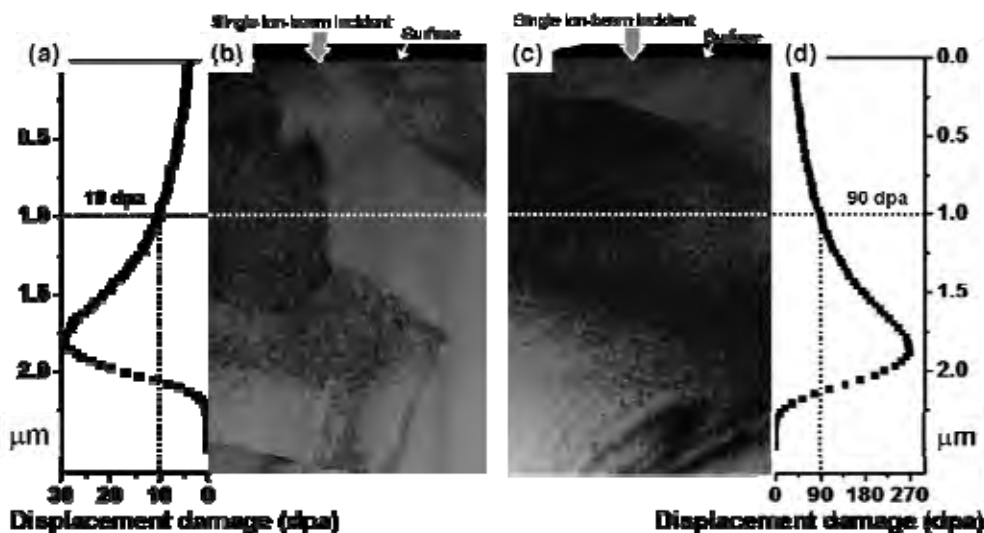
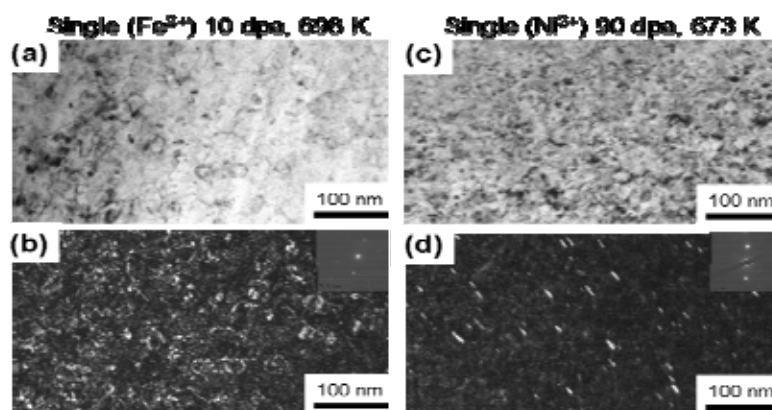


Figure 2 shows typical TEM microstructure for the single (Fe³⁺/Ni³⁺) ion-irradiated EHP (γ') alloys to 10 dpa at 698 K and to 90 dpa at 673 K. In the case of 10 dpa at 698 K, the irradiated microstructure consisted of Frank faulted loops (density: $4.8 \times 10^{21} \text{ m}^{-3}$, d_{ave} : 9.5 nm), unfaulted loops (density: $6.0 \times 10^{20} \text{ m}^{-3}$, d_{ave} : 24.4 nm) and line dislocations (density: $9.5 \times 10^{20} \text{ m}^{-3}$, l_{ave} : 28.6 nm). The d_{ave} and The l_{ave} have an average diameter and length, respectively. In contrast, in the case of 90 dpa at 673 K, the microstructural features were observed to be Frank faulted loops (density: $1.2 \times 10^{22} \text{ m}^{-3}$, d_{ave} : 11.6 nm). Generally, only faulted loops are observed in a low-temperature region, mixture of faulted loops, unfaulted loops and dislocations are observed in an intermediate temperature region and a dislocation structure occurs in a high-temperature region [12] [13]. This behaviour is accelerated with increasing irradiation dose [12]. In this study, but, in the case of 90 dpa at 673 K, unfaulted loops or line dislocations were difficult to see in spite of rather high doses. It can be considered that the temperature factor is higher than the dose factor in high purity Ni-based alloys near 673 K.

Figure 2: Typical TEM micrographs for the single (Fe³⁺/Ni³⁺) ion-irradiated EHP (γ') alloy to 10 dpa at 698 K and to 90 dpa at 673 K, (a) and (c) bright field image, (b) and (d) dark field image



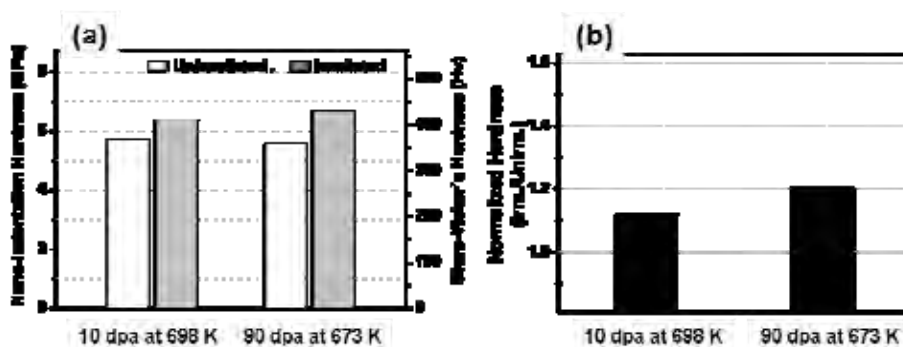
Nanoindentation hardness in EHP (γ') alloy irradiated by single ion-beam near 673 K

Figure 3 compares the nanoindentation hardness at 400 nm indentation depth as a function of dose for specimens irradiated by single ions near 673 K. The nanoindentation hardness of the un-irradiated EHP (γ') alloy was about 5.6 ± 0.2 GPa. In micro-Vickers hardness terms, these hardness values are about 360 HV. A conversion factor between the nanoindentation hardness and the micro-Vickers hardness in EHP (γ') alloy was determined by measuring the un-irradiated EHP alloys, with different hardness values by thermal treatments. From the result of a normalised hardness, the irradiation hardening of EHP (γ') alloys increases the dose about 7%. The irradiation hardening due to Frank faulted loops are suggested by Grossbeck [14] as follows:

$$\Delta \tau_{\text{loop}} = Gb\sqrt{Nd} / \beta \quad (1)$$

Where $\Delta \tau_{\text{loop}}$, G , b , N , d are the increments in shear stress, shear modulus, Burgers vector, loop number density and loop diameter, respectively. β is the constant equal to 2.2 [14]. $\Delta \tau$ of the single ion-irradiated to 10 dpa at 698 K and to 90 dpa at 673 K were calculated using loop data described in the previous section. $\Delta \tau_{10\text{dpa at } 698 \text{ K}}$ and $\Delta \tau_{90 \text{ dpa at } 673 \text{ K}}$ were $Gb (3.48 \times 10^{11}) / \beta$ and $Gb (3.73 \times 10^{11}) / \beta$, respectively. The increase in the irradiation hardening due to Frank faulted loops calculated by Orowan equation with increasing dose is about 7%, which agrees well with the result of hardness increasement. It is considered that the increase in density of small Frank loops mainly contributes to the increase in irradiation hardening.

Figure 3: Dose dependence of nanoindentation hardness (a) and normalised hardness (b) in EHP (γ') alloy irradiated by $\text{Fe}^{3+}/\text{Ni}^{3+}$ single ions

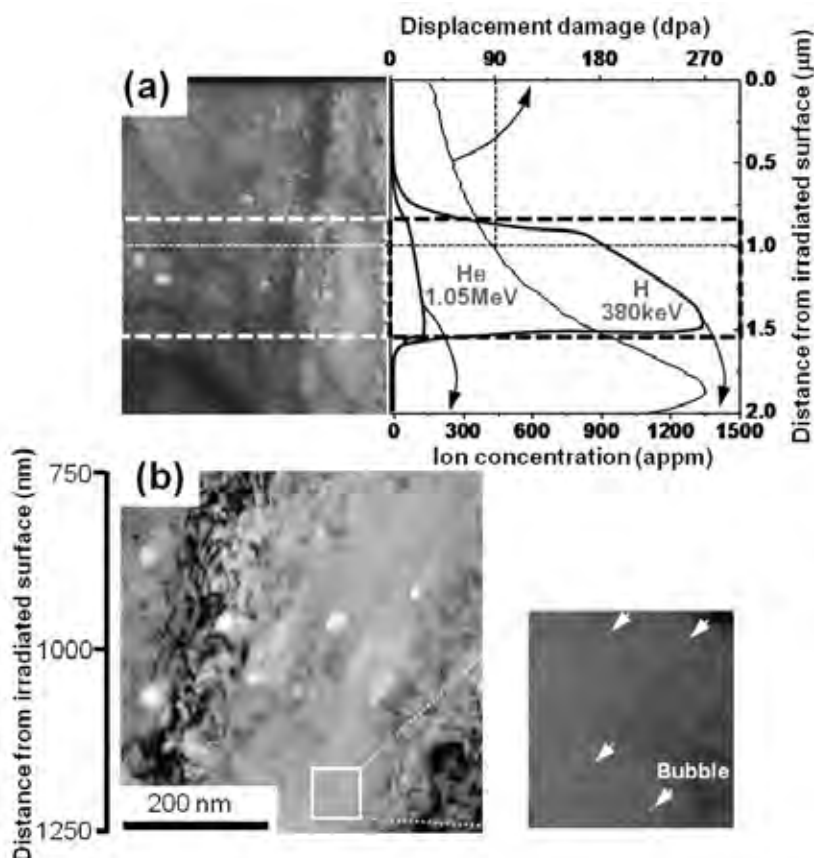


Cavity microstructure in EHP (γ') alloy irradiated by triple ion-beams near 823 K

The cross-sectional cavity microstructure in EHP (γ') specimen irradiated by triple ion-beam to 90 dpa at 823 K is shown in Figure 4(a). Cavities were mainly located from 0.8 to 1.5 μm in depth. The TRIM calculated damage distribution and the profiles of He and H were included. The ions of He and H introduced by ion irradiation distribute mostly in the range of 0.8-1.5 μm in depth from the irradiated surface, which is in good agreement with the range of cavities distribution. In the range of 1.5-2.0 μm in depth cavities were not observed despite being a higher dose than that in 0.8-1.5 μm . This means that the gaseous elements contribute to a cavity stabilisation. Generally, cavity nucleation in high purity alloys is very difficult due to the high surface energy of cavities. Figure 4(b) shows cavity structures around 1 μm in depth in EHP (γ') specimen irradiated by triple ion-beam to 90 dpa at 823 K. Cavities comprised of a two-component distribution consisting of small helium bubbles (diameter < 8 nm) and larger polyhedral cavities which were

arbitrarily classified as voids [Figure 4(b)]. The numbers of density and mean size at 1 μm in depth were $1.57 \times 10^{22} \text{ m}^{-3}$, 3 nm (bubble) and $3.7 \times 10^{20} \text{ m}^{-3}$, 21.5 nm (void), respectively. The swelling was about 0.2%. Bond [15] *et al.* reported that the swelling in Nimonic PE16 alloy, which is similar to γ' phase-strengthened Ni-based alloys, irradiated by dual (Ni^+ and He^+) ion-beams to 80 dpa at 848 K is about 0.25 %. Consequently, the present results showed almost the same level of swelling as the reported value. This result suggests that the impurity level in the present alloy does not affect much the void swelling.

Figure 4: (a) Cross-sectional TEM image and TRIM calculations for EHP (γ') alloy irradiated by triple ion-beams to 90 dpa at 823 K and (b) cavity structures around 1 μm in depth



He/dpa and H/dpa ratios were almost constant.

Conclusions

The EHP Ni-based alloy was irradiated by single ion-beam near 673 K in order to investigate the effects of dose on microstructural evolutions and irradiation hardening. Also, EHP Ni-based alloy was irradiated by triple ion-beams to 90 dpa, 90 appmHe and 1 350 appmH at 823 K to estimate swelling. The following conclusions can be drawn from the data:

- (1) Under single ion-beam irradiation to 10 dpa at 698 K, the dominating radiation defect features of EHP (γ') alloy are Frank faulted loops, unfaulted loops and line dislocation. While in the case of 90 dpa at 673 K, the radiation defect features of EHP (γ') alloy are mainly observed to be Frank faulted loops and point defect clusters.

- (2) In irradiated specimens by single ion-beam at near 673 K, the irradiation hardening of EHP (γ') alloy tended to increase with increasing dose.
- (3) In irradiated specimens by triple ion-beam at 823 K, swelling occurred about 0.2% in EHP (γ') alloy. The dominating cavity features are bimodal (voids and bubbles) cavities.

Acknowledgements

The present study includes the result of “R&D of the third generation irradiation-resistant austenitic alloys” entrusted to Kobe Steel, LTD by the Ministry of Education, Culture, Sports, Science and Technology of Japan.

References

- [1] B. A. Chin *et al.* (1982), *Nucl. Tech.* 57. 426.
- [2] W. J. S. Yang *et al.* (1985), *J. Nucl. Mater.* 132. 249.
- [3] W. J. S. Yang (1982), *J. Nucl. Mater.* 108/109. 339.
- [4] R. S. Barnes (1965), *Nature* 206. 1307.
- [5] JAEA (2006), “Feasibility Study on Commercialized Fast Reactor Cycle Systems, Technical Study Report of Phase II (1) Fast Reactor Plant Systems”, JAEA-Research 2006-042[in Japanese].
- [6] T. Sawai *et al.* (1992), *J. Nucl. Mater.* 191-194. 712.
- [7] E. H. Lee *et al.* (1979), *J. Nucl. Mater.* 83. 79.
- [8] A. A. Bauer *et al.* (1972), *J. Nucl. Mater.* 91. 42.
- [9] L. R. Greenwood (1983), *J. Nucl. Mater.* 137. 115.
- [10] J. P. Biersack, L. G. Haggmark (1980), *Nucl. Instr. Meth.* 174. 257.
- [11] W. D. Oliver, G. M. Pharr (1992), *J. Mater. Res.* 7. 1564.
- [12] G. M. Bond *et al.* (1983), *Nucl. Instr. Meth.* 209/210. 381.
- [13] H. R. Brager, J. L. Straalsund (1973), *J. Nucl. Mater.* 46. 134.
- [14] M. L. Grossbeck *et al.* (1992), *J. Nucl. Mater.* 191-194. 808.
- [15] G. M. Bond, D. J. Mazey (1983), *Nucl. Instr. Meth.* 209/210. 381.

Effects of heat treatments on long-term creep properties of 9Cr-W-Mo-V-Nb steel

Satoshi Obara¹, Takashi Wakai¹, Tai Asayama¹, Yoshiyuki Yamada²,
Takanori Nakazawa³, Masayoshi Yamazaki⁴, Hiromichi Hongo⁴

¹ Japan Atomic Energy Agency, Japan

² Gunma University, now Akebono Brake Industry LTD., Japan

³ Formerly Gunma University, Japan

⁴ National Institute for Material Science, Japan

Abstract

As far as the commercialisation of sodium-cooled fast reactors (SFRs) is concerned, it is essential to reduce construction costs in order to enhance economic competitiveness. For this purpose, employing high chromium (Cr) ferritic steels as main structural materials has been found to be one of the most practical means. Since long-life plant design is required for future SFR plants, long-term creep properties and microstructure stability at high temperature are important characteristics for the structural materials of SFRs. Generally, in high Cr ferritic steels, creep rupture strength is improved by fine MX particles, which precipitate in the tempering process and high dislocation density. Recently, it has been reported that creep strength and ductility have been significantly degraded by high-temperature exposure at 600°C and above for a long time. In order to avoid such degradations of creep properties in the long-term region, it is essential to improve the efficiency of initial microstructure by controlling the heat treatment conditions such as normalising and tempering temperature. In this study, in order to achieve proper initial microstructures, suitable heat treatment conditions were investigated based on the metallurgical examination results. In addition, in order to estimate the degradation of microstructure during creep tests, a series of creep rupture tests were performed and damaged microstructures were examined. Creep tests were carried out at 650°C in the stress range of 80-180 MPa. The microstructures were examined using optical and electron microscopes. Extracted residue analyses were conducted to identify the precipitated elements. Dislocation density was measured by X-ray diffraction analysis. Creep rupture strength increased as normalising temperature increased from 950°C to 1 200°C. Although creep rupture strength of the specimen tempered at 780°C for 1 h was greater than that tempered at 700°C and 750°C in the long-term region exceeding 20 000 hours at 650°C, creep ductility of the former was obviously inferior to those of the latter. Based on the results of creep rupture tests and metallurgical examinations, higher normalising temperature up to 1 150°C is desirable to improve creep strength and ductility in the long-term region. On the other hand, higher tempering temperature and longer tempering time are not desirable to improve creep ductility and strength in the long-term region, respectively.

Introduction

High chromium (Cr) steels such as ASME Grades 91, 92 and 122 are known as structural materials for thermal power plants to promote low thermal expansion and good high-temperature strength. The applicability of high Cr steels to main structural material of sodium-cooled fast reactors (SFRs) has been considered from the viewpoint of the reduction of the construction costs [1]. Creep strength and ductility of structural materials for SFR components need to be improved in the long-term region because, in order to enhance economic competitiveness, the design life of SFRs is intended to be 60 years.

Creep strength in high Cr steel is improved by the addition of strengthening elements such as vanadium (V) and niobium (Nb), because these elements play a role of precipitation strengthening elements as metal carbonitride (MX: VX and/or NbX) particles [2]. Since the precipitation behaviour of MX depends not only on the amounts of V and Nb but also on heat treatment conditions, creep strength also depends on heat treatment conditions [2]. In addition, coarse prior austenite grain produced by normalising at higher temperature also contributes to improvement of creep rupture strength [3].

According to a recent report, creep strength in high Cr steel significantly degrades at 600°C and above in the long-term region [4]. In addition, creep ductility also degrades significantly especially at 600°C and above in the long-term region, as reported by Kimura *et al* [4]. As creep strength depends on heat treatment conditions, it is suggested that significant degradations of creep strength and ductility in the long-term region are inhibited by improving initial microstructures and heat treatment such as normalising and tempering.

In this study, suitable heat treatment conditions to achieve proper initial microstructures were investigated based on metallurgical examination results. In addition, a series of creep rupture tests were performed and damaged microstructures were examined. Based on these results, in order to improve long-term creep properties, the suitable heat treatment conditions were discussed.

Experimental procedure

The chemical compositions of the steel examined in this study are shown in Table 1. This steel is equivalent to ASME Grade 92 steel (9Cr-W-Mo-V-Nb). ASME Grade 92 has superior creep strength to that of ASME Grade 91 at 600°C and 650°C, by contrast, creep ductility of Grade 92 is inferior to that of Grade 91 in the long-term region [4]. In order to improve creep ductility in the long-term region, this study examined ASME Grade 92, which was normalised and/or tempered in various conditions.

Table 2 summarises the heat treatment conditions of the material consisting of normalising followed by tempering. Creep tests were performed in air at 650°C under constant loads. The diameter and gauge length of the smooth round bar specimens were 6.0 mm and 30 mm, respectively.

After the creep tests, microstructures were observed by means of both optical microscope (OM) and field emission transmission electron microscope (FE-TEM) at 200 kV. Prior austenite grain size was measured by OM observation. Precipitated phases were extracted using a 10% acetylacetone-1% tetramethyl ammonium chloride-methanol electrolyte. Each precipitation was analysed by energy dispersion X-ray spectroscopy attached to FE-TEM (TEM-EDX). The amounts of precipitations were quantitatively estimated by the extracted residue analyses. Dislocation density of each specimen was measured by X-ray diffraction, using a modified Williamson-Hall plot [5] as well as modified Warren-Averbach plot [6].

Table 1: Chemical compositions of the steel

C	Si	Mn	P	S	Cr	W	Mo	V	Nb	N	B
0.093	0.16	0.46	0.010	0.001	8.80	1.83	0.42	0.21	0.06	0.049	0.0009

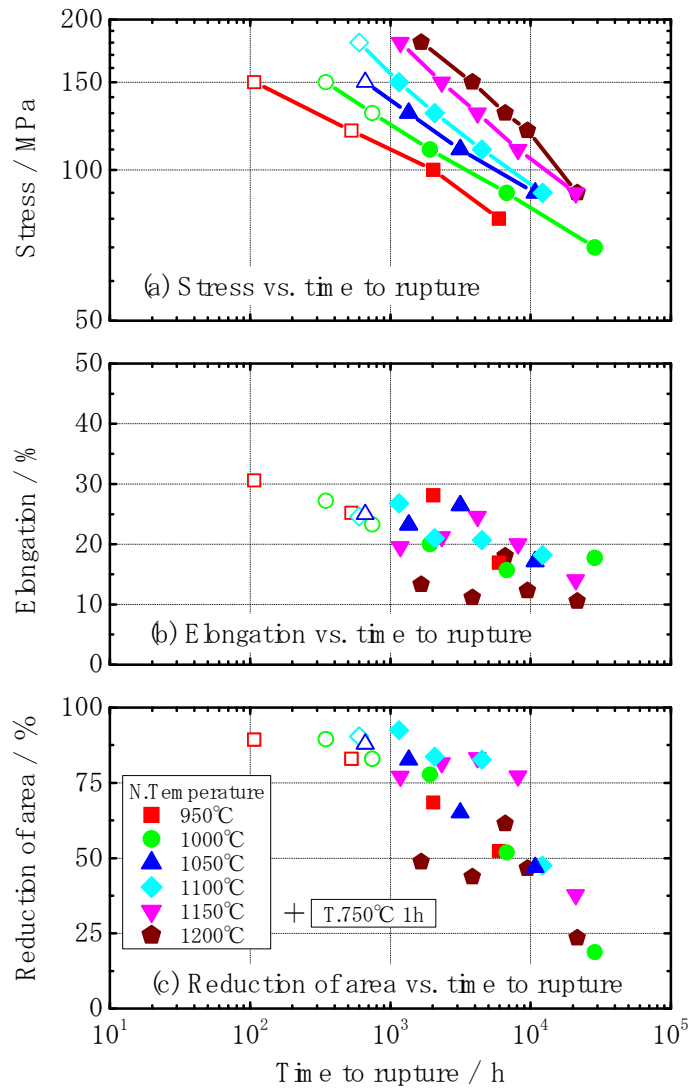
Table 2: Heat treatment conditions of the steel (designations in this study)

Normalising conditions	Tempering conditions		
	700°C	750°C	780°C
950°C×1 h	-	1 h (950°C NT)	-
1 000°C×1 h	-	1 h (1 000°C NT)	-
1 050°C×1 h	-	1 h (1 050°C NT)	-
1 100°C×1 h	-	1 h (1 100°C NT)	-
1 150°C×1 h	1 h (700°C-1T)	1 h (1 150°C NT or 750°C-1T) 10 h (750°C-10T) 100 h (750°C-100T)	1 h (780°C-1T)
1 200°C×1 h	-	1 h (1 200°C NT)	-
Cooling : water quench			

Results and discussions

Effect of normalising temperature on creep properties

Stress vs. time to rupture curves of the steel normalised at various temperatures are shown in Figure 1(a). For 950°C NT steel (normalised at 950°C for 1 h, see Table 2), small creep strength was observed, however, creep strength increased as normalising temperature increased from 950°C to 1 200°C.

Figure 1: Effect of normalising temperature on creep rupture properties

According to Kimura et al. [4], significant degradations of creep strength and ductility correlated to half of 0.2% proof stress (half yield) of corresponding temperature were observed. In Figure 1, solid symbols indicate that the creep tests were performed under the stress level smaller than half yield. As shown in this Figure, no significant degradation of creep strength was observed. Creep ductility is shown in Figures 1(b) and (c). High ductilities were observed in the short-term region, but ductility decreased as time to rupture increased.

A significant degradation in ductility appeared especially in reduction of area, which decreased from 90% in the short-term region to 20% in the long term region. The lower creep ductility was also observed in 1200°C NT. In order to estimate the recovery of microstructure during creep tests in the long-term region, microstructures were observed. The previous study revealed that prior austenite grain size, the amount of MX precipitates and dislocation density were affected by normalising temperature [7] [8]. Therefore, we focused on prior austenite grain size, MX precipitates and dislocation

density. Figure 2 shows the effect of normalising temperature on prior austenite grain size. The higher the temperature at which the steels were normalised, the coarser prior austenite grain sizes were observed. Especially, significant coarsening of prior austenite grain was observed in 1 200°C NT. It was reported that reduction of creep ductility was caused by coarsening of prior austenite grain in ferritic steel [3]. Thus, it was supposed that the difference between creep ductility of 1 200°C NT and that of others result from the difference in prior austenite grain size. Figure 3(a) shows extracted residue analysis results for the specimens as normalised and normalised-tempered (NT). Most of V dissolved even in the specimen as normalised at 1 050°C. By contrast, the amount of precipitated Nb decreased as normalising temperature increased and Nb completely dissolved into the matrices by normalising at 1 200°C. In the specimen as NT, the amount of precipitated V and Nb did not depend on the normalising temperature, as found in this analysis. Therefore, the total amount of precipitated V and Nb in the tempering process was calculated based on the results of the extracted residue analyses for the steels. Relationship between normalising temperature and the total amount of precipitated V and Nb in the tempering process is shown in Figure 3(b). The amount of $\Delta [V + Nb]$ increased as normalising temperature increased. Thus, the number density of the MX precipitates increased as normalising temperature increased.

Figure 2: Effect of normalising temperature on prior austenite grain size [8]

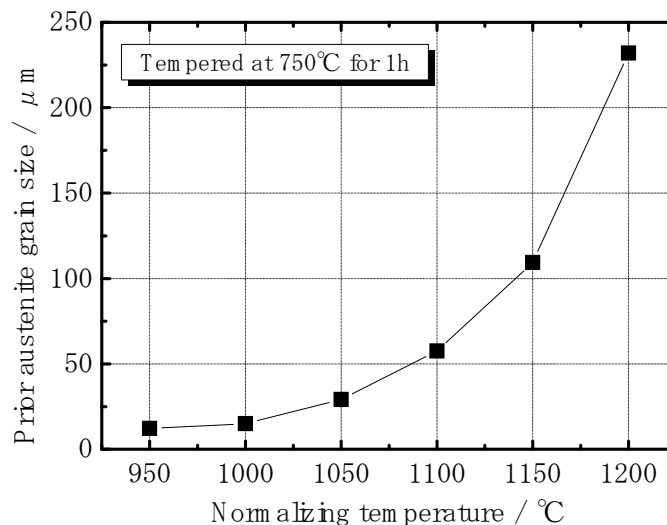


Figure 3: Effect of normalising temperature on the amount of precipitated elements (V and Nb) in normalised and tempered specimens

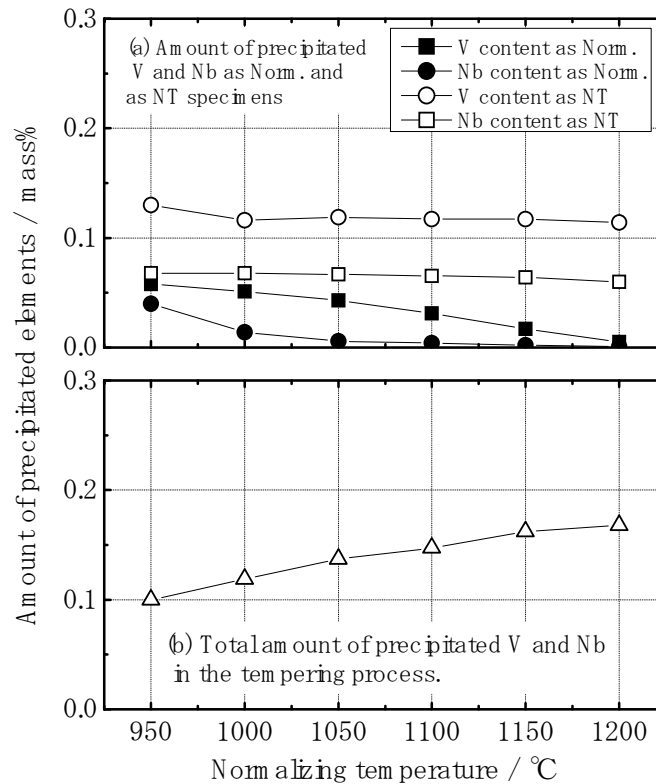


Figure 4 shows bright field TEM images of thin foils produced from specimens as NT and after creep rupture at 600°C in 21 013 h. A typical tempered martensite lath microstructure with high dislocation density was observed in the specimen as NT. Tempered martensite lath microstructure disappeared after creep test. MX precipitates were observed in the creep ruptured specimens as shown in Figures 4 and 5. As can be seen from Figure 5, many fine MX precipitates composed of V and Nb were observed in over 20 000 h creep rupture specimen.

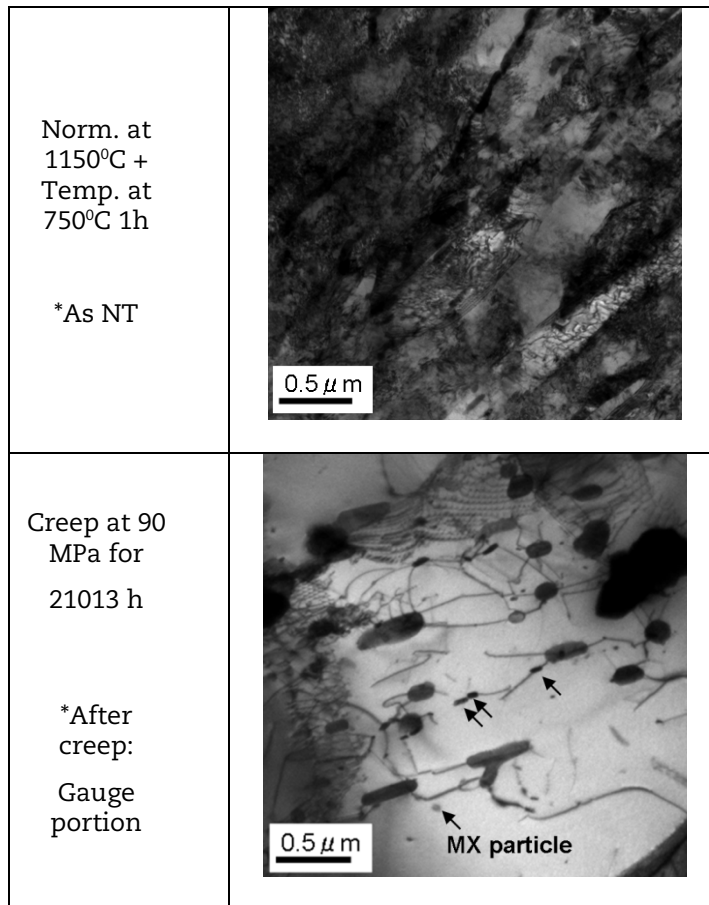
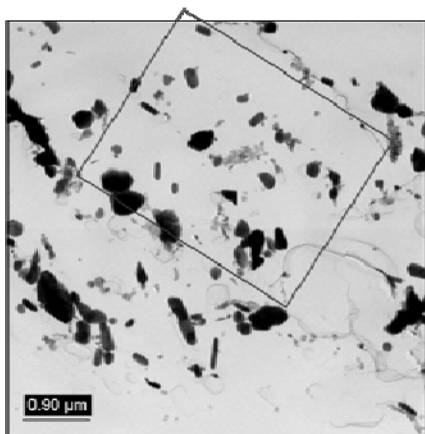
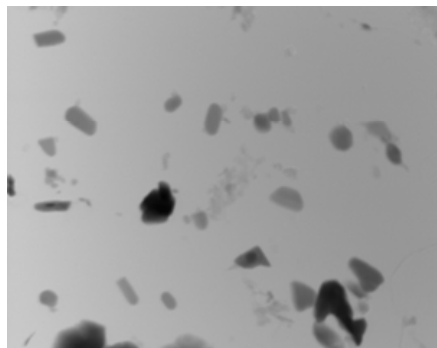
Figure 4: TEM images of thin foil specimens

Figure 5: TEM-EDX images of creep rupture specimen by extracted replica



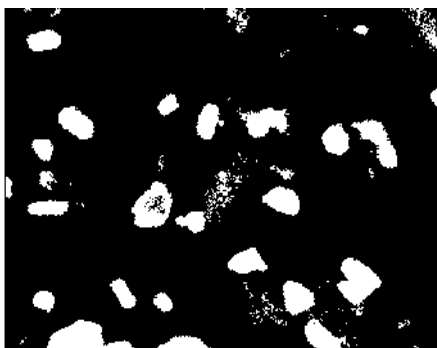
TEM image (Gauge portion)

1 150°C NT (Norm. 1 150°C, Temp. 750 °C for 1 h)

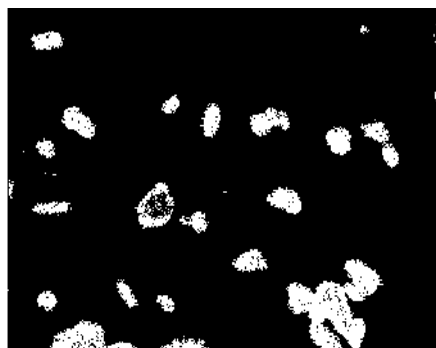


1 μm

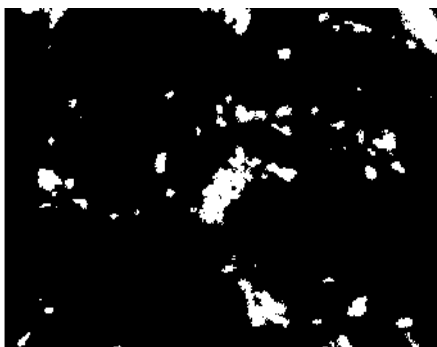
EDX-mapping area



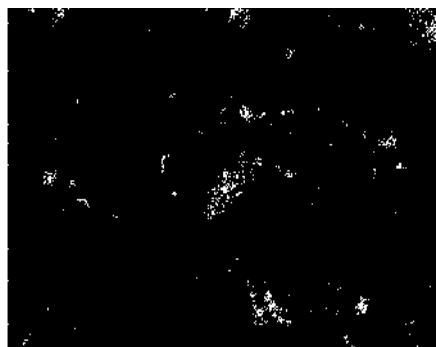
Cr (EDX-mapping image)



Fe (EDX-mapping image)



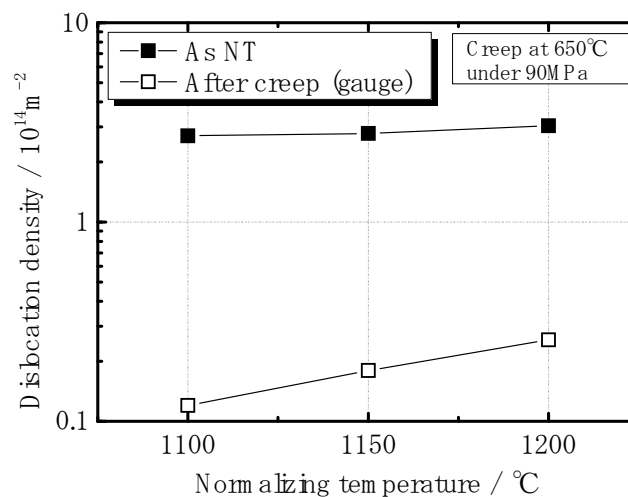
V (EDX-mapping image)



Nb (EDX-mapping image)

After creep rupture, the results of dislocation density measurement by X-ray diffraction analysis for the specimens as NT are shown in Figure 6. It has been shown that dislocation density was observed almost constant in the specimens as NT and that dislocation density of the crept specimens increased as normalising temperature increased. As a result, fine MX inhibits the decreasing dislocation density during creep test. It is clarified that in order to increase the creep strength in the long-term region, higher normalising temperature is desirable, however, in the specimen normalising at 1 200°C, a significant degradation of creep ductility was observed.

Figure 6: Dislocation density of the 1 100°C NT, 1 150°C NT and 1 200°C NT (as NT and after creep) specimens



Effect of tempering conditions on creep properties

Stress vs. time to rupture curves of the steel tempered at various temperatures and time are shown in Figures 7 and 8, respectively. In Figure 7, creep strength of 700°C-1T and 750°C-1T steels was higher than that of 780°C-1T steels in the short-term region. However, creep strength of 780°C-1T steel did not significantly degrade in the long-term region and it became greater than that of 700°C-1T and 750°C-1T steel over 20 000 h. Significant degradations in creep elongation and reduction of area were observed in 780°C-1T steel in the long-term region. In Figure 8, creep strength decreased with the increasing tempering time. The lowest creep strength was observed in 750°C-10T steel in the short- and long-term regions, but it became close to that of 750°C-1T and 750°C-10T steel in the long-term region. Since the creep test is continued, creep properties and long-term stability of microstructure need to be investigated in the future. The prior austenite grain size is not affected by tempering temperature from 700°C to 780°C, because the α - γ transformation temperature of this steel has been calculated to be higher than 800°C by Thermo-Calc. [9]. In addition, since fine MX generally precipitates during the tempering process, the amount of MX precipitates is not affected by tempering temperature. Dislocation density of the specimen as NT decreased as tempering temperature increased, as shown in Figure 9. On the other hand, dislocation density of the crept specimens increased as tempering temperature increased. Thus, the higher tempering temperature resulted in an increase in dislocation density after high-temperature exposure for a long time.

It is clarified that in order to improve the creep strength in the long-term region, higher tempering temperature is desirable, however, tempering at 780°C results in a significant degradation of creep ductility.

Figure 7: Effect of tempering temperature on creep rupture properties

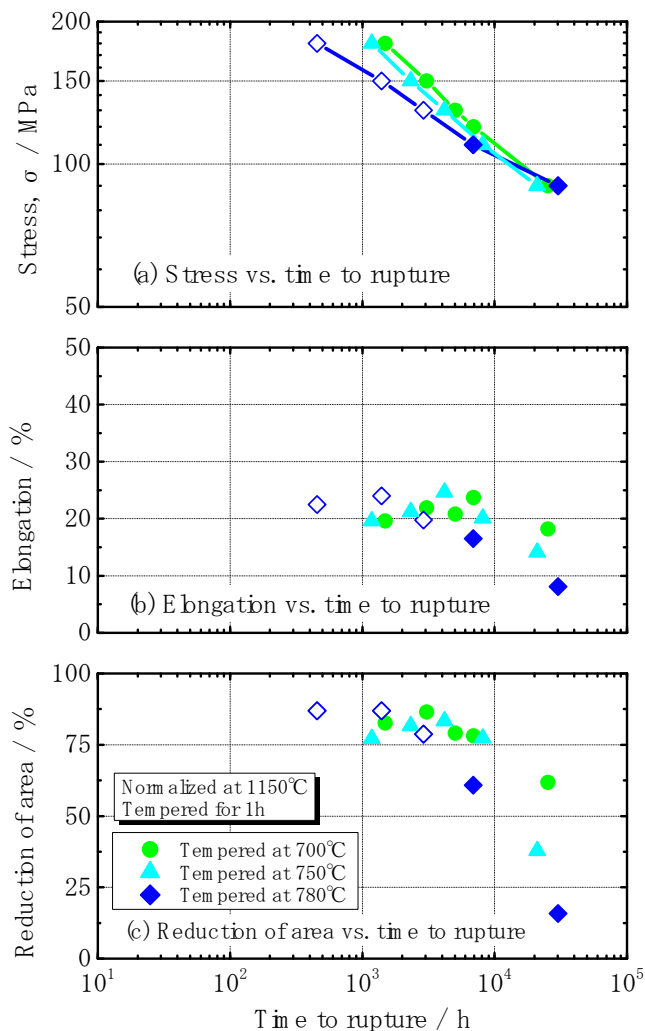
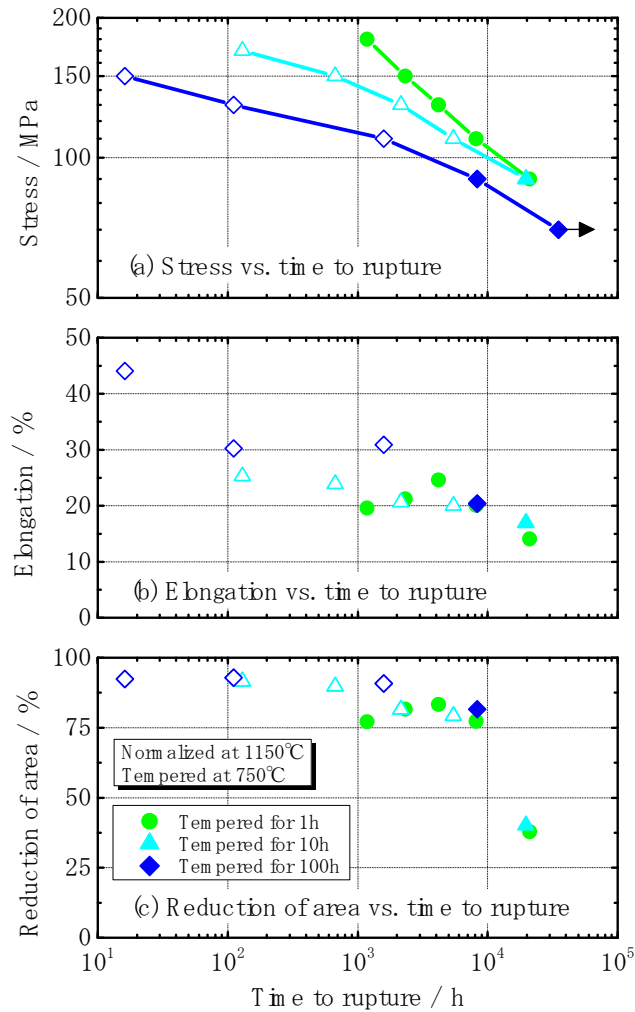


Figure 8: Effect on tempering time on creep rupture properties

Long-term efficiency of heat treatment

Figure 10(a) shows the effect of normalising temperature on creep strength in 150 MPa and 90 MPa at 650°C. Figure 10(b) and (c) show the creep ductilities normalised by those observed in tensile test results [8]. During creep test in 150 MPa, the normalised elongation and reduction of area were constant except in 1 200°C NT. The normalised reduction of area of 1 200°C NT was smaller than that of others. For this reason, higher normalising temperature up to 1 150°C is desirable to improve creep strength and ductility in the long-term region.

Figure 11 shows the influence of tempering conditions on creep properties. Figure 11(a) shows the effect of tempering conditions on creep strength in 150 MPa and 90 MPa. Figures 11(b) and (c) show the creep ductilities normalised by those observed in tensile tests [8]. It should be noted that the horizontal axes of the figures are Larson-Miller parameter (LMP, $C=20$). Creep strength showed a declining trend with the increase in LMP. The normalised creep ductility of 780°C-1T was the smallest for 150 MPa and 90 MPa. For this reason, higher

tempering temperature and longer tempering time are not desirable to improve creep ductility and strength in the long-term region, respectively.

Based on the results of creep rupture tests and metallurgical examinations, the effect of heat treatment on creep rupture properties was confirmed at 650°C up to 30 000 h. Using the Larson-Miller parameter [$C=20$ (10)], 650°C-30 000 h is equivalent to approximately 550°C-28 260 000 h. Although it is necessary to consider the validity of temperature acceleration by a comparison between the fracture morphology and the observation of the microstructure, it can be concluded that these heat treatment conditions are promising ways to improve the creep strength and ductility for the structural materials of SFRs used at 550°C-500 000 h (approximately 60 years).

Figure 9: Dislocation density of the 700°C-1T, 750°C-1T and 780°C-1T (as NT and after creep) specimens

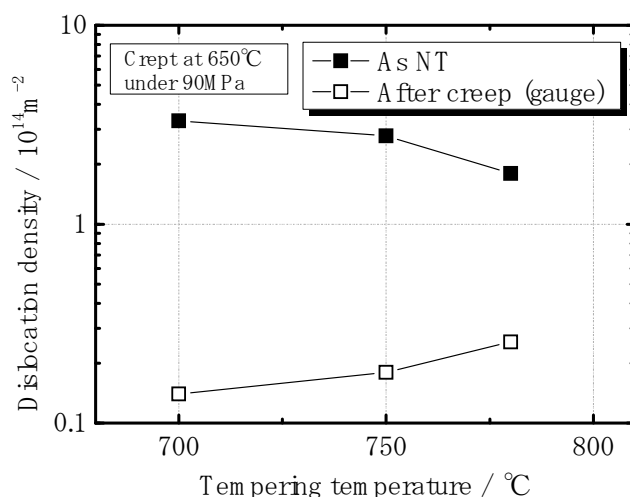


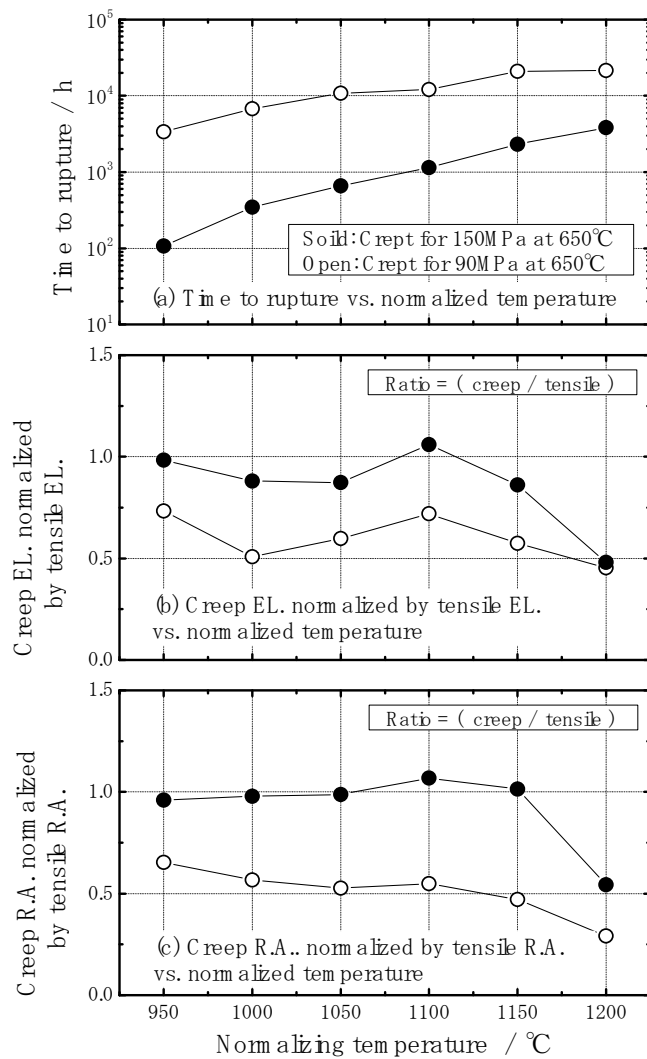
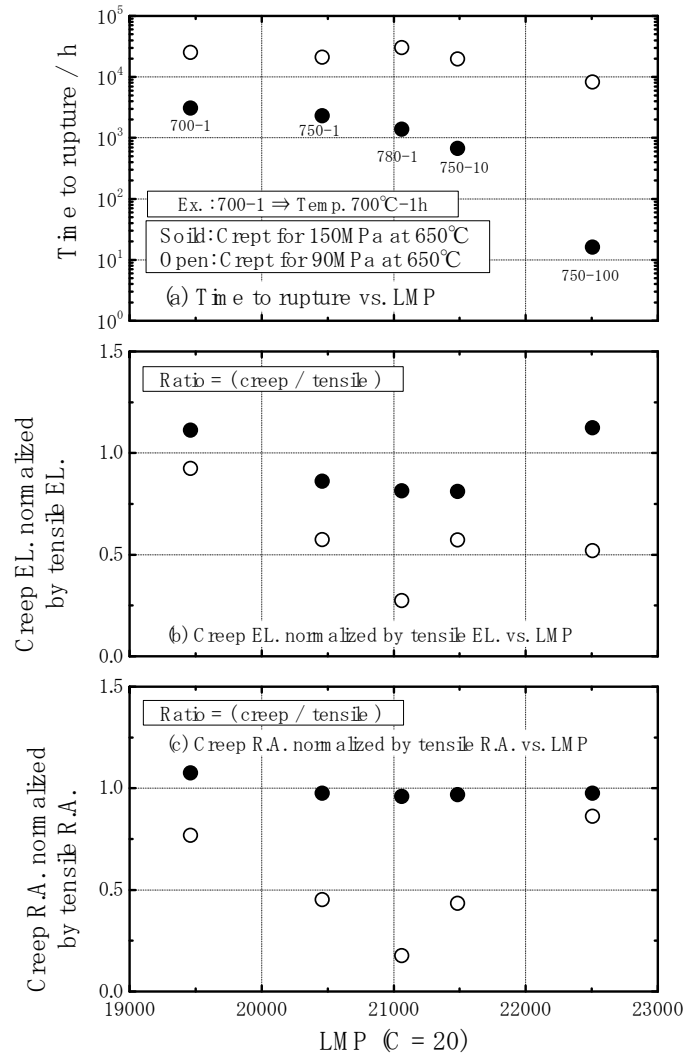
Figure 10: Effect of normalising temperature on creep properties and its stress dependence

Figure 11: Effect of LMP on creep properties and its stress dependence

Conclusions

The effect of heat treatment on the long-term creep properties has been investigated in 9Cr-W-Mo-V-Nb steel. The following results were obtained:

- Creep strength in the short-and long term-region was increased as normalising temperature increased from 950°C to 1 200°C. High ductilities were observed in the short-term region, but ductility decreased as time to rupture increased. A significant degradation in ductility appeared especially in reduction of area, which decreased from 90% in the short-term region to 20% in the long-term region. The lower creep ductility was also observed in 1 200°C NT. This was mainly caused by the coarsening of prior austenite grain, which produces higher normalising temperature.

- Although creep strength of the specimen tempered at 780°C-1 h was greater than that tempered at 700°C and 750°C in the long-term region exceeding 20 000 h, creep ductility of the former was obviously inferior to that of the latter. This was mainly caused by recovery behaviour of dislocation density. Since the recovery rate of dislocation density during creep test was decreased as tempering temperature increased, creep strength of 780°C-1T was greater than that of 700°C and 750°C in the long-term region.
- Based on the results of creep rupture tests and metallurgical examinations, higher normalising temperature up to 1 150°C is desirable to improve creep strength and ductility in the long-term region. On the other hand, higher tempering temperature and longer tempering time are not desirable to improve creep ductility and strength in the long-term region, respectively.
- The effect of heat treatment on creep rupture properties was confirmed at 650°C up to 30 000 h. Although it is necessary to consider the validity of temperature acceleration by a comparison between the fracture morphology and the observation of the microstructure, it can be concluded that these heat treatment conditions are promising ways to improve the creep strength and ductility for the structural materials of SFRs using at 550°C-500 000 h.

References

- [1] T. Asayama *et al.* (2007), Structural Materials for Innovative Nuclear Systems (SMINS) Workshop Proceedings Karlsruhe, June 2007.
- [2] T. Fujita (2001), *3rd EPRI Conference on Advanced Materials Technology for Fossil Plants*, Swansea, April 2001.
- [3] Y. Kadoya *et al.* (1990), *ISIJ International*, Vol. 30. No. 10, p. 829.
- [4] K. Kimura *et al.* (2009), *Welding and Fabrication Technology for New Power Plants: First International EPRI Conference*, Florida, June 2009.
- [5] G.K. Williamson *et al.* (1953), *Acta Metallurgica*, Vol. 1, p. 22.
- [6] B.E. Warren *et al.* (1952), *Journal of Applied Physics*, Vol. 23, p. 497.
- [7] S. Obara *et al.* (2007), Structural Materials for Innovative Nuclear Systems (SMINS) Workshop Proceedings Karlsruhe, June 2007.
- [8] S. Obara *et al.* (2009), *Tetsu-to-Hagane*, Vol.95, p.417 [in Japanese].
- [9] Thermo-Calc. Foundation of Computational Thermodynamics, Version Q, Royal Institute of Technology, Stockholm, Sweden (2000).
- [10] F. Masuyama (2007), *International Journal of Pressure Vessels and Piping*, Vol. 84, p. 53.

Poster Session

Chairs: T. Allen, J-Y.Park

Session I

Fundamental – Irradiation

Chair: J-H. Kwon, G-G. Lee, C-S. Shin

Multi-scale modelling approach to the estimation of radiation hardening of stainless steels in LWR and SFR environments*

Junhyun Kwon, Gyeong-Guen Lee, Chansun Shin
Korea Atomic Energy Research Institute, Republic of Korea

Abstract

Austenitic stainless steels are widely used for structural materials in light-water reactors (LWR) and sodium-cooled fast reactors (SFR) because of their superior resistance to corrosion. In LWR, reactor internals including baffle, core barrel and former are composed of stainless steel 304. Stainless steel 316 is considered to be a candidate material for structural components in SFR. When these steels are exposed to neutrons, radiation hardening occurs due to the formation of microstructures. In this paper, we recommend a method for estimating an increase in yield strength by integrating two theoretical models; molecular dynamics (MD) simulations and point defect cluster (PDC) models based on a reaction rate theory. Firstly, the differences in irradiation condition are taken into account in terms of neutron spectra and operating temperature. The average energy of primary knock-on atoms is about 38 keV for SFR and 5 keV for LWR, which are input to MD calculations. From the MD simulation, we evaluate the primary damage quantitatively. Two major variables relating to the primary damage include the cascade efficiency and the PDC distributions. In the SFR condition, big-size PDCs could be found from the MD simulations. Then, we estimate the evolution of PDCs and finally predict the changes in yield strength by combining the MD results and PDC models. The results show that radiation hardening is strongly affected by temperature, as well as neutron spectra.

* The full paper being unavailable at the time of publication, only the abstract is included.

A study on the change of impact properties by neutron irradiation in modified 9Cr-1Mo steel*

Sung Ho Kim, Woo Seog Ryu, Yong Wan Kim
Korea Atomic Energy Research Institute, Republic of Korea

Abstract

Ferritic/martensitic (FM) steels are widely used as high-temperature materials in power plants due to their high strength and good thermal properties. Modified 9Cr-1Mo (G91) steel is a primary candidate material for the reactor pressure vessel (RPV) of the very-high-temperature gas-cooled reactor (VHTR) of the Korean Hydrogen Production Reactor Programme. Materials for a RPV are required to have adequate fracture toughness so that they can withstand high temperatures and a neutron irradiation environment. The diameter of the VHTR RPV is more than 8 m and the thickness is about 200 mm, so it should be manufactured by a ring forging and a welding. Thus, a fracture toughness test should be performed for a weldment as well as base metal.

Hot-rolled G91 steel with a thickness of 32 mm was procured from commercial product. The welding was done by SMAW method. V-notch Charpy impact properties of base metal and weldment were evaluated for the G91 steel as a preliminary test for the selection of the RPV material for a VHTR. The upper shelf energy (USE) of the un-irradiated base metal was found to be 287 J. The ductile-brittle transition temperature (DBTT) of the un-irradiated base metal was found to be -16°C . The T_{41J} and T_{68J} index temperatures of the irradiated G91 steel were found to be -54°C and -41°C , respectively. The upper shelf energy (USE) of the irradiated G91 base metal was found to be 285 J. The ductile-brittle transition temperature (DBTT) of the irradiated G91 steel was found to be 0°C . The T_{41J} and T_{68J} index temperatures of the irradiated G91 steel were found to be -44°C and -30°C , respectively. The USE of the weldment of G91 was found to be 173 J after irradiation. The DBTT of the weldment was found to be 25°C . The T_{41J} and T_{68J} index temperatures of the irradiated weldment of G91 were found to be 0°C and 15°C , respectively. The USE of the un-irradiated weldment of G91 was found to be 164 J and the DBTT was found to be 1°C . The T_{41J} and T_{68J} index temperatures were found to be -16°C and -4°C , respectively. The upper self energy of G91 steel was changed negligibly by the irradiation both in the base metal and the weldment. But the ductile-brittle transition temperatures were increased after irradiation from -16°C to 0°C for the base metal and from 1°C to 25°C for the weldment. The G91 steel showed hardening effects due to neutron irradiation at 390°C , which was similar to the SA508 steel. The irradiation hardening of G91 steel was more severe in the weldment, but the DBTT of weldment was still below room temperature.

* The full paper being unavailable at the time of publication, only the abstract is included.

Radiation response of ferritic/martensitic cladding steels*

Kevin Field, Alicia Certain, Yong Yang, Todd Allen

Material Science Programme, Engineering Physics Department
University of Wisconsin-Madison, United States

Abstract

Ferritic/martensitic steels are being considered for fast reactor cladding application and the materials are expected to withstand high doses at high temperatures. To understand the microstructural evolution of these candidate F-M steels in expected service environments, ODS alloys (9 Cr and 14 Cr), NF616, 9 Cr model alloy and three lots of HT-9 were selected for this study. The materials were irradiated with a 2 MeV proton beam at various temperatures and doses. Following the irradiation, the microstructures were systematically studied for dislocation loops, voids, radiation-induced-segregation (RIS) at grain boundaries and phase stability. Specifically, the stability of nanosized oxides in irradiated ODS was studied using energy-filtered transmission electron microscopy (EFTEM) and atom probe tomography (APT), the lot-to-lot variability of HT-9 was examined by comparing the irradiated microstructures and radiation-induced hardening among the three different lots; for NF616 and the 9 Cr model alloy, RIS and precipitates were evaluated using STEM-EDS and carbon extraction replicas, respectively.

* The full paper being unavailable at the time of publication, only the abstract is included.

Irradiation-induced shifts in master curve reference temperature of ferritic/martensitic steels and welds*

Ji-Hyun Yoon, Sung-Ho Kim, Do-Sik Kim, Bong-Sang Lee, Woo-Seog Ryu
Korea Atomic Research Institute, Republic of Korea

Abstract

Reduced-activation ferritic/martensitic (F/M) steels are considered to be prime candidates as structural materials for next generation power plants. It is known that F/M steels offer excellent high-temperature strength, but are sensitive to neutron radiation-induced embrittlement. The radiation effect on the fracture toughness of structural steels and their welds is one of the design issues for next generation reactors. Therefore, it is important to investigate radiation effect on the ductile-to-brittle transition temperature shift in F/M steels and welds. The initiation of cleavage fracture can be highly scattered owing to metallurgical heterogeneities. The master curve method appears to adequately describe fracture toughness vs. temperature behaviour for ferritic steels, although fracture toughness data in the transition region are sparse. In this study, the irradiation-induced T_0 reference temperature shifts for T91 and E911 steel and their welds were measured with half size precracked Charpy specimens. Irradiations were performed in the HANARO (High-flux Advanced Neutron Application Reactor) research reactor at the Korea Atomic Energy Research Institute in instrumented capsules. The irradiation range was 4.4×10^{19} ~ 1.2×10^{21} n/cm² ($E > 0.1$ MeV), corresponding to 0.068 dpa~0.85 dpa. The irradiation temperatures ranged from 340°C~400°C. K_{Jc} values and T_0 reference temperature were measured in general accordance with ASTM E 1921. The master curve generated for the fracture toughness data was taken from the tests for T91 and E911 and their welds before and after irradiation. When the K_{Jc} data distribution was expressed in the three-parameter Weibull model, the Weibull slopes were calculated for the K_{Jc} data. The difference in sensitivity to irradiation-induced embrittlement between T91 and E911 steels was discussed. The applicability of the master curve method to FM steels and their welds were assessed.

* The full paper being unavailable at the time of publication, only the abstract is included.

Mechanical properties of welded and irradiated 9Cr-1Mo-1W steel

Dae Whan Kim, Sung Ho Kim, Woo-Seog Ryu

Nuclear Materials Research Division

Korea Atomic Energy Research Institute, Daejeon, Republic of Korea

Abstract

After irradiation, tensile tests were performed for base metal and welds of 9Cr-1Mo-1W steel. It was observed that while yield stress and UTS increased, elongation slightly decreased during welding and irradiation. Tensile properties predicted by the different methods such as polynomial, ANN, and statistics were almost the same. As regards the scattering factor, it was 2 for yield stress, 1.5 for UTS and 3 for elongation.

Introduction

The economic performance of next generation reactors requires the reduction of the amount of materials by employing steel which has excellent thermal properties and high-temperature strength. 9–12Cr–Mo steels were considered for in-core applications (cladding, wrappers, and ducts) for sodium fast reactors (SFR) and pressure vessel for very-high-temperature reactor (VHTR) because of their high thermal conductivity, lower expansion coefficients and excellent irradiation resistance to void swelling [1-3]. Void swelling limited the use of the high swelling austenitic steels for fuel cladding and other in-core applications. 9Cr steel was favoured for next generation reactors, because 12Cr steels were also susceptible to the formation of delta ferrite, which has several detrimental effects on such properties as creep, toughness and could cause embrittlement. The substitution of W for Mo enhanced high-temperature tensile strength, fracture toughness and creep strength because tungsten-containing steels diffused slowly, which slowed recovery and precipitated Laves phase [4] [5].

The pressure vessel of VHTR was fabricated by welding and irradiated during operation. The failure of a component was preferred in weldment because of heterogeneity in microstructure, the differences in the thermal cycles during welding, and residual stress. Irradiation induced the hardening and embrittlement [6-9]. Mechanical properties of the pressure vessel of VHTR were needed under operation condition of VHTR that was high temperature and irradiated. In this study, the tensile properties of W added 9Cr steel were evaluated depending on temperature after welding and irradiation. Tensile properties predicted by some methods are also described.

Experimental procedure

The chemical composition of 9Cr-1Mo-1W steel is shown in Table 1. For this welding process submerged arc welding (SAW) with thermanit MTS 911 wire was used. The post-weld heat treatment was 750°C. The microstructure was tempered martensite. Tensile specimens of base metal and welds were irradiated at 390°C to a fluence of 4.2×10^{19} n/cm² ($E > 1.0$ MeV) in the HANARO reactor, at KAERI.

With respect to the tensile tests performed under displacement control, it can be observed that the strain rate was 2×10^{-3} /s and the test temperature was within $\pm 2^\circ\text{C}$. As regards the tensile test specimen, it was 25 mm gage length, 3.75 mm width and 1 mm thickness. The test temperature ranged from room temperature up to 700°C.

Table 1: Chemical composition of 9Cr-1Mo-1W steel

C	Mn	Si	Ni	Cr	Mo	V	Nb	W
0.12	0.40	0.02	0.80	10.3	1.00	0.20	0.057	1.0

Results

Tensile properties

Figure 1 indicates the tensile properties of base metal and welds with their temperatures. As can be seen, during the welding process there is a slight increase in yield stress and UTS and also a slight decrease in elongation. Elongation decreased slowly below 400°C and increased above 400°C. Yield stress and UTS decreased gradually below 500°C and decreased abruptly above 500°C. Figure 2 indicates the effect of irradiation on tensile properties for base metal and welds. As for base metal and welds, irradiation resulted in an increase in yield stress and UTS and a slight decrease in elongation.

Figure 1: Tensile properties with temperature for base metal and weldment of 9Cr-1Mo-1W steel

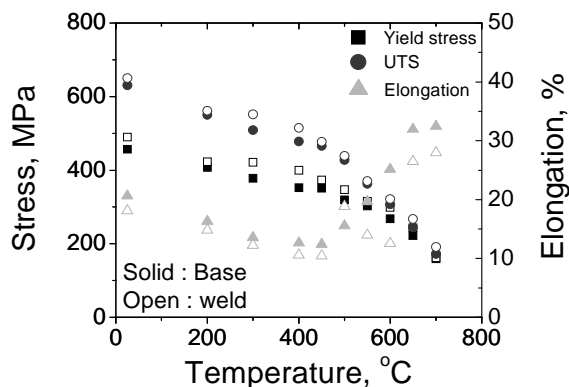
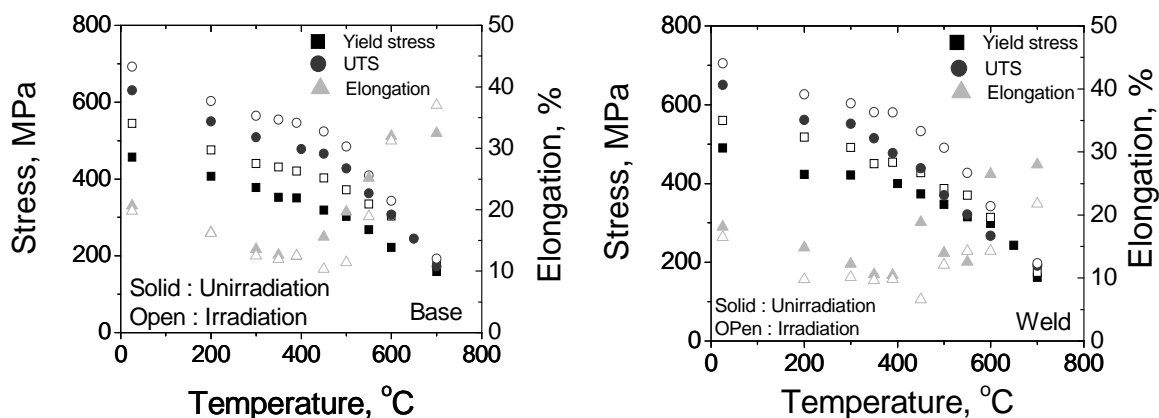
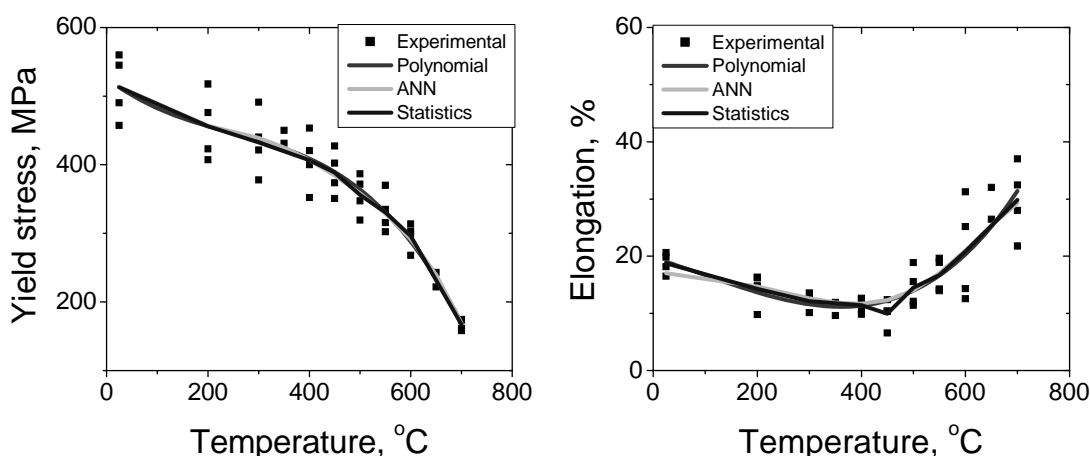


Figure 2: Tensile properties with temperature for base metal and weldment for irradiated 9Cr-1Mo-1W steel



Prediction of tensile properties

Tensile properties of base metal and welds were fitted by applying polynomial regression, artificial neural network (ANN) and statistics methods. Figure 3 shows the different methods applied to tensile properties, which had almost the same values. As regards the scattering factor, it was 2 for yield stress, 1.5 for UTS and 3 for elongation.

Figure 3: Prediction of tensile properties for base metal and weldment for 9Cr-1Mo-1W steel

Conclusion

While yield stress and UTS increased, elongation slightly decreased during welding and irradiation. Tensile properties predicted by the different methods such as polynomial, ANN and statistics were almost the same. As regards the scattering factor, it was 2 for yield stress, 1.5 for UTS and 3 for elongation.

References

- [1] R.L. Klueh and A.T. Nelson (2007), *Journal of Nuclear Materials*, 371. 37–52.
- [2] K.L. Murty and I. Charit (2008), *Journal of Nuclear Materials*, 383. 189–195.
- [3] T. Wakai, K. Aoto, M. Sukekawa, S. Date, and H. Shibamoto (2008), *Nuclear Engineering and Design*, 238. 399–407.
- [4] J.S. Park, S.J. Kim, and C.S. Lee (2001), *Science and Engineering*, A298. 127–136.
- [5] R.L. Klueh, D.J. Alexander, and M.A. Sokolov (2002), *Journal of Nuclear Materials*, 304. 139–152.
- [6] U.E. Klotz, C. Solenthaler, and P.J. Uggowitzer (2008), *Materials Science and Engineering*, A 476. 186–194.
- [7] F. Abe, T. Noda, H. Arakii, M. Narui, and H. Kayano (1989), *Journal of Nuclear Materials*, 166. 265–277.
- [8] Y. Dai, X.J. Jia, and K. Farrell (2003), *Journal of Nuclear Materials*, 318. 192–199.
- [9] J. Henry, X. Averty, Y. Dai, P. Lamagnere, J.P. Pizzanelli, J.J. Espinas, and P. Wident (2003), *Journal of Nuclear Materials*, 318. 215–227.

Computer simulation on the isochronal annealing of irradiated Fe using the kinetic Monte Carlo method*

Gyeong-Geun Lee, Junhyun Kwon
Korea Atomic Energy Research Institute
Daedeok-daero, Yuseong-gu, Daejeon, Republic of Korea

Abstract

An isochronal annealing experiment to measure resistivity has been used as a useful method to analyse the kinetics of irradiation defects. In spite of much information from the experiments, it is difficult to adequately interpret isochronal annealing results because of the limitations of an indirect method. In this study, we analysed an evolution of irradiation defects in Fe using the newly developed kinetic Monte Carlo simulation (KMC). The difference of irradiation methods between electron and neutron irradiation was investigated by comparing defects evolution using KMC simulations. The correlated recombination between vacancies and self-interstitial atoms can be simulated properly during isochronal annealing by the KMC. In particular, electron irradiation induced a significant difference in defects evolution between the KMC and rate theory model because of a correlated recombination. The dose and cascade energy effect were also investigated and the accumulation behaviour was compared to the published results.

* The full paper being unavailable at the time of publication, only the abstract is included.

Creep properties in air and helium environments of Alloy 617 for a VHTR*

Woo-Gon Kim, Song-Nan Yin, Gyeong-Geon Lee, Ji-Yeon Park, Yong-Wan Kim
Korea Atomic Energy Research Institute (KAERI), Nuclear Materials Research Division,
Daedeok-daero, Yuseong, Daejeon, Republic of Korea

Abstract

Very-high-temperature gas-cooled reactors (VHTR) are the most promising reactor types among Generation IV reactors with a cost-effective production of both electricity and hydrogen. The VHTR structural components are designed for a design life of 60 years at 950°C and 3~8 MPa in helium (He) impurities. Compared to other candidate alloys, Alloy 617 is a prime candidate material for the VHTR components due to its superior creep resistance above 800°C. In this paper, creep behaviours for Alloy 617 were investigated in air and He environments at 950°C and their properties were compared. Creep rupture time in air was longer than that in He environment. The relationship between a creep rate and stress showed a good linearity in air and He environments. At this creep condition, Norton's power rule was well-followed by Alloy 617. The creep rate in He environment was higher than that in air and the creep rupture time in He environment was shorter than that in air. It could also be seen that the thickness of Cr-oxide layer in He environment was more significant with increasing creep rupture time than that in air environment.

* The full paper being unavailable at the time of publication, only the abstract is included.

Session II

Metal – Compatibility

Chairs: D.Y. Ku, M.Y. Ahn, I.K. Yu, S. Cho, H.G. Lee, K.J. Jung

Thermal fatigue and thermal ageing test of low activation ferrite/martensitic steel for helium-cooled solid breeder TBM*

D.Y. Ku, M.Y. Ahn, I.K. Yu, S. Cho, H.G. Lee, K.J. Jung

ITER Korea, National Fusion Research Institute, Daejeon, Republic of Korea

Abstract

Test blanket module (TBM) corresponding to DEMO-relevant blanket will be tested in ITER to verify the capability of tritium self-sufficiency and the extraction of high-grade heat suitable for the production of electricity. For this purpose, the Republic of Korea has developed helium-cooled solid breeder (HCSB) TBM. The primary candidate for structural material of the Korean HCSB TBM is the low-activation ferritic/martensitic (LAFM) steel since it has superior swelling resistance under irradiation, excellent thermal properties under high temperatures and good weldability. For the successful fabrication of the TBM and due to the complexity of its structures, it is necessary to develop various joining technologies, such as hot isostatic pressing (HIP) and tungsten inert gas (TIG) welding. In this study, TIG welding and HIP bonding technologies for the LAFM steel were investigated. Thermal fatigue and thermal ageing at the welding joint are especially important phenomena to be investigated for the structural robustness of the TBM. Thermal fatigue cycle tests were performed at 300–550°C with 10, 50 and 100 cycles. A thermal ageing test was also performed at 550°C for 240, 480 and 960 hours. The metallurgical examinations have showed that the size of LAFM steel grain increased after thermal fatigue and thermal ageing test. Based on the mechanical test and the microstructure examination, the TIG welding quality and the applied HIP process have been found to be reasonable.

* The full paper being unavailable at the time of publication, only the abstract is included.

Corrosion behaviour of 316LN in static liquid lead-bismuth eutectic*

**Xiaogang Fu¹, Bin Long¹, Jinquan Zhang¹, Fengmin Chu¹,
Yongli Xu¹, Alessandro Gessi²**

¹China Institute of Atomic Energy, Beijing, China,

²ENEA C.R. Brasimone, Camugnano, Italy

Abstract

The aim of the corrosion tests performed is to focus on the study dealing with corrosion behaviour and the tensile properties of China-made 316LN steel in static liquid Pb-Bi eutectic (LBE). The objectives of the tests are to evaluate corrosion mechanism and to estimate the corrosion rates of 316LN exposed to LBE with high and low oxygen activities. The test temperatures are 673 K and 573 K, the foreseen test times were 1 000 hours, 2 000 hours, 3 000 hours and 5 000 hours.

* The full paper being unavailable at the time of publication, only the abstract is included.

Compatibility of CLAM steel 9Cr2WVTa with flowing lead*

Jinquan Zhang¹, Bin Long¹, Xiaogang Fu¹, Yongli Xu¹, Fengmin Chu¹, Alessandro Gessi²
¹ Institute of Atomic Energy, China, ² ENEA Brasimone Center, Italy

Abstract

The corrosion tests of China low-activity martensitic (CLAM) steel 9Cr2WVTa in flowing Pb started at the ENEA Brasimone Research Center and at the China Institute of Atomic Energy (CIAE) based on a research agreement between China and Italy. The corrosion tests were carried out using CHEOPE-III loop, which was available in Brasimone. The test parameters of this loop were chosen to be representative of a high oxygen potential environment. The test temperature was 773 K and the test times were 5 000 hours and 10 000 hours with a liquid metal velocity on the surface of specimens of about 1 m/s. The specimens exhibited a weight gain after the tests, the thick and compact oxide layer was formed on the surface of specimens, which indicates the oxidation of specimens in lead with saturated oxygen concentration.

* The full paper being unavailable at the time of publication, only the abstract is included.

Ageing effects of nickel-based superalloys on mechanical properties for VHTR applications

Daejong Kim¹, Injin Sah¹, Changheui Jang²

¹Korea Advanced Institute of Science and Technology, Republic of Korea, ²Khalifa University of Science, Technology and Research, Republic of Korea

Introduction

Nickel-based superalloys like Alloy 617 and Haynes 230 are considered to be key candidate materials for the intermediate heat exchanger (IHX) in a very-high-temperature reactor (VHTR). The helium coolant inevitably contains a small number of impurities, such as H₂, CO, CO₂, H₂O, and CH₄, in the operating environment of the VHTR [1]. These gas impurities can lead to low-temperature embrittlement of nickel-base superalloys after high-temperature exposure [2]. In this study, the effects of environmental damage on the ductility of Alloy 617 and Haynes 230 were evaluated after ageing treatment in heavily carburising, decarburising and slightly oxidising helium environments containing H₂, H₂O, CO, CO₂ and CH₄.

Experimental

Commercial wrought nickel-based superalloys, especially Alloy 617 and Haynes 230 were investigated in this study. The chemical compositions of Alloy 617 and Haynes 230 were analysed by ICP-MS and are listed in Table 1. Ageing heat treatment of the small-size, plate-type specimens of 0.5 mm in thickness was carried out for 500 h at 900°C and 1 000°C. The impure helium chemistries to simulate the VHTR environments are listed in Table 2. After ageing heat treatment, tensile tests were carried out at 0.1 mm/min at room temperature.

Table 1: Chemical composition of Alloy 617 and Haynes 230 (in wt%)

	Ni	Cr	Co	Mo	W	Fe	Al	Mn	Si	Ti	C
Alloy 617	Bal.	21.6	11.8	8.92	-	1.14	1.5	.05	.5	.35	.1
Haynes 230	Bal.	21.5	.36	1.09	13.8	2.94	.29	.46	.38	-	.1

Table 2: Composition of impurities in He gases (in μ bar)

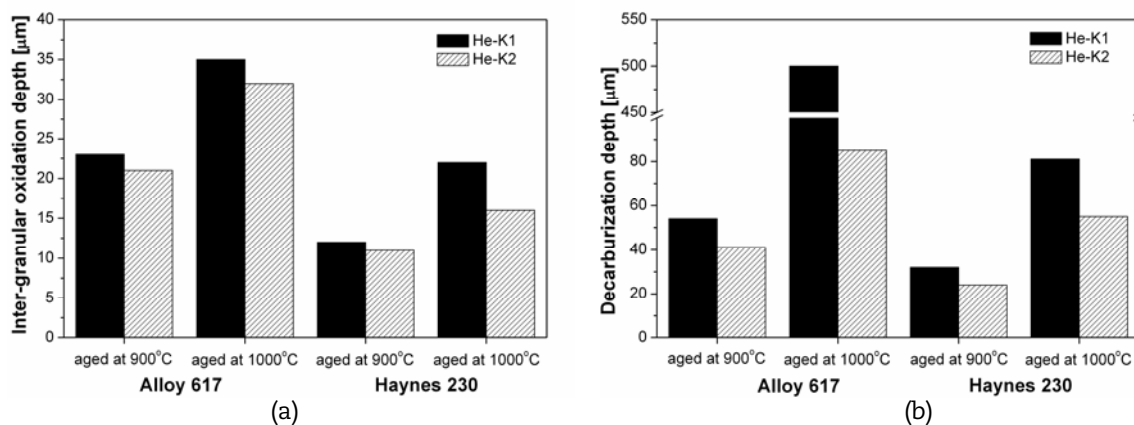
	He	H ₂	H ₂ O	CO	CO ₂	CH ₄
He-K1 at 900°C	Bal.	40	0.7	50	10	20
He-K1 at 1 000°C	Bal.	50	0.7	50	10	15
He-K2 at 900°C	Bal.	-	0.7	50	10	-
He-K2 at 1 000°C	Bal.	-	0.7	50	10	-

Results and discussion

Microstructure after ageing heat treatment

After 500 hours exposure of Alloy 617 and Haynes 230 to He-K1 and He-K2, Alloy 617 and Haynes 230 were oxidised and decarburised. The volume fraction of the intergranular oxides and the depth of the carbide free zone were much greater in Alloy 617 than in Haynes 230, as shown in Figure 1. In particular, the thickness of the 1 mm-thick specimen of Alloy 617 was completely decarburised at 1 000°C in He-K1.

Figure 1: (a) Inter-granular oxidation depth, and (b) decarburisation depth of Alloy 617 and Haynes 230 after ageing in He-K1 and He-K2 at 900°C and 1 000°C

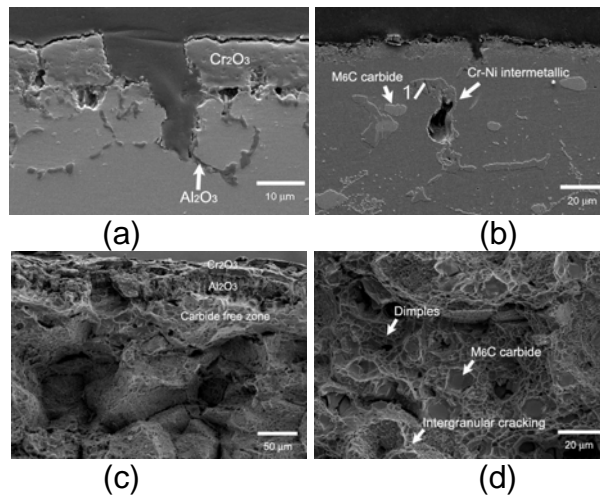


Loss of ductility after ageing heat treatment

Figure 2 shows microstructures of the tensile-tested Alloy 617 and Haynes 230 after ageing for 500 h at 1 000°C in He-K2. For Alloy 617, Al₂O₃ inter-granular oxides below the surface oxide layer and the coarsening of carbides on the grain boundaries caused a loss in ductility. For the same reason, the fracture mode was predominantly inter-granular. For Haynes 230, on the other hand, the localised fracture of globular intermetallic precipitates and grain boundary carbides were the main causes of the loss in ductility for the specimen aged for 500 hours. During the test, fracture of globular M₆C type carbides determined mostly the mixed fracture mode of inter-granular and intra-granular.

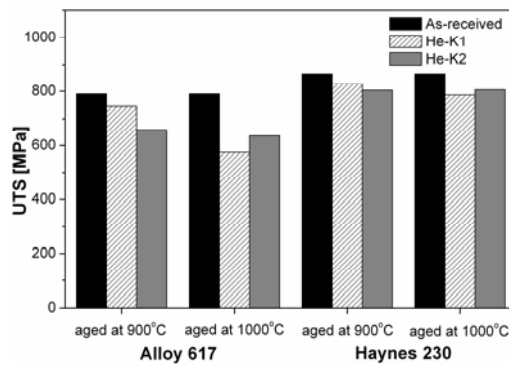
Figure 3 shows the room temperature tensile test results of Alloy 617 and Haynes 230 aged in the impure helium environments for 500 hours at 900°C and 1 000°C. The reduction in elongation was considerable compared to the UTS, particularly in a He-K2 environment. It is indicated that the effect of inter-granular cracking on a fracture mode is reduced by the formation of an extensive carbide free zone in He-K2 and eventually the ductile fracture is more significant. The presence of H₂ probably accelerated the decarburisation rate at higher temperatures by reducing a Cr₂O₃ layer. Substantial decarburisation of Alloy 617 led to the high ductility and the appearance of a fracture surface showed glide plane fracture with ripples and stretch marks as shown in Figure 4.

Figure 2: Fracture behaviours of alloys after 500 hours exposure at 1 000°C in He-K2

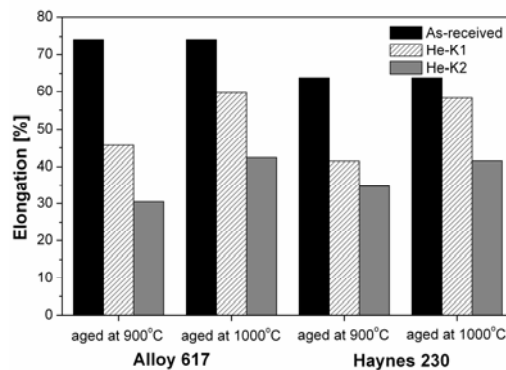


(a) a surface crack of Alloy 617, (b) a surface crack of Haynes 230, (c) a fracture surface of Alloy 617 and (d) a fracture surface of Haynes 230

Figure 3: Change in tensile properties after ageing at 900°C and 1 000°C under He-K1 and He-K2 conditions for 500 hours: (a) UTS, (b) elongation

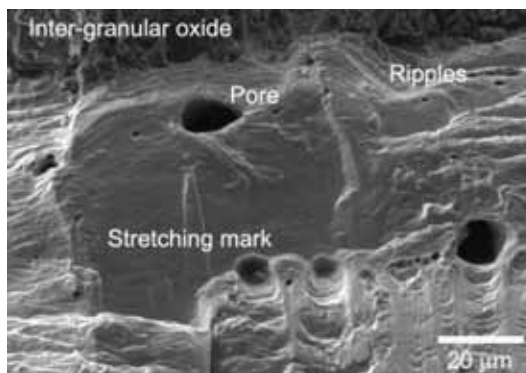


(a)



(b)

Figure 4: Fracture surface of Alloy 617 showing glide plane fracture after ageing for 500 hours at 1 000°C in He-K1



Conclusions

A loss in ductility of Alloy 617 and Haynes 230 occurred after ageing heat treatment in oxidising and decarburising conditions, which resulted from inter-granular cracking along inter-granular oxidation and coarsening of grain boundary carbides. Oxidation and decarburisation were less significant for Haynes 230 because of its good oxidation resistance. The presence of H_2 probably accelerated the decarburisation rate at higher temperatures by reducing the Cr_2O_3 layer. Substantial decarburisation of Alloy 617 led to the high ductility and the appearance of a fracture surface indicated glide plane fracture with ripples and stretching marks. Local brittle fracture was observed in M_6C carbides and intermetallic precipitates which played an important role in the loss of ductility in addition to inter-granular cracking for Haynes 230.

References

- [1] R. Nieder (1980), Specialists Meeting on Coolant Chemistry, Plate-out and Decontamination in Gas Cooled Reactors, Germany, 144-152.
- [2] R. Wright, J. Simpson, A. Wertsching, W. D. Swank (2008), *Proceedings of the 4th International Topical Meeting on High-Temperature Reactor Technology*, United States.

Effects of carburisation and decarburisation on the mechanical properties of nickel-based superalloys for VHTR applications*

Daejong Kim, Injin Sah, Changheui Jang

Korea Advanced Institute of Science and Technology, Republic of Korea

Abstract

This experiment investigated the ageing effects of nickel-based superalloys, such as Alloy 617 and Haynes 230 on low-temperature embrittlement for VHTR applications. Tensile tests were carried out at room temperature after ageing at 900 °C and 1 000 °C in two impure helium environments, such as decarburisation and carburisation environments containing impurities such as CH₄, CO, CO₂, H₂O, in the heavy carburisation environment (He+10%CH₄) and decarburisation environment (air). The susceptibility of Alloy 617 and Haynes 230 to carburisation and decarburisation was discussed. To evaluate the ageing effects on mechanical properties, environmental damage of both alloys such as inter-granular oxidation, the coarsening of grain boundary carbides, the formation of pool-like carbides and fracture of intra-granular carbides were studied and their roles in fracture mode were discussed.

* The full paper being unavailable at the time of publication, only the abstract is included.

Effect of He environment on the microstructure and creep properties of Inconel Alloy 617 at high temperature*

G.G. Lee, D.J. Kim, W.G. Kim, J.Y. Park
KAERI, Republic of Korea

Abstract

Inconel Alloy 617 is regarded as a candidate material for the intermediate heat exchanger (IHX) of the very-high-temperature gas reactor (VHTR), which is one type of next generation nuclear reactors. It has been reported that high operating temperatures and He environment cause a degradation of Alloy 617 during creep test. In this study, the effect of He environment on the integrity of Alloy 617 was investigated from the viewpoint of the microstructure. The thickness of the outer Cr-oxide layer in the creep specimens increased with creep time at 950°C, but the oxide layer was delaminated in the long creep time. The carbides at grain boundaries near the surface disappeared preferentially, the thickness of the decarburised zone in the matrix increased in proportion to the creep time. It has been supposed that the impure gases in the He environment cause a reduction in the strength of the grain boundaries and creep rupture time.

* The full paper being unavailable at the time of publication, only the abstract is included.

Hydrogen effect on nickel and nickel oxide phase transition at hydrogenated water environment

Hyo On Nam¹, Il Soon Hwan¹, Kyu Hwan Lee²

¹Nuclear Materials Laboratory, Seoul National University, Republic of Korea

²Computational Science Center, Korea Institute of Science and Technology, Republic of Korea

Abstract

A number of past studies showed that stress corrosion cracking growth rate of nickel-based alloys in water was affected by dissolved hydrogen and exhibited a maximum susceptibility in the proximity of the nickel/nickel oxide phase transition when the dissolved hydrogen concentrations (C_{aq, H_2}) were varied. Pourbaix diagram of nickel shows that H_2/H_2O equilibrium line is in parallel with Ni/NiO equilibrium line at a distance that can be increased or decreased as a function of hydrogen fugacity (f_{H_2}). This highlights the relationship between Ni/NiO phase transition and the electrochemical corrosion potential of the system with the hydrogen concentration as a factor of primary water stress corrosion cracking. In this work, a thermodynamic model of the Ni/NiO phase equilibrium has been employed to determine the Ni/NiO phase boundary in terms of the hydrogen fugacity at temperatures. In this thermodynamic model, Henry's law coefficient (k_H) of hydrogen, the ratio of partial pressure of hydrogen in atmosphere to the aqueous hydrogen concentration, is identified as a key parameter that should be verified at the temperature and pressure of interest to assure reliable results. Contact electric resistance measurement on nickel coupon was made by Attanasio and Morton to show that corresponding enthalpy and entropy, respectively, of formation for Ni/NiO equilibrium reaction in water ($Ni+H_2O = NiO+H_2$) at room temperature was different from previously reported values. In this paper, hydrogen solubility data in water at various temperatures and pressures were compiled and Henry's law coefficients were determined.

Introduction

Nickel-based alloys, such as Alloy 600 have been used as various tubes and nozzles such as steam generator tubes and control rod drive mechanism (CRDM) nozzles in nuclear water reactors, because of their high strength with necessary toughness and high resistance to aqueous corrosion. These alloys are known to exhibit inter-granular stress corrosion cracking (IGSCC) at high-temperature water environment. In particular, primary water stress corrosion cracking (PWSCC) of Alloy 600 and related 82 and 182 weld metal have become a pressing concern for pressurised water reactor (PWR) plants, because cracks and leaks have been discovered at numerous PWR pressure boundaries and PWSCC of nickel-based alloys have revealed a safety threat to nuclear reactor systems. Therefore, for the reliability of nickel-based alloy components in nuclear reactor systems, it is necessary to understand the PWSCC of nickel-based alloys.

A number of past studies have shown that stress corrosion cracking growth rate (SCCGR) of nickel-based alloys in water was affected by dissolved hydrogen and exhibited maximum susceptibility in the proximity of the nickel/nickel oxide (Ni/NiO) phase transition when the dissolved hydrogen concentrations (C_{aq,H_2}) were varied. A pourbaix diagram of nickel shows that H_2/H_2O equilibrium line is in parallel with Ni/NiO equilibrium line at a distance that can be increased or decreased as a function of hydrogen fugacity (f_{H_2}). This highlights the relationship between Ni/NiO phase transition and the electrochemical corrosion potential (ECP) of the system with the hydrogen concentration as a factor of primary water stress corrosion cracking.

In this work, a thermodynamic model of the Ni/NiO phase equilibrium has been employed to determine the Ni/NiO phase boundary in terms of the hydrogen fugacity at temperatures. In this thermodynamic model, Henry's law coefficient (k_H) of hydrogen, the ratio of partial pressure of hydrogen in atmosphere to the aqueous hydrogen concentration, is identified as a key parameter that should be verified at the temperature and pressure of interests to assure reliable results. Contact electric resistance (CER) measurement on nickel coupon was made by Attanasio and Morton to show that corresponding enthalpy and entropy, respectively, of formation for Ni/NiO equilibrium reaction in water ($Ni+H_2O = NiO + H_2$) at room temperature was different from previously reported values [1].

Thermodynamic modelling of Ni/NiO phase transition

Pourbaix diagram of nickel in aqueous environments

The Ni/ H_2O Pourbaix diagram (Figure 1) is used to understand the effect of various chemical additives and impurities such as B, Li, H⁺ and H_2 fugacity [2]. Reactions of nickel and nickel oxide involving electrons and hydrogen ions are given by Equation (1).



The Nernst equation of this reaction [Equation (2)] gives Ni/NiO equilibrium line.

$$\begin{aligned} E &= E^0 + \frac{RT}{2F} \ln\left(\frac{a_{NiO} a_{H^+}^2}{a_{Ni} a_{H_2O}}\right) \\ &= E^0 + 0.059 \cdot \log(a_{H^+}) \end{aligned} \quad (2)$$

$$\text{where, } E^0 = \frac{\Delta G^0}{nF} = \frac{\mu_{NiO}^0 - \mu_{Ni}^0 - \mu_{H_2O}^0}{2F} \cong 0.11 \text{ V}$$

On the other hand, water solubility lines for H_2O/H_2 can be determined from Equation (3) and its Nernst equation [Equation (4)].

$$(H_2)_g = (H_2)_{aq}, \quad K_{eq} = \frac{[\gamma \cdot c_{aq}]}{[\phi \cdot P_{H_2}]} = \frac{[H_2]_{aq}}{[H_2]_g} = \frac{1}{k_H} \left(\frac{\gamma}{\phi} \right) \quad (6)$$

where, K_{eq} is the equilibrium constant; $[H_2]_{aq}$ and $[H_2]_g$ represent the activity of $(H_2)_{aq}$ and fugacity of $(H_2)_g$, respectively; γ is the activity coefficient of dissolved hydrogen and ϕ is the fugacity coefficient of gaseous hydrogen; k_H is Henry's constant. From the thermodynamic modelling of the Ni/NiO phase transition, the equilibrium concentration of dissolved hydrogen can be determined as shown in Equation (7) as the activity coefficient of solute approaches unity in infinitely dilute solutions [3].

$$C_{aq, H_2}^{Equil.} = \frac{f_{H_2}}{k_H} \quad (7)$$

In this study, Henry's constant was determined by compiling solubility data of hydrogen in water. On the other hand, equilibrium fugacity of gaseous molecular hydrogen was taken from thermodynamic data. Using these compiled data, Ni/NiO phase equilibrium, as a function of temperature, was determined and compared with other thermodynamic predictions and the experimentally observed equilibrium line.

From the works of Attanasio and Morton [1] [4], equilibrium of hydrogen fugacity and equilibrium dissolved hydrogen concentration were presented based on the thermodynamic data and their contact electric resistance (CER) experimental results. However, there is a discrepancy between thermodynamically predicted phase equilibrium and experimentally determined equilibrium. Theoretical NiO thermodynamic values of ΔH_{298}^0 and ΔS_{298}^0 are 46 100 J/mol and 68.0 J/mol-K. Experimental values are 38 400 J/mol and 43.5 J/mol-K [1].

Hydrogen solubility and Henry's constant of hydrogen in water

Calculation of the fugacity coefficient

The thermodynamic model of the nickel/nickel-oxide phase transition needs Henry's constant of hydrogen in water. From the Equation (6), activity coefficient of dissolved hydrogen (γ), fugacity coefficient of gaseous hydrogen (ϕ) and equilibrium constant (K_{eq}) should be determined in advance to obtain the Henry constant. As the activity coefficient of solute approaches unity in infinitely dilute solutions, only fugacity coefficient and reaction constant were compiled from various references.

The fugacity coefficient (ϕ), which was calculated from the relation of the fugacity (f) of a real gas at partial pressure (P) is defined by Equation (8).

$$\gamma = \left(\frac{f}{P} \right) = \exp \left(\frac{- \int_{P=0}^P (V_I - V) \partial P}{RT} \right) \quad (8)$$

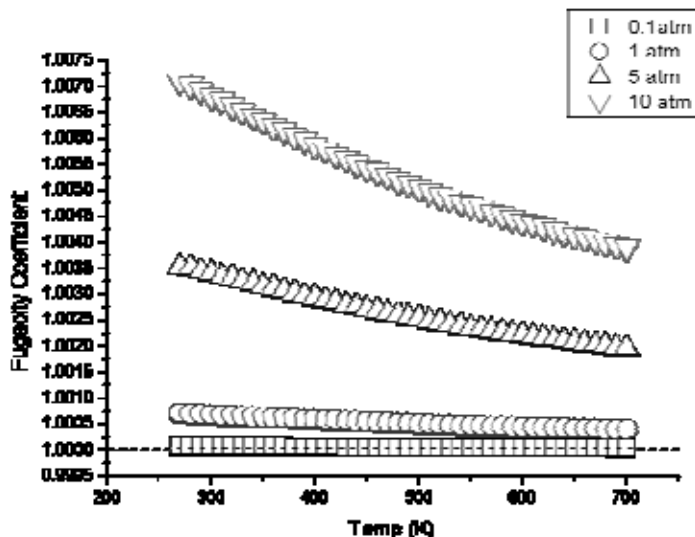
where, V_I and V are the volumes of the ideal gas and real gas, respectively; R is the gas constant (8.3144 J/mol-K); T is the temperature in Kelvin (K).

V_I was determined from the equation of state of ideal gas. On the other hand, Van der Waals equation of state was used to predict the volume of real gas (V) and predicted V was numerically solved by the Newton-Raphson method using derivative [5]. Integration of Equation (8) was conducted numerically with Romberg integration algorithm [6].

Figure 2 shows the numerically calculated fugacity coefficient when various hydrogen partial pressures were applied at different temperature ranges. Operating dissolved hydrogen (DH) condition of primary water reactors (PWR) is around 30 cc/kg, which is

approximately 0.7 atm of hydrogen overpressure. Thus, it can be concluded that the fugacity coefficient effect on Henry's constant in the condition of PWR is very small.

Figure 2: Calculated fugacity coefficient of different hydrogen partial pressures



Determination of Henry's constant of hydrogen (k_H)

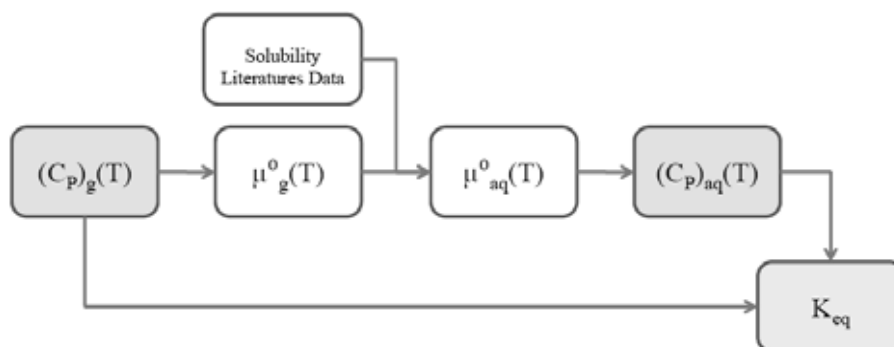
The equilibrium constant of reaction $(H_2)_g = (H_2)_{aq}$, which can be defined by Equation (9), was determined by compiling the solubility data of hydrogen from various literature data [7-11] in advance to determine Henry's constant of hydrogen. Literature on hydrogen solubility which measures the solubility of 1 atm hydrogen partial pressure was chosen at first. All data were measured in the temperature range from 0°C to 100°C.

$$K_{eq} = \exp\left\{\frac{\mu_g^{\circ}(T) - \mu_{aq}^{\circ}(T)}{R \cdot T}\right\} \quad (9)$$

The chemical potential of standard state is defined by Equation (10), which relates the chemical potential to the heat capacity, enthalpy and entropy at constant pressure. 298 K is set as a reference temperature.

$$\mu^{\circ}(T) = \mu_{298}^{\circ} + \int_{298}^T C_p \partial T - T \cdot \int_{298}^T \frac{C_p}{T} \partial T - S_{298}^{\circ} (T - 298) \quad (10)$$

From the heat capacity data of gaseous hydrogen $[(C_p)_g(T)]$, the functional form of chemical potential of gaseous hydrogen $(\mu_g^{\circ}(T))$ was determined. As the heat capacity data of aqueous hydrogen $[(C_p)_{aq}(T)]$ with the variation of temperature is scarce, we need to determine this value indirectly from the hydrogen solubility data. Detailed procedure of calculation is similar to the work of Tromans [3]. With the solubility research data of hydrogen in water [7-11], temperature dependent experimental reaction constant (K) was obtained. Thus, temperature dependent chemical potential of aqueous hydrogen $[\mu_{aq}^{\circ}(T)]$ can be determined, then functional form of heat capacity of aqueous hydrogen $[(C_p)_{aq}(T)]$ can be predicted from $\mu_{aq}^{\circ}(T)$. When the functional form of the heat capacity function of gaseous hydrogen and aqueous (dissolved) hydrogen are known, the functional form of equilibrium constant of reaction $(H_2)_g = (H_2)_{aq}$ can be obtained. Schematic and flow of the calculations are summarised in Figure 3.

Figure 3: Flow chart to determine the equilibrium constant

Molar heat capacity of hydrogen from 200 K-700 K was compiled and fitted to 4th order polynomials, as shown in Figure 4. Heat capacity data of Davis [12] and CRC Handbook [13] were used to fit the data point. From the solubility literature data, thermodynamic data of gaseous hydrogen and dissolved hydrogen were obtained, as shown in Table 1. Molar heat capacity of dissolved hydrogen was fitted into constant using the compiled hydrogen solubility data, as shown in Figure 5. Goodness-of-fit (R^2 value) was 0.99941, which means that the molar heat capacity value of dissolved hydrogen scarcely changes.

Table 1: The standard 298 K thermodynamic data for hydrogen

Species	State	μ° [kJ/mol]	S° [J/mol-K]	Ref.
H ₂	g	0	130.68	HSC [14]
H ₂	aq.	17.741	56.914	calculated (this study)

Figure 4: Specific heat of gaseous hydrogen

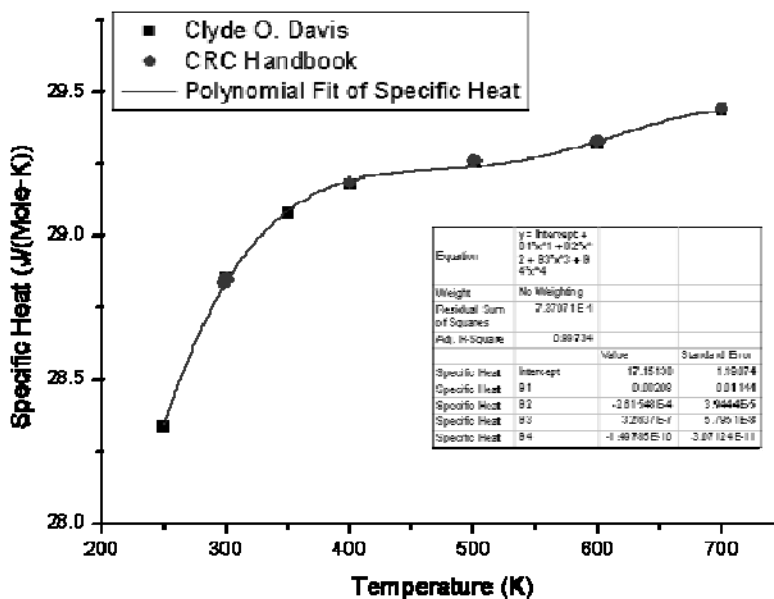
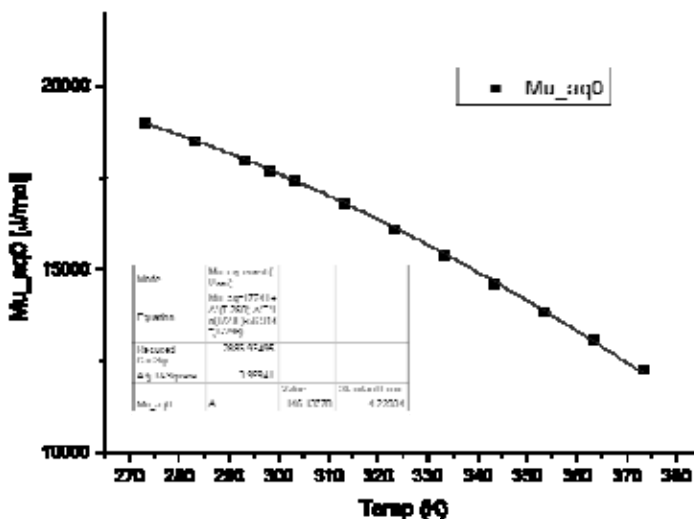


Figure 5: Fitted molar heat capacity of dissolved hydrogen from the $\mu^0_{aq}(T)$



With the molar heat capacity of gaseous hydrogen and dissolved hydrogen function, temperature dependent equilibrium constant of reaction $(H_2)_g = (H_2)_{aq}$ was determined,

$$K_{eq} = \exp \left[\frac{-110.554 + \frac{4849.98}{T} - 0.00553731 \cdot T + 5.2428 \times 10^{-6} \cdot T^2}{-3.27109 \times 10^{-9} \cdot T^3 + 9.00745 \times 10^{-13} \cdot T^4} \right] \cdot T^{15.5137} \quad (11)$$

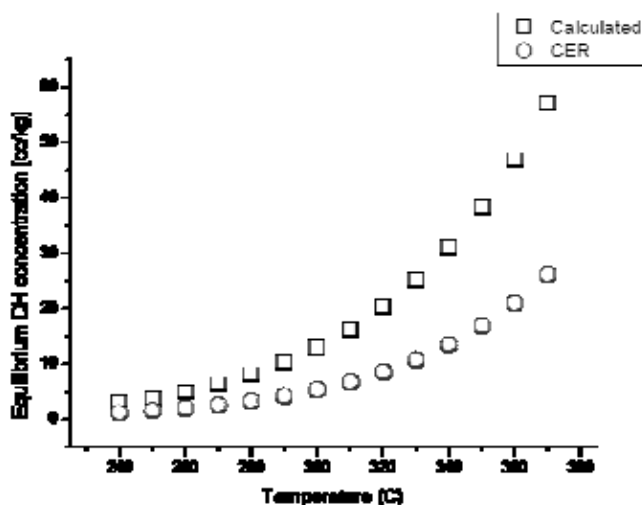
At high temperature and relatively low hydrogen partial pressure, Henry's constant is almost the same as the reciprocal of equilibrium constant as the fugacity and dissolved hydrogen activity coefficients are sufficiently close to unity [see Equation (6)]. Functional form of Henry's constant (k_H), which was obtained in this study, is given below:

$$k_H \cong \frac{1}{K_{eq}} = \frac{\exp \left[\frac{110.554 - \frac{4849.98}{T} + 0.00553731 \cdot T - 5.2428 \times 10^{-6} \cdot T^2}{+3.27109 \times 10^{-9} \cdot T^3 - 9.00745 \times 10^{-13} \cdot T^4} \right]}{22390 \cdot T^{15.5137}} \quad (12)$$

Discussion

Henry's constant was determined from the experimental solubility data of hydrogen in water and was used to model the nickel and nickel oxide phase equilibrium with the thermodynamic data. With Henry's constant [Equation (12)] and the equilibrium fugacity which can be obtained from the thermodynamic free energy of NiO in water environments [13], equilibrium concentration of dissolved hydrogen in primary water was determined, as shown in Figure 6. The discrepancy comes from the inaccuracy of thermodynamic data, because most of the thermodynamic data at high temperatures and high pressures were extrapolated from the experimentally observed data in a low-temperature range and atmosphere. However, an accurate thermodynamic equilibrium modelling of nickel and nickel oxide is still necessary as the CER results can be shifted if a different Henry's constant is used and the cause, which makes the discrepancy between CER experimental equilibrium and thermodynamic equilibrium, is not clear.

Figure 6: Calculated equilibrium dissolved hydrogen concentration and comparison with the Morton's CER equilibrium



Conclusions and future plan

Thermodynamic modelling of nickel and nickel oxide phase transition was conducted based on the thermodynamic handbook data of nickel, nickel oxide phase equilibrium and Henry's constant, which can be derived from the various solubility experimental results. The approach was based on the thermodynamic relation of chemical potentials of gaseous hydrogen and dissolved hydrogen of the equilibrium state. As the chemical potential is a function of temperature dependent molar heat capacity, the molar heat capacity function of gaseous hydrogen and dissolved hydrogen are determined to obtain the general functional form of equilibrium constant and improved Henry's constant. A comparison of equilibrium dissolved hydrogen concentration at the Ni/NiO phase transition between the calculated line from this work and Attanasio and Morton's line based on the CER experiments yields slightly different results. The inaccuracy of thermodynamic data due to the extrapolation of room temperature experimental data to high temperature could be a source of error. However, due to the lack of accurate in-situ experimental data about the phase stability at primary water environments, a thermodynamic modelling of nickel/nickel-oxide phase transition is pursued to determine the cause of the discrepancy.

For future work, *ab-initio* calculation of the free energy of nickel-water system is underway to determine the accurate theoretical phase boundary. Hydrogen concentration effect on the phase transition is also the object of the first-principle computational research. The *ab-initio* thermodynamic modelling results of the nickel/nickel-oxide equilibrium reaction in water will be compared with the thermodynamic and experimental equilibrium to check consistency.

References

- [1] S. A. Attanasio, D.S. Morton (2003), Measurement of the Nickel/Nickel Oxide Transition in Ni-Cr-Fe Alloys and Updated Data and Correlations to Quantify the Effect of Aqueous Hydrogen on Primary Water SCC. *Proc. 11th Int. Conf. Environmental Degradation of Materials in Nuclear Systems*, Stevenson, WA, 10-14 August 2003.
- [2] P.L. Andresen et al. (2007), Effects of PWR Primary Water Chemistry on PWSCC of Ni Alloys. *Proc. 13th Int. Symp. on Environmental Degradation of Materials in Nuclear Power Systems – Water Reactors*.
- [3] D. Tromans (1998), Temperature and pressure dependent solubility of oxygen in water: A thermodynamic analysis. *Hydrometallurgy*, 48(3), pp. 327-342.
- [4] D.S. Morton, S.A.A., G.A. Young (2001), Primary Water SCC Understanding and Characterization Through Fundamental Testing in the Vicinity of the Nickel/Nickel Oxide Phase Transition. *Proc. 10th Int. Conf. Environmental Degradation of Materials in Nuclear Power Systems – Water Reactors*, Stevenson.
- [5] W. H. Press et al. (1992), Newton-Raphson Method Using Derivatives, in *Numerical Recipes in FORTRAN: The Art of Scientific Computing*, Cambridge University Press: Cambridge, England. pp. 355-362.
- [6] W. Romberg (1955), Vereinfachte numerische Integration. *Norske Vid. Sels. Forh*, 28(7).
- [7] H. A. Pray, C.E. Schweickert, and B.H. Minnich (1952), Solubility of Hydrogen, Oxygen, Nitrogen, and Helium in Water - at Elevated Temperatures. *Industrial and Engineering Chemistry*, 44(5), p. 1146-1151.
- [8] U. J. Jáuregui-Haza et al. (2004), Solubility of hydrogen and carbon monoxide in water and some organic solvents. *Latin American Applied Research*, 34(2), p. 71-74.
- [9] R. Wiebe, V.L. Gaddy, and C. Heins (1932), Solubility of hydrogen in water at 25 degrees C. 25 to 1 000 atmospheres. *Industrial and Engineering Chemistry*, 24, pp. 823-825.

- [10] R. Wiebe, V.L. Gaddy (1934), The solubility of hydrogen in water at 0, 50, 75 and 100 °C from 25 to 1000 atmospheres. *Journal of the American Chemical Society*, 56(1), pp. 76-79.
- [11] T. E. Crozier and S. Yamamoto (1974), Solubility of hydrogen in water, seawater, and NaCl solutions, *Journal of Chemical and Engineering Data*, 19(3), pp. 242-244.
- [12] C. O. Davis and H.L. Johnston (1934), Heat Capacity Curves of the Simpler Gases. V. The Heat Capacity of Hydrogen at High Temperatures. The Entropy and Total Energy. A Corrected Table of the Free Energy above 2000°C, *Journal of the American Chemical Society*, 56(5), pp. 1045-1047.
- [13] CRC Handbook, 85th ed. Handbook of chemistry & physics.
- [14] HSC Chemistry(R) 5.0. 2002, Outokumpu.

Session III

Ceramic

Chairs: E-S. Kim, S-H. Chi, Y-W. Kim

Fracture behaviour of nuclear-grade graphite for VHTR*

Eung-Seon Kim, Se-Hwan Chi, Yong-Wan Kim

VHTR Technology Development Group, Korea Atomic Energy Research Institute
Daedeok-daero, Yuseong-gu, Daejeon, Republic of Korea

Abstract

Graphite is designed for use in very-high-temperature gas-cooled reactors (VHTR) not only as a moderator and reflector but also as a major structural component due to its excellent neutronic, thermal and mechanical properties. During a normal operation, these graphite components are subjected to various loadings such as external force and internal stresses resulting from neutron irradiation-induced dimensional and material property changes and a thermal gradient. Fracture mechanics-based structural integrity assessments of graphite components are required to understand the mechanisms and failure criteria of nuclear-grade graphite for the VHTR. The objective of this study was to investigate fracture toughness and the strain energy release rate of selected nuclear grade graphites.

Fracture tests were performed using a 3-point bending specimen with a straight-through notch at a crosshead speed of 0.01 mm/min. Fracture toughness (K_{Ic}) was determined at the maximum load and strain energy release rate-crack extension ($G_I-\Delta a$) curve was obtained by a compliance method. The value of K_{Ic} increased with the coke particle size which may be related to an inherent crack size. The value G_I at the beginning of crack extension increased with coke particle size. Furthermore, as the coke particle size increased the value of G_I grew with crack extension. The influences of the coke particle size and crack-face friction on the K_{Ic} and G_I of the selected nuclear graphites were investigated.

* The full paper being unavailable at the time of publication, only the abstract is included.

Property changes of nuclear grade C_f/C composite by oxidation*

Ji Yeon Park¹, Choong Hwan Jung¹, Weon-Ju Kim¹, Junya Sumita², Taiju Shibata², Kazuhiro Sawa², Ichiro Fujita³, Takashi Takagi⁴, Taiyo Makita⁵

¹Korea Atomic Energy Research Institute, Daejeon, Korea, ²Japan Atomic Energy Agency, Ibaraki, Japan, ³Toyo Tanso Co. Ltd., Osaka, Japan, ⁴IBIDEN Co. Ltd., Gifu, Japan,

⁵Tokai Carbon Co. Ltd., Yamaguchi, Japan

Abstract

The increase in the operating temperature of high-temperature gas-cooled reactors up to 950°C requires ceramic composites as control rod cladding and guide tubes, instead of metallic materials such as Alloy 800H because control rods are exposed to high temperatures, rather high irradiation fluence and slightly oxidising environments under normal operating conditions. These extreme conditions have led to the choice of C_f/C, C_f/SiC or SiC_f/SiC as potential materials for these components. C_f/C composites are considered to be structural components of control rod in short-term options and SiC_f/SiC composites as advanced options in France, Japan and the United States. However, widespread property data, standardisation of characterisation methods and development of design codes are required before the application of ceramic composites for in-core structural components. Oxidation resistance should be estimated at high temperatures under impure He or in air in the case of accidental air ingress.

In this study, baseline thermal and mechanical properties of several nuclear-grade C/C composites were evaluated before and after oxidation. Additionally, oxidation damage of C/C composite was analysed. The oxidation experiments were performed in a range from 500 to 1100°C under air or Ar atmosphere. Thermal properties like heat capacity, thermal conductivity and mechanical properties like flexural strength, tensile strength, inter-laminar shear strength and fracture property of as-received and oxidised specimens were examined.

* The full paper being unavailable at the time of publication, only the abstract is included.

Properties of SiC/SiC_f fabricated by slurry infiltration*

Gun-Young Gil¹, Noviyanto Alfian¹, Dang-Hyok Yoon¹, Weon-Ju Kim², Ji-Yeon Park²

¹School of Materials Science and Engineering, Yeungnam University, Gyeongsan, Republic of Korea, ²Division of Nuclear Materials Technology Development, Korea Atomic Energy Research Institute, Daejeon, Republic of Korea

Abstract

Owing to their excellent mechanical properties, chemical stability and low radioactivity, continuous SiC fiber-reinforced SiC-matrix composites (SiC/SiC_f) are used as structural components for fusion and advanced fission reactors. For these applications, SiC/SiC_f was fabricated by two kinds of slurry infiltration methods: vacuum infiltration and electrophoretic deposition (EPD). 50 nm-sized β -SiC powder and TyrannoTM-SA grade-3 fabrics after coating with pyrolytic carbon (PyC) were used as matrix and fiber-reinforcement. The 10–12 wt. % of Al₂O₃-Y₂O₃-MgO with respect to SiC powder was used as sintering additives. In order to improve composite density, a special infiltration apparatus using a pressure gradient and an alternating tape insertion between fabrics were utilised for vacuum infiltration. In addition, highly-dispersed SiC slurry was prepared for EDP by adjusting the constituent particles' zeta potentials for homogeneous deposition. After hot pressing at 1750°C under 20 MPa for 3 hours in Ar atmosphere, sintered density, microstructure and mechanical strength were evaluated. Overall composite properties fabricated by two different methods were compared to each other. The highest density of composites was 3.13 g/cm³ for 50% fiber content along with a maximum flexural strength of 607 MPa. However, practical applications were needed to solve the problems such as the non-uniform distribution of liquid phase and reaction between PyC and sintering additives during hot pressing.

* The full paper being unavailable at the time of publication, only the abstract is included.

Low-temperature sintering of SiC using ternary aluminium carbides*

Sea-Hoon Lee, Hai-Doo Kim

Korea Institute of Materials Science, Republic of Korea

Abstract

In this study, the application of Al_3BC_3 and Al_4SiC_4 as sintering additives of SiC was investigated. The ternary carbides were synthesised from stoichiometric mixture of aluminium, B_4C , Si and carbon. The effects of the synthetic methods of the additives on the sintering behaviour of SiC were reported. The densification of SiC was attained after spark plasma sintering at 1650°C for 5 minutes under 120 MPa pressure. The hardness, Young's modulus and fracture toughness of sintered SiC specimens were about 21 GPa, 420 GPa and $4\text{ MPa}\cdot\text{m}^{1/2}$, respectively. Both Al_3BC_3 and Al_4SiC_4 were efficient sintering additives of SiC.

* The full paper being unavailable at the time of publication, only the abstract is included.

Determination of the theoretical density and Young's modulus of ceramic ZrO₂ doped with neutron absorbers

Zhang He, Zhengliang Pan

Atomic Energy of Canada Limited, Chalk River Laboratories
Chalk River, Ontario, Canada

Abstract

The Atomic Energy of Canada Limited (AECL) is at present developing an advanced CANDU reactor, ACR-1000¹, which is fuelled with CANFLEX^{®2}-ACR bundles. One of the unique safety features of this fuel is that its central element is designed to control coolant void reactivity during postulated accidents. To satisfy this design requirement, the central element is loaded with zirconia (ZrO₂) pellets as a carrier material, in which burnable neutron absorbers (BNA), dysprosium and gadolinium, are uniformly distributed in the matrix, forming a single-phase solid solution. The carrier material is designed to have a stable fluorite-type cubic crystal structure by adding an appropriate amount of yttria, a structural stabiliser for ZrO₂. In order to be able to do an analysis and develop a reliable computer code for the simulating behaviour of the new material in service condition, various fundamental properties of the material were determined experimentally at AECL Chalk River Laboratories. These properties cover the physical, thermal, mechanical and chemical aspects. In addition, the leaching and oxidation resistance of the material was studied. This paper focuses on reporting the results of the lattice parameter, theoretical density and elastic modulus measurements on the new material.

-
1. CANDU and ACR-1000 (Advanced CANDU Reactor-1000) are registered trademarks of Atomic Energy of Canada Limited.
 2. CANFLEX[®] is a registered trademark of AECL and the Korea Atomic Energy Research Institute (KAERI).

Introduction

The central element of the ACR-1000 bundle is loaded with BNA pellets which contain Gd and Dy. The compositions of the pellets are designed to control the coolant void reactivity during postulated accidents. There is no fissile material in the ZrO₂ matrix. In addition, yttrium oxide (Y₂O₃) is added to the solid solution to ensure that the material has a stable fluorite-type cubic structure [1].

Theoretical density is an important characteristic of the new material. One of its key applications is to calculate the porosity of fabricated pellets. After the theoretical density (ρ_{th}) is determined and the actual density (ρ_s) of the pellets is measured, the porosity of the material (p) can be calculated using the formula $p = 1 - \rho_s / \rho_{th}$ [2].

Young's modulus is one of the most important mechanical properties of materials. In order to simulate the mechanical behaviour of materials, experimental data are needed for analysis and computer code development.

One of the unique safety features of this fuel is that its central element is made of a new material. To provide technical support for the new bundle design, various properties of this material have been studied recently at Chalk River Laboratories under a comprehensive programme [1]. Mechanical properties, including bending strength, fracture toughness and hardness have been experimentally determined. Also, thermal properties, leaching and oxidation resistance of the materials have been investigated; calculations of the theoretical density and determination of Young's modulus of the new material have been conducted.

This paper presents theoretical considerations, experimental setup, results of the theoretical density and Young's modulus work.

Theoretical density

Crystal structure analysis

Zirconia has three crystal structures below its melting point. They are monoclinic (m-ZrO₂), tetragonal (t-ZrO₂) and fluorite-type cubic (c-ZrO₂). They are formed in different temperature ranges. Among them, c-ZrO₂ is the most desirable crystal structure for the central element pellets in the CANFLEX bundle.

In a c-ZrO₂ unit cell with no other additives (see Figure 1 [3]), four Zr⁺⁴ ions occupy the lattice sites and eight O⁻² ions occupy the interstitial sites. The total mass in a c-ZrO₂ unit cell, M , can be calculated using the following expression:

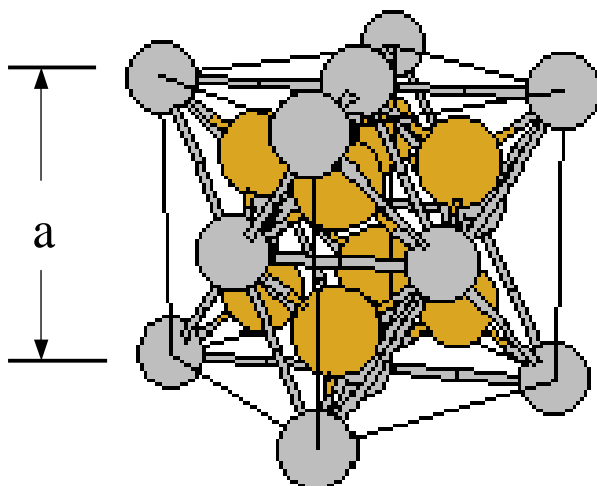
$$M = (4M_{Zr} + 8M_O) / N_A \quad (1)$$

where: M_{Zr} and M_O are the molar masses of Zr (91.22 g/mol) and O (16 g/mol), respectively, and N_A is Avogadro's number (6.023×10^{23}).

The volume of the unit cell (V) can be calculated after the lattice parameter of the unit cell (a) is determined ($V = a^3$). For c-ZrO₂, the lattice parameter determined by X-ray diffraction is 0.5090 nm (i.e. 5.090×10^{-8} cm) [4]. Thus, the theoretical density of the c-ZrO₂, ρ_{th} ($\rho = M/V$), can be determined using the following expression [5]:

$$\rho_{th} = [(4M_{Zr} + 8M_O) / N_A] / a^3 \quad (2)$$

Thereby, the theoretical density of c-ZrO₂ is 6.206 g/cm³ [4].

Figure 1: One unit cell of cubic ZrO₂

Note: Zr⁺⁴ ions occupy all the lattice sites and O⁻² ions occupy the interstitial sites.

The BNA pellet in the ACR central element has a c-ZrO₂ structure due to the addition of Y₂O₃, Dy₂O₃, and Gd₂O₃ oxides. At sintering temperatures, these oxides dissolve in the ZrO₂ cubic matrix. The c-ZrO₂ structure is maintained as the material cools to room temperature.

The addition of the oxides alters the theoretical density of the c-ZrO₂ matrix. Firstly, the lattice parameter and hence, the volume of the unit cell, is altered because the ionic radius of the elements Y, Dy and Gd differ from that of Zr. Secondly, the total mass of the ions in the unit cell is altered. This is because the number of oxygen ions is reduced. The added metal ions are tri-valent (Y⁺³, Dy⁺³ and Gd⁺³). In the unit cell they are substitutes for Zr⁺⁴ ions, occupying the lattice sites. To keep electrical balance, Zr⁺⁴ ion needs two O⁻² ions, but the tri-valent ions only need 1.5 O⁻² ions. The total mass change in the unit cell is also due to the different molar masses of the added elements. Consequently, due to the change in mass (*M*) and volume of the unit cell (*V*), the theoretical density of the Y₂O₃-, Dy₂O₃- and Gd₂O₃-doped material needs to be re-assessed.

With the knowledge that Zr, Y, Gd and Dy ions occupy the lattice sites and the oxygen ions are at the interstitial sites in the unit cells, the theoretical density of the BNA pellet materials, ρ_{th} , can be determined by the following relationship:

$$\rho_{th} = \{4[(\sum x_i M_i + \sum x_j M_j) + (2 \sum x_i + 1.5 \sum x_j) M_o] / N_A\} / a^3 \quad (3)$$

where

$i = \text{Zr}^{+4}, \text{Hf}^{+4}$,

$j = \text{Y}^{+3}, \text{Dy}^{+3}, \text{Gd}^{+3}$,

$x =$ mole fraction of each metal element at the lattice sites,

$M =$ molar mass,

$M_o =$ molar mass of oxygen, occupying the interstitial sites,

$N_A =$ Avogadro's number (6.023×10^{23}), and

$a =$ lattice parameter.

The reason for including Hf (Hf is the element hafnium) in Equation (3) is that HfO₂ is generally present in the ZrO₂ powder that is used for engineering ceramic applications, including the powder used for making the samples discussed in this paper.

X-ray diffraction analysis

Sample preparation

BNA pellet samples with three compositions were made at Chalk River Laboratories by mechanically mixing ZrO₂ with Y₂O₃, Dy₂O₃ and Gd₂O₃, respectively and sintering at high temperatures. The content of each metal element in the samples is shown in Table 1, and the mass of each type of the ions in the unit cell is given in Table 2.

Table 1: Three types of BNA pellet-material with varied content of metal elements

mole fraction	Sample		
	A	B	C
Zr	nominal	low	high
Y	nominal	low	low
Gd	nominal	low	nominal
Dy	nominal	high	nominal
Hf	nominal	low	high
total amount of rare earth oxide	intermediate	high	low

Table 2: Total mass in the unit cell of three types of BNA pellet-material

	Sample		
	A	B	C
total mass of metal ions/cell (g)	7.0977×10^{-22}	8.5801×10^{-22}	7.1168×10^{-22}
# of oxygen ions/cell	7.25	6.95	7.56
mass of oxygen ions/cell (g)	1.9260×10^{-22}	1.8463×10^{-22}	2.0083×10^{-22}
total mass (g)	9.0237×10^{-22}	1.0426×10^{-21}	9.1251×10^{-22}

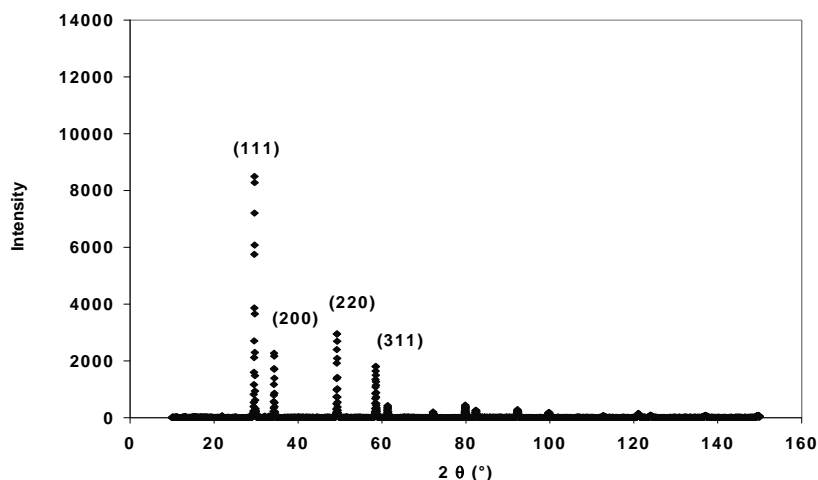
Lattice parameter measurement

The lattice parameter of each sample was measured using X-ray diffraction (XRD) in order to calculate the theoretical density of each sample. The XRD data was obtained using Cu K α radiation with a curved crystal monochromator. The speed for the XRD scan was 0.1°/min in the 2 θ range of 20 to 140°. The diffractometer was calibrated using a silicon standard for accurate 2 θ angular measurements.

XRD results

A typical XRD pattern of the samples is shown in Figure 2. It is a pattern of a single solid solution with a fluorite-type cubic structure, confirming that the doped oxides have been dissolved in the solid solution and no second phase is present. Thus, Equation (3) is valid for calculating the theoretical density of the samples.

Figure 2: Typical XRD pattern for the BNA pellets with a fluorite-type cubic structure

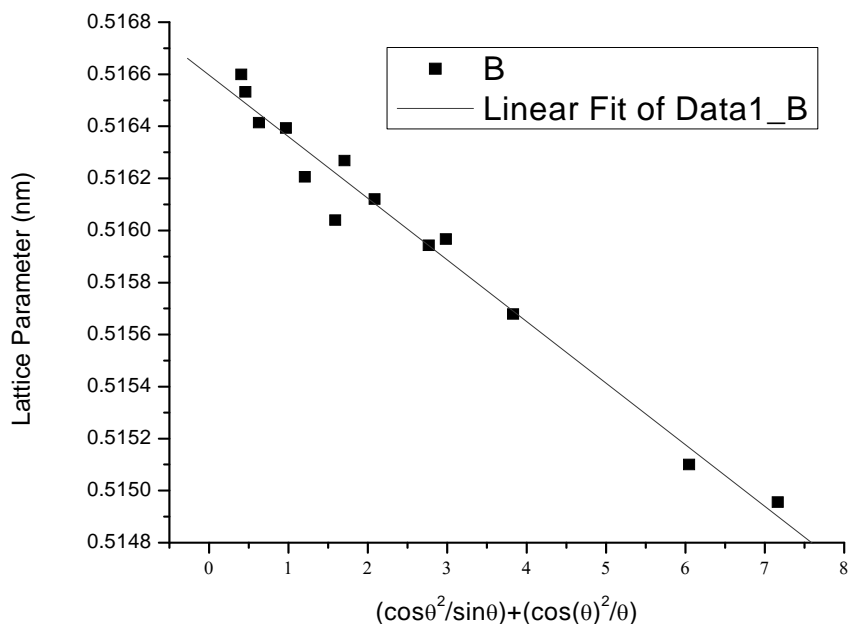


Note: The main diffraction peaks are indexed.

To calculate the lattice parameter of the samples, the “Nelson-Riley” (N-R) method [6] was used. The N-R function of θ [see Equation (4) below] is plotted (on X-axis) against the lattice parameter (on Y-axis) calculated at each given θ angle.

$$\text{N-R function} = \cos^2\theta/\sin \theta + \cos^2\theta/\theta \quad (4)$$

An example of the results is shown in Figure 3. As shown, the linearity is satisfactory. When θ equals 90°, the “ a ” value is the lattice parameter with a minimum error. The lattice parameter value associated with its deviation can be obtained using the least squares approach. For this sample (i.e. sample C), the lattice parameter is 0.5166 nm and the associated uncertainty is ± 0.0001 nm. Table 3 lists the measured lattice parameters of samples with three compositions.

Figure 3: Lattice parameter, a, of a BNA pellet sample deduced from a linear extrapolation

Note: The result of the extrapolation is $a = 0.5166 \pm 0.0001$ nm.

Table 3: Theoretical density of three types of BNA pellet-material

	Sample		
	A	B	C
total mass (g)	9.0237×10^{-22}	1.0426×10^{-21}	9.1251×10^{-22}
lattice parameter (nm)	0.5194	0.5237	0.5166
volume of unit cell (cm ³)	1.4013×10^{-22}	1.4364×10^{-22}	1.3787×10^{-22}
theoretical density (g/cm ³)	6.44	7.27	6.62

Theoretical density calculation

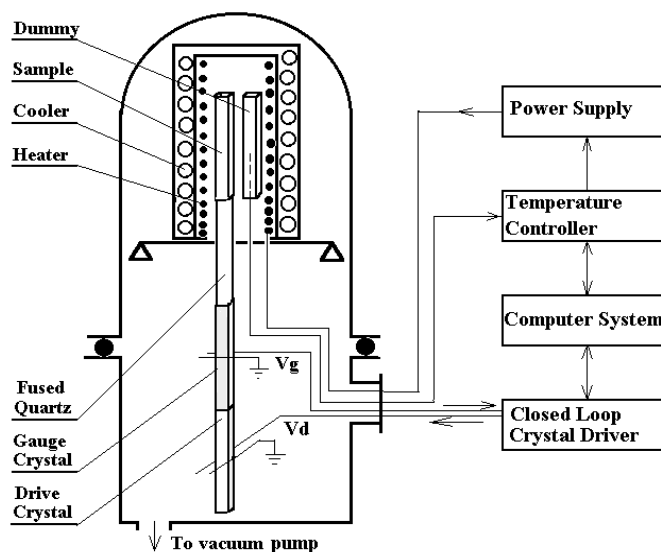
After the total mass of ions in the unit cell is determined and the corresponding lattice parameter is measured by the XRD analysis, the theoretical density can be determined using Equation (3). The results for the three samples are listed in Table 3. As shown, the BNA pellet materials have higher theoretical densities than pure ZrO₂ with a c-ZrO₂ structure.

Young's modulus measurement

Equipment and technique

Young's modulus was determined using the Automated Piezoelectric Ultrasonic Composite Oscillator Technique (APUCOT). This technique was developed by AECL Chalk River Laboratories for measurements of the elastic modulus and internal friction in pressure tube Zr alloys, feeder pipe steels and other materials. The APUCOT is essentially a sonic resonance technique similar to that described in ASTM C1198-01. Its resonant bar is a composite structure containing four components: a bar specimen, two quartz crystals and a fused quartz thermal buffer. The apparatus configuration is schematically shown in Figure 4.

Figure 4: Schematic diagram of the APUCOT



One of the quartz crystals is used to drive the composite oscillator, while the second is a passive pickup crystal to gauge the resonance response. A fused quartz rod is inserted between quartz crystals and the specimen to isolate the heated specimen region from the cold region of the quartz crystals, which are maintained close to room temperatures. The composite oscillator assembly is mounted in a vacuum chamber. A detailed description of the APUCOT has been given elsewhere [7] [8]. Because the quartz crystals and the fused quartz rod have been precisely matched to resonate longitudinally at a frequency of 40 kHz, the required length of the cylinder (or rectangular) specimen must be first decided. The specimen is then carefully machined to that length to achieve the resonance frequency of 40 kHz in the entire composite assembly. To generate the optimum resonance, the specimen length must be an odd multiple of the half wavelength of the longitudinal standing wave at 40 kHz. From the elastic theory of solids, Young's modulus (E) is correlated with the longitudinal resonance frequency (f), wavelength, i.e. double length of specimen (l) and density (ρ) of the specimen with the following Equations (5) (6):

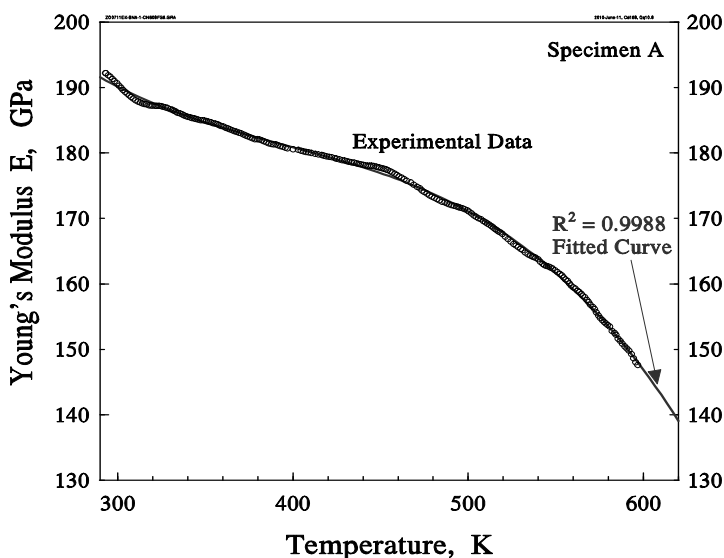
$$E = \frac{\rho}{A_n} \left(\frac{2lf}{n} \right)^2 \quad (5)$$

where n is the overtone mode number ($n = 1$ for basic monotone; $n = 3$ for the 3rd overtone and so on) and A_n is Raleigh's correction factor for specimen dimensions. The value, A_n , is close to one if the cross-section dimensions are much smaller than the specimen length [9], for the present specimens, $A_1 = 0.9998$.

Young's modulus measurement

Young's modulus as a function of temperature in specimen A was determined during heating at a rate of 2 K/min up to 620 K (~350°C). The measurements were repeated for the same specimen more than 10 times. The variation in the Young's modulus measurements at any temperature was observed to be within $\pm 0.1\%$. The typical curve of specimen A is shown in Figure 5.

Figure 5: Young's modulus determined as a function of temperature in specimen A using the APUCOT at 40 kHz and a curve fitted to all measurements



As can be seen, the Young's modulus decreases monotonically with increasing temperature. The fitted polynomial equation is given in Table 4 and is shown as follows:

$$E = 354.01 - 1.16496 T + 2.7584 \times 10^{-3} T^2 - 2.32 \times 10^{-6} T^3 \quad (6)$$

where T is the temperature in K. The associated correlation coefficient R^2 is 0.9988. Values of Young's modulus at several temperatures of interest can be calculated from Equation (6) and are listed in Table 5.

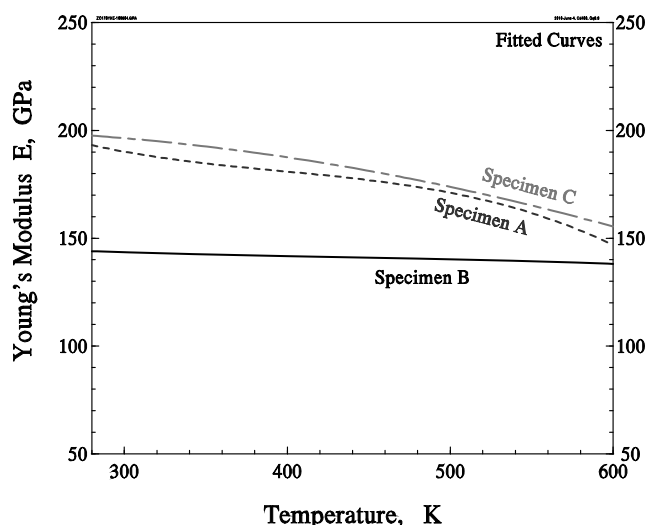
Table 4: E versus T (K) equations from ambient temperature to 600 K (327°C)

Specimen	Equation	R ²
A	$E = 354.01 - 1.16496 T + 2.7584 \times 10^{-3} T^2 - 2.32 \times 10^{-6} T^3$	0.9988
B	$E = 160.30 - 0.1036 T + 2.0597 \times 10^{-4} T^2 - 1.581 \times 10^{-7} T^3$	0.9997
C	$E = 194.275 + 0.078746 T - 2.3932 \times 10^{-4} T^2$	0.988

Table 5: Measurements of Young's modulus (GPa) in BNA pellets

Specimen	300 K	400 K	500 K	600 K
A	190	181	171	147
B	144	142	140	138
C	196	187	174	155

Young's modulus measurements were performed on specimens with the other compositions. The fitted equations for the specimens are provided in Table 4. For comparison, the experimental values of Young's modulus for the three types of specimens are plotted together, as shown in Figure 6. It is observed that the Young's modulus of specimens A and C decreases monotonically with increasing temperature. However, the Young's modulus of specimen B exhibits no significant change in the temperature range from the ambient temperature to 600 K and its Young's modulus value is the lowest.

Figure 6: Variation in the Young's modulus of three BNA specimens as a function of temperature

Values of the Young's modulus of specimens B and C at several temperatures of interest can be calculated from the fitted equations listed in Table 4 and the results are listed in Table 5.

Discussion

Lattice parameter

The addition of Y₂O₃, Dy₂O₃, and Gd₂O₃ oxides apparently increases the lattice parameter of ZrO₂ matrix. For pure cubic ZrO₂, the lattice parameter is 0.5090 nm. After the oxides are added to the matrix, the lattice parameter increases up to 0.5237 nm (see Table 6).

Table 6: Lattice parameter and zirconium concentration in the samples

	Pure ZrO ₂ (cubic)	Sample A	Sample B	Sample C
Zr content (wt%)	74	41.2	27.1	51.0
lattice parameter (nm)	0.5090	0.5194	0.5237	0.5166

The maximum increase is about 2.9%. Apparently, the more Y, Dy and Gd oxides are added, the larger the lattice parameter is. This trend is consistent with the results reported by Pascual *et al.* [11], who studied the variation in lattice parameter as a function of Y₂O₃ addition in the ZrO₂-Y₂O₃ system. It is known that Y⁺³, Dy⁺³ and Gd⁺³ have greater ionic radii than Zr⁺⁴ (see Table 7); thus, it is expected that the addition of these ions to the solid solution would lead to an increase in the lattice parameter.

Table 7: Summary of ionic radii of the metal ions in BNA pellets

	Zr ⁺⁴	Y ⁺³	Gd ⁺³	Dy ⁺³
ion radius (nm)	0.790	0.893	0.938	0.908

Oxygen vacancies

In cubic ZrO₂, eight oxygen ions and four Zr ions are present in each unit cell to keep the electrical balance. However, due to the addition of Y⁺³, Dy⁺³ and Gd⁺³ to the ZrO₂ solid solution, the amount of oxygen ions in the unit cell decreases accordingly, as shown in Table 2. The interstitial sites with no oxygen-ion occupation become oxygen vacancies. Thus, the more tri-valent ions are added, the more oxygen vacancies are generated.

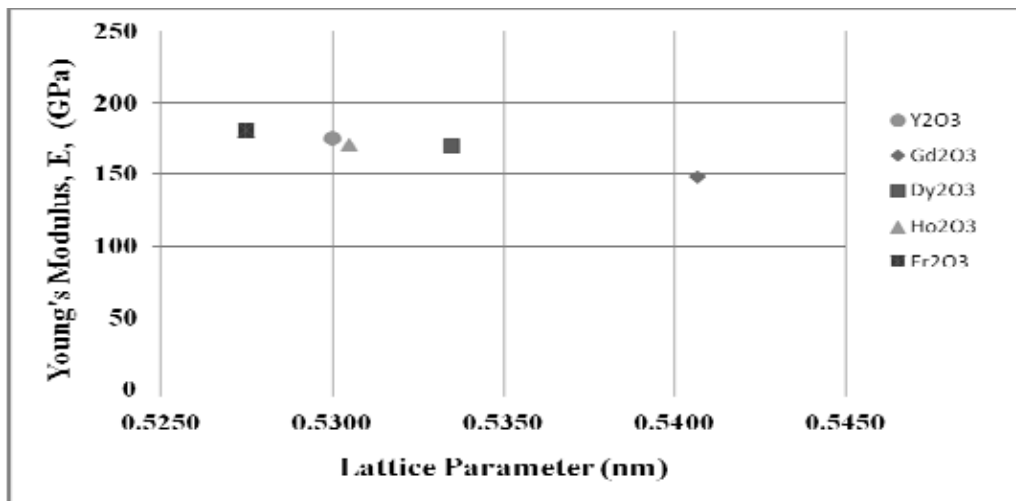
Young's modulus

It is observed that the change in Young's modulus of the material is correlated with the lattice parameter change. As shown in Figure 6, specimen B, which exhibits the lowest Young's modulus, has the greatest lattice parameter (0.5237 nm, see Table 3). Similarly, specimen C, which has the greatest Young's modulus, has the smallest lattice parameter (0.5166 nm; see Table 3). Coincidentally, with more addition of Y₂O₃, Gd₂O₃ and Dy₂O₃, the material exhibits greater lattice parameter, as described in Section 4.1.

Figure 7 shows the relationship between the Young's modulus (measured at room temperature) and the lattice parameter of a group of rare earth oxides [12]. The reason for adding elements Er and Ho is that the data are available. As shown in the Figure, the oxide with greater lattice parameter is associated with lower Young's modulus. Because the chemical and physical properties and the crystal structure of these rare earth oxides are similar, smaller lattice parameter indicates closer distance between the ions with opposite electrical charge in the unit cell and hence stronger ionic bonding between them is expected. As a result, the corresponding Young's modulus is greater. When these oxides are added to a ZrO₂ matrix, leading to an increase in the lattice parameter, the

Young's modulus is reduced accordingly and the more they are added, the lower the Young's modulus is.

Figure 7: Variation in the Young's modulus with lattice parameter of the rare earth oxides [12]



Summary

In this study, the lattice parameters of three compositions of BNA pellets were determined by X-ray diffraction. The corresponding volumes of the unit cells (V) were determined by employing a standard least-squares approach for the cubic structure. With the knowledge that Zr, Y, Gd and Dy ions occupy the lattice sites and the oxygen ions are at interstitial sites in the unit cell, the atomic mass inside the unit cells (M) was calculated and accordingly, theoretical densities (ρ_{th}) of the materials were determined ($\rho_{th} = M/V$).

In addition, the Young's modulus for the materials was determined as a function of temperature and expressions for the temperature-dependant Young's modulus values were derived. It is observed that the Young's modulus decreases with the addition of Y₂O₃, Gd₂O₃ and Dy₂O₃ and it is believed that the increase in the lattice parameter due to the addition of the rare earth oxides is related to this change.

At present, the above results are applied to the development of computer codes to advance ACR-1000 design.

References

- [1] J. Chang, Z. He, M. Gacesa and P. Reid (2008), "BNA pellet material properties test program in support of ACR-1000 fuel design", 29th Annual Conference of the Canadian Nuclear Society, 1-4 June 2008, Toronto, Ontario, Canada.
- [2] R. Ham-Su, J.F. Mouris, and Z. He (2008), "Strength, hardness and toughness testing of BNA-pellets for ACR fuel central element applications", 10th CNS International Conference on CANDU Fuel, Ottawa, Ontario, Canada, 5-8 October 2008.
- [3] U.S. Navy Official Web Site (<http://mstd.nrl.navy.mil>).
- [4] The Joint Committee on Powder Diffraction Standards (JCPDS), JCPDS #27-0997.

- [5] W.D. Callister Jr. (2007), "Materials science and engineering", 7th Edition, published by John Wiley & Sons, Inc. p.414.
- [6] H.P. Klug (1954), "X-ray diffraction procedures", published by John Wiley and Sons, Inc. p.472.
- [7] I.G. Ritchie, Z.L. Pan, K.W. Sprungmann, H.K. Schmidt and R. Dutton (1987), "High damping alloys – the metallurgists cure for unwanted vibrations", *Canadian Metall. Quart.*, Vol. 26, pp.239-250.
- [8] Z.L. Pan and R.R. Hosbons (1998), "Determination of interstitial carbon and nitrogen in low carbon steels", *Proceedings of 39th MWSP Conf*, The Iron & Steel Society, pp. 241-254.
- [9] I.G. Ritchie, H.E. Rosinger, A.J. Shilinglaw & W.H. Fleury (1975), "The dynamic elastic behaviour of a fibre-reinforced composite sheet: I. The precise experimental determination of the principal elastic moduli", *J. Phys. D: Appl. Phys.*, Vol. 8, pp. 1733-1749.
- [10] L. Steven Cook, A. Wolfenden and G.M. Ludka (1990), "Longitudinal and flexural resonance method for determination of variation with temperature of dynamic Young's modulus in 4330V steel", in *Dynamic Elastic Modulus Measurements in Materials*, ASTM, STP 1045, A. Wolfenden, Ed, pp. 75-89.
- [11] C. Pascual, and P. Duran (1983), "Subsolidus phase equilibria and ordering in the system ZrO₂-Y₂O₃", *Journal of American Ceramic Society*, Vol. 66, No. 1, pp. 23-27.
- [12] R.G. Munro (2002), "Elastic moduli data for polycrystalline ceramics", *National Institute of Standards and Technology*, 6853, Gaithersburg, Maryland 20899, United States.

Session IV

Novel Materials Pathways

***Chairs: N.Y. Iwata, T. Liu, R. Kasada, A. Kimura, T. Okuda,
M. Inoue, S. Ukai, S. Ohnuki, T. Fujisawa, F. Abe***

Influence of processing parameters on the microstructure and Charpy impact properties of ODS ferritic steels*

Noriyuki Y. Iwata¹, Tong Liu¹, Ryuta Kasada¹, Akihiko Kimura¹, Takanari Okuda², Masaki Inoue³, Fujio Abe⁴, Shigeharu Ukai⁵, Somei Ohnuki⁵, Toshiharu Fujisawa⁶

¹Institute of Advanced Energy, Kyoto University, Kyoto, Japan, ²Kobelco Research Institute, Inc., Kobe, ³Japan Atomic Energy Agency, Ibaraki, ⁴National Institute for Materials Science, Tsukuba, ⁵Hokkaido University, Sapporo, ⁶Nagoya University, Nagoya

Abstract

Oxide dispersion-strengthened (ODS) ferritic steels have been developed as fuel cladding materials for next generation fast breeder reactors. Al-added ODS ferritic steels have showed good compatibilities with the coolants for supercritical pressurised water (SCPW) reactors and liquid lead-bismuth eutectic (LBE) reactors, however, high-temperature strength has been lower than that of the 9Cr-ODS ferritic steels. Recently, the creep strength of Al-added ODS ferritic steels has also been drastically improved by the addition of Zr.

ODS ferritic steels are usually produced by powder metallurgy techniques, including mechanical alloying (MA) and hot extrusion. Argon atmosphere is the most promising protective medium against oxidation of the powders during MA. However, ODS ferritic steels produced by MA in argon atmosphere have argon bubbles, resulting in the rupture of high-temperature strength. The material performance of ODS ferritic steels depends not only on the milling conditions but also on the atmosphere under which the powders are being milled.

The objective of this study was to examine the influence of processing parameters during MA on the chemical composition, microstructure, micro-hardness and Charpy impact properties of ODS ferritic steels. In order to understand particle properties, the powders prepared by MA in different atmospheres were also examined. As for the milling condition, the effect of ball-to-powder mass ratio was studied to improve the powder metallurgy process, as well as the productivity of planetary ball milling.

Seven types of ODS ferritic steels, with the composition of Fe-(15.5-16)Cr-(0-2)W-(0-4)Al-(0-0.1)Ti-(0-1)Zr-0.35Y₂O₃ (in weight percent), have been prepared by MA of elemental powders with Y₂O₃ particles in different atmospheres and solidification of the MA powders by hot extrusion. Although the pickup of each medium from processing atmosphere causes high excess oxygen and nitrogen content, it has been found that milling in the presence of oxygen and/or nitrogen is effective in reducing the particle size of the MA powders. No formation of argon bubbles has been observed in the matrix of the ODS ferritic steel produced by MA in hydrogen. Relatively large inclusions corresponding to chromium oxide have been observed in the non-Al added ODS ferritic steels. FE-TEM observations have also revealed that many precipitates of Zr(C,N) are present both in grains and on grain boundaries of the Zr-added ODS ferritic steels produced by MA of the nitrogen-containing

* The full paper being unavailable at the time of publication, only the abstract is included.

powders. To enhance the Charpy impact properties, it is important for the oxygen and nitrogen content of ODS ferritic steels to decrease.

The present study includes the results of “Development of super ODS steels with high resistance to corrosion towards highly efficient nuclear systems” entrusted to Kyoto University by the Ministry of Education, Culture, Sports, Science and Technology of Japan (MEXT).

Preliminary results of grain refinement of ODS alloy by equal channel angular pressing*

Jinsung Jang¹, Min Ho Kim¹, Chang Hee Han¹, Hojin Ryu¹,
Xinghang Zhang², David Foley², Karl Ted Hartwig²

¹Korea Atomic Energy Research Institute, Republic of Korea,

²Texas A&M University, United States

Abstract

An experimental Fe-based oxide dispersion-strengthened (ODS) alloy specimen was severely deformed by equal channel angular pressing (ECAP) method. The specimen was prepared by “wet processing” of type 316L powders, fine yttrium oxide particles and hot isostatic pressing (HIP). HIP processed samples were cut into rods and passed through only a single ECAP die at 300°C. Although the hardness of the deformed specimen was twice as high as that of the HIP processed ones, the thermal behaviour of the deformed sample investigated by a differential scanning calorimeter up to 900°C did not show any significant difference. Microstructural evolution due to the severe deformation followed by heat treatment was examined by x-ray diffractometer, TEM and SEM/EBSD. Also, the behaviour of the dispersed oxide particles along with the evolving grain boundaries was studied during the severe plastic deformation and the subsequent heat treatment.

* The full paper being unavailable at the time of publication, only the abstract is included.

Effect of different insert materials on transient liquid phase bonded ODS ferritic steels for advanced nuclear systems

Sanghoon Noh¹, Ryuta Kasada², Akihiko Kimura²

¹Graduate School of Energy Science, Kyoto University, Gokasho, Uji, Kyoto, Japan,

²Institute of Advanced Energy, Kyoto University, Kyoto, Japan

Abstract

The aim of the present study was to investigate diffusion bonding of ODS ferritic steels and the effects of different insert layers on transient liquid phase bonding. In this study, transient liquid phase bonding was performed to join high Cr-ODS ferritic steel (Fe-15Cr-2W-0.2Ti-0.35Y₂O₃) blocks under high vacuum atmosphere using an amorphous insert material based on Fe-3B-5Si compositions with thin pure boron deposited by electron beam physical vapour deposition (EBPVD). Cross-sectional microstructures and mechanical properties of the joint region were investigated and compared. Although the transient liquid phase bonding ODS steel had good tensile strength, it showed lower elongation than before the bonding. It should also be noted that both joint regions show significantly declined fracture energy in the impact test due to residual insert material and agglomerations of complex oxides at the bonding interface.

Introduction

Oxide dispersion-strengthened (ODS) steel is one of the candidate structural materials for Generation IV fission systems and fusion DEMO reactors because of its excellent elevated temperature strength, corrosion and radiation resistance [1-3]. Welding and joining on ODS steels are considered to be important issues in realising these advanced nuclear systems with huge and complex structure. However, joining ODS steels with conventional melting-solidification processes could cause detrimental effects on the joint regions. The reason for this is the possible modification of the microstructure from very small grain size with homogeneously distributed nano-oxide particles in the matrix to rather coarse and inhomogeneous microstructure. Therefore, suitable welding and joining techniques need to be developed with such a process that these featured microstructures are reasonably maintained after the processes [4]. Transient liquid phase bonding (TLPB) is one of the potential joining processes to minimise the disruption of these microstructures at the interface. This process requires an insert material between the two materials to be bonded and its joint is formed when a melting point depressant (MPD; B, Si, P, C and Hf in bonding steels) in the insert material diffuses into the base metal and localised melting and solidification occur in the process [5].

In this study, TLPB was performed to join ODS steel blocks using a commercial amorphous insert foil based on Fe-3B-5Si compositions and electron beam physical vapour deposited (EBPVD) pure boron. Then, the microstructures and mechanical properties on the joint region were investigated to evaluate the applicability of TLPB to ODS ferritic steel joining.

Experimental procedure

The ODS ferritic steel (ODS-FS) used as base metal in this study is Fe (bal.)-15Cr-2W-0.2Ti-0.35Y₂O₃. The chemical compositions of the ODS-FS are shown in Table 1. The ODS-FS was fabricated by mechanical alloying and hot extrusion process. Metallic raw powders and Y₂O₃ powder were mechanically alloyed by attriter under Ar gas atmosphere. The mechanical alloying was performed at a rotation speed of 250 rpm for 48 h with ball to powder weight ratio (BPWR) of 15:1. After mechanical alloying, powders were sieved and charged in the mild steel capsule. A capsule was degassed and hot extruded at 1 150°C in a rod shape. A hot forging and heat treatment process at 1 150°C were performed for the plate shape, followed by air-cooling. As insert material, commercial amorphous foil (Fe (Bal.)-3B-5Si, #2605S-2, 25µm, METGLAS®) and pure boron were used for the TLPB process. To determine the bonding temperature in using the amorphous foil, a thermogravimetry-differential thermal analysis (TG-DTA) was carried out. Its results are shown in the previous paper [6]. The temperature range showing maximum endothermic peaks is the melting point (T_m) of the insert material, which means the insert material begins to transform to liquid phase above 1 180°C. Meanwhile, pure B thin layer was induced by electron beam physical vapour deposition (EBPVD) technique. A substrate (an ODS-FS block to be bonded) and target material (pure B grains, 99.5% purity, 3-7 mm, KOJUNDO Chem. Lab. co.) were vertically located in high vacuum atmosphere (<1.2 × 10⁻³ Pa). The electron beam was discharged to B target in a condition of 7 kV, 180 mA for 15 min.

Table 1: Chemical compositions of high Cr ferritic ODS steel

Elements	Fe	Cr	W	Ti	C	Mn	P	S	Ni	Y ₂ O ₃
Composition	Bal.	14.9	1.9	0.21	<0.02	0.01	0.017	0.003	0.04	0.34

The test pieces were cut into 20×12×12 mm³ and the surfaces to be bonded were buff-polished. Samples were stored in acetone for the purpose of cleaning and preventing surface contamination. For the diffusion bonding process hydrostatic vacuum hot press was used. The two ODS-FS blocks with an insert material were vertically placed and assembled with the carbon sleeves. This assemblage was located between pressing punches and linearly heated up to bonding temperature, 1 200°C at a heating rate of 30°C/min. Then, the bonding temperature was held for 1 h in a high vacuum atmosphere (<5×10⁻⁴Pa) under hydrostatic pressure of 25 MPa in uni-axial compressive loading mode. After the bonding process, the hydrostatic pressure was relieved and the samples were cooled in the furnace.

The grain morphology was observed by FE-EPMA. Joints were buff-polished and electronically polished in 5% HClO₄ + 95% methanol solution in vol. % at 18 V with 0.5 mA at -50°C to remove the work-hardened surface induced by mechanical buff-polishing. To investigate the mechanical property, a nanoindentation hardness test, a tensile test and an impact test were carried out on joint region and base metal. The hardness distribution on each joint region was determined by a Berkovich-type indenter with a load of 1gf. In this study, two ODS-FS were bonded in a longitudinal direction, so that the joint interface was perpendicular to the extruded direction. Tensile tests were performed at a temperature range from room temperature to 700°C at a strain rate of 6.67×10⁻⁴s⁻¹ in a high vacuum atmosphere (5×10⁻⁵torr). Charpy impact test was also carried out to evaluate the impact property on the joint region. The impact tests were carried out in a temperature range from 173 K to 453 K with a load of 500 N by weight-drop-tower type Charpy impact test instrument. The ductile-brittle transition temperature (DBTT) and upper shelf energy (USE) were determined by fitting the plots of the relationship between absorbed energy and temperature to the following hyperbolic functions:

$$R(T) = a + b \tanh \{(T - T_0)/c\} \quad (1)$$

where, T is test temperature and a , b , c and T_0 are regression coefficients. The DBTT and USE are defined to be T_0 and $(a+b)$, respectively. The fracture surfaces were also observed by SEM. Specimen geometry of tensile and impact test are shown in Figure 1. Each specimen was electro-discharge machined, so that the joint interface was located at the center of the specimen at the gage length and in the bottom of the V-notch.

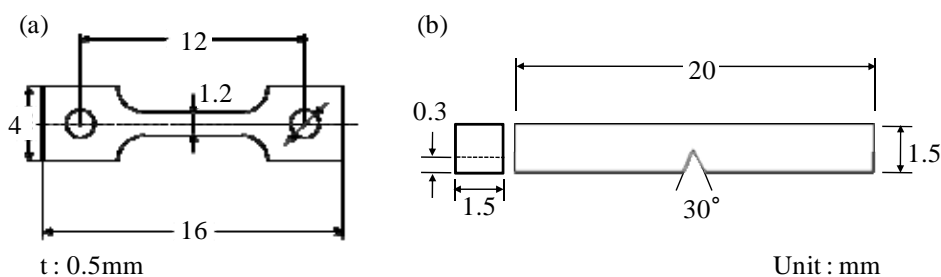
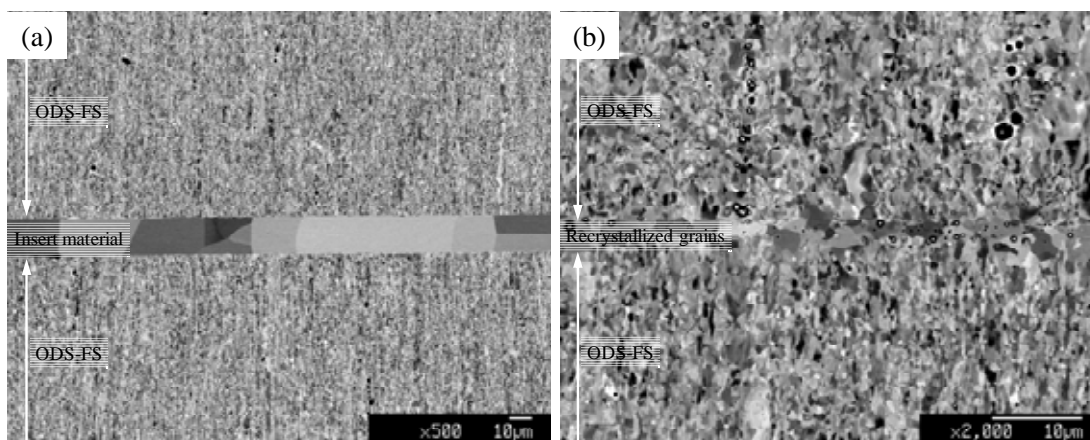
Figure 1: Specimen geometries of SS-J2 miniaturised tensile test (a) and 1.5 mm Charpy V-notched impact test (b)

Figure 2: Cross-sectional microstructures of TLPB joint with (a) amorphous foil and (b) EBPVD B as the insert layer (note the different magnifications)



Results and discussions

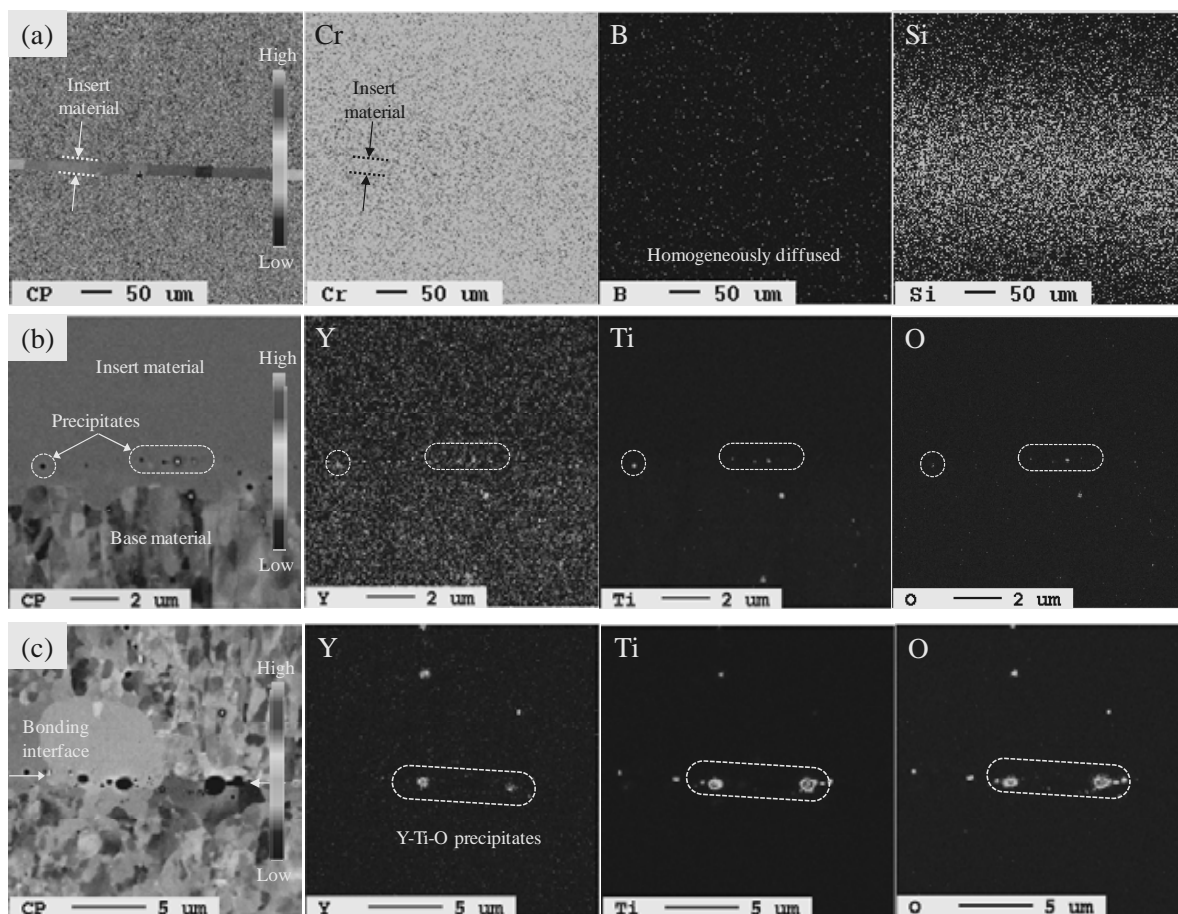
ODS-FS blocks were successfully diffusion-bonded at 1 200°C for 1 h. The surfaces of the bonded sample showed no trace of macroscopic deformation under the hydrostatic pressure of 25 MPa, which is in agreement with the report that the threshold stress for the surface deformation of commercial ODS alloy, Inconel MA956, is about 60 MPa [7]. The cross-sectional microstructures of TLPB ODS-FS joint region are shown in Figure 2. In the TLPB joint with an amorphous foil, the residual insert material of about 15 μm thickness was found and located horizontally in Figure 2(a). During the bonding process, amorphous insert material was melted and crystallised. To investigate the diffusion behaviour of elements, EPMA analysis was conducted in the joint regions. Colour maps show peaks of each element amount in the area for comparative intensity level, as indicated in Figure 3. In Figure 3(a), remarkable element map differences were observed between Si and B in the TLPB joint with amorphous foil; Si was diffused out up to about 100 μm into base metals during the bonding process and B was distributed homogeneously because of its rapid diffusion rate in Fe at the bonding temperature. It is interesting that Cr was also concurrently diffused from base metals to residual insert material. This means that the homogenisation on chemical composition at the joint interface was completed during the TLPB process. Some precipitates exist at the interface of ODS-FS and inset material, although no grain growth occurred in joint region and base material. Some precipitates existing at the interface are considered to be Y-Ti-O complex based on the EPMA analysis, although the yttrium concentration is low and indistinguishable, as shown in Figure 3(b). These precipitates come from the dissolution of base metal due to diffusion of the melting point depressants during the TLPB process.

On the other hand, some recrystallised grains were observed at the bonding interface of TLPB ODS-FS with EBPVD boron, as shown in Figure 2(b). It is evident that ODS-FS matrix near the interface was temporarily melted by the diffusion of pure B into the base metal contacted with EBPVD boron during the bonding process. There is no evidence of eutectic phase or metallic phase such as iron or chromium borides. However, some coarsened precipitates were observed in recrystallised grains at the bonding interface. These agglomerated precipitates are revealed as Y-Ti-O complex oxide by EPMA analysis in Figure 3(c). This indicates that the base metal was dissolved by holding MPD in solution, which was induced by the diffusion of pure B into the base material. In the same manner, with TLPB using Fe-3B-5Si amorphous foil, it is certain that these

recrystallised grains and agglomerated precipitates aligned to the bonding interface can reduce the bonding strength. These can be minimised, but are an unavoidable phenomenon which makes base metal melt partially during the process.

Microstructure observation has revealed that the TLPB joint regions have residual insert material and some Y-Ti-O precipitates at the bonding interface. This observation has also revealed that it is necessary to investigate the effects of microstructural features developed during the bonding process on the mechanical properties. Nano-hardness distributions in the cross-section of both TLPB joint regions are shown in Figure 4(a), as well as TLPB joint with amorphous insert foil and (b) TLPB joint with EBPVD boron. The ODS-FS has high hardness values of about 5 GPa and it is continually varied at the bonding interface. In the TLPB joint with amorphous foil, the hardness of the residual insert material has significantly decreased to about 2 GPa because there is no strengthening phase such as Y_2O_3 in insert material. By contrast, the hardness distribution in the TLPB joint region with EBPVD shows the hardness at the joint boundary to be about 3.5 GPa, which is not very different from that of base metal. This means that thin insert material including MPD is effective in obtaining the comparable mechanical properties to those of base metal.

Figure 3: Elemental distributions of (a) joint region, (b) bonding interface of TLPB with amorphous foil and (c) bonding interface of TLPB with EBPVD B



Tensile tests with miniaturised specimens of the joints were carried out at room temperature and elevated temperature with each bonding orientation relationship. The obtained stress-strain curves of base metal and TLPB joints are presented in Figure 5. TLPB joint regions with an insert material have a high enough tensile strength up to 95% of base materials, although a significant reduction of total elongation (TE) is observed to be a half of base material. Conversely, both tensile strength and TE were fairly good on TLPB joint region with EBPVD B.

Figure 4: Hardness distributions on TLPB joint region with (a) amorphous foil and (b) EBPVD B

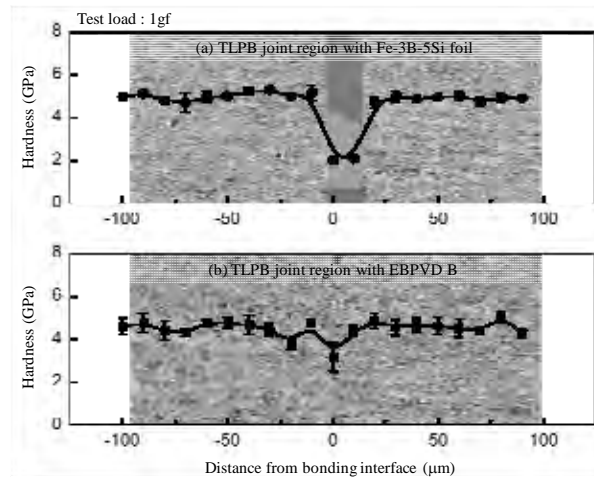
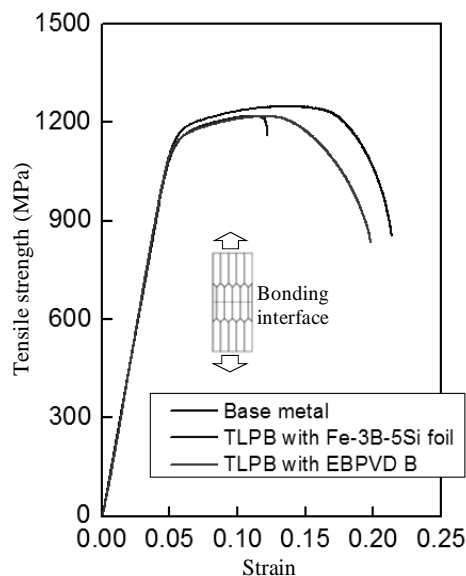


Figure 5: Stress-strain curves of base metal and TLPB joints tested at room temperature



The results of the tensile tests of base metals and TLPB joints at elevated temperatures are shown in Figure 6. Throughout all the temperature ranges tested, TLPB joint regions showed high ultimate tensile strengths (UTS), which were up to 90% of base material. In TLPB joint with amorphous foil, the reduction of total elongation (TE) was also observed at elevated temperatures, which reduced to 30% of that of base metal at 700°C, even though TE of base metal increased slightly at 700°C. However, there was a similarity in the tensile behaviour of the TLPB joint region of EBPVD boron with base material at 600°C, although it decreased at 700°C. Fractography observation revealed that base metals show typical necking behaviour with a significant reduction of area. As for TLPB joint with amorphous foil, all failures occurred at the interface of base metal/insert material, showing a mixture mode of micro-void coalescence and cleavage. It seems that Y-Ti-O precipitates at the bonding interface trigger micro-void formation and crack at the joint region with deformation. These micro-cracks propagated to interface boundaries of ODS-FS/insert material in brittle fracture mode. However, TLPB joints with EBPVD boron show a significantly different fracture behaviour, which is similar to base material showing necking with typical ductile fracture mode even at a 100 μm far from the bonding interface at below 600°C. In conformity with a result of 700°C, the interfacial fracture occurred with lower TE than that of base metal. However, it has a lot of micro-void coalescence dimples. While EBPVD B TLPB joint was elongated by grain-boundary sliding mechanism without area reduction at the beginning of tensile at 700°C, it finally fractured at the interface, because coarsened precipitates aligned at the bonding interface produced the micro-void and then it linked to each other.

Upper shelf energy of base metal and each TLPB joints are shown in Figure 7. It is estimated that USE of base metal is about 0.84 J. However, both the TLPB joint regions show significantly lower USEs about 0.15 J. The fractography observation revealed that dimple patterns were observed in the base metal while the micro-void coalescence with partial exfoliation occurred in the TLPB joint with amorphous foil at high temperatures. TLPB joint with EBPVD B insert layer has similar impact behaviour with a significant reduction of USE.

Figure 6: Tensile test results of base material and TLPB joints at elevated temperature

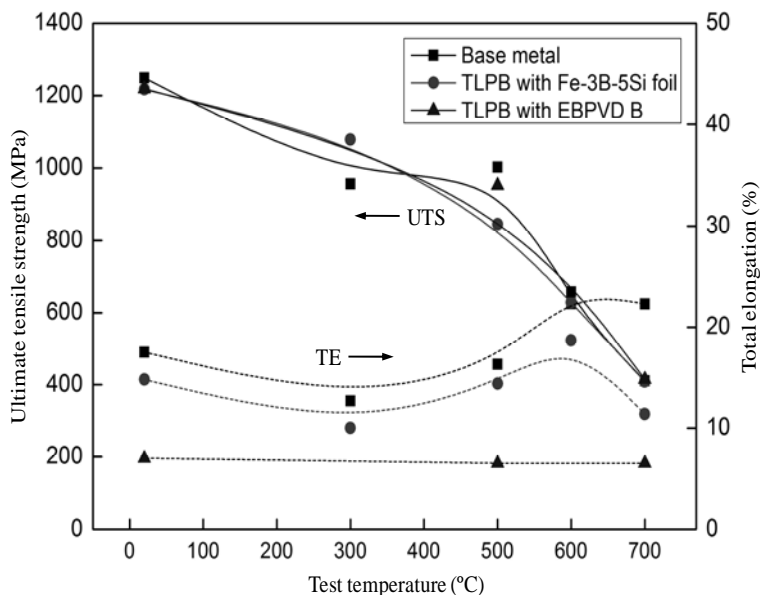
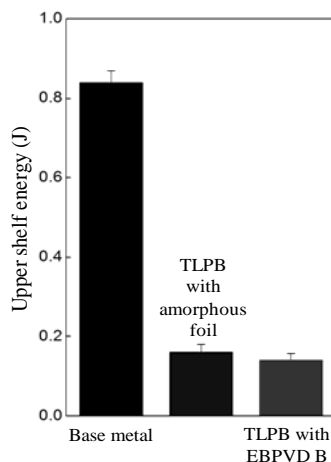


Figure 7: Upper shelf energy of base metal and TLPB joints

Summary

High Cr-ODS ferritic steel was bonded by TLPB with an amorphous foil (Fe-3B-5Si) and EBPVD boron in high vacuum uni-axial hot press. Tensile and impact tests were carried out to investigate the relationship between the microstructure and mechanical property of the joint region. The following main results were obtained:

- The TLPB ODS steel with Fe-3B-5Si amorphous foil showed rather homogeneous elemental distribution in the joint region, while Y-Ti-O complex oxide precipitates and residual insert material were observed at the interface.
- The joints had a fairly good tensile strength which was up to 95% of base metal at 700°C. However, it showed poor elongation compared to base metal showing fractures at the interface between insert material and ODS-FS.
- On the other hand, TLPB joint with EBPVD boron has excellent tensile properties comparable to base metal showing favorable fracture behaviour far from the bonding interface.
- Both the TLPB joints showed a significant reduction of absorbed energy in impact test, because the recrystallised grains and agglomeration of Y-Ti-O complex oxide at the bonding interface were distributed so as to be parallel to the impacting load direction along which cracks propagate more easily with less observed energy.

References

- [1] S. Ukai, T. Okuda, M. Fujiwara, T. Kobayashi, S. Mizuta, H. Nakashima (2002), "Characterization of High Temperature Creep Properties in Recrystallized 12Cr-ODS Ferritic Steel Claddings", *J. Nucl. Sci. Technol.*, 39, 872-879.
- [2] H. S. Cho, H. Ohkubo, N. Iwata, A. Kimura, S. Ukai, M. Fujiwara (2006), "Improvement of compatibility of advanced ferritic steels with super critical pressurized water toward a higher thermally efficient water-cooled blanket system", *Fusion Eng. Design*, 81, 1071-1076.
- [3] S. Yamashita, N. Akasaka, S. Ukai, S. Ohnuki (2007), "Microstructural development of a heavily neutron-irradiated ODS ferritic steel (MA957) at elevated temperature", *J. Nucl. Mater.*, 367-370, 202-207.

- [4] R. Lindau, A. Möslang, M. Rieth, M. Klimiankou, E. Materna-Morris, A. Alamo, A.-A. F. Tavassoli, C. Cayron, A.-M. Lancha, P. Fernandez, N. Baluc, R. Schäublin, E. Diegele, G. Filacchioni, J.W. Rensman, B.v.d. Schaaf, E. Lucon, W. Dietz (2005), "Present development status of EUROFER and ODS-EUROFER for application in blanket concepts", *Fusion Eng. Design*, 75-79, 989-996.
- [5] W. D. McDonald, T. W. Eagar (1995), "Transient liquid phase bonding process", *The Metal Science of Joining*, 93-100.
- [6] S. Noh, R. Kasada, N. Oono, N. Iwata, A. Kimura (2009), *Proceedings of the 9th international symposium on fusion nuclear technology*.
- [7] R. F. Singer, E. Arzt (1986), "Processing, Structure and Properties of ODS Superalloys", *Proc. of High Temperature Alloys for Gas Turbines and Other Applications*, p. 97, D. Reidel, Dordrecht, Netherlands.

Fracture toughness and Charpy impact properties of cold-worked F82H steels

Byung Jun Kim¹, Ryuta Kasada¹, Akihiko Kimura¹, Hiroyasu Tanigawa²

¹Institute of Advanced Energy, Kyoto University, Kyoto, Japan, ²JAEA, Tokai, Ibaraki, Japan

Abstract

Reduced-activation ferritic (RAF) steels are promising candidate structure materials for fusion reactor blanket components, but they may suffer irradiation embrittlement accompanied by a significant shift of the ductile to brittle transition temperature (DBTT) to higher temperature as a consequence of irradiation. In the Broader Approach (BA) Project, the application of small specimen test technologies (SSTT) has been examined to evaluate fracture toughness of F82H and its irradiation-induced degradation. In the present study, constitutive data and widely-obtained fracture toughness data sets at transition temperatures of F82H are investigated to establish the master curve methodology for RAF steels from the viewpoint of fracture mechanics. Small specimen tests on the ductile-to-brittle transition and fracture toughness behaviour have been investigated for F82H with different levels of cold work in order to evaluate the effects of work hardening on the shift of the transition curve. Yield strength (YS) and ultimate tensile strength (UTS) are increased by increasing the level of cold work. It has been found that the DBTT after cold work is shifted to higher temperatures and the upper shelf energy (USE) is decreased. However, shifts of reference temperature (T_0) after cold work have been the reverse of the Charpy test results due to secondary crack in pre-crack. In the highly cold-work level (60%), the effects of anisotropic fracture toughness and Charpy impact properties were evaluated on observing the microstructure of fracture surface. Highly cold-worked steel fractured in a ductile manner, showing dimples accompanied by the delamination even at temperatures of the transition region. The master curve approach for the evaluation of fracture toughness behaviour was carried out by referring to the ASTM E1921.

Introduction

Reduced-activation ferritic (RAF) steels are promising candidate structure materials for fusion reactor blanket components, but may experience significant shift of the ductile to brittle transition temperature (DBTT) as a consequence of irradiation. In order to effectively produce irradiation database, the reduction of the specimen volume is needed. The development and application of small specimen test technology (SSTT) has enabled the evaluation of fusion materials at limited irradiation space. In the Broader Approach (BA) Project, the application of small specimen test technologies (SSTT) was examined to evaluate the fracture toughness of F82H and its irradiation-induced degradation. The most recent SSTT have been pursued within the framework of the master curves-shift, MC- ΔT , a method proposed by Odette *et al.* [1-3] for bcc alloys currently being considered as candidates for fusion reactor structures.

The master curve methodology [4] is specified as a standard test method for determining the reference temperature for ferritic steels in the transition range provided by the American Society for Testing and Materials (ASTM). The MC method is indexed at a reference temperature T_0 at a specific toughness usually equal to $100 \text{ MPa m}^{1/2}$. T_0 is a material dependent parameter. The main advantage of the methodology reduced the fracture toughness testing requirements in terms of both the size and the number of specimens. However, the application of the methodology to RAF steels may have some difficulty passing the requirement of methodology, for example, large constraint loss in small specimens of RAF steels and possible fracture mode change to inter-granular due to precipitation of transmutation helium on to grain boundaries [5-9]. In this paper, we define material fracture toughness (K_{Jc}) for plane strain condition, small scale yielding (SSY) conditions under mode I loading. The measured fracture toughness (K_{Jc}) depends on specimen thickness (B) and the crack front length.

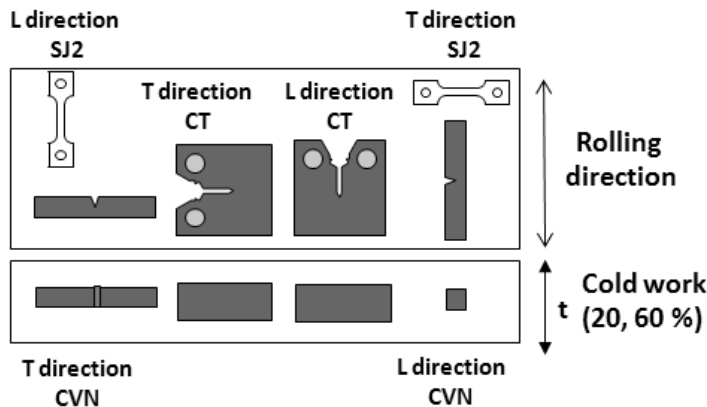
In the present study, in order to evaluate the effects of cold work, fracture toughness and the ductile-to-brittle transition behaviour were investigated for F82H with different levels of cold work. We have discussed and determined the work flow to evaluate the validity of the master curve (MC) methodology for quantification of fracture toughness behaviour of F82H by using small CT specimens (1/4 CT).

Experimental

The standard heat treatment for F82H IEA-heat was austenitisation for 0.5 h at 1040°C followed by an air cooling (normalisation treatment) and then it was tempered for 1 h at 740°C . Its main composition is: 7.65 Cr, 2 W, 0.16 Mn, 0.16 V, 0.02 Ta, 0.11 Si and 0.09 C in wt% and Fe for balance. The cold work on F82H was carried out to increase yield stress so as to evaluate work hardening. A plate of F82H was cold rolled to two different thicknesses of the plates, CW-1 and CW-2, with reductions of the cross-sectional area by 20 and 60%, respectively. Two different sampling directions of specimens were produced so that the gage direction of the tensile specimen and the longitudinal direction of the tested specimens are parallel and perpendicular to the rolling direction.

Tensile tests were performed in accordance with the JIS, which defined the specimen gage length and thickness as 5 mm and 0.5 mm. The tests were carried out by an Intesco machine at a cross head speed of 0.2 mm/min at room temperature.

Charpy impact tests using 1/3 Charpy V-notch specimens (3.3 mm x 3.3 mm x 20.0 mm) were performed to evaluate the ductile-to-brittle transition temperature (DBTT) and upper shelf energy (USE) at temperature from -240°C to 160°C .

Figure 1: Schematic diagram of specimen direction


All the specimens were tested using an instrumented Charpy impact testing machine with an electrically controlled hydraulic system and a load capacity of 50 kN. A specimen was set up in a cold bath filled with isopentane, which was cooled by liquid nitrogen for low-temperature test and used silica oil for high-temperature test. It was held at a desired constant temperature for 15 min before testing. The data were curve fit using a hyperbolic tangent function of the form.

$$E = a + b \tanh [c(T - d)] \quad (1)$$

where E is the absorbed energy (J), a , b , c are constants, $d = \text{constant} = \text{DBTT}$, $a + b = \text{USE}$, T is the temperature ($^{\circ}\text{C}$).

The fracture toughness tests were carried out in accordance with ASTM E 1921-02 standard test method for determining the reference temperature, T_0 , for ferritic steels in the transition range. The unloading compliance method [10] was applied to measuring the J integral with a clip strain gage. The fracture toughness was measured using small specimens. Small size specimens (1/4 CT) of compact tension (CT) were fabricated from 15 mm thickness of F82H plate. The dimension of the 1/4 CT specimen was 12.7 mm in width (W), 6.35 mm in the thickness (B), 6.35 mm in initial crack length (a_0). Fatigue pre-cracking was induced to a ratio of the pre-crack length to specimen width of about 0.5, followed by side grooving by 20% of thickness. A schematic diagram of specimen direction was shown in Figure 1. The master curve (MC) method is very useful in evaluating the shift in the ductile-brittle transition temperature by using a limited number of small specimens. This method is well illustrated by ASTM E 1921 [4].

Results and discussion

Tensile properties and Charpy impact properties [11]

The tensile stress vs strain curves of cold-worked specimens are shown in Figure 2. Yield strength (0.2% offset) and ultimate tensile strength (UTS) are increased by increasing the level of cold work. Strengths of the specimen with transverse direction are higher than those of rolling direction. However, tensile elongation shows an inverse dependence of tensile strength on sampling direction.

Figure 2: The stress vs. strain curves for cold-worked F82H steels [11]

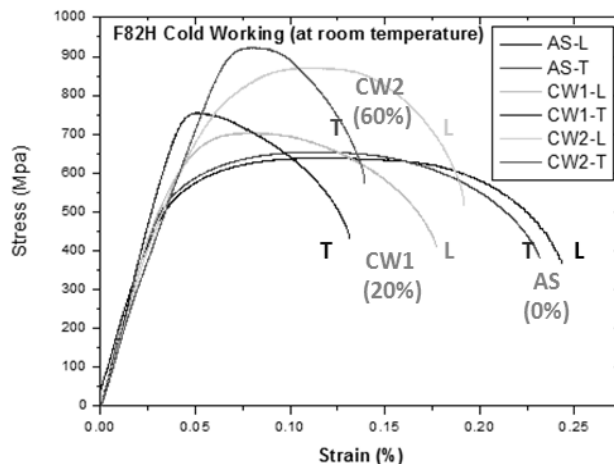


Figure 3: The energy absorbed vs. temperature curves for cold-worked F82H steels [11]

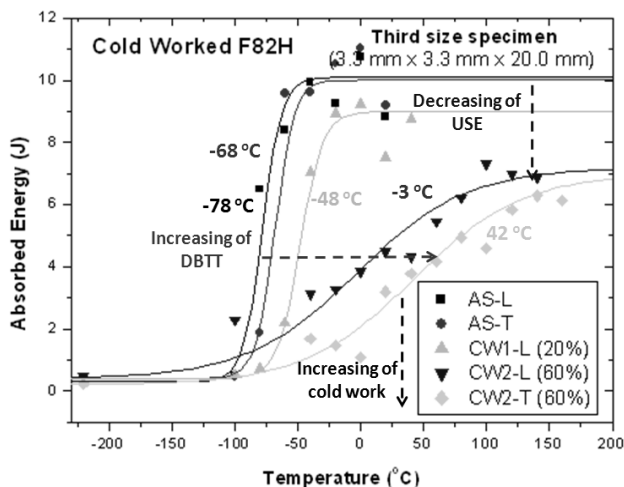


Table 1: Tensile and Charpy impact properties of the tested F82H steels

Specimen ID	YS (MPa)	UTS (MPa)	UE (%)	TE (%)	DBTT (°C)	USE (J)
AS-L	441	638	7.2	22.4	-78	9.4
AS-T	473	653	7.5	20.9	-68	10.0
CW1-L	478	703	4.2	15.4	-48	9.0
CW1-T	656	754	1.3	10.9	-	-
CW2-L	692	870	3.9	14.8	-3	7.0
CW-2T	830	922	1.2	9.7	42	6.5

Yield strength (YS), ultimate tensile strength (UTS), uniform elongation (UE), total elongation (TE), ductile to brittle transition temperature (DBTT), upper shelf energy (USE) [11].

The absorbed energy vs. test temperature curves for F82H IAE-heat with different levels of cold work are shown in Figure 3. It was found that the DBTT after cold work is shifted to higher temperatures and the USE is decreased. The shift of DBTT and the reduction of USE increase with the cold-work level. As for the effects of sampling direction, no significant change in the ductile to brittle transition curve was observed for the as-received F82H IAE-heat, while a rather large reduction of absorbed energy was observed for the transverse specimens of CW2 steel. This is considered to be due to the deformation structure in the heavily cold-rolled materials, in which dislocation cell structures are extended to the rolling direction. The tensile test and Charpy impact properties are summarised in Table 1.

Fracture toughness properties

The master curve (MC) method is very useful in evaluating the shift in the ductile-brittle transition temperature by using limited number of small specimens. This method is used to evaluate the validity for quantification of ductile brittle transition behaviour by using small specimens on cold-worked F82H for work the hardening phenomenon. The following is a brief description of the master curve methodology. Values of J-integral at cleavage instability, J_c , were converted to their equivalent values in terms of stress intensity factor K_{Jc} by the following equation:

$$K_{Jc} = \sqrt{J_c \frac{E}{1-\nu^2}} \quad (2)$$

where E is Young's modulus and $\nu=0.29$ is Poisson's ratio. The K_{Jc} value was considered invalid if it exceeded the validity limit:

$$K_{Jc}(\text{limit}) = \sqrt{\frac{E b_0 \sigma_{ys}}{M(1-\nu^2)}} \quad (3)$$

where b_0 is the ligament size, σ_{ys} is yield strength of the material and M is the constraint factor as defined to $M = 30$ in the ASTM 1 920. All JC data were converted to 1T equivalence, $K_{Jc(1T)}$, using the weakest link size adjustment procedure of ASTM E 1921:

$$K_{Jc(1T)} = K_{\min} + [K_{Jc(xCT)} - K_{\min}] \left(\frac{B_{xCT}}{B_{1CT}} \right)^{4/b} \quad (4)$$

where $K_{\min} = 20 \text{ Mpa m}^{1/2}$ is the minimum of K_{Jc} , B_{xCT} the gross thickness of 1 CT specimen and $b = 4$ is the parameter based on the Weibull model [4]. The data were analysed within the framework of statistical brittle fracture model that yield, for highly

constrained specimens, the cumulative failure probability as a three-parameter Weibull distribution:

$$p_f = 1 - \exp \left\{ - \left[\frac{K_{Jc} - K_{Jcmin}}{K_{Jc} - K_{Jcmin}} \right]^3 \right\} \quad (5)$$

The temperature dependence of the median toughness of 25.4 mm thick specimen (1T) in the transition region of 'ferritic' steels is given by the so-called ASTM master curve as follows:

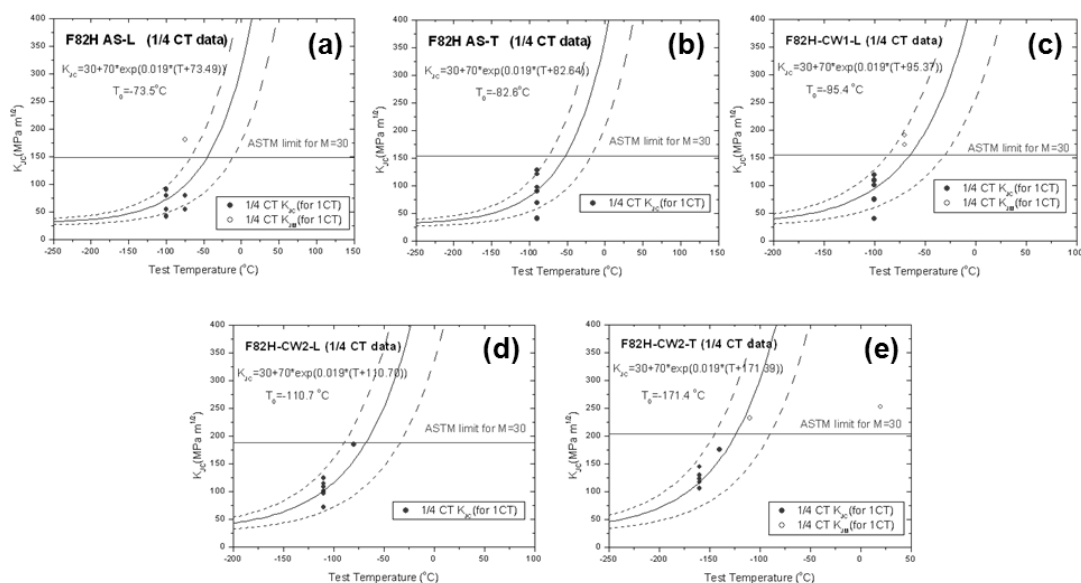
$$K_{Jc(transition)} = 30 + 70 \exp \{ 0.012(T - T_0) \} \quad (6)$$

The reference temperature T_0 corresponds to the temperature where the median fracture toughness for a 25 mm thick specimen has the value $100 \text{ MPa m}^{1/2}$. More detail can be explained by the ASTM 1 921[1].

A total of 46 specimens of F82H steel were tested in the transition region, 9 AS-L 1/4 CT, 9 AS-T 1/4 CT, 12 CW-L 1/4 CT, 8 CW2-L 1/4 CT and 8 CW2-T 1/4 CT. Figure 4 shows the test temperature dependence of the $K_{Jc(1CT)}$ obtained for cold-worked F82H for the 1/4 CT specimen. The $K_{Jc(1CT)}$ for the 1/4 CT specimen has been converted from the $K_{Jc(xCT)}$ data by using Equation (4). The Figure also shows the calculated 5 and 95 % tolerance bounds. The reference fracture toughness temperature, T_0 , for AS-L specimen data is determined to be -73.5°C in Figure 4(a). Reference temperatures (T_0) of AS-T, CW1-L, CW2-L and CW2-T were obtained by -82.6 , -95.4 , -110.7 and -171.4°C respectively from Figures 4(b) to (e). It has been found that the reference temperature (T_0) after cold work is shifted to lower temperatures, which is the reverse of the result of the Charpy test. The shift of reference temperature (T_0) increases with the cold-work level.

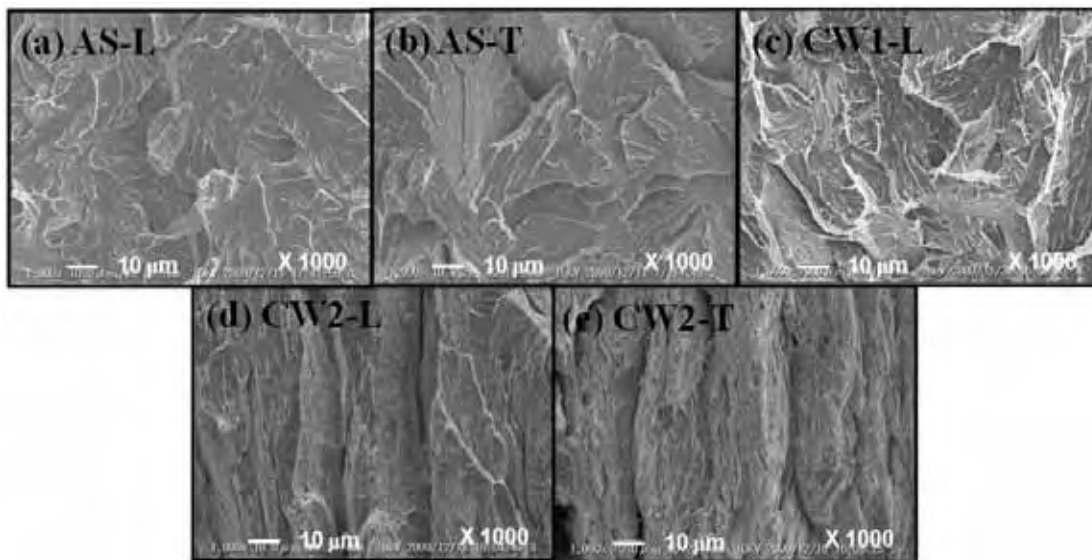
The fracture surfaces of cold-worked F82H at temperatures of the transition region is shown in Figure 5, indicating that as-received and CW1 steel fractured in a brittle manner, showing cleavage fracture (a), (b) and (c), while CW2 steel fractured in a mixed mode with both cleavage and ductile manner showing dimples (d) and (e). This indicates that highly cold-worked F82H has a higher resistance to cleavage fracture in the transition region. In the case of highly cold-worked steel (CW2), the fracture surface shows delaminations, which are in the transverse direction to the main crack and start from the secondary crack in fatigue pre-crack in Figure 6. The occurrence of the delamination acts as internally free surfaces, which enhance the fracture toughness due to changing from plain strain condition to plain stress condition and distributing crack propagation energy. After the formation of the delamination, these dimples arise between neighbouring delaminations due to dominant plain stress condition. The loss of triaxiality allows local shear deformation. This fracture process is simply similar to that of thin thickness specimen in plain stress condition.

Figure 4: The K_{IC} obtained for F82H for 1 CT developed from 1/4 CT data with the master curve



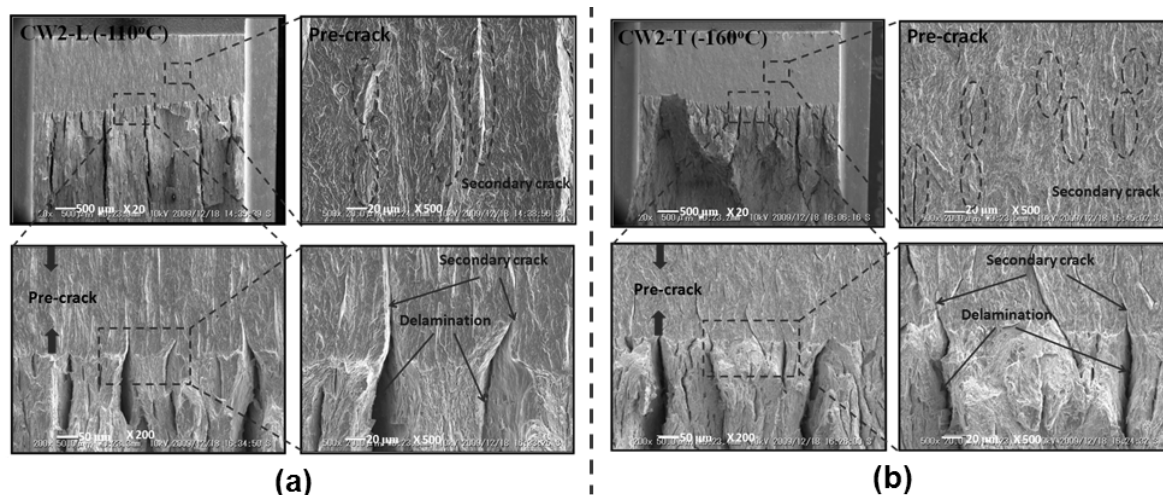
(a) AS-L, (b) AS-T, (c) CW1-L (20%), (d) CW2-L (60 %) and (e) CW2-T (60%)

Figure 5: The fracture surface of cold-worked F82H at temperatures in the transition region



(a) AS-L direction (0 %), (b) AS-T direction (0 %), (c) CW1-L direction (20 %), (d) CW2-L direction (60 %), (e) CW2-T direction (60 %)

Figure 6: The fracture surface and pre-crack of highly cold-worked F82H at temperatures in the transition region: (a) CW2-L direction (60%), (b) CW2-T direction (60%)



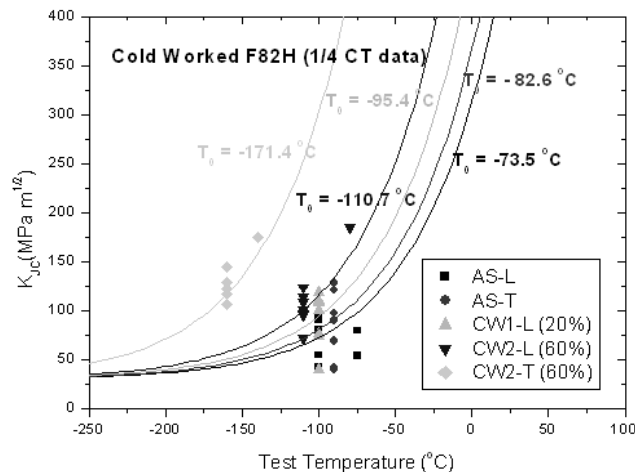
The occurrence of secondary crack can be caused by the compressive residual stress which happens during the cold working process. It is well known that the residual stresses decrease the fatigue cycle number due to the formation of crack, which relieves residual stresses of specimen [12]. The compressive residual stress is decreased during the fatigue pre-crack process. The secondary crack can happen due to a decrease in the compressive residual stress during the pre-crack propagation. The reason for the reverse result between the Charpy and CT test is a secondary crack in pre-crack. The Charpy results of no pre-crack do not show the effect of secondary crack which caused the enhanced fracture toughness.

Anisotropy of the fracture toughness

Figure 7 presents the results of the fracture toughness measurements for the different specimen orientations by parallel and perpendicular to the rolling direction. Comparing the longitudinal orientation sample, the increase (9.1°C) in reference temperature (T_0) was found for specimens with transverse orientation in as-received condition. The difference of fracture toughness between the transverse and longitudinal directions is increased with cold-work level. In the case of 60% cold-work level, the effect of sampling direction is significantly increased around the 59.7 °C. The Charpy result also shows a similar trend, which has the difference between L direction and T direction at 10°C and 39°C, respectively, in as-received and 60% cold-work condition. This character of the anisotropy properties will be presented in more detail.

It has also been found that the difference (60°C) of reference temperature (T_0) between L-direction and T-direction sample is higher than that (39°C) of DBTT in highly cold-worked steel (60%). This indicates that reference temperature (T_0) includes the effects of secondary crack in pre-crack and elongated grain by cold work. However, the result of DBTT has been affected by only elongated grain by cold work. It is well known that fracture toughness after cold work is degraded by the hardening caused by an increase in the dislocation density that hinders the motion of moving dislocations. However, our result shows the reverse trend, which is an increase in the fracture toughness of cold-worked steels due to the presence of secondary crack in pre-crack during the fatigue pre-cracking process. Therefore, anisotropic properties of cold-worked F82H steel may be affected by secondary cracks in pre-crack.

Figure 7: The K_{Jc} obtained for cold-worked F82H steel for 1 CT developed from 1/4 CT data with the master curve



Conclusions

In order to evaluate the effects of work hardening, the fracture toughness and ductile-to-brittle transition behaviour were investigated for F82H with different levels of cold work. A reference fracture toughness vs temperature curve for cold-worked F82H steel was established in the low transition region by using small specimens (1/4 CT). The following main results have been obtained:

Yield strength (0.2% offset) and ultimate tensile strength (UTS) are increased by increasing the level of cold work. The specimen of transverse direction has higher value than that of rolling direction. The DBTT after cold work is shifted to higher temperatures and the USE is decreased. The shift of DBTT and the reduction of USE increase with the cold-work level. It has been found that the reference temperature (T_0) after cold work is shifted to lower temperatures, which is the reverse of the result of the Charpy test. The measured fracture toughness was also strongly affected by specimen orientation. This mechanical anisotropy was affected by the deformation microstructure, which is aligned to rolling direction.

Acknowledgements

The present study includes the result of the Broader Approach Project. The authors would like to express their gratitude to Kyoto University Global COE Programme “Energy Science in the Age of Global Warming” for funding participation in the SMINS-2 meeting.

References

- [1] G. R. Odette, T. Yamamoto, H. J. Rathbun, M. Y. He, M. L. Hribernik, J. W. Rensman (2003), Cleavage fracture and irradiation embrittlement of fusion reactor alloys: mechanisms, multiscale models, toughness measurements and implications to structural integrity assessment, *Journal of Nuclear Materials*, Vol. 323, pp. 313-340.
- [2] M.A. Sokolov, H. Tanigawa (2007), Application of the master curve to inhomogeneous ferritic/martensitic steel, *Journal of Nuclear Materials*, Vol. 367-370, pp. 587-592.
- [3] R. Bonadé, P. Spätig, N. Baluc (2007), Fracture toughness properties in the transition region of the Eurofer97 tempered martensitic steel, *Journal of Nuclear Materials*, Vol. 367-370, pp. 581-586.

- [4] Standard Test Method for Determination of Reference Temperature, T_0 , for Ferritic Steels in the transition Range, ASTM E1921-02, Annual Book of ASTM Standards, Vol. 03.01 (2002).
- [5] Z. Tong, Y. Dai (2009), Tensile properties of the ferritic martensitic steel F82H after irradiation in a spallation target, *Journal of Nuclear Materials*, Vol. 385, pp. 258-261.
- [6] M. Ando, H. Tanigawa, E. Wakai, R.E. Stoller (2009), Effect of two-steps heat treatments on irradiation hardening in F82H irradiated at 573 K, *Journal of Nuclear Materials*, Vol. 386-388, pp. 315-318.
- [7] R.L. Klueh, J.M. Vitek (1991), Tensile properties of 9Cr-1MoVNb and 12Cr-1MoVW steels irradiated to 23 dpa at 390 to 550°C, *Journal of Nuclear Materials*, Vol. 182, pp. 230-239.
- [8] P. Mueller, P. Spätig (2009), 3D finite element and experimental study of the size requirements for measuring toughness on tempered martensitic steels, *Journal of Nuclear Materials*, Vol. 389, pp.377-384.
- [9] G. R. Odette, T. Yamamoto, H. Kishimoto, M. Sokolov, P. Spätig, W. J. Yang, J. -W. Rensman, G. E. Lucas (2004), A master curve analysis of F82H using statistical and constraint loss size adjustments of small specimen data, *Journal of Nuclear Materials*, Vol. 329, pp. 1243-1247.
- [10] Standard Test Method for Measurement of Fracture Toughness, ASTM E 1820-99a, Annual Book of ASTM Standards, Vol.02.01 (2002).
- [11] B. J. Kim, R. Kasada, A. Kimura, H. Tanigawa (2009), Effects of cold work and phosphorous on the ductile to brittle transition behavior of F82H steels, ICFRM-14 conference [ID-00057].
- [12] Y. C. Lin, S. C. Chen (2003), Effect of residual stress on thermal fatigue in a type 420 martensitic stainless steel weldment, *Journal of Materials Processing Technology*, Vol. 138, pp. 22-27.

Study of optimum composition of extra high purity Ni-Cr-W-Si alloy for advanced reprocessing plant

Ikuo Ioka¹, Jun Suzuki¹, Kiyoshi Kiuchi¹, Jumpei Nakayama²

¹ Atomic Energy Agency, Japan, ²Kobe Steel, Ltd., Japan

Abstract

Optimisation of composition for extra high purity Ni-Cr-W-Si alloy (Ni-based EHP alloy) has been used to HNO₃ solution with highly oxidising ions for advanced reprocessing plants. The corrosion resistance of the Ni-based EHP alloy by a new multiple refining technique is superior to that of conventional stainless steels. The Ni-based EHP alloy also has an excellent resistance to weld cracking. Although the Ni-based EHP alloy has a technical limitation in hot workability for practical use, an appropriate temperature region for hot rolling and forging is very narrow compared with conventional stainless steels. This narrow temperature region is attributed to the formation of eutectics at high temperatures and the precipitation of silicides at low temperatures. Several Ni-based EHP alloys with different contents of Si and W were manufactured to choose optimum compositions. Corrosion tests at boiling HNO₃ solution with Cr (VI), hot ductility test and mechanical property tests were carried out to examine the optimum composition range of the Ni-based EHP alloy. A little increase in the corrosion rate of the Ni-based EHP alloys was observed by reducing W or Si content. It is necessary to reduce Si content of the Ni-based EHP alloys less than 2.5% in order to obtain high ductility at the temperature range of 950 °C to 1 150 °C without risking permanent structural damage. The study showed that there was a little influence on mechanical properties, such as tensile, fatigue, impact properties, W and Si content of the Ni-based EHP alloys. The optimum composition range of Ni-based EHP alloy with high corrosion resistance and hot workability was Ni-30Cr-8-10W-2-2.5Si.

Introduction

Reprocessing of spent nuclear fuels is a major area of activities that have attracted efforts to achieve successes in the back-end of nuclear fuel cycle. The most practical process for the reprocessing of spent nuclear fuel is a PUREX process, which could be used for reprocessing high burn-up fuels in advanced water cooling reactors (ALWRs) and MOX fuels in fast breeder reactors (FBRs). The reprocessing plants involve equipment, such as fuel dissolvers, evaporators for various purposes and high active waste storage tanks, which are mainly made of austenitic stainless steels. Nitric acid is the main process medium of reprocessing plants for spent nuclear fuels received from both ALWRs with low plutonium content and from FBRs with high plutonium content. The nitric acid is used in various conditions from dilute to concentrated, room temperature to boiling temperature. The acid is known to be a highly corrosive solution itself and the solution with highly oxidising ions, such as Pu in transuranium (TRU) and Ru in fission products (FP), becomes more corrosive [1] [2]. Moreover, ultra low carbon austenitic stainless steels such as types 304 ULC and 310 Nb are designed for the present reprocessing process like e.g. evaporators would suffer from grain boundary attack as oxidiser ions formed at heat conducting surfaces increase. [3]. Therefore, it is necessary to develop higher corrosion-resistant materials for advanced reprocessing plants.

We have developed an advanced material, an extra high purity Ni-Cr-W-Si alloy (Ni-based EHP alloy), with high corrosion resistance against highly oxidising nitric acid solutions. The composition of the Ni-based EHP alloy was designed to inhibit transpassive corrosion by enriching oxide-former elements such as Cr, W and Si with different electrode potentials for forming the protective films [4]. To achieve extra high purity of Ni-based EHP alloy, a multiple refined melting technique was used which is composed of a cold crucible induction melting (CCIM) and an electron beam cold hearth refining (EBCHR). Purification is also the most effectively practical means of enhancing the maximum solubility limit of Cr, W and Si. The Ni-based EHP alloy has excellent corrosion resistance for corrosion tests simulated to heat conducting surfaces in nitric acid solutions controlled at low boiling point compared with type 304 ULC [4]. Although the Ni-based EHP alloy has a technical limitation in hot rolling and forging for practical use, an appropriate temperature region for hot rolling and forging is very narrow compared with conventional stainless steels. This narrow temperature region is attributed to the formation of eutectics at high temperatures and the precipitation of silicides at low temperatures.

In this paper, the effects of W and Si on hot workability, corrosion resistance and mechanical properties of the Ni-based EHP alloys were investigated to choose optimum compositions range by high strain rate tensile tests at high temperatures, corrosion tests at boiling HNO_3 solution with Cr (VI) and mechanical property tests.

Experimental procedures

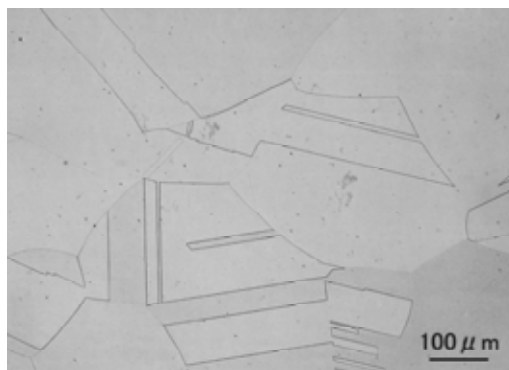
Specimens

Ni-based EHP alloys (Ni-30Cr-10W-3Si, Ni-30Cr-10W-2.5Si, Ni-30Cr-10W-2Si and Ni-30Cr-8W-2Si) were melted from high purity Ni, Cr, W, Si. To make the purified ingot of Ni-based EHP alloys, the multiple refined melting techniques were used.

Table 1: Chemical composition of Ni-based EHP alloys used in the tests (mass%)

ID	Ni	Cr	W	Si	C	Mn	P	S	O	N
10W-3Si	bal.	30.40	10.07	2.77	0.0025	<0.01	<0.003	0.0011	0.0007	0.0011
10W-2.5Si	bal.	30.00	10.03	2.48	0.0025	<0.01	0.0009	0.0008	<0.0005	0.0009
10W-2Si	bal.	30.57	10.24	1.92	0.0016	<0.01	0.0008	<0.0005	0.0007	0.0006
8W-2Si	bal.	27.48	8.13	1.91	0.0014	<0.01	0.0009	<0.0005	0.0010	0.0007

The chemical composition of the Ni-based EHP alloys used is shown in Table 1. Each specimen was machined from the solution-annealed plates for 1 h at 1 200°C. For example, the microstructure of 10W-3Si observed by the optical microscope is shown in Figure 1. These are little precipitates at the grain and grain-boundary. The average grain size is about 150 μm . The hardness of 10W-3Si, 10W-2.5Si, 10W-2Si and 8W-2Si are about 170 Hv, 168 Hv, 150 Hv and 150 Hv, respectively. Dimensions of plate specimens for corrosion tests are 30 mm in length, 15 mm in width and 2 mm in thickness. The bottom-ended test specimens with a gauge section of 6 mm in diameter with the length-axis parallel to the rolling direction were used for tensile and fatigue tests. The surface of the gauge section was ground with 600 grade silicon carbide paper and 3 μm Al_2O_3 powder before the tests. Half size specimens (55x10x5 mm) with a machined V-notch were prepared for Charpy impact tests.

Figure 1: Microstructure of 10W-3Si

Corrosion test

Corrosion tests were performed in boiling 8 kmol/m³ HNO_3 solutions containing 1 kg/m³ Cr (VI) ions. The specimen was corroded in a glass flask containing the boiling test solutions. After an immersion time of 24 hs, the specimen was removed from the flask. The specimen was ultrasonically cleaned for 0.1 h, dried for 0.1 h and then weighted to calculate the corrosion rate. The procedure was repeated periodically until termination (96 hs) of the corrosion test. The test solution was replaced after each weight measurement.

To determine corrosion morphology, surface observation was made by scanning electron microscope (SEM) on the specimen after the corrosion test.

Hot ductility test

Hot ductility tests were conducted using a Gleeble machine, which is essentially a high speed, hot tensile tester instrumented so that heating and cooling of the specimen can be accurately programmed to reproduce the rapid thermal changes that occur during hot rolling. The crosshead speed is 20 mm/s. A reduction of area (RA) of the specimen can predict hot workability. An ultimate tensile strength (UTS) corresponds to deformation resistance. RA and UTS were measured “on-cooling” in hot ductility tests.

Tensile test

A universal testing machine was used for the tensile test. The specimens were tested from room temperature to 450°C with a strain rate of $4 \times 10^{-3} \text{ s}^{-1}$ under air. The 0.2% offset yield strength (YS) and UTS were obtained from the engineering load-elongation curve of each specimen. Fracture elongation (Ef) was determined by the conventional method. RA of some specimens was calculated from the fracture surface area.

Fatigue test

Uniaxial load-controlled cyclic tests were performed on a computer-controlled servohydraulic machine. All tests were performed at room temperature. Specimens were subjected to a triangular tensile load versus time at 1 Hz. Total axial load ranges were from 300 MPa (0.45 UTS) to 550 MPa (0.85 UTS). The fatigue test was discontinued when the specimen broke or the number of cycles exceeded two million cycles.

Charpy impact test

In the Charpy impact test, the energy absorbed by a V-notch half size specimen during fracture at high strain rate was measured. The energy absorbed in fracturing the specimen (measured in Joules) is calculated by the height to which the pendulum rises after breaking the specimen. The Charpy impact value, which is the absorbed energy divided by the minimum cross-sectional area, was calculated. To determine the toughness of a material, the tests were carried out in a variety of temperatures (-196°C-120°C).

Results

Corrosion rates and SEM observation

In the case of corrosion tested in boiling 8 kmol/m³ HNO₃ solutions containing 1 kg/m³ Cr (VI) ions, changes in the corrosion rate during each test interval for Ni-based EHP alloys are shown in Figure 2. The results of type 310 ULC for the reprocessing process were plotted in Figure 2. The corrosion rates of Ni-based EHP alloys were almost constant from the initial stage of the corrosion test. On the other hand, the corrosion rate of type 310 ULC increased with immersion time. The corrosion rate of 8W-2Si was about one seventh lower than that of type 310 ULC at the final stage. The high corrosion rate was attributed to grain dropping caused by severe inter-granular corrosion [5]. A little increase in the corrosion rate of Ni-based EHP alloys was observed by reducing W and Si content of the Ni-based EHP alloys.

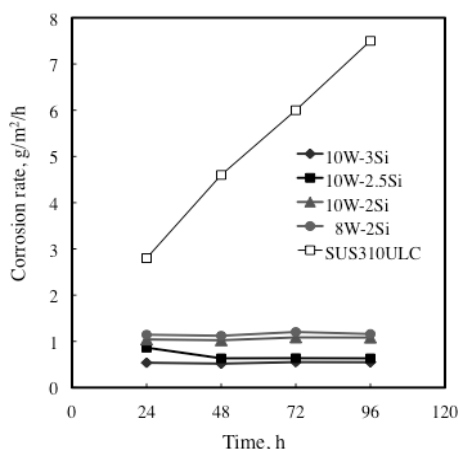
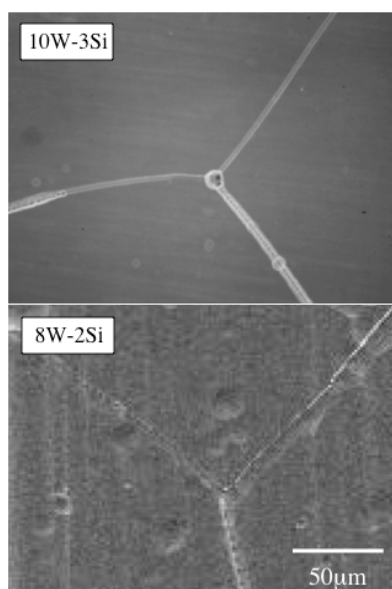
Figure 2: Corrosion rate of Ni-based EHP alloys**Figure 3: Surface of Ni-based EHP alloys after corrosion tests**

Figure 3 shows the surface of Ni-based EHP alloys (10W-3Si and 8W-2Si) after corrosion tests. Inter-granular corrosion occurs owing to the fact that grain boundaries dissolve much faster than the grain. The inter-granular corrosion is an important degradation mechanism of austenitic stainless steels for use in the nuclear fuel reprocessing plant. It is confirmed that the degree of the grain boundary corrosion for each Ni-based EHP alloy was almost the same after corrosion tests.

Hot ductility

The temperature dependence of RA performed by the Gleeble test is shown in Figure 4. RA of 10W-3Si was about 10% at 1050°C. RA of other Ni-based EHP alloys was 50% or more between 950°C and 1150°C. RA of 10W-2Si with less Si content was lower than that of 10W-2.5Si. However, in this study, the effect of Si on hot ductility of Ni-based EHP alloys could not be shown clearly. Figure 5 shows the temperature dependence of UTS performed by Gleeble tests. UTS decreased with increasing temperature. The hot working operation, such as hot rolling and forging, becomes difficult if UTS of Ni-based EHP alloy is too high. According to the results of this study, there was little effect of W and Si content on UTS of Ni-based EHP alloys.

Figure 4: Temperature dependence of RA by the Gleeble test

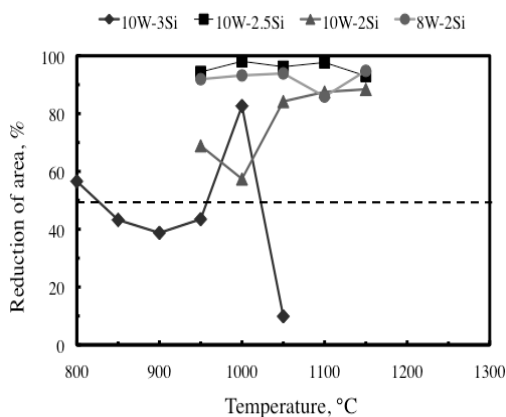
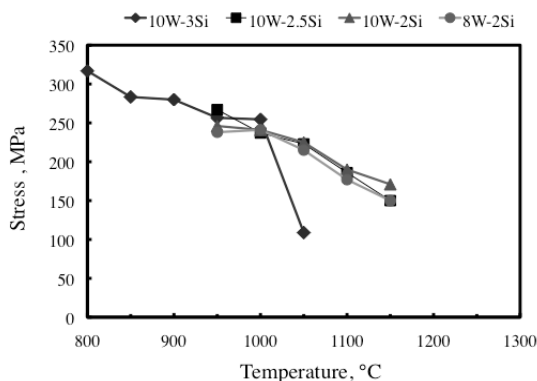


Figure 5: Temperature dependence of UTS by the Gleeble test



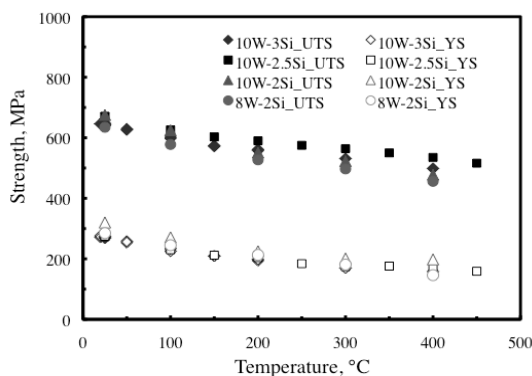
Mechanical properties

Figure 6 shows the relationship between test temperature and tensile properties such as YS, UTS, Ef and RA. The composition dependence of UTS was not observed up to 450°C. UTS decreased monotonously with an increase in the temperature. UTS was about 650 MPa at room temperature, about 500 MPa at 450°C. The present study showed a small influence on the compositions of YS, Ef and RA. The temperature dependence of Ef and RA was extremely

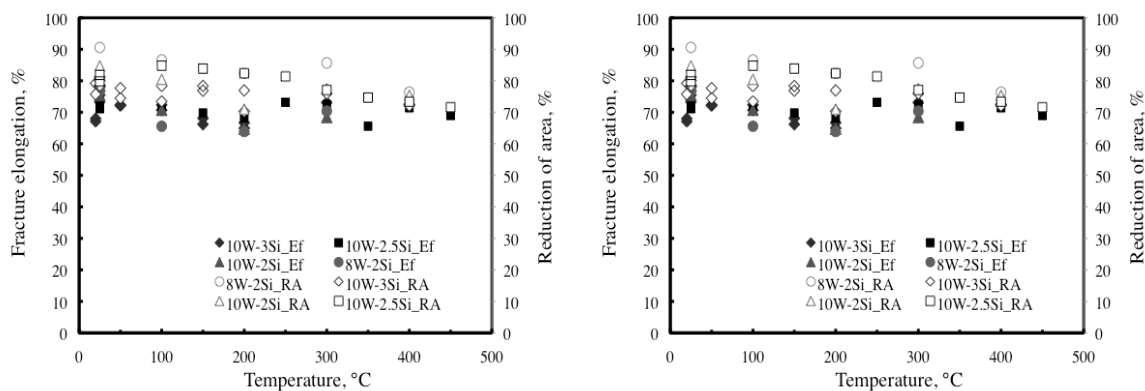
small. Ef changed in the value of about 70% regardless of the temperature and RA changed in the value of about 80%.

Figure 6: Temperature dependence of tensile propertiesg407

(a) 0.2% offset yield strength (YS), ultimate tensile strength (UTS)



(b) fracture elongation (Ef), reduction of area (RA)



The fatigue life of Ni-based EHP alloys is plotted in Figure 7 as the stress amplitude versus the number of cycles to failure on a linear-log scale. The fatigue life of Ni-based EHP alloys expanded with the decrease in the stress amplitude. As can be seen from Figure 7, the fatigue limit of Ni-based EHP alloys is about 300 MPa. Figure 7 also shows no effect of composition on fatigue life. A significant degradation of fatigue life was not observed in Ni-based EHP alloys with different levels of W and Si content.

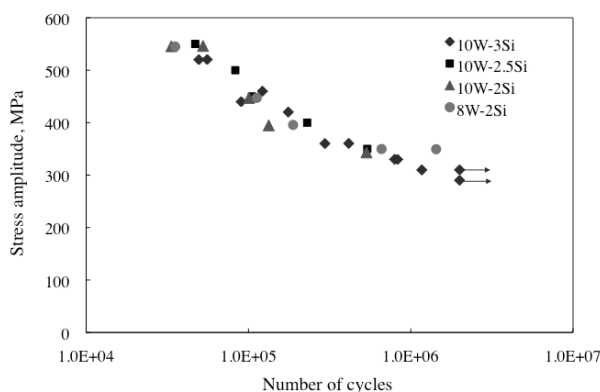
Figure 7: Fatigue life of Ni-based EHP alloys

Figure 8 shows the results of Charpy impact tests. The Charpy impact value of all Ni-based EHP alloys was 400 J/cm² or more at the temperature range of -196°C to 120°C and it was a sufficient value. The fracture modes of all specimens were ductile. The Charpy impact value regarding Ni-based EHP alloys also showed little effect on W and Si content.

The mechanical properties, such as tensile, fatigue and impact properties, of Ni-based EHP alloys were investigated. The present study showed little influence of W and Si contents of Ni-based EHP alloys on mechanical properties.

Discussion

Effect of W and Si on corrosion rate

The relationship between corrosion rate at the final stage and W or Si of Ni-based EHP alloys is summarised in Figure 9. The corrosion rate increased with a decrease in W and Si content. Figure 10 shows the depth profile of the main elements for 8W-2Si using Auger Emission Spectroscopy (AES) after the corrosion test. A horizontal axis, which denotes etching time in Figure 10, corresponds to depth from the surface of the specimen. The surface of the specimen was covered with the protective oxide film mainly composed of Si and Cr. As for the influence of elements on the corrosion rate, it is confirmed that Si is more effective than W.

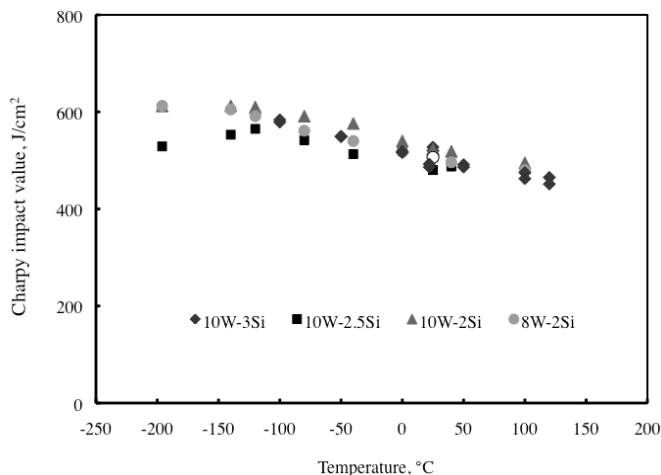
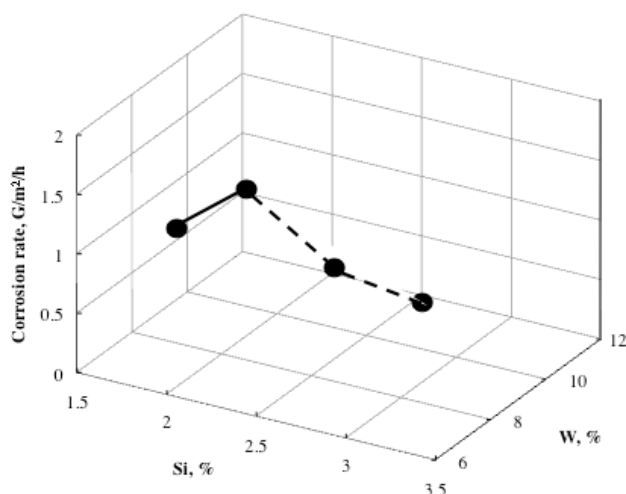
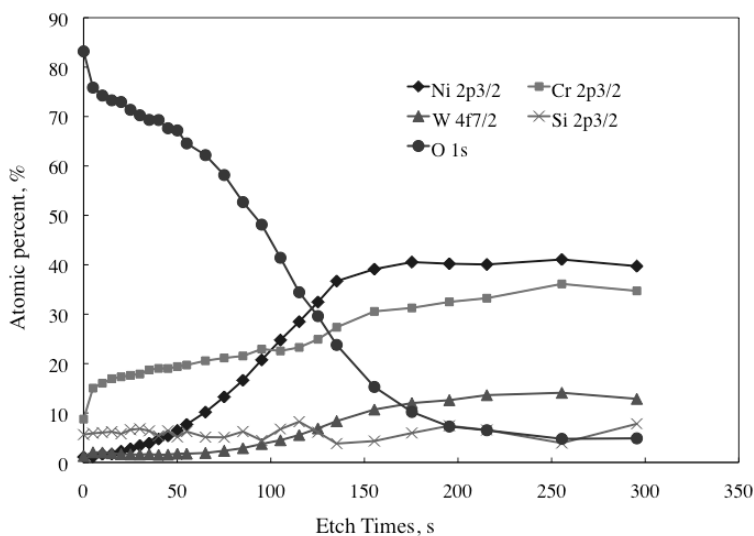
Figure 8: Results of Charpy impact tests

Figure 9: Relationship between corrosion rate and W or Si

Effect of W and Si on hot workability

RA has a very structure-sensitive property, it can be used to detect small ductility variations in materials having moderate ductility, such as superalloys [6]. YS and UTS can be used to select the required load capacity of the production processing equipment. In general, RA can be used by Gleeble tests to predict hot workability and to select hot-working temperature ranges. It is expected that the hot rolling process will provide good hot workability for the generation of a few cracks to the superalloy when RA exceeds 50% [6]. As can be seen from Figure 4, in order to obtain high ductility over the wide temperature range (950°C-1 150°C) without risking permanent structural damage, it is necessary to reduce Si content less than 2.5%. So, it is believed that the optimum composition range of Ni-based EHP alloy with high corrosion resistance and hot workability was Ni-30Cr-8-10W-2-2.5Si.

Figure 10: Depth profile of 8W-2Si using AES after corrosion test

Conclusions

The optimum composition range of Ni-based EHP alloys was examined to improve hot workability of Ni-based EHP alloys from the results of a hot ductility test, corrosion test and mechanical property test. The following results were obtained:

- A little increase in the corrosion rate of Ni-based EHP alloys was observed when W and Si content was reduced.
- In order to obtain high ductility from 950°C to 1 150°C without risking permanent structural damage, it is necessary to reduce Si content less than 2.5%.
- The present study showed little influence of W and Si contents on mechanical properties, such as tensile, fatigue and impact properties, of Ni-based EHP alloys in this study.
- The optimum composition range of Ni-based EHP alloy with high corrosion resistance and hot workability was Ni-30Cr-8-10W-2-2.5Si.

Acknowledgements

The authors express their gratitude to Dr. I. Tsukatani for his contribution to our useful discussions. They would also like to thank Mr. T. Suzuki for preparing the specimens. The present study includes the results of “Research and Development of Nitric Acid Resistant Material Technology Applicable to the Next Generation of Reprocessing Equipment” entrusted to Kobe Steel, LTD by the Ministry of Education, Culture, Sports, Science and Technology of Japan.

References

- [1] M. Okubo, M. Shintani, H. Ishimaru *et al.* (1994), RECOD86, p.1181.
- [2] M. Takeuchi *et al.* (2005), Transactions of the Atomic Energy Society of Japan, 4, 32.
- [3] J.A. Beavers *et al.* (1981), Corrosion, 36, 292.
- [4] K. Kiuchi *et al.* (1999), Technical Committee Meeting of IAEA, Argentina, 210.
- [5] J. Nakayama (2008), *Genshiryoku eye*, 54, 60 [in Japanese].
- [6] G.E. Dieter, H.A. Kuhe and S.L.Semiatin (2003), “Handbook of Workability and Process Design”, ASM international, 72.

Effects of lower nitrogen and higher boron in ferritic/martensitic steels for a SFR fuel cladding*

Jong-Hyuk Baek, C.H. Han, J.H. Kim, T.K. Kim, W.G. Kim, S.H. Kim, C.B. Lee
Korea Atomic Energy Research Institute, Republic of Korea

Abstract

High-chromium (9-12 wt.%) ferritic/martensitic steels are currently being considered as candidate materials for cladding and duct applications in sodium-cooled fast reactors (SFR) because of their higher thermal conductivity and lower expansion coefficient as well as excellent irradiation resistance to void swelling when compared to austenite stainless steels. Since the operation condition in the SFR design would be envisioned to be harsh from the viewpoints of temperature ($\geq 600^\circ\text{C}$) and irradiation dose (≥ 200 dpa), the primary emphasis is on the fuel cladding materials, i.e. high-Cr ferritic/martensitic steels. This study investigated the microstructural and mechanical properties of the experimental steels, which consisted of a lower nitrogen (0.02 wt.%) and higher boron (0.015 wt.%) in the 9Cr-0.5Mo-2W alloying system. The experimental steels were prepared by a serial process of vacuum induction melting, hot-rolling, normalising and tempering. Tensile and creep tests were performed at 650°C and microstructures were evaluated before/after the creep tests. The experimental steels showed a typical tempered martensitic microstructure after the normalising and tempering treatments. $M_{23}C_6$ carbides were observed as major precipitates around the prior-austenite and lath boundaries. Nb-rich MX carbonitrides were also detected on both boundaries and their interiors. The Ta below 10 at.% was incorporated into the Nb-rich MX precipitates. Although the boron content was relatively high up to 150 ppm, BN precipitates were not revealed in the steels due to the lower nitrogen of 0.02 wt.%. The combination of lower nitrogen and higher boron could bring out the $M_{23}C_6$ stabilisation as well as BN precipitation inhibition. The tensile strength at 650°C exhibited 347 MPa, which were much higher than that (290 MPa) of a reference ASTM Gr.92 steel. The creep performance was improved when compared to the Gr. 92 steel due to the increase in Nb as well as the addition of Ta. From the viewpoint of creep resistance, the optimal Ta content would be 0.05 wt.%. The experimental steels showed superior creep performance to the reference steel under the constant load conditions of 140 and 150 MPa. In short, the combination of lower N and higher B could improve creep properties due to the stabilisation of $M_{23}C_6$ precipitates without BN formation during creep testing.

* The full paper being unavailable at the time of publication, only the abstract is included.

Hydrogen cracking of structural materials for innovative nuclear systems: Crack growth mechanism in metals*

YoungSuk Kim, SungSoo Kim, DaeWhan Kim

Hydrogen Cracking Team, Korea Atomic Energy Research Institute, Daejeon,
Republic of Korea

Abstract

Hydrogen, one of the most important fuels for fusion reactors, is considered to be an ideal energy in the foreseeable future which can be produced from water using nuclear energy. One technological challenge for the commercial use of hydrogen energy is how to avoid or lessen degradation due to the hydrogen embrittlement of the structural materials to be used in the transportation, storage and distribution of hydrogen. Furthermore, hydrogen cracking in structural materials is one of the degradation phenomena to be tackled by the current nuclear industry. There are many common features between the degradation mechanisms such as stress corrosion cracking (SCC), hydrogen cracking, hydrogen embrittlement (HE) and liquid metal embrittlement (LME): discontinuous crack growth, temperature dependence of the crack growth rate and the presence of threshold stress intensity factor required to initiate crack. Thus, an understanding of the hydrogen cracking mechanism will lead to the elucidation of the other degradation mechanisms such as SCC, HE and LME. The aim of this work is to show that the kinetics of crack growth in metals is governed by the rate of the slowest one among the processes involved in hydrogen cracking. To this end, we investigated the crack growth rate (CGR) of zirconium alloys containing hydrogen at temperatures ranging from 100°C to over 300°C. The CGR of zirconium alloys increased with increasing temperatures below 300°C but rapidly decreased above that. This abrupt decrease in the CGR cannot be understood if the CGR is assumed to be governed solely by hydrogen diffusion or the hydride growth rate that will increase exponentially at higher temperatures. Hydride cracking resistance, which is represented by the distance between the striations, increased gradually with temperature below 300°C, followed by a sharp increase above 300°C. This fact showed that the hydride cracking rate was fast but slightly lowered with temperatures below 300°C but rapidly dropped at temperatures higher than 300°C. Given that the crack growth consists of the three processes of nucleation, growth and cracking of hydrides in zirconium alloys and nucleation of hydrides occurs faster than the remaining two processes due to higher hydrogen concentrations, the positive temperature dependence of the CGR is due to the rate of hydride growth being the slowest process below 300°C. The negative temperature dependence of the CGR is due to the rate of the hydride cracking being the slowest process above 300°C. Consequently, this study demonstrates that the CGR in zirconium alloys with hydrogen is governed by a slower process between the processes involved in hydrogen cracking. However, the activation energy for the CGR is found to be a sum of the activation energy for the processes involved.

* The full paper being unavailable at the time of publication, only the abstract is included.

A spin-polarised potential for Fe with charge transfer*

Janne Wallenius, Nils Sandberg, Graeme Ackland

Abstract

Within the GETMAT project, formalism for incorporating anti-ferromagnetism into molecular dynamics simulations Fe-Cr alloys is under development. This study presents the first results of spin-dynamic simulations in pure iron, including relaxation of magnetic moments in defect configurations and Curie temperature transition. The model takes into account charge transfer in-between s- and d-bands and hence goes beyond the approach earlier published by Dudarev and co-workers.

* The full paper being unavailable at the time of publication, only the abstract is included.

Session V

General

***Chairs: A. Zeman, N. Dytlewski, V. Inozemtsev, G. Mank, F. Mulhauser,
D. Ridikas, A. Stanculescu***

IAEA activities on co-ordinated research of structural materials for advanced reactor systems

A. Zeman¹, N. Dytlewski¹, G. Mank¹, F. Mulhauser¹, D. Ridikas¹,
A. Stanculescu², V. Inozemtsev²

¹Department of Nuclear Sciences and Applications, International Atomic Energy Agency, Vienna, Austria,

²Department of Nuclear Energy, International Atomic Energy Agency, Vienna, Austria

Abstract

Materials performance and integrity are key issues for the safety and competitiveness of future nuclear installations being developed for sustainable nuclear energy (fission and fusion reactors, fuel recycling and waste transmutation systems or fusion-fission hybrid reactors). These systems will feature, among other things, high thermal efficiency, maximised utilisation of fuel and a minimal production of nuclear waste. This will require the development, qualification and deployment of new structural materials with improved mechanical properties combined with radiation and corrosion resistance. To achieve the required and challenging materials performance parameters, focused research and targeted testing of new candidate materials are necessary.

There have been promising developments in new classes of advanced materials such as fibre-reinforced ceramic composite materials, oxide dispersion-strengthened alloys with nano-structured features or advanced reduced activation ferritic-martensitic steels, exhibiting good radiation resistance and corrosion properties with high-temperature strength and toughness. There is a strong need and demand for experimental support, especially in studies of material behaviour under extreme conditions of high dose and/or temperature. This is being provided at present by charged particle simulation experiments, computer modelling and advanced materials characterisation techniques. These experimental activities form only part of the many different activities required providing reliable and validated data and information leading to the qualification and licensing of materials to be used in future nuclear installations and will have to be supplemented by comprehensive in-pile irradiation programmes.

Such activities require long-term intensive and internationally collaborative and co-ordinated programmes of research and development in which the IAEA can play an important role in the facilitation and co-ordination process. This paper summarises the IAEA programmatic activities in the area of R&D support for advanced reactor systems, including ongoing co-ordinated research projects and future perspectives.

Introduction

The problem of climate change is one of the most significant global challenges confronting the international community. There is growing evidence that greenhouse gas (GHG) emissions, of which carbon dioxide (CO₂) is the most important anthropogenic GHG, are an important contributor to climate change. Global climate change affects livelihoods, threatens life-sustaining resources and weather-related catastrophes are becoming more frequent and more destructive. The danger of climate change may be limited by reducing gas emissions. From the points of view of sustainability and reduction of CO₂ emission, further development and implementation of large-scale GHG free power sources will bring significant benefits to mankind. This demand was emphasised by United Nations Secretary-General during the high-level Summit on Climate Change held in New York, 22 September 2009. Moreover, the critical role of technologies for reducing GHG emission was discussed during the UN Climate Change Conference in Copenhagen (2009). A broad international community of high-level climate experts, decision-makers and business innovators discussed new strategies and technological orientations for future industrial and energy policy with respect to climate change and environment protection.

Today a new generation of evolutionary and innovative nuclear power reactors is in the design phase. These new systems will further enhance safety, improve economics for electricity production and new applications such as hydrogen generation, reduce nuclear wastes and increase proliferation resistance. These innovative systems will feature high thermal operational efficiency, maximised utilisation of fuel and minimal production of nuclear waste and require development, qualification and deployment of new structural materials with improved mechanical properties combined with high radiation and corrosion resistance. The role of the structural materials either for fission or fusion reactors, is to retain functionality of core components; moreover, such materials have to maintain the integrity of individual components, such as fuel rods and assemblies. Another role is to prevent release of radioactivity to the coolant and environment. The requirements for new materials are reaching technological limits. A significant effort has to be made in order to proceed with qualification and development of new structural materials for key reactor components. At present, several development programmes, either for fission concepts or future fusion reactors are ongoing in order to design, characterise and qualify such new materials. The new concepts can solve a number of ongoing issues linked to the need for optimisation of fuel cycles and introduction of advanced nuclear reactors. While a number of physical concepts and innovative reactor designs are available, the absence of reliable materials able to sustain new challenging irradiation conditions represents the real bottle-neck for practical implementation of these promising ideas.

In general, material properties are strongly affected by irradiation, therefore, behaviour of materials under irradiation has been studied for more than 50 years. So far not all scientific and technological aspects have been fully understood and further research is still necessary. In particular, there is a lack of information for new and improved core materials irradiated at very high doses. These materials were originally chosen on the basis of their as-fabricated properties. However, there is an inevitable radiation-induced evolution of properties and most changes have been found to be detrimental. Moreover, most experience has arisen only from the area of thermal reactors where core structural materials are subject to temperatures up to 400°C and damage up to 60 dpa for near-core austenitic internals and 10 dpa for typical LWR fuel cladding materials at a burn-up of 40 GWd/tU. Looking forward, it is projected that core structural components of Generation IV fission reactors will operate at 500°C–1 000°C and reach damage levels of up to 100–200 dpa. For projected fusion devices with greatly differing neutron spectra arising from 14 MeV neutrons, there will also be a wide range of dpa and temperatures. ITER will experience approximately only 100°C–300°C and damage of about 3 dpa. The prototype fusion power reactor DEMO is expected to operate in the range of 500°C–1 000°C and reach ~150 dpa at the end of five years of full power operation.

However, radiation doses in future commercial fusion power reactors might be significantly higher. Such high doses and temperatures will most certainly require the development of improved materials.

Co-ordinated research activities

The IAEA co-ordinated research projects (CRP) aim to enhance the capability of interested Member States to build advanced or innovative nuclear technologies by promotion of information exchange and collaborative R&D to resolve issues associated with specific problems. More information about methodology, principles, formal procedures and all active and planned research projects can be obtained at the following web-page: www-crp.iaea.org.

As already mentioned, today, several Member States have a number of national projects in the area of structural materials of critical components of innovative nuclear reactors. Moreover, international initiatives, like the Generation IV International Forum (GIF) have been active for almost a decade. In line with the statutory objective expressed in Article II *“The Agency shall seek to accelerate and enlarge the contribution of atomic energy to peace, health and prosperity throughout the world. It shall ensure, insofar as it is able, that assistance provided by it or at its request or under its supervision or control is not used in such a way as to further any military purpose”*, the IAEA is assisting Member States’ activities in the area of advanced reactor research and technology development by providing an umbrella for information exchange and collaborative R&D to pool resources and expertise. Specifically, the activities touched upon in this paper are carried out jointly by the Department of Nuclear Sciences and Applications (NA) and Department of Nuclear Energy (NE).

As for IAEA’s fast reactor technology development activities, these are performed within the framework of the Technical Working Group on Fast Reactors (TWG-FR). In responding to strong common R&D needs in the Member States, the TWG-FR acts as a catalyst for international information exchange and collaborative R&D. The TWG-FR is a standing working group within the framework of the IAEA. It provides a forum for exchange of non-commercial scientific and technical information and a forum for international co-operation on generic research and development programmes on advances in fast reactors and fast spectrum accelerator-driven systems. Its present members are the following 14 IAEA Member States: Belarus, Brazil, China, France, Germany, India, Italy, Japan, Kazakhstan, the Republic of Korea, the Russian Federation, Switzerland, the United Kingdom, and the United States of America, as well as the ISTC, OECD/NEA and the EU (EC). The TWG-FR has also welcomed, as observers, Belgium and Sweden.

Within the framework of the TWG-FR, the IAEA sustains an excellent platform for the fast reactor specialists to share their experience related to the design, development, construction and operation of nuclear power plants with fast reactors, organises regular topical technical meetings to exchange information as well as large conferences on different aspects of fast reactor research and technology, establishes a forum for broad exchanges on technical requirements for 4th generation fast reactor systems, carries out CRPs of common interest to the TWG-FR Member States, also provides technical expertise and support to the IAEA Department of Nuclear Safety and Security with the development of fast reactor safety standards and secures training and education in the field of “Fast neutron physics, technology and applications”.

Accelerator simulation and theoretical modelling of radiation effect

The overall objective of the co-ordinated research project on “Accelerator Simulation and Theoretical Modelling of Radiation Effects” in the first phase is focused mostly on the improvement, development and testing of core structural materials for higher burn-up in advanced water-cooled and fast reactors. The identified goals are addressed by

accelerator simulation of high-dose irradiation and complementary application of theoretical modelling. The approach of coupling accelerator studies with modelling has tremendous potential to increase understanding of radiation damage in high-dose materials, validation of complex materials models and increased use of novel characterisation techniques for enhanced understanding of the basic problems and processes. A new era for studies with charged particle accelerators coupled with characterisation using high-tech instrumentations has been entered since charged particle simulation experiments, backed up by theoretical modelling of radiation effects, have been proven methodology to study microstructural evolution. Of course, this type of experiments cannot substitute for the full qualification scale tests, however, they are extremely useful in the R&D stage, as a key tool which can be used effectively to reduce both the cost and duration of experimental testing. Since there is no or very limited activation of samples caused by ion irradiation, specialised techniques can be applied for characterisation down to the atomic scale. In addition, exchange of specimens for international collaborations can be more easily accomplished [1].

The objectives of this research project are defined as follows; (1) better understanding of radiation effects and mechanisms of material damage and basic physics of accelerator irradiation under specific conditions, (2) improvement of knowledge and data for the present and new generation of structural materials, (3) contribution to the development of theoretical models for radiation degradation mechanism and (4) fostering of advanced and innovative technologies by support of round robin testing, collaboration and networking.

The specific research outputs of the co-ordinated research include specific tests and cross-examination of selected materials with the use of different accelerator techniques and material characterisation methods (with special attention to scaling issues of small testing samples). In the final stage of the project a database of jointly qualified accelerator experiments and results of materials will be compiled.

From the beginning of 2009, extensive theoretical and experimental studies are being carried out among participating laboratories in Belgium, China, the European Commission, France, India, Japan, Kazakhstan, the Republic of Korea, Poland, the Russian Federation, the Slovak Republic, Spain, Switzerland, Ukraine and the United States. In total, 18 full CRP members are active. In addition, OECD/NEA participates as a permanent observer. The programme activities fall into three broad categories, namely modelling, ion or neutron bombardment studies and material characterisation studies, all directed toward the use of modelling and ion simulation to predict the behaviour of high-dose neutron irradiation of simple Fe-Cr model alloys, conventional ferritic-martensitic alloys and especially dispersion-hardened ferritic-martensitic steels. The preliminary results reported in 2010 showed interesting achievements regarding dual and triple beam irradiations. A number of research papers have already been published under these co-ordination research activities. Further emphasis of research will be given to the correlation of nano-dispersoid microstructure data obtained by microscopy and non-destructive techniques. According to the project plan, the CRP will be finished by the end of 2012.

Benchmarking of structural materials pre-selected for advanced nuclear reactors

The aim of the research project on “Benchmarking of Structural Materials Pre-Selected for Advanced Nuclear Reactors” is to respond to an ongoing demand related to the enhanced operating regimes of innovative reactor concepts, which face higher temperatures and doses than existing power reactors as well as design life extension of fast reactors up to at least 60 years. The fast reactors with coolants like sodium, lead or lead-bismuth have several advantages. On the other hand, they could cause a potentially more aggressive environment, which has also a negative impact on the degradation of structural materials of key primary components. In order to solve such pending issues, a significant effort is needed to develop and qualify new materials for key primary

components. In view of this, international efforts should be focused on full testing of new materials. Several recently developed structural materials have very promising characteristics, especially for application in both fission and fusion reactors. A very good example is ferritic-martensitic steel with oxide dispersion-strengthened (ODS) features. Today, several classes of ODS alloys are being developed and tested by different national laboratories in several EU countries and also in India, Japan, China and the United States. It has been recognised that several synergies and similarities exist between R&D effort of fission and fusion. Considering design aspects of magnetic fusion reactors, it has been decided that austenitic stainless steel chosen for ITER vacuum vessel and in-vessel components would not be suitable for DEMO and future fusion power reactors, where, neutron doses will be significantly higher. The parallelism of the ITER activities exists under the IEA implementing agreement on the fusion materials development. This initiative focused on reducing the activation of ferritic-martensitic steels. First heats of RAFM steels were produced in Japan (F82H) and fully tested. However, the European programme has been focused on development of RAFM steel EUROFER'97 for fabrication of the fusion reactor test blanket modules, specifically, helium-cooled lithium lead and helium-cooled pebble bed. The recent achievements co-ordinated by EFDA and F4E agencies have quite positive results. Newly developed EUROFER'97 steel with ODS features is a unique and promising candidate material, which is being qualified for fusion applications. Nevertheless, there are several issues to be addressed, specifically (1) microstructure optimisation (alloying elements, size and distribution of oxide particles, etc.) and (2) larger scale fabrication process (anisotropy and homogeneity) as well as (3) technological aspects like welding and joining procedures.

The issue related to deficiencies in the high-temperature structural materials' design criteria, particularly in the domain of creep-fatigue interaction must also be addressed. It is important to note that this problem is not fully resolved for well-known materials, such as the austenitic stainless steel type 316L (N). It becomes even more challenging for martensitic steels that show cyclic softening during fatigue or creep-fatigue loading when trend towards longer reactor lifetimes (60 years) is considered. The next subject of the project is focused on advanced materials capable of operating through a wide range of elevated temperatures to high radiation damage levels. In this regard, many of the innovative reactor concepts propose to use high-temperature materials, capable of resisting irradiation doses of 200 dpa or higher (e.g. for cladding and ducts). Currently, the cycle of examinations necessary for an improved material for industrial employment in existing reactors requires 20 or more years. These factors make it very difficult to conduct direct reactor experiments for developing new materials of advanced nuclear systems. From this point of view, very careful screening of candidate materials needs to be done in order to optimise further testing and final qualification of selected structural materials [2].

To start with the benchmarking of radiation degradation, ageing and phase stability mechanisms for recently developed pre-selected materials for new innovative reactor systems are needed. The performance testing of pre-selected materials for innovative nuclear reactors can be done by using nuclear techniques, based on accelerators and research reactors. These tools can contribute strongly to the assessment of the material properties at the micro scale. The results of such R&D work can lead to the technological improvement of materials under investigation. At present, extensive characterisation and testing of recently developed candidate materials using the most advanced techniques of as-fabricated materials are needed as a necessary precursor to the subsequent understanding of radiation degradation, ageing and phase stability mechanisms. In addition, improved design methodologies to ensure the safe application of these advanced materials in high-temperature reactor environments are needed. Since such activities are being pursued separately in various national programmes, co-ordination of these activities by means of an IAEA international co-ordinated research is warranted. This broader initiative will indeed accelerate technological improvements of the materials and design methodologies.

The CRP on Benchmarking of Structural Materials Pre-Selected for Advanced Nuclear Reactors (2010–2013) aims to support the IAEA Member States interested in internationally co-ordinated R&D activities related to the core structural materials of innovative reactor systems. Many countries with fully developed national nuclear energy programme have demonstrated interest in fast reactors technology, either sodium-(SFR) or lead-cooled concepts (LFR). Nevertheless, structural materials development and their qualification remain a significant challenge. The SFR concept is quite well-proven technology; however, further improvement of fuel performance and other internal components of reactor is still an issue. In this particular case, structural materials of highest interest for these concepts were austenitic stainless steels, particularly type 316L (N) and martensitic steels of the 9Cr-1Mo class. For the cladding, the choices varied between well-known materials, such as Ti-modified 316 SS and 15/15Ti, but for advanced concepts all countries were investigating higher temperature and/or higher dose-resistant materials such as conventional and oxide dispersion-strengthened (ODS) grades of ferritic-martensitic steels, ceramic composites (SiC/SiC), or refractory metal alloys (vanadium alloys). This is also considered as a parallel initiative with R&D trends in materials development for proposed future fusion reactors. The research synergies between innovative fission and fusion programmes are clear in the case of the ODS alloys.

The objectives of the co-ordinated research are primarily focused on the following issues: (1) high-temperature structural materials design criteria, particularly in the domain of creep-fatigue interaction and (2) round-robin testing of advanced ODS ferritic-martensitic steels. The CRP is addressed to research groups with expected interest in the subject and/or to participants with direct involvement in research linked to the development of radiation-resistant materials, primarily for fast reactor critical, replaceable and non-replaceable components in order to analyse the long-term behaviour of these components related to the operational temperature and transition regimes, neutron flux, chemical compatibility with coolant and mechanical stress. The CRP is open for submission of research proposals from individual research groups until end of 2010.

Examination of advanced fast reactor fuel and core structural materials

It is foreseen that the development of fast reactor technology for nuclear power application will be vital towards meeting security and sustainability of energy for the growing economy. Yet, at a number of recent IAEA international meetings it was indicated that, despite the high priority of fast reactor technologies for optimisation of nuclear fuel cycles, there is a lack of information exchange in R&D on materials for FR fuels and core components, combined with a crucial shortage of testing irradiation facilities with fast neutron spectra.

The Russian Federation is now the only country that operates commercial fast power reactor BN-600 (which is also used to a limited extent for R&D projects) and has large-scale fast neutron irradiation testing and PIE capabilities. Nowadays, only a few research and experimental reactors are used as a test bed for the development of fuel and structural materials for fast reactors. It is important to emphasise that, existing material test reactors with thermal neutron spectrum do not fulfil necessary requirements of irradiation experiment, specifically flux, fluence, helium ratio, etc. The suitable test fast reactors are located in India (FBTR), Japan (JOYO) and the Russian Federation (BOR-60). However, these reactors have limited capacity since the programmes are pre-booked for forthcoming years. Nevertheless, in the case of an internationally co-ordinated effort with an optimised set of materials, the testing and pre-qualification work can be accelerated.

The experience obtained from previous generation of sodium-cooled fast reactors operated in France (PHÉNIX), Kazakhstan (BN-350) and the United States (BR-2) have provided a solid base for design and development of new reactors. The sodium-cooled fast reactor in the Russian Federation BN-600 as well as the recently restarted MONJU in Japan can bring additional information on long-term behaviour and degradation

processes of core structural materials. The end of life experiments and post-irradiation analysis of core materials as well as samples loaded in irradiation rigs could give additional support to the R&D of new materials. From this point of view, further enhancement of international co-ordination, information exchange as well as joint experiments will help to optimise cost and limit the timeframe necessary to finalise individual national projects [3].

For necessary economic efficiency, liquid metal-cooled fast reactors should operate at very high neutron fluxes up to doses of about 200 dpa and at higher temperatures (up to about 650°C) compared to those in light-water reactors. So their structural components are subjected to much higher rates of atomic displacement and microstructural-microchemical evolution, phase instability and dimensional changes. This stability of structural materials should be maintained long enough for the fuel to reach the maximum burn-up consistent with neutronic and economic considerations.

Extensive experimental studies and actual operating experience have shown that austenitic stainless steels commonly used in both thermal and fast reactors will eventually swell at ~1%/dpa after an incubation period which is very dependent on compositional, processing and environmental variables. This high steady-state swelling rate of 1%/dpa limits the use of austenitic steel to <150 dpa. Ferritic and ferritic-martensitic steels in general have much longer incubation periods before the onset of swelling and also possess an inherently lower steady-state swelling rate estimated to be a maximum of 0.2%/dpa. But, in their turn, they have non-sufficient high-temperature strength (above about 550°C) and suffer radiation-induced shifts in their ductile-brittle transition temperature. That is why the most promising candidate materials are currently ODS alloys that maintain strength to much higher temperatures but also appear to contribute to additional resistance to swelling at lower temperatures. However, these ODS alloys are often rather difficult to manufacture and their development is still very much in the R&D phase.

Despite the structural materials (mostly fuel cladding), the option for fast reactor fuels is also open and discussed. This also brings about a need for irradiation testing as a necessary component of R&D efforts and defines incentives for international co-operation in the present circumstances of the acute deficiency and skyrocketing costs of irradiation testing facilities.

This is the reason why the IAEA initiates international co-ordinated research on "Examination of advanced fast reactor fuel and core structural materials for fast reactors" planned to start in 2011. It aims at facilitation of collaboration among interested Member States and is to initiate internationally co-ordinated fast neutron irradiation experiments and post-irradiation examination of samples provided by CRP members.

The IAEA Member States with active fast reactor programmes are to be members of the CRP. The objectives of the new co-ordinated research project are (1) support for R&D of advanced fuel and core structural materials of sodium fast reactors, (2) co-ordinated access to irradiation testing and post-irradiation examination and (3) enhance information exchange among Member States active in the fast reactor technology. It is expected that CRP will start early in 2011 and its detailed test programme will be set up during its first Research Co-ordination Meeting Q1/2011. In principle, various types of reactor experiments related to the core structural materials will be included into the test matrix of the project. The following research topics are open in this CRP:

- review of accumulated fast neutron irradiation data and experience;
- characterisation, in-pile performance analysis and PIE of (a) advanced cladding and wrapper steels for fast reactors (austenitic, ferritic-martensitic and ODS) and (b) fuel materials for fast reactors, specifically (U, Pu)O₂, (U, Pu)N, metallic, minor actinides;

- fast neutron irradiation within national programmes;
- joint IAEA co-ordinated fast neutron irradiation programme with the following entries to be considered: (a) pre-irradiation characterisation, (b) definition of irradiation facilities, (c) definition of PIE facilities and (d) design, manufacturing and licensing of test fuel assemblies.

Following the irradiation experiments, post-irradiation examination (PIE) is to be carried out preferably at the same laboratory site. It is important to emphasise that any long-distance transports or international shipments will be extremely complicated. In respect of recent expert's advice the CRP will be open for submission of research proposals early in Q1/2011.

Conclusion

This paper summarises the IAEA initiatives related to the R&D support of structural materials for innovative nuclear reactor systems. Further support of international co-operation in the area of innovative nuclear reactor systems has been requested by the delegates of the 53rd IAEA General Conference held in Vienna, 14-18 September 2009. Resolutions GC(53)/ES/10 on "Measures to strengthen international co-operation in nuclear, radiation, transport and waste safety" and GC(53)/RES/13 on "Strengthening the Agency's activities related to nuclear science, technology and applications" have specifically stressed that secretariat activities related to the technological and safety aspects of new reactor designs should be continuously supported in order to develop services and tools that support Member States in promoting the safety of such new reactor technology. In addition, peaceful use of fusion energy should also be advanced through increased international efforts and with the active collaboration of interested Member States and organisations in fusion-related projects.

References

- [1] IAEA (2008), CRP 1488 on Accelerator Simulation and Theoretical Modelling of Radiation Effects, Vienna (Austria), (RCS project proposal).
- [2] IAEA Consultants Meeting (1007110) on Benchmarking of advanced materials pre-selected for innovative nuclear reactors, Vienna (Austria), 9-12 March 2010 (working materials).
- [3] IAEA Consultants Meeting on Examination of advanced fast reactor fuel and core structural materials, Zarechny (Russia), 22-24 June 2010 (working materials).

Contribution of ITER to research of internal component materials

C.S. Kim, V. Barabash, M. Merola, R. Raffray

ITER Organization, St-Paul-Lez-Durance, France

Abstract

ITER is the first experimental fusion facility now under construction at Cadarache Site, France, which provides the key physics, materials and technological issues related to the development of fusion reactors. Although operational conditions and the design of ITER internal components may differ from the design for reactors producing electricity, the operation of ITER will provide a wide range of tests of materials and components under combined 14 MeV neutron, heat and particle fluxes within the available fluence.

During previous ITER phases, the specific ITER requirements have been identified and the main materials for various components have been selected based on a comprehensive assessment. The results from the ITER materials R&D programme have indicated the feasibility of the selected materials and joining technologies to provide the required operational lifetime and structural integrity.

The ITER plasma-facing components are those parts of the machine which directly face the thermonuclear plasma. They cover an area of about 850 m² and consist of the divertor, the blanket and the test blanket modules (TBMs) with their corresponding frames.

The divertor is located at the bottom of the plasma chamber and is aimed at exhausting the major part of the plasma thermal power (including alpha power) and at minimising the helium and impurity content in the plasma. CFC is the reference design solution for the armour of the lower part of the targets. This material promises to facilitate the development of techniques for ELM control and disruption mitigation taking advantage of the larger tolerance of the plasma to carbon because of absence of melting and lesser impact of C impurities on the plasma as compared with tungsten (W) armour. However, the resultant high erosion rate and co-deposition with T could potentially limit machine operation in the DT phase. Therefore, prior to the DT phase, the divertor plasma-facing components (PFCs) will be replaced with a new set entirely covered with W armour.

The blanket covers the largest fraction of the plasma-facing surface. Each of the 440 blanket modules consists of a first wall (FW) panel, which is mechanically attached to a shield block (SB). The design heat flux depends on the module location and is set up to 1 or 5 MW/m². The FW panels are covered by beryllium (Be) tiles, which are joined onto a copper alloy (CuCrZr) heat sink, which is in turn intimately joined onto a 316L (N) stainless steel part. The SB is a block of 316L (N)-IG steel with an array of cooling channels produced by machining and welding.

The TBMs are mock-ups of DEMO breeding blankets. There are three ITER equatorial ports devoted to TBM testing, each of them allocating two TBMs, inserted in a thick steel frame. The frame is a water-cooled 316L (N) steel port structure, similar to the one used in all other equatorial ports and based on the same materials and manufacturing process as those used for the blanket SB. At the back of the frame a water-cooled steel shield is located on which TBMs are mechanically attached.

This paper discusses the main directions of the project-oriented materials activity and main challenges related to selection of materials for the ITER internal components with supporting design activity.

Introduction

ITER will be the first experiment to bring together the physics, materials and key technologies of an operating fusion-power-generating reactor. During the earlier ITER design phases, a rigorous materials R&D programme in support of materials selection was carried out by the participating parties to address the unique operational conditions including 14 MeV neutron irradiation for internal (in-vessel) components, high heat and particle fluxes for plasma facing materials, etc.) and to provide the necessary materials properties databases for design justification.

The calculated level of radiation damage (in dpa) and He production (in appm) for DEMO-relevant materials for ITER conditions (maximum fluence of 0.5 MWa/m²) cannot fully meet the materials testing needed for DEMO at its maximum fluence limit. However, ITER can provide valuable understanding of fusion materials behaviour in a fusion neutron spectrum: dpa/gas production ratio, etc. Direct information about the effect of the fusion neutron spectrum on materials properties could be very important for the possible licensing of DEMO materials.

The main advantages of materials testing in ITER are:

- correct fusion spectrum;
- large volume (large samples and quantity);
- possibility to test materials under combined loads (synergetic effects);
- possibility for specific in-pile designed tests.

At the same time, the following ITER features have to be taken into account:

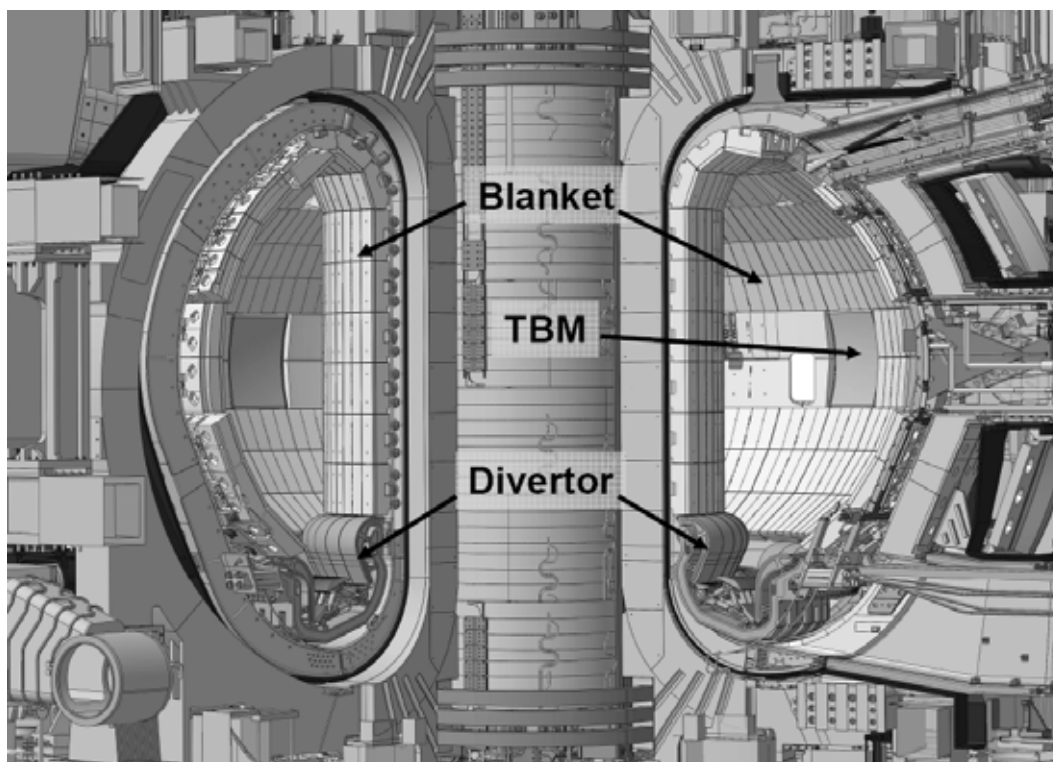
- pulsed operation;
- variable irradiation temperature.

In the immediate future, only ITER will provide high flux and fluence of 14 MeV neutrons. A worldwide programme to understand the fundamental features of radiation defects produced with fission and fusion neutrons is underway. Based on recent results on molecular dynamic simulations, it has been concluded that there are some similarities in defect production. However, the effect of He on the properties of materials is not yet well understood. Targeted experiments using IFMIF and fission reactors could be designed and ITER could provide some data for the correct fusion neutron spectrum. Another important feature of ITER is that it provides simultaneously the effects of different factors (neutrons, stress, heat flux, hydrogen atmosphere, etc). The understanding of these effects is important for ITER itself because the prediction of the materials performance has been based on conventional experimental techniques. In addition, by combining these factors, the materials performance could be significantly different. Similar synergetic effects could be expected for DEMO materials and must be tested in the IFMIF facility. To validate the ITER design, especially for the high fluence phase, the properties of the ITER materials under combined loads have to be known. A possible solution is to establish a Materials Testing Programme. This programme has to include a materials test matrix, the design of possible irradiation rigs (irradiation temperature, etc). Clearly, there is a continuing need for the co-ordination of the ITER test programme and tests of the ITER materials in other facilities.

The ITER internal components include the divertor, the blanket and the test blanket modules with their corresponding frames inside the vacuum vessel torus (Figure 1). The

materials for internal components are summarised elsewhere including the results of the previous R&D programme [1] [2]. The selection of materials was based on a general engineering approach, taking into account key factors including operational conditions, safety requirements, physical and mechanical properties, reliability, maintainability, corrosion performance and join-ability. For some materials, detailed reasons will be discussed later in the paper. The total thermal power, which is deposited onto the internal components, can reach a value of 850 MW and is removed by pressurised water.

Figure 1: ITER internal components



Divertor

Selection of plasma-facing armour materials for divertor

The divertor PFCs consist of a plasma-facing material, the armour, which is made of either carbon fibre reinforced carbon composite (CFC) or tungsten (W). The armour is joined onto an actively cooled substrate, the heat sink, made of precipitation hardened copper-based alloy CuCrZr.

Carbon based material, CFC, is the present reference design solution for the lower part of the vertical targets (VTs) due primarily to a long history of experience in present and past tokamaks.

Operation with a CFC target is considered to have advantages for the start of ITER operations given its proven range of compatibility with a number of plasma conditions in present devices, particularly at low densities with significant additional heating. CFC also promises to make easier the development of techniques for edge localised mode (ELM) control and disruption mitigation, taking advantage of the larger tolerance of the plasma

to C due to its lower atomic number versus W and its absence of melting. Finally, even if the onset for material damage for transient loads in CFC is similar to that of W, vapour shielding effects are more effective in protecting the CFC from further erosion at high power fluxes. On the other hand, W suffers from macroscopic cracking, melting and possible melt layer loss, thus making the potential damage to the plasma facing units (PFUs) more serious for W. These conditions of low densities with additional heating and high frequency of disruptions would constitute a significant fraction of ITER's initial operation.

The main disadvantage of CFC is co-deposition of eroded carbon atoms with tritium. Excessive co-deposition raises safety concerns as it relates to tritium inventory limits. While the exact magnitude of the fuel retention associated with CFC operation in ITER conditions remains uncertain, its foreseen magnitude in the DT phase may require frequent interventions to remove T with techniques that remain to be developed. It is these features of carbon that have triggered the decision to move to a full-tungsten divertor before the start of the nuclear phase of the ITER operation. CFC materials have great advantages due to their high thermal shock and thermal fatigue resistance and their high thermal conductivity in comparison with conventional graphite materials (in addition to the absence of melting). As important material parameters, optimum thermal conductivities and tensile strengths are required as well as mean density ($> 1.65 \text{ g/cm}^3$) and minimum impurity content (carbon $>99.99\%$).

The power handling parts of the upper region of the VTs and the Dome (DO) will be manufactured in W because of its high threshold for physical sputtering, low tritium retention, high melting temperature and good thermal conductivity.

As tungsten material, sintered and deformed tungsten grade (minimum required content and density are 99.94% and 19.0 g/cm^3 , respectively) has been selected for the divertor armour materials. The key issue is the proper design of the W armour (size of tiles, grain orientation). The selected grain orientation is parallel to the direction of the heat flow, in which case possible delamination is not so critical.

Selection of structural materials for divertor

The main structural material for the divertor components are the steel grade 316L (N)-IG (IG means ITER Grade) and XM-19. The 316L (N)-IG plates and forgings were selected due to good corrosion resistance, weldability, availability and sufficient strength. These properties are achieved as a result of an optimal combination of the main alloying elements such as carbon, nitrogen, nickel, chromium, manganese and molybdenum, low carbon content and controlled nitrogen with a tight specification of their allowable range. Furthermore, Co and Nb contents were restricted to minimise the activation of corrosion products and waste for the nuclear phase of the operation of ITER. For piping application, the tubes made of common industrial 316L grade were selected. Chromium-manganese-nickel austenitic stainless steel XM-19 (UNS No. S20910) was selected as a material for the attachment elements. This steel has almost twice higher yield strength values than 316L (N)-IG steel. It also has very good corrosion resistance to the coolant water and has been proposed for use at contact surfaces.

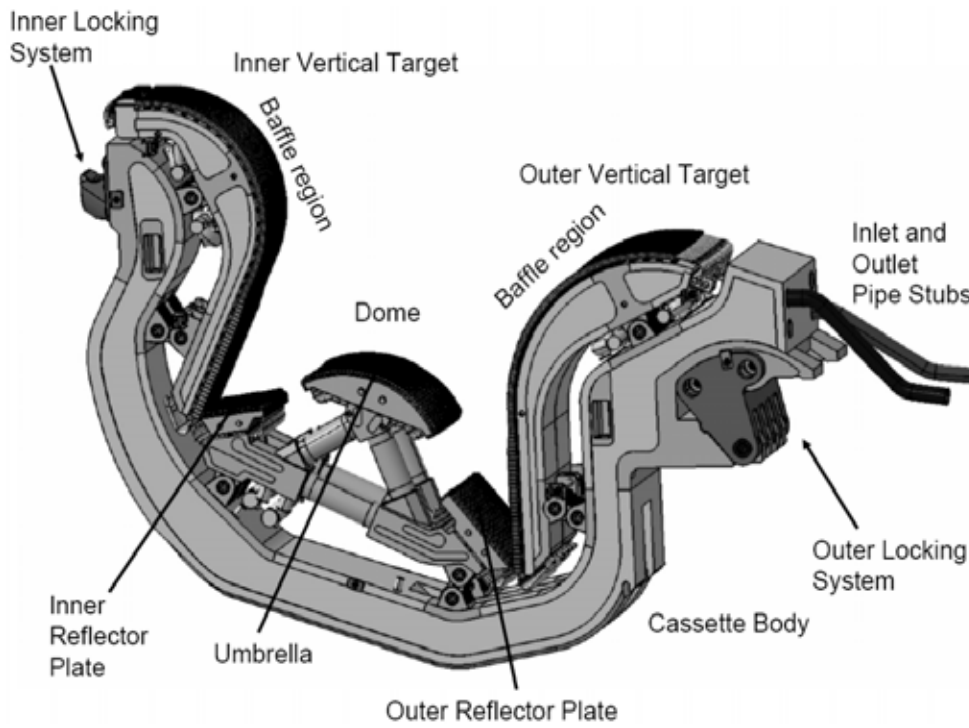
As heat sink and structural material, a precipitation hardened CuCrZr alloy (UNS number C18150) has been selected because of its high thermal conductivity and sufficient strength, good post-irradiation fracture toughness, weldability, availability and cost. Since CuCrZr is a precipitation hardened alloy, particular attention has to be paid to the heat cycles applied to the component during manufacture. Over-precipitation of the Cr will result in some loss of its mechanical properties that are obtained with an optimal heat treatment. Nevertheless, the remaining strength is sufficient to provide the required performance.

Divertor design description

The ITER divertor is installed in the bottom part of the vacuum chamber. Its main function is to exhaust the scrape-off layer (SOL) power, which arrives at the divertor target plates by plasma conduction and convection or by radiation (photons and neutral particles) from the divertor plasma volume. It must perform this function while maintaining acceptable core plasma impurity (both due to helium ash produced by fusion reactions and impurities released as a consequence of the plasma-surface interaction). As the main interface component between the plasma and material surfaces, the divertor must tolerate high heat loads while at the same time providing neutron shielding for the VV and magnet coils in its vicinity. Its design must provide an engineering solution compatible with today's plasma physics expectations but, given the uncertainties inherent in such predictions, should also allow for flexibility to ensure a means for rapid replacement and refurbishment [3] [4].

The ITER divertor consists of 54 cassette assemblies which are inserted radially through three lower level ports and moved toroidally before being locked into position. Each cassette assembly includes a cassette body (CB) that supports three separate components: the inner and outer VTs, and the DO (Figure 2).

- The inner and outer VTs constitute the highest heat flux components – their lower regions interact directly with the SOL plasma and the upper (curved) regions, or baffles, mostly with charge exchange (CX) neutral particles.
- The DO is located in the private flux region (the space below the separatrix which has no field line connection to the main plasma) and consists of:
 - The umbrella, located below the X-point, which protects the CB and is exposed mainly to radiation and CX neutrals. It plays the important role of baffling neutral particles in the sub-divertor region, preventing excessive backflow to the main plasma.
 - The inner and outer neutral particle reflector plates (PRPs) that stop the plasma strike points from falling down below the divertor in case of loss of control, or if confinement transitions result in a displacement of the strike points.
- The CB, which is reusable to minimise activated waste. It routes the coolant and provides both neutron shielding and a mechanical support for different possible arrangements of PFCs.
- Inner and outer locking systems are integrated into the CB to provide locking and alignment of the divertor cassettes against the VV through the hard cover plates on the inner and outer divertor rails.
- Inlet and outlet cooling pipe stubs, located in the outboard region of the CB, interface with the radial cooling pipes, which are connected to the three cassettes in each 20-degree VV sector. These are cut and orbitally re-welded from outside the pipe.

Figure 2: Divertor cassette assembly

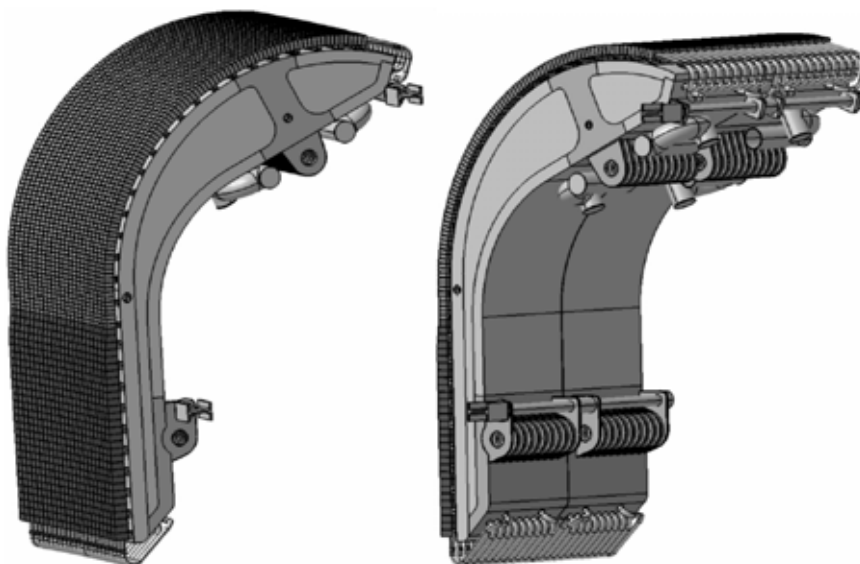
The coolant flow is supplied to and returned from each divertor cassette through two separate pipes. The inlet water temperature is 100°C with a pressure of 4.2 MPa. The total flow rate is 934 kg/s, with a coolant temperature increase of about 50°C, a maximum pressure drop of 1.6 MPa and a critical heat flux (CHF) margin of at least 1.4. The coolant circuit allows the bake-out of the divertor components at 240°C by pressurised hot water flow and at 350°C by hot He or nitrogen gas flow.

During normal operation, a steady state design heat flux is 5-10 MW/m² at the bottom segment of the VT. However, the capability to remove up to 20 MW/m² during transient events ("slow transient" phase) of 10 seconds must also be provided. The upper segment of the VT is designed to handle steady state heat fluxes of up to 5 MW/m² to allow for configuration flexibility (for example during operation with raised strike points but at lower input power) and the high plasma radiation densities in the X-point vicinity which can occur when full performance plasmas operate in partially detached conditions. The DO is designed for 5 MW/m² in steady state condition, in addition to the capability to remove 10 MW/m² for duration of up to 2 seconds.

Table 1: Summary of main divertor design parameters

Parameter	Value
Size	
- Toroidal extent of a cassette	6.67°
- Number of cassettes	54
Coolant type:	Water
Inlet temperature (C)	100
Inlet pressure at pipe stubs (MPa)	4.2
Max permissible pressure drop (MPa)	1.6
Max permissible total flow rate (kg/s)	1 000
Materials	
- Cassette body and supporting structures of PFCs	SS 316L(N)-IG and XM-19
- Heat sink of PFUs	CuCrZr-IG alloy
- Armour	CFC, pure sintered and deformed W
- Pipes	316L
- Pins of multilink attachments	C63200 Ni-Al bronze
- Inner and outer locking system: nose and knuckle	C63200 Ni-Al bronze
- Hard cover plates of divertor rails	Steel 660
- Shear pins of hard cover plates	C63200 Ni-Al bronze
Design load for target in strike point region	~ 10 MW/m ²
Design load of target in baffle region	~ 5 MW/m ²
Min critical heat flux margin	1.4
Thickness of carbon fibre composite (CFC) at end of life	> 4 mm
Plasma-facing surface area	~ 190 m ²

Each outer VT (Figure 3) has 22 PFUs (11 per component) and two steel supporting structures (one per component). At the inner target, each VT has 16 PFUs (8 per component) and two steel supporting structures (one per component). The PFU geometry is based on the so-called “monoblock” concept, consisting of armour tiles with a drilled hole. A cooling tube made of CuCrZr copper-based alloy (12/15 mm ID/OD) is inserted into these holes and is intimately joined to the tiles. Each PFU has a CFC monoblock segment in the lower part and a curved W monoblock segment in the upper part. The reference armour thicknesses at the start-of-life are 15 mm for CFC and 8 mm for W above the heat sink tube.

Figure 3: 3D views of outer vertical targets consisting of two similar components

The steel supporting structure of the VT is a box fabricated structure made of austenitic stainless steel 316L (N)-IG plates and austenitic steel XM-19 forged pieces.

The CB supports the PFCs and is designed to withstand the EM forces, provide neutron shielding of the VV and coils and incorporate internal coolant channels which cool the CB and act as manifolds for the PFC coolant. The design of all CBs is identical and independent of location in the tokamak, with the sole exception of the cassette accommodating the lower vertical neutron camera. The CB is a welded component made of forged austenitic stainless steel XM-19 and 316L (N)-IG plates. Each has dimensions of 3.3 m length, ~ 2.0 m high, 0.4 to 0.8 m wide and a mass of 5.15 tonnes (the mass of whole divertor cassette assembly, namely CB +PFCs, is 8.6 tons). The minimum radial thickness of the CB is 240 mm and includes a 40 mm steel front plate, a 60 mm steel back plate and 140 mm of water. The front and back plates are welded to side and internal plates (both with 40 mm thickness).

Manufacturing technologies

Manufacturing of PFUs is one of the most challenging operations. The PFUs of OVT are manufactured by one brazing and/or hot isostatic pressing (HIP) cycle for CFC and W monoblocks on CuCrZr tube after preparation of the joining surface and soft Cu interlayer. This process is followed by quenching and ageing in order to recover the mechanical strength of CuCrZr tube [5]. The PFUs of IVT are manufactured by HIPping or brazing process after the preparation of the joining surface and Cu interlayer [6] [7]. The PFUs of DO are manufactured by brazing W flat tiles to bimetallic (CuCrZr/316L (N)-IG) heat sink through a soft Cu interlayer. The bimetallic heat sink is considered to be manufactured by the explosion-bonding process. The CB and steel support-structures of PFCs have a box-type design to route coolant water to PFCs and from PFCs to PFUs. The CB and steel support-structure is considered to be manufactured by welding of a number of 316L (N)-IG plates and XM-19 forgings or milling out of large single pieces of XM-19 forging followed by the closing of the cavities by side plates. As regards the divertor cooling tubes, standard seamless steel 316L pipes are used.

Blanket

Selection of first wall panel material for blanket

The first wall (FW) panel is composed of an array of plasma-facing fingers (to reduce loads due to eddy currents) assembled into a stainless steel central support beam. The fingers can be manufactured and inspected separately and then assembled into the support beam via mechanical attachments or HIPping. The finger cooling circuits are then joined to the central beam circuit using a bore welding process.

Plasma-facing fingers are designed for either “enhanced” (up to 5 MW/m²) or “normal” (1-2 MW/m²) heat flux levels and with both variants employing the same interfaces and attachment features. Each finger comprises a series of beryllium (Be) armour tiles, a copper-based alloy (CuCrZr) water-cooled heat sink and stainless steel (SS) support structure. They are assembled on the central support beam with a toroidal orientation to equalise the thermal load distribution as much as possible.

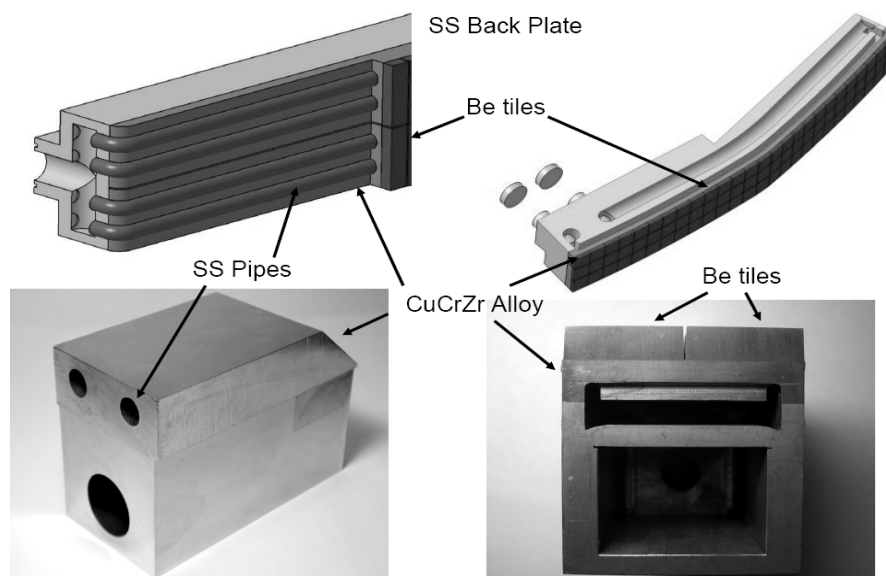
Be has been chosen for the plasma facing armour material for blanket to minimise fuel dilution caused by impurities released from these surfaces, which are expected to have the largest contamination efficiency and the consequences of Be contamination on fusion performance and plasma operations are relatively mild. This has been demonstrated by experiments in tokamaks UNITOR, ISX-B and JET.

The main issues related to the use of Be in ITER are: a) the possible damage (melting) during transients such as ELMs, disruptions and runaway electron impact and its implications for operations and b) the co-deposition of tritium with Be which is eroded from the FW and deposited at the divertor targets (and possibly also locally re-deposited into shadowed areas of the shaped ITER FW). Both issues are part of ongoing research, the initial results of which are being taken into account in the ITER design so that the influence of these two factors on ITER operation and mission are minimised. As mentioned in the previous section, carbon is selected for the high power flux area of the divertor strike points for its compatibility with operation over a large range of plasma conditions and the absence of melting under transient loads. Both of these characteristics are considered to be essential during the initial phase of ITER exploitation, in which plasma operational scenarios will require development and transient load control and mitigation systems will need to be demonstrated.

Two plasma-facing finger types are considered necessary for the heat flux levels for blanket FW panel [8]:

- SS tube for FW panels with normal heat flux level, in which the SS tubes are embedded into a copper-based alloy (CuCrZr);
- CuCrZr alloy rectangular or circular channels for FW panels with enhanced heat flux level.

The joining of Be armour tiles to the CuCrZr heat sink is a critical process that has been validated through a number of processing techniques including HIP and fast brazing. The FW panel central support beam is made of SS and provides the mechanical support for the fingers. A matrix of water cooling channels is drilled and plugged within the beam and connected to the fingers through $\phi 24$ (ID) mm pipes. The FW surface of each panel is defined by the toroidal shaping of the individual fingers assembled into the two lateral sides of the central support beam. The sides are separated by a 60 mm wide slot running poloidally in the center of the panel. The recess is protected from the open plasma flux tubes by the shadowing effect of the FW shaping. The panels are shaped so that the heat loads on the lateral sides of the panels are reduced down to acceptable levels.

Figure 4: Illustration of the basic FW panel structure and fingers

Left: normal heat flux fingers (concept with steel cooling pipes).

Right: enhanced heat flux fingers (concept with rectangular channels).

The selection of the optimum Be grade for ITER PFC applications is driven mainly by the requirements of ITER operation structural integrity and stability against various thermal loads and in particular, the absence or minimisation of macro-damage. It is believed that ion and thermal erosion at elevated temperatures of various Be grades is identical, however, performance at heat fluxes, especially under transient thermal loads such as disruptions, VDE, ELMs resulted in different behaviour and damage mechanisms. It is also considered that in general, the ease of joining beryllium to copper-alloys is not so sensitive to BeO content, impurities level and method of consolidation, which define the grade of beryllium material.

It should be noted that for tokamak applications beryllium is used in the form of tiles. Some surface cracking of the tiles could be acceptable, if there are no macro-damages and delaminations along the surface of tiles and loss of macroscopic parts.

The resistance to thermal fatigue is the most important factor that affects the grade selection because cracking could not only lead to enhanced armour erosion, delamination and loss of parts, but also potentially to crack propagation to the heat sink structure. Neutron irradiation resistance is another factor to be taken into account because it may affect the thermal performance and structural integrity. Due to some of the uncertainties on the ITER thermal loads, especially during transient events, preference is given to Be grade(s) with potentially higher resistance to transient thermal loads.

The selection of the reference grades was made based on the comprehensive assessment of the results of various tests carried out. Among the various studies, the following shall be mentioned:

Screening low cycle fatigue test of various beryllium grades was performed in the past. It was shown that the grades with the best thermal fatigue resistance are S-65C VHP, DShG-200, TShG-56 and TShGT.

Various Be grades also were tested in conditions simulating the disruption heat loads. The tests show that crack formation and behaviour after surface layer melting in different grades are quite different. For Be S-65C, all cracks stopped in the molten zone, whereas for some grades the cracks propagated to the bulk of the sample.

VDE simulation tests have been done. Severe melting of Be was observed for energy densities of 60 MJ/m^2 (~1 s pulse duration), however no cracks were observed between molten and un-molten material and in the bulk of un-molten parts for S-65C VHP grade.

On the basis of the available data, Be S-65C VHP (Brush Wellman, United States) was selected as reference based on excellent thermal fatigue and thermal shock behaviour and more in general for the good available data base on materials properties, including neutron irradiation effects. Recently, China and the Russian Federation, two of the seven international parties engaged in the construction of ITER, have proposed to use it for their contribution to the fabrication of the first-wall additional grades. In order to accept these newly proposed beryllium grades, a specific qualification programme is underway.

Selection of structural materials for blanket

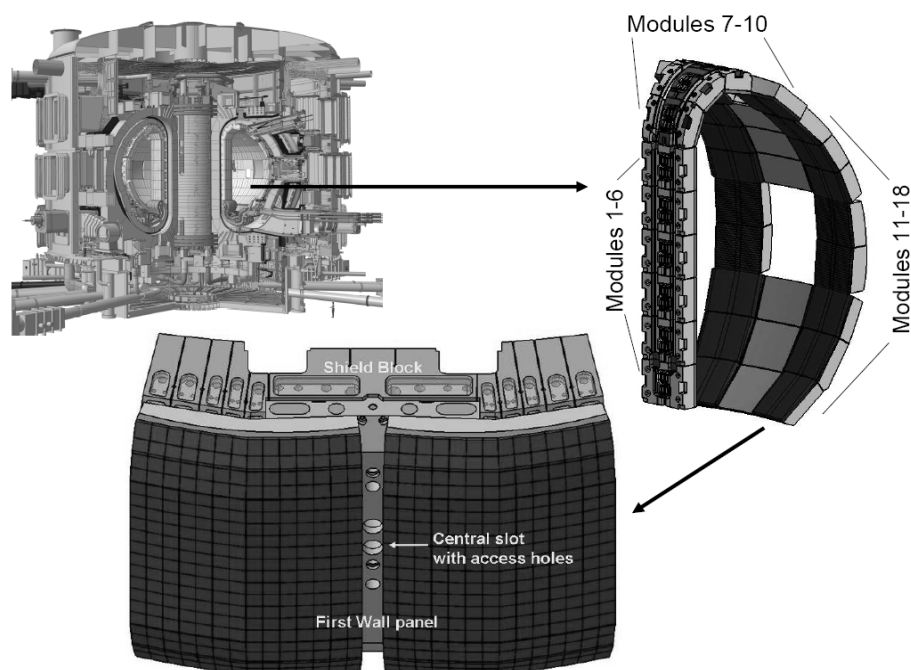
Austenitic stainless steel designated as 316L (N)-IG has also been selected as the main structural material for the ITER blanket system. Its advantages are the same as for the ITER divertor case.

Other materials should be included for SB supporting such as Ti-alloy and Inconel 718 for flexible cartridges due to their high strength, low Young's modulus and adequate toughness after irradiation, NiAl bronze for pads and collars due to its large thermal conductivity, higher strength, and high creep resistance up to 350°C , CuCrZr alloy for electrical straps due to its high thermal and electrical conductivity and high strength at the operating temperature and Al_2O_3 or MgAl_2O_4 ceramic coatings for the electrical insulation of the flexible cartridge, collar and key due to sufficient adhesion strength, high compression strength and satisfactory electrical resistance both with and without irradiation.

Blanket design description

The basic function of the blanket module (BM) system is to provide the main thermal and nuclear shielding of the vacuum vessel (VV) and ex-vessel components such as the poloidal field (PF) and toroidal field (TF) coils during plasma operations. The blanket system is also a plasma limiter and therefore its plasma-facing part is designed to withstand the plasma heat loads generated during the transition phases including plasma "start-up" and "shut-down".

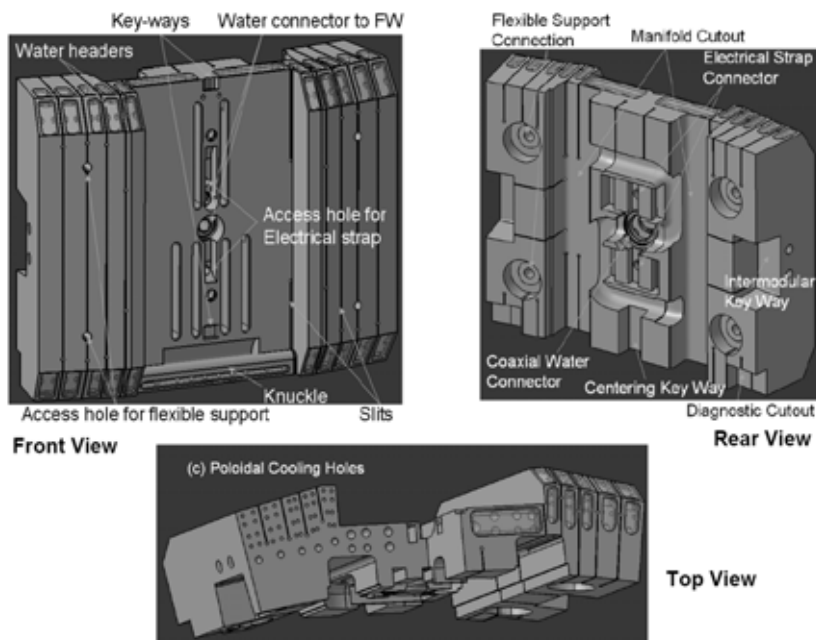
The blanket system comprises two different sub-systems that cover the ITER inner vessel wall: the wall-mounted and port-mounted BMs, covering $\sim 600 \text{ m}^2$ and $\sim 30 \text{ m}^2$, respectively. The wall-mounted BMs consist of two major components: a plasma-facing first wall (FW) panel and its supporting shield block (SB). The BMs are segmented into 18 poloidal locations: rows 1 to 6 constitute the inboard region, rows 7 to 10 the upper region and rows 11 to 18 the outboard region.

Figure 5: Blanket module: overall configuration**Table 2: Summary of main blanket design parameters**

Parameter	Value
Number of BMs	440
Typical module dimension	1.4m x 1.0m x 0.45m
Max allowable mass of one module	4.5 t
Total mass on BMs	1 530 t
Coolant type	Water
Inlet temperature (C)	100
Inlet pressure at chimney bulk head (MPa)	3.0
Minimum FW panel flow velocity (m/s)	1.5
Minimum SB flow velocity (m/s)	0.8
Materials	
- Heat sink of FW panels	CuCrZr-IG alloy
- Armour	Beryllium (S-65C or equivalent)
- Pipes and hydraulic connections	316L
- Shield block	316L(N)-IG
Design heat flux on FW panels	1-2 and 5 MW/m ² depending on location
Max neutron damage in Be / heat sink / steel pipe / SB	1.6 / 5.3 / 3.4 / 2.3 dpa

The main function of the SB is to provide nuclear shielding and supply the FW panel with cooling water. The steel / water / void ratios (86: 10: 4 and 85: 12: 3 for the inboard and outboard BMs, respectively) have been optimised with respect to neutron shielding. Each SB is electrically joined to the VV by electrical straps. They are formed and louvered from two sheets of CuCrZr alloy to achieve flexibility in all three directions.

Figure 6: Illustration of the SB structure



Test blanket modules

A key element of the worldwide fusion programme is the development of breeding blankets for commercial fusion power stations. The various programmatic goals of ITER include the “test of tritium breeding module concepts that would lead in a future reactor to tritium self-sufficiency, the extraction of high-grade heat and electricity production”. The test blanket modules (TBMs) are mock-ups of DEMO breeding blankets. They are installed in three ITER equatorial ports (Nos. 2, 16 and 18) devoted to TBM testing, each of them allocating two TBMs, inserted inside a steel frame. The TBMs and the related TBM programme will be described elsewhere [9]. Testing of breeding blanket modules must not interfere with ITER availability or decrease ITER reliability and safety. This means that supporting R&D and finalisation of the TBM design must be completed soon.

All materials used for TBMs must be qualified at least for the ITER operational conditions (neutron effect on properties of structural materials and breeding materials). All modules before installation in ITER must be qualified. Here, only a description of the TBM frame and dummy TBM will be given.

The TBM frame is a water-cooled 316L(N)-IG steel port structure, which is based on the same materials and manufacturing process as those used for the blanket SB. It has a radial length of 3 330 mm, a poloidal height of 2 160 mm and a toroidal width of 1 170 mm. It can accommodate up to two TBMs, having a plasma-facing surface of 500 (toroidal) x 1 690 (poloidal) mm². Since such surface is relatively small compared to the total FW area and recessed 120 mm, it is expected that the TBMs do not need a plasma-facing beryllium-

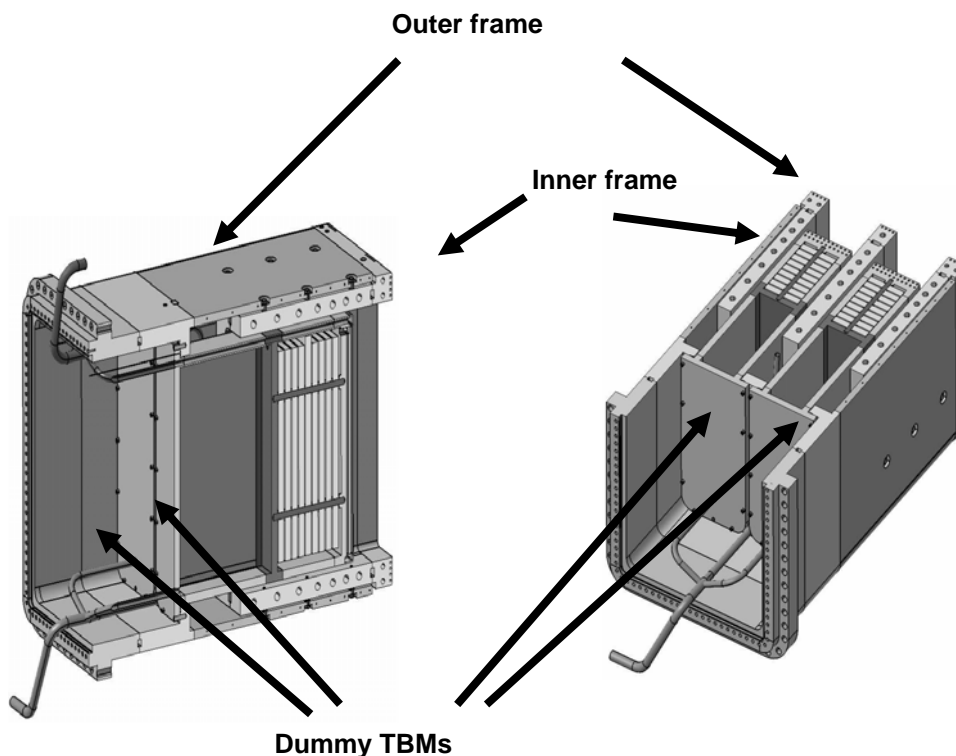
armour as required for the BM FW panels. Behind each TBM, there is a shield block that has a function to protect the cryostat/magnets region. Both components form the so-called TBM-Set.

The water-coolant circuit of the frame is connected in parallel with the water-coolant circuit of the shield blankets and with the shield part of each TBM-Set.

The TBM frame comprises two parts: a structural part, called the “outer frame” and a shield part, the “inner frame”. These are steel fabricated structures, where the cooling channels are obtained by drilling. The outer frame has a design similar to that of the ITER generic equatorial port plug frame and is obtained by welding 60 mm thick plates. It is welded to the equatorial port closure plate. The inner frame is bolted inside the outer frame and has a more massive structure with 155 mm wall thickness. It has the function to neutronically and thermally insulate the two TBMs between themselves and from the surrounding environment.

A TBM-Set can be replaced by a dummy TBM in the form of a steel box structure which, like the outer frame, is also obtained by welding 60 mm thick plates. The box contains an array of 60 mm thick plates, which, together with the water coolant, ensures the shielding function. Each dummy TBM can be mounted and dismounted from the frame via a set of M20 bolts located on the rear side. This operation is performed in the hot cell, once the whole TBM port plug is removed through the port. The dummy TBM and the TBM frame are cooled in parallel with the coolant connections located inside the equatorial ports (Figure 7).

Figure 7: Illustration of the TBM frame: poloidal (left) and toroidal (right) cut-out



Conclusions

ITER will be the most important experiment in support of the design of a following power reactor, providing the vital information about plasma performance and operational conditions for key reactor elements. ITER, when built, will provide a unique opportunity to test different reactor components and reactor materials for the next step fusion reactor. It is proposed that this programme should include tests on materials, test blanket modules, plasma surface interaction and safety. This programme has to be co-ordinated with other programmes such as IFMIF, materials tests in fission reactors, blanket developments, etc.

In this paper, the materials selected and supporting design for the set of internal components in the ITER tokamak were presented.

Acknowledgements

This report was prepared as an account of work by the ITER Organisation. The members of the organisation are China, the European Atomic Energy Community, India, Japan, the Republic of Korea, the Russian Federation, and the United States of America. The views and opinions expressed herein do not necessarily reflect those of the Members or any agency thereof. The dissemination of the information in this paper is governed by the applicable terms of the ITER Joint Implementation Agreement.

References

- [1] V. Barabash et al. (2007), *J Nucl Mater* 367–370. 21–32.
- [2] ITER Materials Properties Handbook, (internal project document distributed to the ITER Participants, IDM_D_29DDBF).
- [3] R. A. Pitts, A. Kukushkin, A. Loarte, A. Martin et al. (2009), “Status and physics basis of the ITER divertor”, *Physica Scripta*, in press.
- [4] A.S. Kukushkin, H.D. Pacher, V. Kotov, D. Reiter et al. (2007), “Effect of Dome on divertor performance in ITER”, *J. Nucl. Mater.* 363-365. 308-313.
- [5] S. Suzuki et al. (2009), *Phys Scr* T138. 014003.
- [6] T. Huber et al (2009), *Plansee Seminar-17 International Conference on High Performance P/M Materials*, Reutte Austria, 25-30 May 2009.
- [7] E. Visca et al. (2009), *Fusion Eng Des*, 84. 309-313.
- [8] R. Mitteau, P. Stangeby, C. Lowry, M. Merola et al. (2009), “Heat loads and shape design of the ITER first wall”, *Proceedings of ISFNT-9*, Dalian, China.
- [9] L. Giancarli, V. Chuyanov, M. Abdou, M. Akiba et al. (2007), “Test blanket modules in ITER : an overview on proposed design and required DEMO-relevant materials”, *J. Nucl. Mater.* 367-370. 1271-1280.

Annex 1: List of participants

OECD Nuclear Energy Agency International Workshop on Structure Materials for Innovative Nuclear Systems

Australia

EDWARDS, Lyndon
Head, Institute of Materials Engineering
Australian Nuclear Science & Technology
Organisation
PMB 1, Menai, Sydney
NSW 2234, AUSTRALIA

Tel: +61 0 297 173 652
Fax: +61 0 295 439 225
Eml: led@ansto.gov.au

Belgium

COEN, Gunter
Boeretang 200
B-2400 Mol
Belgium

Tel: +32 14 33 31 77
Fax:
Eml: gcoen@sckcen.be

Canada

HE, Zhang
Chalk River Laboratories
Chalk River, Ontario
K0J 1P0

Tel: +1 (613)-584-8811 + 44186
Fax: +1 (613) 584-8214
Eml: hez@aecl.ca

China

FU, Xiaogang
China Institute of Atomic Energy,
P.O.Box 275(92),
102413, Beijing, China

Tel:
Fax:
Eml: fuxiaogang@ciae.ac.cn

GUO, Xunzhong
College of Material Science and Technolog
Nanjing University of Aeronautics and Ast
29 Yudao Street,
Nanjing 210016,
P. R. China.

Tel:
Fax:
Eml: 3466008@qq.com

LONG, Bin
China Institute of Atomic Energy
P.O.Box 275 (92)
102413, Beijing
P.R.China

Tel: 86 0086 10 6935 7613
Fax: 86 0086 10 6935 7008
Eml: binlong@ciae.ac.cn

ZHANG, Jinqun
China Institute of Atomic Energy,
P.O.Box 275(92),
102413, Beijing, China

Tel:
Fax:
Eml: zunking@ciae.ac.cn

ZHOU, Zhangjian
Lab. of Special Ceramic and P/M,
School of Materials Science and Engineeri
University of Science and Technology Beij
Beijing 100083, China

Tel: +86 13366878092
Fax: +86 10 62334951
Eml: zhouzhj@mater.ustb.edu.cn

ZHU, Shengyun
P.O. Box 275-50, Beijing 102413

Tel: +86-10-69358003
Fax: +86-10-69357787
Eml: zhusy@ciae.ac.cn

Czech Republic

BRUMOVSKY, Milan
Nuclear Research Institute
Division of Integrity & Materials
25068, REZ

Tel: +420 724 030 765
Fax: +420 220 940 519
Eml: bru@ujv.cz

France

BALBAUD, Fanny
DEN/DPC/SCCME/LECNA
CEA Saclay
91991 Gif-Sur-Yvette

Tel: +33 1 69 08 16 51
Fax: +33 1 69 08 15 86
Eml: fanny.balbaud@cea.fr

DUBUISSON, Philippe
Departement des Materiaux
pour le Nucleaire
Direction de l'Energie Nucleaire
CEA - Saclay Bt 520 - PC 97

Tel: +33 1 69 08 22 78
Fax: +33 1 69 08 80 70
Eml: philippe.dubuisson@cea.fr

KIM, Chang Shuk
ITER Organization
Bat 524/004
Route de Vinon
CS 90 046
F-13067 Saint Paul lez Durance Cedex

Tel: +33 4 4217 6937
Fax: +33 + 33 4 4225 7261
Eml: changshuk.kim@iter.org

PAILLERE, Henri J.
TPNU, 4 avenue Andre Malraux
92309 Levallois Perret Cedex

Tel:
Fax:
Eml: henri.paillere@power.alstom.com

Germany

ALTSTADT, Eberhardt
Forschungszentrum Dresden-Rossendorf(FZD)
Institute of Safety Research
P.O.B. 51 01 19
D-01314 Dresden

Tel: +49 351 260 2276
Fax: +49 351 260 12276
Eml: e.altstadt@fzd.de

FAZIO, Concetta
KIT-Nuclear Safety Research Programme
Hermann von Helmholtz Platz 1
76344 Eggenstein-Leopoldshafen

Tel: +49 7247 82 5517
Fax: +49 7247 82 5508
Eml: concetta.fazio@kit.edu

HOFFMANN, Michael
 Materialprüfungsanstalt
 Universität Stuttgart

Tel: +49 711 685 62596
 Fax: +49 711 685 63053
 Eml: michael.hoffmann@mpa.uni-stuttgart.de

Abteilung Berechnung

LINDAU, Rainer
 Karlsruhe Institute of Technology KIT
 Institute for Materials Research I
 Hermann-von-Helmholtz-Platz 1
 D-76344 Eggenstein-Leopoldshafen

Tel: +49 7247 82 6402
 Fax: +49 7247 82 4567
 E-mail: rainer.lindau@kit.edu

Hungary

HORVATH, Akos
 Head, Materials Department
 Hungary Academy of Sciences
 KFKI Atomic Energy Research Institute
 Konkoly Thege ut 29-33
 1121 BUDAPEST

Tel: +36 1 392 2296
 Fax: +36 1 395 9162
 Eml: akos.horvath@aeki.kfki.hu

India

MATHEW, Mannarathu Devasia
 Mechanical Metallurgy Division
 Kalpakkam
 Tamil Nadu

Tel: +914427480075
 Fax: +914427480075
 Eml: mathew@igcar.gov.in

P.V., Durgaprasad
 #223, Hall-7, Reactor Safety Division
 Bhabha Atomic Research Centre
 Trombay, Mumbai
 INDIA-400085

Tel:
 Fax:
 Eml: pvd@barc.gov.in

Italy

AGOSTINI, Pietro
 ENEA
 C.R. ENEA Brasimone
 Bacino del Brasimone
 Camugnano 40032

Tel: +390534801170
 Fax: +390534801225
 Eml: pietro.agostini@enea.it

Japan

MUSTARI Andi, PRAMUTADI Asril
 Department of Nuclear Engineering
 Tokyo Institute of Technology, Japan

Tel:
 Fax:
 Eml: pramutadi.a.aa@m.titech.ac.jp

DOHNOMAE, Takako
 Japan Atomic Energy Agency

Tel:
 Fax:
 Eml: donomae.takako@jaea.go.jp

DOU, Peng
 Kyoto University
 Gokasho, uji shi
 kyoto fu

Tel:
 Fax:
 Eml: doupeng99@tsinghua.org.cn

IOKA, Ikuo
Tokai-mura
Ibaraki-ken, 319-1195
Japan

Tel: +81-29-282-6385
Fax: +81-29-282-6367
Eml: ioka.ikuo@jaea.go.jp

ISSELIN, Jerome
Kyoto University
Gokasho, uji shi
Kyoto fu
611-0011

Tel: +81-774-38-3482
Fax: +81-774-38-3479
Eml: jerome.isselin@iae.kyoto-u.ac.jp

IWATA, Noriyuki
Kyoto University
Gokasho, Uji
Kyoto 611-0011

Tel: +81-774-38-3478
Fax: +81-774-38-3479
Eml: noriyuki76@iae.kyoto-u.ac.jp

KIM, BYUNG JUN
Institute of Advanced Energy,
Kyoto University, Kyoto, Japan

Tel:
Fax:
Eml: byungjun_kim@iae.kyoto-u.ac.jp

KIM, Gwang-Ho
Japan Atomic Energy Agency,
Tokai, Naka, Ibaraki 319-1195,
Japan

Tel:
Fax:
Eml: metalkkh@gmail.com

KIMURA, Akihiko
Kyoto University
IAE
Kyoto University
Gokasho

Tel:
Fax:
Eml: kimura@iae.kyoto-u.ac.jp

KURATA, Yuji
Japan Atomic Energy Agency
Tokai-mura, Naka-gun
Ibaraki-ken, 319-1195

Tel: +8129 282 5059
Fax: +8129 282 6489
Eml: kurata.yuji@jaea.go.jp

LEE, Jae Hoon
Institute of Advanced Energy
Kyoto University
Uji, Kyoto
611-0011
Japan

Tel:
Fax:
Eml: jhlee.ods@gmail.com

NOH, Sanghoon
Kyoto University
Gokasho, Uji
Kyoto

Tel:
Fax:
Eml: sh-noh@iae.kyoto-u.ac.jp

OBARA, Satoshi
JAEA
Oarai-machi
Higashiibaraki-gun
Ibaraki-ken

Tel:
Fax:
Eml: obara.satoshi@jaea.go.jp

OHNUKI, Somei
Hokkaido University
Materials Science
Graduate School of Engineering
Japan

Tel:
Fax:
E-mail: ohnuki@eng.hokudai.ac.jp

SHIBATA, Taiju
4002 Oarai-machi
Ibaraki-ken
311-1393

Tel: +81 29 266 7705
Fax: +81 29 266 7710
Eml: shibata.taiju@jaea.go.jp

SHIKAMA, Tatsuo
Institute for Materials Research,
Tohoku University
Katahira, Sendai, 980-8577

Tel: +81 29-267-4205(-3181)(Oarai);
Fax: +81 29 267-4947; 022 215 2061
Eml: shikama@imr.tohoku.ac.jp

TAKAHASHI, Minoru
Research Laboratory for Nuclear Reactors
Tokyo Institute of Technology
2-12-1-N1-18, O-Okayama, Meguro-ku, Tokyo

Tel: +81 3-5734-2957
Fax: +81 3-5734-2959
Eml: mtakahas@nr.titech.ac.jp

UKAI, Shigeharu
N13, W8, Kita-ku
Sapporo 060-8628

Tel: +81-11-706-6355
Fax: +81-11-706-6355
Eml: s-ukai@eng.hokudai.ac.jp

Kazakhstan

KISLITSIN, Sergey
Institute of Nuclear Physics
National Nuclear Center of Kazakhstan,
Almaty, Kazakhstan

Tel: +7 727 386 52 62
Fax: +7 727 386 52 61
Eml: skislitsin@inp.kz

Republic of Korea

BAEK, Jong Hyuk
KAERI
Daekeokdaero 1045 Yuseong
305-353 Daejeon

Tel: +82 42 868 8623
Fax:
Eml: jhbaek@kaeri.re.kr

CHANG, Jonghwa
Chief Research Advisor, KAE Research Inst
P.O. Box 105, Yuseong
Daejeon, 305-600

Tel: +82 42 868 2884
Fax: +82 42 868 4717
Eml: jhchang@kaeri.re.kr

CHO, SEUNGYON
ITER Korea,
National Fusion Research Institute, Gwaha
Daejeon, 305-333, Republic of Korea

Tel:
Fax:
Eml: sycho@nfri.re.kr

HONG, Jun-Hwa
Vice President
Nuclear Safety Research
Korea Atomic Energy Research Institute
1045 Daedeok-daero, Yuseong-gu,
Daejeon, 305-353, Republic of Korea

Tel: +82 42 868 2386
Fax: +82 42 868 8583
Eml: jhhong@kaeri.re.kr

HWANG, Ilsoon Nuclear Engineering Dept. Seoul National University Rm32-211 56-1, Shinlim-Dong, Gwanak-Ku SEOUL, 151-742	Tel: +82 2 880 7200 Fax: Eml: hisliune@snu.ac.kr
JANG, Changheui KAIST 373-1 Guseong-dong Yuseong-gu Daejeon	Tel: +82 42 3503824 Fax: +82 42 3503810 Eml: chjang@kaist.ac.kr
JANG, Jinsung 1045 Daedeok-daero Yuseong-gu Daejeon	Tel: +82-42-868-2376 Fax: +82-42-868-8549 Eml: jjang@kaeri.re.kr
KIM, Daejong KAIST 373-1 Guseong-dong Yuseong-gu Daejeon	Tel: Fax: Eml:
KIM, Dong-Jin 1045 Daedeokdae-ro Yuseong-gu, Daejeon	Tel: +82-42-868-8387 Fax: +82-42-868-8686 Eml: djink@kaeri.re.kr
KIM, Eung-Seon Daeduk-daero 1045 Yuseong-gu Daejeon	Tel: Fax: Eml: kimes@kaeri.re.kr
KIM, Dae Whan Korea Atomic Energy Research Institute Daeduk-daero 1045 Yuseong-gu, Daejeon	Tel: +82-042-868-2046 Fax: +82-042-868-8549 Eml: dwkim1@kaeri.re.kr
KIM, Ji Hyun Ulsan National Institute of Science and Technology	Tel: Fax: Eml: kimjh@unist.ac.kr
KIM, Min-Chul Korea Atomic Energy Research Institute Daeduk-daero 1045 Yuseong-gu, Daejeon	Tel: ++82-42-868-2761 Fax: Eml: mckim@kaeri.re.kr
KIM, Sung Ho Korea Atomic Energy Research Institute Daeduk-daero 1045 Yuseong-gu, Daejeon	Tel: +82-42-868-2266 Fax: +82-42-868-8549 Eml: shkim7@kaeri.re.kr
KIM, Whung-Whoe Korea Atomic Energy Research Institute Daeduk-daero 1045 Yuseong-gu, Daejeon	Tel: Fax: Eml: wwkim@kaeri.re.kr

KIM, Young Do Division of Materials Science and Engineering, Hanyang University, Republic of Korea	Tel: Fax: Eml: ydkim1@hanyang.ac.kr
KIM, Young Suk Korea Atomic Energy Research Institute Daeduk-daero 1045 Yuseong-gu, Daejeon	Tel: +82-42-868-2359 Fax: +82-42-868-8549 Eml: yskim1@kaeri.re.kr
KWON, Junhyun Korea Atomic Energy Research Institute 1045 Daedeok-daero, Yuseong-gu, Daejeon 305-353	Tel: +82 42 868 8588 Fax: +82 42 868 8549 Eml: jhkwon@kaeri.re.kr
LEE, Gyeong-Geun Korea Atomic Energy Research Institute Daeduk-daero 1045 Yuseong-gu, Daejeon	Tel: Fax: Eml: gglee@kaeri.re.kr
LEE, Sea-Hoon Korea Institute of Materials Science 66 Sangnam-dong, Changwon, Kyungsangnam-do, 641-010 Republic of Korea	Tel: Fax: Eml: seahoon1@kims.re.kr
NAM, Hyo On Seoul National University, Bldg 31-1, SNU Shinlim-Dong, Gwanak-Gu, SEOUL 151-744	Tel: Fax: Eml: hyon99@snu.ac.kr
NOVIYANTO, Alfian School of Materials Science and Engineering Yeungnam University 214-1 Dae-dong Gyeongsan, Gyeongbuk, 712-749	Tel: +82-53-810-3970 Fax: Eml: alfian@ynu.ac.kr
PARK, Ji Yeon Nuclear Materials Research Division Korea Atomic Energy Research Institute Daedeok Daero 1045, Deokjin-dong, Yuseong-gu, Daejeon 305-353, Republic of Korea	Tel: +82 42 868 2311 Fax: +82 42 868 5496 Eml: jypark@kaeri.re.kr
SHIN, Chansun Korea Atomic Energy Research Institute Daeduk-daero 1045 Yuseong-gu, Daejeon	Tel: Fax: Eml: cshin@kaeri.re.kr

YOON, Dang-Hyok
School of Materials Science and
Engineering
Yeungnam University
214-1 Dae-dong
Gyeongsan, Gyeongbuk, 712-749

Tel: +82-53-810-2561
Fax: +82-53-810-4628
Eml: dhyoon@ynu.ac.kr

YOON, JI-HYUN
Korea Atomic Energy Research Institute
Daeduk-daero 1045
Yuseong-gu, Daejeon
Eml: zhusy@ciae.ac.cn

Tel:
Fax:
Eml: jhyoon4@kaeri.re.kr

Russian Federation

IGNATIEV, Victor V.
Head of Laboratory, Inst. of Nuclear Reac
RRC - Kurchatov Institute
Kurchatov sq. 1, 123182 Moscow

Tel: +7 499 196 71 30
Fax: +7 499 196 86 79
Eml: ignatiev@vver.kiae.ru

NIKITINA, Anastasia
Joint Stock Company
High-technological Institute
(JSC VNIINM), Moscow

Tel:
Fax:
Eml: ageev-val@yandex.ru

Sweden

WALLENIUS, Janne
Associate Professor & Head of Division
Reactor Physics
Royal Institute of Technology (KTH)
AlbaNova University Centre
S-106 91 Stockholm

Tel: +46-8-5537 8200
Fax: +46-8-5537 8216
Eml: janne@neutron.kth.se

Switzerland

DAI, Yong
ODGA/114
Paul Scherrer Institute (PSI)
CH-5232 Villigen PSI

Tel: +41 56 310 4171
Fax: +41 56 310 4529
Eml: yong.dai@psi.ch

United Kingdom

ACKLAND, Graeme
University of Edinburgh
Kings Buildings
Edinburgh EH93JZ

Tel: +44 13 16 50 52 99
Fax:
Eml: g.j.Ackland@ed.ac.uk

BUCKTHORPE, Derek Edward
AMECNNC Limited
Booths Park
Chelford Road
Knutsford

Tel:
Fax:
Eml: derek.buckthorpe@amec.com

United States of America

ALLEN, Todd
University of Wisconsin
1500 Engineering Drive
Madison, WI 53706

Tel: +1 608 265 4083
Fax: +1 608 263 7451
Eml: allen@engr.wisc.edu

NANSTAD, Randy
 P.O. Box 2008
 MS 6138
 Oak Ridge
 Tennessee, 37831
 Tel: +1-865-574-4471
 Fax: +1-865-242-3650
 Eml: nanstadrk@ornl.gov

PASAMEHMETOGLU, Kemal O.
 Division Dir., Nuclear Fuels and Material
 Idaho National Lab., P.O. Box 1625, MS 38
 Idaho Falls, ID 83415
 Los Alamos National Laboratory,
 PO. Box 1663, MS-B296
 Los Alamos, NM, 87545
 Tel: +1 208 526 5305
 Fax: +1 208 526 2930
 Eml: kemal.pasamehmetoglu@inl.gov
 STAN, Marius Tel: +1 505 667 8726
 Fax: +1 505 667 5921
 E-mail: mstan@anl.gov

TOLOCZKO, Mychailo
 Pacific Northwest National Laboratory
 MS P8-15, PO Box 999
 Richland, WA 99354, US.
 Tel: +1 509 376 0156
 Fax: +1 509 376 0418
 Eml: mychailo.toloczko@pnl.gov

YANG, Yong
 1500 Engineering Dr.
 Madison, WI 53706
 Tel:
 Fax:
 Eml: yyang@cae.wisc.edu

YANG, Youngki
 1500 Engineering drive
 Madison, WI 53706
 Tel:
 Fax:
 Eml: ykyang@wisc.edu

International organisations

INOZEMTSEV, Victor
 Nuclear Fuel Cycle and Materials Section
 IAEA
 P.O.Box 100
 A-1400 WIEN
 Tel: +43 1 2600 22760
 Fax: +43 1 26007
 Eml: v.inozemtsev@iaea.org

CHOI, Yong-Joon
 OECD Nuclear Energy Agency
 12 Boul. des Iles
 92130 Issy-les-Moulineaux
 Tel: +33 145241091
 Fax: +33 145241128
 Eml: yongjoon.choi@oecd.org

ZEMAN, Andrej
 Vienna International Centre, PO Box 100,
 1400 Vienna Austria
 Tel: +431 2600 21705
 Fax: +431 2600 7
 Eml: a.zeman@iaea.org

NEA PUBLICATIONS AND INFORMATION

The full **catalogue of publications** is available online at www.oecd-nea.org/pub.

In addition to basic information on the Agency and its work programme, the **NEA website** offers free downloads of hundreds of technical and policy-oriented reports.

An **NEA monthly electronic bulletin** is distributed free of charge to subscribers, providing updates of new results, events and publications. Sign up at www.oecd-nea.org/bulletin/.

You can also visit us on **Facebook** at www.facebook.com/OECDNuclearEnergyAgency or follow us on **Twitter** @OECD_NEA.



Structural Materials for Innovative Nuclear Systems (SMINS-2)

Materials research is a field of growing relevance for innovative nuclear systems, such as Generation IV reactors, critical and sub-critical transmutation systems and fusion devices. For these different systems, structural materials are selected or developed taking into account the specificities of their foreseen operational environment. Since 2007, the OECD Nuclear Energy Agency (NEA) has begun organising a series of workshops on Structural Materials for Innovative Nuclear Systems (SMINS) in order to provide a forum to exchange information on current materials research programmes for different innovative nuclear systems. These proceedings include the papers of the second workshop (SMINS-2) which was held in Daejeon, Republic of Korea on 31 August-3 September 2010, and hosted by the Korea Atomic Energy Research Institute (KAERI).

OECD Nuclear Energy Agency
12, boulevard des îles
92130 Issy-les-Moulineaux, France
Tel.: +33 (0)1 45 24 10 15
nea@oecd-nea.org www.oecd-nea.org

ISBN 978-92-64-99209-2



9 789264 992092